NASA/OHIO SPACE GRANT CONSORTIUM

2024-2025 ANNUAL STUDENT RESEARCH SYMPOSIUM PROCEEDINGS XXXIII



A Massive Cluster is Born (N79) This image from the Webb telescope shows N79, a massive star-forming region within the Large Magellanic Cloud (a satellite galaxy of the Milky Way).**Photo Courtesy of NASA's James Webb Telecope**

April 4, 2025
Held at the Ohio Aerospace Institute
Cleveland, Ohio

Follow OSGC on:

Just click on any name, and it will link you to the page immediately!

TABLE OF CONTENTS

	Page(s)
Table of Contents	2-6
Foreword	7
Member Institutions	8
Acknowledgements	9-10

Fellows	*University*	*Page*
Baird, Nicholas	Kent State University	12
Barnhouse, Alex	The Ohio State University	16
Clawson, Jonthan	The University of Akron	22
Curtician, Grace	The University of Akron	28
Dillon, Davin	Ohio University	33
Falkosky, Erin	The University of Akron	35
Frankowski, Andew	The University of Akron	37
Greene, Sophia	Cleveland State University	42
Hyland, Emily	Cleveland State University	47
Jacques, Henry	University of Dayton	52
Langin, Joshua	Cleveland State University	59
Megazzini, Mathew	The Ohio State University	63
Miller, Dane	The Ohio State University	68
Morton, Caleb	The Ohio State University	74
Murray, Justin	Ohio University	79
Nguyen-Huynh, Tammy	The Ohio State University	84
Reindl, Joseph	Miami University	91
Seggi, Lukas	The University of Akron	98
Sharkey, Andrew	Kent State University	104
Sluder, Isaac	The University of Akron	111
Steffen, Nathan	University of Cincinnati	116
Verderico, Carter	Kent State University	123
Wilson, Austin	Case Western Reserve University	130
Yarlagadda, Abhilash	The Ohio State University	137

Scholars	College/University	Page
Abrams, Margo	Wilberforce University	145
Amoroso, Chloe	Cleveland State University	147
Ballentine, Rachael	Wright State University	154
Borovich, Michael	Cleveland State University	158
Boyer, Abigail	University of Dayton	165
Brockway, Megan	Miami University	167
Brucchieri, Alyssa	The Ohio State University	171
Carlson, Caleb	Ohio Northern University	174
Chaffey, Andreas	Case Western Reserve University	177
Chambers, Lisa	Cleveland State University	182
Core, Emma	The University of Toledo	184
Culp, Kamryn	The University of Akron	186
Damiano, Dylan	Central State University	193
Daubon, Jeremiah & Thomas, Stephon	Central State University	195
DeHaven, Lincoln	Wright State University	197
Doughman, Nicholas	Bowling Green State University	202
Douglas, Katherine	Bowling Green State University	205
Drexler, Robert	University of Dayton	207
Dulani, Rahul	Case Western Reserve University	209
Dunlap, Julie	Baldwin Wallace University	211
Escobar, Mario	Baldwin Wallace University	213
Faison, Love	Wilberforce University	216
Fokine, Coline	Wright State University	219
Foster, Michael	University of Dayton	222
Frank, Kavanugh	Ohio University	229
Frith, Kyle	The Ohio State University	231
Gaetano, Gianni	University of Cincinnati	235
Gillum, JD	Wright State University	239
Gilman, Emily	Baldwin Wallace University	244
Hackett, Liam	Wright State University	246
Hagan, Anna	Wright State University	248
Hall, Abigail	Cedarville University	250

Scholars	College/University	Page
Hamid, Zain	The Ohio State University	256
Hammontree, Adrienne	Marietta College	262
Hefler, Joseph	Kent State University	264
Hensley, Elyse	Ohio University	267
Hopfensperger, Claire	Miami University	270
Imran, Sania	Cleveland State University	276
Jackson, Jeremy	Central State University	278
Johnston, Kevin	University of Dayton	280
Keichel, Kaleb	Ohio University	288
Kennedy, Brooke	Cleveland State University	294
Kerg, George	Youngstown State University	299
Khatri, Nabeel	The University of Toledo	305
Kitchen, Henry	The Ohio State University	308
Lawal, Suraju	Central State University	310
Lewan, Nathan	Wright State University	314
Lynn, Nathan	Wright State University	319
Lyons, James	The University of Akron	321
Lyons, Joseph	Cleveland State University	327
Madden, LyDel	Wilberforce University	330
Mahoney, Daniel	University of Toledo	334
Manu, Arnav	Case Western Reserve University	340
Melnikov, Dimitry	The University of Akron	342
Miller, Ethan	Marietta College	349
Miller, Sydney	Baldwin Wallace University	351
Mitchell, Mason	The Ohio State University	354
Mitchell, Seth	Cedarville University	361
Montunnas, Lincoln	The Ohio State University	368
Moore, Madisyn	Cleveland State University	372
Ng, Elias	Cedarville University	374
Nomina, Jack	Miami University	376
Pabon, Julian	University of Dayton	378
Patel, Jinit	The Ohio State University	385

Scholars	College/University	Page
Paul, Kira	Kent State University	387
Phelps, Brady	Ohio University	389
Phillips, Maxwell	Ohio Northern University	395
Posey, Alex	Marietta College	400
Quear, Anthony	The University of Akron	402
Radey, John	Ohio Northern University	404
Ressler, Caely	Baldwin Wallace University	410
Richards, Collin	Youngstown State University	414
Rodriguez, Aliah	Cleveland State University	416
Scheideger, Caleb	Ohio Northern University	418
Shartle, Abigail	Marietta College	424
Shenal, Andrew	Kent State University	426
Shultz, Mason	Miami University	428
Stallone, Mark	Kent State University	434
Stammen, Lucas	The University of Toledo	440
Stoller, Adin	University of Dayton	442
Stoltz, Bryce	Kent State University	444
Tack, Auna	Wright State University	449
Tan, Michael	Ohio University	451
Toth, Zachary	Ohio Northern University	455
Tyler, Sri	Central State University	462
Upadhyay, Jayanti	Baldwin Wallace University	466
Vanderhorst, Cael	Ohio Northern University	468
Verhosek, Justin	Baldwin Wallace University	475
Webber, Cory	Miami University	479
Whipkey, Isaac	Ohio University	486
Wible, Leo	Kent State University	488
Wilson, Brady	The Ohio State University	491
Wood, Johanna	Cedarville University	498
Wynter Mitchell, Isabella	Central State University	501
Zayac, Jennifer	Ohio Northern University	503
Zhang, Lisa	Miami University	508

Community College Scholars	***Community College***	***Page***
Bogna, Olivia	Lorain County Community College	512
Fullilove, Tyler	Cincinnati State Technical and Community College	514
Manley, Noah	Cincinnati State Technical and Community College	516
Mateo, Jocelyn	Lorain County Community College	518
Mathis, Amari	Cincinnati State Technical and Community College	520
Roberts, Noah	Cincinnati State Technical and Community College	522
Zbornik, Stephen	Lorain County Community College	524

Education Scholars	***College/University***	***Page***
Briley, Morgan	Baldwin Wallace University	526
Burket, Kristina	Baldwin Wallace University	528
Denman, Elizabeth	Kent State University	530
Gill, Cora	University of Cincinnati	532
Grasse, Taylor	Kent State University	533
Hart, Alyssa	Cedarville University	535
Levans, Jenna	Marietta College	537
Penno, Rachel	Ohio Northern University	539
Somers, Alice	University of Cincinnati	541
Taylor, Joslyn	Ohio Northern University	543

FOREWORD

The Ohio Space Grant Consortium (OSGC), a member of the NASA National Space Grant College and Fellowship Program, awards graduate fellowships and undergraduate scholarships to students working toward degrees in Science, Technology, Engineering and Mathematics (STEM) disciplines at OSGC-member universities. The awards are made to United States citizens, and the students are competitively selected. Since the inception of the program in 1989, 1,737 undergraduate scholarships and 324 graduate fellowships have been awarded.

By helping more students to graduate with STEM-related degrees, OSGC provides more qualified technical employees to industry. The research conducted for the Master's fellowship must be of interest to NASA. A prime aspect of the scholarship program is the undergraduate research project that the student performs under the mentorship of a faculty member. This research experience is effective in encouraging U. S. undergraduate students to attend graduate school in STEM. The Education scholarship recipients are required to attend a workshop conducted by NASA personnel where they are exposed to NASA educational materials and create a lesson plan for use in their future classrooms.

Matching funds are provided by the 26 member universities/community colleges, the Ohio Aerospace Institute (OAI), and the Ohio Department of Higher Education (State of Ohio).

Affiliate Members

- The University of Akron
- Baldwin Wallace University
- Bowling Green State University
- Case Western Reserve University
- Cedarville University
- Central State University
- Cleveland State University
- University of Cincinnati
- University of Dayton
- Kent State University
- Marietta College
- Miami University
- University of Mount Union
- Ohio Northern University
- The Ohio State University
- Ohio University
- University of Toledo
- Wilberforce University
- Wright State University
- Youngstown State University

Community Colleges

- Cincinnati State Technical and Community College
- Columbus State Community College
- Cuyahoga Community College
- Lakeland Community College
- Lorain County Community College
- Sinclair Community College

MEMBER INSTITUTIONS

Affiliate Members	***Campus Representative***
• Baldwin Wallace University	James W. McCargar, Ph.D.
• Bowling Green State University	Andrew Layden, Ph.D.
• Case Western Reserve University	Christian A. Zorman, Ph.D.
• Cedarville University	Robert Chasnov, Ph.D., P.E.
• Central State University	Augustus Morris, Jr., Ph.D., P.E.
• Cleveland State University	Liqun Ning, Ph.D.
• Kent State University	Joseph D. Ortiz, Ph.D.
• Marietta College	Andrew Beck, Ph.D.
• Miami University	Jeong-Hoi Koo, Ph.D.
• University of Mount Union	Chad Korach, Ph.D.
• Ohio Northern University	David Sawyers, Ph.D., P.E.
• The Ohio State University	Mo Samimy, Ph.D.
• Ohio University	Roxanne Male'-Brune, Ph.D.
• The University of Akron	Julie Zhao, Ph.D.
• University of Cincinnati	Kelly Cohen, Ph.D.
• University of Dayton	Rydge Mulford, Ph.D.
• The University of Toledo	Lesley M. Berhan, Ph.D.
• Wilberforce University	Deok Hee Nam, Ph.D.
• Wright State University	Mitch Wolff, Ph.D.
• Youngstown State University	Byung-Wook Park, Ph.D.

Community Colleges	***Campus Representative***
• Cincinnati State Technical and Community College	Professor Abigail Yee
• Columbus State Community College	Professor Erik Aagard
• Cuyahoga Community College	Professor Michelle S. Davis
• Lakeland Community College	Professor Rick Bartlett
• Lorain County Community College	Regan L. Silvestri, Ph.D.
• Sinclair Community College	Professor Jay Jayanth

NASA Glenn Research Center - Representatives

- Dr. Gerald Volts
- Mr. Robert F LaSalvia

ACKNOWLEDGMENTS

Thank you to all who helped with the OSGC's 33rd Annual Research Symposium!

Keynote Speaker: Butch Reynolds - Olympian, Gold Medalist, World Record Holder

Campus Representatives – 4-Year Universities

- Dr. James W. McCargar, Baldwin Wallace University
- Andrew Layden, Ph.D., Bowling Green State University
- Dr. Chris Zorman, Case Western Reserve University
- Robert Chasnov, Ph.D., P.E., Cedarville University
- Augustus Morris, Jr., Ph.D., P.E., Central State University
- Liqun Ning, Ph.D., Cleveland State University
- Dr. Joseph D. Ortiz, Kent State University
- Dr. Andrew Beck, Marietta College
- Jeong-Hoi Koo, Ph.D., Miami University
- Chad Korach, Ph.D., University of Mount Union
- David Sawyers, Ph.D., Ohio Northern University
- Dr. Mo Samimy, The Ohio State University
- Dr. Roxanne Male'-Brune, Ohio University
- Dr. Julie Zhao, The University of Akron
- Dr. Kelly Cohen, University of Cincinnati
- Dr. Rydge Mulford, University of Dayton
- Dr. Lesley M. Berhan, The University of Toledo
- Deok Hee Nam, Ph.D., Wilberforce University
- Mitch Wolff, Ph.D., Wright State University
- Dr. Byung-Wook Park, Youngstown State University

Campus Representatives - Community Colleges

- Professor Abigail Yee, Cincinnati State Technical and Community College
- Professor Erik Aagard, M., Columbus State Community College
- Professor Michelle S. Davis, Cuyahoga Community College
- Professor Rick Bartlett, Lakeland Community College
- Regan L. Silvestri, Ph.D., Lorain County Community College
- Professor Jay Jayanth, Sinclair Community College

Special thanks go out to the following:

- Dennis Andersh, President and CEO – Parallax Advanced Research & Ohio Aerospace Institute, for supporting the OSGC and embracing our position within Parallax.
- Timothy McCartney, Executive VP Cleveland Operations and Advanced Air and Space Systems – Parallax Advanced Research & Ohio Aerospace Institute, for supporting the OSGC and hosting this event.
- Robert Romero, Director – OSGC, for his enthusiasm, vigor, and inspired leadership. Robert's passion for education and citizenship has pushed the program in a bold new direction.
- Mark Cline, Senior Manager, Information Technology – OAI, whose expertise ensured the hardware and software operated seamlessly.
- Sam Santos, Program Assistant – OSGC, who is on the spot to assist team and students alike throughout the school year and the day of the event.
- Olivia Bogna, Outreach – OSGC, for contributing her experience as a scholar to smooth out details and create a student-centered event.
- Anthony Bogna, Social Media Marketing – OSGC, for getting the word out to every possible person through social media and seeing to the needs of every student throughout the day.

- Jill Marconi, K-12 Specialist – OSGC, who brings in the inner child out in the team and the STEM professional out of our pre-college students.
- All of our presentation evaluators providing insight to our students: Dr. Monroe Kennedy, Leigh Oldham, Dr. Jeffrey Piggott, Dr. Rydge Mulford, Dr. John Sankovic, Christopher Morris, Dr. Mitch Wolff, Bob Bodi, Dr. Sarah Wyatt, Dr. Othmane Benafan, Dr. James Gilland, Halle Buescher, Dr. Andrew Layden, Paul Penko, Dr. Richard Bachmann, Dr. Julie Zhao, John Rindy, Dr. James McCargar, Dr. Byung-Wook Park, Dr. David Sawyers.

Most importantly, thank you to our students, whose efforts and contribution makes this program possible!



Fellows

Advanced Computational Techniques for Optimal Control of a 3-DOF Robotic Manipulator Using Nonlinear Model Predictive Control and Proportional Control

Student Researcher: Nicholas Baird

Advisor: Hossein Mirinejad

Kent State University
College of Aeronautics and Engineering

Abstract
This paper presents the development and implementation of control strategies for a four-degree-of-freedom robotic manipulator, the Quanser QArm. Specifically, it focuses on the implementation and refinement of Nonlinear Model Predictive Control (NLMPC). Simulation and hardware tests were conducted to optimize controller parameters, enhance trajectory tracking, and ensure robust performance during practical operations such as pick-and-place tasks. Results highlighted the necessity of careful modeling and fine-tuning to bridge the gap between simulation and real-world behavior.

Project Objectives
The primary objectives of this project were to develop and implement Nonlinear Model Predictive Control (NLMPC) for a four-degree-of-freedom robotic manipulator to improve trajectory tracking performance and efficiency compared to traditional control approaches. Utilizing proportional control as a baseline comparison, demonstrating the effectiveness and limitations of linear versus nonlinear control strategies in a nonlinear system. This requires validating and refining simulation models of the robotic manipulator for accurate representation of physical dynamics, including friction, actuator limitations, and motor characteristics. Assessing and enhancing the manipulator's operational efficiency and accuracy in practical tasks, such as precise positioning and pick-and-place operations. Identifying and mitigating discrepancies between simulated results and physical hardware behavior through iterative testing, analysis, and refinement of control parameters and system modeling.

Methods
System Setup
The Nonlinear Model Predictive Control (NLMPC) strategy was implemented using MATLAB and Simulink, utilizing the MPC toolbox. The QArm dynamic model was discretized to incorporate gravity torque, PWM-to-voltage conversion, motor dynamics, and friction effects, accurately predicting system behavior for determining optimal control actions. Key parameters for tuning include Sampling Time, Prediction Horizon, Control Horizon, Cost Function Weights, and Manipulated Variable Constraints. These parameters balanced accuracy with computational constraints for real-time hardware implementation.

Torque-to-PWM conversion was approximated using motor specifications, incorporating back-EMF effects to refine voltage-to-torque calculations. Friction was modeled as a static offset and considered in torque computations.

Nonlinear Model Predictive Control (NLMPC)
NLMPC was chosen for its ability to handle complex nonlinearities and explicit constraints within the system. Parameter tuning determined optimal settings of:

- Sampling Time: 0.002 seconds
- Prediction Horizon: 0.006 seconds (3 time steps)
- Control Horizon: 0.002 seconds (1 time step)

The MATLAB solver fmincon with sequential quadratic programming (SQP) was employed without additional solver constraints.
The cost function was defined as:

$$J = \sum_{k=0}^{N_p-1} Q\|x(k) - r(k)\|^2 + \sum_{k=0}^{N_c-1} R\|\Delta u(k)\|^2 + P\|x(k+1) - r(k+1)\|^2$$

- Weight Q: 1 for each joint position error, 0.8 for joint velocity error.
- Weights R and P: set to 0.

Proportional Controller Development

Proportional controllers were designed independently for each joint. The proportional gain (Kp) was tuned to a final value of 5.5. Two modes were explored:

- PWM control: External proportional control implemented via Simulink.
- Position control: Integrated proportional control using built-in Dynamixel motor controllers.

Simulation and Hardware Testing

Simulation tests utilized a Simulink dynamic model incorporating noise (up to 5% of max signal output) to mimic real-world conditions without risking hardware. Reference trajectories were generated using random target points at 60-second intervals, validated through inverse kinematics.

Following successful simulations, hardware tests were conducted on the QArm. Real-time data logging identified discrepancies between simulation and hardware results, prompting further model refinement, parameter adjustments, and incorporation of noise-filtering techniques to achieve improved alignment with practical behavior.

Results and Discussion

Proportional Control Results:

The proportional control demonstrated rapid response and effective tracking of reference trajectories. However, it experienced significant sensitivity to sensor and actuator noise, causing noticeable fluctuations in positioning accuracy (see Figure 1). This sensitivity shows the need for the introduction of filtering techniques to reduce noise-induced tracking deviations and stabilize control outputs.

Nonlinear Model Predictive Control (NLMPC) Results:

The NLMPC approach exhibited promising performance in simulations, demonstrating smooth trajectory tracking even under noisy conditions. Hardware testing revealed notable discrepancies between simulated and real-world outcomes, showing the need for precise state-space modeling and accurate representation of physical constraints. Specific issues observed included persistent offset errors, particularly in joint 3 after approximately 90 seconds (see Figure 2), and instances of joints reaching physical limits (see Figure 3), attributed to the uniform weighting strategy used in the cost function.

Comparative Analysis:

The proportional controller's average mean absolute error across 64 runs was 0.107 rad (6.1°), indicating relatively accurate but noise-sensitive tracking.
NLMPC exhibited a higher average mean absolute error of 0.472 rad (27°), influenced by discrepancies between simulation and hardware, and uniform weighting within the cost function.

The results clearly highlight the need for customized cost functions tailored specifically to individual joint dynamics and operational priorities to improve NLMPC's practical effectiveness.

Future Considerations:

Results suggest potential for real-world performance of NLMPC through further refinement of model accuracy, parameter tuning, and integration of advanced optimization methods.

Future work includes exploring customized cost functions, integrating obstacle avoidance, and testing alternative optimization methods, potentially offering superior robustness and performance compared to conventional optimization approaches.

Figures

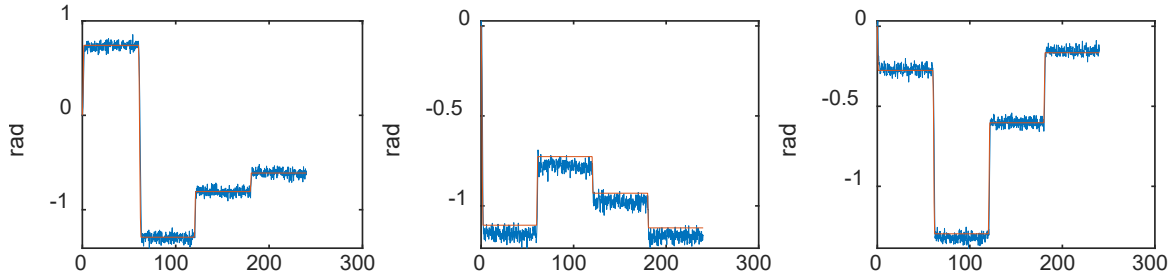


Figure 1 Proportional Control Performance

Figure 1: Shows the rapid response and trajectory tracking accuracy of the proportional controller,

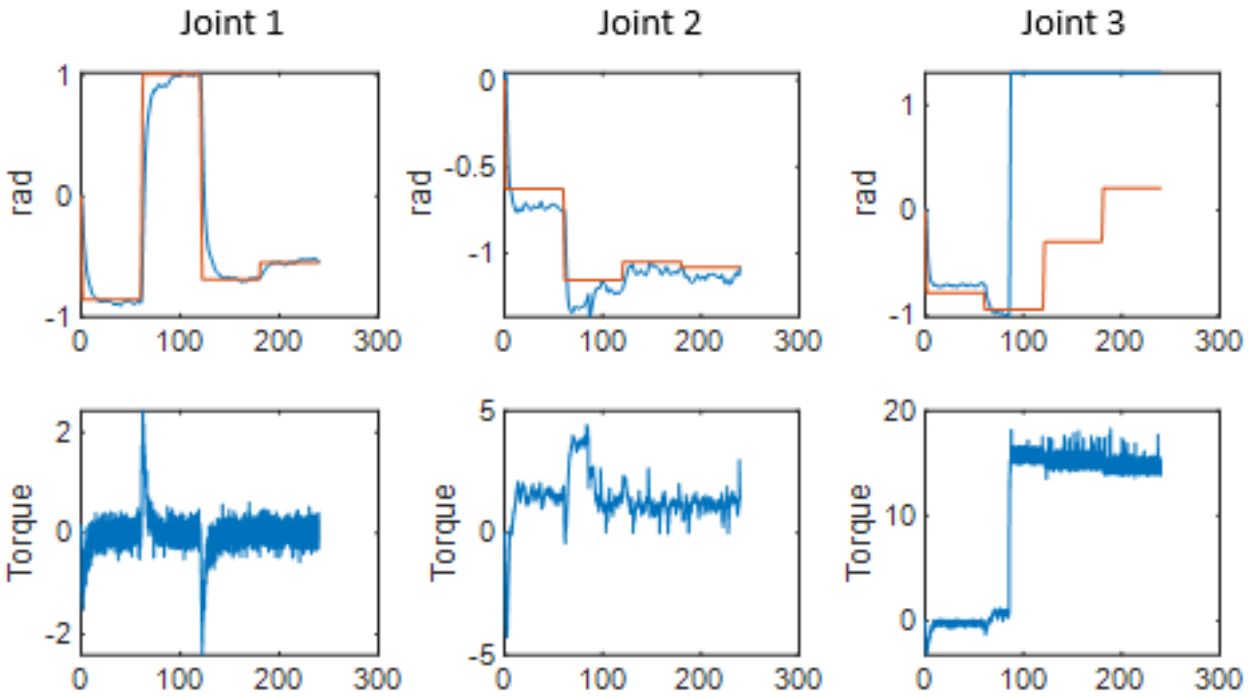


Figure 2 NLMPC Trajectory Tracking Performance (Joint 3 Offset Error)

highlighting its sensitivity to noise. Fluctuations indicate the controller's responsiveness to sensor and actuator disturbances, motivating the need for filtering.

Figure 2 shows the persistent offset error in joint 3 trajectory tracking observed approximately after 90 seconds during hardware tests. This demonstrates the limitations of the current cost function.

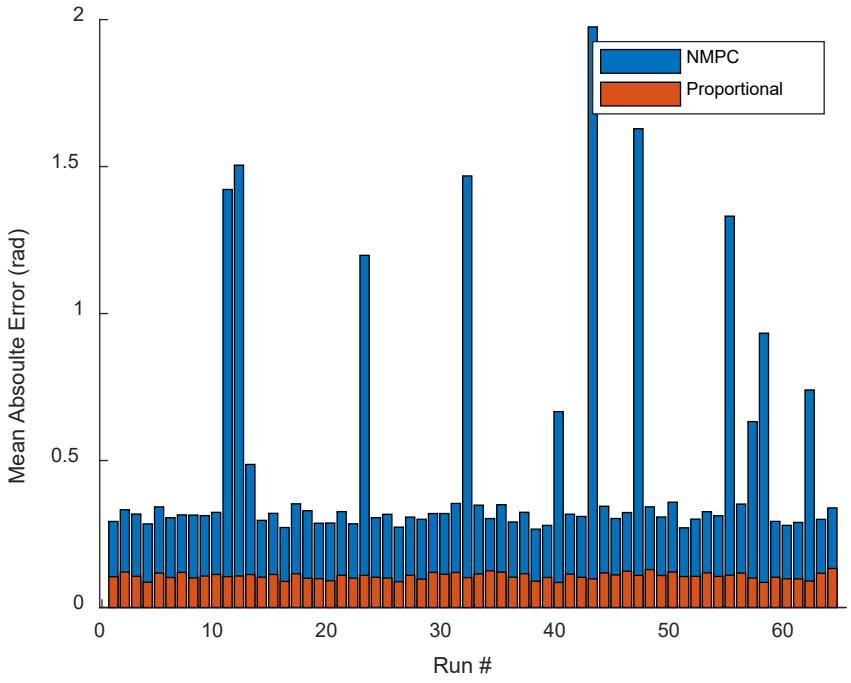


Figure 3 Mean Absolute Error (NLMPC vs Proportional)

Figure 3 demonstrates scenarios where the cost function optimization solves one or more joint positions to have large errors. The operational limits due to cost function weighting issues highlight the importance of accurately modeled constraints and tailored optimization criteria in NLMPC design.

Acknowledgements

I would like to acknowledge the following for their support and contributions to this research:

- The Ohio Space Grant Consortium (OSGC) for funding support through the OSGC Fellowship.
- Quanser, for providing the QArm robotic manipulator platform and assistance with default PID gain values.
- My advisor, Dr. Hossein Mirinejad, and Kent State University, for academic support and guidance.
- Levent Bozcu, a fellow graduate student at Kent State University, for valuable discussions, support, and assistance throughout the project.

References

Quanser (2021). QArm Dynamics. Quanser Documentation.

MathWorks (2024). Nonlinear MPC Design, MATLAB Help Center. Retrieved December 10, 2024, from https://www.mathworks.com/help/mpc/nonlinear-mpc-design.html.

Robotis (2024). e-Manual XM540-W270-T/R. Retrieved December 10, 2024, from https://emanual.robotis.com/docs/en/dxl/x/xm540-w270/.

Effect of Reaction Surface Geometry on Control Authority of Asymmetric Plasma Actuation over Subsonic Axisymmetric Jet Aerodynamics

Student Researcher: Alex Barnhouse

Advisor: Dr. Nathan Webb

The Ohio State University
Department of Mechanical and Aerospace Engineering

Abstract

Thrust vectoring, the controlled deflection of a jet to alter the angle of developed thrust, is currently implemented using complex, heavy, variable geometry nozzles to obtain hyper-maneuverability and vertical takeoff/landing capabilities. Previous work investigated the deflection of a subsonic, axisymmetric jet by localized arc-filament plasma actuators (LAFPAs) azimuthally distributed at the jet exit, upstream of a fixed-geometry "reaction surface" which curves away from the jet axis. The LAFPAs demonstrated the ability to induce pressure asymmetries on the reaction surface which were confirmed by streamwise PIV to be suggestive of jet deflection. This investigation focuses on the effects of reaction surface geometry on the LAFPAs' control authority on the development of coherent structures within the jet shear layer. The effect of control at various excitation frequencies was documented using an array of static pressure taps embedded in the reaction surface to compare the induced pressure asymmetries for reaction surfaces with varying step heights. It was determined that 1mm is near the optimal step height and step heights of 1.5mm and larger induce audible resonance that disrupts the LAFPAs' control authority.

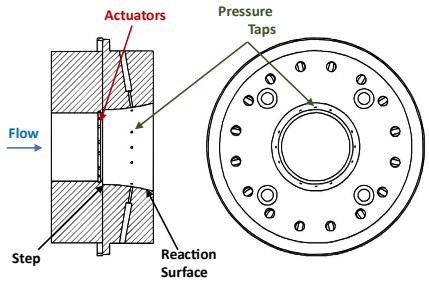
Project Objectives

Vertical take-off/landing (VTOL) vehicles, particularly tail-sitter aircrafts, require a high degree of maneuverability to maintain their attitude control while in hover. One possibility to achieve high maneuverability out of a single exhaust is to influence the direction and magnitude of the exit flow, i.e., the thrust. The Navy and Department of Defense are interested in this possibility as this would enable the operation of fixed-wing, unmanned aerial vehicles (UAVs) from vessels without a flight deck. Historically, thrust vectoring can be achieved using mechanical control surfaces to alter the nozzle exit geometry, but this introduces additional weight and mechanical complexity to the nozzle. An active flow control method, Coanda-based Thrust Vectoring (CTV) leverages the Coanda effect by adding flow momentum to deflect the exit flow and attach it to fixed "reaction surfaces" which curve away from the jet axis [1]. While this method has proven effective for light-weight UAVs, significant bleed air is required to attach the flow [2]. In an attempt to achieve significant thrust vectoring while eliminating heavy mechanical actuation or costly bleed air of CTV, localized arc-filament plasma actuators (LAFPAs) will be investigated to change the flow angle near a nozzle exit. LAFPAs connect an arc between charged and grounded pins, causing rapid deposition of small amounts of thermal energy. This instantaneous addition of thermal energy has been shown to perturb the flow, exciting the Kelvin-Helmholtz instability and inducing the formation of coherent structures (CS) to develop [3–6]. Controlling the spacing and size of the CS by altering the frequency of the LAFPAs can provide significant control authority and attach the flow to the nozzle's reaction surfaces [7]. Since the frequency of actuation can be quickly modified electronically, the degree and direction of flow deflection can be altered just as rapidly. The objective of this project is to investigate if this method could provide a fixed geometry, low power means of vectoring the thrust from a jet without bleed flow.

The novel concept of this project is the combination of CTV inspired, plasma-actuated control of a flow, with the inclusion of a fixed reaction surface geometry. While others have demonstrated the LAFPAs' ability to alter flow characteristics such as far-field acoustic noise reduction [8] or even thrust vectoring in a supersonic jet [9], this project uses the reaction surface to provide a location of attachment for the flow as does CTV. Previous work [7,10] from this project demonstrated that the LAFPAs can control the jet shear layer mixing and entrainment properties to attach the jet to a curved reaction surface (as employed in CTV), thereby inducing cross stream momentum and deflecting the flow. By examining the effect of altering the actuation frequency, it was hypothesized (consistent with the body of literature on instability-based flow control) that lower frequency actuation induces larger CS which entrain more flow, thereby decreasing the (azimuthally) local pressure and increasing the subsequent jet deflection toward the active LAFPAs. The objective of this work is to experimentally examine the effect of reaction surface geometry on the LAFPAs' ability to deflect the jet. This will be accomplished by testing multiple reaction surface geometries in conjunction with LAFPA excitation. This will allow an assessment of more ideal geometric parameters to produce a final nozzle extension configuration with a greater magnitude of pressure asymmetries and jet deflections.

Methodology

The LAFPAs' capabilities and control mechanism have been investigated in a blow down facility at the Gas Dynamics and Turbulence Laboratory. This facility is located at Ohio State University's Aerospace Research Center. The facility can precisely control the stagnation pressure of the jet to maintain the nozzle pressure ratio (NPR) and therefore Mach number, at the desired condition. During the reported experiments, the NPR was set to 1.17 (M_j = 0.48). However, the facility can accommodate a wide range of Mach numbers from subsonic to supersonic. The current nozzle extension configuration (internal contours shown in Figure 1) includes a boron nitride, constant-diameter extension containing the LAFPAs, followed by a fixed, but detachable, reaction surface containing the static pressure taps. By 3D printing each new reaction surface, test configurations can be manufactured and tested much quicker than traditional manufacturing. The new reaction surfaces will individually vary the backward facing step height, length, and termination angle. These parameters affect the shear layer development, if the jet will attach to the reaction surface, and the maximum angle at which the jet could deflect. The current portion of this study details results of varying the backward facing step height.



(a) (b)

Figure 1: Subsonic axisymmetric jet with reaction surface: (a) Side view (flow left-to-right) of actuators, static pressure taps, and reaction surface contour and (b) Front view (flow out-of-the-page) highlighting static pressure tap azimuthal distribution.

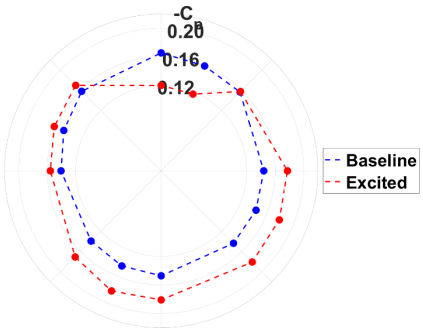
Control was implemented by eight LAFPAs evenly distributed azimuthally around the nozzle exit. Each LAFPA consists of a pair of 1 mm diameter tungsten electrodes with a center-to-center tip separation of 4.0 mm. The electrodes were mounted with the tips flush to the internal nozzle extension surface, within a 1 mm wide by 0.5 mm deep groove to shield and stabilize the arc. The groove is located 0.5 mm upstream

of the step to the curved reaction surface. Each actuator is driven by an in-house built power supply which periodically applies an 8 kV potential across the electrodes, resulting in breakdown of the air between electrode tips and the introduction of a localized thermal perturbation. As mentioned above, these actuators function via the excitation of instabilities, rather than the introduction of significant energy. Accordingly, the time-averaged power consumption of each actuator is quite low (10's of Watts). The excitation frequency is a critical parameter, as it determines the induced CS spacing, development, and eventual effects on the flow field. The power supply individually controls each actuator, allowing different groups to be activated, and each active actuator to be operated at a unique excitation frequency and delay relative to the others. In all cases reported in this work, all active actuators were operated at the same frequency and in-phase with one another.

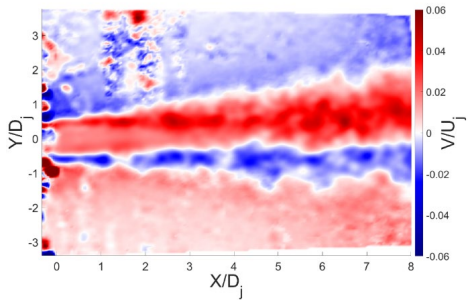
The flow was interrogated by measurements from a static pressure tap array embedded in the reaction surface (see Figure 1). Twelve static pressure taps are azimuthally distributed 13.3 mm downstream of the step to the reaction surface. The tap pressures were recorded by a Scanivalve DSA 3217 16-channel pressure transducer, operated by an in-house developed LabVIEW code. The static pressure measurements displayed below are averages of 50 points acquired at a rate of 10 Hz. Each recorded point is the average (performed internally by the Scanivalve transducer) of 50 samples. Particle Image Velocimetry (PIV) was used on the previous configuration to interrogate the flow confirm the present of jet deflection by the control. The PIV system used an EverGreen HP laser system of two lasers combined to produce two 532 nm laser pulses at 25 Hz. The laser was used to illuminate oil particles introduced to the flow using a core flow seeder: a LaVision Aerosol Generator, able to withstand a maximum back pressure of 145 psi, and an ambient flow seeder: a TSI 6 Jet Atomizer 9306. The images were collected using two LaVision Imager sCMOS cameras able to capture 50 frames per second at a resolution of 2560 x 2160 pixels. The cameras were directed toward the nozzle plane from the side, capturing the streamwise flow field.

Results

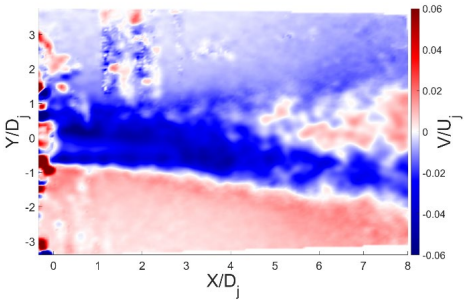
Previous work demonstrated the LAFPAs' ability to induce asymmetric pressure distributions and deflect the jet. That nozzle extension configuration was similar to the current one but was contained in a single nozzle extension made from boron nitride rather than two attachable parts. Additionally, the previous configuration had a slightly shorter straight length before the backward facing step, a 1mm step height, 18.9mm reaction surface length, and a 15° termination angle. Shown below in Figure 2 are static pressure and PIV results for the most evident jet deflection from that configuration. For these results, the active LAFPAs were at the top of the jet, exciting at 45 kHz, which is hypothesized to decrease the spacing between the CS, discouraging mixing within the shear layer near the center of excitation (CE). This decreased spacing and mixing would decrease the size of the induced vortices relative to the shear layer opposite the CE and deflect the jet away from the active LAFPAs. The polar plot in Figure 2a contains the baseline pressure distribution as well as the excited pressure distribution, using a metric of $-C_p$ on the radial axis. A higher magnitude indicates a lower pressure value and thus a higher local suction. This pressure data showcases that the LAFPAs can induce pressure asymmetry near the jet exit. The PIV images in Figure 2b and Figure 2c support that this asymmetry is indicative of jet deflection. The images were captured from the side of the jet, so red and blue indicate upward and downward vertical velocity at each streamwise location, respectively. The baseline flow shown in Figure 2b is deflected downward in Figure 2c, consistent with what the pressure distributions suggested. These experiments validate that the LAFPAs can induce asymmetric pressure profiles and jet deflections.



(a)



(b)



(c)

Figure 2: (a) Suction coefficient for baseline and excited cases, (b) normalized vertical velocity field for baseline case, and (c) normalized vertical velocity field for excited case.

With the results of previous work displaying that this could be a viable active flow control technique, the effects of reaction surface geometry on the LAFPAs' control authority can be determined. While this is not an optimization study, the aim of this project is to better understand how each geometric parameter impacts the LAFPAs' control authority and to produce a final nozzle extension configuration with greater jet deflections.

To quantify the overall effect of excitation at a given frequency and allow general trends to be extracted from sweeps of actuation frequency, the time-averaged static pressure measurements of the array were reduced to a single metric which is here referred to as "pressure asymmetry". Each azimuthal pressure measurement is used to define a vector with a magnitude of the pressure and a direction based on the tap location relative to the jet centerline. These vectors are summed and the component of the resultant vector directed toward the center of the active group of LAFPAs is the pressure asymmetry. This metric approximates the level of cross-stream force on the jet produced by one excitation condition as compared to another. PIV results displayed above also further validate the use of this metric. Figure 3 displays the pressure asymmetry for three different backward facing step heights for a range of actuation frequencies from 1 kHz to 83.3 kHz for a Mach number of 0.48. Based on the definition of the metric, a positive value

indicates that the net cross-stream force on the reaction surface is directed toward the CE while a negative value indicates the cross-stream force is directed away from the CE.

For the 1mm step height, the lowest excitation frequencies do not have a significant impact on the flow attachment until near 2 kHz. At that point the pressure asymmetry increases, suggesting that the jet begins to deflect toward the CE. The pressure asymmetry peaks near 10 kHz then decreases to 0 near 25 kHz. This is consistent with the working hypothesis: as the spacing of the larger CS decreases as the excitation frequency increases, inducing more time averaged entrainment and pressure asymmetry, while at higher frequencies beyond the peak toward CE, the close spacing of the induced structures results in reduced growth and entrainment, and therefore decreasing pressure asymmetry. The greatest magnitude of pressure asymmetry away from the CE is around 40 kHz. At this high excitation frequency, the vortices are known, from significant previous experience with the LAFPAs, to be spaced much more closely, further discouraging growth and reducing entrainment beyond the level present in the unexcited shear layer at the side opposite the CE. The result is the observed pressure asymmetry away from the CE. Thus, the 1mm step height paired with the LAFPAs displays the desired control authority on the jet, encouraging pressure asymmetries toward and away from the CE depending on the excitation frequency. This 1mm step height configuration shows similar trends to the previous nozzle extension configuration, which contained the same step height. This suggests that the trends are consistent despite differences in material and assembly.

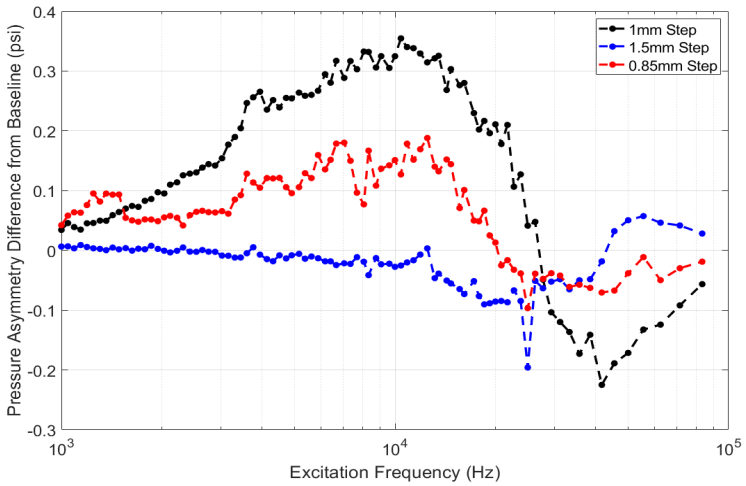


Figure 3: Pressure asymmetry along center of excitation axis difference from baseline for three different backward facing step heights.

The 0.85mm step height displays similar trends in pressure asymmetry, but with lower magnitudes relative to the baseline values. This step height also shows little to no pressure asymmetry away from the CE at high frequency excitation, likely due to the smaller step height encouraging flow attachment to the reaction surface in the baseline flow. The presumed partial baseline attachment reduces the maximum difference from baseline which is achievable by the actuators attempting to attach the flow and mitigates the effect of attempting to detach the flow near CE. The 1.5mm step height paired with the LAFPAs displays minimal control authority over the flow, with little to no pressure asymmetry toward or away from the CE. During this experiment, there was significant audible resonance created from the flow and reaction surface. This resonance was immediately heard when the Mach number reached the desired conditions and was much louder than the baseline noise caused by the jet. Acoustic waves can alter and/or induce CS, controlling the aerodynamics of the flow. Since this resonance was dominant, the LAFPAs'

control authority over the flow was lessened and thus the active flow control technique was unable to induce significant pressure asymmetries.

Step heights of 0.5mm and 2mm were also tested. The 0.5mm step height displayed strong baseline attachment to the reaction surface and pressure asymmetry which were unable to be affected by the LAFPAs. The 2mm step height produced stronger resonance than the 1.5mm step height during baseline tests and thus the entire frequency sweep was not completed. The mechanism causing the resonance in these configurations is currently unknown but will be the subject of future investigation.

Conclusion

Reaction surface geometry does have an impact on the LAFPAs' control authority, evident by the different trends in Figure 3. It is likely that the most ideal step height is near 1mm, which allows the LAFPAs to induce significant pressure asymmetries toward and away from the CE, which is suggestive of jet deflection. More generally, the reaction surface geometry paired with the LAFPAs should avoid strong baseline attachment and resonance that lower the active flow control technique's authority on the flow aerodynamics. Future work will include investigating the effects of altering the length and termination angle of the reaction surface. Combining those results with this step height study will provide insight to produce a more ideal reaction surface geometry in the hopes of achieving a greater deflection than previous results have shown.

Acknowledgements

The support of this research by the Office of Naval Research through Dr.'s David González and Leighton Meyers is greatly appreciated. Support from the Ohio Space Grant Consortium of Alex Barnhouse through a summer internship and graduate fellowship, and Zain Hamid and Jinit Patel through and undergraduate research scholarship is also gratefully acknowledged.

References

[1] Gill, K., "The Development of Coflow Fluidic Thrust Vectoring Systems," Dissertation. University of Manchester, Manchester, UK, 2008.

[2] Warsop, C., and Crowther, W. J., "Fluidic Flow Control Effectors for Flight Control," *AIAA Journal*, Vol. 56, No. 10, 2018, pp. 3808–3824. https://doi.org/10.2514/1.J056787

[3] Samimy, M., Adamovich, I., Webb, B., Kastner, J., Hileman, J., Keshav, S., and Palm, P., "Development and Characterization of Plasma Actuators for High-Speed Jet Control," *Experiments in Fluids*, Vol. 37, No. 4, 2004, pp. 577–588. https://doi.org/10.1007/s00348-004-0854-7

[4] Samimy, M., Webb, N., and Crawley, M., "Excitation of Free Shear-Layer Instabilities for High-Speed Flow Control," *AIAA Journal*, Vol. 56, No. 5, 2018, pp. 1770–1791. https://doi.org/10.2514/1.J056610

[5] Moore, C., "The Role of Shear-Layer Instability Waves in Jet Exhaust Noise," *Journal of Fluid Mechanics*, Vol. 2, 1977, pp. 231–327.

[6] Michalke, A., "On Spatially Growing Disturbances in an Inviscid Shear Layer," *Journal of Fluid Mechanics*, Vol. 3, 1965, pp. 521–544.

[7] Mills, D., Cartwright, E., and Webb, N. J., "Asymmetric Control of Subsonic Axisymmetric Jet Aerodynamics Using Plasma Actuators," presented at the AIAA AVIATION 2023 Forum, San Diego, CA and Online, 2023. https://doi.org/10.2514/6.2023-3954

[8] Kearney-Fischer, M., Kim, J.-H., and Samimy, M., "Noise Control of a High Reynolds Number High Speed Heated Jet Using Plasma Actuators," *International Journal of Aeroacoustics*, Vol. 10, Nos. 5–6, 2011, pp. 635–658. https://doi.org/10.1260/1475-472X.10.5-6.635

[9] González, D. R., Gaitonde, D. V., and Lewis, M. J., "Large-Eddy Simulations of Plasma-Based Asymmetric Control of Supersonic Round Jets," *International Journal of Computational Fluid Dynamics*, Vol. 29, Nos. 3–5, 2015, pp. 240–256. https://doi.org/10.1080/10618562.2015.1053877

[10] Barnhouse, A., Mills, D., Cartwright, E., and Webb, N. J., "Controlled Deflection of a Subsonic, Axisymmetric Jet Using Plasma Actuators," presented at the AIAA Aviation 2024 Forum, Las Vegas, NV, 2024. https://doi.org/10.2514/6.2024-3544

Elevated Temperature Solid Particle Erosion of a Ceramic Matrix Composite

Student Researcher: Jonathan Clawson

Advisor: Dr. Gregory Morscher

The University of Akron
Department of Mechanical Engineering

Abstract

Ceramic matrix composites (CMCs) consist of a ceramic matrix reinforced by continuous or discontinuous (chopped) ceramic fibers or ceramic particulates. Additionally, a CMC may include a weak fiber-matrix interface, usually in the form of a coating. CMCs possess the characteristic high melting point and high thermal stability at elevated temperatures of their constituent materials coupled with improved fracture toughness and damage tolerance compared to monolithic ceramics. Ceramic matrix composites are enabling improvements in the thermal and propulsive efficiency of gas turbine engines due to weight savings and advanced thermomechanical properties. The integration of CMCs into gas turbine engines in the aerospace industry exposes the material to harsh, erosive environments, especially in the military sector. Solid particle erosion is a common phenomenon that occurs in gas turbine engines when particles that have not exceeded their melting point are ingested at a high velocity, resulting in material removal after impact. This occurrence is particularly apparent along aerodynamic channels such as the leading edges of turbine blades. It has been reported in literature that CMCs are more susceptible to erosion than nickel (Ni)-based superalloys currently in-service and monolithic ceramics [1]. Therefore, the influence of erosive environments on the mechanical properties and failure mechanisms of CMCs must be extensively characterized to accurately predict material performance.

Project Objectives

The objective of this study was to characterize the elevated temperature solid particle erosion behavior of a CMC system, representative of the cutting-edge material architecture currently in-service, in a simulated combustion environment. The influence of temperature, erodent particle velocity, and erodent particle concentration were quantified with respect to the mass basis erosion rate and damage morphology of the impact crater. Additionally, the ambient temperature residual tensile strength of the material was evaluated, and the net stress concentration effect of the impact crater was determined. Non-destructive evaluation (NDE) techniques were employed to investigate the damage accumulation and failure mechanisms.

Methodology

The CMC target material is a vintage GE Aviation prepreg laminate. The composite consists of individual unidirectional laminas in the form of a tape of continuous Hi-Nicalon^{TM} Type S (HNS) fibers. In the prepreg process, the SiC fibers are coated with a boron nitride (BN)-based fiber-matrix interface and a protective silicon nitride (Si_3N_4) overcoating using a proprietary chemical vapor deposition (CVD) process and then formed into unidirectional prepreg sheets via wet drum winding [2]. The prepreg sheets are then laid up and laminated to form the composite preform. At this stage, the matrix of the composite consists of powders (commercially available SiC and C) in a mixed polymer binder. A binder burnout/pyrolysis step converts part of the polymer to carbon. Final densification takes place when molten silicon infiltrates the porous preform, during which the silicon reacts with the free carbon present in the preform to form a continuous SiC phase in the matrix [2]. The composite structure is comprised of eight plies that are oriented in a symmetrical cross-ply lay-up ($[0/90]_{2s}$). The nominal volume fraction of the composite is approximately 20-25%.

The erodent material used in this study is 120 mesh commercially available white aluminum oxide particles obtained from Kramer Industries, Inc. with in average particle diameter of 125 μm. As explained by Panakarajupally et al. [3], the alumina particles resemble a rhombohedral shape with sharp edges that are ideal for solid particle erosion impact testing. Two distinct erodent particle velocity conditions, 200 and 350 m/s (Mach ≈ 0.6 and Mach ≈ 1.0, respectively), and two different erodent particle concentrations, 0.2 g/iteration and 0.4 g/iteration, were investigated at both ambient temperature and an elevated temperature of 1315°C, which corresponds to a hot-section turbine component design condition.

The ambient temperature erosion testing was conducted using a pneumatic impact gun. The experimental setup utilizes pressurized helium (He) gas to propel erodent particles through a 300 mm steel barrel before impacting the target material at a 90° (normal) impingement angle. A normal impingement angle was selected for both the ambient and elevated temperature experimental setup since it is the condition for maximum erosion of brittle ceramics [3]. The standoff distance between the target material and the barrel was set to 15 mm with the barrel aligned to impact the center of the target material test specimen. The helium reservoir was pressurized to 100 and 200 psi to achieve the target erodent particle velocities of 200 and 350 m/s, respectively, and verified using a double disc method that has been commonly applied to erosion studies [4]. Five impact iterations were conducted at the aforementioned erodent particle concentrations totaling 1 g and 2 g, respectively. Between iterations the mass loss of the specimen was measured, and the damage morphology was analyzed using a Keyence VHX 7000 optical microscope. The crater damage morphology was quantified with respect to the crater depth, axial cross-sectional area, and transverse cross-sectional area. Each variation of erodent particle velocity and erodent particle concentration were tested twice, except for the minimum condition of 0.2 g of erodent per iteration at 200 m/s which was only tested once since it produced only negligible erosion damage compared to the surface roughness of the specimen.

The elevated temperature erosion was performed using The University of Akron burner rig system that consists of a Plasma Powders high-velocity oxygen fuel (HVOF) gun, gas flow control panel, and powder feeder capable of mixing erodent particles into the combustion flow stream using nitrogen as the carrier gas. For this work, natural gas was selected as the fuel as it is readily available and oxygen as the oxidizer with an air-cooled converging nozzle. The combustion conditions were controlled by adjusting the flow rates and pressures of the fuel, oxidizer, and compressed air. The velocity of the erodent particles was verified by using a high-speed camera at 30,000 frames per second and an open-source software called Tracker [5] to measure particle velocity. The amount of erodent entering the combustion flow stream was controlled by adjusting the angular velocity of the disc inside the powder feeder canister, flow rate and pressure of nitrogen carrier gas, and time of erodent exposure. Test specimens were held in a specially designed superalloy fixtures (Inconel 601) fixed in the grips of a horizontal mounted hydraulic MTS mechanical test frame. A forward-looking infrared camera (FLIR – T650sc) was used to monitor the front surface temperature of the target material test specimen by employing the emissivity of the material that was determined using a small resistive furnace with a window opening. The temperature reading of the furnace k-type thermocouple was matched with the FLIR camera by adjusting the emissivity value. Since the furnace is limited to a temperature of 1200°C, the material emissivity was plotted over a temperature range and extrapolated to the target temperature of 1315°C. During testing, the flame was started far away from the test specimen and held there while the necessary flow rates and pressures were adjusted for the desired erosion condition. The flame was advanced slowly until the surface temperature reached 1315°C. The specimen was allowed to dwell at this condition for 30 seconds to a minute to achieve a steady temperature distribution. After the erosion impact, the specimen was allowed to cool to ambient temperature naturally.

Dogbone specimens, characterized by a reduced cross-sectional area in the gage region, were used to collect baseline material properties and baseline residual tensile strength when exposed to the elevated temperature condition whereas straight-edge specimens were used to evaluate the retained strength at each combination of erodent particle velocity and cumulative erodent particle mass. The average dogbone specimen dimensions are 152 mm × 10.2 mm × 1.8 mm. The average straight-sided specimen dimensions are 152 mm × 12.7 mm × 1.8 mm. All specimens were machined from three distinct panels of the target material. The baseline material properties and retained strength of the eroded specimens were both evaluated by an ambient temperature monotonic tensile test at a displacement rate of 0.15 mm/min. An extensometer, with a standard 25.4 mm (one inch) gage region, collected strain data for the baseline dogbone specimens and elevated temperature straight-sided eroded specimens. Conversely, digital image correlation was employed to collect strain data on the pristine backside of the ambient temperature straight-sided eroded specimens. Acoustic emission and electrical resistance NDE monitoring techniques were applied to both the baseline and eroded tensile tests.

Results & Discussion

Erosion Behavior

The influence of erodent particle velocity, erodent particle concentration, and temperature on the erosion behavior of a melt-infiltrated cross-ply laminate SiC-based CMC system was explored at a 90° (normal) impact angle. Figures 1 and 2 show the cumulative mass loss of the target material with respect to cumulative erodent particle mass at ambient temperature and 1315°C, respectively. The legend indicates distinct material panels by their respective identification number (e.g., 0025, 0028-09, and 0028-10).

A linear mass loss progression is observed from both experimental setups. The ambient temperature erosion shows general agreement between specimens tested at the same erosive conditions, verifying consistency in the erosion behavior between material panels. An initial sharp increase in CMC mass loss is followed by a gradual decrease to a steady-state erosion rate. However, the elevated temperature erosion showed rapid material removal approaching near through-thickness crater depths and the same cumulative erodent particle mass quantities as the ambient temperature setup could not be reached nor steady-state erosion. One elevated temperature test specimen at conditions of 350 m/s and 0.4 g/iteration with a maximum crater depth of 1.39 mm fractured during a subsequent erosion test while approaching the desired temperature. As a result, any test specimens with a maximum crater depth at or exceeding 1.40 mm were not subjected to further elevated temperature erosion iterations.

The effect of the erosive conditions was quantified in terms of the erosion rate on a mass basis as defined in equation (1) where E is the erosion rate (g/g), m_i and m_f are the initial and final mass quantities of the target material, and m_e is the mass of the erodent material.

$$E = \frac{(m_i - m_f)}{m_e} \quad (1)$$

At ambient temperature, the erodent particle velocity and erodent particle concentration had a similar influence on the erosion rate of the CMC. For a constant erodent particle velocity, doubling the erodent particle concentration resulted in a 3.16 times increase in the erosion rate at 200 m/s and 2.63 times increase in the erosion rate at 350 m/s. Conversely, for a constant erodent particle concentration, increasing the erodent particle velocity by 1.75 times led to a 3.82 times increase in the erosion rate at 200 m/s and 3.18 times increase in the erosion rate at 350 m/s. This indicates only a slight difference in erosion rate influence of approximately 6% between the two variables which may be due to inherent statistical deviation that could be elucidated with further testing. The same trend is observed in elevated temperature solid particle erosion. However, an outlier in the elevated temperature solid particle erosion is the

200 m/s, 0.4 g/iteration condition for specimen from the 0028-09 panel. Figure 3 illustrates the eye-shaped morphology of the crater that formed as a result of alumina particles that adhered to the center of the crater in an early erosion impact iteration. Subsequent iterations slowly removed the bonded alumina particles, but the alumina provided additional erosion protection resulting in reduced mass loss and the aforementioned crater morphology. This appears to be an artifact of the test setup and was not repeated on the other samples shown here.

With exception of the eye-shaped crater outlier, both ambient and elevated temperature erosion showed linear crater growth progression with respect to the crater depth, axial cross-sectional area, and transverse cross-sectional area. The ambient temperature experimental setup produced nearly symmetrical hemisphere-shaped crater morphology whereas the elevated temperature experimental setup produced paraboloid-shaped crater morphology. Compared to a 2D woven melt-infiltrated SiC-based CMC tested under identical ambient temperature erosion conditions in the same facility, the cross-ply laminate CMC exhibited greater resistance to erosion damage, resulting in a crater depth only two-thirds that of the woven counterpart [4].

Material Strength

An ambient temperature monotonic tensile test was conducted to assess the pristine material strength, residual material strength after exposure to the burner rig environment at the testing temperature of 1315°C, and retained material strength after exposure to the erosive environments tested. Figure 4 depicts the engineering tensile strength degradation of the material due to ambient temperature solid particle erosion damage. Given the proprietary nature of the material performance, the y-axis has been hidden to conceal the exact engineering tensile strength values. Notably, even under the most severe erosive conditions, with the crater depth exceeding half the thickness of the specimen, there was only a minor amount of degradation in engineering tensile strength. Conversely, elevated temperature solid particle erosion led to an average engineering tensile strength reduction of nearly 50% as shown in Figure 5. Although the maximum crater depth from the elevated temperature test methodology only exceeded the maximum crater depth from the ambient temperature test methodology by approximately 26%, the cross-sectional area of the crater increased by three times using the elevated temperature burner rig setup. Based upon the residual engineering tensile strength of pristine material exposed to the burner rig without solid particle erosion at the maximum velocity condition of 350 m/s and the testing temperature of 1315°C for 15 minutes, a duration far exceeding the combined exposure time of eroded test specimens, it is observed that exposure to the burner rig environment did not result in tensile strength reduction.

Net section tensile strength, which accounts for the transverse cross-sectional area reduction at the impact crater, was calculated to further evaluate and compare the strength degradation of the eroded specimens. The values have been normalized to examine the impact of the crater, functioning as a stress concentrator, on the degradation of strength. This involved dividing both the baseline and retained tensile strength values by the average baseline tensile strength obtained from the pristine dogbone test specimens. The results in Figure 8 show that despite the presence of a crater, there is no net stress concentration effect from ambient temperature erosion due to the crater. However, the elevated temperature erosion led to approximately a 20% net stress concentration effect at the crater.

List of Figures

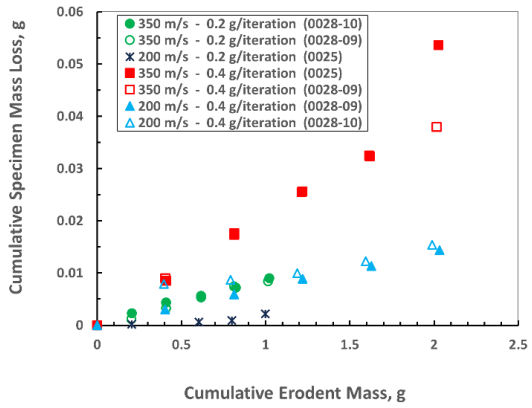


Figure 1: Ambient temperature erosion mass loss.

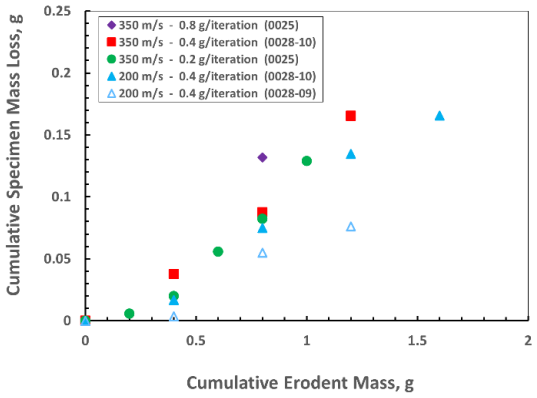


Figure 2: Elevated temperature erosion mass loss.

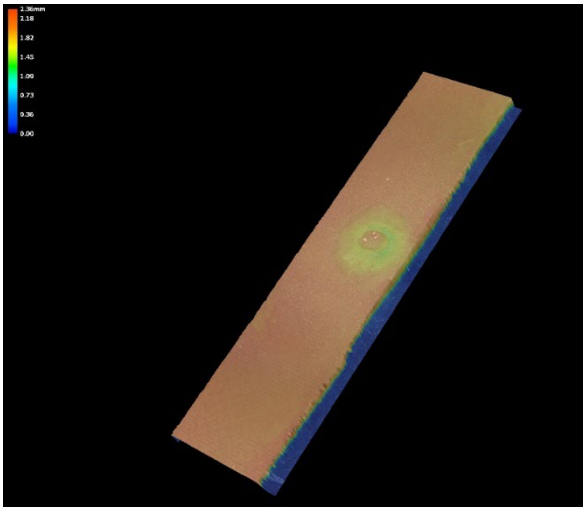


Figure 3: High temperature eye-shaped crater outlier.

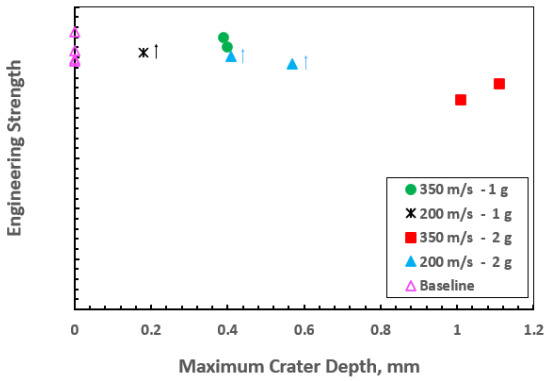


Figure 4: Ambient temperature erosion engineering residual strength.

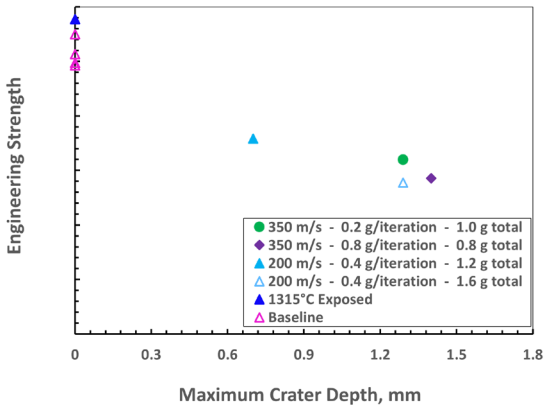


Figure 5: Elevated temperature erosion engineering residual strength.

Acknowledgements

The author wishes to express sincere gratitude to the Ohio Space Grant Consortium for supporting this work. Appreciation is also extended to Dr. Gregory Morscher and Dr. Julie Zhao from The University of Akron for their roles in facilitating this work. Lastly, the author acknowledges the contributions of colleagues at The University of Akron for their assistance.

References

[1] Kedir, N., Gong, C., Sanchez, L., Presby, M.J., Kane, S., Faucett, D.C., Choi, S. R., "Erosion in Gas-Turbine Grade Ceramic Matrix Composites," *Journal of Engineering for Gas Turbines and Power*, vol. 141, no. 1, Sep. 2018. https://doi.org/10.1115/1.4040848.

[2] Corman, G.S., and Luthra, K.L., "Silicon Melt Infiltrated Ceramic Composites (HiPerComp™)," in *Handbook of Ceramic Composites*, 1st, Bansal, N.P., Springer-Verlag, New York: Springer, 2005, pp. 99–115.

[3] Panakarajupally, R.P., Mirza, F., El Rassi, J., Morscher, G.N., Abdi, F., and Choi, S., "Solid particle erosion behavior of melt-infiltrated SiC/SiC ceramic matrix composites (CMCs) in a simulated turbine engine environment," *Composites Part B: Engineering*, vol. 216, no. 12, p. 108860, Jul. 2021, https://doi.org/10.1016/j.compositesb.2021.108860.

[4] Ruff, A.W., and Ives, L.K., "Measurement of Solid Particle Velocity in Erosive Wear," *Wear*, vol. 35, no. 1, pp. 195–199, Nov. 1975, https://doi.org/10.1016/0043-1648(75)90154-4.

[5] Douglas Brown, Wolfgang Christian, Robert M Hanson. (2023). Tracker Video Analysis and Modeling Tool for Physics Education. https://tracker.physlets.org.

Thermal Properties of Elastin-like Polypeptides for Drug Delivery

Student Researcher: Grace Curtician

Advisor: Dr. Nolan B. Holland

Cleveland State University
Department of Chemical and Biomedical Engineering

Abstract

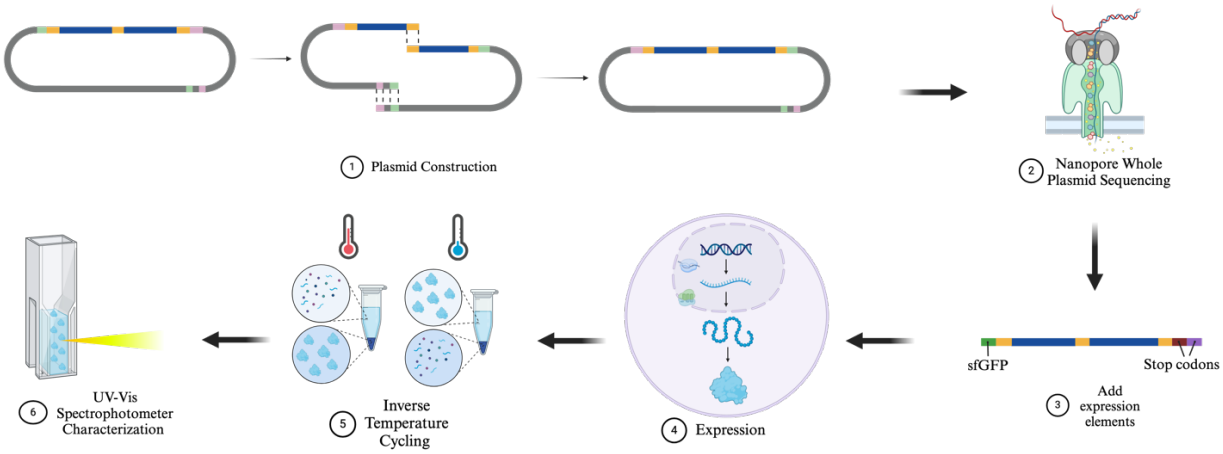


Figure 1. Graphical abstract detailing the plasmid construction, sequencing, expression element addition, expression, purification, and characterization.

Elastin-like polypeptides (ELPs) are a promising biomaterial for drug delivery due to their admirable characteristics such as biocompatibility, biodegradability, and thermal responsiveness. This study investigated the thermal properties of ELPs by genetically engineering polypeptides with repetitive GVGVP based sequences. Through iterative doubling of the target sequence, we successfully constructed and verified sequences encoding ELPs up to 880 pentapeptide repeats. We then expressed and purified a hydrophobic segment designed by a previous lab member. UV- Vis spectroscopy revealed the transition temperature of this segment of the ELP triblock was below 3□C, indicating premature micelle formation. These findings highlight the need to redesign the hydrophobic block to achieve gelation at physiological temperatures. This work establishes a foundational framework for the precise design of thermo-responsive ELPs, enabling future development of injectable, site specific drug delivery systems.

Project Objectives

This project aimed to investigate the structure-function relationships of ELP hydrogels by systematically exploring how the polypeptide structure influences their physical and chemical properties. Specifically, we wanted to produce ELPs with varied block sizes and compositions and characterize their thermal properties. Most conventional drug delivery systems struggle with issues like non-specific distribution, poor bioavailability, and rapid systemic clearance [1]. That means medication may reach healthy tissue instead of the target site, degrade too quickly, have increased side effects, higher dosages, reduced therapeutic impact, or just be inefficient overall. One promising

solution to this issue is the use of hydrogels. Hydrogels are 3D networks of water-swollen polymers [2] that can act as a drug depot, allowing for controlled, localized release over time. This means fewer injections, longer-lasting effects, and ideally, better patient outcomes. To make a good hydrogel, we need a smart biomaterial.

A biomaterial for drug delivery needs several key features including, mechanical tunability, to match the properties of the tissue it's going into, biocompatibility and biodegradability, so it doesn't cause inflammation and naturally breaks down over time. Elastin-like Polypeptides (ELPs) check all of these boxes and more. They're genetically encoded, which means we can control their exact sequence, length, and architecture, giving us precise control of the design at the molecular level. This is incredibly useful in drug delivery, where minor changes can affect release profiles, targeting, and degradation rate. ELPs are also thermo-responsive, which allows them to self-assemble into gels at body temperature, and highly modular, meaning we can attach targeting domains, or drug conjugates to them.

All of these features make ELPs an excellent platform for injectable, site-specific, and long- lasting drug delivery systems. ELPs are synthetic proteins inspired by human elastin. They're made up of repeating pentapeptide sequences like GVGVP — which stands for glycine-valine- glycine-valine-proline [3]. What's particularly interesting is that one of the valines in the GVGVP repeat can be substituted with another amino acid, as long as it's not proline, to tune the physicochemical properties of the ELP. This allows us to adjust things like solubility, transition temperature, and interaction with other molecules. In our design, we use a triblock architecture: hydrophobic end blocks that dictate aggregation, and a hydrophilic midblock, that provides water retention and elasticity. This design allows injectable delivery that gels inside the body.

Methods

Plasmid Construction (2.1) was repeated iteratively to achieve plasmid repeats of 17x, 33x, 65x, 129x, 257x, 513x, and 880x.

Plasmid Construction

Designed plasmids, were ordered from Twist Bioscience. Kanamycin agar plates were incubated at 37°C. DNA was thawed at 4°C in a cold block, and 40 µL of chemically competent *E. coli* cells were combined with 1 µL of DNA in thermocycle tubes. The BIORAD T100 Thermal Cycler was run at 4°C (5 min), 42°C (45 sec), and 4°C (5 min). The mixture was transferred to 2 mL LB media, incubated at 30°C (250 rpm, 20 min), and plated (100 µL) on kanamycin agar for 24–48 hours at 37°C. Plates were parafilmed and stored at 4°C for later use. Approximately 24 hours later, one colony, not encroaching on any other colonies, was harvested from the plate and inoculated into a culture tube with 10 mL of LB Kanamycin media. This culture was grown for 12-16 hours until turbidity was observed. Using a Monarch® Spin Plasmid Miniprep Kit, 2 mL of culture was centrifuged using an Eppendorf 5424 R at 24,000 rpm for 5 min at 20°C. The pellet was sequentially treated with resuspension, lysis, neutralization, and wash buffers, followed by elution with 50 µL buffer. Eluted plasmid DNA was stored for further steps. DNA and standards were stored at 4°C. Standards were diluted with sample buffer, and samples were prepared by combining DNA with buffer (199 µL buffer + 1 µL DNA). Fluorescence measurements were taken using an Invitrogen Life Technologies Quibit® 3.0 Flurometer. Plasmid DNA (10 µL) were sent to Eurofins Genomics LLC for nanopore whole plasmid sequencing. Digestions were set up with 1 µL enzyme (BamHI or HindIII), 5 µL buffer, calculated amounts of DNA, and nuclease-free water to 50 µL.

Reactions were run in the BIORAD T100 Thermal Cycler at 37°C (30 min), 80°C (20 min), and 4°C (30 min). Digested DNA was mixed with binding buffer and processed through a spin column system with wash steps, using a Monarch® Spin PCR & DNA Cleanup Kit. The final product was eluted with 20 µL buffer and stored at 4°C. Thermocycle tubes contained 16 µL Milli-Q water, 1 µL of each digest, and 2 µL HiFi MasterMix from New England Biolabs. Tubes were incubated at 50°C for 1 hour and stored at 4°C. Samples were prepared by combining DNA, sample buffer, and ladder. An E-Gel (1% agarose) was loaded with 20 µL of each and run for 10 minutes. Gel images were captured.

2.1 Protein Manufacturing

After turbidity was observed from colony culture, the 10 mL culture was added to 1L of LB Kanamycin media in a 2L flask and grown at 37°C, 250 rpm, until OD600 ≥ 0.6. Arabinose (2 g) was added, and cultures were induced for 4 hours. Cells were harvested by centrifugation, in a ThermoScientific Sorvall Legend XTR at 4,200 rpm for 45 minutes, resuspended in phosphate buffer (PBS), and stored. Pellets were sonicated, using a FisherbrandTM Model 505 Sonic Dismembrator (level 8, 10 sec on/off cycles for 90 sec) and chilled on ice between runs. Lysis products were processed for purification. Samples underwent alternating cold (10,000 rpm, 4°C, 30 min) and hot (11,000 rpm, 40°C, 25 min) centrifugation cycles, with resuspension in PBS and pH adjustment (6) as required. Final purified products were collected after the third cold cycle.

2.2 Thermal Characterization

A UV-Vis Spectrophotometer Shimadzu UV-1800 Spectrophotometer with temperature control was used to determine the transition temperature of purified ELPs. Protein samples were placed in a 1cm path length quartz cuvette, and absorbance at 280 nm was measured during a temperature ramp from 3°C to 70°C in 1°C increments. Absorbance vs temperature was plotted in Microsoft Excel. The aggregation temperature was identified as the point of a sharp absorbance increase, confirmed by the first derivative of the curve, which highlighted the temperature with the steepest change.

Results and Discussion

The motivation for this work lies in creating a smart biomaterial to be used for hydrogels in the clinical application of drug delivery systems. By using modern synthetic biology tools, we were able to produce highly repetitive DNA sequences to produce biomedically useful proteins. These proteins enable environmentally responsive behaviors such as temperature dependent solubility, making them valuable in drug delivery applications. Despite advances in DNA synthesis and assembly techniques, constructing large repetitive sequences like GKGVP880 remains challenging.

The plasmid design and construction framework successfully enabled the efficient assembly of highly repetitive DNA sequences, encoding the elastin-like polypeptides GKGVP17, GKGVP33, GKGVP65, GKGVP129, GKGVP257, GKGVP513, and GKGVP880. Nanopore whole plasmid sequencing verified the accurate assembly of the GVGVP880 sequence, confirming the integrity of the repetitive DNA.

In the second portion of our project objectives, we were able to express, purify, and characterize the hydrophobic segment of the triblock with UV-Vis Spectroscopy. Expression and purification yielded proteins in sufficient quantities for characterization. UV-Vis spectroscopy demonstrated an unexpected

temperature-dependent solubility of the synthesized ELPs. Absorbance measurements at 280nm did not reveal a distinct aggregation temperature, which leads us to believe that the micelles were already formed and stable below 3□C. This shows us that the transition temperature is below 3□C. We then,

will need to redesign this hydrophobic portion to have a transition temperature closer to that of human body temperature, to be useful in drug delivery applications.

Ultimately, we were able to construct hydrophilic segments from 17x pentapeptide repeats to 880x pentapeptide repeats. Future work for the hydrophilic segment includes adding a GFP-rbs site to the DNA sequence to further express and purify this portion of the triblock ELP. We were also able to thermally characterize the hydrophobic segment made by a previous lab member, which revealed a lower transition temperature than expected. Future work on the hydrophobic segment includes redesigning and constructing new plasmids to lower the transition temperature closer to that of the human body temperature, for drug delivery applications.

Figures/Charts

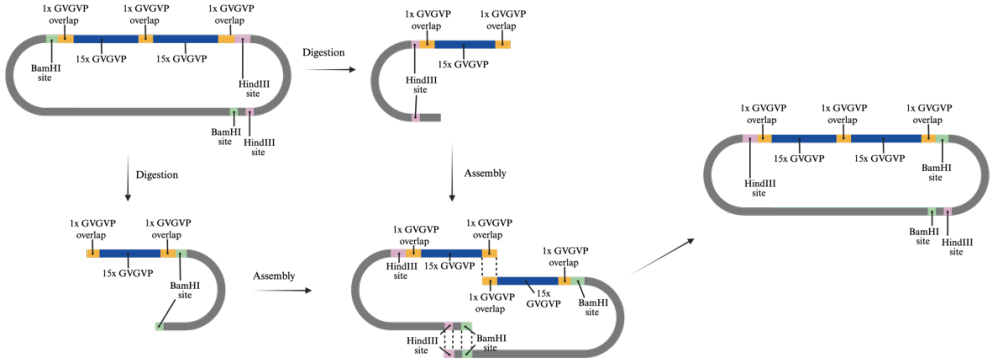


Figure 2. Construction of repetitive DNA encoding 33x Glycine-Valine-Glycine-Valine-Proline, GVGVP33, repeat.

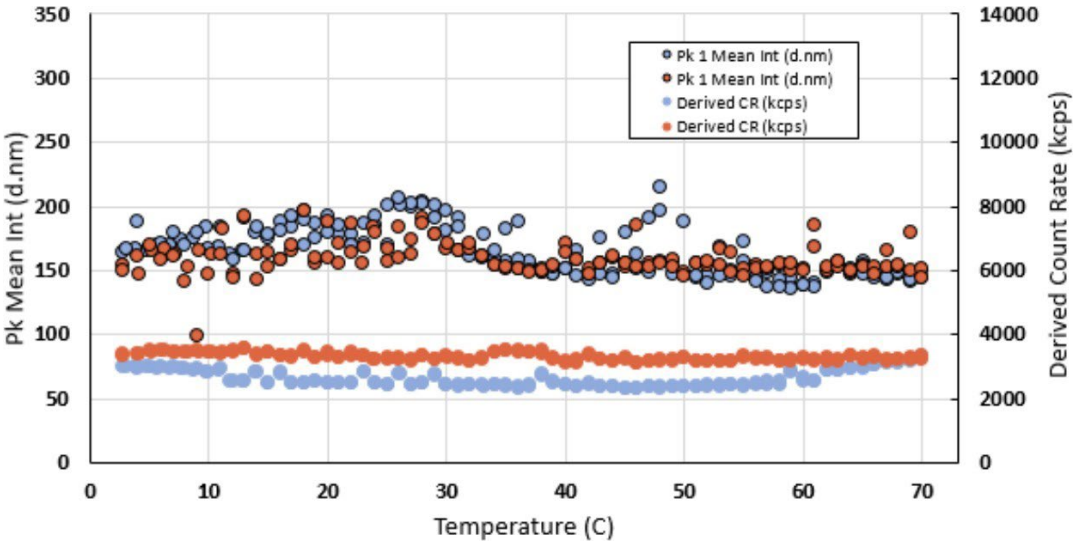


Figure 3. Thermal Characterization using UV-Vis Spectrophotometer with a temperature sweep from 3 C to 70 C of hydrophobic segment of the triblock.

Acknowledgments

I would like to thank Dana Aramouni for her assistance with the thermal characterization of the hydrophobic segment. I would also like to thank Dr. Nolan Holland, and Dr. Edward Turk for their

support throughout this project. Finally, thank you to the Ohio Space Grant Consortium for funding this research.

References

[1] S. Adepu and S. Ramakrishna, “Controlled Drug Delivery Systems: Current Status and Future Directions,” *Molecules*, vol. 26, p. 5905, Sep. 2021, doi: 10.3390/molecules26195905.

[2] “Hydrogel - an overview | ScienceDirect Topics.” Accessed: Apr. 17, 2024. [Online]. Available: https://www.sciencedirect.com/topics/chemistry/hydrogel

[3] Y. Guo, S. Liu, D. Jing, N. Liu, and X. Luo, “The construction of elastin-like polypeptides and their applications in drug delivery system and tissue repair,” *J Nanobiotechnol*, vol. 21, no. 1, p. 418, Nov. 2023, doi: 10.1186/s12951-023-02184-8.

Deep Reinforcement Learning for Autonomous Robot Navigation in Simulation Through Reward Shaping

Student Researcher: Davin Dillon

Advisor: Dr. Jundong Liu

Ohio University
Electrical Engineering and Computer Science

Abstract
This paper investigates the application of Deep Reinforcement Learning (DRL) for autonomous navigation of a TurtleBot v3 robot within simulated environments using LiDAR data. Focusing on the foundational stage of model development, we explore the impact of different reward function designs on the learning performance of a Deep Deterministic Policy Gradient (DDPG) agent in obstacle-filled scenarios. While significant and consistent improvement in navigation performance has not yet been demonstrated, the initial experimental results provide valuable insights into the learning process and the influence of reward shaping, building upon established DRL principles [2]. These findings will inform future work aimed at deploying and evaluating DRL-based navigation on real-world robots, including TurtleBot v3 and potentially drone platforms. The core DDPG agent architecture and the simulation environment setup utilized in this research are largely based on the open-source implementation provided by tomasvr in the turtlebot3_drlnav repository [3]. Our work extends this foundation by exploring the impact of novel reward function designs.

Project Objectives
The primary objectives of this research were to:

1. Develop a DRL-based autonomous navigation agent for a simulated TurtleBot v3 robot using LiDAR sensor input, leveraging continuous control techniques [1].
2. Implement and compare the effectiveness of different reward function designs on the agent's learning speed and navigation performance, drawing from fundamental reinforcement learning concepts [2].
3. Evaluate the trained DDPG agent's success rate, efficiency, and collision avoidance capabilities in various simulated obstacle courses, with visual context informed by existing simulation examples [3].
4. Lay the groundwork for future deployment and testing of DRL-based navigation on real-world robotic platforms, including TurtleBot v3 robots and drones, inspired by the success of DRL in continuous control tasks [1].

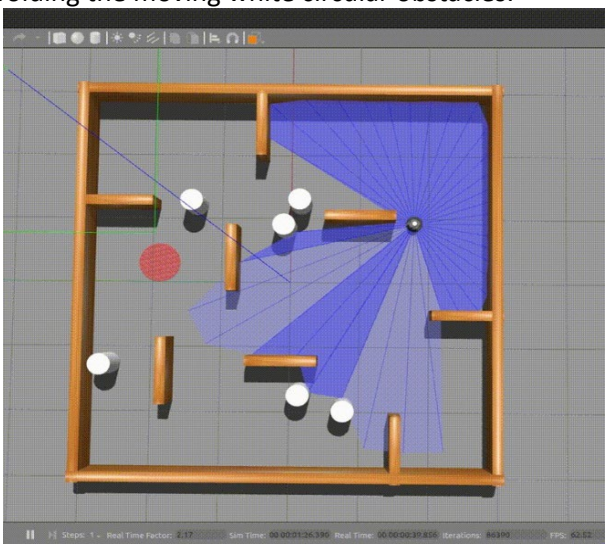
Methodology
The research methodology involved training a DDPG agent in a simulated Gazebo environment with a TurtleBot v3 robot model equipped with a simulated LiDAR sensor. The state space included LiDAR readings, robot velocities, and relative goal pose. The continuous action space controlled the robot's linear and angular velocities, aligning with approaches suitable for DDPG [1]. Several reward functions were designed and tested, guided by principles of reinforcement learning [2]. The DDPG agent, with actor and critic networks implemented in PyTorch, was trained over numerous episodes. Experience replay and target networks were used for stable learning, consistent with the methodology described for continuous control tasks [1]. The agent's performance was evaluated based on success rate, time to goal, distance

traveled, and collision rate across different simulated environments, visually represented in similar setups [3].

Results and Discussion

The current stage of our research has focused on systematically evaluating the impact of various reward function designs on the DDPG agent's ability to learn autonomous navigation within the simulated TurtleBot v3 environment. While a clear and substantial improvement in performance over a baseline has not yet been demonstrated, the data gathered from these initial experiments is essential for informing the next iteration of our model development. For instance, our analysis of the agent's behavior under different reward schemes revealed that when increasing the penalty for obstacle collision the TurtleBot tended to stay in the center of the map and travel in a small circle without advancing toward the target, highlighting the complexities of reward shaping in DRL [2]. Looking ahead, future work will build upon this foundational understanding gained in simulation to address the complexities of deploying these DRL techniques on real-world robotic platforms, including TurtleBot v3 robots and potentially more agile systems like drones, drawing from the established successes of continuous control in robotics [1]. The challenges associated with real-world sensor noise, dynamic environments, and the transition from simulated to physical actuators will necessitate further investigation and adaptation of the learning algorithms and reward structures explored in this initial phase.

Figure 1: Simulated Gazebo environment for autonomous navigation experiments. The TurtleBot v3 robot (black circle) uses a LiDAR sensor (blue) to perceive its surroundings. The objective is to reach the red circular target goal while avoiding the moving white circular obstacles.



Acknowledgments

This work was supported by the Ohio Space Grant Consortium (OSGC) Fellowship.

References

[1] T. P. Lillicrap, J. J. Hunt, A. Pritzel, N.ъем, H. Heess, T. Erez, Y. Tassa, D. Silver, and D. Wierstra, “Continuous control with deep reinforcement learning,” *arXiv preprint arXiv:1509.02971*, 2015.

[2] R. S. Sutton and A. G. Barto, *Reinforcement learning: An introduction*. MIT press, 2018.

[3] tomasvr, “turtlebot3_drlnav (Image file of simulation),” GitHub. [Online]. Available: https://github.com/tomasvr/turtlebot3_drlnav/blob/main/media/simulation.gif. [Accessed: April 18, 2025].

Hypersonic CMC TBC Testing

Student Researcher: Erin Falkosky

Advisor: Dr. Manigandan Kannan

University of Akron
Dept. of Mechanical Engineering

Abstract
Ceramic matrix composites (CMCs) are looking to replace superalloys in the hot section of jet engines. Concerns for this switch include CMCs brittle nature and their oxidation at high temperatures. To combat this, thermal barrier coatings (TBCs) are being studied in burner rigs to simulate jet engine conditions. While TBCs were used on superalloys, the interaction with the CMC substrate needs to be studied, along with conditions for spallation. A literature review was completed on a background of CMCs, and various TBCs. Samples are currently on order to test a variety of TBCs in the University of Akron's burner rig.

Project
Ceramics matrix composites, or CMCs, are ceramics that consist of a ceramic matrix with embedded fibers. While traditional ceramics are known for their low fracture resistance, CMCs have high crack resistance due to the fiber integration into the matrix (Cao, et al., "Advanced Ceramics…"). The proposed usage of CMCs is to replace nickel-based superalloys in the hot sections of jet engines. This is due to their high temperature capacity being higher than that of the superalloys, along with weight savings and high specific strength (Panakarajupall, et al, "Tension-tension fatigue"). The increase in turbine inlet temperature will create more efficient and powerful engines (Presby, et al., "Characterization and…"). Some concerns with making the switch to CMCs include the fact that CMCs undergo oxidation and surface recession at high temperatures with the presence of water vapor (Panakarajupall, et al, "Tension-tension fatigue"). In addition, there are concerns of fast degradation due to impact damage when compared to their ductile metallic counterparts (Presby, et al., "Characterization and…").

The initial testing method to test the capability of CMCs in high temperature turbine environments was done inside furnaces, but that was not reflective of real life conditions. A study done by Panakarajupall, et al concluded that burner rigs reflect more real life conditions to test CMCs. Fatigue life of burner rig samples decreased by a whole magnitude as a result of thermal gradient stresses by heating only one side of the sample and convection occurring on the other side. The longitudinal cracking in both types of samples proved the contribution of thermal gradients (Panakarajupall, et al, "Tension-tension fatigue").

An additional study done by Panakarajupally, et al. found that when testing C/SiC composites if a high temperature preload is exerted then unloaded, the samples last longer during further testing. The fibers in the sample when under high temperature and load before failure begin to stretch, resulting in permanent stretching as the sample is cooled. This improves the uniformity of the fiber length and increases the load bearing area. Samples were found to increase fracture resistant capability by almost 39% (Panakarajupally, et al., "Thermo-mechanical…").

One method to help push the temperature limits of CMCs are thermal barrier coatings (TBCs). These coating systems consist of an insulating ceramic layer, reducing creep and oxidation rates, and a metallic bond layer, which also reduces oxidation and allows for strong adhesion to the substrate (Watson, Levine, "Deposition stress…"). Although there are also concerns with the coating. Spallation is a major concern

for the ceramic layer, which is usually a result of oxidation. In addition, the differences in thermal expansion coefficients between the coating and substrate may result in transient or steady state stresses (Watson, Levine, “Deposition stress…”).

An experiment completed by Watson and Levine tested the failure of a plasma spray TBC at two different plasma arc currents, three different cooling methods and two different numbers of passes. The coating was made of a “Ni-Cr-A1-Y bond coat and a partially yttria- stabilized zirconia ceramic coat” at a thickness of 0.1 millimeters with either one pass or eight passes (Watson, Levine, “Deposition stress…”). Three cylindrical samples of Waspaloy were being tested in a burner rig environment: a hollow tube with no airflow, a hollow tube with 20C airflow, and a solid tube. Scanning electron microscopy was used to view the microstructural features of the coating. Coating life was found to increase when the plasma spray power level was lower, the substrate had the opportunity to dissipate heat (ie cooled or solid sample), and when time span the heat was applied to the specimen at a specific location (number of passes) (Watson, Levine, “Deposition stress…”).

A study completed by Mauget, et al. tested two AM1 single crystal disks with a SAFRAN– SNECMA coating system made of a yttria stabilized zirconia top coat and a NiAlPt bond coat. The bond coat was deposited using aluminum phase vapor Snecma (Snecma’s aluminising process), and the top coat was deposited by electron beam physical vapor deposition (EB-PVD). The burner rig tests were completed at 1100 C at 120 MPa and 500 C at 700-800MPa, and an over-aging was completed at 1100 C for 100 hours for about half the samples. The tests showed that prior thermal aging increased cyclic ratcheting while in compression due to the degradation of the substrate’s creep strength in the 1100 C samples. In addition, lowering the maximum tensile stress from 800 to 700MPa increased the thermomechanical fatigue lifetime. Finally, introducing internal cooling leads to an increased thermomechanical fatigue life due to a reduction in crack propagation rate along the specimen’s thickness (Mauget, et al., “Damage mechanisms…”).

References

Cao, Peng, et al. Advanced Ceramics for Energy Storage, Thermoelectrics and Photonics. Elsevier, 2023.

Mauget, Florent, et al. “Damage mechanisms in an EB-PVD thermal barrier coating system during TMF and TGMF testing conditions under Combustion Environment.” International Journal of Fatigue, vol. 99, June 2017, pp. 225–234, https://doi.org/10.1016/j.ijfatigue.2016.08.001.

Panakarajupally, Ragav P., Manigandan Kannan, et al. “Tension-tension fatigue behavior of a melt-infiltrated sic/sic ceramic matrix composites in a combustion environment.” Journal of the European Ceramic Society, vol. 41, no. 5, May 2021, pp. 3094–3107, https://doi.org/10.1016/j.jeurceramsoc.2020.10.007.

Panakarajupally, Ragav P., Michael J. Presby, et al. “Thermomechanical characterization of SiC/Sic Ceramic Matrix Composites in a combustion facility.” Ceramics, vol. 2, no. 2, 17 June 2019, pp. 407–425, https://doi.org/10.3390/ceramics2020032.

Presby, Michael J., et al. “Characterization and simulation of foreign object damage in curved and flat SiC/Sic Ceramic Matrix Composites.” Ceramics International, vol. 45, no. 2, 1 Feb. 2019, pp. 2635–2643, https://doi.org/10.1016/j.ceramint.2018.10.207.

Watson, James W., and Stanley R. Levine. “Deposition stress effects on the life of thermal barrier coatings on burner rigs.” Thin Solid Films, vol. 119, no. 2, 14 Sept. 1984, pp. 185–193, https://doi.org/10.1016/0040-6090(84)90533-9.

Performance of Complex Geometry Composite Hydrogen Storage Tanks Using Additive Manufacturing

Student Researcher: Andrew P. Frankowski

Advisor: Dr. K. T. Tan

The University of Akron
Mechanical Engineering

Abstract
Recent advances in hydrogen fuel cell technology have made hydrogen powered air vehicles increasingly viable. One of the key challenges for such vehicles is the space-efficient storage of liquid hydrogen. This research aims to take advantage of the complex geometry capabilities of Additive Manufacturing to create non-traditional, space-optimized pressure vessels. In particular, this research is investigating the performance of a pressure tank that conforms to an airfoil shape.

Recent advancements in composite pressure vessel (CPV) technology have significantly influenced the development of next-generation hydrogen storage tanks. Carbon Fiber Reinforced Polymers (CFRP) are particularly well-suited for this application due to their high strength-to-weight ratio, which is crucial for the aerospace industry. Type V CPVs, which are pressure vessels entirely constructed with composite materials without a metallic or polymer liner, are the state-of-the-art technology for high-pressure fluid storage. As described by Air et al. these vessels depend solely on the carbon fiber laminate for both structural integrity and fluid containment, eliminating the need for an internal liner, further reducing the weight of the components (Air et al., 2023).

Magliano et al. conducted a literature review analyzing over 50 studies related to hydrogen safety and storage. Their findings emphasize the growing reliance on composite materials in hydrogen infrastructure, particularly for thin-walled, lightweight storage tanks for aerospace and mobile energy systems (Magliano et al., 2024).

Zhou et al. provide a detailed review on the value of using Finite Element Analysis (FEA) as a tool for assessing the structural integrity of pressure vessel designs (Zhou et al., 2022). Building on these approaches, this study utilizes FEA in Abaqus to compare circular pressure vessels of varying inner diameters and wall thicknesses with airfoil-shaped designs. Additionally, the effect of incorporating an internal stringer within the airfoil geometry was evaluated to improve structural stiffness and reduce deformation within the pressure vessel.

Preliminary results from FEA simulations show that while circular geometries perform predictably under internal pressure, the airfoil design experiences localized stress concentrations which lead to excessive deformation. By introducing strategic reinforcement, such as a stringer, these high deformations can be reduced. These findings support the potential of CFRP airfoil-shaped tanks which can serve as dual-purpose components for both hydrogen storage and structural load bearing in an aircraft. Experimental validation via burst pressure testing is planned for future work.

Project Objectives
The objective of this study is to investigate the structural behavior of non-circular composite pressure vessels (CPVs). Utilizing Additive Manufacturing allows us to create non-traditional cross-section designs

that incorporate geometrical features that are not feasible with traditional filament winding for CPV manufacturing. By introducing structural features, this research aims to explore alternative tank geometries that allow for improved space efficiency for hydrogen fuel storage in aerospace applications.

FEA is used to evaluate and compare how stresses propagate through various CPV designs and to identify critical regions for targeted reinforcement. The study begins with circular cross-sections of varying inner diameters to isolate the influence of curvature on the pressure vessel performance. Then the wall thickness of these circular geometries is varied to understand its effect as well. These results are then compared to an airfoil-shaped vessel, with and without an internal stringer as structural reinforcement, to assess how complex geometries influence their strength and stability. Ultimately the goal is to inform the design of lightweight, structural hydrogen tanks suitable for advanced air vehicles.

Methods

The material being used is a composite nylon-carbon fiber 3D printer filament called Onyx from the company Markforged. It is being reinforced with an additional continuous carbon fiber bundle which is printed as a perimeter of the cross-section. This orientation for the reinforcement material provides increased hoop strength and increased resistance to deformation caused by internal pressure. These materials are manufactured using the Markforged Mark Two composite 3D printer, which allows for dual-material extrusion.

FEA was conducted using Abaqus to evaluate the structural performance of each pressure vessel cross-section design. A composite layup was defined within Abaqus to accurately represent the anisotropic behavior of the reinforced specimens, with fiber orientation aligned around the perimeter of the geometries to match those of the 3D printed specimens. The simulations were conducted under idealized boundary conditions to isolate the radial stresses induced by internal pressure.

The material properties for Onyx and the continuous carbon fiber reinforcement will be validated utilizing experimental materials testing to be conducted in the future. The current values are placeholders to enable preliminary design comparison and exploration of structural designs. The results of this study will be quantified by comparing the performance of the airfoil shaped pressure vessel with its corresponding circular counterpart.

Future work will involve conducting experimental burst pressure testing on the 3D printed specimens. The specimens will be clamped firmly between two solid steel plates to replicate the boundary conditions used in the FEA simulations. The results of these experiments will then be used to validate the Abaqus simulations. Once validated, the model can then be used to analyze a larger variety of non-circular designs with different structural reinforcement geometries.

Results and Discussion

FEA was performed on a range of CPV designs to evaluate the structural response to internal pressurization. The specimens were subjected to an internal pressure of 0.2 MPa. The boundary conditions constrained all three rotational degrees of freedom along the profile of the CPV. The translation normal to the cross section was also constrained, limiting the specimen to experiencing only radial deformation.

Circular geometries with an inner diameter of 80 mm, 100 mm, and 120 mm (Figure 1) were analyzed with three wall thicknesses: 2.8 mm, 3.7 mm, and 4.6 mm. These wall thicknesses correspond to having one, two, and three reinforcement perimeters respectively, which we refer to as “Single Reinforced”,

“Double Reinforced”, and “Triple Reinforced” (Figure 2). Results showed that decreasing the number of reinforcement perimeters lead to an increase in both maximum stress and overall deformation. Additionally, specimens with smaller internal diameters exhibited lower maximum stress and displacement, indicating that increased curvature contributes to improved resistance under internal pressure (Figure 3a and 3b).

The airfoil-shaped pressure vessel exhibited a significantly different stress distribution leading to varied deformation along the profile. Under internal pressure, the airfoil’s leading and trailing edges were pulled inward, while the top and bottom surfaces bulged outward (Figure 2a). This deformation caused the airfoil to approach a more circular shape, which aids in equalizing the internal stresses caused by the pressurization. Stress concentrations were observed at the leading edge, trailing edge, and near the center of the upper and lower surfaces.

The results of our circular profiles and airfoil design suggest that the high stress regions observed in the airfoil-shaped vessels are largely driven by induced bending stresses resulting in large deformations under pressure, rather than inherent geometric stress concentrations. This distinction highlights the importance of controlling deformation in non-circular designs through internal structural reinforcement.

To mitigate these extreme deformations, a structural stringer was introduced inside the airfoil. This style of reinforcement is typically not available for the traditionally manufactured filament wound CPVs. The stringer substantially reduced the deformation in the airfoil, particularly along the top and bottom surfaces of the airfoil. However, it should be noted that local stress concentrations were introduced at the connection between the stringer and the airfoil profile. These stresses could be addressed in future designs by modifying the interface geometry, such as adding a fillet or gradually tapering the stringer to distribute the loads more evenly.

Additionally, the position of the stringer had a notable impact on the performance of the pressure vessel. Two stringer locations were compared, one with the stringer located at the midpoint of the chord line, the other with the stringer located one-third of the distance from the leading edge. The design placing the stringer one-third of the distance from the leading edge reduced the peak stresses at the leading edge more effectively than a centered placement, however it allowed for greater deflection in the rear section of the profile. This suggests that strategic placement of the internal reinforcement geometry can be used to redistribute stress away from critical regions, as well as resisting deflection which can cause additional high stress concentrations.

Although the material properties used in the simulations are unverified placeholders, the trends observed provide a valuable example of the concept of selective reinforcement to achieve non-circular pressure vessel designs. The ability to resist deformation through internal geometry and reinforcement design demonstrates the potential of airfoil-shaped tanks for dual-function use, both as fuel storage and structural support in aerospace applications. Ongoing work will include the validation of the FEA model through physical burst pressure testing.

Figures/Charts

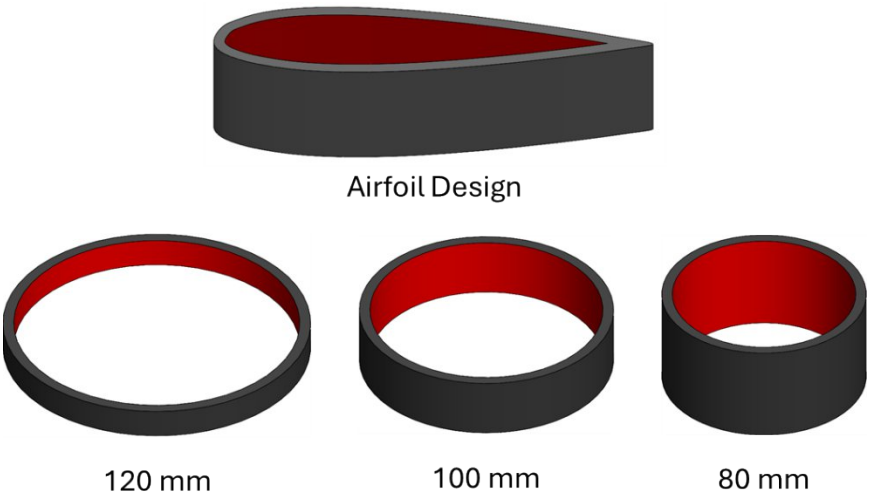


Figure 1. Selection of specimen geometries which were simulated using Abaqus Finite Element Analysis

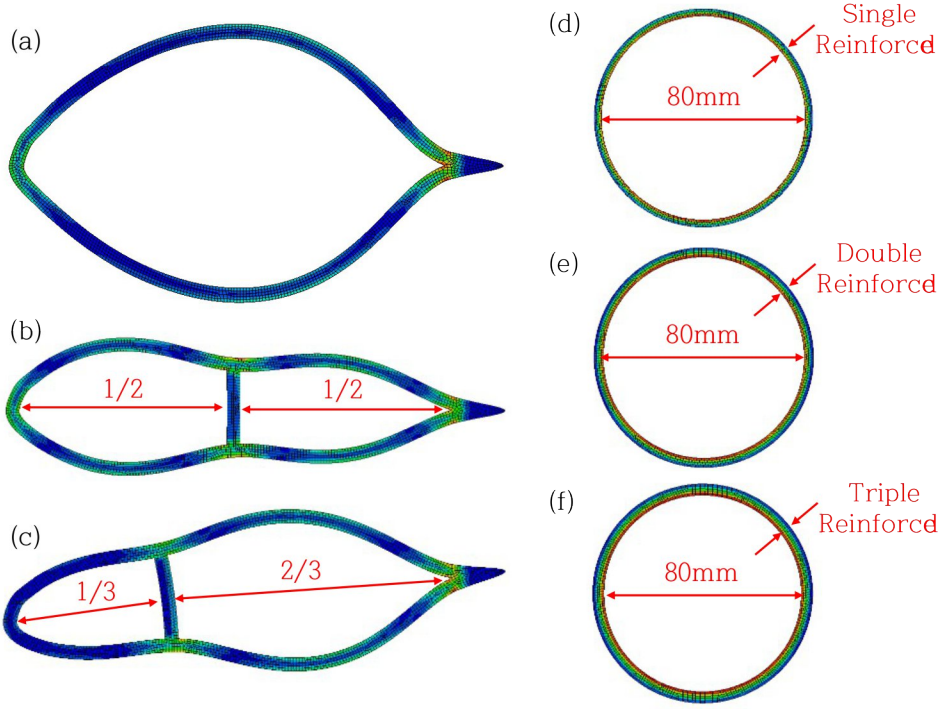


Figure 2. Stress distributions within deformed airfoil designs (a) No Stringer, (b) Midpoint Stringer, (c) Thirds Stringer and deformed circular designs (d) Single Reinforced, (e) Double Reinforced, (f) Triple Reinforced.

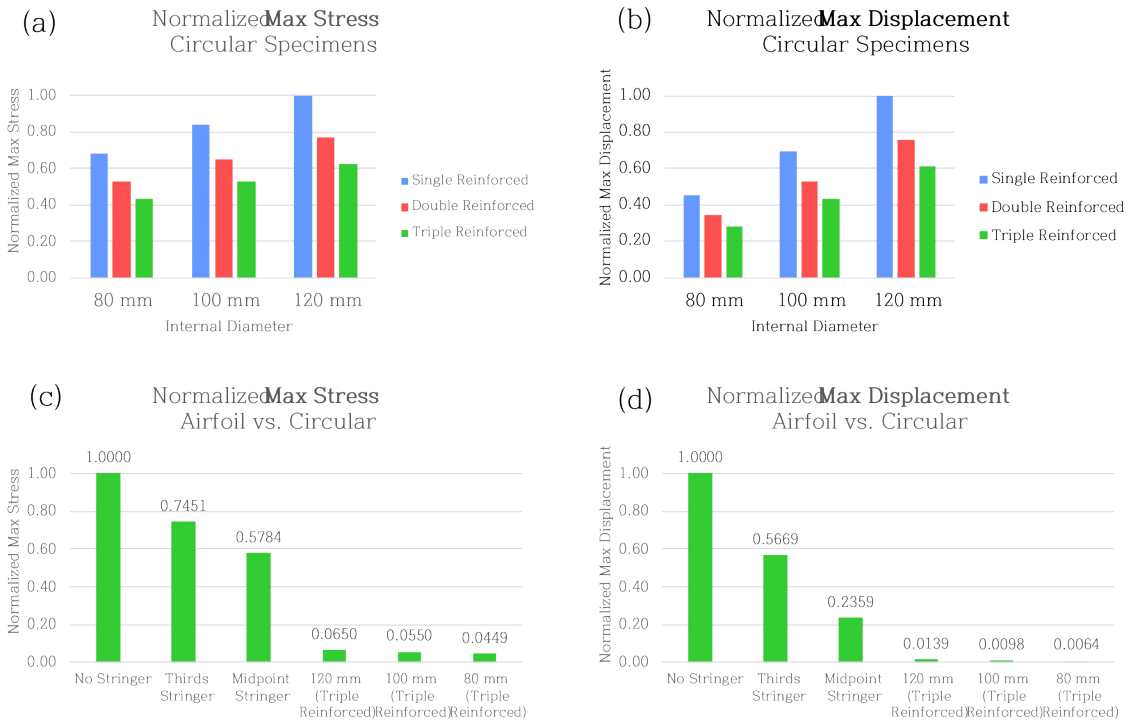


Figure 3. Normalized maximum stress and displacement of circular and airfoil-shaped designs

Acknowledgments

The author gratefully acknowledges the support of the Ohio Space Grant Consortium for funding this research. Special thanks to Dr. K. T. Tan for his guidance and mentorship throughout the project. Appreciation is also extended to the Department of Mechanical Engineering at the University of Akron for providing access to the necessary equipment and facilities that made this work possible.

References

[1] Air, A., Shamsuddoha, M., & Gangadhara Prusty, B. (2023). A review of Type V composite pressure vessels and automated fibre placement based manufacturing. Composites Part B: Engineering, 253, 110573. https://doi.org/10.1016/j.compositesb.2023.110573

[2] Magliano, A., Perez Carrera, C., Pappalardo, C. M., Guida, D., & Berardi, V. P. (2024). A Comprehensive Literature Review on Hydrogen Tanks: Storage, Safety, and Structural Integrity. Applied Sciences, 14(20), Article 20. https://doi.org/10.3390/app14209348

[3] Zhou, W., Wang, J., Pan, Z., Liu, J., Ma, L., Zhou, J., & Su, Y. (2022). Review on optimization design, failure analysis and non-destructive testing of composite hydrogen storage vessel. International Journal of Hydrogen Energy, 47(91), 38862–38883. https://doi.org/10.1016/j.ijhydene.2022.09.028

The Impact of Longwave Radiation on the Formation of Marine Stratocumulus Clouds

Student Researcher: Sophia Greene

Advisor: Dr. Thijs Heus

Cleveland State University

M.S. Applied Physics

Abstract

Marine stratocumulus clouds (MSc) play a significant role in the Earth's climate, yet their sensitivity to atmospheric conditions remains a subject of ongoing research. This work focuses on the radiative effects of water vapor on MSc formation, specifically investigating how the liquid water path (LWP) is influenced by changes in lower tropospheric stability (LTS) and the free-tropospheric humidity difference relative to the surface (often related to Δqt, the difference in specific humidity between the sea surface and the free troposphere). While previous studies have primarily focused on entrainment and mixing processes, the impact of increased free tropospheric water vapor on the longwave radiative flux (LW-Flux) into the cloud layer warrants further investigation [cf. 1]. To explore this, Large Eddy Simulations (LES) were run across a range of LTS and humidity difference values under constant nocturnal ('eternal night') conditions, utilizing DYCOMS-II RF02 flight data for initial conditions. The analysis centered on the relationship between LW-Flux at the cloud layer and LWP, as well as how LW-Flux is modulated by LTS and humidity differences. Results demonstrate that increased humidity in the free troposphere leads to enhanced downwelling longwave radiation, which warms the cloud layer. This warming effect increases the saturation mixing ratio within the cloud layer, leading to a decrease in LWP with an increase in free tropospheric moisture under stable conditions, a potentially counterintuitive result challenging traditional views focused solely on entrainment.

Introduction

Clouds exert a profound influence on Earth's climate system, yet accurately modeling their complex and dynamic behavior remains a significant challenge due to non-linear feedback cycles between solar radiation, cloud cover, and turbulent flow [6]. This is especially true for marine stratocumulus (MSc) decks, which cover vast ocean areas and significantly impact the Earth's radiative budget. These clouds typically form under conditions of strong lower tropospheric stability (LTS) and exhibit significant sensitivity to changes in humidity, particularly the difference between the sea surface and the overlying free troposphere [3]. Understanding how these key factors influence cloud formation, evolution, and response to environmental changes is crucial for improving regional and global climate projections [11].

Existing research provides a valuable foundation. Studies using Large Eddy Simulations (LES) illuminate the sensitivity of these clouds to their environment [11]. Observational studies, using remote sensing, reanalysis, and airborne data, have identified factors like sea surface temperature (SST), air temperature (e.g., T850), and specific humidity (e.g., q950) as influential in MSc dynamics and dissipation [8], highlighting the need to connect models with real-world variability. Research suggests that overall warming may thermodynamically favor cloud thinning [4]. Furthermore, intercomparisons using LES and single-column models (SCMs) predict overall positive feedback in response to climate perturbations [2, 11], though discrepancies exist. LES results suggest positive feedback from SST increase is primarily due to LWP decrease [cf. 5], while SCM results show dependence on both LWP and total cloud cover [11]. SCMs also tend to simulate boundary layers that are too shallow, cool, and moist compared to LES [10], underscoring the need for further refinement.

Building upon these insights, this research aims to advance our understanding of how LTS and humidity modulate stratocumulus behavior, focusing particularly on the role of longwave radiation. We hypothesize that two primary effects significantly impact cloud formation and persistence:

1. **Entrainment and Mixing:** Entrainment mixes drier air from aloft into the cloud layer. Increasing atmospheric stability generally suppresses entrainment [11]. This research investigates these dynamics across a wider parameter space.

2. **Infrared Radiation:** Changes in humidity above the boundary layer impact infrared downwelling radiation [cf. 1]. This affects cloud temperature, internal saturation levels, and potentially the entrainment rate itself. This work dissects how these radiative processes vary under diverse humidity and stability conditions.

By exploring these interactions, particularly the radiative effects often overlooked in relation to LWP, this research strives to bridge high-resolution modeling insights with real-world dynamics.

Project Objectives

The central objectives of this research are:

1. **Expand Parameter Space Understanding:** To increase the known range of possible Liquid Water Path (LWP) values as a function of Lower Tropospheric Stability (LTS) and the humidity difference between the surface and free troposphere (Δqt). Current literature presents a limited view, particularly regarding the radiative influence.

2. **Describe LW-Flux Influence:** To describe how the Longwave Radiative Flux (LW-Flux) at the cloud layer influences LWP in steady state, detailing how LW-Flux itself changes in response to variations in LTS and Δqt. This addresses a gap where the radiative effect of water vapor on LWP has often been disregarded [cf. 1].

3. **Quantify Humidity and Stability Impacts:** To gain a better understanding of how MSc respond to varying fluxes of moisture and energy, including entrainment drying, and *specifically* the effects of increased humidity in the free troposphere (leading to enhanced downwelling longwave radiation and cloud layer warming).

4. **Improve Model Representation:** Ultimately, to improve the representation of MSc clouds in climate models, addressing current uncertainties [3]. This involves understanding processes within domains of real-world LTS and Δqt where water vapor's radiative effect is significant for LWP. This can lead to improved predictions of phenomena like the morning breakup of clouds, crucial for solar energy, farming, and aviation [cf. 8].

Methodology

To investigate the interplay between stability, humidity, and longwave radiation on stratocumulus clouds, we employed Large Eddy Simulations (LES). This project explored a regime of Lower Tropospheric Stability (LTS) and free tropospheric humidity difference (Δqt) designed to investigate potential phase transitions in cloud behavior, informed by preliminary research suggesting that for high stability, a more moist free troposphere results in less LWP.

The simulations were conducted using the MicroHH LES package [12 - *Note: Add van Heerwaarden et al. (2017) reference*], chosen for its efficiency in running GPU-accelerated simulations. Computational resources included Dr. Heus's personal cluster (2x V100 GPUs), the CSU Vikings cluster (2x H100 GPUs), and the NSF-MRI funded cluster (30x A100 GPUs).

Simulation Setup:

- **Model:** MicroHH LES [12]
- **Resolution:** 25m horizontal and vertical grid spacing within a 6.4km x 6.4km x Z domain (where Z is sufficiently large to contain the boundary layer and relevant free troposphere).
- **Initial Conditions:** Based on the DYCOMS-II RF02 case, a well-established benchmark for nocturnal stratocumulus [cf. 7].
- **Microphysics:** Interactive two-moment microphysics scheme (e.g., SB06 or similar, specify if known).
- **Radiation:** Interactive longwave radiation scheme capable of responding to humidity profiles. Shortwave radiation was excluded, simulating constant nocturnal ('eternal night') conditions.
- **Parameter Space Explored:**
    - **LTS Proxy (Temperature Difference):** The difference in potential temperature between the free troposphere (e.g., at 1-2 km) and the sea surface was varied systematically across a range representing weakly to strongly stable conditions (e.g., corresponding roughly to the [5 to 23] K range mentioned, clarify exact definition).
    - **Humidity Proxy (Specific Humidity Difference, Δqt):** The difference in specific humidity between the sea surface and the free troposphere was varied systematically (e.g., [-6.5 to -2.5] x 10^{-3} kg/kg range mentioned).
    - *Initial Humidity Profile:* Specific details of the initial humidity profile setup, including the humidity layer above the clouds (e.g., Z [500] m mentioned, clarify meaning - base height? thickness?), are crucial for the radiative effects.

All simulations were run under 'eternal night' conditions (excluding the diurnal cycle and solar radiation) to isolate the effects of longwave radiation, thermodynamics, and turbulence, and were run to a quasi-steady state to analyze the resulting cloud properties (LWP, cloud top/base height, thickness) and radiative fluxes (especially LW-Flux at cloud top/base) as a function of the imposed LTS and Δqt conditions.

Results and Discussion

The LES simulations reveal a strong interplay between tropospheric moisture (represented by Δqt) and atmospheric stability (represented by LTS) in determining marine stratocumulus properties and radiative balance. Our analysis focused on characterizing cloud structure and LWP across different regimes, conceptually categorized as Moist-Unstable, Moist-Stable, Dry-Unstable, and Dry-Stable based on the combinations of humidity difference and stability parameters explored.

Influence of Tropospheric Moisture (Δqt): A key finding confirms the significant impact of free tropospheric moisture on cloud properties, but highlights the crucial role of longwave radiation. Consistent with the hypothesis, higher free tropospheric humidity (smaller magnitude of negative Δqt, i.e., 'Moist' conditions) leads to enhanced downwelling longwave radiation warming the cloud top [cf. 1]. This warming increases the saturation specific humidity within the cloud. Consequently, for a given total water content, less water condenses, leading to thinner clouds and lower LWP compared to drier free tropospheric conditions ('Dry' cases, larger magnitude negative Δqt) *under stable conditions*. This radiative warming effect counteracts and can dominate over potential moisture supply effects from reduced entrainment dryness. The overall atmospheric cooling effect was lower in moist conditions due to this enhanced

downwelling radiation trapping outgoing heat, whereas dry conditions with a large humidity gradient facilitated stronger radiative cooling from the cloud top.

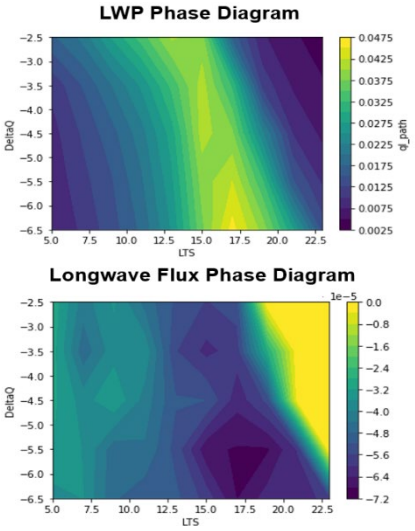
Influence of Atmospheric Stability (LTS): Atmospheric stability primarily governed the vertical structure and placement of the cloud layer. Higher LTS (Stable conditions) suppressed vertical mixing, leading to lower cloud tops and often sharper radiative flux divergence near the cloud top. Lower LTS (Unstable conditions) allowed for deeper vertical mixing, resulting in higher cloud tops. The Dry-Unstable regime (low stability, dry free troposphere) exhibited the highest cloud tops and thickest clouds, benefiting from both convective potential and strong radiative cooling driving turbulence. Cloud base height also varied, being highest in the Moist-Unstable case and lowest in the Dry-Stable case.

Interaction Effects and Mechanisms: The simulations showed that the relationship between moisture and LWP is strongly modulated by stability.

- **Stable Regimes (Moist-Stable, Dry-Stable):** In highly stable conditions, the radiative effect of free tropospheric moisture becomes dominant. Increased moisture (Moist-Stable) leads to significantly less LWP compared to the Dry-Stable case, driven by the enhanced downwelling LW radiation warming the cloud top, despite potentially reduced entrainment drying [cf. 1, 11]. The Dry-Stable case developed thick clouds due to strong radiative cooling at the cloud top in the absence of significant overlying moisture.
- **Unstable Regimes (Moist-Unstable, Dry-Unstable):** In less stable conditions, entrainment plays a more vigorous role [11]. The Dry-Unstable case developed the thickest, highest clouds due to strong radiative cooling enhancing turbulence and entrainment of dry air, which fuels condensation lower down. The Moist-Unstable case resulted in the thinnest clouds overall, likely reflecting a complex balance where weaker radiative cooling (due to moist overlying air) and entrainment of relatively moist air limit the LWP development compared to the Dry-Unstable case.

These results underscore the importance of including accurate representations of water vapor's radiative effects, particularly the downwelling longwave component, when modeling MSc LWP sensitivity to environmental conditions. The finding that increased free tropospheric humidity can lead to *decreased* LWP under stable conditions, driven by radiative warming, contrasts with simpler frameworks focused solely on entrainment drying and has significant implications for climate model parameterizations [cf. 3, 10].

Figures



References

[1] Ackerman, A. S., Kirkpatrick, M. P., Stevens, D. E., & Toon, O. B. (2004). The impact of humidity above stratiform clouds on indirect aerosol climate forcing. *Nature*, 432(7020), 1014-1017. https://doi.org/10.1038/nature03174

[2] Blossey, P. N., Bretherton, C. S., Zhang, M., Cheng, A., Hill, A. A., Solomon, S., ... & Stevens, B. (2013). Marine low cloud sensitivity to an idealized climate change: The CGILS LES intercomparison. *Journal of Advances in Modeling Earth Systems*, 5(2), 234-258. https://doi.org/10.1002/jame.20025

[3] Bony, S., & Dufresne, J. L. (2005). Marine boundary layer clouds at the heart of tropical cloud feedback uncertainties in climate models. *Geophysical Research Letters*, 32(20). https://doi.org/10.1029/2005GL023851

[4] Bretherton, C. S., and P. N. Blossey (2014), Low cloud reduction in a greenhouse-warmed climate: Results from Lagrangian LES of a subtropical marine cloudiness transition, *J. Adv. Model. Earth Syst.*, 6, 91–114, https://doi.org/10.1002/2013MS000250

[5] Bretherton, C. S., P. N. Blossey, and C. R. Jones (2013), Mechanisms of marine low cloud sensitivity to idealized climate perturbations: A single-LES exploration extending the CGILS cases, *J. Adv. Model. Earth Syst.*, 5, 316–337, https://doi.org/10.1002/jame.20019

[6] Chen, T., Rossow, W. B., & Zhang, Y. (2000). Radiative effects of cloud-type variations. *Journal of Climate*, 13(1), 264-286. https://doi.org/10.1175/1520-0442(2000)013<0264:REOCTV>2.0.CO;2

[7] Chlond, A., Wolkau, A. Large-Eddy Simulation Of A Nocturnal Stratocumulus-Topped Marine Atmospheric Boundary Layer: An Uncertainty Analysis. *Boundary-Layer Meteorology* 95, 31–55 (2000). https://doi.org/10.1023/A:1002438701638

[8] Dadashazar, H., Crosbie, E., Majdi, M. S., Panahi, M., Moghaddam, M. A., Behrangi, A., Brunke, M., Zeng, X., Jonsson, H. H., and Sorooshian, A.: Stratocumulus cloud clearings: statistics from satellites, reanalysis models, and airborne measurements, *Atmos. Chem. Phys.*, 20, 4637–4665, https://doi.org/10.5194/acp-20-4637-2020 , 2020.

[9] Dal Gesso, S., Siebesma, A.P., de Roode, S.R. and van Wessem, J.M. (2014), A mixed-layer model perspective on stratocumulus steady states in a perturbed climate. *Q.J.R. Meteorol. Soc.*, 140: 2119-2131. https://doi.org/10.1002/qj.2282

[10] Dal Gesso, S., J. J. van der Dussen, A. P. Siebesma, S. R. Roode, I. A. Boutle, Y. Kamae, R. Roehrig, and J. Vial (2015), A single-column model intercomparison on the stratocumulus representation in present-day and future climate, *J. Adv. Model. Earth Syst.*, 7, 617–647, https://doi.org/10.1002/2014MS000377

[11] van der Dussen, J. J., S. R. de Roode, S. Dal Gesso, and A. P. Siebesma (2015), An LES model study of the influence of the free tropospheric thermodynamic conditions on the stratocumulus response to a climate perturbation, *J. Adv. Model. Earth Syst.*, 7, 670–691, doi:10.1002/2014MS000380.

[12] van Heerwaarden, C. C., van Stratum, B. J. H., Heus, T., Gibbs, J. A., Fedorovich, E., and Mellado, J. P.: MicroHH 1.0: a computational fluid dynamics code for direct numerical simulation and large-eddy simulation of atmospheric boundary layer flows, Geosci. Model Dev., 10, 3145–3165, https://doi.org/10.5194/gmd-10-3145-2017, 2017.

Using Imaging Spectroscopy to Assess Shifts in Phytoplankton Community Composition

Student Researcher: Emily Hyland

Advisor: Dr. Brice Grunert

Cleveland State University
Biological, Geological, and Environmental Sciences Department

Abstract
For years, chlorophyll has been the main water quality parameter in coastal aquatic systems. However, individual optical constituents like colored dissolved organic matter and phytoplankton absorption are more representative of specific stressors than chlorophyll is. Using bio-optical modeling, we can effectively represent the contributions of these parameters to satellite-observed reflectance. This helps to assess our ability to observe these optical parameters in coastal waters and assess uncertainty in our observations. This research project will build on demonstrations of phytoplankton absorption and community composition in the Great Lakes from satellite retrievals. Using select satellite imagery (from PACE) paired with an open-source bio-optics Python package to compare individual biogeochemical components to typical water quality indices including chlorophyll and harmful algal bloom indicators. Using code and workflows established by Dr. Grunert and other scientists, I will examine the extent to which phytoplankton absorption and associated pigments are observable in remotely sensed reflectance. I will then use this information to look at how accurately we can assess compositional shifts in phytoplankton community composition in optically complex coastal waters like the Great Lakes.

Project Objectives
The central goal of this research is to explore whether we can move beyond generalized assessments such as “the water is green” and begin identifying specific phytoplankton communities from remote sensing data. To this end, we aim to:

1. Characterize and quantify the sensitivity of remote sensing reflectance (Rrs) to variability in inherent optical properties (IOPs) in optically complex waters.

2. Evaluate our ability to retrieve phytoplankton pigments from reflectance spectra and relate these retrievals to community composition, with a focus on Lake Erie.

Methods
This project utilizes a 2024 data set that was collected as part of the PACE Validation Science Team project in the Great Lakes. Data includes radiometry, hyperspectral backscattering, discrete particulate and colored dissolved organic matter absorption, and biogeochemical variables including HPLC pigments, dissolved and particulate organic carbon concentrations, and suspended particulate matter concentrations. This data was used to validate a theorical open-source bio-optics model. This bio-optics model is a python package that provides a framework for forward and inverse modeling of above water multispectral and hyperspectral observation of natural water bodies. Using this model, I modified the phytoplankton absorption component to analyze its impact on variability in remote sensing reflectance (Rrs). Additionally, I applied the Derivative Analysis and Iterative Spectral Evaluation of Absorption (DAISEA2) algorithm, which enables Gaussian decomposition of absorption spectra, to investigate the contribution of individual pigments to overall phytoplankton absorption.

Results and Discussion

In order to characterize and quantify the sensitivity of remote sensing reflectance I used two different phytoplankton absorption spectra. The purpose of using two different phytoplankton absorption spectra is to see the differing effects of a higher or lower phytoplankton signal in a reflectance spectra. Figure one shows the two phytoplankton spectra I used for modification. The WLE4 phytoplankton absorption is used to make the water bluer and essentially remove phytoplankton signal from the reflectance spectra. The GB2 phytoplankton absorption is used to make the water greener and add more phytoplankton signal to the reflectance spectra. Figure two highlights the first station where the different phytoplankton spectra were applied. In figure two, WLE2 is a station within the western basin of Lake Erie that generally has blue water, so I wanted to focus specifically on adding more phytoplankton, essentially making that stations water greener. From this figure we can highlight three spectral changes that occur in the reflectance spectra. These changes can be seen in the colored circles that are highlighting the addition of troughs. The reason for these differences is due to the added pigments removing photons. We can also see that added pigments and more absorption decreases the overall reflectance spectra, which is expected. These emerging spectral features are affiliated with specific pigment differences and these differences are associated with both the biomass and composition of phytoplankton. In figure three the percent change plots allow us to once again see these troughs and associate the trough with specific phytoplankton pigments based on the wavelengths where the changes occur. Figure three also provides a way to not only see a loss in reflectance from the removal of photons but also allows us to quantify the magnitude of these spectral changes. Figures four and five are similar to figures two and three but this time are highlighting a station in Green Bay. This GB8 station has very green water so the idea was to focus on removing phytoplankton, essentially making the water bluer. In figure four, we can see that the modified spectra is higher in magnitude compared to the modeled and this is due to less absorption by phytoplankton so there is more light able to be scattered instead. Unlike WLE2, GB8 is losing troughs, and the reflectance spectra is flattening out due to more photons. This is seen in figure five where on the percent change figures there are peaks instead of troughs. Overall, both of these examples show that by modifying the amount of phytoplankton absorption contributing to a reflectance spectra we can start characterizing and quantifying the change in reflectance.

Figures/Charts

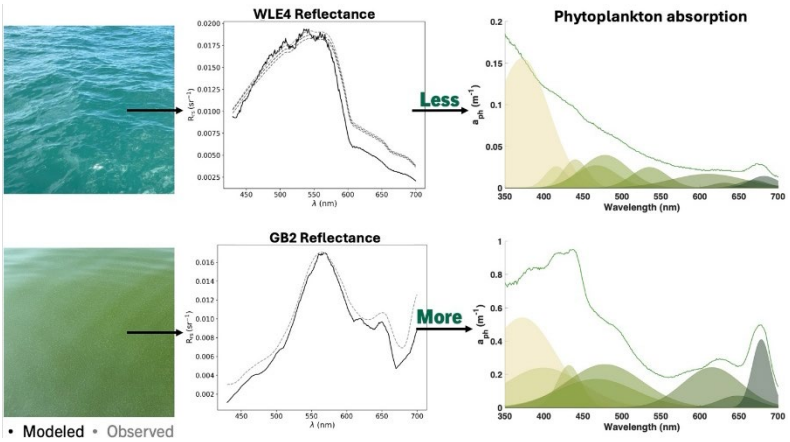


Figure 1: Phytoplankton absorption spectra used for modification. On the left is an image of the water color associated with the stations in the middle. The middle figures are remote sensing reflectance spectra for a station in western Lake Erie and Green Bay. The figures on the right are phytoplankton absorption figures with corresponding pigment contribution for both sites.

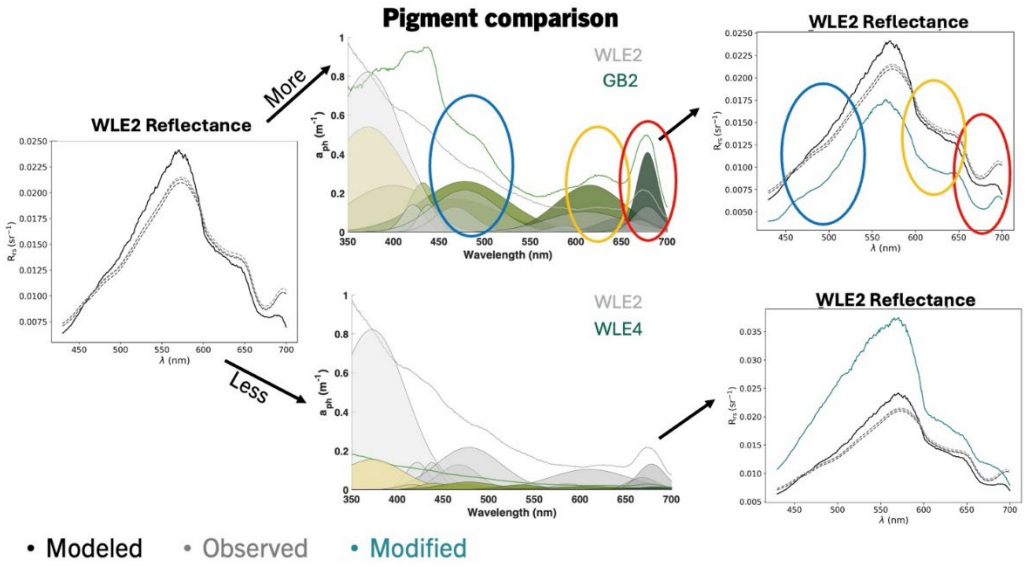


Figure 2: Western Lake Erie site 2 (WLE2) phytoplankton modification comparison. On the left is the remote sensing reflectance spectra for WLE2. The middle figures are phytoplankton absorption comparisons between the original absorption spectra (gray) and modified absorption (green). On the right is the corresponding reflectance comparison between the original reflectance (black) and the modified reflectance (blue). The colored circles are highlighting the changes in spectral shape and the corresponding difference in the pigment comparison.

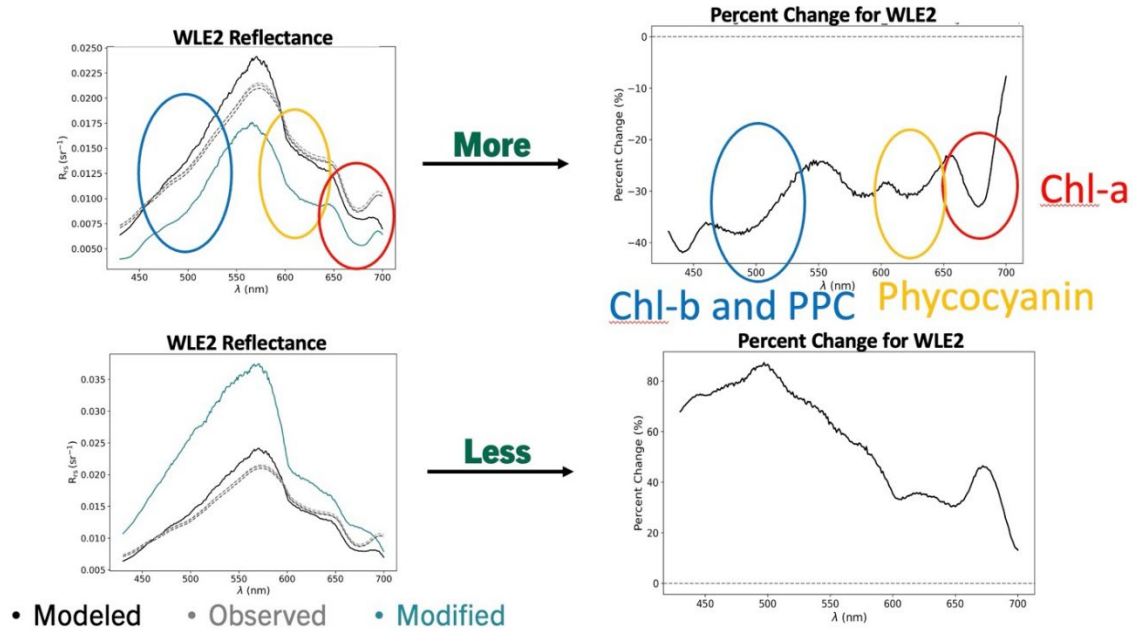


Figure 3: Western Lake Erie site 2 percent change comparison. On the left are the two reflectance spectra with the modified phytoplankton absorption. On the right is the percent change figures showing the difference between the modified and modeled reflectance spectra. The colored circles are highlighting the changes in spectral shape and the corresponding difference in the percent change.

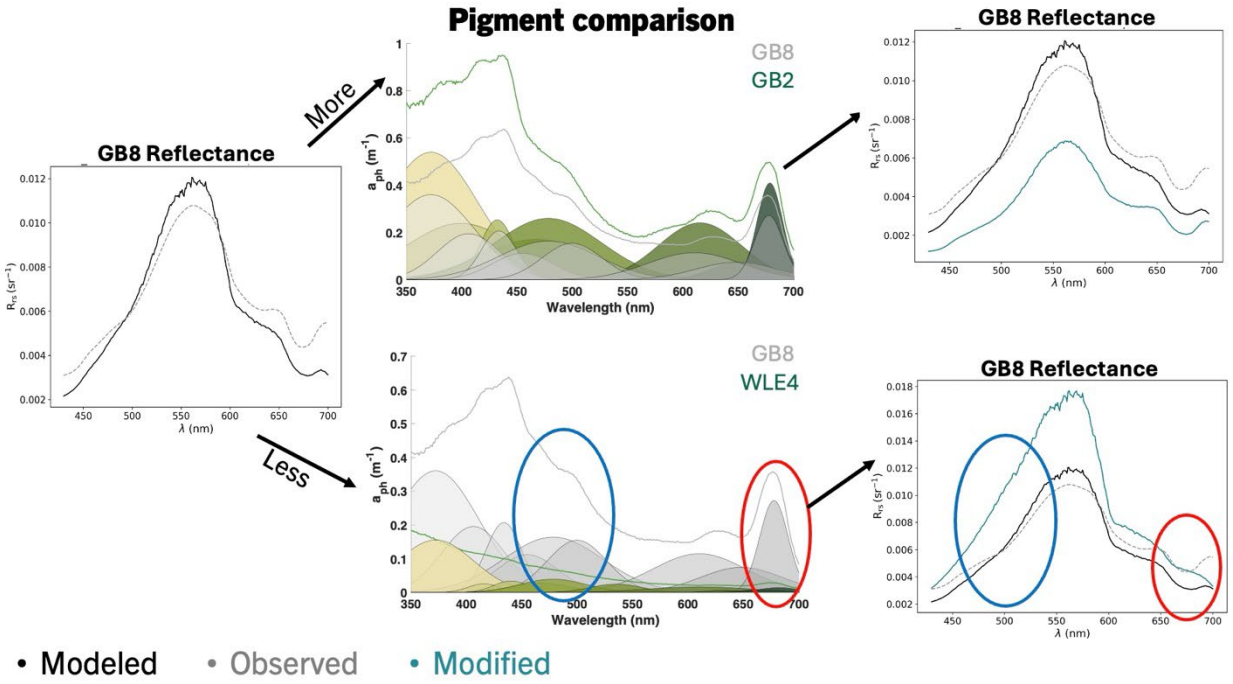


Figure 4: Green Bay site 8 (GB8) phytoplankton modification comparison. On the left is the remote sensing reflectance spectra for GB8. The middle figures are phytoplankton absorption comparisons between the original absorption spectra (gray) and modified absorption (green). On the right is the corresponding reflectance comparison between the original reflectance (black) and the modified reflectance (blue). The colored circles are highlighting the changes in spectral shape and the corresponding difference in the pigment comparison.

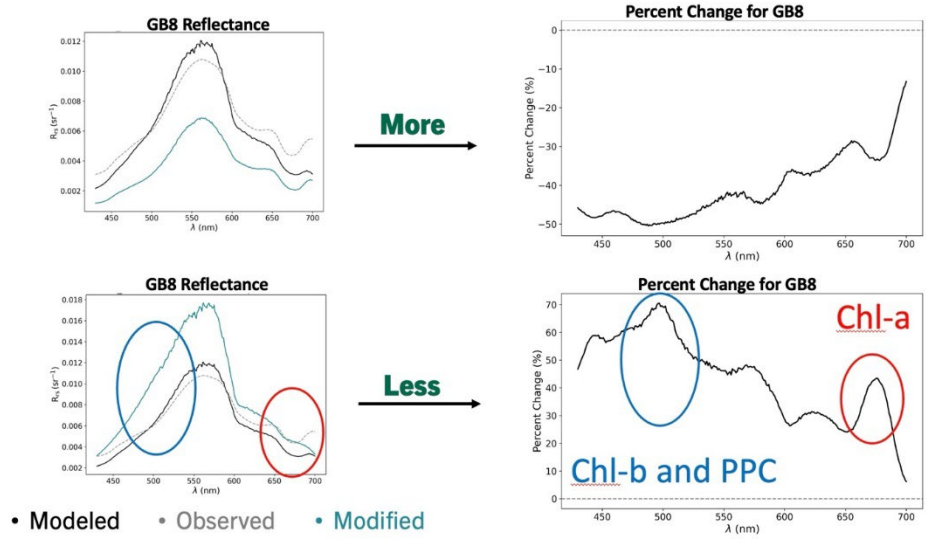


Figure 5: Green Bay site 8 percent change comparison. On the left are the two reflectance spectra with the modified phytoplankton absorption. On the right is the percent change figures showing the difference between the modified and modeled reflectance spectra. The colored circles are highlighting the changes in spectral shape and the corresponding difference in the percent change.

Acknowledgments

This work would not have been possible without the support of the Ohio Space Grant Consortium, my advisor, Dr. Brice Grunert, Audrey Ciochetto, Dr. Marcel König, Dr. Kelly Hondula, the entire Carbon and H_2(Optics) lab, and NASA. Thank you!

References

Grunert, B. K., Mouw, C. B., & Ciochetto, A. B. (2019). Deriving inherent optical properties from decomposition of hyperspectral non-water absorption. *Remote Sensing of Environment*, *225*, 193–206. https://doi.org/10.1016/j.rse.2019.03.004

König, M., Noel, P., Hondula. K.L., Jamalinia, E., Dai, J., Vaughn, N.R., Asner, G.P. (2023): bio_optics python package (Version x) [Software]. Available from https://github.com/CMLandOcean/bio_optics. [https://doi.org/10.5281/zenodo.10246860]

Quantitative Evaluation of Supercritical Fuel Injection for Rocket Applications via Rainbow Schlieren Deflectometry

Student Researcher: Henry Jacques

Advisor: Dr. C. Taber Wanstal

University of Dayton
Mechanical Engineering

Abstract
Schlieren imaging, a non-intrusive method for visualizing density gradients, has been predominantly qualitative since its inception in the mid-20th century. Recently, its application has expanded to quantitative measurements using Rainbow Schlieren Deflectometry (RSD), a method that uses color filters to encode deflection information.

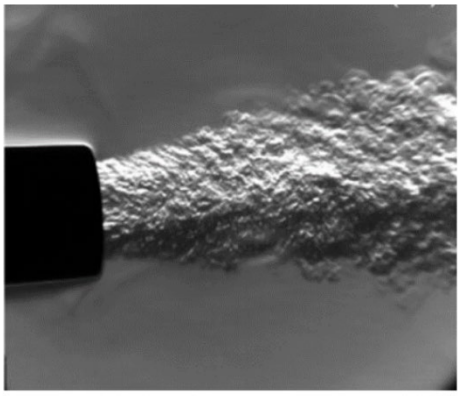


Figure 1. Conventional schlieren applied to a turbulent heated jet [1].

Conventional knife-edge schlieren setups create high-contrast images by blocking or passing deflected light, producing light and dark regions that correspond to density gradients. RSD replaces the knife edge with a rainbow filter, correlating hue with deflection distance to quantify fluid properties such as concentration and density.

This technique has been validated in applications such as turbulent jets and fuel injection studies, offering a valuable tool where intrusive measurement methods would disturb the flow. Recent works by Agrawal, Wanstall, and others have demonstrated RSD's potential in both subcritical and supercritical mixing regimes.

Project Objectives
This study aims to:

- Validate RSD in a turbulent subsonic helium jet, comparing results with Rayleigh scattering.
- Apply RSD to a supersonic helium jet for quantitative density measurements

Methods/Figures and Charts

Subsonic Case

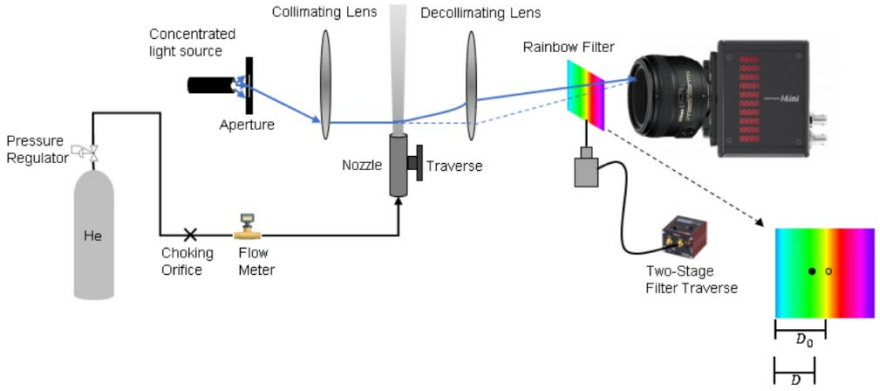


Figure 2.Schematic of subsonic experimental setup and RSD system

- **Helium Source:** Pressure-regulated and metered via Dakota GM3.
- **Flow Path:** Stainless steel tube (0.19 in. ID), ending in a 500 µm orifice.
- **Environment:** Ambient air at standard conditions.

Supersonic Case

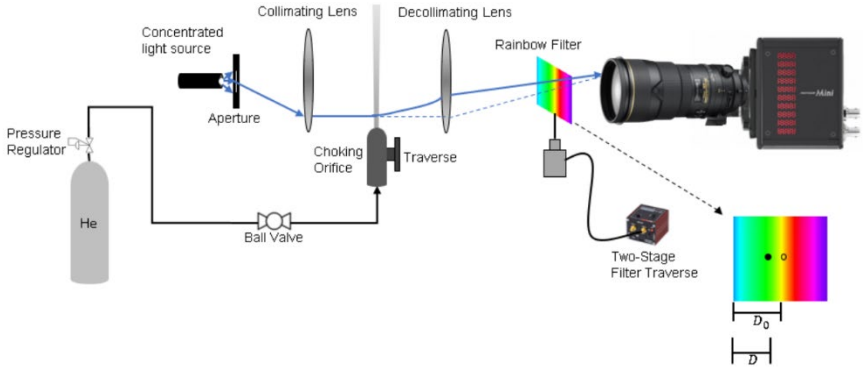


Figure 3. Schematic of supersonic experimental setup and RSD system

- **Higher Flow Rate**: Exceeds GM3 meter capacity; controlled via ball valve.
- **Jet Expansion**: Choked flow through the same orifice creates an under-expanded jet.

Optical System (Both Cases)

- **Light Source**: High-intensity broadband, passed through 30 µm aperture.
- **Lenses**: Two achromatic lenses (250 mm focal length, 76 mm diameter).
- **Filter**: 0.6 mm-wide rainbow filter on a motorized stage (ThorLabs KDC101).
- **Camera**: Photron AX Mini at 2000 fps, 14 µs exposure.
- **Lenses**: 50 mm (subsonic), 300 mm (supersonic) Nikon Nikkor lenses.

RSD images were processed in MATLAB. Images were captured in RGB, then converted to HSI space to extract hue values, essential for assigning unique deflection distances.

Calibration & Deflection Measurement

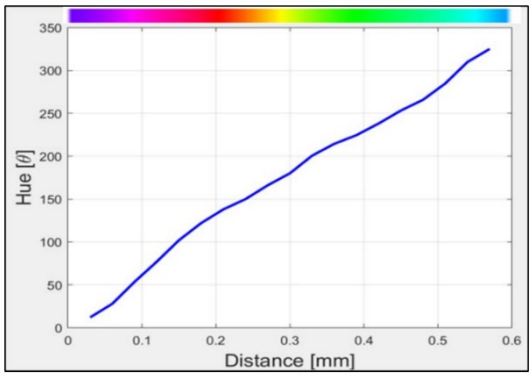


Figure 4. Hue to distance calibration curve. The shifted rainbow filter is shown above.

- A pixel-by-pixel calibration was performed by scanning across the filter in 0.03 mm increments.
- Hue–distance correlation is linear; used to calculate deflection angle (θ) via:

From Deflection to Concentration

- The transverse deflection angle $\theta_x(x, z)$ relates to the refractive index gradient through line integration.
- Assuming axial symmetry, the Abel transform is used to invert the measured angles into a 2D refractive index field:

η(ri,t)=∑j=1N+1Dijθx(xj,t)\eta(r_i,t) = \sum_{j=1}^{N+1} D_{ij} \theta_x(x_j,t)η(ri,t)=j=1∑N+1Dijθx(xj,t)

- Using the Gladstone–Dale equation, the refractive index field is translated into helium mole fraction:

n−1=PRT∑Miκixin - 1 = \frac{P}{RT} \sum M_i \kappa_i x_in−1=RTP∑Miκixi

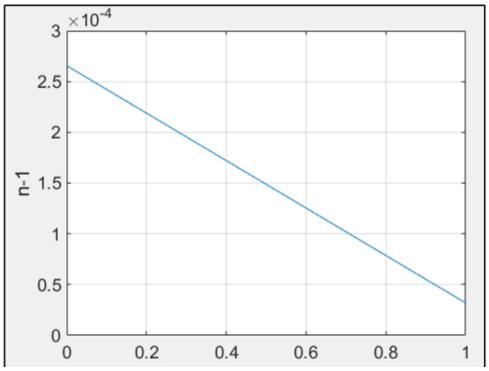


Figure 5. Refractive index of the helium-air mixture versus helium mole fraction.

Refractive index is nearly linear with helium mole fraction, enabling accurate concentration estimates.

Subsonic Jet Validation

Flow Characterization

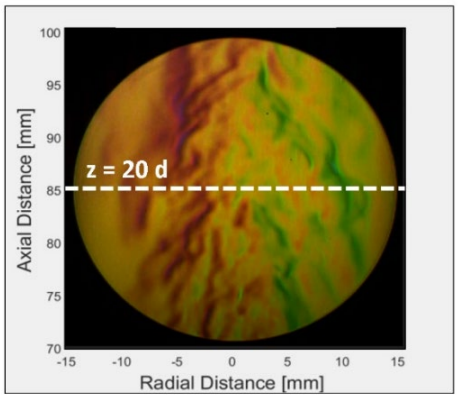


Figure 6. Instantaneous RSD Image

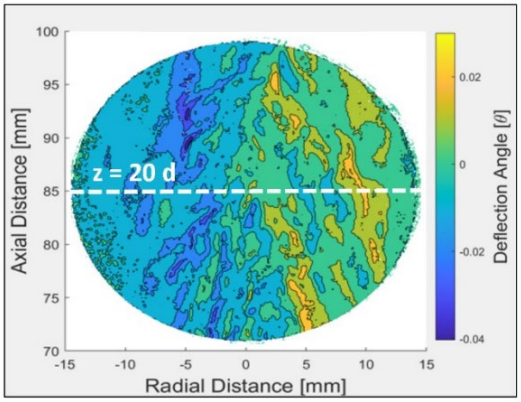


Figure 7. Instantaneous deflection angle

At Re = 800, RSD revealed turbulent structures at z = 20d, showing high deflection near eddies. Positive (yellow/red) and negative (blue/green) hues captured the fluctuating density gradients.

Time-Averaging for Quantification

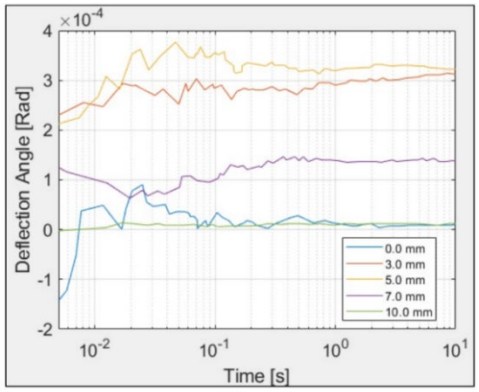


Figure 8. Time average deflection angle at different radial locations

Using over 1000 images, time-averaged deflection angles were obtained at various radial positions. A software averaging method was used due to exposure time constraints. Past research confirms negligible difference between software and hardware averaging [5].

Validation with Rayleigh Scattering

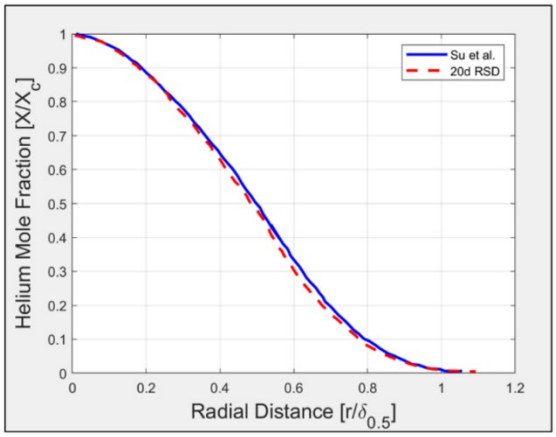


Figure 9. Nondimensional helium mole fraction

Deflection angles were converted to helium mole fraction and normalized by centerline mole fraction and jet width at half-maximum ($\delta_{o.5}$). As shown in Fig. 9, RSD data closely matched existing Rayleigh scattering results, validating the method's accuracy for turbulent free jets.

Results and Discussion

Supersonic Jet Results

Qualitative Observations

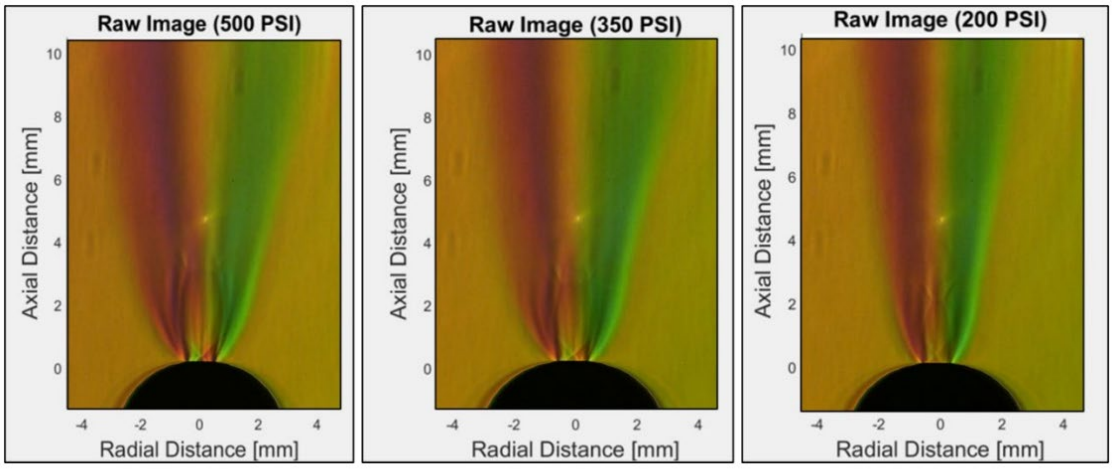


Figure 10. Supersonic RSD images at 500 PSI, 350 PSI, and 200 PSI.

At 200, 350, and 500 PSI, RSD images revealed:

- Expansion waves near the nozzle exit,
- Formation of Mach disks and shock triple points,
- Periodic shock cells and free jet boundaries.

As pressure increased, shock strength and jet width also increased. Minor optical anomalies included:

- Central reflections,
- Diffraction artifacts near the nozzle base.

Quantitative Results

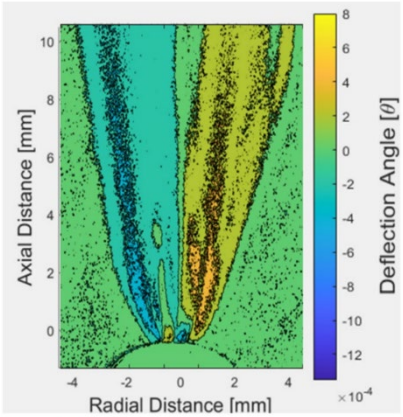


Figure 11. Instantaneous deflection angle

Deflection angles (Fig. 11) show a sharp boundary between the helium core and surrounding helium-air plume, marking the edge of the Mach barrel.

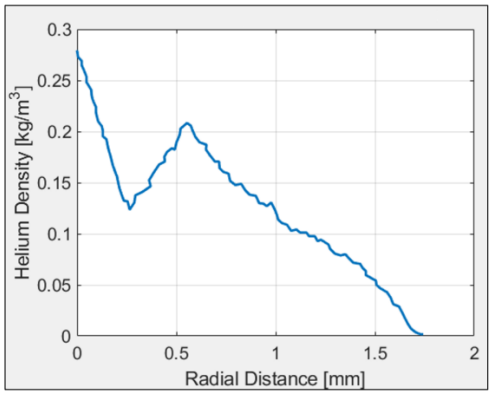


Figure 12. Helium density 1mm downstream

Helium density profiles (Fig. 12) reveal:

- High central density inside the shock cell,
- Gradual radial decrease due to mixing,
- Slight increase at the free jet boundary,
- Eventual decay to ambient values at the plume edge.

These results support RSD's capability for mapping density fields in supersonic turbulent environments. Further validation using alternative methods is recommended.

This study demonstrates that Rainbow Schlieren Deflectometry can provide accurate, quantitative measurements in both subsonic and supersonic helium jets.

Key Findings:

- Pixel-by-pixel calibration significantly improves measurement accuracy.
- Implementing a hue-prime filter mitigates light throughput loss.
- For turbulence studies, averaging over >1000 images ensures statistical convergence.
- RSD-derived mole fraction profiles align with Rayleigh scattering data.

Future Work

- Extend RSD validation for supersonic jets using independent techniques.
- Investigate real-gas behavior (e.g., CO_2), replacing the ideal gas assumption.
- Apply RSD to complex, multi-phase flow systems such as fuel injection in combustion applications

References

[1] Dobrosotskaya, J., Alrefaie, A., & Schmidt, B. E. (2023, January). *A Quantitative Comparison of Background Oriented and Conventional Schlieren Visualization*. AIAA SCITECH 2023 Forum. https://doi.org/10.2514/6.2023-2439

[2] Agrawal, A. K., & Wanstall, C. T. (2018). *Rainbow schlieren deflectometry for scalar measurements in fluid flows*. *Journal of Flow Visualization and Image Processing*, 25(3–4), 329–357. https://doi.org/10.1615/jflowvisimageproc.2018028312

[3] Al-Ammar, K., Agrawal, A. K., Gollahalli, S. R., & Griffin, D. (1998). *Application of rainbow schlieren deflectometry for concentration measurements in an axisymmetric helium jet*. *Experiments in Fluids*, 25(2), 89–95. https://doi.org/10.1007/s003480050211

[4] Pasumarthi, K. S., & Agrawal, A. K. (2003). *Schlieren measurements and analysis of concentration field in self-excited helium jets*. *Physics of Fluids*, 15(12), 3683–3692. https://doi.org/10.1063/1.1623490

[5] Wanstall, C. T., Bittle, J. A., & Agrawal, A. K. (2021). *Quantitative concentration measurements in a turbulent helium jet using rainbow schlieren deflectometry*. *Experiments in Fluids*, 62(3). https://doi.org/10.1007/s00348-021-03154-2

[6] Wanstall, C. T., Agrawal, A. K., & Bittle, J. A. (2019). *Phase boundary detection in transient, evaporating high-pressure fuel sprays by rainbow schlieren deflectometry*. *Applied Optics*, 58(25), 6791. https://doi.org/10.1364/ao.58.006791

[7] Wanstall, C. T., Agrawal, A. K., & Bittle, J. A. (2017). *Quantifying liquid boundary and vapor distributions in a fuel spray by rainbow schlieren deflectometry*. *Applied Optics*, 56(30), 8385. https://doi.org/10.1364/ao.56.008385

[8] Parker, A., Wanstall, C. L., Reggeti, S. A., Bittle, J. A., & Agrawal, A. K. (2021). *Simultaneous rainbow schlieren deflectometry and OH* chemiluminescence imaging of a diesel spray flame in constant pressure flow rig*. *Proceedings of the Combustion Institute*, 38(4), 5557–5565. https://doi.org/10.1016/j.proci.2020.05.045

[9] Wanstall, C. T., Bittle, J. A., & Agrawal, A. K. (2022). *Transient mixing behavior of a supercritical fluid injected into supercritical and subcritical environments*. *Physics of Fluids*, 34(2). https://doi.org/10.1063/5.0072291

[10] Mastorakos, E., Shibasaki, M., & Hishida, K. (1996). *Mixing enhancement in axisymmetric turbulent isothermal and buoyant jets*. *Experiments in Fluids*, 20(4), 279–290. https://doi.org/10.1007/bf00192673

[11] Gopal, V., & Maddalena, L. (2021). *Review of Filtered Rayleigh Scattering technique for mixing studies in supersonic air flow*. *Progress in Aerospace Sciences*, 120, 100679. https://doi.org/10.1016/j.paerosci.2020.100679

[12] Tan, J., Zhang, D., Li, H., & Hou, J. (2018). *Detailed experimental investigations on flow behaviors and velocity field properties of a supersonic mixing layer*. *Acta Astronautica*, 144, 30–38. https://doi.org/10.1016/j.actaastro.2017.12.010

[13] Traxinger, C., & Pfitzner, M. (2021). *Effect of nonideal fluid behavior on the jet mixing process under high-pressure and supersonic flow conditions*. *The Journal of Supercritical Fluids*, 172, 105195. https://doi.org/10.1016/j.supflu.2021.105195

[14] Davis, M. R. (1975). *Intensity, scale and convection of turbulent density fluctuations*. *Journal of Fluid Mechanics*, 70(3), 463–479. https://doi.org/10.1017/s0022112075002133

[15] Kolhe, P. S., & Agrawal, A. K. (2009). *Density measurements in a supersonic microjet using miniature rainbow schlieren deflectometry*. *AIAA Journal*, 47(4), 830–838. https://doi.org/10.2514/1.37332

[17] Su, L. K., Helmer, D. B., & Brownell, C. J. (2009). *Quantitative planar imaging of turbulent buoyant jet mixing*. *Journal of Fluid Mechanics*, 643, 59–95. https://doi.org/10.1017/s0022112009991856

[18] Richards, C. D., & Pitts, W. M. (1993). *Global density effects on the self-preservation behaviour of turbulent free jets*. *Journal of Fluid Mechanics*, 254, 417–435. https://doi.org/10.1017/s0022112093002204

Transient Modeling of Catalytic Deactivation of Carbon Blacks During Thermo-Catalytic Methane Decomposition

Student Researcher: Joshua Langin

Advisor: Maryam Younessi

Cleveland State University
Mechanical Engineering

Abstract
With growing concerns over climate change and sustainability, many alternatives to fossil fuels are being investigated. Hydrogen is a promising alternative to fossil fuels because it does not emit greenhouse gases when used and can be sustainably sourced. An attractive method for producing hydrogen is the catalytic decomposition of methane, CDM. This process does not emit greenhouse gases and has the potential for high rates of hydrogen production. This paper builds on an existing CHEMKIN model of the CDM process. This study develops empirical equations that describe the deactivation of three commercially available carbon black catalysts. These equations are then used to define inputs to model the CDM process. This model is then applied to perform a net energy production analysis. Results of this analysis indicate the main factor affecting the net energy produced is the amount of methane conversion.

Project Objectives
The main objective of the project is to develop a model to describe the deactivation of 3 carbon black catalyst over time. While there have been numerous experimental studies on this subject, accurate modeling of the process is limited. At the time of this project, the only models found to accurately describe the reaction were limited to the initial conditions of the reaction. This project seeks to use available experimental data over extended CDM runs to develop a model for the catalyst deactivation. This model will be able to help guide further experimental research, as well as provide a tool for those in industry to use to simulate the process to obtain preferable operating conditions.

After the model is obtained it will then be applied to perform a net energy production analysis. This analysis will provide insight to what conditions are suitable for energy production by comparing the rate of energy produced in the form of hydrogen fuel, and the rate of energy that is actively consumed to run the process at the given reaction conditions.

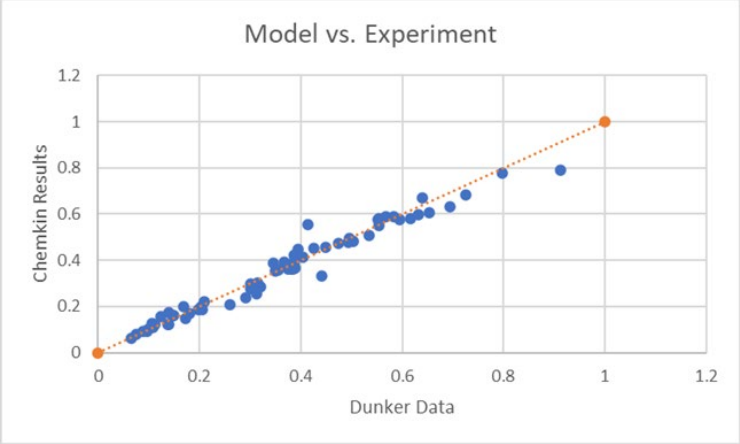
Methods
Computer modeling with the CHEMKIN software.

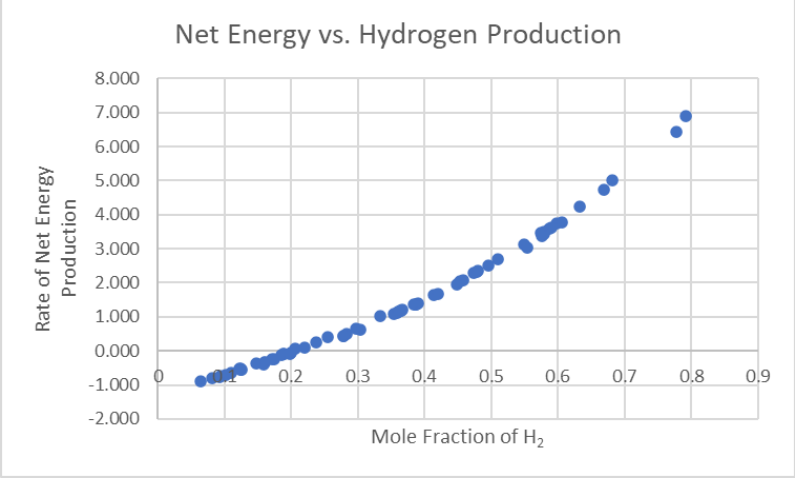
Results and Discussion
Previously existing models were expanded upon by implementing a new variable, X into the rate reaction equation. This X value accounts for the changing surface area and site activity throughout the reaction. Functions for how this X value changes as a function of both time and temperature were found for 3 different carbon catalysts. This model was then compared to existing experimental data and the initial cases were compared to existing models as well. The developed model is able to predict hydrogen production as a function of both time and temperature where existing models were limited to predicting conditions at the start of the run and could not accurately predict the hydrogen production as the runs were extended through time.
This model was then used to perform an energy analysis to show which conditions are most effective at producing energy. It was found that higher values of methane conversion we correlated to higher net

energy production values. A breakeven point was observed around 20% hydrogen gas in the outlet gas flow.

Figures/Charts

Catalyst	Trial	X Model Error %	Klosinski Error %	Younessi Error %
BP120	6	**0.0%**	15.6%	12.8%
	7	**4.9%**	6.2%	12.4%
	8	**2.6%**	14.6%	6.2%
	9	-1.2%	7.6%	**1.1%**
V72	10	27.5%	**11.3%**	24.2%
	11	**-18.5%**	26.5%	44.4%
	12	**4.2%**	9.9%	5.0%
	13	4.0%	8.9%	**3.1%**
	14	-6.0%	**2.8%**	7.0%
BP2000	15	**-1.2%**	5.3%	21.3%
	16	-24.7%	15.8%	**14.0%**
	17	**4.8%**	20.5%	15.8%
	19	-13.2%	**6.5%**	8.9%
	20	-2.5%	7.0%	**2.0%**





Acknowledgments
I would first like to thank my advisor, Dr. Younessi for the guidance she offered during my work on this. Her expertise in the subject area was appreciated and helped me to learn and have a deeper appreciation for research projects.

I would also like to thank my friends and family for their support as I worked many late nights on this project.

Lastly, I would like to thank my lovely fiancée, Lauren, who through the late nights, and long weekends supported and encouraged me.

References

[1] A. M. Dunker, S. Kumar, and P. A. Mulawa, "Production of hydrogen by thermal decomposition of methane in a fluidized-bed reactor—Effects of catalyst, temperature, and residence time," *International Journal of Hydrogen Energy*, vol. 31, no. 4, pp. 473–484, Mar. 2006, doi: https://doi.org/10.1016/j.ijhydene.2005.04.023.

[2] M. Younessi Sinaki, "Numerical Modeling of Methane Decomposition for Hydrogen Production in a Fluidized Bed Reactor," Ph.D. thesis, Dept. Mechanical Engineering, University of Waterloo, Ontario, Canada, 2014.

[3] A. Klosinski, "MODELING OF CATALYTIC DECOMPOSITION OF METHANE OVER CARBON BLACKS AND PLASMA-GENERATED CARBON IN CHEMKIN," Master thesis, Dept. Mechanical Engineering, Cleveland State University, Cleveland, OH, 2024.

[4] World Nuclear Association, "Heat Values of Various Fuels - World Nuclear Association," *world-nuclear.org*, Nov. 18, 2020. https://world-nuclear.org/information-library/facts-and-figures/heat-values-of-various-fuels

[5] E. B. Agyekum, C. Nutakor, A. M. Agwa, and S. Kamel, "A Critical Review of Renewable Hydrogen Production Methods: Factors Affecting Their Scale-Up and Its Role in Future Energy Generation," Membranes, vol. 12, no. 2, p. 173, Feb. 2022, doi: https://doi.org/10.3390/membranes12020173.

[6] E. K. Lee *et al.*, "Catalytic decomposition of methane over carbon blacks for CO2-free hydrogen production," *Carbon*, vol. 42, no. 12–13, pp. 2641–2648, Jan. 2004, doi: https://doi.org/10.1016/j.carbon.2004.06.003.

[7] M. J. Lázaro, J. L. Pinilla, I. Suelves, and R. Moliner, "Study of the deactivation mechanism of carbon blacks used in methane decomposition," *International Journal of Hydrogen Energy*, vol. 33, no. 15, pp. 4104–4111, Aug. 2008, doi: https://doi.org/10.1016/j.ijhydene.2008.05.072.

[8] "Financial Incentives for Hydrogen and Fuel Cell Projects," *Energy.gov*. https://www.energy.gov/eere/fuelcells/financial-incentives-hydrogen-and-fuel-cell-projects

[9] A. A. Ibrahim, A. S. Al-Fatesh, W. U. Khan, M. A. Soliman, R. L. Al-Otaibi, and A. H. Fakeeha, "Thermo-Catalytic Methane Decomposition: A Review of State of the Art of Catalysts," Jan. 2015.

[10] N. Muradov, F. Smith, and A. T-Raissi, "Catalytic activity of carbons for methane decomposition reaction," *Catalysis Today*, vol. 102–103, pp. 225–233, May 2005, doi: https://doi.org/10.1016/j.cattod.2005.02.018.

[11] N. Sánchez-Bastardo, R. Schlögl, and H. Ruland, "Methane Pyrolysis for Zero-Emission Hydrogen Production: A Potential Bridge Technology from Fossil Fuels to a Renewable and Sustainable Hydrogen Economy," *Industrial & Engineering Chemistry Research*, vol. 60, no. 32, pp. 11855–11881, Aug. 2021, doi: https://doi.org/10.1021/acs.iecr.1c01679.

[12] C. D. Fulhage, D. Sievers, and J. R. Fischer, “Generating methane gas from manure,” Nov. 2018. Available: https://extension.missouri.edu/publications/g1881

[13] J. G. F. Madeira *et al.*, “Hydrogen production from swine manure biogas via steam reforming of methane (SRM) and water gas shift (WGS): A ecological, technical, and economic analysis,” *International Journal of Hydrogen Energy*, vol. 46, no. 13, pp. 8961–8971, Feb. 2021, doi: https://doi.org/10.1016/j.ijhydene.2021.01.015.

[14] I. Suelves, J. L. Pinilla, M. J. Lázaro, and R. Moliner, “Carbonaceous materials as catalysts for decomposition of methane,” *Chemical Engineering Journal*, vol. 140, no. 1–3, pp. 432–438, Jul. 2008, doi: https://doi.org/10.1016/j.cej.2007.11.014.

[15] J. Appel, H. Bockhorn, and M. Frenklach, “Kinetic modeling of soot formation with detailed chemistry and physics: laminar premixed flames of C2 hydrocarbons,” *Combustion and Flame*, vol. 121, no. 1–2, pp. 122–136, Apr. 2000, doi: https://doi.org/10.1016/s0010-2180(99)00135-2.

[16] “Chemkin Theory Manual Chemkin ® Software,” 2016. Available: https://personal.ems.psu.edu/~radovic/ChemKin_Theory_PaSR.pdf

[17] “ANSYS Chemkin-Pro Input Manual : ANSYS Inc : Free Download, Borrow, and Streaming : Internet Archive,” *Internet Archive*, 2020. https://archive.org/details/ansys-chemkin-pro-input-manual/page/94/mode/2up (accessed Mar. 23, 2025).

Investigation of Hypersonic 3D SBLI

Student Researcher: Matthew Megazzini

Advisor: Prof. Jesse Little

The Ohio State University
Aerospace Engineering

Abstract
Shock/boundary layer interactions (SBLIs) are inevitable in hypersonic flight, and despite decades of research, there remain many open questions. These interactions generate elevated and unsteady surface pressure and heat flux loads which can reduce vehicle control authority and lead to structural failure. The purpose of this study is to determine the influence of leading-edge sweep, which causes a three-dimensional incoming boundary layer, on the SBLI generated by a two-dimensional compression surface (i.e., flap). The outcome of this research can be generalized to better understand hypersonic vehicle design and is most relevant to external flows associated with control surfaces. Experimental testing is being conducted in the 45-inch diameter Mach 6 Large Area Reflected Shock (LARS) Tunnel at The Ohio State University Aerospace Research Center.

Project Objectives
Researchers have extensively explored SBLIs for nominally 2D incoming boundary layers interacting with 3D compression surfaces [1]. The objective of this study is to explore the influence of high sweep angle on the SBLI produced by a compression surface at Mach 6, as this configuration more closely resembles the aerodynamics encountered by hypersonic vehicles. An understanding of the incoming 3D boundary layer is essential for this SBLI investigation. Boundary layer separation occurs when the adverse pressure gradient caused by a shock wave is too strong for the near-wall flow to overcome. The low momentum, laminar boundary layer is known to separate earlier than the more energized turbulent boundary layer. This study aims to explore these 3D SBLI phenomena for a range of boundary layer states.
In the case of a delta wing, the flow along the centerline of the vehicle travels a longer streamwise distance to the flap hinge, compared to outboard spanwise locations. This may cause the inboard boundary layer to begin to transition into turbulent flow, while the outside remains laminar. Whitehead Jr. and Keyes [2] observed a “dumbbell” shaped separation pattern developing from outboard laminar separation transitioning into inboard turbulent separation on a delta wing with a flap (Figure 1a). This phenomenon was further examined by Kaufman and Freeman [3] for a 3D boundary layer interacting with a forward-facing step. Figure 1b identifies the expected “Laminar Separation Line”, “Turbulent Separation Line”, and “Laminar-Transitional-Turbulent Separation Line” that result due to this SBLI. Although previous studies have outlined the general structure of the separation patterns, they provide limited insight into the unsteady dynamics of the interaction.

Methodology
The test article (Figure 2a) was 3D-printed using Formlabs Grey V4 resin. The model features a 75-degree sweepback angle and a 5mm leading-edge radius. The centerline chord length from the leading edge to the flap hinge is 18 inches, with a flap deflection angle of 15 degrees. The delta wing is integrated with 12 Kulite XCE-062 pressure sensors. These sensors are positioned spanwise along both quarter-chord lines and the centerline, and in the streamwise direction at 80%, 86%, 92% and 98% of the centerline chord length to the flap hinge (Figure 2b).
Testing was conducted at the Ohio State LARS facility. This Mach 6 reflected shock tunnel has blowdown capability, enabled by a Fast-Acting Valve. The present test campaign was conducted in blowdown mode,

exploring unit Reynolds numbers ranging from 1.5 to 2.75 million per meter. The total temperature and model surface temperature are 295K. The steady state test time for these runs was approximately 100 milliseconds.

Results and Discussion

Trends in the data remained consistent across different Reynolds number conditions; therefore, this report will focus exclusively on the highest unit Reynolds number tested. Power Spectral Density (PSD) plots were generated to compare the frequency content between pressure sensors at different locations. The PSD magnitude is a measure of the fluctuating pressure signal normalized by the mean pressure of the signal over the steady state time. At the most upstream location, x/L= 0.80, a small discrepancy is observed between the centerline and outboard sensors, as shown in Figure 3a. The centerline signal exhibits a frequency peak near 8 kHz, while the starboard and port sensors do not have distinguishable peaks present. Further downstream at x/L = 0.86, the centerline frequency peak becomes more pronounced, broadening between 5 and 9 kHz and increasing in magnitude (Figure 3b). There are still no major peaks across the outboard locations.

Advancing downstream to x/L = 0.92, the largest discrepancy between the centerline and outboard sensors is seen (Figure 3c). The centerline PSD is nearly an order of magnitude higher than the port and starboard sensors between 7 and 8 kHz. Additionally, small peaks are introduced to the outboard sensors between 10 and 11 kHz. These trends continue in the furthest downstream location, x/L=0.98, as presented in Figure 3d. At this position, the centerline sensor exhibits a prominent PSD peak at a lower frequency compared to the outboard sensors. No distinct turbulent spectral content is observed, which is expected given the relatively low unit Reynolds number.

Figure 4 shows the streamwise variation in the PSD across all sensor locations. As the flow moves downstream, the PSD peaks increase in magnitude and shift to lower frequencies. This trend aligns with the expectation that the separated shear layer grows as it moves downstream resulting in lower frequency content. More specifically, a larger separation bubble, bounded by a thicker shear layer, is expected to display lower-frequency content in comparison to smaller separation bubbles for the same boundary layer state. Indeed, higher frequency content is observed for the port and starboard locations suggesting smaller separated regions here.

Collectively, these experimental results suggest that a laminar separation pattern is present for the cases examined here. This is characterized by initial separation along the centerline, followed by the outboard locations (see Figure 1b “Laminar Separation Line”). This hypothesis is supported by the distribution of frequency peaks, which appear at lower frequencies along the centerline and higher outboard. Future investigations will examine how incoming transitional and turbulent boundary layers influence the SBLI topology, surface heat flux, and unsteadiness.

Figures/Charts

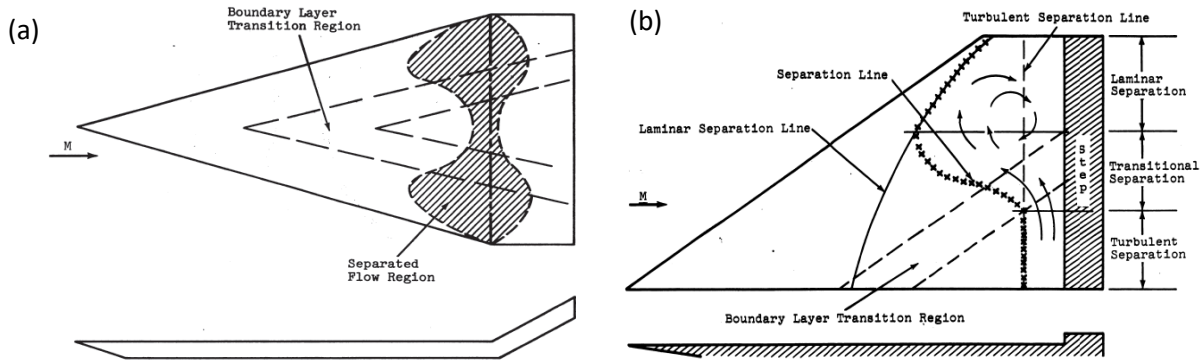


Figure 1: (a) Dumbbell shaped separation pattern resulting from a transitional incoming 3D boundary layer [2] (b) Expected separation patterns corresponding to different incoming boundary layer states [3].

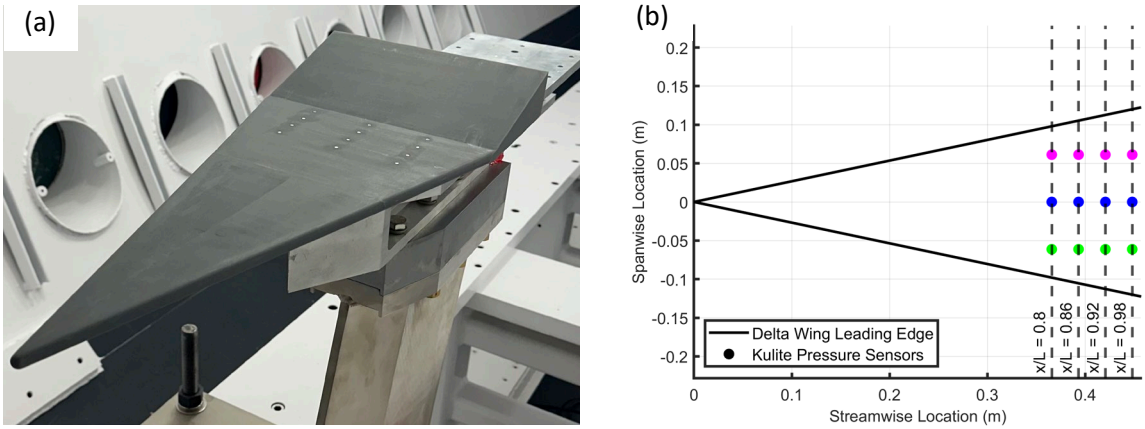
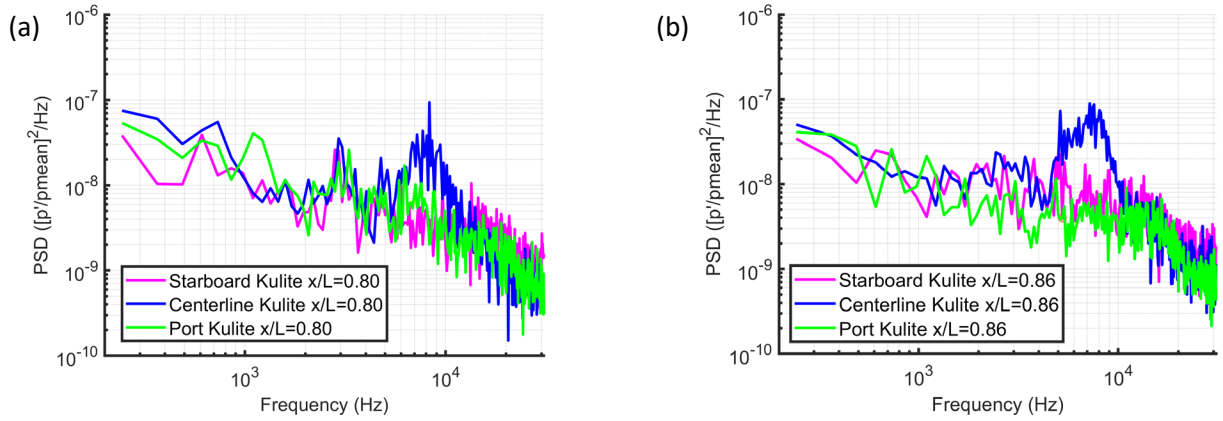


Figure 2: (a) Resin 3D-printed test article installed in the LARS facility (b) Schematic showing Kulite pressure sensor locations on the model.



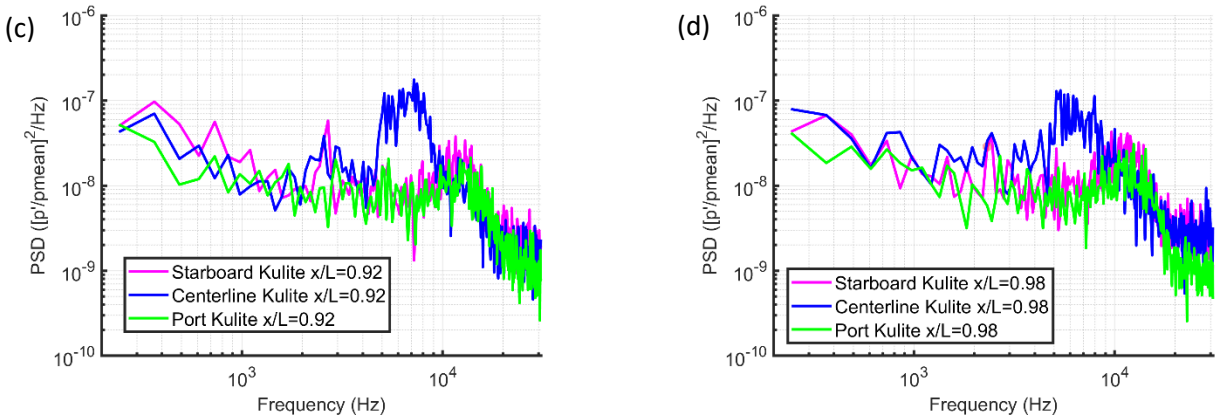


Figure 3: (a) Power Spectral Density (PSD) plot showing spanwise variation in pressure signals at x/L = 0.80 (b) PSD showing spanwise variation at x/L = 0.86. (c) PSD showing spanwise variation at x/L = 0.92 (d) PSD showing spanwise variation at x/L = 0.98.

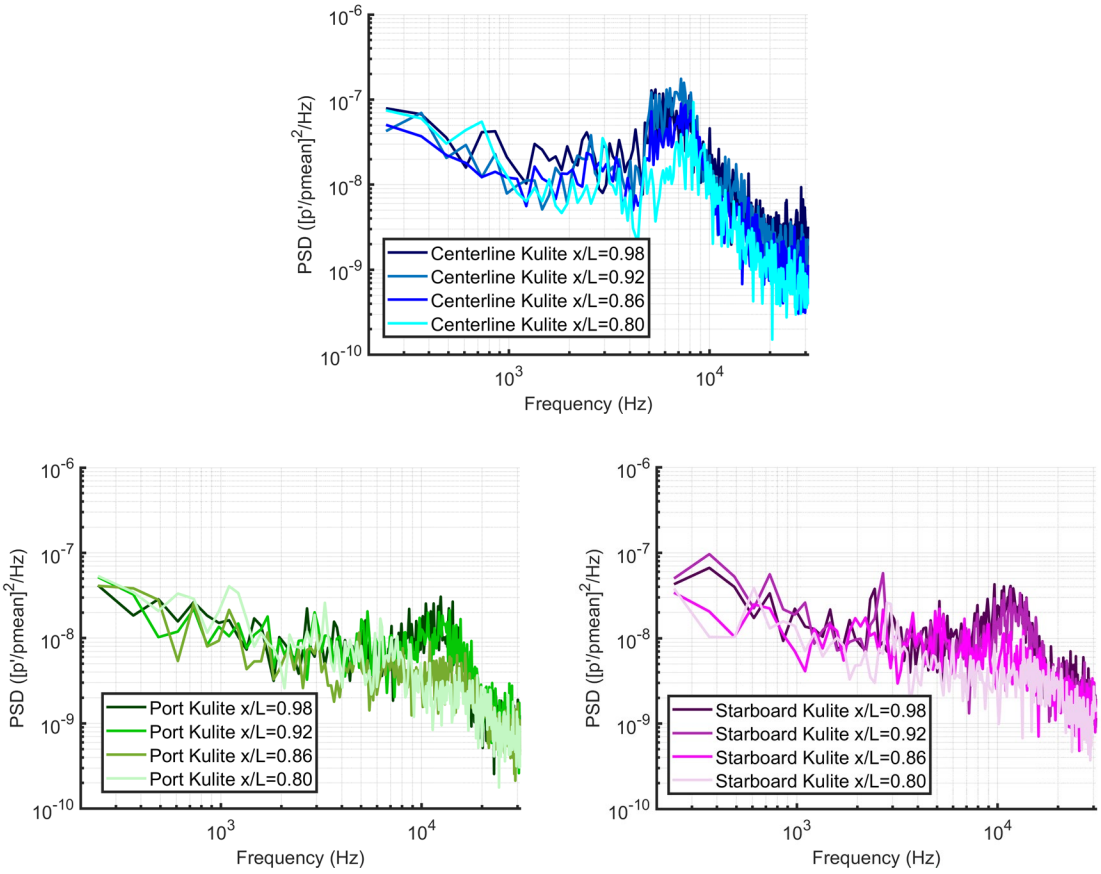


Figure 4: PSD plots showing the development and shift of spectral peaks to lower frequencies across all spanwise sensor locations moving downstream.

Acknowledgments
The author would like to thank the Ohio Space Grant Consortium for this fellowship opportunity. They would also like to acknowledge Prof. Jesse Little, Prof. Nathan Webb, Owen Brown, Luke Paxton, and Josh Petro for their contributions to this work.

References
[1] Gaitonde, D. V. and Adler, M. C. "Dynamics of three-dimensional shock-wave/boundary-layer interactions". Annual Review of Fluid Mechanics 55.1 (2023), pp. 291‑321.

[2] Whitehead Jr, A. H. and Keyes, J. W. "Flow phenomena and separation over delta wings with trailing-edge flaps at Mach 6." *AIAA Journal* 6.12 (1968), pp. 2380–2387.

[3] Kaufman, L. G. and Freeman, L. M. "Separation ahead of steps on swept wings". *Journal of Aircraft* 13.12 (1976), pp. 1016–1017.

Evaluation of Multiple Processing Methods for PTFE-PI Composites

Student Researcher: Dane Miller

Advisor: Dr. Mark Sidebottom

Miami University
Department of Mechanical and Manufacturing Engineering

Abstract

The aim of this research was to evaluate the effects of three different chemical pathways and two different manufacturing processes on the tribological properties of PTFE-PI composites. PTFE-PI composites are known to have excellent thermal and tribological properties: high thermal resistance, low coefficient of friction (COF), and low wear rate. However, they are limited in their manufacturability. Polyimide (PI) is generally produced as insoluble particles that have no melting point. Due to this limitation in processability, composites are produced by dry mixing polytetrafluoroethylene (PTFE) and PI and then sintering. This investigation used two different soluble precursors of PI, polyamic acid (PAA) and polyisoimide (PII), to allow the use of an uncommon processing method: rotary evaporation.

The materials tested used PI as a filler within bulk granular PTFE. Unfilled PTFE along with dry mixed PTFE-PI samples were used as controls. These were compared to a dry mixed PTFE-PII sample and rotary evaporated PTFE-PAA and PTFE-PII samples. The rotary evaporated samples may lead to a microstructure in which the PI envelopes the PTFE, leading to better wear performance. The composites were investigated for COF, wear rate, and thermal degradation temperature. Improvement in these properties could increase the applications of polyimide fillers, bulk materials, and composites in many industries.

Project Objectives

Create PTFE-PI composites utilizing PI fillers synthesized through different chemical processes. Use the soluble PI precursors of PAA and PII to allow the use of rotary evaporation. It is hypothesized that using the soluble precursors, more specifically PII, will create an uncommon morphology in which the PII 'coats' the PTFE. This morphology could be more favorable and demonstrate better tribological properties. *Figure 1(a)* shows the morphology of dry mixed PI-PTFE composites, while *Figure 1(b)* shows the hypothesized morphology in which the PI coats the PTFE particles. To the author's knowledge rotary evaporation is novel in the creation of PTFE-PI composites and has not previously been tested. Once these composites were created, thermal and tribological analysis was performed to assess the performance of the different chemical and processing pathways.

Methodology

Materials

To test the PTFE-PI composites, bulk PTFE-PI samples were created that used 10 wt % PI filler. All samples used Teflon™ PTFE 7A-X powder (average diameter size of 38 μm). All the PI materials start with PAA and follow the same PAA synthesis process. To create the PAA for this project, Oxydianiline (ODA) was used for the diamine monomer and (hexafluoroisopropylidene)diphthalic anhydride (6-FDA) was used as the dianhydride monomer. The solvent used for this reaction was dimethylacetamide (DMAc).

To create the PAA precursor, the PAA-DMAc solution was then poured into (hexafluoroisopropyl)methyl ether (HFMOP). This caused the PAA to precipitate and it was then dried. To create the insoluble PI particles, the PAA was chemically imidized using acetic anhydride and triethylamine (TEA). To create the PII precursor, the PAA was dehydrated using trifluoroacetic anhydride (TFAA) and TEA. The TFAA removes

water and traps the intermediate in the kinetic product (the PII precursor). This isomer tends to be more soluble than the final PI form and will isomerize to make PI at modest temperatures (100-250 ℃).

To test the different combinations of chemical and processing pathways, five different types of materials were created. *Figure 2* summarizes the types of samples with what PI filler they used and the method in which the PTFE and PI were mixed. All the combinations once mixed, either dry mixed or rotary evaporated, were compression molded in a 25.4 mm diameter cylindrical die at 44.5 kN for 15 minutes. Following that, they were put into an oven and baked in air. The temperature was ramped at 5 ℃/min until 380℃ where it sits for 2 hours before ramping the temperature down at 5 ℃/min. These 25.4 mm wafers were then machined into their final shapes for testing.

Thermal Analysis

Differential scanning calorimetry (DSC) was performed on the PAA and PII to better understand the imidization and isomerization processes, respectively. This was done by ramping the temperature from 25 ℃ to 400 ℃ at 10 ℃ per minute. The samples were then held at 400 ℃ for one minute before dropping the temperature back to 25 ℃ at the same rate. This heating cycle was repeated one more time. Thermogravimetric Analysis (TGA) was performed on the PI and PII to investigate the thermal resistance of both materials. This analysis was done by increasing the temperature up to 800 ℃ and measuring the mass loss. This theoretically should be equivalent for the PI and PII as they have the same chemical composition.

Tribological Analysis

To conduct tribological analysis a custom-made reciprocating flat-on-flat tribometer, shown in *Figure 3*, was used. This tribometer uses load cells to measure the friction and normal force which is then used to calculate the COF. Mass-based wear measurements were taken to calculate the wear rate of the samples. These measurements were done at intervals throughout the testing. All the samples used the same experimental conditions: applied load of 250 N (pressure of 6.25 MPa), stroke length of 25 mm, sliding velocity of 50 mm/s, and a total sliding distance of 20 km (400,000 cycles). All tests used polished 304 SS counterbodies with a mirror finish.

Results and Discussion

Thermal Analysis

Figure 4a and *4b* show the DSC first and second heat results, respectively. Both curves, PAA and PII, have thermal events towards the beginning of the first heat. This most likely is due to trapped solvent evaporating from the material. The PII having a large change in heat flow at this event possibly points towards it having a substantial amount of trapped solvent. Both PAA and PII also have a second thermal event during the first heat. For the PAA, this is the thermal imidization process and for PII it is the isomerization process. Throughout the second heat, there are no thermal events for both the PAA or PII and this indicates that they successfully transformed into the final PI material that is thermally stable through 400 ℃.

Figure 5 shows the results of running the PI and PII through TGA. Looking at the PI curve (blue) there is practically no mass loss until it reaches a temperature of approximately 530 ℃. This is what is expected as PI materials generally have very high thermal resistance. However, the PII curve (green) has a mass loss of roughly 20 wt % at around 200 ℃. The PII should be as thermally resistant as the PI, so this drop also points towards the possibility of significant amounts of trapped solvent. After the initial drop the curve levels out and has minimal mass loss until it reaches a degradation temperature of 530 ℃ that matches its PI counterpart.

Tribological Analysis

It should be noted that the unfilled PTFE samples (7AX) failed after 0.5 km due to wear. *Figure 6* shows the average COF for all samples throughout the entire test. All the samples had comparable COFs that were all very respectable ranging from 0.15-0.18. The two samples that used PII (PIICR,PIICD) had the lowest COFs, with the rotary evaporated sample (PIICR) being the best. *Figure 7* shows the volume lost through the duration of the test. The slope of this graph essentially shows the wear rate of the materials. The unfilled PTFE samples' (7AX) wear rates were so large that they had to be excluded from this graph, which is expected from virgin PTFE. The graph shows that both rotary evaporated samples (PIT,PIICR) had very high wear rates. It can also be seen that the two dry mix samples (PIC,PIICD) had comparable volume loss, with the PII sample performing slightly better (PIICD). *Figure 8* is a table summarizing the results of the tribological testing. The table contains the weighted average COF, total wear rate, and 3-point wear rate for all the samples. The 3-point wear rate is a wear rate that accounts for uncertainties in the experimental setup. The table shows that while they all have good weighted average COFs the dry mix PII sample has the lowest (0.15). The rotary evaporated samples (PIT,PIICR) both had high total wear rates on the scale of 10^{-6} (mm^3/Nm), while the dry mix samples (PIC,PIICD) had lower wear rates ($4.4*10^{-7}$ and $3.4*10^{-7}$ mm^3/Nm). The trends were similar with the 3-point wear rate, except that the dry mix PII sample (PIICD) had a wear rate ($9.2*10^{-8}$ mm^3/Nm) of less than half of the next lowest wear rate (PIC: $1.9*10^{-7}$ mm^3/Nm). To summarize, the rotary evaporated samples had very poor wear performance and the dry mixed PII sample performed the best through all categories.

Future Work

To better understand why these materials performed the way they did the next step will be performing scanning electron microscopy (SEM) to look at the surface of these materials. Energy-dispersive X-ray spectroscopy (EDS) mapping will be performed to check the morphologies of the samples to see if the hypothesized morphology was achieved through rotary evaporation. The SEM and EDS may give insights into the results and point towards changes that can be made to improve these materials.

Figures/Charts

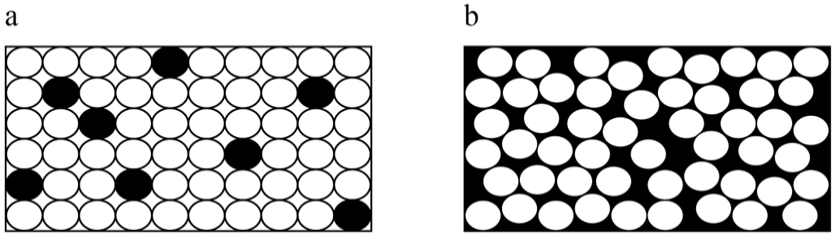


Figure 1. Expected Morphologies (White-PTFE, Black-PI) (a) Dry Mixed (b) Rotary Evaporated

PTFE Samples			
Sample Type Name	**Polyimide Filler**	**Description of Polyimide Filler**	**Mixing Method**
7AX	No	N/A	N/A
7AX PIC	Yes	Chemically Imidized Polyimide	Dry Mixing
7AX PIT	Yes	Thermally Imidized Polyamic Acid	Rotary Evaporation
7AX PIICR	Yes	Chemically Imidized Polyisoimide	Rotary Evaporation
7AX PIICD	Yes	Chemically Imidized Polyisoimide	Dry Mixing

Figure 2. Summary of PTFE-PI Composite Sample Types

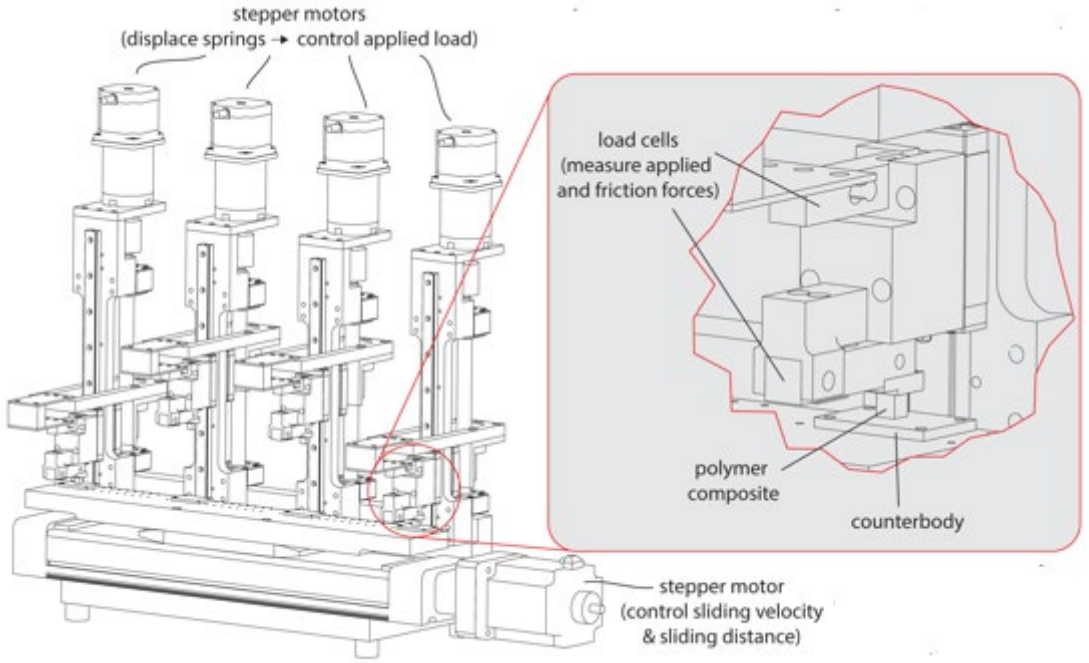


Figure 3. Custom-Made Flat-on-Flat Tribometer

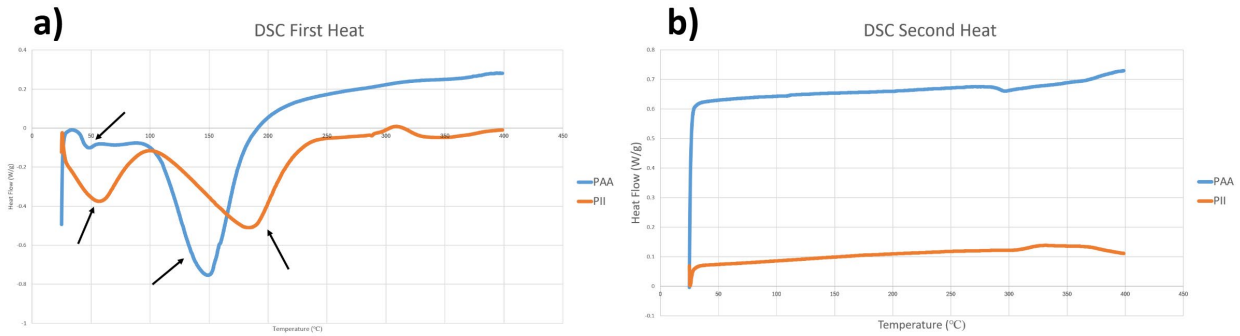


Figure 4. DSC Results for PAA and PII (a) First Heat (b) Second Heat

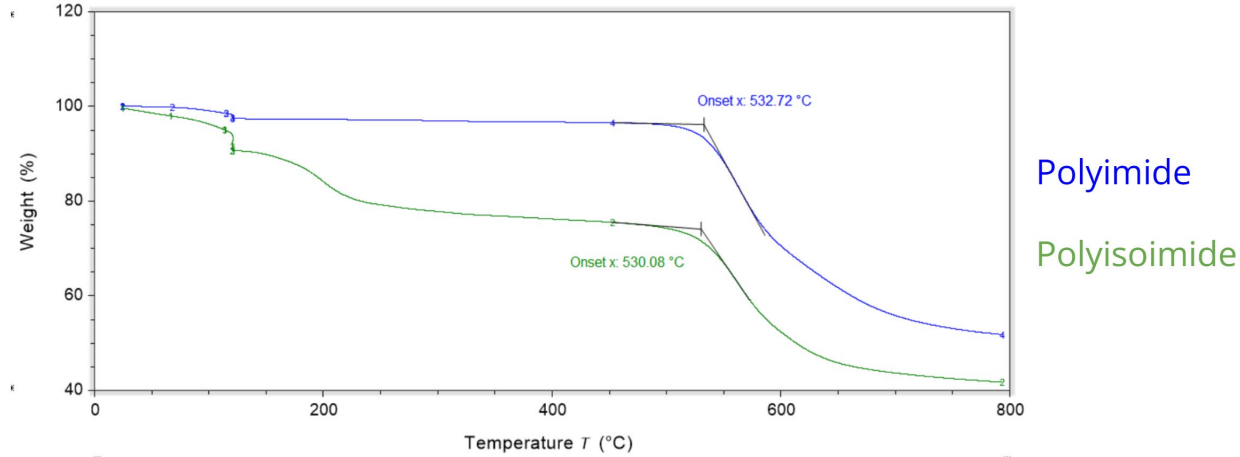


Figure 5. TGA Results for PI and PII

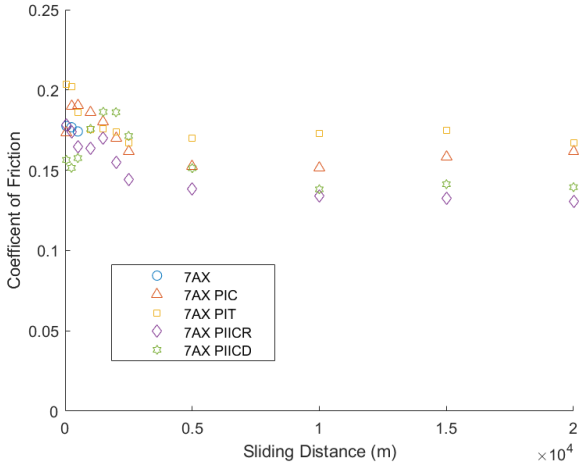


Figure 6. Sliding Distance (m) vs Coefficient of Friction

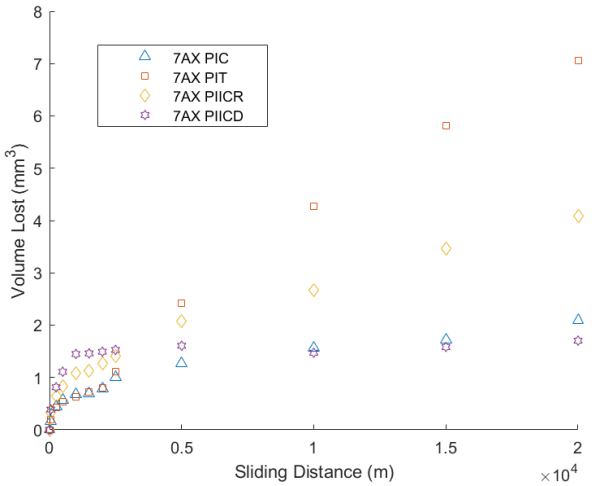


Figure 7. Sliding Distance (m) vs Volume Lost (mm^3)

Tribology Test Results			
Filler Type	**Weighted Average COF**	**Total Wear Rate (mm^3/Nm)**	**3-Point Wear Rate (mm^3/Nm)**
Unfilled	0.18	7.2E-04	7.0E-04
Dry Mix PI	0.16	4.4E-07	1.9E-07
Rotary Evaporation PAA	0.17	1.6E-06	1.2E-06
Rotary Evaporation PII	0.15	1.4E-06	1.4E-06
Dry Mix PII	0.15	3.4E-07	9.2E-08

Figure 8. Tribological Testing Results Summary

Acknowledgments

I would like to acknowledge my advisor Dr. Mark Sidebottom along with the rest of the Miami University Tribology Team. I would also like to thank Dr. Chris Junk for the use of his lab and for providing materials. Lastly, I would like to thank the Ohio Space Grant Consortium for providing funding for this research.

Modeling Turbulence Using Generative AI with a Multi-Scale Latent Space

Student Researcher: Caleb Morton

Advisor: Dr. Jack McNamara

The Ohio State University
Aerospace Engineering

Abstract

While a decade old, several challenges identified in the NASA-funded CFD Vision 2030 study still remain. We target one such challenge: rapid knowledge extraction and generalization from large computational fluid dynamics (CFD) datasets of highly resolved turbulent flow behavior. Traditional, successful, data-driven models rely upon low-dimensional, broadly scoped training data. However, CFD data on turbulent flows are inherently high-dimensional and narrowly scoped, presenting a challenge for traditional data-driven models. To address this challenge, this research aims to develop a transformative data-driven modeling framework for high Reynolds number turbulent flows using generative artificial intelligence (AI) and multi-scale latent space representations.

Data-informed Local Subspaces (DLS) show promise as a low-dimensional representation, i.e., latent space, due to its use of interpolation functions from the Generalized Finite Element Method (GFEM), which are designed to simultaneously capture large- and small-scale behavior. In addition, the DLS representation can be learned using only one time solution. Thus, large reductions in the dimensionality of CFD data, as well as achieving even larger reductions in the data necessary to generate a latent space. For synthesizing the underlying physics in the DLS latent space, Transformer neural networks are promising for complex spatio-temporal datasets. This is due to their great success in Large Language Models, where they demonstrate the capability to scale up to massive data sets of training data for complex tasks by synthesizing knowledge for text generation. Combining these methods, we hope to create successful, data-driven models of practical scale problems.

Project Objectives

Turbulence is a complex multi-scale phenomenon at the root of many practical problems in engineering. We need reduced order models (ROMs) to generalize high fidelity turbulent data for systems analysis. This requires effective spatial and temporal modeling techniques for post processing of complex of turbulent data sets. The objective of this project is to combine Data-informed Local Subspaces (DLS) with Transformer architectures to create data-driven, reduced order models of turbulent flow data.

Methods

For this project, data of a two-dimensional lid driven cavity flow at $\mathrm{Re} = \mathcal{O}(10^4)$ will be used, with boundary conditions pictured in Figure 1. This data set was generated through direct numerical simulation of the non-dimensionalized Navier-Stokes equations, sampled at 100 Hz over 25 non-dimensional time units, giving 2499 snapshots of high-fidelity data. The data will be compressed to a low-dimensional representation, i.e., latent space, with DLS. With the flow data mapped to this latent space, the Transformer model will be used to model the physics in this reduced latent space.

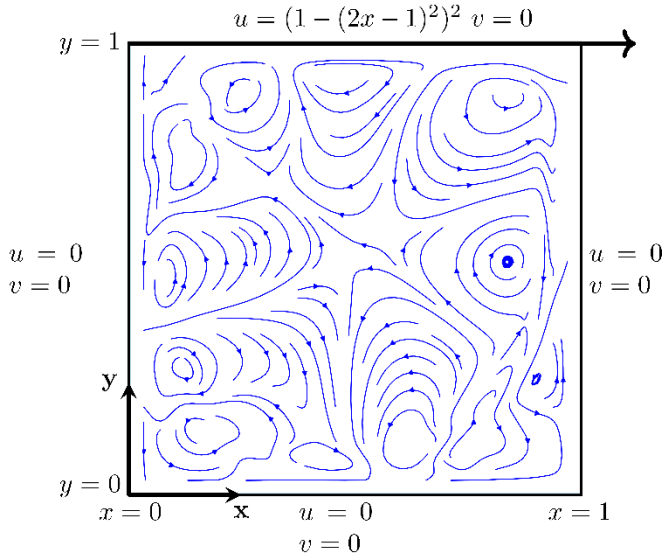


Figure 1: Lid-driven cavity flow diagram, with streamlines showing flow trajectories

Latent Space Methodology

Data-informed Local Subspaces is a data compression method that has been effective in decomposing high Reynold's number flow in turbulent flow data produced by computational fluid dynamics (CFD) [1]. It combines the proper orthogonal decomposition (POD) [2], to learn spatially redundant shapes in the data, and the generalized finite element method (GFEM) [3] as a mathematical framework to apply the shapes to the entire computational domain. The local shapes are learned by randomly sampling 'patches' from *one, singular snapshot*, assembling them into a snapshot matrix, and decomposing them with POD into the dominant local shapes.

Through the finite element matrix assembly process, we create a matrix, ϕ_G, that when multiplied by coefficients, S_G, approximates the high-fidelity data set, Q ($Q \approx \phi_G S_G$). The coefficient matrix S_G represents the data in the compressed latent space and can be found by inverting the system $S_G = \phi_G^{-1} Q$. The hyperparameters we choose to control the compression level of our data are the number of local shapes to use, as well as the patch size, or the size of the local shapes. By increasing the patch size, we increase the compression, where a patch size equal to the size of the computational domain returns the global POD solution. A patch size equal to one grid point of the computational domain returns the original, uncompressed data set.

Machine Learning Methodology

Transformer neural networks have been transformative in the world of natural language processing due to their ability to capture sequential relationships without recurrent architectures using attention layers. The attention layers allow the model to weigh the relevant sequential information from input sequences when producing its output. By removing recurrence, these models can process information in parallel, allowing for greater computational efficiency [4].

The original implementation of the Transformer architecture used an encoder-decoder structure to process language translation, as translated language sequences will not always have the same length. The encoder encodes the information of the input sequence to an abstract latent representation, and the decoder decodes the latent representation into the target language by generating the sequence until an 'end of sequence' output is reached. For a reduced order model, we may only want to generate one output

at a time. Feeding this output back into the model as an input allows for an auto-regressive training approach. Since we only want to output one target at a time, the decoder architecture can be entirely removed, opting for an encoder only architecture, pictured in Figure 2.

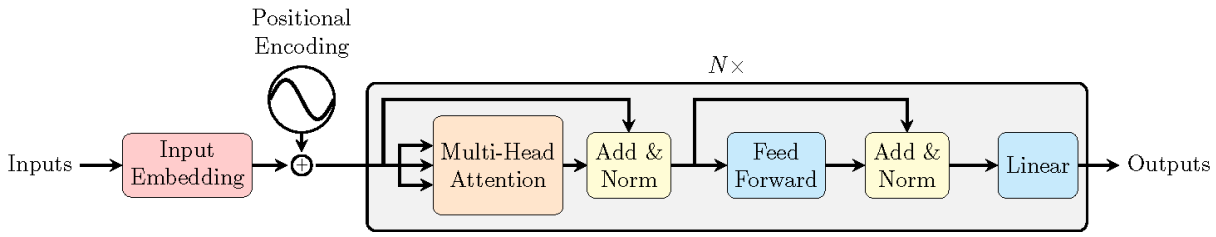


Figure 2: Transformer encoder architecture

The architecture hyperparameters include the time delay, the number of layers, the number of attention heads, as well as the size of the feed-forward layers. The time delay, i.e. the number of snapshots as model input, is selected based on the 'memory' of the fluid, which can be found by analyzing the autocorrelation of the flow. We select the time delay that captures the majority of the correlation in time. The rest of the hyperparameters are manually selected through a guess and check method for optimal model performance.

Results and Discussion

A data-driven reduced order model of a 2D lid-driven cavity flow was created using PyTorch for Python, utilizing an NVIDIA 3090 Ti GPU for Transformer model training [5]. All computational times necessary for each component of ROM creation and inference can be found in Table 1. Due to the chaotic nature of turbulence, pointwise error metrics such as the mean squared error are not reliable metrics to evaluate model accuracy, so second order flow statistics will be compared. The considered flow statistics for comparison include the turbulent kinetic energy (TKE), the root mean square (RMS) of the fluctuating velocity data, and the power spectral density (PSD) [6].

Task	Snapshots Used	Total Time (s)	Time/Snapshot (s)
DLS Compression	2499	274.98	0.11
DLS Reconstruction	2499	44.72	0.018
Model Training	2000	93.80	N/A
Model Inference	499	0.71	~0.002

Table 1: Computational Time

Of the 2499 snapshots, the last 499 of snapshots are used to evaluate the ROM on unseen data. Checking the TKE of the prediction allows for preliminary analysis of model stability, as rapidly increasing or vanishing TKE may indicate model instability. Over the 499 predicted snapshots, the ROM predicts general fluctuations in the TKE with good accuracy, with a normalized L2 error of 1.76%. The RMS of the velocity fluctuation serves as a measure of relative turbulence intensity in the domain over time and is an important qualitative measure for comparing turbulent flows. Our ROM predicts the RMS of the data with 1.84% error. Finally, checking the PSD of the flow at points of interest, we can estimate the power of the respective frequency bins of the data. Our ROM shows good agreement with the low frequency content of the flow, up to ~12 Hz, this equates to over 99% of the total power in the system being captured.

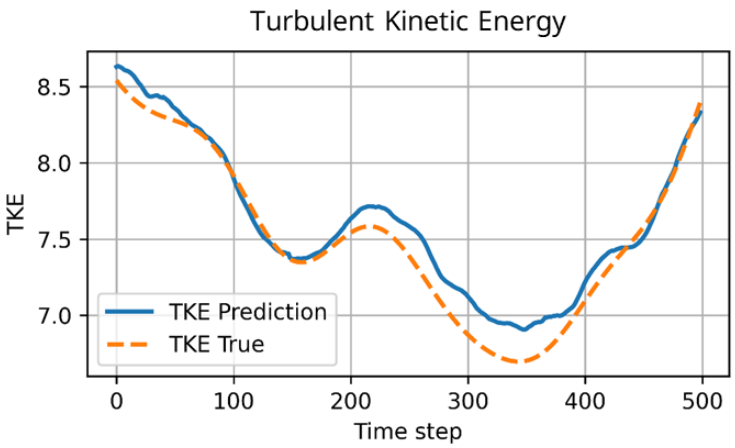


Figure 3: Comparison of turbulent kinetic energy

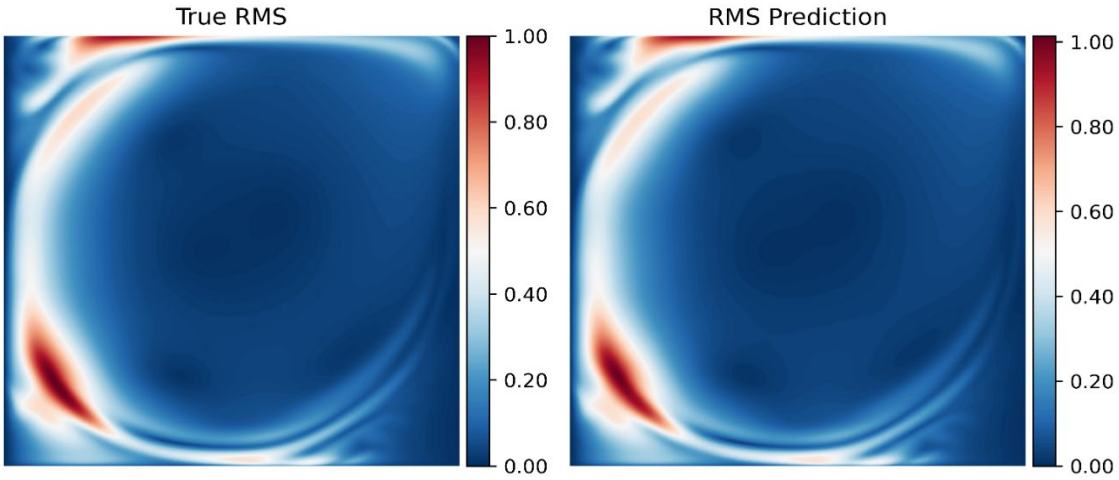


Figure 4: Comparison of root mean square of velocity fluctuation

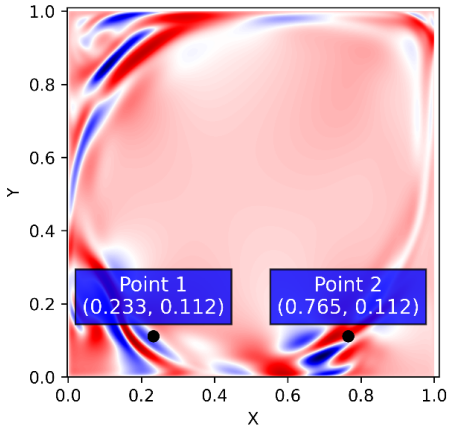


Figure 5: Points used for PSD plots

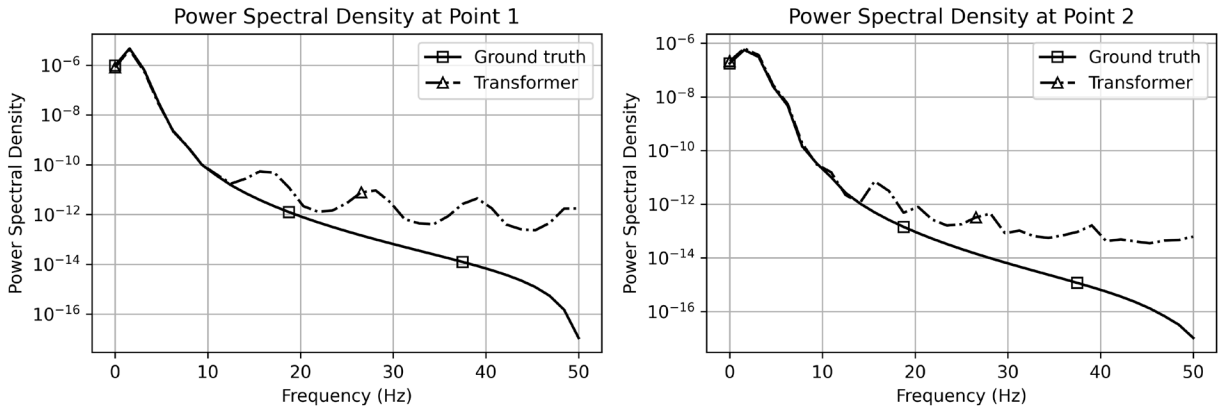


Figure 6: Comparison of power spectral densities at point probes

Acknowledgments

This research was supported by the Office of Naval Research and the Ohio Space Grant Consortium, whose funding has made this research possible. The author would like to thank Dr. Jack McNamara for his guidance and support throughout this project, as well as Dr. Rohit Deshmukh for his codes and datasets.

References

[1] Deshmukh, R., Shilt, T., and McNamara, J. J., "Efficient Representation of Turbulent Flows Using Data-Enriched Finite Elements," *International Journal for Numerical Methods in Engineering*, Vol. 121, No. 15, 2020, pp. 3397–3416. https://doi.org/10.1002/nme.6364

[2] Berkooz, G., Holmes, P., and Lumley, J. L., "The Proper Orthogonal Decomposition in the Analysis of Turbulent Flows," *Annual Review of Fluid Mechanics*, Vol. 25, No. Volume 25, 1993, 1993, pp. 539–575. https://doi.org/10.1146/annurev.fl.25.010193.002543

[3] Babuška, I., Banerjee, U., and Osborn, J. E., "GENERALIZED FINITE ELEMENT METHODS — MAIN IDEAS, RESULTS AND PERSPECTIVE," *International Journal of Computational Methods*, Vol. 01, No. 01, 2004, pp. 67–103. https://doi.org/10.1142/S0219876204000083

[4] Vaswani, A., Shazeer, N., Parmar, N., Uszkoreit, J., Jones, L., Gomez, A. N., Kaiser, Ł., and Polosukhin, I., "Attention Is All You Need," Vol. 30, 2017.

[5] Ansel, J., Yang, E., He, H., Gimelshein, N., Jain, A., Voznesensky, M., Bao, B., Bell, P., Berard, D., Burovski, E., Chauhan, G., Chourdia, A., Constable, W., Desmaison, A., DeVito, Z., Ellison, E., Feng, W., Gong, J., Gschwind, M., Hirsh, B., Huang, S., Kalambarkar, K., Kirsch, L., Lazos, M., Lezcano, M., Liang, Y., Liang, J., Lu, Y., Luk, C. K., Maher, B., Pan, Y., Puhrsch, C., Reso, M., Saroufim, M., Siraichi, M. Y., Suk, H., Zhang, S., Suo, M., Tillet, P., Zhao, X., Wang, E., Zhou, K., Zou, R., Wang, X., Mathews, A., Wen, W., Chanan, G., Wu, P., and Chintala, S., "PyTorch 2: Faster Machine Learning Through Dynamic Python Bytecode Transformation and Graph Compilation," Vol. 2, New York, NY, USA, 2024, pp. 929–947. https://doi.org/10.1145/3620665.3640366

[6] Pope, S. B., "Turbulent Flows," Cambridge Univ. Press, Cambridge, 2015.

Convolutional Deep Learning for Atmospheric Visibility Estimation in Aviation

Student Researcher: Justin Murray

Advisor: Dr. Chad Mourning

Ohio University
Electrical Engineering and Computer Science

Abstract
Accurate measurement of atmospheric visibiltiy is an important part of safe aircraft operation. Usually, these measurements are made using forward scatter sensors in Automated Weather Observing Systems (AWOS) located at airports. These sensors are accurate and reliable, but only provide point measurements for the airports at which they are located. This is an issue for Advanced Air Mobility (AAM) where aircraft may be in operation at low altitude over and between urban areas. Deploying many forward scatter sensors to meet the coverage needs for AAM would be prohibitively expensive. A deep learning model that can estimate atmospheric visibility from photos would be more feasible. Such a model could be deployed on single-board computers are run on a mobile phone. To this end, a dataset of real photos with truth data from AWOS has been compiled, and three existing models for the purpose of visibility estimation trained on it. The results show similar performance between models, but with one consistently performing better. Attempts to improve one of the models through changes to image processing were made, but no significant improvement was made in this regard.

Project Objectives
This project's objective is to evaluate atmospheric visibility prediction performance of existing convolutional deep learning models on a dataset of FAA weather camera images tagged with visibility data from colocated AWOS. Methods of improving the performance of these models are also tested. These methods include changes to image processing, training parameters, and combining of visibility classes.

Methods
The the dataset used in this research, which will be referred to as the FAA Webcams dataset, consists of images taken from publically available cameras on the FAA WeatherCams website. Using a script, images and their corresponding atmospheric visibility data from over 300 cameras are saved at a time. This script was run manually many days, often multiple times a day, over the past year. This resulted in about 80,000 images with varying levels of visibility. Many of these images have quality issues including but not limited to: excessive glare, dirty lenses, obstructions, poor lighting, and camera artifacts. To filter out these images, a ResNet34 [1] model was trained on a small set of manually selected images to differentiate good and bad images. After using this model on the dataset, about good 40,000 images were left. To verify that this made an improvement when training models, two VisNet models trained before and after cleaning the dataset are compared. A small of example images can be seen in Figure 1, and Figure 2 shows the distribution of the image across the visibility classes.

In addition to removing poor quality images from the dataset, the dataset was also balanced across ten visibility classes. These classes are the atmospheric visibility in miles from one to ten. In addition to the integer labels, some images in the dataset are labeled as 1.25, 1.5, 1.75, 2.25, and 2.5 miles. To balance the dataset, 1.5 and 2.5 are excluded and 1.25, 1.75, and 2.25 are rounded to the nearest integer. Then,

each class is limited to 521 images. This ensures the model attempts to learn to predict visibility rather than only guess the most common visibility classes.
Four models are tested: VisNet [2], Retrieval of Multiple Environmental Parameters (RMEP) [3], Integrated model [5], and ResNet50 [1]. ResNet50 was not created to be used for atmospheric visibility estimation and serves as a baseline comparison for the other models designed specifically for this problem. The percentage splits for training, validation, and testings sets are 0.70, 0.10, and 0.20 respectively. Each model is trained for 60 epochs. Loss, accuracy, and a confusion matrix are recorded at each epoch.

The input to VisNet consists of three images, one of which is a high-pass filtered version of the original using the fast fourier transform (FFT). Multiple bands for this filter are tested and compared, as well as a filter where frequency ranges are separated into the three image color channels.

To find out if models are better able to differentiate between a smaller number of visibility classes, the dataset is split into five classes instead of ten and the models are trained and tested on this. The classes are, in miles, 1-2.5, 3-4, 5-6, 7-8, and 9-10. The lower number of classes also allows the dataset to be larger overall while still being balanced, as the smallest size of any class is 2,269 images.

Results and Discussion
The results from training each model on the dataset with ten classes is shown in Table 1. The metrics were taken from the epoch with the lowest loss for each model. The best performing model was RMEP with a loss of 1.91 and accuracy of 0.305. More interesting, however, is that ResNet50 had the second best performance with a loss of 1.97 and accuracy pf 0.276. This is interesting because ResNet50 is the only model not created for the purpose of atmospheric visibiltiy estimation. Although the other models may have shown better performance than non-specialized models in their respective papers, it seems that perhaps performance on synthetic datasets does not transfer to datasets of real images. The integrated model was notably worse than the others with an accuracy of 0.236.
Changing the frequency range of the highpass filter used in one of the VisNet inputs had little to no effect on loss and accuracy, as seen in Table 3. The shape of the loss and accuracy curves was slightly changed, with wider ranges resulting in the model reaching its lowest loss sooner. Separating frequency ranges into the three color channels of the input image had no effect when using the same frequency range for the highpass portion of the filter. These results indicate that VisNet may not be properly utilizing the FFT filtered input, instead extracting features from the original and pseudo-colored input images. It is not clear whether the model cannot find a way to utilize the image or if it simply does not provide any information that cannot already be extracted from the other two images. Using a more complex image processing technique than highpass filtering may be beneficial to the model's performance.

The results for models trained on five classes are shown in Table 2. A similar pattern to those trained on 10 classes. All four models have an accuracy of at least 0.40, with RMEP having the highest accuracy at 0.462. The increase in accuracy is not proportional to the decrease in the number of classes. Comparing the confusion matrices in Figures 3 and 4, the five class model has a more unimodal distribution of predictions. This means that even when the model's prediction is incorrect, it is likely to be close to the correct class. There are methods that address the problems with ordinal classification problems like this, and implementing these methods would be a good path forward in future work.

Figures



Figure 1: A set of 25 random images from the FAA Webcams dataset

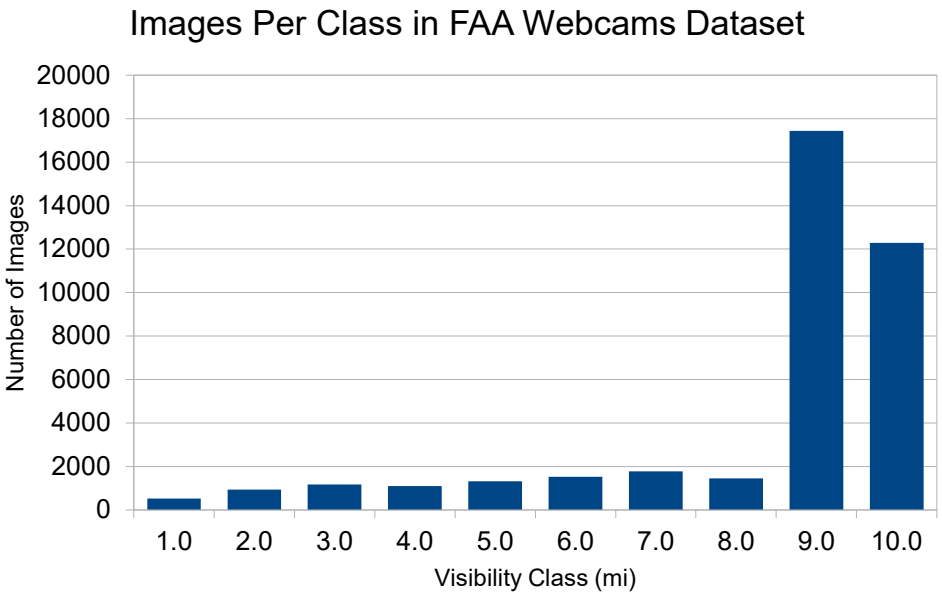


Figure 2: Distribution of number of images in each visibility class after cleaning the dataset

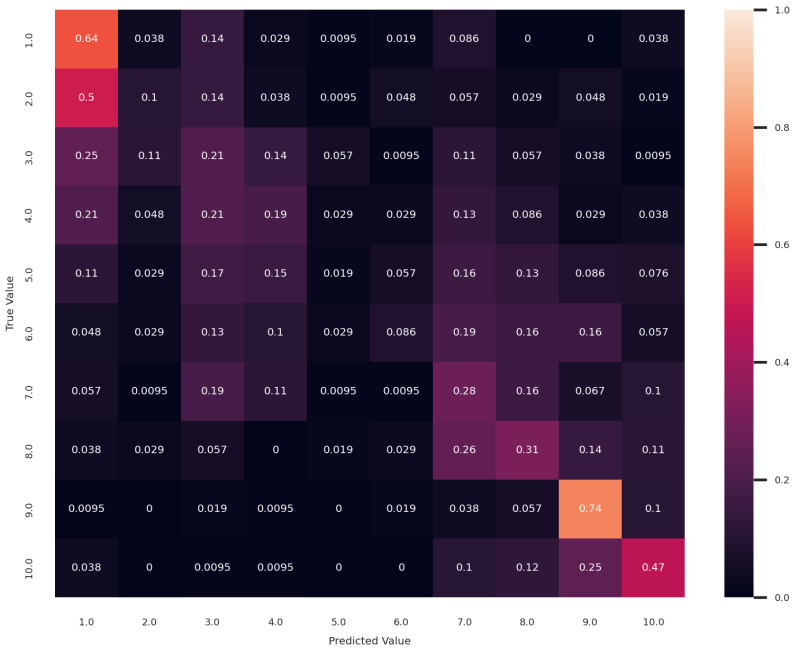


Figure 3: Confusion matrix for the ten class RMEP model. Shows the percentage of images with a certain label that are predicted as each class.

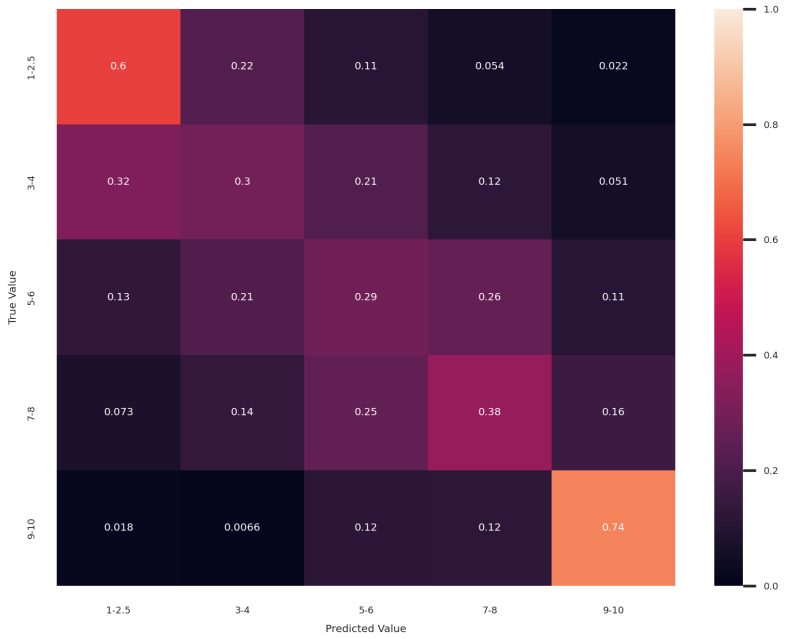


Figure 4: Confusion matrix for the five class RMEP model.

Table *1*: Loss and accuracy at epoch with lowest loss for each model trained on 10 classes

10 Classes		
Model	**Loss**	**Accuracy**
VisNet	2.05	0.263
RMEP	1.91	0.305
Integrated	2.07	0.236
ResNet50	1.97	0.276

Table *2*: Loss and accuracy at epoch with lowest loss for each model trained on 5 classes

5 Classes		
Model	**Loss**	**Accuracy**
VisNet	1.38	0.413
RMEP	1.24	0.462
Integrated	1.35	0.427
ResNet50	1.28	0.443

Table *3*: Loss and accuracy for each highpass frequency range and the multipass filter

VisNet FFT Filters		
Filter Type/Size	**Loss**	**Accuracy**
Highpass Narrow	2.03	0.241
Highpass Medium	2.07	0.249
Highpass Wide	2.06	0.249
Multipass	2.06	0.254

References

1. K. He, X. Zhang, S. Ren, and J. Sun, “Deep Residual Learning for Image Recognition”, arXiv [cs.CV]. 2015.
2. Palvanov, Akmaljon, and Young Im Cho. 2019. "VisNet: Deep Convolutional Neural Networks for Forecasting Atmospheric Visibility" Sensors 19, no. 6: 1343. https://doi.org/10.3390/s19061343
3. P. Su et al., "Retrieval of Multiple Atmospheric Environmental Parameters From Images With Deep Learning," in IEEE Geoscience and Remote Sensing Letters, vol. 19, pp. 1-5, 2022, Art no. 1005005, DOI: 10.1109/LGRS.2022.3149045.
4. Zhen Liu, Yihan Chen, Xingyu Gu, Justin K.W. Yeoh, Qipeng Zhang, Visibility classification and influencing-factors analysis of airport: A deep learning approach, Atmospheric Environment, Volume 278, 2022, 119085, DOI: 10.1016/j.atmosenv.2022.119085.
5. R. Belaroussi and D. Gruyer, "Impact of reduced visibility from fog on traffic sign detection," 2014 IEEE Intelligent Vehicles Symposium Proceedings, Dearborn, MI, USA, 2014, pp. 1302-1306, DOI: 10.1109/IVS.2014.6856535.
6. Sakaridis, C., Dai, D. & Van Gool, L. Semantic Foggy Scene Understanding with Synthetic Data. Int J Comput Vis 126, 973–992 (2018). https://doi.org/10.1007/s11263-018-1072-8.
7. M. Cordts, M. Omran, S. Ramos, T. Rehfeld, M. Enzweiler, R. Benenson, U. Franke, S. Roth, and B. Schiele, “The Cityscapes Dataset for Semantic Urban Scene Understanding,” in Proc. of the IEEE Conference on Computer Vision and Pattern Recognition (CVPR), 2016.

Development of an Adjoint Optimization System for Improvement of Turbine Cooling Passages

Student Researcher: Tammy Nguyen-Huynh

Advisor: Randall Mathison

The Ohio State University
Department of Mechanical and Aerospace Engineering

Abstract
In gas turbine engines, turbine stages are cooled to protect them against high temperature flows from the combustor. One such method of cooling is with blade internal passages. While the structure of these passages promote heat transfer, loss in flow pressure is a direct consequence, decreasing the thermal efficiency of the engine. In this study, adjoint optimization is used to optimize the geometry of a single u-bend passage with no turbulators to maximize heat transfer while minimizing pressure loss. The motivation behind using adjoint optimization, which utilizes freeform deformation, is the opportunity to investigate the new design space available with the rise of additive manufacturing. The baseline geometry is based upon the NASA HOST experiment and is additively manufactured. This geometry is to be integrated into a heat transfer rig to serve as a matching experiment for the computational component of the study. The computational model and adjoint scheme are contained within STAR-CCM+. This report summarizes current progress on this study for both experimental and computational aspects. Once the computational model of the baseline geometry could be experimentally validated, the geometry can be optimized. Ultimately, this work aims to assess the real-world capability of adjoint optimization in turbomachinery design.

Project Objectives
Turbine blades require cooling through methods such as blade internal passages to withstand the high temperatures of the flows exiting the combustor. However, these cooling flows decrease the thermal efficiency of a gas turbine engine due to pressure losses attained during the cooling process. To mitigate this effect, the geometry of these passages could be optimized to reduce pressure loss while maximizing heat transfer. The selected optimization method is the adjoint method, a design optimizer based on computational fluid dynamics (CFD). The adjoint method optimizes designs using freeform deformation, allowing for the exploration of the expanded design space provided by the rise of additive manufacturing. An advantage of this method is that optimization speed is not dependent on the quantity of design variables, which in this case are grid points that define the geometry of the object of interest. In the context of turbomachinery design, the application of adjoint methods in design optimization is fairly new and this research provides a basis on which confidence in the tool could be built.

In this study, the effectiveness of adjoint optimization in internal cooling passages will be assessed. Adjoint optimization will be applied to a u-bend passage with objective functions of maximized heat transfer and minimized pressure loss.

Methodology
This research consists of computational and experimental components. A flowchart for the organization of the project is shown in Figure 1.

The baseline geometry to be optimized is based on the heat transfer model geometry from NASA's Hot Section Technology (HOST) experiment [1]. From this model, a single u-bend passage with no turbulators was extracted to serve as the baseline geometry, as seen in Figure 2. The baseline geometry is additively manufactured using resin. The resin selected for the geometry is Formlabs' Rigid 10K V1. This material

was selected because its thermal properties are available in the open literature [2]. Additional structures used to interface with the experimental setup include the inlet and outlet plenums and nozzle pieces, also seen in Figure 2. Only three walls of the passage are additively manufactured. The fourth wall is a clear acrylic plate to provide visual access to the passage floor for the purpose of heat transfer assessment. Figure 3 shows a test print of the baseline geometry.

The full experimental setup is detailed in the flowchart in Figure 4. The baseline geometry is integrated into an existing heat transfer rig from [3]. However, in this study, heat transfer is assessed visually using thermochromic liquid crystals (TLC). TLCs display the temperature distribution of the surface on which it coats via a visual spectrum of rainbow colors, starting with red at the activation point (temperature range start) and blue at the clearing point (temperature range end). TLC paint from LCR Hallcrest with a range of 30-33°C was selected to evaluate the passage floor temperature.

To confirm that the selected temperature range was appropriate for the experiment, a semi-infinite solid analysis for a surface convection case was performed, as seen in Figures 5a and 5b. The mean flow temperatures through the passage were determined using a steady-state straight pipe flow model with heat transfer coefficients evaluated using empirical Nusselt number data from NASA HOST [1]. According to Figure 5b, ~10 seconds elapse before the surface at the passage exit reaches the activation point of the TLC paint and ~20 seconds elapse before the same surface attains the temperature of the paint's clearing point. The semi-infinite solid assumption remains valid for the passage floor through the entirety of the experiment, which lasts approximately 30 seconds. This deems the paint's temperature range appropriate.

A steady CFD model of the baseline geometry was developed in STAR-CCM+. Though the experiment is transient, it is necessary for the numerical model to be steady state so that adjoint optimization could be applied. Figure 6 displays the inputs to the model. These inputs were selected based on the experimental setup of NASA HOST or on this study's experimental setup.

Results and Discussion

Initialization of the numerical model is currently in progress. Convergence of the current iteration of the model is poor, as evidenced by Figure 7. Velocity contours on the midspan plane display unsteady behavior in the inlet and outlet regions. This is expected as the inlet and outlet geometries contain elements that encourage the formation of vortices and other unsteady flows. Additionally, this unsteady behavior is being modeled in a steady model. To improve convergence, an inlet study was performed with two alternate configurations. These configurations are pictured in Figure 8.

Convergence was optimal in Case A, however, it is also necessary to assess how well the solutions for these configurations match with the solution of the original baseline model from Figure 7. Relative differences with respect to baseline distribution range of temperature and pressure through the passage were calculated. These results can be seen in Figures 9 and 10, respectively.

In Figure 9, the largest relative difference in temperature with respect to baseline passage temperature range is located at the passage inlet region for both configurations. This difference is approximately 100%. The largest relative difference in pressure distribution with respect to baseline pressure drop is in the outgoing leg of the passage for both configurations. In Figure 10, this difference is about -130% in Case A. This difference is smaller in Case B, but the pressure drop in this configuration is still larger than that seen in the baseline model.

The inlet and outlet can be designed to smooth many of the corners present in the plenum to reduce the formation of vortices. Other undesirable phenomena may also be mitigated by centering the jet in these

regions. Flow can be made uniform in the plenum by inserting a screen or baffle. An alternative solution to attaining a well-converging CFD model of the baseline geometry is to run a model with passage inlet conditions that were extracted at the exit of the inlet plenum in the poorly converging model.

Once a baseline computational model could be initialized and validated, adjoint optimization could be applied. This optimized geometry would then be manufactured and experimentally assessed.

Figures/Charts

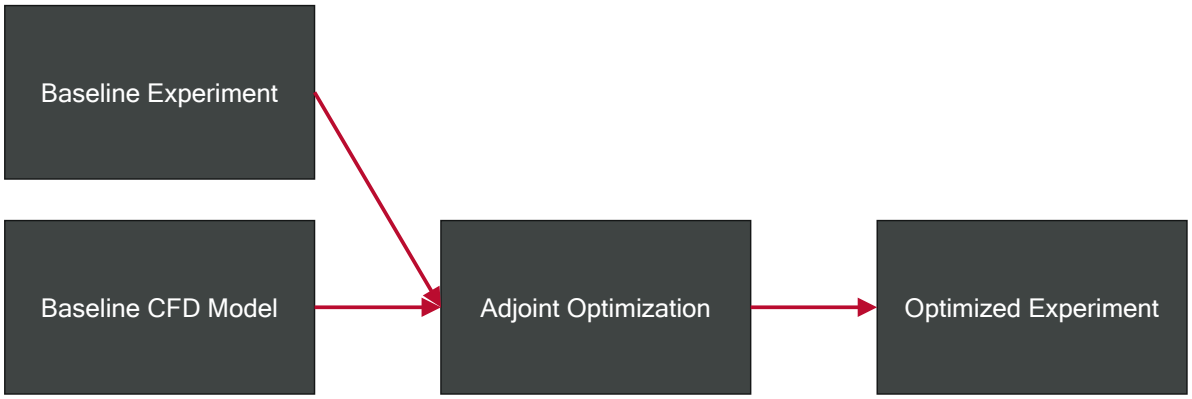


Figure 1: Project flowchart

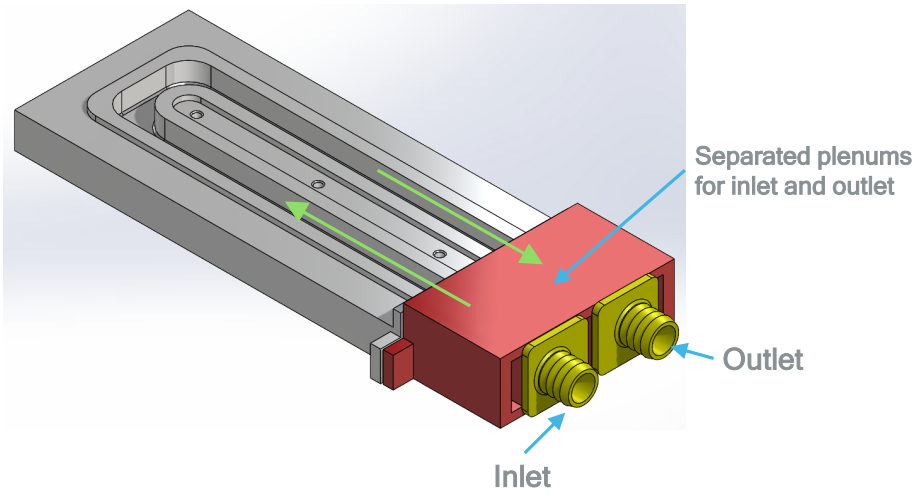


Figure 2: Baseline geometry CAD

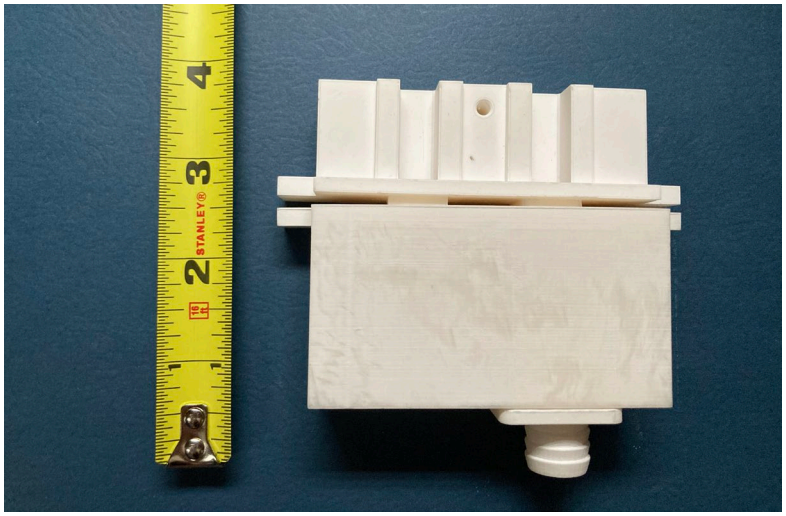


Figure 3: Baseline geometry test print

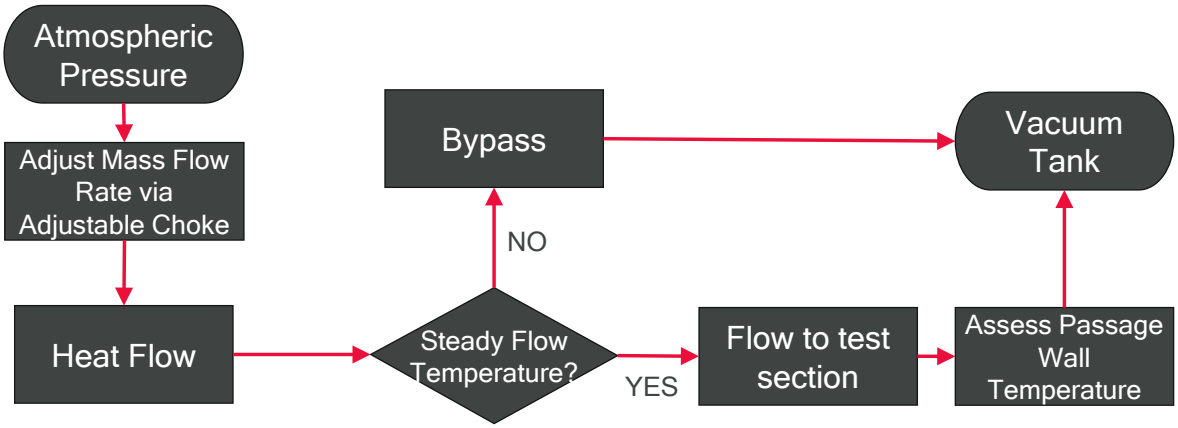
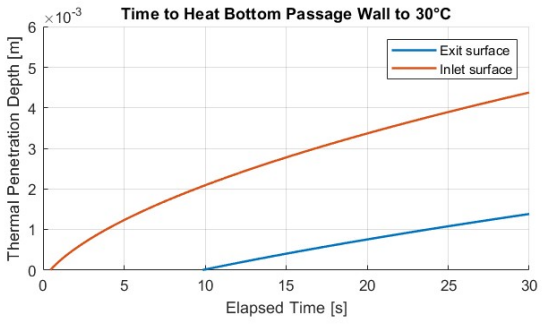


Figure 4: Experimental setup flowchart



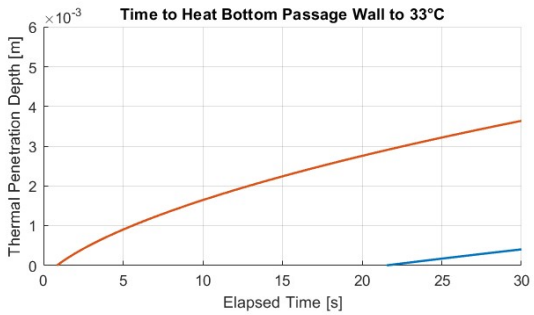


Figure 5a (left): Semi-infinite solid analysis for passage floor temperature of 30°C

Figure 5b (right): Semi-infinite solid analysis for passage floor temperature of 33°C

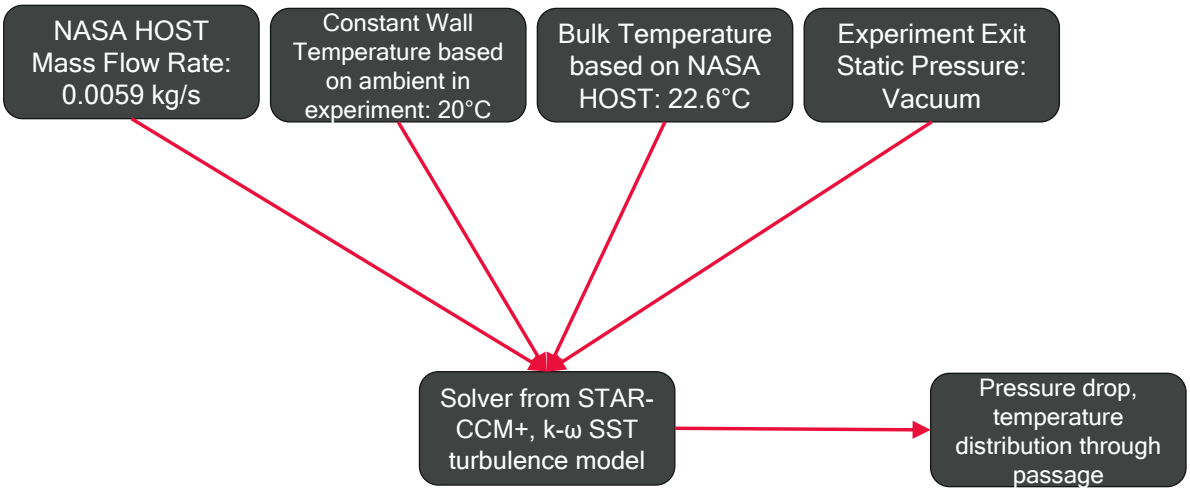


Figure 6: Baseline CFD model inputs and outputs

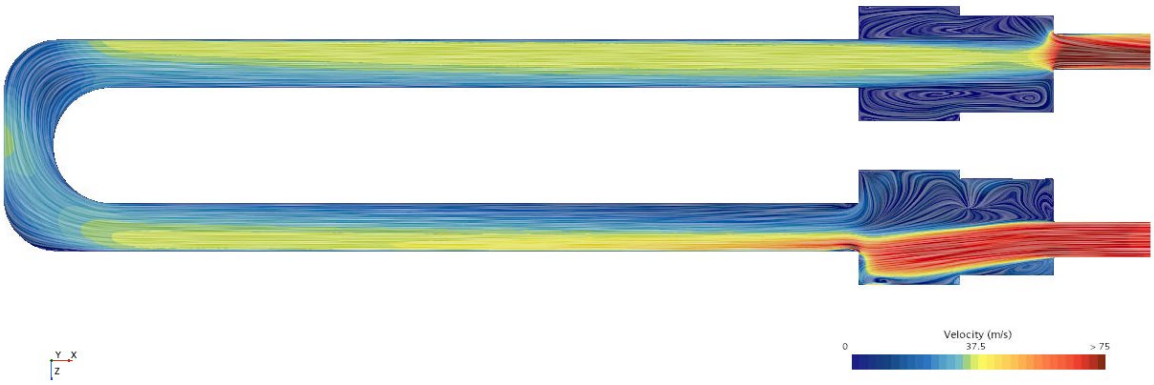


Figure 7: Baseline midspan plane velocity contour

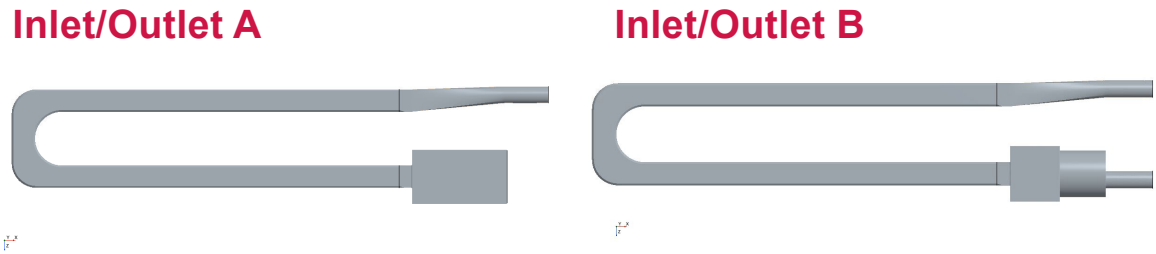


Figure 8: Inlet study configurations

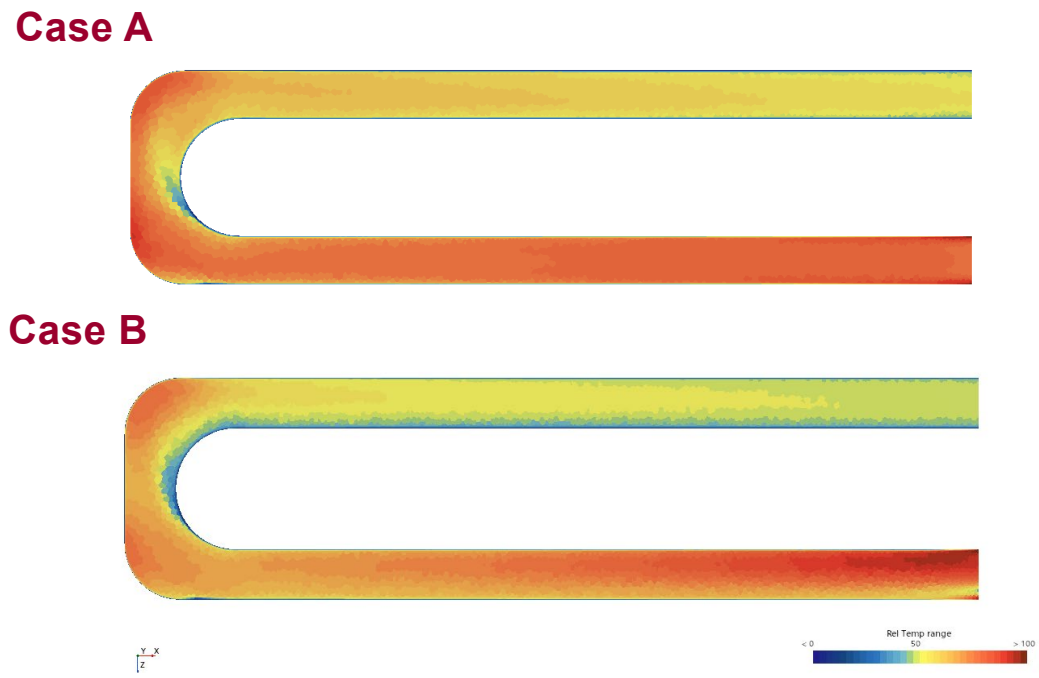


Figure 9: Midspan contours for relative difference in temperature with respect to baseline temperature range

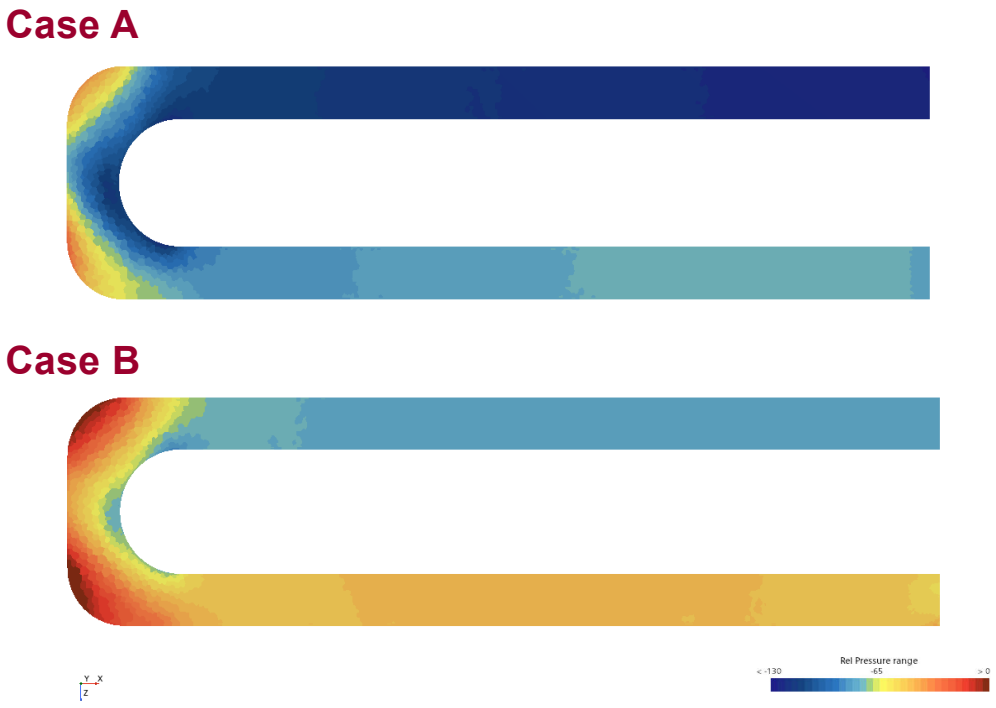


Figure 10: Midspan contours for relative difference in pressure with respect to baseline pressure drop

Acknowledgments
This research is funded by Honeywell Aerospace and the Ohio Space Grant Consortium. Their support is greatly appreciated.

References

[1] Hajek, T. J., Wagner, J. H., Johnson, B. V., Higgins, A. W., and Steuber, G. D., 1991, *Effects of Rotation on Coolant Passage Heat Transfer: Volume I-Coolant Passages With Smooth Walls*. [Online]. Available: https://ntrs.nasa.gov/citations/19910021175.

[2] Kinsey, B., Skora, A., Mokler, M., Wheeler, M., Dahl, K., Craig, S. A., Portoni, P., Basore, K., Strauss, T., Dean, T., Arndt, A., and Wernz, S., 2024, "Measurement of Heat Flux on a 3D Printed Hemisphere With IR Thermography," *AIAA AVIATION FORUM AND ASCEND 2024*, American Institute of Aeronautics and Astronautics, Las Vegas, Nevada. https://doi.org/10.2514/6.2024-4284.

[3] Christensen, L. E., and Mathison, R. M., 2018, "Measurement of Heat Transfer Inside a Channel Using External Infrared Thermography," *2018 Joint Propulsion Conference*, American Institute of Aeronautics and Astronautics, Cincinnati, Ohio. https://doi.org/10.2514/6.2018-4430.

In situ carbonization of PEEK and PEKK by pyrolysis of lignin

Student Researcher: Joseph Reindl

Advisor: Dr. Luigi Giancarlo Corti

Miami University
Department of Mechanical and Manufacturing Engineering

Abstract

Composites of Carbon with Polyetheretherketone and Polyetherketoneketone were made by in situ pyrolysis of organic material during melt processing in an extruder as a candidate precursor thermoplastic pitch for Carbon/Carbon composite production. The effects of rice husk (RH) and lignin (L) concentrations on the processability and residual carbon content were investigated. The effects of processing temperature and time were investigated. GC/MS analysis of residual oils collected during the extrusion process indicates the onset of thermal decomposition of PEEK and PEKK at temperatures as low as 370℃ and 350℃, respectively, when compounded with organic material. Thermogravimetric analysis shows an increase in retained mass when heated to 900℃ in Argon. Differential scanning calorimetry indicates a loss in thermoplastic properties after 20 hours at melt processing temperatures.

Project Objectives

In this work, the effects of in situ carbonization of PEEK-(Rice Husk) and PEEK-(Lignin) composites on the residual carbon content post-carbonization are investigated, as well as the mechanism by which PEEK interacts and degrades in the presence of lignin and rice husk at melt processing temperatures. It is hypothesized that the degradation byproducts of lignin accelerate the degradation of PEEK at melt processing temperatures and that the formation of graphite-like carbon structures combined with cross-linking of the polymer may increase the stiffness and strength of the final PEEK-Carbon composite as well as increase the potential residual carbon content of the polymer for carbon/carbon composite production applications..

Methods

PEEK and PEKK were purchased from 3DXTech (3DXTech, Grand Rapids, MI, USA). Pulverized rice husk powder with a maximum particle size of 74µm was purchased from Ribus (Nu-FLOW™ Nu-FLOW SMBG PO, Ribus, Sparks, NV, USA). Alkali lignin (CAS 8068-51) was purchased from Sigma-Aldrich (Sigma-Aldrich, St. Louis, MO, USA).

The raw PEEK and PEKK pellets, rice husk powder, and lignin powder were dried in a vacuum at 80°C overnight. Samples were mixed into 50g batches of 3% and 6% rice husk by weight and 0.6% and 1.2% lignin by weight. The lignin values were selected based on the reported 20% lignin content of rice husk [1]. Each batch underwent four passes through a Filabot EX6 extruder (Filabot, Barre, VT, USA) with a standard profile nitride coated screw at one of two mixing temperatures for each polymer, as described in Table 1, to ensure a homogeneous mixture throughout the material. For the fifth and final pass, the extruder temperature was increased during the pass to 400℃, 420℃, and 440℃ for the PEEK samples and to 380℃, 390℃, and 400℃ for the PEKK samples.

Table 1 Zone Heater Settings for Filabot EX6

Material	Front Heater (℃)	Middle Heater (℃)	Back Heater (℃)	Feed (℃)
PEEK	370	370	350	60
PEEK	380	380	350	60
PEKK	350	350	320	60

Gas chromatography/mass spectrometry analysis was carried out on an Agilent 789O gas chromatography coupled to an Agilent 5975 electron impact mass spectrometer (Agilent Technologies Inc., Santa Clara, CA, USA). The GC analysis started at 90℃ and was heated at 15℃/min to 325℃ with a 5-minute isothermal at 323℃. The column was a ZB-5 HT with a length of 30 m, an internal diameter of 0.25 mm, and a film thickness of 0.25 µm. The helium column flow rate was 37/1 cm/s. The front inlet temperature was 250℃ with a pressure of 68.6 kPa, a flow rate of 24 mL/min, and a septum purge of 3 mL/min.

Thermogravimetric Analysis (TGA) was conducted on a TA TGA550 (TA Instruments, New Castle, DE, USA). Samples of each final temperature pass from each mixing temperature of each material concentration were heated in an argon atmosphere up to 900℃ at a rate of 10℃/min to determine the residual carbon concentration.

Differential Scanning Calorimetry (DSC) was conducted on a TA DSC2500 (TA Instruments, New Castle, DE, USA). All samples were 5-10 mg and were prepared in sealed aluminum DSC pans. Each sample underwent four heating and cooling cycles, ranging from 40℃ to 400℃ at a rate of 5℃/min in both directions.

Results and Discussion

A previous research project aimed to improve the mechanical properties of PEEK by direct compounding pyrolysis of PEEK with rice husk to form a PEEK-silica composite. The goals of this project were not met, however, as it was observed that the PEEK started to carbonize and decompose at melt processing temperatures much lower than the typical onset of thermal degradation for PEEK [2]. This was evidenced by notable gas formation at the nozzle of the extruder, rubbery hot extruded material, and a lightweight and brittle cooled filament.

To investigate the pyrolysis effects on the rice husk alone, thermogravimetric analysis was conducted on a sample of dried rice husk powder. The rice husk was heated in a nitrogen atmosphere to 400℃ at a rate of 10℃/min, then allowed to cool to 30℃ before repeating the heating and cooling cycle three more times. The mass loss curves for each pass are shown in Figure 1.

Figure 1 shows that approximately 60% of the original mass of the rice husk sample is lost during the first heating pass, primarily due to the cellulose and hemicellulose components. After 350℃, the mass loss continues again, dropping off more significantly near the 400℃ maximum temperature. This is likely the beginning of the thermal decomposition of the lignin in the rice husk, which occurs primarily between 350℃ and 450℃ [3]. This is proven by the second to the fourth cycle, where the RH does not lose any significant amount of mass below 400℃, but it loses approximately 3.5%, 2.5%, and 1.9% on the second, third, and fourth cycles, respectively.

GC/MS analysis was performed to identify the volatile compounds released during the decomposition contained in the extruder. It was observed that an oily substance tended to accumulate in the feed section of the extruder during processing.The resulting chromatographs can be seen in Figure 2 (PEEK) and Figure 3 (PEKK). Each peak was correlated using the NIST database, and the contents of the condensed liquid were determined. Cross-referencing these volatiles to existing literature on the decomposition products of PEEK, PEKK, and lignin, it was determined that none of the present volatiles are unique to lignin [4,5]. All of the components are decomposition products of PEEK and PEKK, however phenol is also produced in the thermal decomposition of lignin, so it is uncertain if the phenol content is primarily from the polymer or the lignin [4]. It was observed that decomposition products started appearing at temperatures well under what is expected for the thermal decomposition of PEEK and PEKK. Thus suggesting an accelerated thermal degradation of PEEK and PEKK.Figure 4 shows the mass loss curves for samples of PEEK-3% RH, PEEK-0.6% L, and PEEK-1.2% L, each mixed at 380℃ with a final pass temperature of 400℃. It can be seen that the residual mass increase is similar between the three PEEK blends, with the 3% RH increasing by 6.25%, the 0.6% L increasing by 7.44%, and the 1.2% L increasing by 8.44%. Despite containing double the lignin concentration, the 1.2% L sample only increased the relative residual mass by 1%. This suggests that the mechanism of accelerated decomposition may be limited by the availability of its PEEK components rather than the availability of lignin.

Figure 5 shows the mass loss curves for samples of PEKK-3% RH, PEKK-0.6% L, and PEKK-1.2% L mixed at 350℃ with a final pass at 400℃. It can be seen that the PEKK-3% RH and PEKK-0.6% L samples do not show the same large increase in residual carbon content as the PEEK samples did, however the base residual mass for PEKK is ~18.99% higher than that of PEEK. The PEKK-1.2% L samples did show an increase in residual mass compared to pure PEKK. For PEEK, increasing the concentration of lignin did not significantly increase the residual carbon content because the accelerated degradation reaction may be reliant on the presence of polymer components rather than lignin, but as increasing the concentration of lignin in PEKK does increase the residual carbon content, insight into the potential mechanism can be gleaned. If increasing the lignin concentration of PEEK does not increase its carbon content, but it does increase the carbon content of PEKK, it is possible that the accelerated degradation reaction occurs between the decomposition products of lignin and the carbonyl bonds in the PEEK and PEKK structure. As PEKK has two carbonyl bonds per unit to PEEK's one, and the most likely starting point for the onset of the regular pyrolytic decomposition of PEEK is at the carbonyl bonds [6], it follows that an increase in high molecular weight degradation products and radicals released from lignin could induce the chain propagation phase of PEEK and PEKK thermal decomposition.

Figure 6 shows the mass loss curves for samples of PEEK-1.2% L that were left in the extruder for 1 hour, 2 hours, and 20 hours. It can be seen that the final mass increases the longer the material is kept at temperature in the extruder. This suggests that the accelerated decomposition continues slowly over time. Figure 7 shows the mass loss curves for samples of PEEK-1.2% L mixed at 350℃ and left in the extruder for 0, 1 , 2, and 22 hours. It can be seen that the material that spent the most time in the extruder once again has the highest residual carbon content. The 1-hour and 2-hour samples are comparable to the base residual mass of pure PEKK, though they do show an increase from the 0-hour PEKK-1.2% L sample. The 20-hour sample, however, shows a marked increase in residual mass.

Differential scanning calorimetry was used to investigate the crystallinity and thermoplastic properties of the pre-carbonized PEEK. Figure 8 shows the results of the thirds DSC cycle for a sample of PEEK-0.6% L mixed at 380℃ with a final pass at 420℃. It can be seen that the melting point is consistent with the reported 343℃

value. The slight positive slope on the high-temperature end of the heating curve indicates that the reaction between PEEK and lignin is ongoing and exothermic. The hump on the lower-temperature side of the recrystallization peak is evidence of non-polymeric material in the mixture, most likely primarily Carbon.

Material was again collected from the extruder after it had sat at 420℃ for 20 hours. The results of DSC analysis on the sample can be seen in Figure 9}. It can now be seen that there is no evidence of semi-crystalline polymer properties at all and the reaction is again exothermic until the end of the test. This implies that there is an upper limit for how much of the reaction can be allowed to take place before the polymer is no longer able to be worked with.

Figures

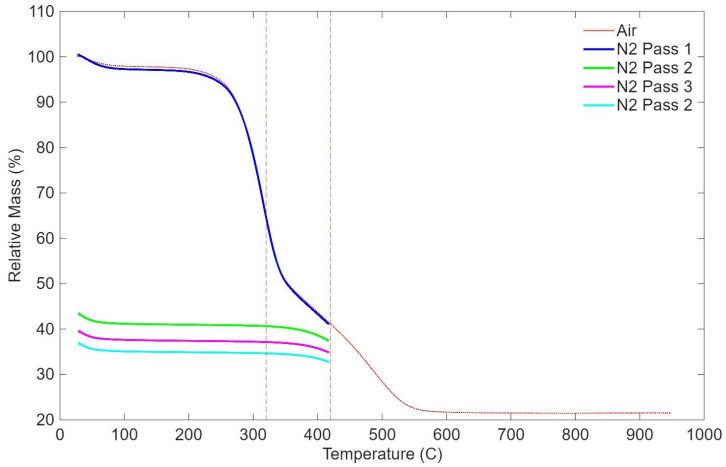


Figure 1 Mass loss curves for rice husk heated from 40℃ to 400℃ in N2.

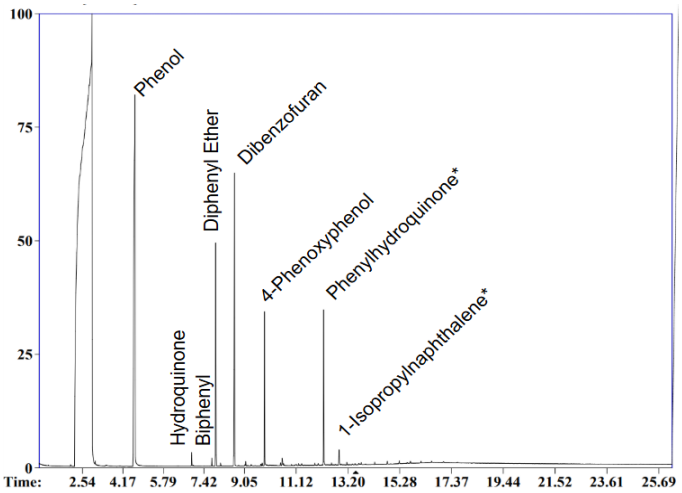


Figure 2 Chromatograph of residual oil collected during PEEK-1.2% L production.

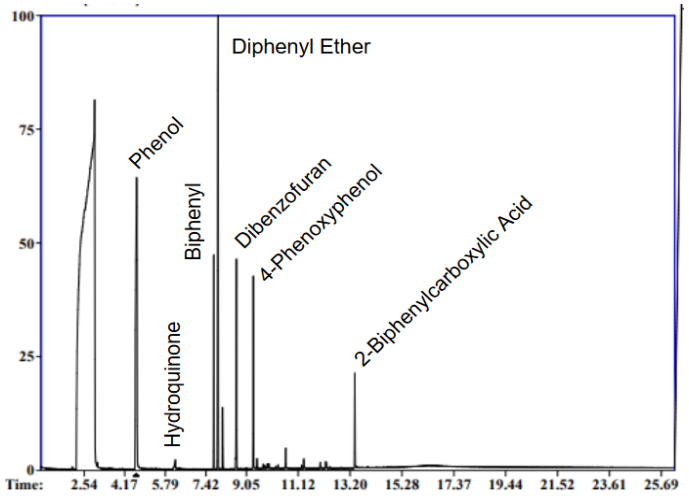


Figure 3 Chromatograph of residual oil collected during PEKK-1.2% L production.

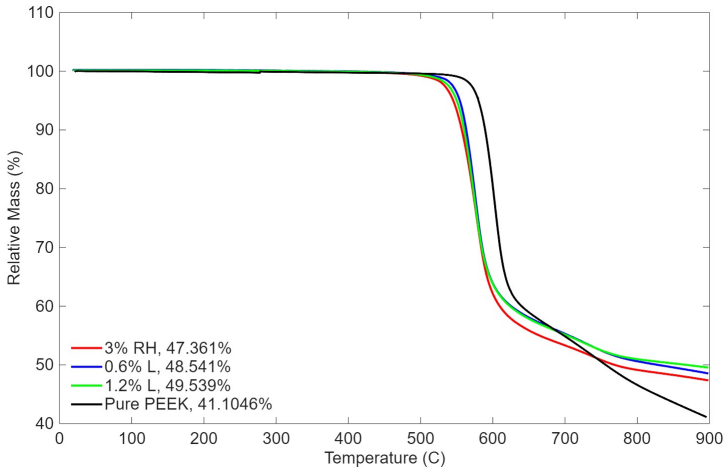


Figure 4 Mass loss curves for PEEK with 3% RH, 0.6% L, 1.2% L, and pure control.

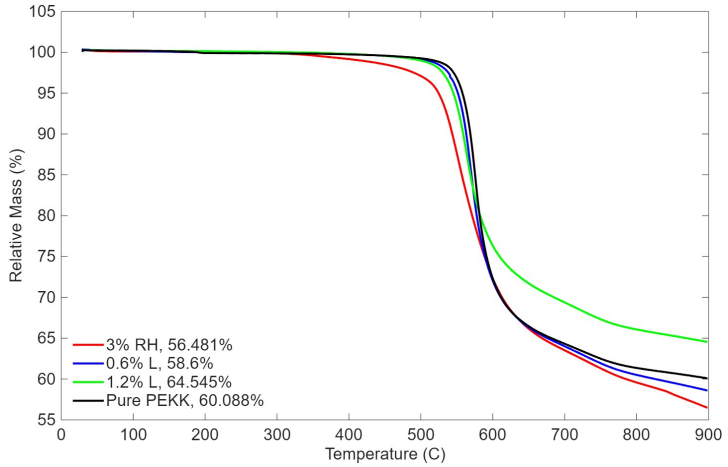


Figure 5 Mass loss curves for PEKK with 3% RH, 0.6% L, 1.2% L, and pure control.

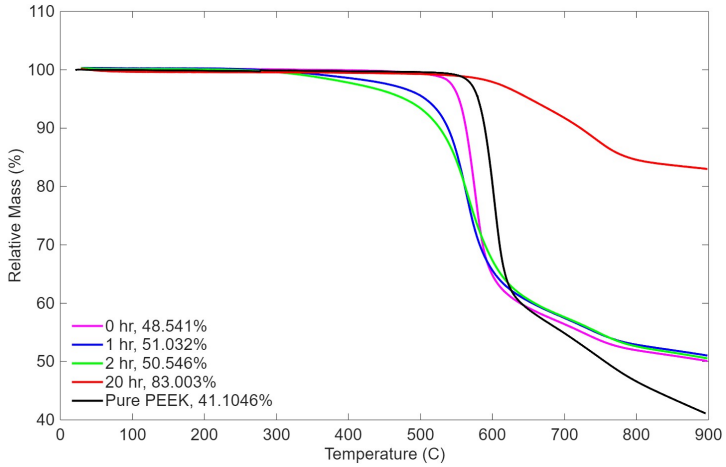


Figure 6 Mass loss curves for PEEK-1.2% L held at 420℃ for 0, 1, 2, and 20 hours following production.

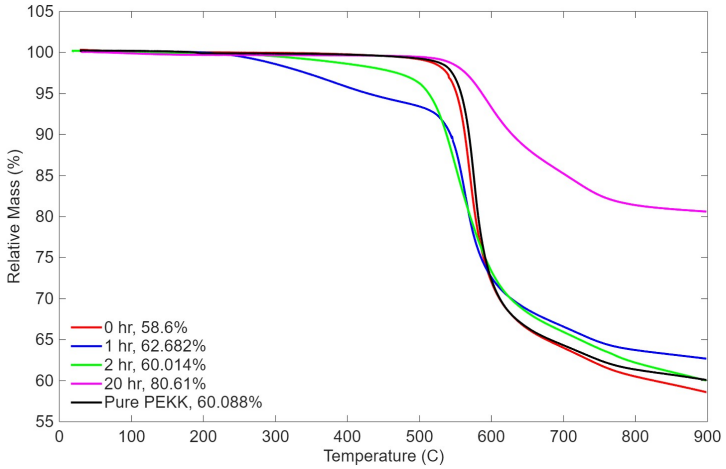


Figure 7 Mass loss curves for PEKK-1.2% L held at 420℃ for 0, 1, 2, and 20 hours following production.

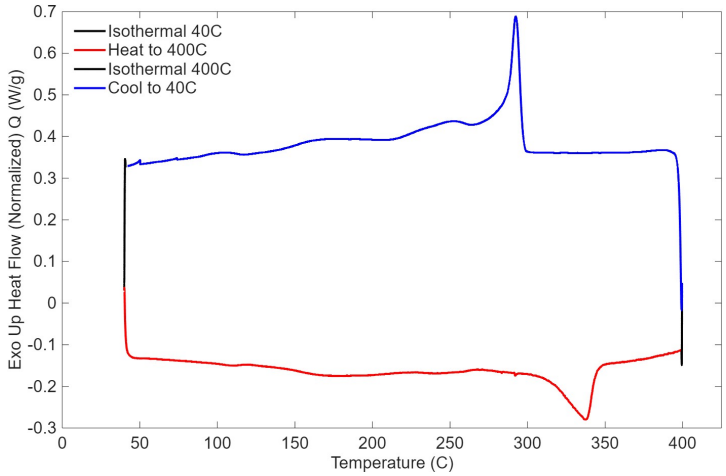


Figure 8 Heat flow curve of PEEK-1.2% L with no isothermal hold.

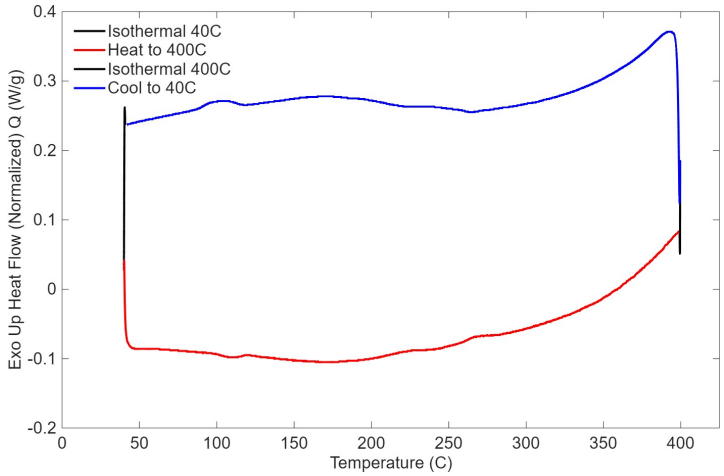


Figure 9 Heat flow curve of PEEK-1.2% L after 20-hour isothermal hold.

Acknowledgments

I thank the Ohio Space Grant Consortium for providing the Award that enabled me to conduct this research. I also thank my advisor, Dr. Luigi Giancarlo Corti, and my thesis committee member, Dr. Fazeel Khan, Dr. Mark Sidebottom, and Dr. Scott Iacono for their mentorship and support. I thank the United State Air Force Research Lab and the United States Air Force Academy for facilitating parts of this research. Finally, I thank my friends and family for always encouraging me to keep moving forward.

References

[1] Jha, P., 2024. Characterization of Biomass and Studies of Pyrolysis on Rice Husk in a Lab-Scale Pyrolyzer: A Step Toward Environmental and Energy Sustainability. Springer Nature Switzerland, Cham, pp. 75–90.

[2] Patel, P., Richard Hull, T., W. McCabe, R., Flath, D., Grasmeder, J., and Percy, M., 2010. “Mechanism of thermal decomposition of poly(ether ether ketone) (peek) from a review of decomposition studies”. Polymer Degradation and Stability.

[3] Liu, W.-J., Jiang, H., and Yu, H.-Q., 2015. “Thermochemical conversion of lignin to functional materials: a review and future directions”. Green Chemistry.

[4] Har, J. N., and Kemmish, D. J., 1987. “Thermal decomposition of poly(aryl ether ketones)”. Polymer.

[5] Chu, S., Subrahmanyan, A., and Hubert, G., 2013. “The pyrolysis chemistry of a β-o-4 type oligomeric lignin model compound”. Green Chemistry.

[6] Tsai, C. J., Perng, L. H., and Ling, Y. C., 1997. “A study of thermal degradation of poly(aryl-ether-ether-ketone) using stepwise pyrolysis/gas chromatography/mass spectrometry”. Rapid Communications in Mass Spectrometry.

Repair and Enhancement of Titanium Turbine Blades through Direct Energy Deposition (DED) Additive Manufacturing (AM)

Student Researcher: Lukas Seggi

Advisor: Dr. Manigandan Kannan

University of Akron
Department of Mechanical Engineering / Mechanical Engineering

Abstract

The recent advances in additive manufacturing (AM) have opened many new possibilities for various industries and applications, one of them being to use the technology to create new parts and repair existing parts using AM. In this research, wire-based Direct Energy Deposition (DED) AM is investigated as a tool to repair damages in titanium parts and the vibrational suppression technology i-DAMP is utilized within the DED-AM parts to enhance lifetime performance in the field. To understand the viability of this technology, samples were manufactured by printing Ti-6Al-4V on top of printed and conventional Ti-6Al-4V using a Meltio M450 DED system. These samples will be tested for the strength of the bond between the substrate and the printed material, as well as the application of i-DAMP vibration suppression technology towards the material's vibrational properties.

Introduction and Background

For aerospace industry purposes, metal additive manufacturing (AM) is a process of fabricating models in a layer-by-layer through a combination of energy delivery and material deposition, with one of the most common industry methods for this being direct energy deposition (DED) (Shrestha et al., 2021). DED involves a wire being continuously fed into a laser or electron beam to form a continuous deposited material structure in the presence of an inert environment (Frazier, 2014, pg. 1919). DED-AM has been investigated as a repair mechanism for damaged aerospace parts, especially for turbine blade applications. Traditionally when turbine blades are damaged it would require a full replacement; with DED-AM, the blades could be repaired due to DED's low material porosity characteristics. Further material surface modifications such as surface grinding could be utilized to improve compressive residual stresses on the part surface (Rakurty et al., 2023). In conjunction with material processes, a vibration suppression technology called i-DAMP developed by Hyphen Innovations has been used to increase part life by a factor of ten and lead to a ninety-five percent decrease in vibrational output. This technique involves placing powder-filled pockets within the part during the DED-AM process in high stress areas to absorb energy during the use of the part. This research involves combining all avenues of the previously mentioned technologies into an encompassing repair and enhancement method for aerospace parts.

Project Objectives

The main objective of this project is to combine vibration suppression technology with laser wire Direct Energy Deposition (DED) Additive Manufacturing (AM) to develop a repair and enhancement method for Aerospace components. These types of aerospace components can range in size and shape, but for the purposes of this project the chosen application is titanium turbine blades in jet turbine engine compressors. To fully determine the properties of the repaired surface method and the enhancement technology, mechanical property testing through tensile and fatigue testing as well as vibrational testing through specialized high-cycle fatigue testing will be conducted. Beyond traditional property testing, microstructure analysis of the printed material is desired. This is due to determine how the printed material bonds to conventional material, the overall microstructure of the printed material compared to

the conventional material, as well as the effects the energy of the printing process has on the conventional material. Following this general material testing and results, future testing will involve material performance after various surface modification methods, with the goal to be to improve the compressive residual stress on the material surface thereby slowing down the crack initiation and other surface properties in the material.

Methods and Materials

To achieve the project objectives, a project strategy to test the capability of DED-AM with multiple materials and part geometries and sample fixtures was developed. First, create a procedure to print material onto existing objects using DED-AM utilizing the Meltio M450 DED system. Following that, develop a procedure to machine an i-DAMP-representative pocket, fill the pocket with nicked-based superalloy powder utilized in powder bed fusion AM, and continue the DED-AM process above the pocket without significant powder fusion within it. Following the completion of the manufacturing procedures, manufacture DED-AM samples to test the method's mechanical properties through tensile and fatigue dogbone samples and the method's vibrational properties through DED-AM plate samples enhanced with i-DAMP technology. Once these samples are manufactured and tested, the results, procedures, and strategies developed concurrently will be applied to manufacturing DED-AM turbine blade specimens and testing will be repeated. Regarding material utilization, initial tests will be conducted with DED-AM Stainless Steel 316L and then the results and strategies developed through these initial tests will be applied to Titanium Ti-6Al-4V. For the utilized damping powder, nicked-based superalloy powder that is utilized in powder bed fusion AM was selected to reduce the likelihood of powder fusion during the DED-AM process while still providing vibration suppression through i-DAMP.

Experiment Methodology

The experimental testing for this project is split into two main categories: mechanical property testing and vibration testing. In addition to these major testing goals, additional microstructure analysis will be conducted to visually determine how the printed and conventional materials bond to one another, as well as how the materials are affected by the high temperatures during the printing process.

The mechanical property testing will be conducted by comparing standard Ti-6Al-4V to its repaired counterpart, consisting of standard Ti-6Al-4V with DED-AM Ti-6Al-4V printed above. These specimen groups will be comprised of dogbone tensile specimens as per ASTM E8 (ASTM); the standard group will be dogbones comprised of all standard stock Ti-6Al-4V, while the repair group will be dogbones comprised of half standard Ti-6Al-4V and half DED-AM Ti-6Al-4V separated at the midline of the dogbone. See Figure 1 for visual representation of these specimens. Through tensile and fatigue testing of these specimens, the material properties will be determined for each specimen group will be determined and the results will be compared between the two groups. As stated previously, the results of these tests will be compared to repair specimens subjected to surface modification methods to improve crack initiation and other surface properties.

The vibrational testing will be conducted by manufacturing Ti-6Al-4V plate specimens consisting of half standard Ti-6Al-4V with DED-AM Ti-6Al-4V printed above it, similar to the mechanical property test samples. However, as the goal of this testing is to incorporate i-DAMP vibration suppression technology, the top of the plates will be machined and then will have void pockets machined into the plate and filled with Ni-based superalloy powder. A Ti-6Al-4V shim will be placed atop the machined surface to act as a covering. The final portion of the plate will be printed above this covering, with the heat generated by the DED-AM process fusing the shim to the rest of the Ti-6Al-4V specimen. See Figure 2 for visual representation of these specimens. These vibrational plate specimens will be tested using high-cycle fatigue testing and the results of it will be compared to stock Ti64 plates tested in the same configuration

and style. Following the plate specimen testing, the manufacturing and testing process designated for the vibrational specimens will be repeated with Ti-6Al-4V DED-AM turbine blade specimens. As with the mechanical property specimens, plate and blade specimens subjected to surface modification methods to improve crack initiation and other surface properties will be manufactured and tested, with the results compared to the non-modified surface vibrational specimens.

Results and Discussion

Over the current duration of the project, many of the project objectives have been accomplished or are actively in progress. Through iterative manufacturing segments, DED-AM print strategies have been developed as well as specimen fixtures and orientations have been produced. Through this, multiple DED-AM specimens have been manufactured. With these strategies proven, manufacturing of mechanical property and vibrational specimens is underway.

In accordance with the first project objective to create a procedure to DED print material onto existing objects, initial testing was conducted on the viability of printing on top of existing prints and objects. Using the Meltio M450, stainless steel 316L specimens were printed, their top surface machined flat, and then another specimen was printed atop this flat surface (see Figure 3). This specimen allowed for a better understanding of how printing above existing surfaces could work and aided in the development of the procedure for sample manufacturing.

In accordance with the second project objective to create a procedure to machine the i-DAMP pocket and DED print on top of the pocket without significant powder fusion within the pocket, samples were manufactured using this structure and then x-ray images were taken of the resulting powder fusion using computed tomography (CT) scanning technology. Following the sample manufacturing procedure developed in the first project objective, stainless steel 316L samples were produced through DED-AM on the Meltio M450. After the print surface was machined flat, a void pocket was machined into the specimen and filled with Ni-based superalloy powder. A 316L shim was welded to the top surface to ensure the pocket was covered. The rest of the specimen was then printed above the shim (see Figure 4 for the final print as well as a schematic of the specimen internal structure). Following this, the sample was machined down to be CT scanned (see Figure 5). The resulting CT scan for this sample revealed the internal pocket, as well as the powder within the pocket and its approximate fusion amount. The CT scanned specimen image can be seen in Figure 6 below. From the results of the scan, there was a larger amount of fused powder within the void pocket than expected. Due to this, a larger shim will be utilized in future samples to account for this powder fusion.

Following the completion of project objectives one and two, the procedures and strategies developed for stainless steel were applied to titanium. For DED-AM Ti-6Al-4V samples, a new fixture was developed to allow for easier removal and adjustment of printed samples. Ti-6Al-4V presented a new challenge in printing different from 316L as it required a significantly higher Argon gas flow rate for the inert print chamber. To find an effective range to utilize Argon gas, a trial specimen was manufactured that had three separate printed sections with each printed using a varied Argon flow rate. The values used were determined by the wire filament Ti-6Al-4V manufacturer's guidelines of an argon flow rate range of seventeen to twenty liters per minute, as well as five liters per minute to show a significant difference in argon flow. The first section was printed at twenty liters per minute, the second section at five liters per minute, and the third section at seventeen liters per minute. The resulting specimen can be seen in Figure 7 along with the aforementioned specimen fixture. Note the distinct differences in print quality from the higher argon flow rates to the low argon flow rate, as the lower argon flow allowed for a surrounding oxide layer on the printed surface to form with increased exposure to oxygen. To further study the material structure of the fusion between standard and printed Ti-6Al-4V as well as the impact of argon

flow on the print structure, microstructure analysis will be investigated on these areas of interest on this sample. These areas include the stock Ti-6Al-4V, the area where stock and printed Ti-6Al-4V fused, Ti-6Al-4V printed at twenty liters per minute, Ti-6Al-4V printed at five liters per minute, and Ti-6Al-4V printed at seventeen liters per minute. The microstructure analysis will investigate both along the print face and at the layer level, by taking samples from both the front and side of the specimen (see Figure 8). Along with microstructure analysis, further investigations into these areas will include the oxygen content within each section as well as CT scans of the specimen.

Figures

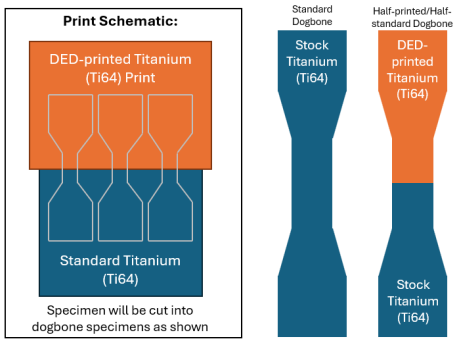


Figure 1: Mechanical property dogbone sample diagram, visualizing the difference between the 'standard' sample group and the 'repair' sample group.

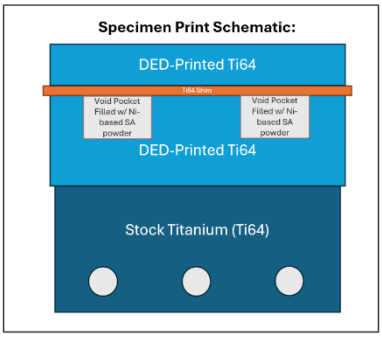


Figure 2: Vibrational plate specimen diagram, visualizing the components of the sample and how i-DAMP and DED-AM will be incorporated into the sample manufacturing process.

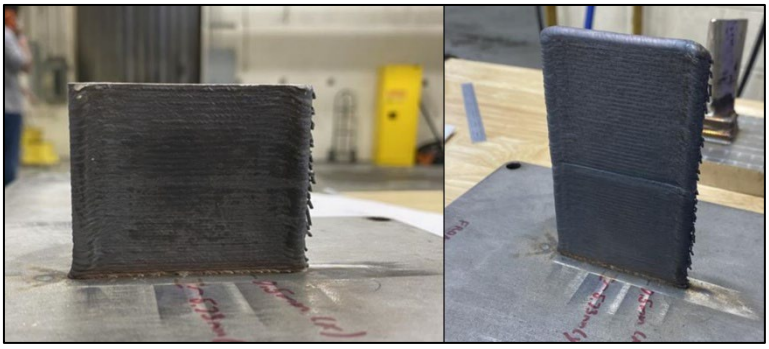


Figure 3: (Left) 316L print sample with top surface machined flat. (Right) Final specimen with 316L sample printed above original 316L sample.

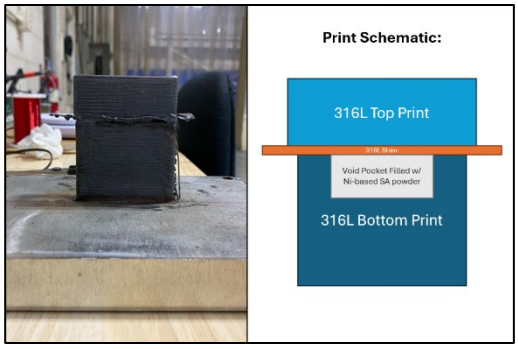


Figure 4: (Left) 316L void pocket sample post-print. (Right) Schematic of internal structure of DED-AM 316L void pocket sample.

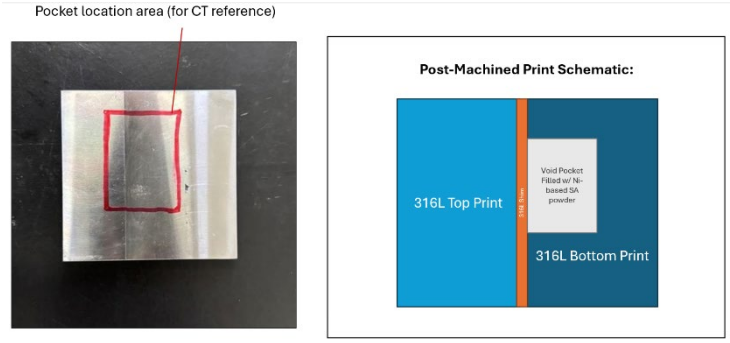


Figure 5: (Left) 316L void pocket printed sample post-machining. (Right) Schematic of internal structure of DED-AM 316L void pocket sample post-machining.

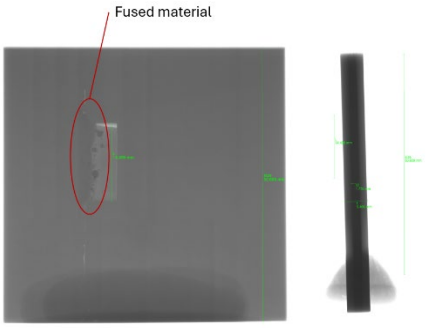


Figure 6: CT scan of 316L void pocket sample - note the circled fused material area.

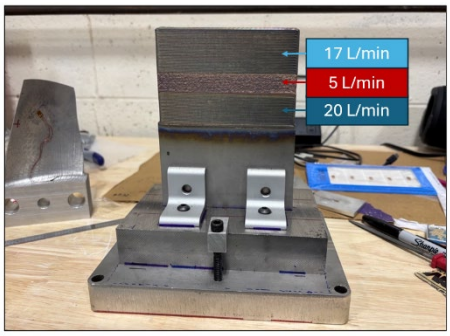


Figure 7: DED-AM Ti-6Al-4V printed specimen with argon rates noted.

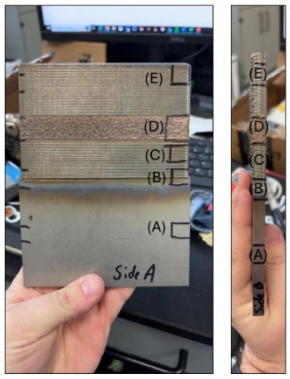


Figure 8: DED-AM Ti-6Al-4V argon sample separated into specified sections, from front and side views. From Bottom: (A) Rolled Ti64, (B) Fusion b/w Stock and Printed Ti64, (C) Ti64 printed at 20 L/min Argon, (D) Ti64 printed at 5 L/min Argon, (E) Ti64 printed at 17 L/min Argon.

Acknowledgments

The author would like to thank Dr. Manigandan Kannan for his continuous work and constant support of the author's graduate research and studies as their advisor. The author would also like to thank Dr. Onome Scott-Emuakpor, Philip Johnson and the team at Hyphen Innovations for providing the author with this opportunity and supporting specimen manufacturing. The author would also like to thank Dr. KT Tan for their support with testing and validation. The author would finally like to thank Jordan Craft and Erin Falkosky for their support and help through various aspects of this project.

References

ASTM, "E8 Standard Test Methods of Tension Testing of Metallic Materials," Annual Book or ASTM Standards, American Society for Testing and Materials, Vol. 3.01

C.S. Rakurty, Manigandan K, Blake Bowser, Nithin Rangasamy, Satya Kakaraparthi, Ryan Dippolito, Riley Myers, Grinding EB-PBF based additive manufactured Ti6Al4V: A surface integrity study, Advances in Industrial and Manufacturing Engineering, Volume 7, 2023, 100131, ISSN 2666-9129

Sulochana Shrestha, Ragavendra P. Panakarajupally, Manigandan Kannan, Gregory Morscher, Andrew L. Gyekenyesi, Onome E. Scott-Emuakpor, Analysis of microstructure and mechanical properties of additive repaired Ti–6Al–4V by Direct Energy Deposition, Materials Science and Engineering: A, Volume 806, 2021, 140604, ISSN 0921-5093.

William E. Frazier, Metal additive manufacturing: a review, J. Mater. Eng. Perform. 23 (6) (2014) 1917–1928.

Mathematical Model of Regenerative Fuel Cell for System Optimization

Student Researcher: Andrew Sharkey

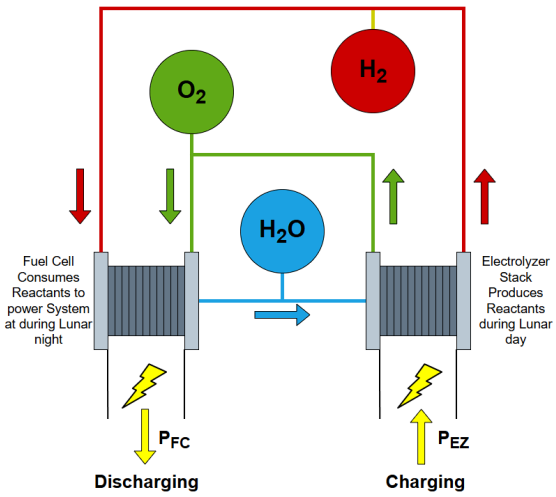
Advisor: Xiaoyu Zheng

Kent State University
Department of Mathematical Sciences
Applied Mathematics

Introduction

No energy storage technology enables lunar night survival within existing technical and programmatic constraints. While promising, advanced rechargeable energy storage solutions like regenerative fuel cells (RFC) require architecture-level optimization efforts across dozens of design parameters to maximize the overall system specific energy (measured in Wh/kg) and enable persistent human operations on the lunar surface (Guzik et al., 2017).

The goal of this project is to develop a robust and integrated model of the regenerative fuel cell system, considering operational characteristics of the fuel cell, electrolysis, and fluidic systems within a lunar environment to accurately estimate the system's specific energy for optimization purposes. In addition, we seek to apply optimization algorithms to the RFC model to maximize specific energy of the system, and identify critical design parameters by conducting a sensitivity analysis.



Mathematical Model

This model seeks to maximize specific energy of the system. Thus, we need the following equation:

$$SE = \frac{1}{m_{sys}} \int_{T_{EZ}}^{T_{FC}+T_{EZ}} P_{Req} - P_{cons} dt. \tag{2.1}$$

Here, T_{EZ} is the operation time for EZ cell and T_{FC} is the Fuel Cell operation time per cycle, and P_{Req} is the required power supplied by the Fuel Cell during that time, while P_{cons} is the power consumed during the Fuel Cell operation. In this model, P_{cons} is zero and we consider T_{FC} and P_{Req} to be parameters. In this model, we consider P_{Req} to be a given constant, therefore, the integral is just a constant, and equation 2.1 simplifies to:

$$SE = \frac{1}{m_{sys}} P_{Req} T_{FC}. \tag{2.2}$$

For ease, the mass of the system can be split into four parts: the mass of the fuel cell, electrolyzer, stored gases, and the balance of plant systems,

$$m_{sys} = m_{FC} + m_{EZ} + m_{Gas} + m_{bop}. \tag{2.3}$$

Mass of the Fuel Cell

First, we examine how the mass of the fuel cell is calculated:

$$m_{FC}(N_{FC}, k_{FC}, A_{FC})$$

$$= 1.2 \cdot N_{FC} \left(k_{FC} \left(m_{MEA}^{FC}(A_{FC}) + m_{bp}^{FC}(A_{FC}) + m_{fr}^{FC}(A_{FC}) \right) + 2m_{ep}^{FC}(A_{FC}) + m_{aux}^{FC} \right). \tag{2.4}$$

Here, $N_{FC} = N_{SFC} \cdot N_{PFC}$ and is the total number of fuel cell stacks. N_{SFC} and N_{PFC} is the number of fuel cell stacks in series and in parallel respectively, A_{FC} is the area in each cell, and k_{FC} is the total number of cells per fuel cell stack.

m_{aux}^{FC} is the auxiliary masses, e.g., wires and piping, that are needed for each fuel cell stack. We also use 1.2 to estimate the mass of auxiliary cells such as humidifiers or degasser cells.

The mass of each individual cell contains m_{MEA}^{FC}, which is the mass of the cell membrane electrode assembly (MEA) where the reaction takes place, m_{bp}^{FC} is the mass of the bipolar plate which separates each cell and directs the gasses along the MEA, and m_{fr}^{FC} is the mass of each cell frame. This model assumes that the fuel cell is circular, thus these three masses, are calculated using the following equations:

$$m_{MEA}^{FC}(A_{FC}) = \sigma_{MEA}^{FC} A_{FC}, \quad (2.5)$$

$$m_{bp}^{FC}(A_{FC}) = \rho_{bp}^{FC} A_{FC} t_{bp}^{FC}, \quad (2.6)$$

$$m_{fr}^{FC}(A_{FC}) = \rho_{fr}^{FC}\left(\pi r_{fr}^{FC^2} - A_{FC}\right) t_{fr}^{FC}, \quad (2.7)$$

Here σ_{MEA}^{FC} is the area density of the MEA, while t_{bp}^{FC} and ρ_{bp}^{FC} are the thickness and density of the bipolar plate. The t_{fr}^{FC} and ρ_{fr}^{FC} are the thickness and density of the cell frame. The outer radius of the frame r_{fr}^{FC} is calculated from the fuel cell area A_{FC} by

$$r_{fr}^{FC} = \alpha_{FC} \cdot \sqrt{\frac{A_{FC}}{\pi}} + r_{ext}^{FC}, \quad (2.8)$$

where α_{FC} is the radial factor of the fuel cell frame, and r_{ext}^{FC} is the constant extra radius of the frame.

The mass of the endplate is given by

$$m_{ep}^{FC}(A_{FC}) = \rho_{ep}^{FC} \pi r_{fr}^{FC^2} t_{ep}^{FC}, \quad (2.9)$$

where $\rho_{ep,FC}$and $t_{ep,FC}$ are the density and thickness of the endplate of the stack.

Mass of the Electrolyzer

The electrolyzer mass equation has similar structure as the fuel cell with a few differences.

$$m_{EZ} = N_{EZ}\left(k_{EZ}\left(m_{MEA}^{EZ} + m_{sc,an}^{EZ} + m_{sc,ca}^{EZ} + m_{fr}^{EZ}\right) + 2m_{ep}^{EZ} + k_{bolt}^{EZ} m_{bolt}^{EZ} + m_{aux}^{EZ}\right). \quad (2.10)$$

where N_{EZ} is the number of electrolyzer stacks, k_{EZ} is the number of electrolyzer cells, and m_{aux} is the mass of auxiliary components such as wiring and tubing.

Similar to the fuel cell, the m_{MEA}^{EZ} is the mass of electrolyzer MEA, and m_{fr}^{EZ} is the mass of the cell frame. In the electrolyzer, $m_{sc,an}^{EZ}$ and $m_{sc,ca}^{EZ}$ are the masses of the cell screens on the anode and cathode side respectively. These screens replace the bipolar plate in distributing the fluids in the electrolyzer cells. Between the anode screen and cathode screen of adjacent cells, there will be a thin sheet of material to separate the two cells. We assume this sheet's mass to be negligible. Just like the fuel cell, the electrolyzer is assumed to be cylindrical, and thus these terms are calculated by the following equations

$$m_{MEA}^{EZ} = \sigma_{MEA}^{EZ} A_{EZ}, \quad (2.11)$$

$$m_{sc,an}^{EZ} = \left(1 - \phi_{sc,an}^{EZ}\right)\rho_{sc,an}^{EZ} A_{EZ} t_{sc,an}^{EZ}, \quad (2.12)$$

$$m_{sc,ca}^{EZ} = \left(1 - \phi_{sc,ca}^{EZ}\right)\rho_{sc,ca}^{EZ} A_{EZ} t_{sc,ca}^{EZ}, \quad (2.13)$$

$$m_{fr}^{EZ} = \rho_{fr}^{EZ}\left(\pi\left(r_{fr}^{EZ}\right)^2 - A_{EZ}\right) t_{fr}^{EZ}, \quad (2.14)$$

with ρ_{fr}^{EZ}, $\rho_{sc,an}^{EZ}$, $\rho_{sc,ca}^{EZ}$, and ρ_{MEA}^{EZ} the density, t_{fr}^{EZ}, $t_{sc,an}^{EZ}$, $t_{sc,ca}^{EZ}$, and t_{MEA}^{EZ} being the thickness of the corresponding component. Also A_{EZ} is the area of each electrolyzer cell, and $\phi_{sc,an}^{EZ}$ and $\phi_{sc,ca}^{EZ}$ are the porosity of the anode screen and the cathode screen respectively. The outer radius of the frame r_{fr}^{EZ} is given by:

$$r_{fr}^{EZ} = \alpha_{rad}^{EZ}\sqrt{\frac{A_{EZ}}{\pi}} + r_{ext}^{EZ}, \quad (2.15)$$

where α_{rad}^{EZ} is the radial factor of the frame, and r_{ext}^{EZ} is the additive radial increase.
The mass of the endplate m_{ep}^{EZ} is given by

$$m_{ep}^{EZ} = \rho_{ep}^{EZ} \pi \left(r_{fr}^{EZ}\right)^2 t_{ep}^{EZ}. \tag{2.16}$$

Different from the Fuel cell, the EZ is operating at much higher pressure than that of the FC. For this reason, the thickness of the endplate t_{ep}^{EZ} needs to be sufficient such that the maximum deflection of endplate is within the limit δ_{max} to ensure no leaking of the reactant gas. The thickness is derived from the equation of deflection of a simply supported circular plate under a uniform pressure [x],

$$t_{ep}^{EZ} = \left(\frac{12 p_{EZ} \left(r_{fr}^{EZ}\right)^4 (1-\nu^2)}{64 \delta_{max} E} \right)^{1/3}. \tag{2.17}$$

Here, ν is Poisson's ratio, which is assumed to be 0.3, E is the elastic modulus of the endplate.
The last term of Eq. 2.10 is the mass of the electrolyzer clamping bolts. The bolts are distributed evenly near the perimeter of each stack. For each individual bolt, the shape is assumed as a cylindrical shape, then the mass is given by

$$m_{bolt}^{EZ} = \rho_{bolt}^{EZ} \pi \left(r_{bolt}^{EZ}\right)^2 t_{total}^{EZ}, \tag{2.18}$$

where r_{bolt}^{EZ} and ρ_{bolt}^{EZ} is the radius and density of the bolt. We calculate t_{total}^{EZ} as the total length of the electrolyzer stack, plus an additional length for clamping:

$$t_{total}^{EZ} = 2 t_{ep}^{EZ} + k_{EZ} \left(t_{fr}^{EZ} + t_{sc,an}^{EZ} + t_{sc,ca}^{EZ} + t_{MEA}^{EZ} \right) + 5. \tag{2.19}$$

The number of bolts are calculated so that the combined clamping force of the bolts is greater than the force of the pressurized stack as

$$k_{bolt}^{EZ} = \left\lceil \frac{6 p_{EZ} A_{EZ}}{s} \right\rceil, \tag{2.20}$$

where s is the clamp force per bolt, and the 6 is the factor of safety for the clamp. We use the $\lceil\rceil$ as a ceiling function, which rounds the value to the next highest integer.

Mass of the Reactant Gases

To derive the total mass of the reactant gas, we first need to understand the dynamics of the gas flow. The gas flows from electrolyzer to storage tank, and from storage tank to fuel cell. To ensure the gas flow without extra compressors, the following relations need to be hold

$$p_{FC} < p_{tank,min} \leq p_{tank} \leq p_{tank,max} \leq p_{EZ}. \tag{2.21}$$

Similarly, the water flows out from the fuel cell and into the water reservoir, and from the reservoir into a water compressor into the electrolyzer. In this model, we do not consider the mass of the water compressor.
The total amount of gas is conserved throughout the operation. We can split the calculation as

$$m_{Gas}\left(N_{FC}, k_{FC}, A_{FC}, p_{FC}, p_{EZ}\right) = m_{H_2,cons} + m_{O_2,cons} + m_{H_2,res} + m_{O_2,res}. \tag{2.22}$$

where $m_{X,cons}$ is the gas of corresponding species that will be consumed by FC during its operation, the $m_{X,res}$ is the gas left in the tank to avoid the back-flow of the gas from the fuel cell to the tank.
The mass of the gases consumed by the fuel cell needs to meet the required output power P_{req}. The power output P_{FC} is given by

$$P_{FC} = i_{FC} V_{FC} A_{FC,total}. \tag{2.23}$$

Here $A_{FC,total}$ is the total active area of the fuel cell, and is calculated by multiplying the total number of cells by the area of each cell:

$$A_{FC,total} = N_{FC} k_{FC} A_{FC}. \tag{2.24}$$

The voltage of the fuel cell V_{FC} is a function of i_{FC} can be calculated using the following equation (Spiegel, 2018):

$$V_{FC}(i_{FC}, p_{FC}) = -\frac{\Delta G_F}{2F} + \frac{RT}{2F}\ln\left(\frac{p_{H_2} p_{O_2}^{1/2}}{p_{H_2O}}\right) + \beta_{FC}\ln\left(i_{FC} + i_{FC,offset}\right) + i_{FC} R_{FC} + c\ln\left(1 - \frac{i_{FC}}{i_{FC,lim}}\right), \tag{2.25}$$

where the constant ΔG_F is the Gibbs free energy of formation of water $-237.14\ kj/mol$, while R is the universal gas constant, and F is Faraday's constant. The partial pressures p_{H_2}, p_{O_2}, and p_{H_2O} are the pressures exerted by respective species. For pure reactant gases, the partial pressure is simply equal to the pressure of the fuel cell, which is

$$p_{FC} = p_{H_2} = p_{O_2}. \tag{2.26}$$

Our model assumes a liquid water product, so the partial pressure p_{H_2O} is simply one atmosphere. The remaining values in the equation are parameters, $\beta_{FC} = -0.0287\ V$, $i_{FC,offset} = 2.9998\ mA/cm^2$, $R_{FC} = -4.211 \cdot 10^{-5}\ k\Omega \cdot cm^2$, $c_{FC} = 0.1000V$, and $i_{FC,lim} = 1500\ mA/cm^2$, all depend on the design of the fuel cell.
The dependence of masses on i_{FC} and $A_{FC,total}$ are given by (Spiegel, 2018),

$$m_{X,cons} = \frac{M_X}{n_X F} A_{FC,total} i_{FC} T_{FC}, \tag{2.27}$$

The constants $M_{H_2} = 2.0159\ g/mol$ and $M_{O_2} = 31.9988\ g/mol$ are the molar mass of hydrogen and oxygen, while $n_{H_2} = 2$ and $n_{O_2} = 4$ are the number of moles of electrons transferred per mole of hydrogen and oxygen consumed. Faraday's constant $F = 96485.3321\ C/mol$ is the amount of electrical charge carried by each mole of electrons. Here i_{FC} is the current per area supplied by the fuel cell for T_{FC} hours. Also, the voltage produced by the fuel cell stacks must remain between 9 volts and 150 volts:

$$9 \le V_{FC} k_{FC} N_{SFC} \le 150. \tag{2.28}$$

This constraint represents the capabilities of the power management system to convert the fuel cell power into power usable by the customer system.
Setting

$$i_{FC} V_{FC} A_{FC,total} = P_{req} \tag{2.29}$$

we have

$$i_{FC} A_{FC,total} = \frac{P_{req}}{V_{FC}}, \tag{2.30}$$

To minimize $m_{X,cons}$, we need to minimize $i_{FC} A_{FC,total}$, which means we need to maximize V_{FC}. We observe that V_{FC} is strictly decreasing function of i_{FC}, since

$$V'_{FC} = \frac{\beta}{i_{FC} + i_{FC,offset}} + R_{FC} - \frac{c}{i_{FC,lim} - i_{FC}} \tag{2.31}$$

is negative for all i_{FC} with the values of the parameters. In addition, the current density i_{FC} needs to satisfy

$$i_{FC} \ge i_{FC,min} \tag{2.32}$$

where the $i_{FC,min}$ is the minimum current density needed for proper fuel cell operation. Thus if the fuel cell is operating at $i_{FC,min}$, the consumed mass will be minimized. However, at times, operating at the smallest $i_{FC,min}$ might lead to large $A_{FC,total}$, which might not be optimal for the total mass. If $A_{FC,total}$ is large, the mass of fuel cell will be

large. Correspondingly i_{FC} will be small, leading to small $i_{FC} \cdot A_{FC,total}$ and small mass of the gas. Otherwise, if $A_{FC,total}$ is small, corresponding to large value of i_{FC}, leading to large value $i_{FC} \cdot A_{FC,total}$ and mass of gas. The minimizer is determined by the intrinsic balance of those masses.

So in our minimization process, our strategy is to solve Eq. 2.29 for i_{FC} given p_{FC} and $A_{FC,total}$ to satisfy the output power requirement $P_{FC} = P_{req}$, where we use Newton's iteration after a few steps of bisection on the interval $\left[i_{FC,min}, i_{FC,max}\right]$.

For any given $A_{FC,total}$, there is a maximum power that can be supplied by the fuel cell $P_{FC,max}$. Thus using equation 2.32, we get

$$P_{FC,max} = i_{FC,max} V_{FC}(i_{FC,max}) A_{FC,total}. \tag{2.33}$$

Now let's move to reserved gas. The amount $m_{X,res}$ needs to ensure the pressure in the storage tank is at least p_{FC}. We set the minimum pressure in the storage tank to be $1.25p_{FC}$, where 1.25 is a buffer factor to assure adequate back-pressure to the fuel cell. Using the equation of

$$n_{X,res} = \frac{p_{tank,min} V_{in,X}}{RTZ_X\left(p_{tank,min}\right)} \tag{2.34}$$

which leads to

$$m_{X,res} = M_X \frac{1.25p_{FC} \cdot V_{X,in}}{Z_X(1.25p_{FC}) \cdot R \cdot T}. \tag{2.35}$$

The only quantity unknown from above equation is the $V_{X,in}$. To obtain it, we need to relate back to $m_{X,cons}$. When the tank is full, the expected pressure in the storage tank is p_{EZ}. With this we have

$$n_{X,total} = \frac{p_{tank,max} V_{X,in}}{RTZ_X\left(p_{tank,max}\right)} \tag{2.36}$$

Subtracting the equation for $n_{X,res}$ from $n_{X,total}$, we obtain

$$n_{X,cons} = \frac{p_{tank,max} V_{X,in}}{RTZ_X\left(p_{tank,max}\right)} - \frac{p_{tank,min} V_{X,in}}{RTZ_X\left(p_{tank,min}\right)}. \tag{2.37}$$

Solving for $V_{X,in}$ we get

$$V_{X,in} = \frac{n_{X,cons} RT}{p_{tank,max}/Z_X\left(p_{tank,max}\right) - p_{tank,min}/Z_X\left(p_{tank,min}\right)} \tag{2.38}$$

In order for the fuel cell to run indefinitely, we also require that the electrolyzer be able to produce more reactant gases than the fuel cell consumes. To allow for some tolerance, we use a factor of 0.95. Thus we have

$$m_{X,cons} \leq 0.95 m_{X,max,prod}. \tag{2.39}$$

The mass of the gases produced by the electrolyzer is calculated similar to Eq. 2.27

$$m_{X,prod} = \frac{M_X}{n_X F} A_{EZ,total} i_{EZ} T_{EZ} = \frac{M_X}{n_X F} \frac{P_{EZ}}{V_{EZ}} T_{EZ}, \tag{2.40}$$

where T_{EZ} is the operation duration of electrolyzer. Here i_{EZ} is calculated from the electrolyzer power, which we set equal to the solar array power or the maximum power, whichever is smaller:

$$P_{EZ} = \min\left(P_{SA}, P_{EZ,max}\right), \tag{2.41}$$

where

$$P_{EZ,max} = i_{EZ,max} V_{EZ,max} A_{EZ,total}. \tag{2.42}$$

For any i_{EZ}, the voltage V_{EZ} can be calculated using the following equation.

$$V_{EZ}(i_{EZ}, p_{EZ}) = -\frac{\Delta G_F}{2F} + \frac{RT}{2F}\ln\left(\frac{p_{H_2} p_{O_2}^{1/2}}{p_{H_2O}}\right) + \beta_{EZ}\ln(i_{EZ}) + i_{EZ}R_{EZ} + c_{EZ}\ln\left(1 - \frac{i_{EZ}}{i_{EZ,lim}}\right). \quad (2.43)$$

Similarly to the fuel cell, p_{H_2} and p_{O_2} are taken to be the pressure of the electrolyzer p_{EZ}, and p_{H_2O} is one atmosphere. Additionally, the parameters in Eq. 2.43 are based on the design of the electrolyzer stack: $\beta_{EZ} = 0.029\ V$, $R_{EZ} = 0.000165\ k\Omega \cdot cm^2$, $c_{EZ} = -0.1900\ V$, and $i_{EZ,lim} = 1145\ mA/cm^2$.

In the case that $P_{EZ,max}$ is bigger than P_{SA}, we calculate i_{EZ} by applying Newton's iteration method similar to the fuel cell calculation:

$$i_{EZ} = \frac{P_{EZ}}{V_{EZ}A_{EZ,total}}, \quad (2.44)$$

where i_{EZ} is in the interval $\left[i_{FC,min}, i_{FC,max}\right]$. Here $i_{FC,min}$ is the minimum current current density for proper electrolyzer operation.

Mass of Storage Tanks

For the balance of plant mass m_{bop}, we have three terms, m_{tank,H_2}, m_{tank,O_2}, and m_{tank,H_2O}, the masses of the H_2 and O_2 tanks, and the mass of the water reservoir respectively:

$$m_{bop} = m_{tank,H_2} + m_{tank,O_2} + m_{tank,H_2O}. \quad (2.45)$$

This model assumes spherical containers for ease of implementation, thus

$$m_{tank,X} = \rho_{tank}\frac{4\pi}{3}\left(r_{out,X}^3 - r_{in,X}^3\right), \quad (2.46)$$

where X is the molecule species. Here ρ_{tank} is the density of the tank and is assumed to be the same for hydrogen, oxygen, and water, while $r_{in,X}$ and $r_{out,X}$ is the inner and outer radius of the tank. For the hydrogen and oxygen, $r_{in,X}$ calculated from the previously calculated gas volume:

$$r_{in,X} = \left(\frac{3V_{X,in}}{4\pi}\right)^{1/3}. \quad (2.47)$$

The minimum required thickness is calculated from the allowable stress from the internal pressure of the tank:

$$t_{tank} = \frac{p_{tank,max}r_{in,tank}}{2\sigma_{stress}} \quad (2.48)$$

where σ_{stress} is the maximum allowable stress of the tank walls. To safeguard, we make the thickness bigger, and we use the following equation for thickness of the storage tank, which comes from the ASME pressure vessel code UG-27:

$$t_{tank,X} = \frac{p_{EZ} \cdot r_{in,X}}{2\frac{YS}{SF} - 0.2p_{EZ}}, \quad (2.49)$$

where YS is the yield strength of the container material, and SF is the factor of safety.

For the water, the maximum mass in the tank is the sum of the masses of the hydrogen and oxygen gases. Since water is incompressible, the volume of the water can be calculated by dividing the total mass by the density of water ρ_{H_2O}:

$$V_{H_2O} = \frac{m_{H_2,cons} + m_{O_2,cons}}{\rho_{H_2O}}. \quad (2.50)$$

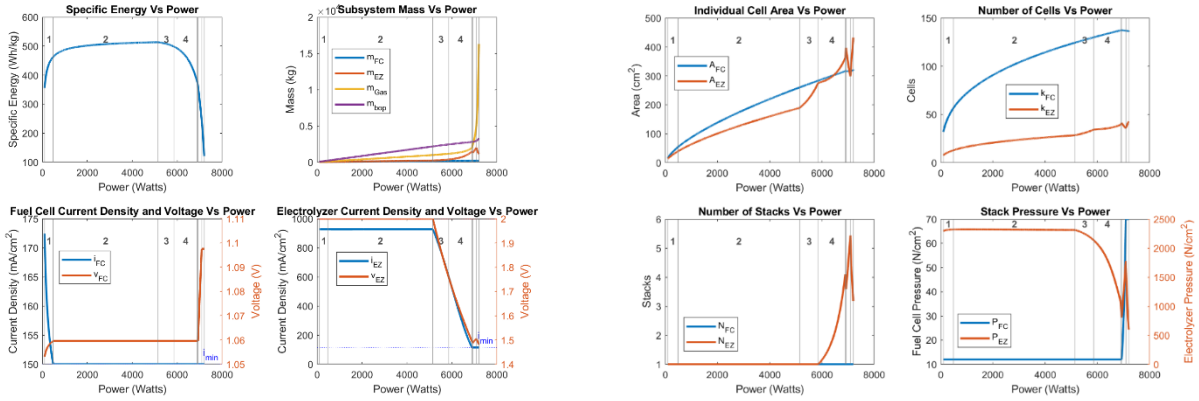
Additionally instead of calculating it based on the pressure, we set the tank radial thickness to be $0.6\ cm$.

Results

In this chapter, we present our numerical results. We use the *fmincon* function in MATLAB (MATLAB 2025b, The MathWorks, Natick, MA) to solve the constrained nonlinear optimization problem. *fmincon* takes the initial values of the independent variables, the objective function, and the constraints, and returns the optimal values of the independent variables. The initial values are generated by randomly selecting values within the allowed ranges and retaining only those that satisfy the additional constraints. From the resulting set of feasible initial points, we choose the one that yields the smallest objective function value.

Sensitivity Analysis

For this run $P_{SA} = 10000$ W, $T_{EZ} = 351$ h, and $T_{FC} = 359$ h. We look at the optimal solution at for varying P_{FC} from 100 Watts, to 7200 Watts. Note: when applicable, O2 is labeled as green, H2 is red, and Water is blue, as is commonly used in industry.



In these graphs, we can see that the best solutions occur when the power of the fuel cell P_{FC} lies between 500 and 6000 Watts. Note that this range would change for different values of P_{SA}.

Conclusion

This model offers an approximation of a Regenerative Fuel Cell system, taking into account the fuel cell and electrolyzer mass and behavior, as well as gas and storage masses, to optimize the system for specific energy. Sensitivity analysis showed that the best solution occurs when the power of the fuel cell is approximately 50% of the power provided by the solar array.

In addition to the work already discussed in this paper, some further work can be done. First, sensitivity analysis performed on the fuel cell and electrolyzer operational time T_{FC} and T_{EZ}, as well as the solar array power, will show how the solution changes with these mission parameters and how they impact the system solution. Additionally, running the model for common variable values to see how model compares to known systems will show how well the model represents real world solutions. Subsequently, implementing electrical and thermal subsystems and including improvements to the model based on results from sensitivity analysis will yield more accurate approximations.

Bibliography

Guzik, M., Jakupca, I., Gilligan, R., Bennett, W., Smith, P., & Fincannon, J. (2017). *Regenerative Fuel Cell Power Systems for Lunar and Martian Surface Exploration*. https://ntrs.nasa.gov/api/citations/20170009088/downloads/20170009088.pdf

Spiegel, C. (2018). *PEM Fuel Cell Modelling and Simulation using MATLAB*. Academic Press.

Extreme Environmental Effects on 3D Printed Composites for Space Applications

Student Researcher: Isaac Sluder

Advisor: Dr. Kwek Tze Tan

The University of Akron
Mechanical Engineering

Abstract
3D printed components frequently operate in humid environments, where moisture can degrade polymer properties over time. As 3D printing advances beyond prototyping and into end-use applications, understanding material behavior in real-world conditions becomes essential. This study investigates the long-term humidity resistance of two carbon fiber-reinforced nylon filaments: Onyx (PA6-based, Markforged) and PAHT-CF (PA12-based, Bambu Labs). Motivated by Bambu Labs' claim that PAHT-CF absorbs less moisture, specimens were printed using each filament's proprietary printer and conditioned at 55% RH and 22 °C [1]. Mass gain and mechanical performance (tensile and flexural) were analyzed over 14, 32, and 42 days. PAHT-CF retained its mechanical properties better due to its PA12 matrix, though degradation still occurred. Onyx absorbed more moisture but eventually stabilized, exhibiting a surprising increase in ductility. While Onyx has been widely tested—particularly in the context of continuous carbon fiber (CCF) reinforcement on the Mark Two printer—independent testing of PAHT-CF is limited [2, 3, 4]. This research offers a direct performance comparison and provides valuable insights for selecting reinforced nylon materials in moisture-prone industrial applications.

Project Objectives
This project aims to evaluate the long-term effects of humidity on the mechanical performance of two carbon fiber-reinforced nylon filaments used in 3D printing: Onyx and Paht (short for PAHT-CF). These materials are of particular interest for aerospace applications, where dimensional stability and mechanical reliability under environmental stressors are essential.

The specific objectives of this project are:

1. Characterize moisture absorption behavior of both filaments under controlled environmental conditions (55% RH, 22 °C) over an extended period.

2. Assess mechanical degradation by conducting mechanical testing at multiple conditioning duration intervals (14, 32, and 42 days).

3. Compare material performance to evaluate Bambu Lab's claim that Paht exhibits superior moisture resistance compared to the industry-standard Onyx filament.

4. Inform material selection strategies for aerospace components produced through additive manufacturing, particularly in environments where humidity exposure is unavoidable.

These objectives support the broader goal of improving the reliability and environmental resilience of 3D printed polymers in advanced engineering applications, including space systems and atmospheric vehicles.

Methods

1.1 Materials

The two materials to be tested are commonly used in engineering prototyping applications. The first material, Onyx, is 3D printed on the Markforged Mark Two composite printer. Onyx is a proprietary nylon-based filament reinforced with chopped carbon fibers. Many researchers have investigated what constitutes the Onyx filament, typically indicating it to be either PA6 or PA66 (a polyamide). This filament is often frequently used with the Continuous Carbon Fiber material made by Markforged for more advanced fiber-matrix combinations not explored in this study.

Our second material is the Paht material from Bambu Labs. Paht is a new material recently released by Bambu Labs in 2024. Bambu's focus is on its improvement upon its older iteration of nylon-chopped-carbon-fiber filament. Paht contains "PA 12 and other long-chain PA, carbon fiber" in the filament and has properties that make the material desirable in environmental conditions such as low moisture absorption with great mechanical properties, strong layer adhesion and more reported by the company [1]. Paht is 3D printed on the Bambu Lab X1E 3D printer.

1.2 3D Printing

As previously noted, printing will be carried out on two different machines: the Mark Two and the X1E. Each printer will use its corresponding filament—Onyx and Paht—following the manufacturer's recommended material settings. The consistent build parameters across both setups are:

- Layer Height: 0.125 mm
- Infill Density: 100%
- Infill Direction: In the 45˚ and -45˚ direction, alternating layers (zig zag)
- Orientation: Thin Section to Z Direction

To minimize cost and print time four samples were chosen to represent every testing condition, in our case that is material type and time spent in a conditioning chamber. Samples were printed in batches, as Celestine et al., indicated no real correlation between placement on the build plate and performance [4]. The samples were stored in an air-tight container with desiccant and a small humidity monitor inside to ensure samples stayed dry until all samples were printed.

1.3 Conditioning

After 3D printing the samples will be placed in an Espec BTX-475 benchtop humidity chamber. The temperature and humidity will be set to 22˚C and 55% RH respectively. Before the samples are placed in the chamber an initial reading of the weight of each sample is measured. The samples will then be removed at intervals of 0, 14, 32, and 42 days. After removal the samples will be weighed, and the relative water weight increase is calculated using the following equation [4, 5, 8]:

(1)

Where $\boldsymbol{m_i}$ is the initial mass, $\boldsymbol{m_f}$ is the final mass, and $\boldsymbol{m_{RH\%}}$is the percentage of water inside of the sample. After $\boldsymbol{m_{RH\%}}$ is calculated the samples are immediately mechanically tested. A dry test was formulated later after the results pointed towards interesting finding in that direction. The reverse of the

process above was done by drying the materials at 60˚C for 48 hours. These conditions were specified by the manufacturer for Onyx. Note that the Tg for Onyx is around 61˚C [2]

1.4 Testing

The Tensile testing is conducted on an Instron 5582 Series Universal Testing Machine following the ASTM D638 Standard [5]. Our test specimen follows the Type 1 Dog Bone geometry requirements, measuring 165 x 19 x 4 mm. The speed of the test was determined experimentally by finding a rupture time between 0.5 to 5 minutes of testing. This was determined to be 10 mm/min. The test was configured to collect force, displacement and time data.

Results and Discussion

The first set of results evaluated the moisture absorption behavior of each material over the testing period. Figure one shows these results for the tensile samples with each respective material. As expected Paht exhibits minimal mass gain like Bambu stated [1]. It also maintains consistency over the duration showcasing low moisture absorption between 0.3% to 0.5%. Onyx has much higher variance in its $\boldsymbol{m_{RH}}_{\%}$ value. Onyx absorbs over 2.5% initially then stabilizes to just over 2.0%. Both materials show they've reached saturation and Onyx's numbers agree with the results from Nikiema [2]. The column in figure 1 shows the dried samples. During testing, it was observed that the saturation stayed consistent between the materials. A few samples were selected to dry to test the material's ability to recover its strength. This also highlighted a limitation of this study. Because the samples were temporarily stored inside what was thought of as a dry container, the materials absorbed moisture even before the test started. Drying wasn't initially considered because there was a lack in confidence as to whether the drying process would damage the material. This is disproven in figure 2 and future work will incorporate drying procedures to prevent this.

Figure 2 shows the tensile stress strain curves of all specimens highlighted in different colors to indicate different states. Onyx is displayed in the teal color, while Paht is the orange (with the exception of the dried category in which Onyx is red and Paht is light blue). The general trend of Onyx between the two tests is that Onyx shows a large initial drop in performance of around 10 MPa for tensile after saturation. It appears Onyx's strength is that it does not degrade any farther after saturation. Onyx becomes around 2 times more ductile during the tensile test before failure. Eftekhari et al. explains that this is common for polyamides and is caused by the separation of polymer chains by the absorption of water molecules which allows for more mobility (resulting in the perceived ductility) and results in the loss of strength and stiffness [7]. This can also be viewed at a smaller scale for the Paht material as well, at the lighter colored region representing 0 days, the Paht material has the highest tensile strength but the lowest strain break. As the period moves farther, strain increases slightly while the strength decreases. It can also be inferred that Paht seems to continue to degrade well after saturation. This is more apparent in figure 3. Both materials when dried yielded a full recovery, beyond the unconditioned specimens. This is expected because while the unconditioned samples were not exposed to higher humidity levels the materials still absorbed some water in the time they were exposed to the room environment.

Figure 3 breaks out the tensile strength. Onyx unconditioned (0 day) specimens yielded between 30-40 MPa on average. This agrees with research done on plain Onyx, for example, Imburgia et al. [3], but is a little lower than Nikiema et al. (50-60 MPa) [2] This further indicates Onyx may have absorbed some moisture during the dry storage before testing. Paht also shows a small decline in tensile strength, pointing

towards a rather slow plasticization effect. Paht may show longer resistance to plasticization even after absorbing moisture as seen in figure 1. Both materials, Onyx and Paht show a full recovery after being dried indicating stiffer performance in dryer environments, highlighting their suitability for dry environments such as vacuum systems or spaceborne applications, where moisture-induced degradation is not a concern

In summary, Paht demonstrated greater resistance to moisture uptake compared to Onyx, with both materials exhibiting saturation over time. Onyx experienced higher initial strength loss but showed stability post-saturation and a significant increase in ductility, consistent with known polyamide plasticization behavior. Paht maintained higher strength throughout exposure, though evidence suggests it continues to degrade gradually beyond saturation. Notably, both materials fully recovered their tensile performance after drying, emphasizing the reversible nature of humidity-induced degradation in nylon-based composites. These findings highlight the importance of environmental conditioning in additive manufacturing applications and suggest that both materials, particularly in controlled environments, remain viable for mechanically demanding applications.

Figures/Charts

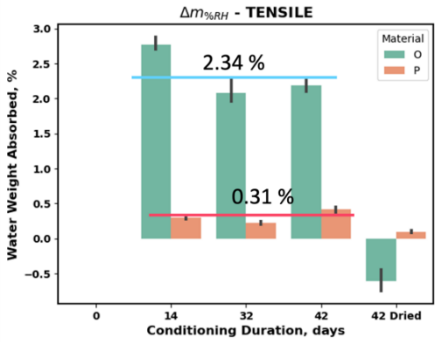


Figure 1 - Relative humidity gained, m_(RH%), O represent Onyx and P is Paht.

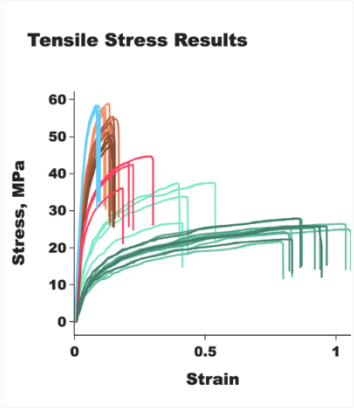


Figure 2 - Stress-strain curves for tensile tests, darkening color indicates longer trial run.

Blue is dried Paht and red is dried Onyx

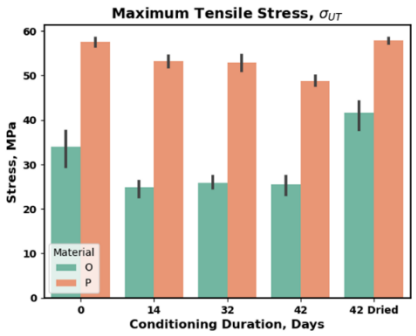


Figure 3 - Strength charts for tensile tests, tensile strength is defined to be the highest stress value recorded on the stress-strain curves.

Acknowledgments

I sincerely thank Dr. Manigandan Kannan for generously providing lab access, which was essential to this research. I'm also grateful to my lab-mates—Jason Mack, Andrew Frankowski, Rafsun Mridha, and Faizan Mirza—for their valuable support and input. I extend my appreciation to M. K. Morse for supplying key materials and 3D printers, and especially to Dr. Sekhar Rakurty, Roan Kirwin, and Michael Lambert for their ongoing support throughout the project. Thanks also to the University of Akron for the resources that enabled this work. Finally, I deeply appreciate the guidance and dedication of my advisor, Dr. Tan, whose mentorship was critical to this project's success.

References

[1] Bambu Lab: PAHT-CF. https://us.store.bambulab.com/products/paht-cf, last accessed 2024/07/15.

[2] Nikiema, D., Balland, P., Sergent, A.: Study of the mechanical properties of 3D-printed Onyx parts: Investigation on printing parameters and effect of humidity. Chinese Journal of Mechanical Engineering: Additive Manufacturing Frontiers 2, 100075 (2023).

[3] Imburgia, M. J., Faust, J. L., Buitrago, J. O., Enfield, R. E., Roy-Mayhew, J. D.: Environmental Stability of Additively Manufactured Thermoplastic Polyamide Composites. Polymers 2023, 15(16), 3385; https://doi.org/10.3390/polym15163385

[4] Celestine, A.-D.N., Agrawal, V., Runnels, B.: Experimental and numerical investigation into mechanical degradation of polymers. Composites Part B 201, 108369 (2020).

[5] ASTM International: Standard Test Method for Tensile Properties of Plastics. Designation: D638−14. ASTM International, West Conshohocken (2015). DOI:10.1520/D0638-14.

[6] ASTM International: Standard Test Methods for Flexural Properties of Unreinforced and Reinforced Plastics and Electrical Insulating Materials. Designation: D790−10. ASTM International, West Conshohocken (2010). DOI:10.1520/D0790-10.

[7] Eftekhari, M., Fatemi, A.: Tensile behavior of thermoplastic composites including temperature, moisture, and hygrothermal effects. Polymer Testing 51 (2016) 151-164

Explainable AI for Safety-Critical In-Orbit Proximity Operations

Student Researcher: Nathan Steffen

Advisor: Dr. Kelly Cohen

University of Cincinnati
College of Engineering and Applied Science/Aerospace Engineering

Abstract
As the number of satellites and volume of debris in Earth's orbit increases, interest in the development of autonomous robotic systems capable of performing maintenance and debris removal increases as well [1]. Current approaches to automate such procedures use artificial intelligence (AI) techniques like deep reinforcement learning (DRL) and other methods based on DRL, but these techniques struggle with trustworthiness as it is difficult to interpret their outputs, and they become unpredictable in situations outside their training set. This work employs the use of explainable AI via Genetic Fuzzy Systems (GFS) to offer trust in the controllers used for these autonomous systems. Additionally, run time assurance (RTA) is coupled with the trained GFS to uphold safety specifications that were not considered for training. It was found that the trained GFS outperforms a widely used optimal control law by 18.5% on average, that it is extremely robust to uncertainty in the system, and that when coupled with RTA, safety specifications can be upheld without sacrificing an unnecessary amount of performance. These results show that this designed and trained GFS would be effective in the automation of satellite servicing tasks, and that this method should be applied to other proximity operation modes to form a robust autonomous robotic system overall.

Project Objectives

- Develop an effective simulation environment for a two degree-of-freedom planar robotic manipulator
- Design GFS to dynamically tune gains for Linear Quadratic Regulator (LQR) control scheme
- Train hybrid Genetic Fuzzy-LQR controller for minimizing settling time and control effort
- Perform stochastic robustness analysis to compare performance between Genetic Fuzzy-LQR and optimal LQR under system uncertainty
- Couple Genetic Fuzzy-LQR controller with RTA method and demonstrate its use

Methods
As a foundation to the implementation of the control techniques to be shown, the robotic system being investigated is a two degree-of-freedom planar robotic manipulator. The configuration for this environment is seen in Figure 1. This is meant to represent the arm on a servicing satellite that would be performing maintenance. The generalized coordinates of the system are the angles of each link, θ_1 and θ_2. Knowing this, the dynamics can be derived utilizing the Euler-Lagrange equations to take the form below:

$$\boldsymbol{M}(\boldsymbol{\theta})\ddot{\boldsymbol{\theta}} + \boldsymbol{C}\left(\boldsymbol{\theta}, \dot{\boldsymbol{\theta}}\right) + \boldsymbol{G}(\boldsymbol{\theta}) = \boldsymbol{\tau} \tag{1}$$

Here, $\boldsymbol{M}(\boldsymbol{\theta})$ is the generalized mass matrix, $\boldsymbol{C}\left(\boldsymbol{\theta}, \dot{\boldsymbol{\theta}}\right)$ is the Coriolis matrix, $\boldsymbol{G}(\boldsymbol{\theta})$ is the gravity matrix, and $\boldsymbol{\tau}$ is the torque input. $\boldsymbol{G}(\boldsymbol{\theta})$ is a matrix of zeros since the system is in space and gravity is negligible. $\boldsymbol{M}(\boldsymbol{\theta})$ and $\boldsymbol{C}\left(\boldsymbol{\theta}, \dot{\boldsymbol{\theta}}\right)$ are defined in Equations 2 and 3.

$$\boldsymbol{M}(\boldsymbol{\theta}) = \begin{bmatrix} m_1 r_1^2 + m_2 (l_1^2 + l_2^2)_{I_1} + m_2 l_1 r_2 \cos\theta_2 & m_2 r_2^2 + \frac{1}{2} m_2 l_1 r_2 \cos\theta_2 \\ m_2 r_2^2 + \frac{1}{2} m_2 l_1 r_2 \cos\theta_2 & m_2 r_2^2 + I_2 \end{bmatrix} \tag{2}$$

$$\boldsymbol{C}(\boldsymbol{\theta}, \dot{\boldsymbol{\theta}}) = \begin{bmatrix} -\frac{1}{2} m_2 l_1 r_2 \dot{\theta}_2 (2\dot{\theta}_1 + 1) \sin\theta_2 \\ -\frac{1}{2} m_2 l_2 r_2 \dot{\theta}_1 \dot{\theta}_2 \sin\theta_2 \end{bmatrix} \tag{3}$$

Here, m_i is the mass of each link, l_i is the length of each link, r_i is considered the length along the arm to be tracked, and I_i is the inertia of each link, all of these for $i = 1, 2$.

To control this manipulator, linear control techniques are typically used. One popular technique is the Linear Quadratic Regulator (LQR) [2]. It was revolutionary when it was first introduced because of how its optimal control problem was set up. Equation 11 shows the cost function that is minimized for LQR.

$$J = \int_0^\infty [\boldsymbol{x}^T \boldsymbol{Q} \boldsymbol{x} + \boldsymbol{u}^T \boldsymbol{R} \boldsymbol{u}]\, dt \tag{4}$$

Here, $\boldsymbol{x}$ is the state, $\boldsymbol{u}$ is the applied controls, $\boldsymbol{Q}$ is the state gain matrix, and $\boldsymbol{R}$ is the control effort gain matrix. $\boldsymbol{Q}$ and $\boldsymbol{R}$ allow a controller designer to specify the importance of reaching a state versus preserving control effort. They are typically diagonal matrices. To calculate the appropriate feedback gains for this system, the linearized dynamics must be computed such that they are represented by $\boldsymbol{A}$ and $\boldsymbol{B}$ matrices. Then, the optimal control is computed with the state-feedback law in Equation 5.

$$\boldsymbol{K} = \boldsymbol{R}^{-1} \boldsymbol{B}^T \boldsymbol{P} \tag{5}$$

Where $\boldsymbol{P}$ is the solution to the continuous-time algebraic Ricatti equation shown in Equation 6.

$$\boldsymbol{A}^T \boldsymbol{P} + \boldsymbol{P} \boldsymbol{A} - \boldsymbol{P} \boldsymbol{B} \boldsymbol{R}^{-1} \boldsymbol{B}^T \boldsymbol{P} + \boldsymbol{Q} = 0 \tag{6}$$

Despite its effectiveness, LQR is still a linear controller. This means that in a non-linear system, like the robotic manipulator being investigated, this simplification can yield sub-optimal behavior. The optimality guarantees of LQR can be utilized to form a non-linear controller when paired with AI, however. This control loop can be seen in Figure 2.

The specific kind of AI utilized is Fuzzy Logic-based AI [3]. This technique has a simple means of tracing the logic that causes inputs to yield certain outputs, and it is capable of generalizing its solution space well. For this reason, Fuzzy Logic-based AI was chosen instead of other popular AI techniques like Deep Reinforcement Learning that struggle with both of those categories. This is intended to boost overall confidence and trust in the controller utilized.

Fuzzy Logic-based AI relies on membership functions and rules. As opposed to Classical Logic which classifies values entirely into certain sets, Fuzzy Logic assigns values to have degrees of membership to different sets, otherwise known as membership functions. Linguistic rules can then be formed with these fuzzy sets, and these can be translated into mathematical operations to produce outputs.

This process is known as a Fuzzy Inference System (FIS). Multiple FISs can be connected to form a network/tree. This minimizes the number of rules required in the overall inference process and can increase explainability through the resulting simplicity as well. The membership functions and rules are then optimized using a Genetic Algorithm (GA) [4]. For this reason, this technique is often referred to as

a Genetic Fuzzy Tree (GFT). The specific implementation of GFTs is through Thales' TrUE AI Toolkit™ [5]. This toolkit allows a GFT to be designed with ease and provides its own GA that specializes in the training of GFTs.

The specific GFT design is shown in Figure 3. This first layer is intended to prioritize the error in each link by considering the normalized error and normalized derivative error, and the second layer is intended to use these importance rankings to produce the $\boldsymbol{Q}$ gains. It is assumed that the $\boldsymbol{R}$ gains are to be kept constant, and performance benefits will be found in the variation of the $\boldsymbol{Q}$ gains.

The cost function used to train the GFT is shown in Equation 7. First, optimal static LQR gains are found according to this cost function. Then, this optimal static LQR cost is used in the GFT cost function so that the GFT can train against the best static LQR possible. In Equation 7, T_s is the settling time and IAC is the integral over absolute control, and that is defined in Equation 8.

$$cost = T_s + \frac{IAC_1}{\tau_{1_{max}}} + \frac{IAC_2}{\tau_{2_{max}}} \tag{7}$$

$$IAC_i = \sum_{j=1}^{N} \left|\tau_i(t_j)\right| \times \left(t_j - t_{j-1}\right) \; for \; i = 1, 2 \tag{8}$$

With the controller designed and trained according to this cost function, RTA can be paired with it to enforce safety constraints. In this problem, only the angular velocity in each link is limited as a proof of concept. The specific RTA technique used is the active set invariance filter. This is essentially a quadratic programming problem that balances the desired control from some performance controller with a safe control to satisfy a safety constraint. For the sake of space, the specific math is omitted, but one should see [6] if details regarding this implementation are desired. Figure 4 shows the control loop that includes RTA.

Results and Discussion

The Genetic Fuzzy-LQR controller was trained on over 88 cases. Each case started from rest at either $\theta_1 = 0^o$, $\theta_2 = 0^o$ or $\theta_1 = 180^o$, $\theta_2 = 0^o$ and the target states were at increments of 45° for both links. The training history of this controller can be seen in Figure 5. The final cost for this was around 71. Since each case is normalized with respect to the optimal static LQR case, one would expect the cost to be around 88 if the Genetic Fuzzy-LQR controller is as good as optimal static LQR. By normalizing this cost over each case (i.e. 71/88), the average Genetic Fuzzy-LQR run produces about 81.5% of the cost of the optimal static LQR case. In other words, it is about 18.5% more efficient than optimal static LQR on average.

Figure 6 shows the control surface produced by each FIS in Genetic Fuzzy-LQR's GFT. This visualization gives important insight to the behavior of the system, and shows which gains are prioritized given the normalized error and normalized derivative error in each link.

A single case comparison between the two controllers is shown in Figure 7. This shows the non-linear behavior in the Genetic Fuzzy-LQR compared to optimal static LQR, and how exactly it performs better. Figure 8 shows the results of the stochastic robustness analysis. Essentially, 1,001,088 simulations were ran where the mass and length of each link varied uniformly randomly by +/- 10%. Genetic Fuzzy-LQR succeeded in 100% of the cases whereas optimal static LQR only succeeded in 89.8% of cases. This figure shows the settling time and control statistics only over the mutually successful cases, and here Genetic Fuzzy-LQR appears to be way more performant with respect to settling time.

The coupled RTA-Genetic Fuzzy-LQR approach is shown in Figure 9. Here, the arm starts at 0 degrees for both links at rest and must go to 60 degrees in the first link and 45 degrees in the second link. The specification put on both links is that the angular velocity must be in the range +/- 30 degrees per second. In the angular velocity chart for Figure 9, it can be seen that the system never exceeds these bounds and is capable of compromising with Genetic Fuzzy-LQR to produce optimal controls while maintaining this constraint.

Figures/Charts

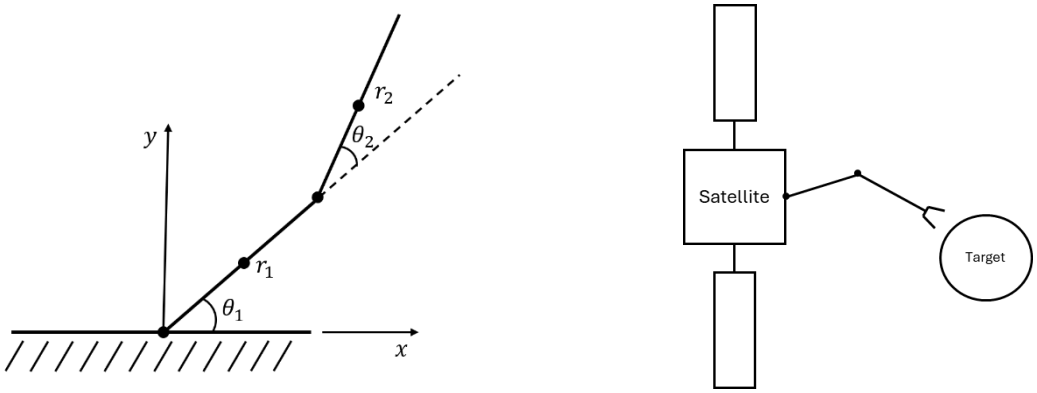


Figure 1. Representation of System.

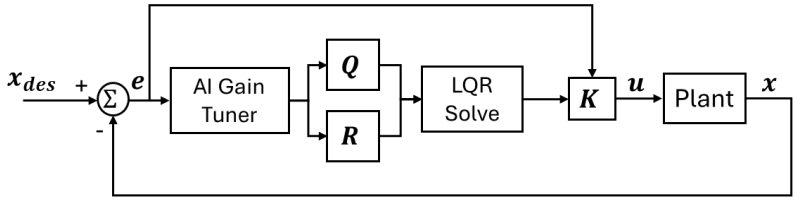


Figure 2. Dynamic Gain Tuning LQR Control Loop.

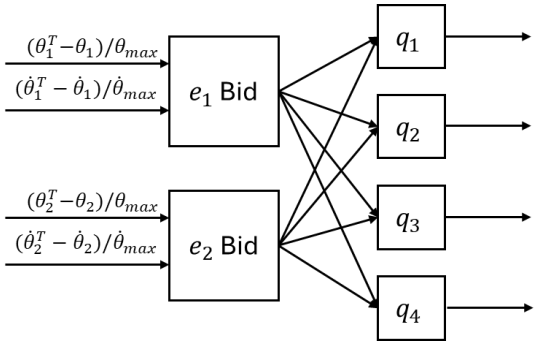


Figure 3. Genetic Fuzzy Tree for Determining LQR Gains.

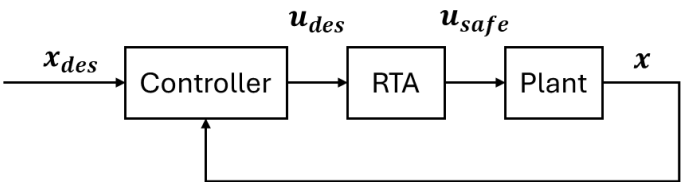


Figure 4. Run Time Assurance Control Flow Diagram.

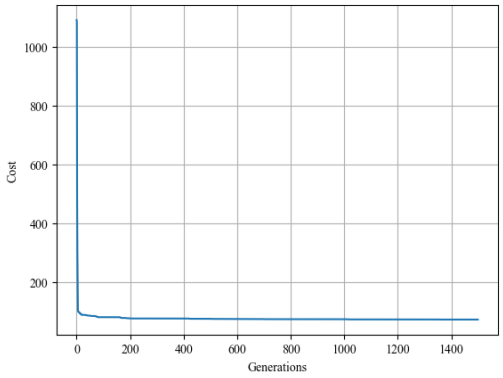


Figure 5. Training History of Genetic Fuzzy Tree.

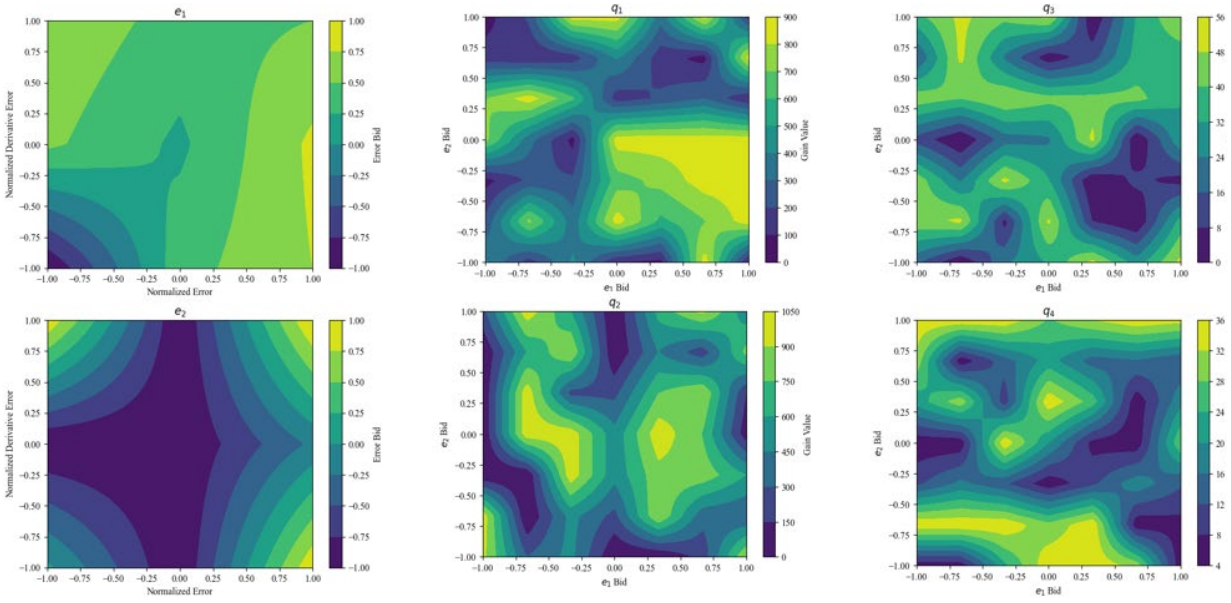


Figure 6. Control Surface Visualization of Fuzzy Inference Systems.

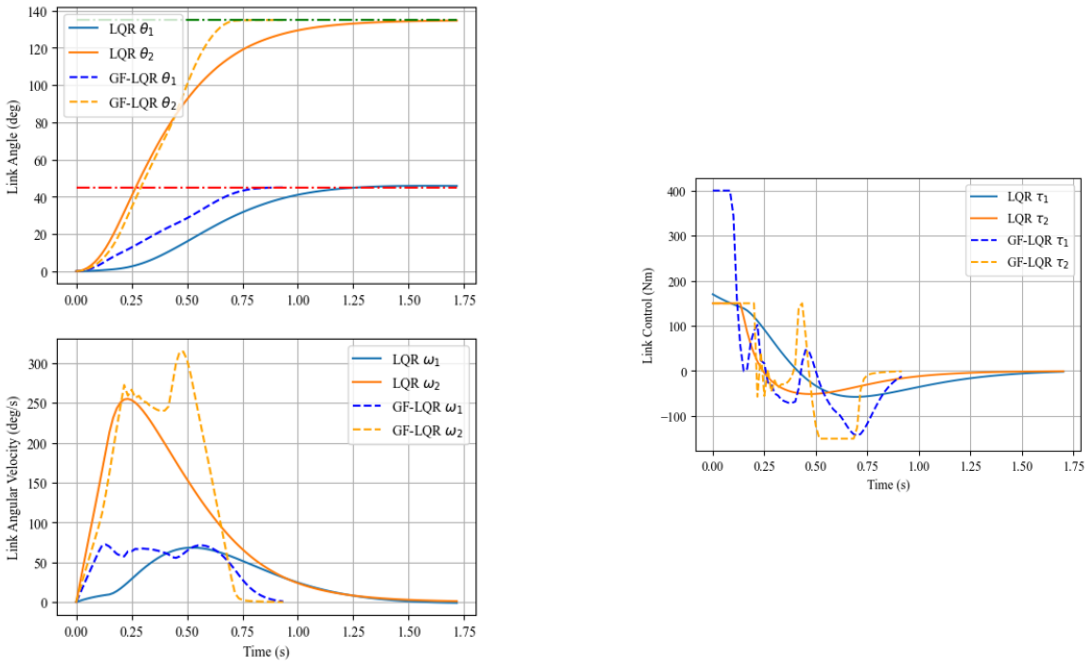


Figure 7. Single Case Comparison Between Optimal LQR and Genetic Fuzzy-LQR.

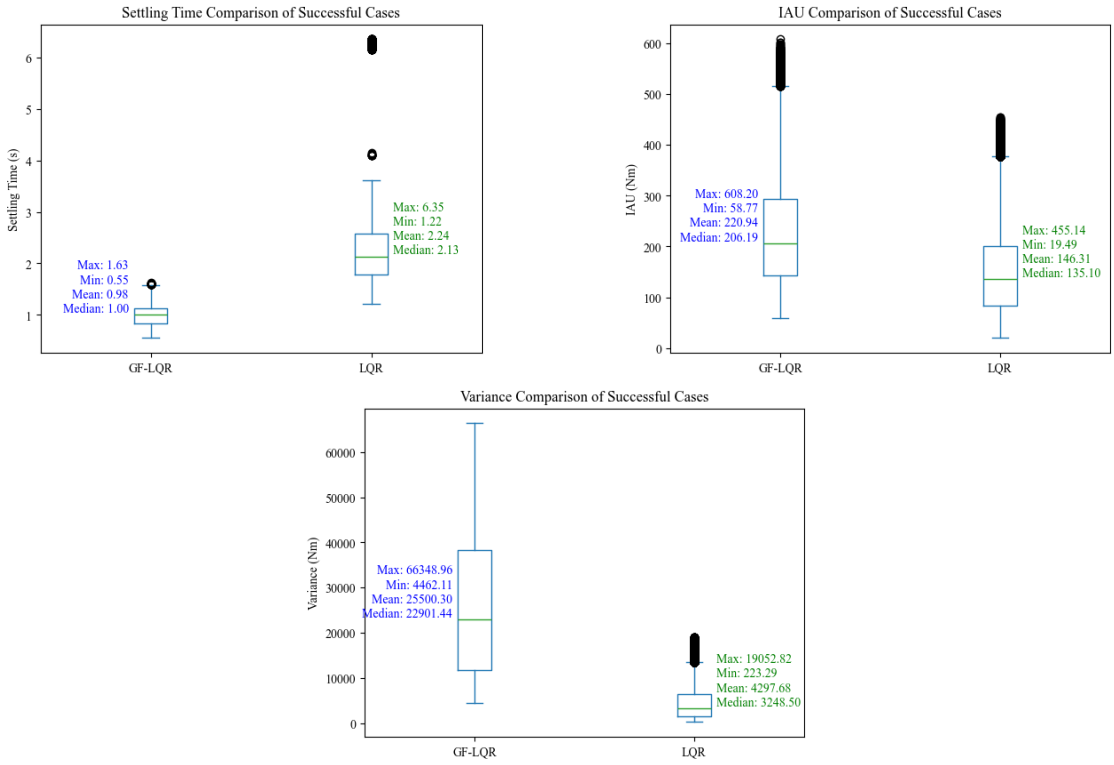


Figure 8. Robustness Analysis Results.

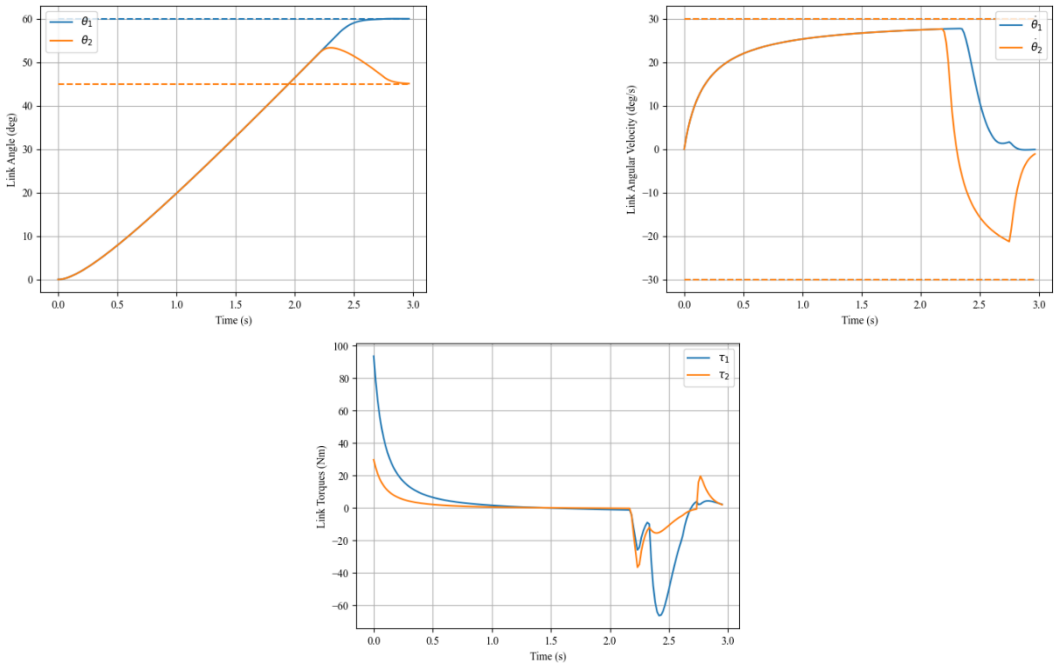


Figure 9. Run Time Assurance Paired with Genetic Fuzzy-LQR Example.

Acknowledgments

I would like to thank Dr. Kelly Cohen for his help and support throughout this research project. Additionally, I would like to thank the AI Bio Lab for the discussions and collaborations that yielded great progress in this research. Finally, I would like to thank the Ohio Space Grant Consortium for funding this research and for providing the opportunity to present it to peers and experts.

References

[1] Flores-Abad, A., Ma, O., Pham, K., Ulrich, S.: A review of space robotics technologies for on-orbit servicing. Progress in Aerospace Sciences 68, 1–26 (Jul 2014)

[2] Ogata, K.: Modern Control Engineering. Pearson (2010)

[3] Zadeh, L.A.: Fuzzy sets. Information and Control (Nov 1964)

[4] Sastry, K., Goldberg, D., Kendall, G.: Genetic Algorithms, pp. 97–125. Springer US, Boston, MA (2005), https://doi.org/10.1007/0-387-28356-0_4

[5] (Jun 2019), https://www.thalesgroup.com/en/group/journalist/press release/ thales-true-ai-approach-artificial-intelligence-be-unveiled-paris

[6] Hobbs, K.L., Mote, M.L., Abate, M.C., Coogan, S.D., Feron, E.M.: Runtime assurance for safety-critical systems: An introduction to safety filtering approaches for complex control systems. IEEE Control Systems 43(2), 28–65 (Apr 2023)

Identifying the Relationship Between Photophobia and Simulator Sickness Through Blue Light Exposure in VR

Student Researcher: Carter Verderico

Advisor: Dr. Stephanie Fussell

Kent State University
Aerospace Engineering

Abstract
Virtual reality (VR) systems are used increasingly in learning environments to promote acquisition of desired KSAs (knowledge, skills, and abilities) while meeting learning outcomes. However, the design of the virtual environment can negatively impact user experience and cause simulator sickness (sometimes called cybersickness). The objective of this research is to investigate the impact of different display modes in a VR headset (light settings: night, normal, and vivid) to determine if the modes contribute to simulator sickness. Participants completed a scripted flight procedure using the three different built-in headset display modes and reported usability and simulator sickness symptoms. The data set in this study was too small to prove significance, but the vivid display mode had slightly higher SSQ scores than the rest of the modes.

Project Objectives
In modern virtual reality (VR) systems, between 40 and 70 percent of people can experience the negative impacts of simulator sickness (also referred to as cybersickness, the differentiation of which is beyond the scope of this paper) within 15 minutes [1, 3]. Researchers have tried to determine what causes simulator sickness, but the answer is complicated as many factors related to hardware, software, and personal attributes can contribute to different symptoms. Symptoms include nausea, sweating, vomiting, fatigue, and dizziness; these can be quite drastic and negatively impact the user's experience in VR or cause them to stop the experience entirely. Eyestrain is another symptom, a condition many experience when their eyes become fatigued from long exposure to an intense amount of light [4, 5, 8].

VR headsets produce an abundance of blue light which may cause people with photophobia to experience symptoms of simulator sickness [2, 4, 5, 8]. According to the Cleveland Clinic, "The literal definition of photophobia is 'fear of light.' However, in medicine, it refers to your eyes' sensitivity to light, especially bright light, which can cause discomfort and even pain" [6]. When someone with photophobia is exposed to bright light it not only causes them to experience discomfort or pain, but it can also negatively impact the person's experience [5] in VR if the exposure occurs while in a virtual environment. Understanding how the light emitted from VR headsets affects people, especially those with photophobia, and contributes to simulator sickness is an area of research that has received little attention [2, 14].

Purpose
VR technology is being increasingly incorporated into learning and training environments [3]. Aviation is exploring VR as a training tool to reduce the time required for someone to achieve a private pilot certificate [11]. However, if a user experiences simulator sickness while training in VR, the training benefits can be compromised. The goal of this research is to understand the relationship between simulator sickness and photophobia, contributing to the body of knowledge of the causes of simulator sickness as well as mitigation strategies. To accomplish this, the study manipulated the different display modes in a

VR headset to determine if the modes contribute to simulator sickness, especially in people with photophobia.

Research Questions and Hypotheses:

How do display modes impact the symptoms of simulator sickness in people with or without photophobia?

H1: Participants with photophobia will experience significantly higher levels of simulator sickness on different display modes than participants without photophobia.

H0: There will be no significant difference in levels of simulator sickness on different display modes in participants with or without photophobia.

Methods

Study design:

This was a quantitative, quasi-experimental, 3x2 two-way design that held display modes (night, normal, and vivid) as an independent variable, photophobia or no photophobia as a quasi-independent variable, and simulator sickness as the dependent variable. Due to the small sample size, only trends in the data were assessed.

Population and sampling:

The research was conducted in Kent State University's (KSU) Extended Reality Research Lab. The convenience sample of KSU staff, faculty, and students who held a private pilot certificate (PPC) or higher and were at least 18 years and older were recruited using Canvas (a web-based learning management system) and email messaging. Each participant was asked to partake in three separate sessions of equal duration on different days. The VR headset had a different display mode setting for each session. Participants were not compensated for their participation. They were informed that their participation was voluntary, that they could stop the experiment at any time, and that they were not obligated to return for the other session(s). The research was approved by the Kent State Institutional Review Board.

Materials and apparatus:

The software applications used for this study were X-Plane 11 and 12, accessed through the XR Research Lab's Steam account and using Alienware PCs. The HTC Vive Pro 2 VR headset was used to fly a virtual Cessna 152 in X-Plane 11 and 12. The software was flown using a CKAS OpenFRM Single, a six-degrees-of-freedom motion platform [12]. The motion simulator was equipped with Logitech flight instrument panels, a Redbird Alloy YK1 (yoke system), a Redbird Alloy TH1 (flight simulator controls for single-engine airplanes), and a Redbird Alloy RD1 (rudder pedal system). As the participant flew in VR, the motion platform moved, and the flight instruments reacted in a realistic manner to give participants the physical sensation of flying. Participants could have experienced the negative impacts of motion or simulator sickness without the platform due to sensory-conflict theory [1, 2, 7]. According to this theory, sickness could have been caused by the participants flying in VR where their eyes and brain are moving with the airplane, but their physical body remained stationary in the chair due to a lack of motion. This would have confounded the study in terms of understanding the relationship between photophobia and simulator sickness. The flight platform minimized motion sickness by giving participants the normal sensations of flight, allowing the difference in light emissions from the VR headset to remain the manipulated variable that could cause simulator sickness. Figure 1 shows the software set up and Figure 2 shows a mock participant sitting on the motion platform, flying the aircraft, while wearing the VR headset.



Figure 1



Figure 2

Survey instruments:

The study used Google Forms as the instrument platform for collecting data. There were two separate questionnaires used in the project: a pre-study questionnaire and a post-study questionnaire. The pre-study questionnaire included participant consent items, demographics, the Visually Induced Motion Sickness Susceptibility Questionnaire (VIMSSQ) [15], and a Photophobia Questionnaire. The participants only took this before the first VR flight. The post-study questionnaire was comprised of the Simulator Sickness Questionnaire (SSQ) and participants completed this questionnaire after each VR flight [13].

The demographics section allowed the team to 1) confirm the participant was eligible for the study (age 18+ and held an FAA Private Pilot Certificate) and 2) learn about their eyes (color, vision, etc.), use of VR, experience with motion sickness, and if they have been diagnosed with photophobia.

The VIMSSQ was utilized in the pre-study questionnaire to get a baseline of the participants' susceptibility to simulator sickness. The participants filled out the VIMSSQ which compares the five subscales (nausea, headache, dizziness, fatigue, and eyestrain) when they use visual display devices. The questionnaire lists four responses for each subscale, zero which signifies never, one which signifies rarely, two which signifies sometimes, and three which signifies often. It has been cited in eight other papers and the "VIMSSQ alone explained 34% of VIMS variance" [10].

The research team developed a Photophobia Questionnaire based on the validated Utah Photophobia Symptom Impact Scale (UPSIS) [9]. The UPSIS has been cited in nine other papers and was evaluated with "Rasch analysis to evaluate instrument targeting, including internal consistency and reliability" [9]. The Photophobia Questionnaire is a modified UPSIS with phrasing changes to better align with the VR study to non-medically determine if a participant has photophobia. The Photophobia Questionnaire was reviewed by a local eye doctor for face validity of the items. In addition to reviewing the questions, the expert told the team to add questions about eyes to the demographics, such as eye color, because the answer to these can significantly increase the likelihood of a participant having photophobia. The information from the questionnaires was used to relate the participants' likelihood of having photophobia with how they felt after the VR flight from their SSQ results.

The post-study questionnaire utilized the SSQ for participants to evaluate how they felt with the symptoms of simulator sickness and rate the severity. The symptoms listed in the questionnaire are general discomfort, fatigue, headache, eyestrain, difficulty focusing, increased salivation, sweating,

nausea, difficulty concentrating, fullness of head, blurred vision, dizzy (eyes open), dizzy (eyes closed), vertigo, stomach awareness, and burping. The severity scale has four possible responses, zero which is none, one which is slight, two which is moderate, and three which is severe. The subscales and total score are calculated using their respective formulas [13]. The SSQ was created in 1993 and has been cited more than 3,000 times [13].

Results

Demographics:

A total of 26 people showed interest in the study. Ten people started the study, but only eight finished all three flight sessions. The eight participants had never been diagnosed with photophobia, had prior experience with VR, and confirmed that light sensitivity had never affected their ability to use VR and that VR had never made them sick. Only one participant had prior experience with motion sickness which was due to the temperature being too warm. Two participants believed that the Cleveland Clinic's definition of photophobia applied to them [6]. The same two participants responded that they had been diagnosed with an eye condition, one being an astigmatism and the other being myopia. Eye color was another question asked because it is believed that lighter-colored eyes (e.g., blue, green, and hazel) are more likely to experience photophobia, according to the expert. There were three blue-eyed participants, three brown-eyed participants, one hazel-eyed participant, and one green-eyed participant. The two participants who believed photophobia affected them and have been diagnosed with eye conditions have blue eyes and green eyes, respectively. Traumatic brain injury can also affect photophobia and only one participant had experienced that. Lastly, all the participants had earned their PPC, which was a requirement to participate in the study. Age (other than verification that the participant was 18+) and gender information were not collected as these personal characteristics are not thought to be related to photophobia.

VIMSSQ results

The participants VIMSSQ scores are shown in Table 1. The prevalence of low scores (i.e. 0 and 1) across the subscales indicates that susceptibility to VIMS is low for each participant. The VIMSSQ also asks if participants have stopped using the equipment due to these symptoms, shown in the last column.

Score of	Nausea	Headache	Dizziness	Fatigue	Eyestrain	Symptoms Stop Use
0	7	4	7	7	3	6
1	1	3	1	1	4	1
2	0	0	0	0	1	1

Table 1. VIMSSQ Scores

Photophobia Questionnaire

The participants filled out the research team's photophobia symptom impact scale which consisted of 26 possible item questions and a maximum possible score of 93. Some of the items had decision trees where an answer of yes or no led to slightly different questions or were skipped because they were irrelevant. Table 2 shows the participants photophobia scores with their eye colors, the VIMSSQ eyestrain score, and if they had to stop using a visual display device. The participant group had relatively low photophobia scores, a wide range of eye colors, low VIMSSQ Eyestrain scores (except for one participant with a higher photophobia score), and low VIMSSQ device stopped usage (except for one participant with a higher photophobia score).

Photophobia Score	Eye Color	VIMSSQ Eyestrain	VIMSSQ Stopped Use
18	Blue	Rarely	Sometimes

21	Green	Sometimes	Rarely
19	Brown	Never	Never
9	Blue	Rarely	Never
8	Blue	Rarely	Never
6	Brown	Never	Never
5	Hazel	Never	Never
8	Brown	Rarely	Never

Table 2. Participants with Higher Photophobia Scores

SSQ

The SSQ scores are calculated using the formulas presented in [13]. The research team compared the SSQ scores of participants who believe photophobia impacts them with the group's average, highlighted in bold in Table 3. Table 4 includes the averages for each subscale. The data demonstrates that the SSQ total average for the participants who believe they have photophobia were similar to those of the group for session one (night mode) but the photophobia impact group's score became higher than the average of the rest of the participants for sessions two and three (normal and vivid modes, respectively).

Photophobia Score	Eye Color	Night Mode Total	Normal Mode Total	Vivid Mode Total
18	Blue	11.22	3.74	0
9	Blue	18.7	26.18	18.7
8	Blue	22.44	56.1	41.14
6	Brown	18.7	41.14	37.4
5	Hazel	7.48	0	0
8	Brown	26.18	14.96	11.22
21	Green	11.22	18.7	56.1
19	Brown	7.48	3.74	7.48

Table 3. SSQ Scores by Flight

Subscales	Night Mode	Normal Mode	Vivid Mode
Nausea	10.73	11.93	9.54
Oculomotor	17.06	20.85	20.85
Dizziness	10.44	20.88	27.84
Total	15.43	20.57	21.51

Table 4. Participant Group SSQ Average Score

Discussion

This study required 54 participants to test significance, but unfortunately, we only had eight participants finish. Preliminary results indicate that eye color may not impact the likelihood of someone having photophobia, as eye color did not align with higher Photophobia Questionnaire scores. Despite two participants indicating that the definition of photophobia may apply to them, only one participant had a higher score on the Photophobia Questionnaire. Of note, none of the participants had a high enough score to confidently assert that they may suffer from photophobia. Although the SSQ subscale and total scores were slightly higher for the Vivid Mode, only the disorientation mode was much higher. Disorientation is not related to photophobia, indicating that the display modes may not cause simulator sickness at all, let alone in people who may be more sensitive to light. However, the data set is too small to come to definitive conclusions.

We were unable to reach the 54-participant threshold for a few reasons: 1) this study occurred over the course of a single semester, 2) we did not compensate participants for their participation, and 3) only people with a PPC could participate, which significantly reduced our sample size.

Conclusion

In conclusion, we would like to run a similar study with more participants, except change the requirements on who can participate. We cannot demonstrate significance with our sample size, but we believe the relationship between photophobia and simulator sickness must be further explored and that it may negatively impact those with photophobia more than those without it. More research needs to be done on this topic as researchers need to understand these relationships so symptoms of simulator sickness can be mitigated, allowing VR to reach its maximum potential.

Acknowledgements

We would like to thank the Ohio Space Grant Consortium for sponsoring this research as well as Kent State University for the space to conduct this study.

References

[1] Kim, M. (2019, August 14). Cybersickness: *Why People Experience Motion Sickness During Virtual Reality.* American Institute of Physics. https://ww2.aip.org/inside-science/cybersickness-why-people-experience-motion-sickness-during-virtual-reality

[2] McIntosh, C. W. (2018, November 15). *Understanding simulator sickness*. Children's Hospital of Philadelphia. https://injury.research.chop.edu/blog/posts/understanding-simulator-sickness

[3] Saredakis, D., Szpak, A., Birckhead, B., Keage, H. A. D., Rizzo, A., & Loetscher, T. (2020, March 31). Factors associated with virtual reality sickness in head-mounted displays: a systematic review and meta-analysis. *Frontiers in Human Neuroscience*, *14*(96). https://www.ncbi.nlm.nih.gov/pmc/articles/PMC7145389/

[4] Vision Specialists of Michigan (n.d.). The link between motion sickness, nausea & eye muscle strain. https://www.vision-specialists.com/the-link-between-motion-sickness-nausea-eye-muscle-strain/

[5] Debaun, T. (2021, July 23). Virtual reality: EMF & blue light concerns for VR technology. Defender Shield. https://defendershield.com/blogs/blue-light/vr-technology-emf-and-blue-light-concerns-for-virtual-reality

[6] Cleveland Clinic. (2023, October 4). Photophobia. https://my.clevelandclinic.org/health/symptoms/photophobia

[7] Dreyer, J. (2016, July 1). *Virtual reality headsets and vision*. Crystal Vision Ltd. https://www.contactlenses.co.uk/education/virtual-reality-headsets-and-vision

[8] Mayo Clinic. (2024, July 2). *Eyestrain*. https://www.mayoclinic.org/diseases-conditions/eyestrain/symptoms-causes/syc-20372397

[9] Cortez MM, Digre K, Uddin D, Hung M, Blitzer A, Bounsanga J, Voss MW, Katz BJ. Validation of a photophobia symptom impact scale. Cephalalgia. 2019 Oct;39(11):1445-1454. doi: 10.1177/0333102419845641. Epub 2019 May 22. PMID: 31116567; PMCID: PMC6999072.

[10] Keshavarz, B., Murovec, B., Mohanathas, N., & Golding, J. F. (2021). The Visually Induced Motion Sickness Susceptibility Questionnaire (VIMSSQ): Estimating Individual Susceptibility to Motion Sickness-Like Symptoms When Using Visual Devices. Human Factors, 00187208211008687. https://doi.org/10.1177/00187208211008687

[11] Hunt, C., M. (2022, February 9). Embry-Riddle trims student start-to-solo time by 30 percent. Aircraft Owners and Pilots Association. https://www.aopa.org/news-and-media/all-news/2022/february/09/embry-riddle-trims-student-start-to-solo-time-by-30-percent

[12] CKAS Mechatronics Pty Ltd. (2019). *CKAS OpenFRM Single*. https://www.ckas.com.au/ckas_openfrm_single_58.html

[13] Kennedy, R. S., Lane, N. E., Berbaum, K. S., & Lilienthal, M. G. (1993). Simulator Sickness Questionnaire: An Enhanced Method for Quantifying Simulator Sickness. *The International Journal of Aviation Psychology*, *3*(3), 203–220. https://sci.bban.top/pdf/10.1207/s15327108ijap0303_3.pdf

[14] Gluck, A., & Huth, L. (2024). Supporting Individuals with Photophobia in VR: A Case Study of VR Shades, an Accessible VR Application Feature Prototype. In *Proceedings - 2024 IEEE Conference on Virtual Reality and 3D User Interfaces Abstracts and Workshops, VRW 2024* (pp. 311-315). (Proceedings - 2024 IEEE Conference on Virtual Reality and 3D User Interfaces Abstracts and Workshops, VRW 2024). Institute of Electrical and Electronics Engineers Inc.. https://doi.org/10.1109/VRW62533.2024.00062

[15] Golding, J. F., Rafiq, A., & Keshavarz, B. (2021). Predicting Individual Susceptibility to Visually Induced Motion Sickness by Questionnaire. Frontiers in Virtual Reality, 2. https://doi.org/10.3389/frvir.2021.576871

AstroPsych: A Therapist-Guided Multimodal AI Framework for Real-Time Mental Health Support

Student Researcher: Austin Wilson

Advisor: Dr. Alexis E. Block

Case Western Reserve University
Electrical, Computer, and Systems Engineering / Master of Science in Computer Engineering

Abstract
AstroPsych is a modular, multimodal AI-driven framework that provides empathetic, real-time mental health support in environments where immediate access to a human therapist is unavailable, whether due to the isolation of deep-space missions or the physical, social, or systemic barriers that restrict access to care on Earth. By integrating physiological sensing, natural language processing, and adaptive interaction modalities, AstroPsych personalizes support based on each user's emotional and physiological state. Crucially, AstroPsych is designed to function with therapist oversight: sessions are logged and shared asynchronously with mental health professionals, enabling expert review, guidance, and continuity of care. This therapist-guided approach ensures that immediate emotional support does not replace, but rather augments, traditional therapy. AstroPsych is a scalable, autonomous, human-centered solution to closing mental health accessibility across terrestrial and extraterrestrial frontiers.

Project Objectives
As NASA prepares for extended human spaceflight missions to Mars and beyond, astronauts will encounter unprecedented psychological challenges. One of the most significant is *temporal isolation*, the communication delay that increases with distance from Earth, which can reach up to twenty-two (22) minutes one way [1]. This time lag fundamentally disrupts the ability to receive immediate technical or psychological support, rendering real-time therapeutic intervention infeasible. In deep space, astronauts experiencing stress, anxiety, or emotional distress will be expected to self-regulate without the benefit of live interaction with mental health professionals.

This issue is not unique to space. On Earth, many individuals also experience temporal or physical isolation, particularly those in underserved or remote regions with limited access to mental health care or other real or perceived barriers. In the United States alone, the severe shortage of mental health professionals has resulted in wait times of several months for therapy appointments [2]. During these delays, individuals in distress are left to navigate mental health challenges alone, mirroring the isolation experienced during deep space missions.



Fig. 1. *[A] Example of the Text modality, [B] Voice modality, [C] Avatar modality, [D and E] front and rear isometric views of Robot modality (the NAO with AstroPsych modifications).*

Integrating large language models (LLMs) into human-robot interaction (HRI) and mental health applications has significant potential [3], but key limitations remain. Existing AI-driven conversational agents and robots often fall short due to:

- **Lack of multimodal feedback:** Most existing systems rely exclusively on text or speech features like sentiment, linguistic content, or prosody, without incorporating real-time physiological data, limiting their ability to accurately assess user states [3].
- **Poor adaptation to user stress:** Humans under stress often exhibit cognitive rigidity, frustration, and uncooperative behaviors [4], yet current AI systems lack mechanisms to dynamically adapt responses to a user's stress levels.
- **Limited focus on emotional well-being:** Previous research has prioritized LLM usability [5] and dialogue coherence with default voices [3], often neglecting the goal of affective support [6].

In the mental health domain specifically, prior research has explored using LLMs for automated therapy [7] and mental health condition detection [8]. However, these efforts are limited by:

- Use of generalized, unvalidated datasets, which undermines clinical applicability [2].
- Inadequate safety mechanisms when engaging with sensitive or high-risk topics, which raises ethical concerns [2].
- Insufficient empathy generation, particularly in high-stress or crisis scenarios [9].
- Delayed system responses, which disrupt conversational flow, and damage user trust and engagement [6].

To address these limitations, we propose a therapist-guided, multimodal, adaptive framework that combines physiological sensing, behavioral cues, and AI-driven language models to deliver empathetic, responsive support. Rather than replace human therapists, the system is designed to extend their reach by enabling real-time intervention in situations where access to professional care is delayed or unavailable. The platform-agnostic framework allows it to be deployed via text, voice, avatar, or robot, depending on the user's context and preferences.

This research bridges the gap between AI-driven conversation and real-time emotional support by evaluating how different expert-guided interaction modalities influence the system's ability to promote psychological recovery and reduce stress. Our work is guided by the following research questions:

1. To what extent can **expert-guided prompts enhance** the **appropriateness** and **effectiveness** of **LLM**-generated responses?
2. How does the **fidelity** of an LLM-powered **interaction modality influence** the users' **perceived emotional support** and engagement?

Methods

Hardware and Software

AstroPsych uses custom-built and commercially available hardware and software to enable real-time physiological monitoring and adaptive, multimodal interactions. Key components include:

- **Meta Quest 3:** A wireless mixed-reality headset with a high-resolution display and full-color passthrough, enabling immersive virtual-physical transitions and seamless research integration.
- **Hexoskin ProShirt:** A breathable, machine-washable smart garment that continuously records heart rate (256 Hz), respiratory rate (128 Hz), and physical activity. This system is the foundation for Astroskin devices, which are currently used on the International Space Station (ISS) [10, 11].

- **Custom Sensor Shirt:** Equipped with five ICM20948 inertial measurement units (IMUs) for upper-body movement tracking and an electrodermal activity (EDA) sensor to measure skin conductance to track emotional arousal.
- **Camera System:** Two Raspberry Pi v3 RGB cameras and a Seek thermal camera (S314SPX) for facial and thermal pattern tracking [12], supplemented by an Intel RealSense D455 Depth Camera for IMU movement validation.
- **NAO V6 Humanoid Robot: M**odified with custom PCBs, Raspberry Pi Compute Module, microphone array, integrated RGB and thermal camera system, and custom housings, to support physically embodied AI-driven interaciton.

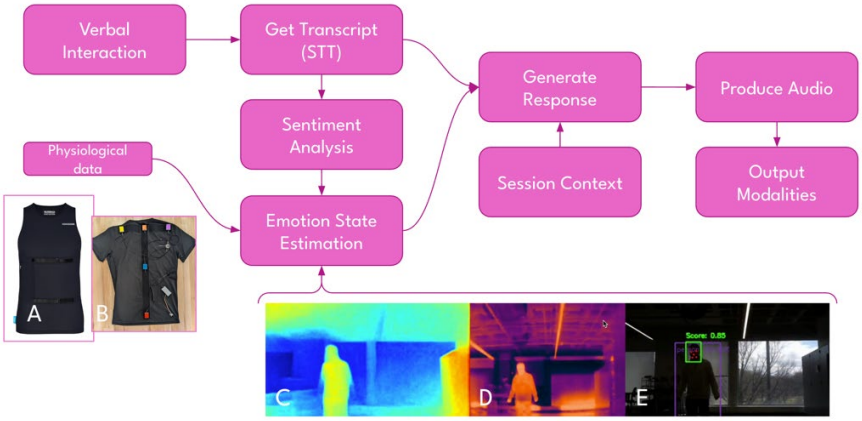


Fig 2. The *AstroPsych system architecture. The framework processes multi-modal inputs (speech, text, physiological data using [A] Hexoskin ProShirt and [B] custom sensor shirt, and behavioral data using [C] depth map from stereoscopic camera system and [D] thermal camera for [E] person, face, and facial landmark detection) to determine sentiment and emotional state. Then, AstroPsych integrates these data with static documents for context and sends a generated response to our output modalities (which may include audio production).*

The AstroPsych framework (Fig. 2) processes and synthesizes real-time multimodal physiological, behavioral, and speech data, to estimate a user's emotion state. AstroPsych then uses LLM-powered natural language generation to produce a response. Key components include:

- **Real-time streaming input:** Text or speech is streamed via WebSocket for low-latency communication.
- **Emotion state estimation:** Physiological data are continuously streamed via Bluetooth Low Energy (BLE) from the Hexoskin ProShirt (heart and respiration rate, RR-interval at ≥ ~ 20Hz) and the custom sensor shirt (IMU and EDA data at ~ 50Hz). Camera input is processed for facial landmarks, person tracking, and thermal and depth-based features. Using a custom model, these data streams are processed at ≥ ~ 1Hz to generate affective state predictions [1].
- **Personalization layer:** Static documents (e.g., patient background, therapist notes, and environment details) are injected into the LLM prompts to tailor responses and promote therapeutic continuity.
- **LLM-based response generation:** The core decision-making engine integrates physiological and affective state estimates, sentiment analysis, and historical memory to generate emotionally sensitive, context-aware responses.

- **Multimodal Outputs:** AstroPsych supports output through multiple modalities: text, speech, immersive avatars, and humanoid robots, automatically routed via WebSocket to the currently active interface.

To ethically and reliably induce stress, we use a virtual reality (VR)-based implementation of the Trier Social Stress Test (VR-TSST) [13, 14], deployed via Unity 3D on the Meta Quest 3. This self-contained module includes real-time speech transcription and consistent stressor delivery. Additionally, we may integrate the Database for Emotion Analysis Using Physiological Signals (DEAP) [15] dataset with our experimental data to refine affective state classification and identify recovery patterns across interventions.

Focus Group Study Design

To address Research Question 1 (effectiveness of expert-guided LLM prompts), we designed a focus group study with licensed mental health professionals (e.g., psychologists, psychiatrists, social workers, and school counselors). Participants are divided into multiple cohorts. Each cohort collaboratively develops mental health scenarios, including a) patient personas (demographics, medical history, concerns), b) session contexts (session goals, past notes), and c) sample dialogues (example patient statements with ideal supportive responses).

After development, each cohort evaluates a set of scenarios created by a different cohort through a structured Qualtrics survey. Each survey includes about 50 rank-order questions, each presenting a mental health scenario and a single patient statement expressing mental health difficulties, and multiple possible responses, generated by various LLMs (e.g., Anthropic's Claude, OpenAI's GPT-4o, Meta's LLaMA 3, Google's Gemma, ChatPsychiatrist, MentaLLaMA), and the original human-generated one.

Professionals will rate responses based on emotional sensitivity, appropriateness, and clinical effectiveness. This evaluation will determine whether LLM models can approximate human-like support and which LLM should be used in the modality user study.

Modality User Study Design

To address Research Question 2 (impact of modality on stress recovery), we designed a between-subjects, repeated measures study. Participants undergo acute stress via the VR-TSST and are randomly assigned to one of five conditions: 1) no intervention (control), 2) text-based chat, 3) voice-based conversation, 4) immersive avatar interaction (VR), or 5) physical robot interaction (NAO). Each condition delivers the same structured intervention generated by the selected LLM, with modality being the only manipulated variable to isolate the effects of embodiment and fidelity. Physiological signals are continuously recorded and self-reported affective data are collected at three time points: baseline, post-stress, and post-intervention.

An a priori power analysis (repeated measures between-subjects ANOVA, power = 0.8, medium effect size d = 0.25), determined a required sample size of 180 participants, (36 per condition). The study balances for biological sexes while remaining inclusive of all gender identities.

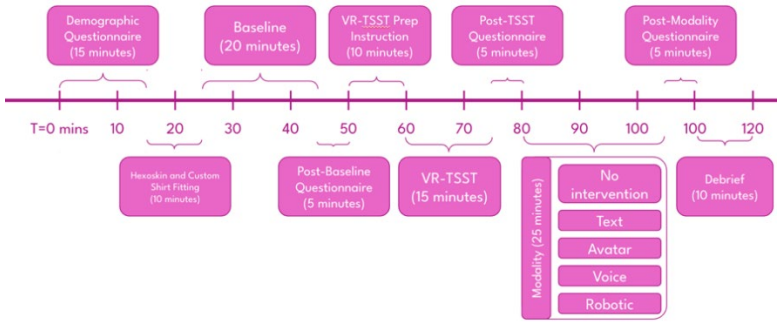


Fig. 3. *Modality user study timeline: A participant completes a demographic questionnaire (15 min), sensor fitting (10 min), baseline rest period (20 min), and initial emotional state (ES) questionnaire (5 min) before the VR tutorial (10 min) and the VR-TSST stress induction (15 min), and a second ES questionnaire. Then, they experience one intervention modality (25 min): no intervention, text, voice, avatar, or robot before completing a final ES and concluding questionnaire, and being debriefed. Total experiment time is ~120 minutes per user.*

As shown in Fig. 3, each study session begins with the participant completing a brief demographic questionnaire (age, self-described gender identity, and other relevant background information). Height and weight are recorded for accurate physiological data; however, these values are not shared with the participant to avoid introducing unnecessary stress.

Next, the participant is fitted with a Hexoskin ProShirt and our custom sensor shirt. To ensure comfort and privacy, the participant may request assistance from a researcher of the same-gender.

Following sensor setup, the participant is guided to a quiet room and instructed to sit quietly for 20 minutes to allow physiological signals to stabilize. During this period, baseline affective state measurements are collected using the Self-Assessment Manikin (SAM) [16] and the short-form Positive and Negative Affect Schedule (PANAS-SF) [17].

After the baseline assessment, the participant is guided to the TSST room, where a research assistant fits them with a Meta Quest 3 VR headset and walks them through a brief tutorial to ensure familiarity with the VR environment and check for VR-induced discomfort. Once ready, the participant undergoes the VR-TSST, a validated protocol for acute stress induction, which consists of three phases: ten minutes of speech preparation, then five minutes of public speaking followed by five minutes of oral mental arithmetic, all in front of a virtual panel of judges. The session is monitored throughout, and the participant is reminded they may withdraw at any time, without penalty.

Immediately following the VR-TSST, the participant completes an emotional state assessment (SAM and PANAS-SF) [16, 17] and is guided to the intervention room. Based on the assigned condition, the participant receives an intervention or enters a control condition for 25 minutes.

- Control: The participant sits alone in a quiet room while journaling.
- Intervention: The participant engages with one of the four LLM-powered supportive modalities (text, voice, avatar, or robot). For the avatar condition, the user keeps wearing the VR headset.

All interventions are monitored via a live audio-visual feed, and the participant is informed they may request assistance at any time.

After the intervention, the participant completes a final emotional state assessment (SAM and PANAS-SF) [16, 17], followed by additional Likert-scale and open-ended questions about the experience and the perceived effectiveness of the intervention.

The session concludes with a debriefing. The purpose of the VR-TSST is explained, and the participant is reassured their performance and feelings of stress were typical. A take-home flyer with evidence-based stress management techniques is provided. The participant then removes the Hexoskin ProShirt and custom sensor shirt. Each study session is expected to last approximately 120 minutes per participant.

Results and Discussion

Due to the nature of our research involving human participants, all study protocols require approval from the Case Western Reserve University Institutional Review Board (IRB). Unanticipated delays in the IRB approval process prevented us from fully executing our planned studies within the academic year. Nevertheless, we conducted preliminary trials for the focus group and modality studies, which were instrumental in refining our procedures ahead of formal IRB approval.

The focus group received IRB approval in February, and we have since conducted several sessions with licensed mental health professionals. These early interactions yielded valuable insights into the structure and dynamics of therapeutic conversations. Notably, participants emphasized the importance of *validating a patient*, *asking clarifying questions*, demonstrating *mindful engagement*, and using *reframing* to promote emotional understanding and resilience. These clinician-identified strategies are now being integrated into the LLM prompting pipeline to enhance the emotional sensitivity and appropriateness of system responses. The modality user study is still pending IRB approval. However, internal pilot testing helped identify key logistical and technical issues, which are currently being addressed to streamline the study protocol and ensure data quality upon deployment.

Although formal results are not yet available, extensive development and testing of the AstroPsych system have yielding promising process, particularly in optimizing response latency, which is important for preserving conversational flow and user trust. We explored strategies on the input and output sides of the interaction pipeline: On the input side, we tested a hybrid approach using voice-activity detection (VAD) and time-since-last-word (TSLW). VAD proved highly responsive in low-noise environments, but faltered under high-noise conditions, often resulting in unintended continuous transcription. In contrast, TSLW relies on word-level timestamps to infer conversational pauses, performing better in noisy conditions but introducing unnecessary latency in quiet settings. By combining VAD and TSLW, AstroPsych adapts to environmental noise levels and optimizes input responsiveness dynamically.

On the output side, we evaluated two response generation paradigms: think-then-speak and think-and-speak. The traditional think-then-speak approach requires full text-response generation before audio output begins. Think-and-speak, leveraging recent advances in streaming generative audio, allows the system to begin producing speech as the response is being generated. In our testing, think-and-speak consistently initiated audio playback in about one and a half seconds, substantially improving perceived responsiveness compared to think-then-speak, which remained constrained by text generation time.

Over the next year, we will finalize executing both studies. In parallel, we are extending the AstroPsych framework to support multi-user interactions to address interpersonal conflict resolution. These improvements will broaden the framework's applicability beyond individual support to emotion emotionally intelligent facilitation of group dynamics.

Acknowledgments

This research was made possible through the generous support of the Ohio Space Grant Consortium. I also thank Case Western Reserve University and the Social and Physical Human-Robot Interaction (SaPHaRI) Lab and Human Fusions Institute. Special thanks to Dr. Alexis E. Block and her students—Noah Medrano, Alice Liu, Kaleb Kim, and Andrew Chen—for their contributions and support of this work.

References

[1] K. T. McBrayer, P. Chai and E. Judd, "Communication Delays, Disruptions, and Blackouts for Crewed Mars Missions," 2022.

[2] Y. Hua, F. Liu, K. Yang, Z. Li, H. Na, Y.-h. Sheu, P. Zhou, L. V. Moran, S. Ananiadou, A. Beam and others, "Large language models in mental health care: a scoping review," *arXiv preprint arXiv:2401.02984,* 2024.

[3] C. Y. Kim, C. P. Lee and B. Mutlu, "Understanding Large-Language Model (LLM)-Powered Human-Robot Interaction," in *ACM/IEEE International Conference on Human-Robot Interaction*, Boulder CO USA, 2024.

[4] S. Cohen, "After effects of Stress on Human Performance and Social Behavior: A Review of Research and Theory," *Psychological Bulletin,* vol. 88, pp. 82--108, 1980.

[5] N. Dimitropoulos, P. Papalexis, G. Michalos and S. Makris, "Advancing Human-Robot Interaction Using AI – A Large Language Model (LLM) Approach," *Advances in Artificial Intelligence in Manufacturing,* pp. 116--125, 2024.

[6] T. Onorati, Á. Castro-González, J. Cruz del Valle, P. Díaz and J. C. Castillo, "Creating Personalized Verbal Human-Robot Interactions Using LLM with the Robot Mini," *International Conference on Ubiquitous Computing and Ambient Intelligence,* pp. 148--159, 2023.

[7] Z. Ma, Y. Mei and Z. Su, "Understanding the Benefits and Challenges of Using Large Language Model-Based Conversational Agents for Mental Well-Being Support," *arXiv,* 2023.

[8] K. Yang, S. Ji, T. Zhang, Q. Xie, Z. Kuang and S. Ananiadou, "Towards Interpretable Mental Health Analysis with Large Language Models," in *Conference on Empirical Methods in Natural Language Processing*, Singapore, 2023.

[9] S. B. Loh and A. S. Raamkumar, "Harnessing Large Language Models' Empathetic Response Generation Capabilities for Online Mental Health Counselling Support," *arXiv,* 2023.

[10] W. Toscano, P. Cowings, P. Sullivan, A. Martin, J. Roy, M. Krihak, S. Winther, A. Hanson and T. Shaw, "Wearable Biosensor Monitor to Support Autonomous Crew Health and Readiness to Perform," 2017.

[11] M. Krihak, S. Wolfe, A. Lindsey, C. Middour, W. Toscano, S. Winther, N. Marker and T. Shaw, "Biosensor Integration Development ExMC/Canadian Space Agency Collaboration," 2017.

[12] V. Kosonogov, L. De Zorzi, J. Honoré, E. S. Martínez-Velázquez, J.-L. Nandrino, J. M. Martinez-Selva and H. Sequeira, "Facial thermal variations: A new marker of emotional arousal," vol. 12, no. 9, pp. 1--15, 09 2017.

[13] C. Kirschbaum, K.-M. Pirke and D. H. Hellhammer, "The 'Trier Social Stress Test'--a tool for investigating psychobiological stress responses in a laboratory setting," *Neuropsychobiology,* vol. 28, pp. 76--81, 1993.

[14] E. C. Helminen, M. L. Morton, Q. Wang and J. C. Felver, "Stress Reactivity to the Trier Social Stress Test in Traditional and Virtual Environments: A Meta-Analytic Comparison," *Psychosomatic Medicine,* vol. 83, pp. 200--211, 2021.

[15] S. Koelstra, C. Muhl, M. Soleymani, J.-S. Lee, A. Yazdani, T. Ebrahimi, T. Pun, A. Nijholt and I. Patras, "Deap: A database for emotion analysis; using physiological signals," *IEEE transactions on affective computing,* vol. 3, pp. 18--31, 2011.

[16] M. M. Bradley and P. J. Lang, "Measuring emotion: The self-assessment manikin and the semantic differential," *Journal of Behavior Therapy and Experimental Psychiatry,* vol. 25, pp. 49-59, 1994.

[17] A. Mackinnon, A. F. Jorm, H. Christensen, A. E. Korten, P. A. Jacomb and B. Rodgers, "A Short Form of the Positive and Negative Affect Schedule: Evaluation of Factorial Validity and Invariance across Demographic Variables in a Community Sample," *Personality and Individual Differences,* vol. 27, pp. 405--416, 1999.

High-Frequency Active Control of Far-field Noise in a Supersonic Rectangular Twin Jet

Student Researcher: Abhilash Yarlagadda

Advisor: Dr. Mo Samimy and Dr. Nathan Webb

The Ohio State University
Department of Mechanical and Aerospace Engineering

Abstract
The effect of high-frequency, plasma-based excitation on the radiated noise of a supersonic rectangular single jet (SRSJ) was investigated. Rectangular nozzles are desired by the military because of their ease of integration among other reasons, and twin rectangular jet configurations are common in fighter jets. After conducting an experimental campaign with a twin jet, the focus of the group shifted to study the more fundamental physics of the single jet. Our previous research was also limited to a lower range of excitation frequencies, but this work is the first to examine the effect of higher frequencies on the far-field (FF) noise in the overexpanded regime. As a preliminary work on this topic, the acoustic measurements were limited to the minor axis plane where the noise of the jet is known to be greatest. It was found that a sufficiently high excitation frequency produces broadband noise reduction in the FF, particularly in the downstream direction, but the reduction reaches a maximum before dropping off as the frequency increases. In addition, the actuation pattern, or mode, made little difference at high frequencies.

Project Objectives
Noise in supersonic jets is an issue for military personnel who spend a great deal of time near these aircraft and communities that live near military bases. For the latter, this is more of an inconvenience. Care must be taken when planning a new installation to place it far enough away from ordinary buildings to avoid noise complaints. On the other hand, jet noise can cause hearing loss and other health problems for the soldiers on deck during launches, particularly in the Navy [1]. This research is part of a broader campaign to study plasma actuator excitation as a method of supersonic jet noise reduction.

We first consider the sources of supersonic jet noise. In any shear layer, the difference in velocity between the two sides makes the flow susceptible to the Kelvin-Helmholtz (K-H) instability. If the flow is slightly perturbed, the K-H instability causes a small vortical wavepacket known as a coherent structure (CS) to be produced and travel downstream [2]. There are typically countless, tiny, random fluctuations in a flow that lead to CS being produced over a wide range of frequencies, but certain frequencies may be amplified or attenuated depending on the flow physics.

CS interact with another major flow element to generate much of the noise in a supersonic jet: the shock waves. When the pressure achieved by the fluid at the exit of a nozzle does not match the pressure of the ambient environment, a series of shock and expansion waves are created. For nozzles designed with the method of characteristics, the smoothly curved internal geometry ensures that the flow will be shock-free for a single design condition. In this work, a military-style nozzle was used, which has straight sides and a sharp throat. Due to the discontinuity at the edge, a shock wave emerges at the throat regardless of the pressure condition, but it is always relatively weak. Whether they originate at the exit or the throat, the pressure waves form a pattern called a shock train in the downstream direction as they reflect toward and away from the jet centerline. The units between each pair of Mach disks are known as shock diamonds or shock cells.

In a rectangular jet, the short sides of the nozzle have a negligible impact on the shock structure and noise characteristics, so it can be thought of as 2D. If seen along the major axis, a shear layer would grow along the top and bottom sides of the jet. The points where the shocks in Figure 1 reflect off the sonic line lie within the shear layer, so the CS discussed earlier pass over them as they convect downstream. Each CS passes over shock tips until one or both are too weak, and the combined noise is known as broadband shock-associated noise (BBSAN). When a CS passes a shock tip, an acoustic wave is emitted in all directions, including back toward the nozzle. This wave can produce a perturbation at the nozzle exit when it impacts the nozzle lip, causing a CS to be created in turn. If the timing of the waves radiated from a particular shock tip to the nozzle aligns with the timing of the CS arriving from the nozzle to that shock tip, the process becomes self-sustaining. This feedback loop is associated with screech, a component of supersonic jet noise marked by a distinct tone and high amplitude [3]. Each shear layer hosts a screech feedback loop, and the two can become coupled. The shedding pattern of the jet is known as its mode. The mode of the SRSJ observed in our lab was always flapping; this is characterized by the alternating shedding of CS from each of the two shear layers. Other modes are possible naturally, especially in an axisymmetric jet, but even excitation could not induce them in the flow. Both BBSAN and screech are key targets for noise reduction efforts in supersonic flow control.

Flow control can be used to provide an assortment of benefits to aircraft, like mixing enhancement, thrust vectoring, and noise control, and falls into either the passive or active category. Passive flow control often means a geometric change geared toward a single design condition. These devices are usually simple in design and require no power input, but they can be difficult to retrofit onto vehicles, and they cannot be adapted to different flight conditions. On the other hand, active flow control (AFC) tends to involve complex systems with some kind of power requirement. As a plus, AFC features adjustable parameters to ensure that the actuators can switch off when they would be a detriment or to operate in other modes for optimal performance in all cases. In this work, localized arc filament plasma actuators (LAFPAs) were used to excite the flow. These devices use Joule heating to supply a burst of thermal energy to the flow and are located strategically near the nozzle exit to take advantage of the K-H instability [4]. By perturbing the flow where it is most sensitive, the LAFPAs can be used to disrupt or alter the development of natural CS and even create their own. There are two characteristic frequency ranges for CS in a jet, and the lower of the two was previously studied by our lab [5, 6]. The LAFPAs exhibited good control authority over the jet in this range and produced large CS that competed with the natural CS to reduce screech. It was thought that using actuation in the higher frequency range could help weaken CS in the flow by causing them to dissipate faster, thus reducing BBSAN by affecting a broad range of the spectrum and providing the motivation for this research.

Methods

An anechoic chamber at the Gas Dynamics & Turbulence Laboratory at The Ohio State University's Aerospace Research Center was used for this research. The stagnation pressure of the flow is set by a computer-controlled valve, which automatically maintains the desired nozzle pressure ratio (NPR). Figure 2a shows part of the assembly of the SRSJ and the coordinate system used. A bi-conic, rectangular, converging-diverging nozzle (Figure 2b) with a sharp throat, a design Mach number of 1.5 (M_d = 1.5 or NPR = 3.67), and an aspect ratio of 2 (AR = 2) was used. The nozzle exit measures 1 in. wide and ½ in. tall. φ is the azimuthal angle of the SRSJ in the y-z plane and refers to the angle between the major axis plane and the plane of the FF microphones. In the results shown here, all data was collected at φ = 90°. The jet noise levels are the highest at this angle due to the presence of CS and the screech feedback loops in the shear layers along the long sides of the nozzle. Previous research indicates that trends in jet behavior along all azimuthal angles are similar, but future work will examine φ = 0° cases for completeness. The assembly of the SRSJ within the anechoic chamber room is shown in Figure 2b. The angle θ, measured

with respect to the downstream jet axis, is the polar angle for the FF microphone locations. The FF array consists of ¼ in. microphones mounted at polar angles ranging from 30° to 120° and aimed at the origin of the jet coordinate system (Figure 2a). Only the eight microphones from 30° to 90° were used since the line of sight of the microphones at higher angles is blocked. The individual microphone distances from the SRSJ origin range from $99D_e$ to $196D_e$. The acoustic data was processed to produce sound pressure level (SPL) spectra, which are in turn integrated to find the overall sound pressure levels (OASPL). The spectra allow for the examination of noise level distinguished by frequency, and the OASPL values serve as an overview of the noise level across the range of frequencies most annoying and damaging to humans. In jet noise research, frequencies are often normalized by the jet velocity and diameter to make it easier to compare results between facilities. The normalized frequency is called the Strouhal number and is calculated as follows, where f is a frequency, D is the exit diameter of the nozzle and U is the exit velocity of the flow:

$$St = \frac{f * D}{U}$$

The same Strouhal number can correspond to different frequencies if comparing flows with different velocities. As a reference for the results later, plots are shown for jet Mach numbers (M_j) of 1.35 and 1.50 with an excitation Strouhal number (St_e) of 1.50 for both Mach. However, the physical frequency is ~20 kHz when M_j = 1.35 and ~31 kHz when M_j = 1.50. Another note about the results: ΔOASPL is often shown instead of OASPL for cases using the actuators. The OASPLs of the natural jet are subtracted from the OASPLs calculated for the excited jet case, resulting in ΔOASPLs that express the change in noise level due to actuation.

The other crucial part of the experimental setup is the LAFPAs. As implied by the name, these devices generate a small arc of plasma when actuated, and as mentioned in the last section, take advantage of a flow instability at the nozzle exit. Each LAFPA consists of two, 1-mm tungsten electrodes connected to a high-voltage power supply. The system was built in-house to handle the voltage requirements and the high-frequency switching capabilities of the actuators. In Figure 2a, one can see that the front face of the nozzle is a separate piece from the ones with the bolt holes behind it; it is also composed of a different material. The baseplate and convergent section of the nozzle are made of stainless steel, but the divergent section at the end is made of boron nitride (BN). BN is a ceramic with extremely high thermal and electrical resistance, which makes it ideal for housing the LAFPAs and withstanding their arcs. The LAFPAs are inserted through the BN such that their tips emerge in a shallow groove just upstream of the nozzle exit. This allows the arc to sit in the flow without the electrodes extending into the path as well, and it provides a gap that prevents the flow from disrupting the formation of the arc as much. Three LAFPAs (i.e., six electrodes) are positioned along each of the long sides of the nozzle. The actuation parameters of each LAFPA can be independently varied, but they are typically used with all firing at the same frequency. When testing at a given frequency, the mode of excitation is altered. In this work, excitation frequencies ranged from Ste = 0.75 to Ste = 2.50, and five modes were tested at most frequencies. For brevity, a limited set of cases will be presented. The actuation patterns are shown in Figure 3.

Results and Discussion

The results will focus on a variety of excitation cases at M_j = 1.35 and 1.50. The baseline or natural jet spectra for each Mach number are shown in Figures 4a and 4b respectively. Certain microphones' spectra are selectively plotted to get a look at differences in noise directivity at varying polar angles. As the angle increases, the spectrum is further offset by -30 dB for readability. Thus, only the dB values of the 30° are accurate as plotted.

The leftmost peak in each figure is the signature of screech. M_j = 1.50 is the design Mach number, so there are no shocks produced at the nozzle exit. The presence of the throat shock train means the baseline jet still screeches, albeit weakly. The M_j = 1.35 case is fairly overexpanded, so a strong shock system is generated at the exit. This difference is key to explaining the differences in LAFPA effectiveness between the two Mach numbers and will be returned to later. More harmonics are visible at all angles in the M_j = 1.35 case, and the first harmonic is very prominent at the sideline (90°) in both cases.

Only one case of high-frequency excitation at each Mach number will be examined. Figures 4c and 4d show spectra with excitation of Ste = 1.50 in FM at M_j = 1.35 and 1.50 respectively. The black lines in each are the same spectra as Figs 4a and 4b, and the colored lines now show the results of actuation in relation to the baseline.

In the M_j = 1.35 case, almost no change is observed at the downstream angles, but a slight broadband decrease is seen from about 3-30 kHz at θ = 60° and 90°. The screech peak is not altered at any angle. In the M_j = 1.50 case, screech is absent at all angles, and the broadband decrease now extends to all angles as well. Because the screech is so much weaker in the design case, the LAFPAs are able to get rid of the tone. There is no longer a preferred frequency to organize CS in the shear layer, so the LAFPAs exhibit strong control authority. When screech is stronger, the effect of the LAFPAs is less apparent.

Figures 5a and 5b show the ΔOASPL at all measured polar angles for Ste = 1.50 at M_j = 1.35 and 1.50 respectively. These plots include the results of all the actuation patterns that were tested at each frequency.

Clearly, there is little distinction between the different excitation modes. Starting from about Ste = 1.00, the effects of each mode become quite uniform as in the figures above. This frequency provides the best overall noise reduction at each Mach number, with up to 2 dB reduction at M_j = 1.35 and nearly 3 dB at M_j = 1.50. The effects of excitation seen in the FM spectra are apparent here as well. Once integrated, the large gaps between the baseline and excited spectra for M_j = 1.50 correspond directly to the reductions over all angles in the ΔOASPL. The largest reductions for M_j = 1.50 occur at θ = 50° and beyond, which also agrees with the observations of the spectra from earlier. When the excitation frequency is sufficiently high, the CS generated by the LAFPAs are so small that they dissipate too quickly to establish a coherent pattern. It therefore makes no difference what mode of actuation is attempted, but they are all similarly effective since they disrupt larger CS over a range of length scales, leading to the broadband noise reduction effect.

Figures

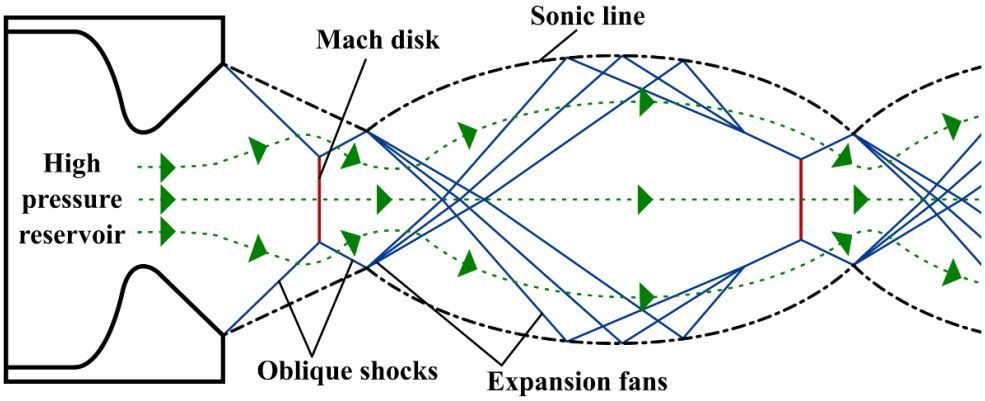
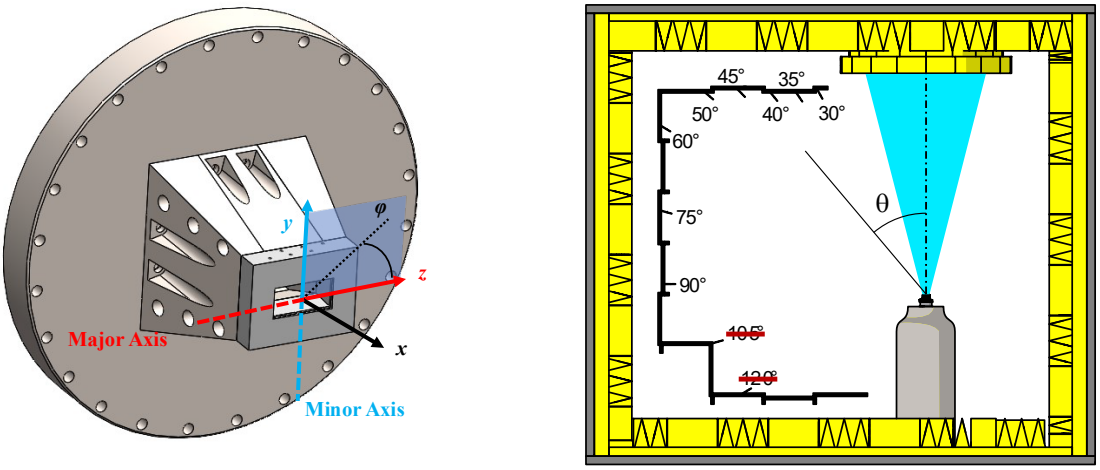
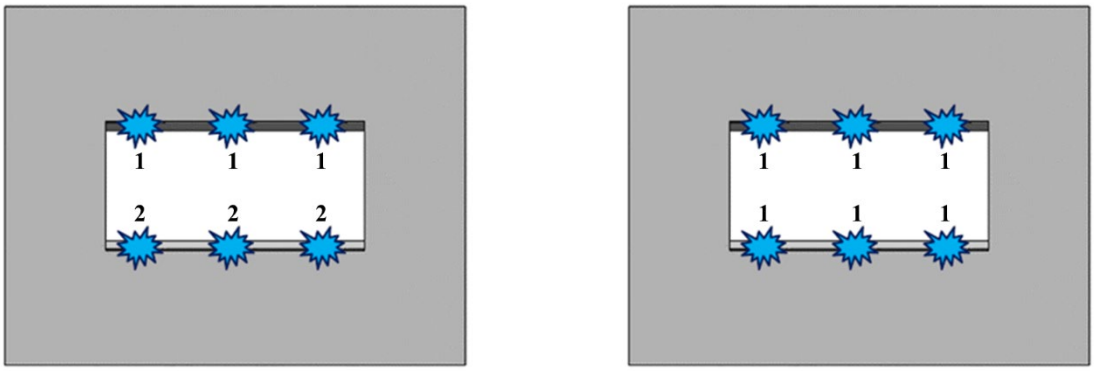


Figure 1. Diagram of important flow structures in an overexpanded supersonic jet.

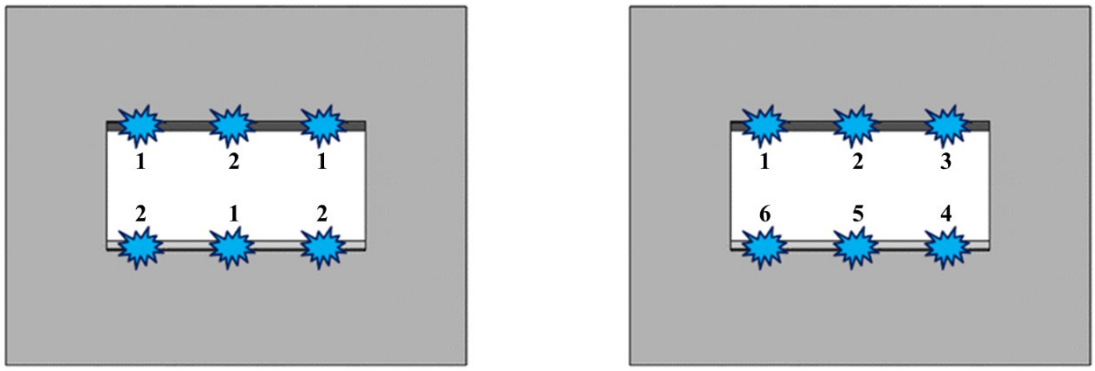


(a) **(b)**

Figure 2. SRSJ assembly with referenced coordinate system (a) and top view of anechoic chamber with FF microphone positions (b).



(a) **(b)**



(c) **(d)**

Figure 3. Actuation patterns used with the LAFPAs in this work: (a) flapping mode, FM; (b) symmetric mode, SM; (c) combined helical mode 3, CH3; (d) helical mode, H1. The numbers in each figure indicate which actuators fire simultaneously and in what order over the course of a period.

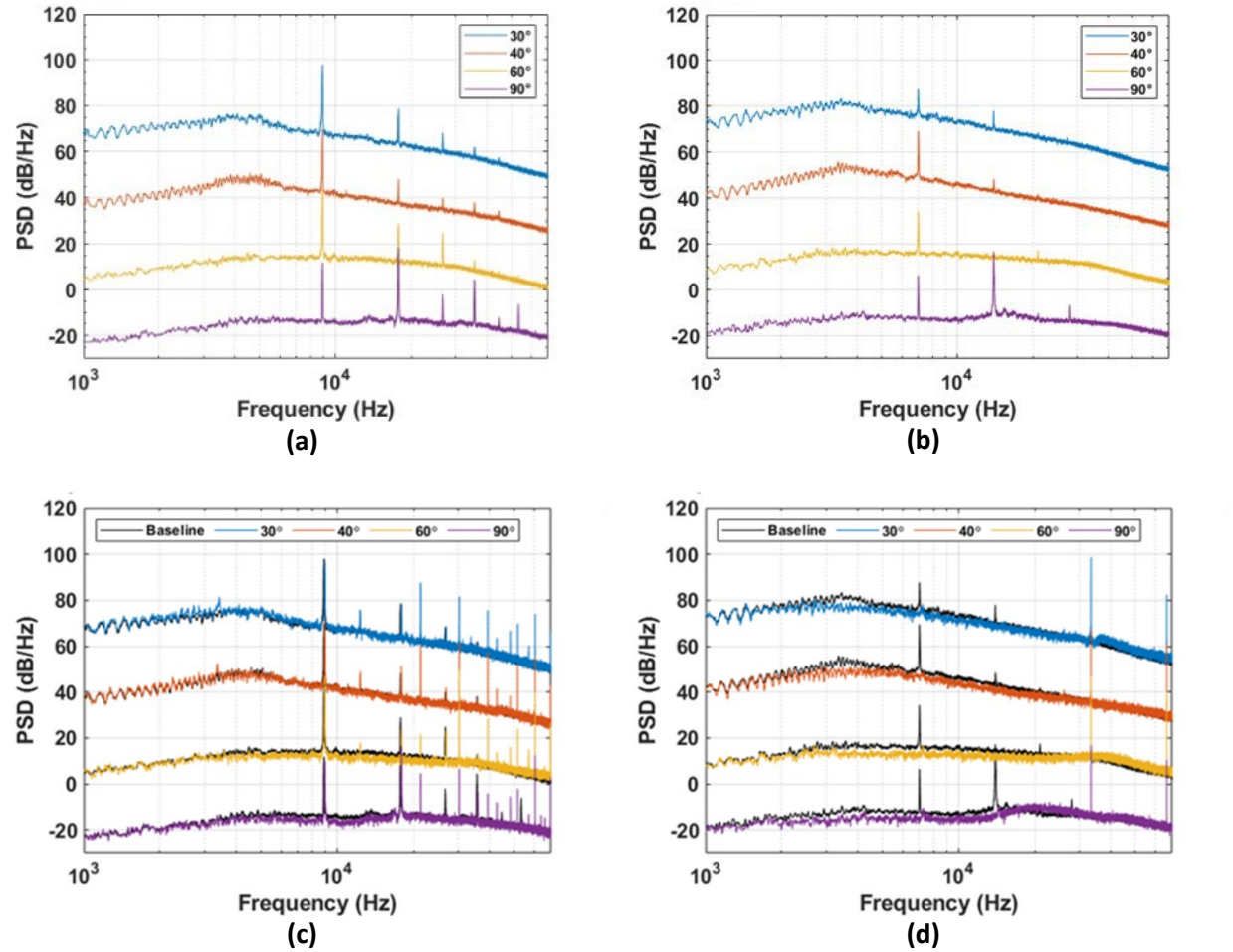


Figure 4. Noise spectra of (a) baseline M_j = 1.35 jet and (b) baseline M_j = 1.50 jet, and comparison spectra of (c) M_j = 1.35 jet excited at Ste = 1.50, and (d) M_j = 1.50 jet excited at Ste = 1.50.

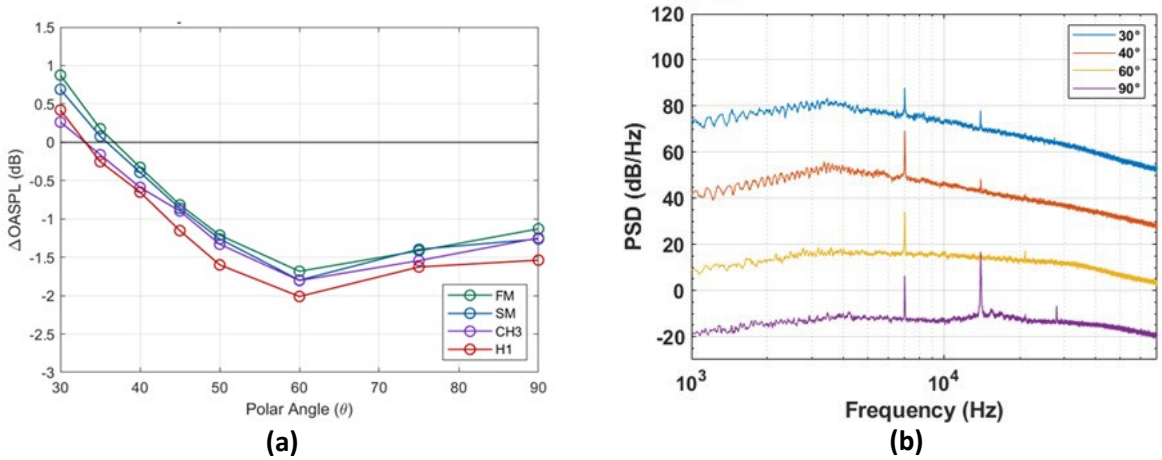


Figure 5. ΔOASPL over all measured polar angles and modes for Ste = 1.50 in (a) the M_j = 1.35 jet and (b) the M_j = 1.50 jet.

Acknowledgements

This work was supported primarily by the Office of Naval Research. However, my experience would not have been possible without the support of the Ohio Space Grant Consortium. In addition, my advisors Dr. Mo Samimy and Dr. Nathan Webb have served as excellent guidance during my time at The Ohio State University's Gas Dynamics and Turbulence Laboratory. Last and certainly not least, I appreciate the help of my fellow graduate students, Karli Katterle and Noah Hiler, and our undergraduate assistants, Mason Mitchell and Alyssa Brucchieri, who make the lab an excellent place to work on a personal and professional level.

References

[1] Aubert, A., and McKinley, R. Measurements of Jet Noise Aboard US Navy Aircraft Carriers. Presented at the AIAA Centennial of Naval Aviation Forum "100 Years of Achievement and Progress," Virginia Beach, VA, 2011.

[2] Brown, G., and A. Roshko, "On density effects and large structure in turbulent mixing layers," Journal of Fluid Mechanics Vol. 64, No. 4, 1974, pp. 775-816.

[3] Powell, A. "On the Mechanism of Choked Jet Noise." Proceedings of the Physical Society B, Vol. 66, 1953, pp. 1039–1056.

[4] Ho, C.-M., and P. Huerre, "Perturbed free shear layers," Annual Review of Fluid Mechanics Vol. 16, 1984, pp. 365-424.

[5] Samimy, M., Webb, N., Esfahani, A., and Leahy, R., "Perturbation-Based Active Flow Control in Overexpanded to Underexpanded Supersonic Rectangular Twin Jets," Journal of Fluid Mechanics, Vol. 959, A13, March 2023. http://doi:10.1017/jfm.2023.139.

[6] Samimy, M., Katterle, K., Leahy, R., Webb, N., Yarlagadda, A. and Hiler, N. "Active Control of Flow and Near Field Pressure Fluctuations in Heated Supersonic Rectangular Twin Jets," Journal of Fluid Mechanics, Vol. 984, p. A36, April 2024. doi:10.1017/jfm.2024.222

Scholars

Understanding The Bidirectional Reflectance Distribution Function

Student Researcher: Margo Abrams

Advisor: Dr. Nkorni Katte

Wilberforce University
Computer Science

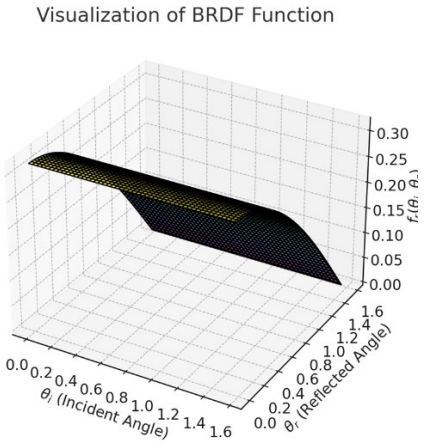
Abstract
The Bidirectional Reflectance Distribution Function (BRDF) is a fundamental concept in radiometry and computer graphics, describing how light is reflected at an opaque surface. This project examines what BRDF is, its significance, its mathematical formulation, how it is calculated, and methods of measurement. Various models for BRDF estimation are discussed, including Lambertian, Phong, and Cook-Torrance approaches. This project also reviews the three most common measurement techniques associated with BRDF to provide further insight into how to calculate it.

Significance
BRDF is required for accurately modeling light interaction with surfaces, which is essential in many fields like optics and illumination engineering, material science and quality control, remote sensing and earth observation, realistic rendering in computer graphics, and defense and stealth technology. BRDF is essential in optics and illumination engineering because controlled reflectance is required when designing optical devices, sensors, and lighting systems. BRDF's value is also recognized in material science due to how it analyzes surface roughness and material properties to help with industrial manufacturing and quality assurance. Thirdly, when it comes to remote sensing and earth observation, BRDF helps interpret satellite imagery by distinguishing between different surface materials based on their reflectance properties. Next, there is realistic rendering in computer graphics. BRDF enhances the realism of images by accurately simulating how light interacts with materials. Finally, regarding defense and stealth technology, BRDF helps radar and optical camouflage by optimizing material reflectance to reduce detectability.

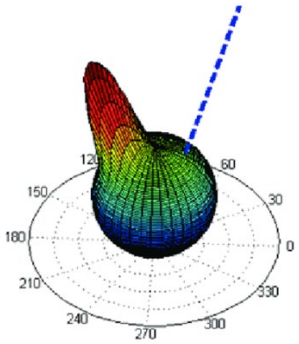
Mathematical Formulation

$$f(\theta_o, \phi_o, \theta_i, \phi_i) = \frac{dL(\theta_o, \phi_o)}{dE(\theta_i, \phi_i)}$$

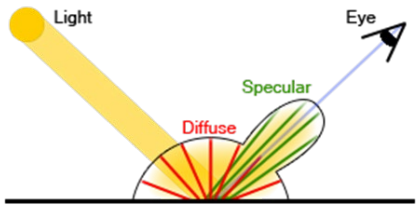
How BRDF is Calculated
To calculate BRDF, you must first define the measurement setup by identifying the light source direction (theta i, phi i) and the observation direction (theta 0, phi 0) and ensure the environment is controlled to minimize unnecessary reflections. Next, you need to measure the incident radiance with a calibrated light source to determine the amount of incoming light per unit area and measure the power distribution over the surface. Thirdly, the reflected radiance must be measured with a sensor or photodetector to capture the amount of light reflected in the specified direction. Also, ensure there is accurate alignment of the detector with the reflection angle. Fourthly, compute the BRDF value by applying the BRDF formula and normalizing the measured values to ensure consistency across different measurement setups. Finally, you need to validate and compare the measured BRDF values with known models like Lambertian, Phong, or Cook-Torrance to verify accuracy.



Lambertian Model



Phong Model



Cook-Torrence Model

Measurement Techniques

Measuring BRDF is challenging due to its reliance on various variables. Some common methods utilized for measurement are gonio reflectometers, because they measure reflectance at different angles using a controlled light source and detector. Another option is image-based techniques that capture BRDF using computer photography and machine learning for efficient approximation. A third option is hemispherical reflectance measurements, which is a technique that utilizes an integrating sphere to capture hemispherical reflectance data.

Conclusion

The Bidirectional Reflectance Distribution Function (BRDF) is a crucial tool in understanding and modeling light reflection across various scientific and industrial fields. By defining how light interacts with opaque surfaces, BRDF allows accurate simulations in computer graphics, remote sensing, and material science. Through its mathematical formulation, measurement techniques, and various models such as Lambertian, Phong, and Cook-Torrance, BRDF provides a structured approach to capturing surface reflectance properties.

References

- Nicodemus, F. E., Richmond, J. C., Hsia, J. J., Ginsberg, I. W., & Limperis, T. (1977). Geometrical considerations and nomenclature for reflectance. *National Bureau of Standards*.
- Cook, R. L., & Torrance, K. E. (1982). A reflectance model for computer graphics. *ACM Transactions on Graphics, 1*(1), 7-24.
- Ward, G. J. (1992). Measuring and modeling anisotropic reflection. *ACM SIGGRAPH Computer Graphics, 26*(2), 265-272.
- Bacour, C., & Bréon, F. M. (2005). Variability of biome optical properties: Implications for remote sensing of the Amazon forest. Remote Sensing of Environment, 98(2-3), 212-228. Retrieved from https://www.theia-land.fr/wp content/uploads/2018/12/Bacour_and_Breon_RSE_2005.pdf
- Surface Optics Corporation. (n.d.). BSDF, BRDF, and BTDF: A review of measurement approaches. Retrieved from https://surfaceoptics.com/bsdf-brdf-and-btdf-a-review-of-measurement-approaches/

Energy And Exergy Analysis of the Strayton Generator Quad Configuration for Performance Optimization

Student Researcher: Chloe Amoroso

Advisor: Maryam Younessi Sinaki

Cleveland State University
Department of Mechanical Engineering

Abstract
Researching combined cycles is essential for advancing turbo/hybrid-electric propulsion systems because they enhance energy efficiency, allowing engines to attain higher performance with less fuel and emissions. Using energy and exergy analyses, the effect of irreversibilities that occur throughout the Brayton portions of the Strayton Generator Quad Configuration are quantified. This analysis models He-Ar gas as the working fluid, incorporating 80% effective coolers and recuperator. It considers turbine and compressor efficiencies ranging from 50% to 95%, turbine inlet temperatures ranging from 1373.15 K to 2073.15 K, and pressure ratios spanning from 1.25 to 2.5. As a result of these variations, the analysis identifies key sources of useful energy loss and provides a systematic thermal evaluation of the system. By inputting specific operating parameters, this evaluation can generate corresponding performance results, making it directly applicable to defined operating conditions.

Nomenclature

	Symbols		
BP	Brayton power	T	temperature (K)
ε	effectiveness of heat exchanger	w	specific work ($\frac{kJ}{kg}$)
h_i	enthalpy at state (*i*) ($\frac{kJ}{kg}$)	X_{dest}	exergy destroyed ($\frac{kJ}{kg}$)
η	efficiency		**Subscripts**
η_{th}	overall thermal efficiency	a	actual
ψ	flow exergy ($\frac{kJ}{kg}$)	c	compressor
P	pressure (MPa)	s	isentropic
q	heat transfer per unit mass ($\frac{kJ}{kg}$)	rev	reversible
r_p	pressure ratio	t	turbine
s	entropy ($\frac{kJ}{kg}$)	net	net

Introduction
To address challenges in energy consumption, emission reduction, and operational efficiency, a novel combined cycle system developed at the NASA Glenn Research Center demonstrates a promising approach that delivers high efficiency in the 1 MW range while also taking advantage of an aircraft's electric system: the Strayton Cycle. The Strayton Cycle merges the Stirling and Brayton cycles in a way that optimizes energy use and enhances overall performance [1]. Due to the cycle's high power specific fuel consumption (PSFC), this cycle represents a transformative approach to turbo and hybrid-electric propulsion, offering a highly efficient, lightweight, zero-emission alternative for modern aviation and aerospace applications [2].

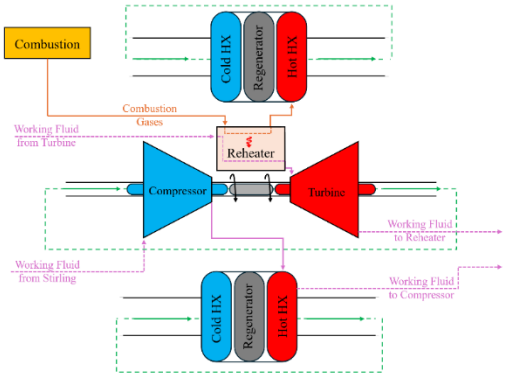


FIGURE 1: SCHEMATIC DEMONSTRATING ONE ITERATION OF THE STRAYTON GENERATOR QUAD CONFIGURATION; TOP LAYER: THERMOACOUSTIC STIRLING ENGINE; MIDDLE LAYER: BRAYTON ENGINE WITH THERMOACOUSTIC STIRLING ENGINE EMBEDDED IN SHAFT; BOTTOM LAYER: THERMOACOUSTIC STIRLING ENGINE

There are three main assemblies that make up each of the four iterations of the Strayton cycle. Firstly, a thermoacoustic Stirling engine is embedded within the shaft of the turbine-compressor of the Brayton engine. In this configuration, the Stirling engine naturally absorbs heat through conduction from the turbine, enabling operation at higher temperatures and improving overall system efficiency [1]. Since the absorbed heat is recycled rather than wasted, this process enhances performance without reducing efficiency. A thermoacoustic Stirling engine is also placed after the compressor, extracting heat from its outlet in preparation for future compressor stages. Finally, waste heat from combustion is recycled and directed to a third Stirling engine. In each of these configurations, the Stirling engine uses the heat it absorbs to generate power using bi-directional turbine generators, maximizing energy recovery and significantly reducing exhaust heat [2]. *Fig. 1* demonstrates the components of a single iteration of the Strayton cycle.

Taking this explanation a step further, the Strayton Generator Quad Configuration incorporates four iterations in series, with a single recuperator enhancing the system's efficiency through inter-stage cooling, reheating, and the formation of a complete acoustic wavelength loop. This quad arrangement is ideal because both the compressor and turbine's efficiencies increase up to four stages (with efficiency gains diminishing for each additional stage) and power output is further maximized by effectively utilizing waste heat from one cycle as energy for the next. This approach significantly increases Stirling power output, enhances internal Brayton recuperation, provides effective turbine cooling, minimizes thermal losses, and boosts overall thermal efficiency [2].

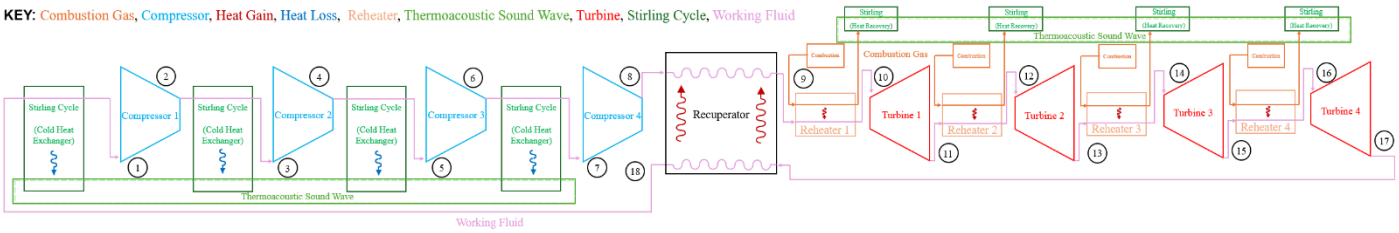


FIGURE 2: SHEMATIC OF THE BRAYTON AND STIRLING COMPONENTS IN THE STRAYTON CYCLE DEMONSTRATING THE FLOW PATH OF THE COMBUSTION GAS AND WORKING FLUID AND HEAT GAINS/LOSSES OF THE WORKING FLUID

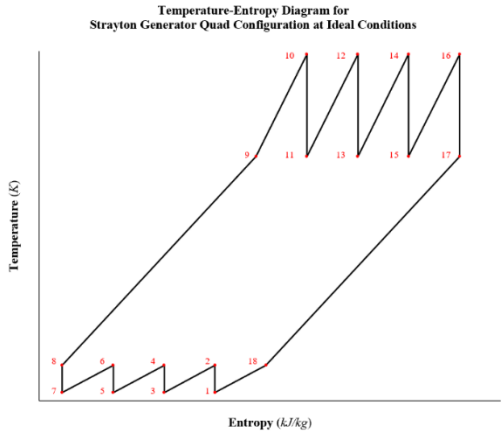


FIGURE 3: TEMPERATURE-ENTROPY DIAGRAM FOR THE QUADLY-ARRANGED BRAYTON CYCLE IN THE STRAYTON CYCLE; ISENTROPIC COMPRESSION/EXPANSION AND IDEAL HEAT EXCHANGERS/RECUPERATOR

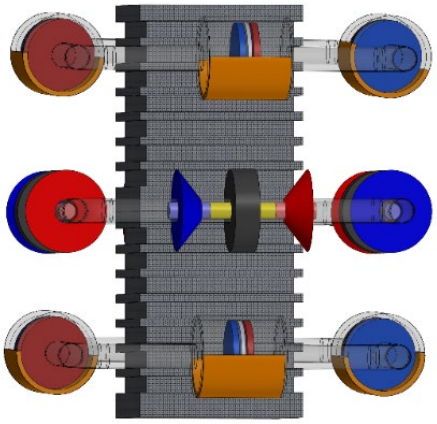


FIGURE 4: STRAYTON GENERATOR QUAD CONFIGURATION MODEL; TOP/BOTTOM: STIRLING ENGINES; MIDDLE: BRAYTON TURBINES AND COMPRESSORS

The Brayton cycle serves as the primary driver of energy production within the Strayton system, generating approximately 80% of the total power output. Its seamless integration into the hybrid system is crucial to optimizing overall efficiency and unlocking the system's full potential. Consequently, analyzing and optimizing the key parameters of the Brayton cycle is pivotal to the successful design of a Strayton engine.

Project Objectives

This paper focuses on the Brayton portion of the Strayton Generator Quad Configuration, contributing to Strayton research by introducing a practical investigation that incorporates realistic operational values and working fluid consideration. Through energy and exergy analyses, the study quantifies irreversibilities within the turbine and compressor components, identifying significant sources of useful energy loss. These insights serve as a foundation for further optimization efforts based on various operating parameters. The analysis evaluates the impact of varying isentropic efficiencies for turbines and compressors on overall thermal efficiency. Additionally, it simulates a range of turbine inlet temperatures (TIT) and pressure ratios (PR) to assess the performance of different turbine and compressor configurations and their influence on system efficiency. Exergy analysis further pinpoints specific regions of the Brayton cycle that experience the highest irreversibilities, allowing engineers to target and optimize these components effectively.

Methods

The analysis of the Strayton cycle's thermodynamic performance is guided by various key elements: Firstly, the National Institute of Standards and Technology's (NIST's) Reference Fluid Thermodynamic and Transport Properties (REFPROP) [3] database is utilized to accurately determine thermodynamic properties of Helium-Argon (the working fluid) including entropy, enthalpy, and flow exergy across various temperature and pressure conditions. A streamlined, idealized analysis of common reference parameters in typical turbine engines establish operating conditions and provides a foundation for assessing the impact of turbine inlet temperatures and pressure ratios on overall efficiency and system behavior. The study then incorporates real-world inefficiencies, accounting for the Striling coolers and recuperator's effectiveness to evaluate how varying turbine inlet temperatures and pressure ratios influence the cycle's thermal performance. Finally, an exergy analysis quantifies irreversibilities, identifying key areas for efficiency improvements.

With states (i) ranging from 1 to 18:

Efficiencies of Turbines and Compressors:

$$\eta_t = \frac{h_{i-1} - h_{ia}}{h_{i-1} - h_{is}}, \quad h_{ia} = h_{i-1} - \eta_t (h_{i-1} - h_{is}) \tag{1}$$

$$\eta_c = \frac{h_{is} - h_{i-1}}{h_{ia} - h_{i-1}}, \quad h_{ia} = \frac{h_{is} - h_{i-1}}{\eta_c} + h_{i-1} \tag{2}$$

Heat Transfer:

$$q_{in} = \Sigma_{reheaters}(h_i - h_{(i-1)a}) \tag{3}$$

The net work *(Eqn. 4)* and thermal efficiency of the system *(Eqn. 5)* are also found as follows:

Work:

$$w_{net} = \Sigma_{turbines}(h_{i-1} - h_{ia}) - \Sigma_{compressors}(h_{ia} - h_{i-1}) \tag{4}$$

Thermal Efficiency:

$$\eta_{th} = \frac{w_{net}}{q_{in}} \tag{5}$$

Compressor Inlet Temperatures:

$$T_c = \varepsilon\left(T_1 - T_{c,out}\right) + T_{c,out} \tag{6}$$

Enthalpy Values at Recuperation:

$$h_9 = h_8 + \varepsilon(h_{17} - h_8) \tag{7}$$

$$h_{18} = -h_9 + h_8 + h_{17} \tag{8}$$

TABLE 1: TURBINE INLET TEMPERATURES REPRESENTATIVE OF VARIOUS TURBINE TYPES

TIT (K)	1373.15	1673.15	1873.15	1973.15	2073.15

Exergy Destroyed:

$$X_{dest} = -(\psi_{out} - \psi_{in}) - \Sigma_{turbines}(h_{i-1} - h_{ia}) + \Sigma_{compressors}(h_{ia} - h_{i-1}) - (\psi_{out} - \psi_{in})$$

Results and Discussion

This section presents the results of the thermodynamic analysis of the Strayton Generator Quad Configuration, focusing on energy and exergy performance under various operational conditions. *Fig. 3* is the temperature-entropy diagram for the idealized case of the Brayton portion of the Strayton Generator Quad Configuration at the reference parameters: turbine inlet temperature of 1500 K, compressor inlet temperature of 300 K, inlet pressure of 0.1 MPa (ambient conditions), and a pressure ratio of 2 [2].

To obtain a base for comparison of more realistic cases, the properties of the working fluid were obtained for the quadly arranged Brayton portion of the Strayton cycle at the same reference points but assuming an 80% effective recuperator and cooling Stirling engines. From this data, the temperature-entropy diagram presented in *Fig. 5* has been made to model the new relationship.

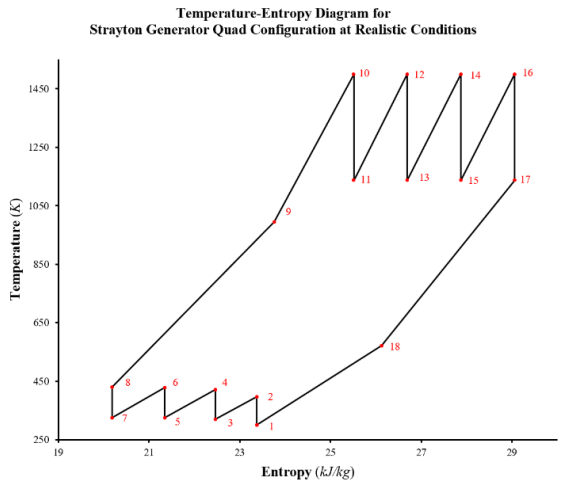


FIGURE 5: TEMPERATURE-ENTROPY DIAGRAM FOR THE QUADLY-ARRANGED BRAYTON CYCLES IN THE STRAYTON CYCLE, ASSUMING AN 80% EFFECTIVE RECUPERATOR AND COOLING STIRLING ENGINES

Combining the ideal and realistic scenario results found, *Fig. 6* exhibits both trends in an effort to underscore the gap between theoretical maximum efficiency and actual operational performance and examine the two scenarios differ most:

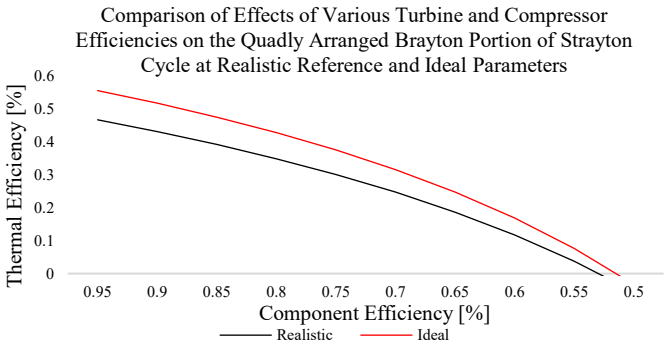


FIGURE 6: IMPACT OF COMPONENT EFFICIENCIES ON THE PERFORMANCE OF THE QUADLY-ARRANGED BRAYTON PORTION OF THE STRAYTON CYCLE UNDER REALISTIC AND IDEAL REFERENCE CONDITIONS

While both trends exhibit a decline in thermal efficiency, the deviation between them widens at lower component efficiencies, emphasizing that inefficiencies in recuperation and cooling become increasingly detrimental as turbine and compressor performance degrades. For instance, at component efficiencies such as 60%, thermal efficiency in the realistic reference is around 11% - a change of 6% compared to the ideal case. Additionally, as component efficiencies improve to 95%, thermal efficiency in the realistic scenario only increases to approximately 47%. *Fig. 7* exhibits the effect of six distinct turbine inlet temperatures on the overall thermal efficiency of the Brayton portion of the Strayton cycle, including the reference.

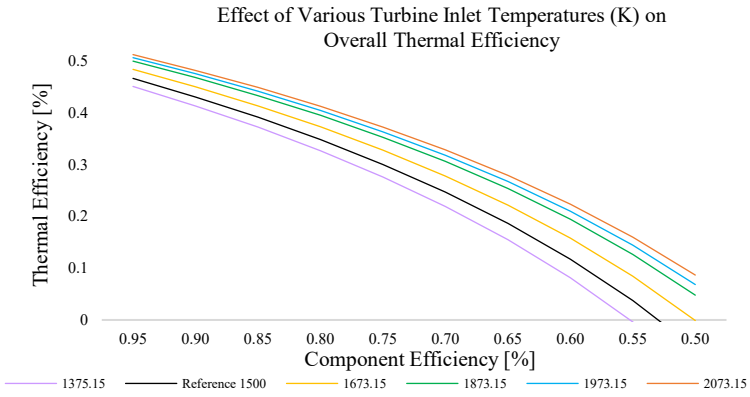


FIGURE 7: PLOT DEPICTING THE IMPACT OF VARIOUS TURBINE TYPES AND TURBINE INLET TEMPERATURES ON THE OVERALL EFFICIENCY OF THE BRAYTON PORTION OF THE STRAYTON CYCLE

As component efficiency decreases, the thermal efficiency across all the systems declines. Higher TIT values correspond to improved thermal efficiency due to greater energy input into the cycle. For example, a TIT of 2073.15 K achieves higher efficiencies than TITs coming in at only 1373.15 K. *Fig. 8* illustrates the effect of various pressure ratios on the overall thermal efficiency of the Brayton portion of the Strayton cycle as component efficiencies decrease.

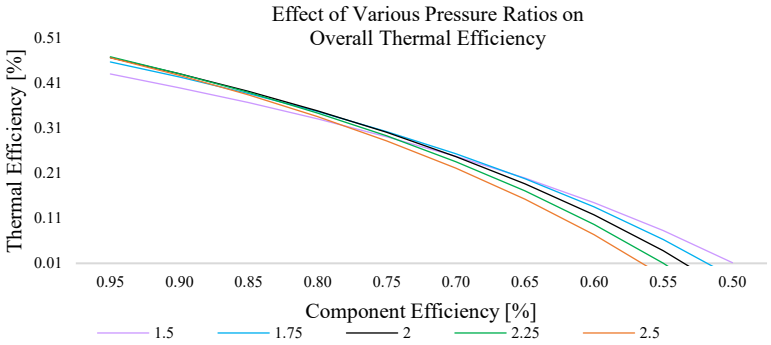


FIGURE 8: PLOT DEPICTING THE IMPACT OF VARIOUS PRESSURE RATIOS ON THE OVERALL EFFICIENCY OF THE BRAYTON PORTION OF THE STRAYTON CYCLE

Higher overall pressure ratios ($r_p = 2, 2.25, 2.5$) result in greater overall thermal efficiency compared to lower pressure ratios ($r_p = 1.5, 1.75$) at equivalent component efficiency levels. This is consistent with thermodynamic principles: higher pressure ratios lead to better cycle performance. However, this is only true up to a certain degree. As seen in the contrasting cases between $r_p = 1.5$ and $r_p = 2.5$, a high pressure ratio initially returns high thermal performance at high component efficiency levels, but reaches a point of diminishing returns once components reach efficiencies around 80%. In contrast, $r_p = 1.5$ might start off with returning a low performance, but when component efficiencies begin to diminish, this pressure ratio is most beneficial.
Investigating the specific trend in values this study provides, between component efficiencies of 0.9 and 0.95, the individual component pressure ratio that achieves the highest thermal efficiency of the Brayton portion of the Strayton cycle is $r_p = 2.25$. This demonstrates how an increase in pressure ratios is not necessarily proportional to higher thermal efficiency but is dependent on other quantified values the engine is operating at.

These results, in conjunction with the variations in TITs, display results that coincide with the claims made about Strayton's high efficiency capabilities. When comparing results with previous work [1, 2], these findings are valuable in that the research not only holds additional data, but quantifies the values of efficiency utilizing realistic scenarios capable of being practiced in real life prototypes. *Fig. 9* illustrates the exergy values at each state within the Brayton portion of the Strayton Generator Quad Configuration evaluated at the realistic reference conditions.

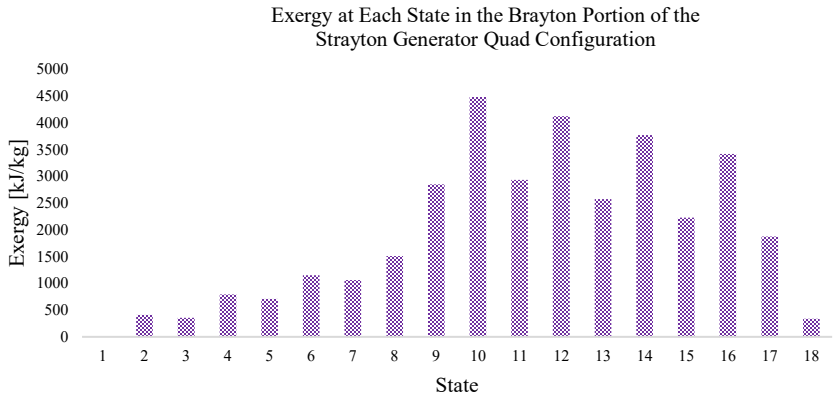


FIGURE 9: EXERGY DISTRIBUTION ACROSS STATES IN THE BRAYTON PORTION OF THE STRAYTON GENERATOR QUAD CONFIGURATION AT REALISTIC REFERENCE CONDITIONS

A sharp increase in exergy is observed at state 10, corresponding to significant energy input through heat addition. Beyond this point, exergy fluctuates due to energy transfers, with most work extraction seen in the turbines and

reheating processes. Eventually, the exergy declines as energy is lost through the final recuperation stage. When compared to *Fig. 5*, the exergy variations closely align with changes in temperature and pressure, highlighting the interconnected processes within the cycle. *Fig. 10* compares the average amount of exergy destroyed through the turbines and compressors operating at 85% efficiency to visually demonstrate the difference between the two components.

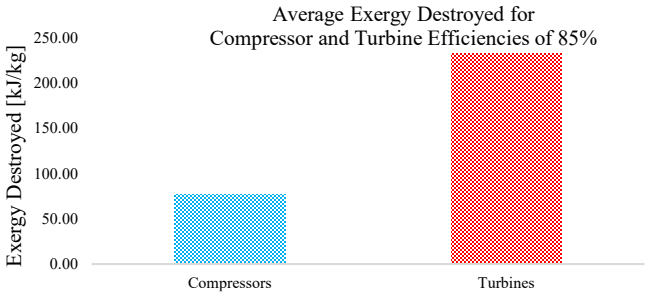


FIGURE 10: COMAPRING AVERGAE AMOUNT OF EXERGY DESTROYED THROUGH TURBINES AND COMPRESSORS

Comparatively analyzing the average amount of exergy destroyed in the compressor and turbine components of the Strayton cycle, the turbine quantifies approximately 75% of the destruction while the compressor approximately 25%. This is due to the turbine operating at higher temperatures than the compressor.

Conclusion

This study provides a comprehensive and scalable framework for analyzing the Brayton portion of the Strayton Generator Quad Configuration, applicable to any range of operational parameters. By integrating energy and exergy analyses, it quantifies thermal efficiency trends and irreversibility sources, offering data-driven insights into the effects of turbine and compressor efficiencies, pressure ratios, and turbine inlet temperatures on overall cycle performance. The results demonstrate that higher component efficiencies significantly enhance thermal efficiency, while lower efficiencies lead to a rapid increase in exergy destruction, underscoring the importance of turbomachinery optimization. Unlike previous studies, this work incorporates realistic operational parameters to produce quantifiable results, bridging the gap between idealized predictions and practical performance expectations. The findings highlight the need for advanced recuperation and cooling strategies to mitigate energy losses and improve system efficiency. Ultimately, this research lays the foundation for optimizing the Strayton cycle as a highly efficient, zero-emission, and lightweight propulsion system, positioning it as a promising low-emission alternative for hybrid-electric aerospace and energy applications.

Acknowledgements

Special thanks to Dr. Roger Dyson and Dr. Luis Rodriguez from NASA Glenn Research Center for their unwavering support and expertise, which were instrumental in navigating the complexities of the Strayton cycle. Their contributions have been pivotal to the success of this research.

References

[1] R. Dyson, “Novel Thermal Energy Conversion Technologies for Advanced Electric Air Vehicles.” Accessed: Feb. 11, 2025. [Online]. Available: https://ntrs.nasa.gov/api/citations/20180005343/downloads/20180005343.pdf

[2] R. W. Dyson, “True Zero Emission Electric Aircraft Propulsion Transport Technology,” Nasa.gov, Jun. 12, 2023. https://ntrs.nasa.gov/citations/20230006407 (accessed Nov. 08, 2024).

[3] E. W. Lemmon, M. L. Huber, and M. O. McLinden, NIST Reference Fluid Thermodynamic and Transport Properties Database (REFPROP), version 10.0, National Institute of Standards and Technology, Standard Reference Data Program, Gaithersburg, MD, 2018. [Online]. Available: https://www.nist.gov/srd/refprop

[4] C. Amoroso and M. Younessi Sinaki, “Energy and exergy analysis of the Strayton Generator Quad Configuration for performance optimization,” in *Proc. ASME Turbo Expo 2025: Turbomachinery Technical Conf. and Exposition (GT2025)*, Memphis, TN, USA, Jun. 2025, Paper No. GT2025-151501.

Exploration of Data Science and Machine Learning Concepts for Wildfire Prediction

Student Researcher: Rachael Ballentine

Advisor: Dr. Michael Raymer

Wright State University
Department of Mechanical and Materials Engineering

Abstract
Wildfires are defined as unplanned and uncontrolled fires that occur in areas with combustible materials. According to the National Interagency Fire Center, there were over 64,000 wildfires across the US in 2024 alone, affecting almost 8 million acres of land [1]. Ignition and spread of these fires depend on a number of factors, including seasonal weather conditions, available fuel, topography, and proximity to populated areas. Prediction and management of wildfires is a complex but critical problem, as the wildfire crisis continues to develop in conjunction with the rise of global temperature and greenhouse emissions. In this project, data science and machine learning techniques will be applied to a prediction problem in this field. A range of methods will be applied to an identified data set, from exploratory data analysis and interpretive techniques to more complex approaches like neural networks.

Project Objectives
The primary goal of this project was to develop a foundational understanding of data science and machine learning concepts by investigation of a practical problem. A previous study that developed a Convolutional Autoencoder model for wildfire spread prediction was examined, with the secondary objective of reconstructing the model and improving its prediction results.

Methods
The first step in this project was a review of relevant literature, primarily to identify an available wildfire dataset. Several previous studies were considered, encompassing a variety of wildfire prediction problems, including severity label prediction, risk level classification, rate of spread estimation, and next-day spread prediction. The study "Next Day Wildfire Spread: A machine learning dataset to predict wildfire spreading from Remote-Sensing Data" by F. Huot, et al. [2] was selected as the starting point for this project. The study provided an open-access dataset on Kaggle.com (referred to as the *Next Day Wildfire Spread* dataset) and included a neural network model with relatively low prediction performance, which made it an appropriate basis for reconstruction and potential improvement.
After identifying an appropriate study, the dataset from Huot et al. was extracted and analyzed. The model source code was investigated to understand the model architecture, and the model was rebuilt to obtain baseline results before hyperparameter tuning to improve performance results.

Results and Discussion
The *Next Day Wildfire Spread* dataset [2] captures historical data for square 64-by-64 kilometer regions across the continental US, broken into 1km by 1km pixels. Each region contained an active fire and was described by 12 environmental features and a single label. The 12 features were minimum and maximum temperature, wind direction and velocity, precipitation, humidity, Palmer Severity Drought Index, Normalized Difference Vegetation Index, elevation, population, Energy Release Component, and previous fire mask, and the label was the next-day fire mask. The fire at time t days was considered the Previous Fire Mask, and the location of the fire spread or retreat at time $t + 1$ days was the predicted next-day Fire Mask label. Both fire mask features were binary, with 0 indicating no fire and 1 indicating fire. An overlay of the Previous Fire Mask and predicted next-day Fire Mask can be seen in Figure 1 in the Figures/Charts

section below. The full dataset contained files for 19 different regions, each containing 4096 data points, and was split into 15 training, 2 testing, and 2 evaluation files.
Data visualization was performed using t-distributed Stochastic Neighbor Embedding (t-SNE) to understand the relationships between the chosen features and their impact on the presence of fire the following day. This method was chosen for its ability to handle complex, non-linear data, and allows high-dimensional data to be visualized by reducing dimensionality to a 3D space. To accomplish this, the t-SNE algorithm first randomly projects all data points onto 3D space. A conditional probability for similarity is calculated between each two data points, then each data point in the 3D space is moved iteratively until the differences between the two spaces are minimized. The conditional probability equation can be seen below in Equation 1 [4].

$$P_{i,j} = \frac{\exp\left(-\frac{|x_i - x_j|^2}{2\sigma_i^2}\right)}{\sum_{k \neq i} \exp\left(-\frac{|x_i - x_k|^2}{2\sigma_i^2}\right)} \quad (1)$$

The 3D representations for one of the 15 dataset files can be seen in Figures 2 and 3 in the Figures/Charts section below. Because of the strong influence the Previous Fire Mask was assumed to have on the Fire Mask prediction results, t-SNE was performed both with and without this feature. The 3D data representations showed clear clusters in the data for both cases. These results meant that the low performance results of the Huot et al. model could be improved with model hyperparameter tuning, as the clustering in the data representations showed that the chosen features were very sufficient for prediction.

In their study, Huot et al. approached wildfire spread prediction as a semantic image segmentation problem. Semantic image segmentation identifies objects in an image and assigns each pixel to a specific class, as seen in the 3-channel RGB images shown in Figure 4. For this study, the input was a 12-channel image composed of the 12 feature variables, and the segmented output was the next-day FireMask with two classes: fire or not fire.

Investigation of the model source code revealed that a Convolutional Autoencoder architecture was used for prediction. Like a Convolutional Neural Network, the Convolutional Autoencoder model processes multi-dimensional matrices as input rather than flattened vectors, which preserves spatial relationships in the data. The model architecture is constructed similarly to an Autoencoder with an encoder and decoder, where the encoder identifies the key defining characteristics of the input and the decoder reconstructs the segmentation map output. For their model, Huot et al. used the Keras TensorFlow deep learning framework to implement a MobileNetV2 architecture for the encoder and Pix2Pix upsampling layers for the decoder. Four skip connections from intermediate MobileNetV2 layers were used to aid in preserving detail in the encoder. Finally, a single convolutional layer with sigmoid activation flattened the decoder output into the binary FireMask segmentation map.

For greater flexibility and ease of customization, this project aimed to rebuild the Huot et al. model in the PyTorch deep learning framework. The reconstructed model was intended to establish a baseline for model prediction performance. However due to time constraints, a complete rebuild of the model was not finished within the scope of this project. In future work, the PyTorch model implementation will be finished and the model hyperparameters will be tuned to improve the performance results from those obtained in Huot, et al [2].

Figures/Charts

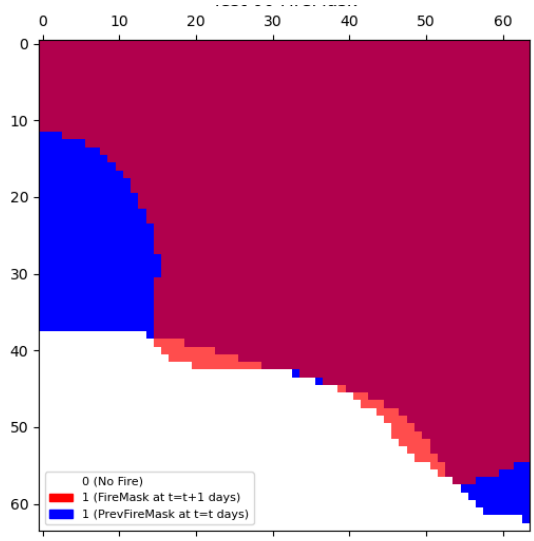


Figure 1: Previous Fire Mask (Blue) at time t days overlaid with Fire Mask (red) at time t+1 days [2].

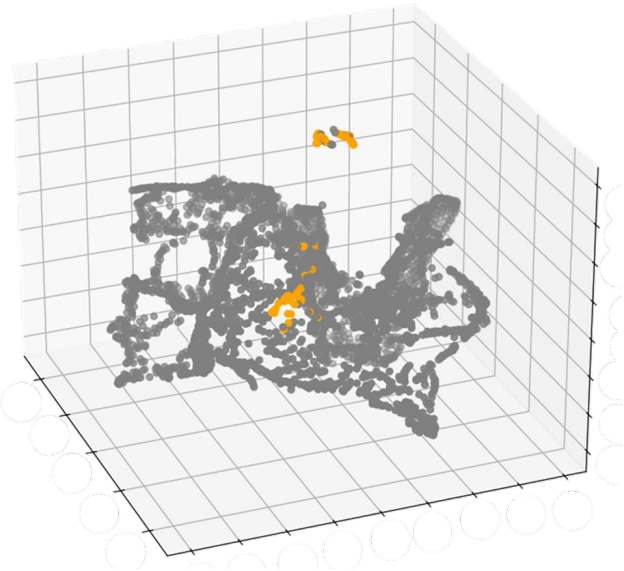


Figure 2: t-SNE representation of Eval 00 file with Previous Fire Mask feature included.

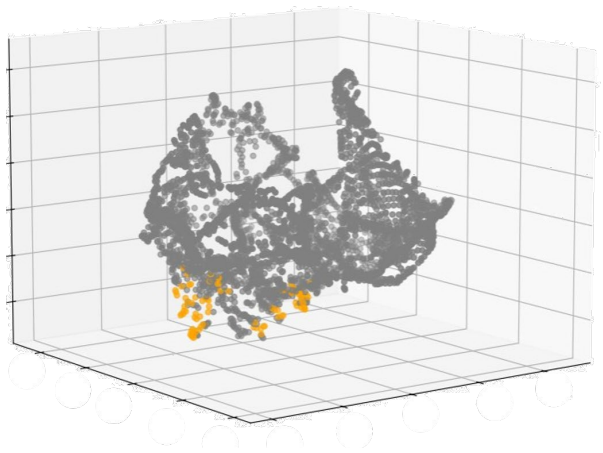


Figure 3: t-SNE representation of Eval 00 file with Previous Fire Mask feature excluded.

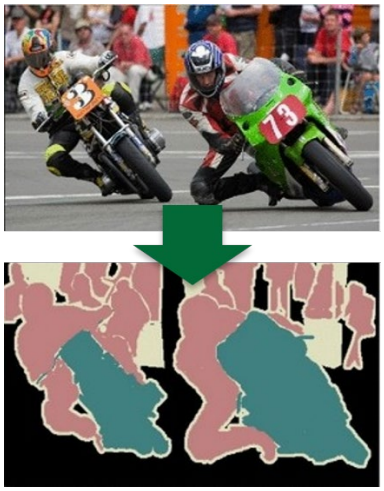


Figure 4: RBG Semantic Image Segmentation example [4]

Acknowledgments
Special thanks to my advisor, Dr. Michael Raymer, for his guidance and support, without which this project would not be possible. I would also like to thank Dr. Mitch Wolff for the opportunity to work with OSGC.

References
[1] "Total Wildland Fires and Acres (1983-2024)," *National Interagency Fire Center*, 2024. https://www.nifc.gov/fire-information/statistics/wildfires

[2] F. Huot, R. L. Hu, N. Goyal, T. Sankar, M. Ihme, and Y.-F. Chen, "Next day Wildfire spread: A machine learning dataset to predict wildfire spreading from Remote-Sensing Data," IEEE Transactions on Geoscience and Remote Sensing, vol. 60, pp. 1–13, Jan. 2022, doi: 10.1109/tgrs.2022.3192974.

[3] L. Van Der Maaten and G. Hinton, "Visualizing Data using t-SNE," *Journal of Machine Learning Research*, vol. 9, no. 86, pp. 2579–2605, Jan. 2008, [Online]. Available: http://isplab.tudelft.nl/sites/default/files/vandermaaten08a.pdf

[4] Y. Guo, Y. Liu, T. Georgiou, and M. S. Lew, "A review of semantic segmentation using deep neural networks," International Journal of Multimedia Information Retrieval, vol. 7, no. 2, pp. 87–93, Nov. 2017, doi: 10.1007/s13735-017-0141-z.

Developing Methods for Testing the Electrical Conductivity of Hydrogel/Conductive Nanoparticle Composites and Subsequent Electrical Stimulation Studies

Student Researcher: Michael Borovich

Advisor: Dr. Liqun Ning

Cleveland State University
Department of Mechanical Engineering

Abstract

Peripheral nerve injuries (PNIs) affect millions and severely impact an individual's quality of life[1]. Nerve guidance conduits (NGCs) have emerged as a promising treatment option for large-gap PNIs. These conduits, often constructed from hydrogels, aim to mimic the native environment of nervous tissue, with electrical conductivity being an important consideration. This work focuses on developing a simple, reliable, cost-effective method for easily measuring the bulk electrical conductivity of hydrogel/conductive nanoparticle composites, specifically relating to gelatin methacrylate (GelMA) with single-walled carbon nanotubes (SWCNTs). An iterative design process was utilized to establish an effective two-point probe protocol. This protocol ultimately consists of sandwiching a sample (of known dimensions) between two flat electrodes, held parallel in an adjustable fixture, which connect to a high resistance ohmmeter. The screen readout of the ohmmeter is recorded, then processed using a custom optical character recognition (OCR) MATLAB script, which generates a resistance versus time plot. This plot is used to find an average resistance value, which in combination with the sample's known dimensions, is used to calculate the material's bulk electrical conductivity. These conductivity values will be used to guide the development of an electrical stimulation (ES) setup for subsequent in vitro ES studies on cell types relevant to PNI regeneration.

Introduction

Peripheral nerve injuries (PNIs) have devastating effects, often resulting in reduced or complete loss of function or sensation in the affected areas[2]. Peripheral nerve gaps exceeding a critical length (>5cm for humans) are unable to heal on their own, requiring medical intervention to reestablish function[1,3]. Current treatment options for large-gap PNIs are limited by donor availability and donor site morbidity, leading to interest in the development of nerve guidance conduits (NGCs)[1,4]. NGCs are fabricated using biomaterials with specific properties designed to help the body bridge larger nerve gaps than would otherwise be possible without intervention. In PNI applications, NGCs should be flexible with high tensile strength, permeability, and electrical conductivity[1]. Electrical conductivity is of particular relevance for PNI treatments due to the nervous system operating based on electrical potential differences[1]. Thus, electrically conductive NGCs would allow for increased regenerative capabilities through exogenous electrical stimulation (ES) or endogenous electrical signaling[5].

Hydrogels, being polymers, typically have very low intrinsic electrical conductivity values. Thus, conductive nanoparticles can be incorporated to create a composite with appropriate electrical conductivity[6]. Existing methods for measuring the electrical conductivity of hydrogels require expensive, highly specialized equipment[7]. The goal of this work is to develop a simple, reliable, cost-effective process for easily measuring the bulk electrical conductivity of hydrogel/conductive nanoparticle composites, specifically focused on gelatin methacrylate (GelMA) with single-walled carbon nanotubes (SWCNTs). These measurements will then be used to inform the development of an electrical stimulation (ES) setup for future in vitro ES studies on relevant cell types involved in peripheral nerve regeneration.

Methods

Due to challenges associated with accurately measuring the electrical resistance of these composites, an iterative design process was utilized to establish an effective measurement technique. Various combinations of electrical equipment, electrode types, sample geometries, and data processing techniques were trialed. The knowledge gained from each iteration was used to inform testing parameters as this process evolved.



Figure 1. Preliminary two-point probe testing setup with electrodes across the sample.

A two-point probe configuration, with pointed electrodes contacting a circular sample across its diameter, was initially tested as a proof of concept to assess the feasibility of acquiring resistance measurements from the composite material (**Fig. 1**). This setup utilized a DC voltage source (Agilent E3649A) and an amp meter (Keithley 2000 Multimeter). The principle used in this test is to run a known voltage across the sample while measuring the current through the sample and applying Ohm's Law ($V = IR$) to calculate resistance. This initial setup exhibited various issues, namely sample damage, electrode corrosion, and inadequate equipment sensitivity, leading to the development of the second design.

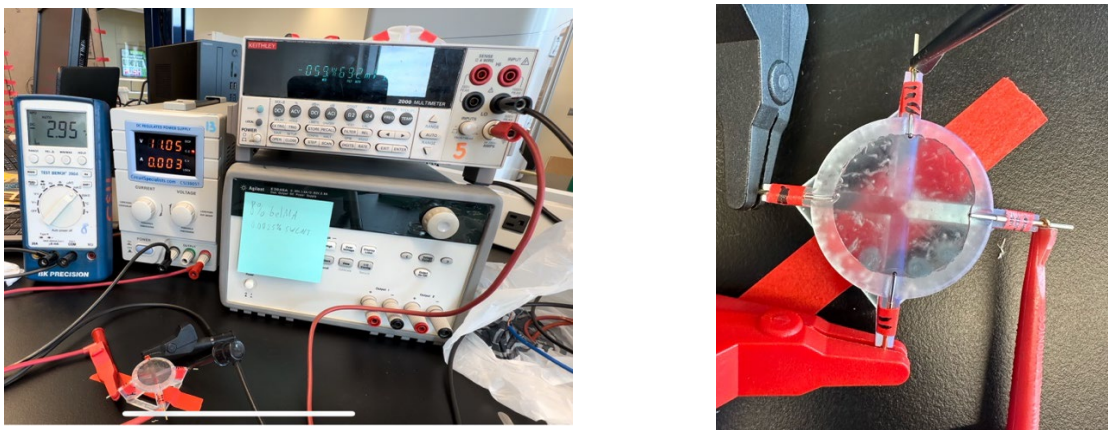


Figure 2. Four-point probe Van der Pauw method setup.

The Van der Pauw four-point probe method was tested in the second configuration to calculate electrical conductivity. In this method, a circular sample was placed on a 3D printed pedestal, with four pointed electrodes evenly spaced out around its circumference (**Fig. 2**). This setup utilized a current source (Circuit Specialists CSI300ST), and two multimeters (B&K Precision 390A & Keithley 2000). In the Van der Pauw method, a known current is applied through two adjacent electrodes and the subsequent electrical potential difference across the remaining electrodes is measured. The composites tested were too resistive for readings to be taken using this method with the available equipment and therefore, conductivity calculations were performed. However, the formulas used with this technique are:

$$R = \frac{V}{I}, \quad R_S = \frac{\pi R}{\ln(2)}, \quad \& \ \sigma = \frac{1}{R_S t}$$

Where measured voltage (V) and applied current (I) are used to calculate a resistance (R). This resistance is used to calculate a sheet resistance (R_S), which in combination with the sample thickness (t) is used to find the bulk electrical conductivity (σ). As previously stated, this setup did not provide any measurements, so a third configuration was developed.

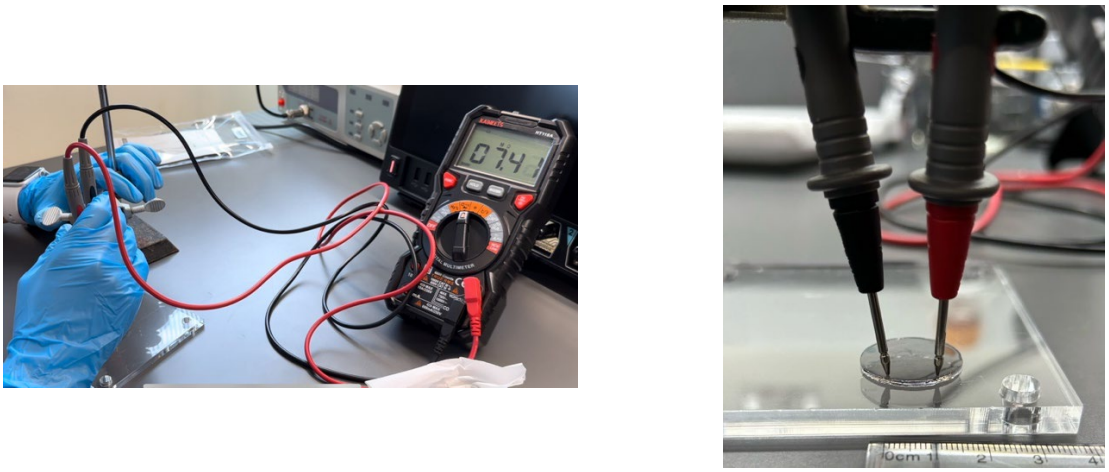


Figure 3. Two-point probe testing setup with electrodes on the face of the sample.

The two-point probe method was reevaluated for the third setup, with this iteration placing the pointed electrodes on the face of the sample rather than along the edge, as in the initial configuration (**Fig. 4**). A high resistance meter (Kaiweets HT118A) was connected and gave a direct electrical resistance readout. This setup produced inconsistent resistance measurements and posed a high risk of sample damage with the pointed electrodes contacting the face of the delicate composites. Due to these limitations, a more refined measurement strategy was needed.

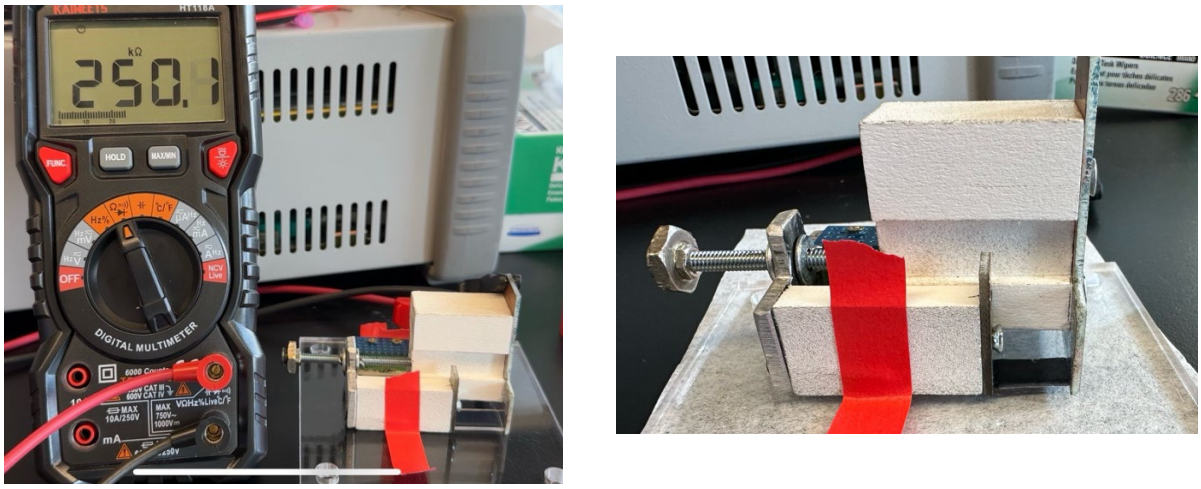


Figure 4. Final two-point probe setup with flat electrodes in a custom adjustable fixture.

Despite the shortcomings of the previous three iterations, they provided invaluable insight into how to approach measuring the electrical conductivity of these composites and were necessary steps in developing an effective method. The final equipment protocol consists of sandwiching a rectangular prism sample between two flat electrodes, held parallel in a custom adjustable fixture (**Fig. 5**). The electrodes are then connected to a high resistance meter (Kaiweets HT118A). The use of flat electrodes circumvents the sample damage issues seen in previous attempts in two major ways. Replacing pointed electrodes with flat electrodes greatly reduces the chances of physically damaging the delicate sample when contacting the surface, along with reducing electrochemical damage by decreasing the current density through the sample.

While this configuration provided more consistent resistance readings, the measured values varied with time, and the available equipment does not have data logging capabilities, as expensive specialized equipment would. Thus, a cost-effective data logging and processing procedure was developed. With the measured electrical resistance changing with time, a camera was set to record the multimeter screen for the duration of a trial. A custom MATLAB code was developed that extracts frames from the video at predetermined intervals and logs the screen readout using optical character recognition (OCR), along with their corresponding timestamps. This resistance and time data is then plotted, revealing an average, steady-state resistance value (**Fig. 6**). This resistance value (R), along with the measured distance between the electrodes (l) and the cross-sectional area of the sample (A) can be used to calculate the bulk electrical conductivity (σ) using the following equation.

$$\sigma = \frac{l}{RA}$$

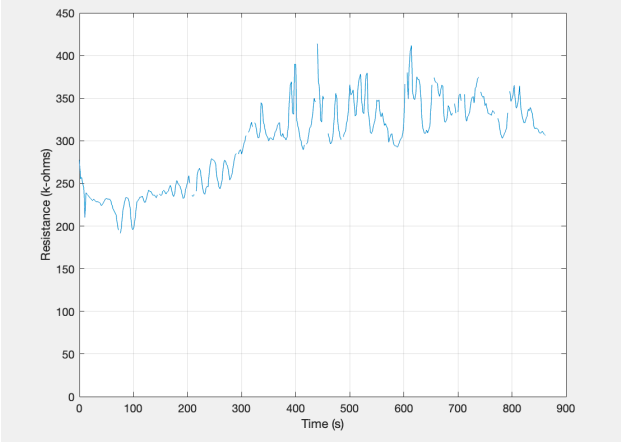


Figure 6. Resistance vs Time plot from OCR MATLAB script.

Results and Discussion

The goal of this research was to develop a simple, reliable, cost-effective method for measuring the electrical conductivity of hydrogel/conductive nanoparticle composites. Through iterative testing, a final measurement protocol was successfully developed using flat electrodes connected to a high resistance meter. A key innovation of this work was the development of a novel MATLAB script that enables data logging using cost effective equipment. This approach significantly lowers the barrier to entry to measuring the electrical conductivity of these composites, allowing these critical measurements to be taken when access to highly specialized equipment is limited.

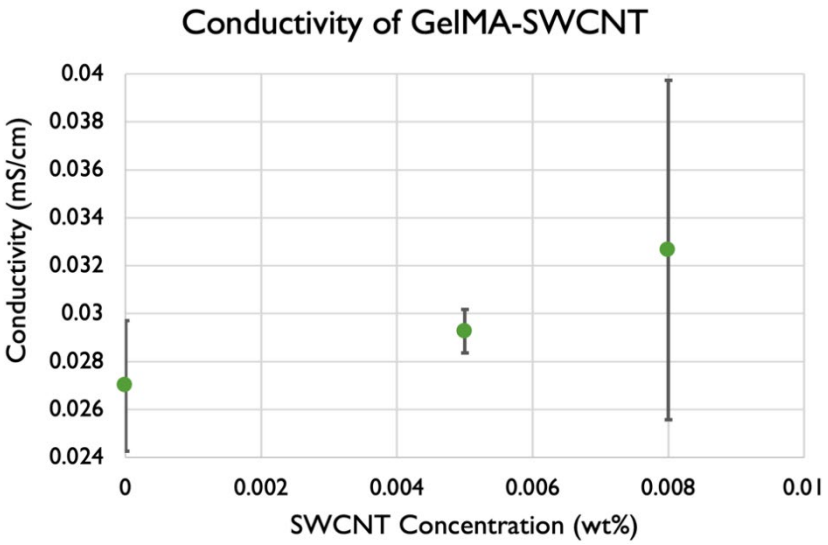


Figure 6. Electrical conductivity vs SWCNT concentration.

Preliminary testing was conducted on GelMA samples with various concentrations of SWCNTs. The results reveal a positive correlation between SWCNT concentration and electrical conductivity of GelMA-SWCNT composites (**Fig. 7**). Large variability was observed in the higher concentration samples, likely due to inconsistent material preparation. In addition, the electrical conductivities observed are lower than ideal for applications in NGCs, necessitating further testing with higher concentrations and improved material preparation techniques.

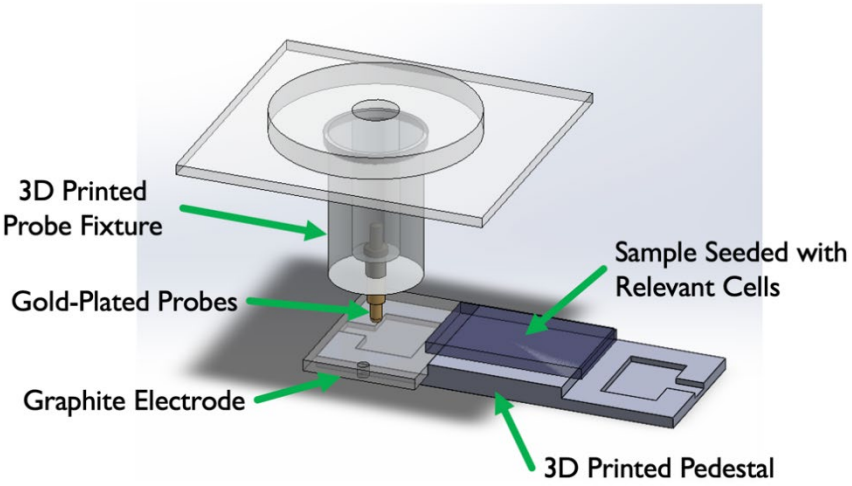


Figure 7. Preliminary electrical simulation design.

In addition to conductivity measurements, preliminary work on an electrical stimulation (ES) setup for in vitro testing with relevant cell types has begun (**Fig. 8**). This system must meet a number of criteria, including being simple and cost effective, able to be sterilized, non-cytotoxic, and allow easy access to samples. The first preliminary design involves a 3D printed pedestal with two graphite electrodes secured to it which sits in a modified petri dish. A sample seeded with cells will be placed to span the gap between the electrodes and an electrical field will be applied across the electrodes by two gold-plated probes contacting them through the petri dish lid.

Acknowledgments

I would like to acknowledge Miroslav Bogdanovski for his contributions to the conductivity test fixture, as well as Dr. Hans Richter, Miroslav Bogdanovski, and Tara Peppard for providing equipment used in this research. I would also like to thank the Ohio Space Grant Consortium for supporting this project through their undergraduate research scholarship.

References

1. Park J, Jeon J, Kim B, et al. Electrically Conductive Hydrogel Nerve Guidance Conduits for Peripheral Nerve Regeneration. *Adv Funct Mater*. 2020;30(39):2003759. doi:10.1002/adfm.202003759

2. Vijayavenkataraman S. Nerve guide conduits for peripheral nerve injury repair: A review on design, materials and fabrication methods. *Acta Biomater*. 2020;106:54-69. doi:10.1016/j.actbio.2020.02.003

3. Zhang M, Yannas IV. Peripheral Nerve Regeneration. In: Yannas IV, ed. *Regenerative Medicine II: Clinical and Preclinical Applications*. Springer; 2005:67-89. doi:10.1007/b100000

4. Zhu W, Ye T, Lee SJ, et al. Enhanced neural stem cell functions in conductive annealed carbon nanofibrous scaffolds with electrical stimulation. *Nanomedicine Nanotechnol Biol Med*. 2018;14(7):2485-2494. doi:10.1016/j.nano.2017.03.018

5. Wang J, Cheng Y, Chen L, et al. *In vitro* and *in vivo* studies of electroactive reduced graphene oxide-modified nanofiber scaffolds for peripheral nerve regeneration. *Acta Biomater*. 2019;84:98-113. doi:10.1016/j.actbio.2018.11.032

6. Ahadian S, Ramón-Azcón J, Estili M, et al. Hybrid hydrogels containing vertically aligned carbon nanotubes with anisotropic electrical conductivity for muscle myofiber fabrication. *Sci Rep*. 2014;4:4271. doi:10.1038/srep04271

7. Kaviani S, Talebi A, Labbaf S, Karimzadeh F. Conductive GelMA/alginate/polypyrrole/graphene hydrogel as a potential scaffold for cardiac tissue engineering; Physiochemical, mechanical, and biological evaluations. *Int J Biol Macromol*. 2024;259:129276. doi:10.1016/j.ijbiomac.2024.129276

Design and Testing of CubeSat Radiator Prototype

Student Researcher: Abigail C. Boyer

Advisor: Dr. Rydge Mulford

University of Dayton
Mechanical Engineering

Abstract
This research, part of the NASA CubeSat Launch Initiative, focuses on designing and testing a CubeSat radiator prototype. CubeSats are cuboidal nanosatellites that are 10 cm in length. They are research satellites, primarily used for collecting weather data. They face rapid temperature fluctuations in space, which can cause damage, and only about 50% complete their missions due to this issue. Current temperature modulation technology is too large for CubeSats, so this research aims to develop an effective system to maintain the CubeSats' radiator's operating temperature.

The design includes fins coated with phase change material (PCM) that actuate outward to disperse heat. PCM is effective at storing thermal energy and helps removes heat when exposed to the environment in space. Nickel-titanium (nitinol) wires, a shape memory alloy, are used to achieve at least 45 degrees of actuation. These wires can be manipulated into desired shapes and revert to their original form when heated. The prototype was tested in a vacuum chamber to simulate space conditions.

Laboratory testing confirmed that the nitinol wire could be manipulated and return to its original shape when heated, and it was strong enough to actuate the fins under excessive heat. The use of PCM and shape memory alloys opens up new possibilities for satellite and spacecraft innovations, enabling complex technology movement without traditional equipment.

Project Objectives
Primarily used for research purposes, a CubeSat is a cuboidal nanosatellite with side dimensions of 10 centimeters. Due to the harsh environment of space, the CubeSat experiences rapid temperature fluctuations, leaving it susceptible to damage. Currently, only 50% of CubeSats are able to complete their mission without fail. The objective of this research is to design an effective system to maintain the operating temperature of the CubeSat radiator.

Methods
Through the use of shape memory alloys, nitinol, we created a fin that would actuate out into space when heated. The fin would be coated with phase change material, allowing for the release of heat and energy, thereby supporting the operation of the CubeSat. Once we were able to confirm actuation, we began testing in a controlled environment. Testing in a vacuum chamber was critical to ensure that our design could withstand the temperature and pressure conditions in space. Through electric and thermocouple feedthroughs, we were able to heat the apparatus in the chamber with polyimide heaters and collect the data with the software Labjack.

Results and Discussion
The nitinol wire proved to be able to be geometrically manipulated and then return to its original configuration following exposure to heat. The best wire configurations were L-shaped wires and nitinol springs that we developed in the lab. As verified through laboratory testing, the nitinol wire can be geometrically manipulated and then returned to its original configuration following exposure to heat. Additionally, the nitinol was strong enough to actuate the fins when excessive heat was applied. To

conclude, the phase change material opens up endless opportunities for innovation within satellites and spacecraft innovations, supporting the actuation and movement of complex technology without the use of bulky, heavy equipment.

PFA-PAEK Polymer Blends: Candidate Material for Improved Friction and Wear at Extreme Temperatures

Student Researcher: Megan Brockway

Advisor: Dr. Sidebottom, Dr. Corti

Miami University
Department of Mechanical and Manufacturing Engineering

Abstract

The primary research aim of this project is to develop a unique blend of melt-processable (i.e. 3D printable, extrudable, injection moldable) polymer blends of perfluoroalkoxy polymer (PFA) and polyaryletherketone (PAEK) to minimize wear and friction of sliding interfaces. PFA is a fluoropolymer that has low friction and a large temperature range (-200° C - 260 °C). PAEK, in the form of polyetheretherketone (PEEK), has high mechanical strength (90-100 MPa) and a large operating temperature range (-70° C - 250 °C) [1]. Another member of the PAEK family, polyetherketoneketone (PEKK), also has promising material characteristics. It exhibits 105 MPa of tensile strength and can operate at up to 150°C [2]. PFA- PAEK blends have the potential to be among the most wear-resistant of any polymer-based system with a lifetime of 10-100x longer than most commercially available composite systems while reducing energy consumed during friction. Additionally, their ease of processing over existing composite systems would make them attractive for aerospace applications.

A series of PFA-PAEK blends using different volumetric percentages to create variety of microstructures (e.g. PAEK matrix with PFA filler and PFA matrix with PAEK filler) were manufactured in partnership with another institution. After processing, the blends will be tested for mechanical, thermal, and frictional properties using tensile loading, differential scanning calorimetry/thermogravimetric analysis, and flat-on-flat wear experiments. These experiments will quantify the performance metrics of the material such as its frictional properties, expected lifetime, strength, and thermal limits.

Project Objectives

1. Process a series of PFA-PAEK blends with varying weight percent combinations
2. Manufacture and test PFA-PEEK samples for tribological properties, wear rate and coefficient of friction.

Methods

The PFA-PAEK samples used in this experiment were manufactured through compression molding. Six total samples were prepared:

1) 41/59 wt.% PFA-PEEK
2) 41/59 wt.% PFA-PAEK
3) 80/20 wt.% PFA-PEEK
4) 80/20 wt.% PFA-PEKK
5) 100% Pure PEEK
6) 100% Pure PEKK

Each sample was compacted into a compression mold assembly and compressed into a ~115 mm sheet of ~10 mm uniform thickness required for the test part samples, instead of using individual sample molds. This process was completed at one of DuPont's research facilities. The molded sheet was returned to the lab, and a final subtractive machining process was completed. The samples were machined down to

roughly 10 x 10 x 20 mm before being polished. The samples were then cleaned in a sonicating alcohol bath to prepare for tribological testing.

Wear rate and coefficient of friction were found through tribological testing completed on a linear reciprocating flat-on-flat tribometer, shown in Figure 1. Testing was completed according to the methods laid out by Schmitz et al. in the 2003 Wear-Rate Uncertainty Analysis [3]. Each sample was individually mounted to a multi-axis load cell used to monitor normal load and friction coefficient. The standard normal load was held constant for this series of tests at 250 N. The PFA-PAEK samples ran against a stainless-steel counter sample mounted to the system's linear ball screw stage driven by a stepper motor. This motor controls the stage's velocity and stroke length for the tests. The standard parameters for the sliding velocity and the stroke length were 50 mm/s and 25mm, respectively. The mixed blends ran for a total of 25 km while the pure PAEK blends ran for 2.5 km. The pure samples' testing was stopped early because previous research indicated the samples had reached steady state and would not experience further variation.

Since the environment can pose effects on the experiment mechanisms, the relative humidity was controlled to 30% RH. MATLAB (MathWorks, Natick MA) performed the system controls and data acquisition for this set of experiments. The wear rate, K, for each test run was calculated according to the general equation shown in Figure 1. V_L is the volume lost during the wear tests, measured as the quotient of the sample mass change during the experiment and the initial sample density, F_n is the average normal force regulated to a set value during the experiment, and d is the total sliding distance.

Results and Discussion

The tribological performance of the PFA-PAEK blends was evaluated based on their wear rate and coefficient of friction, as shown in Figures 2 and 3 and summarized in Table 1. Each test was completed in the same controlled environment, which allows for direct comparison of results between samples. The figures show variation in both wear rate and coefficient of friction in the early transient phase of testing, and stabilized values toward the end of the test. The mixed blends ran for a longer distance (25 km) than the pure blends (2.5 km) because previous research indicated the samples had reached steady state and would not experience further variation. Wear rate was calculated in MATLAB using a Monte Carlo 3-point simulation to reduce uncertainty and increase accuracy of the estimate.

Among all samples tested, 41/59 wt.% PFA-PEEK demonstrated the most ideal material properties. It achieved the lowest wear rate (2.67E-7 mm^3/Nm) and the lowest coefficient of friction (0.18). This is considerably better performing than pure PEEK alone (exhibited a wear rate of 2.0E-6 mm^3/Nm and a coefficient of friction of 0.39).

Although the 20/80 wt.% blends of PFA-PAEK did not perform as strongly as 41/59 wt.% PFA-PAEK blends, they still outperformed the pure PAEK samples. This suggests that each component of the blend was able to improve the material properties of the overall blend. The PFA component likely imparts lubricity and thermal stability to the blend, while the PAEK family component improves the blend's structural integrity and load-bearing capacity.

These results indicate strong reasoning for an interest in PFA-PAEK polymer blends based on their tribological properties for applications requiring low friction rates, extended wear life, and high thermal tolerance. Further research should be completed to evaluate mechanical, thermal, and electrical properties before materials applications can be fully identified. Still, these blends may have widespread applications as lubricants in the aerospace industry based on the results of this study.

Figures/Charts

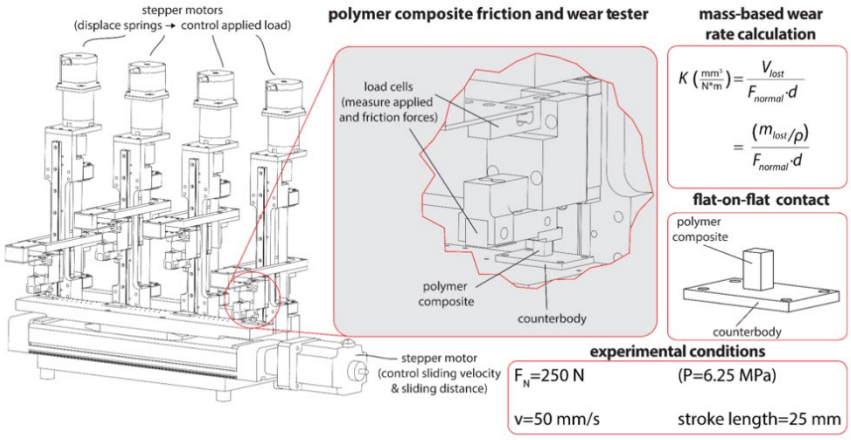


Figure 1: *Schematic of flat-on-flat tribometer and guiding equations*

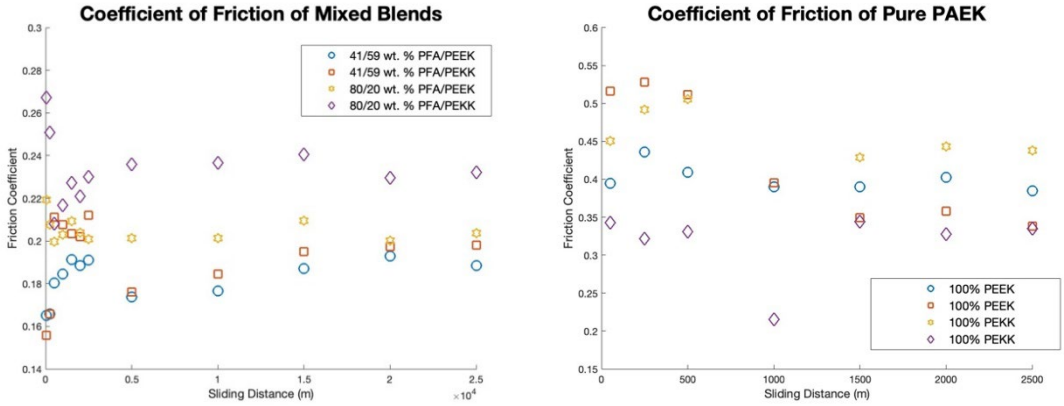


Figure 2: *Coefficient of friction results for PFA-PAEK blends and pure PAEK samples*

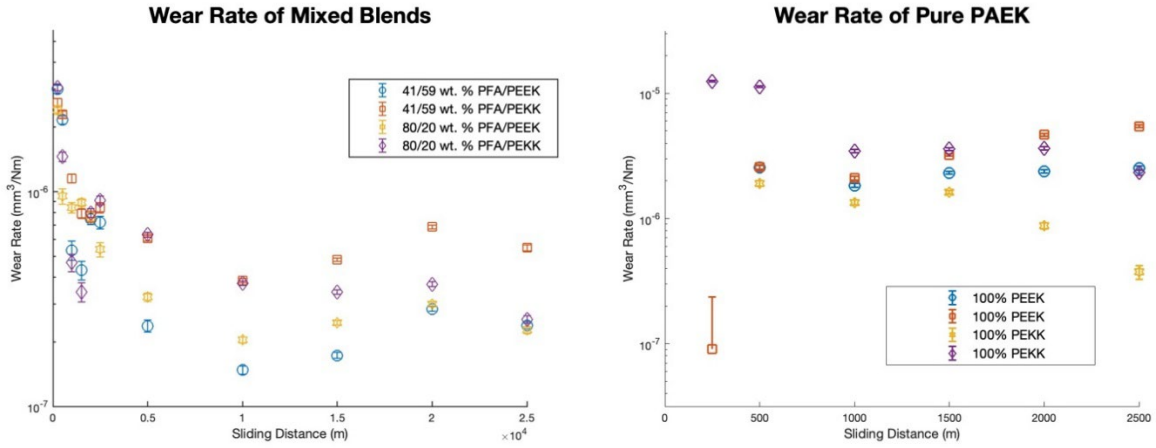


Figure 3: *Wear rate results for PFA-PAEK blends and pure PAEK samples*

Table 1: *Summary of tribological testing results*

	PFA	PEEK	PEKK	Total Sliding Distance	CoF	Wear Rate
	wt.%	wt.%	wt.%	km		mm^3/Nm
1	**41**	**59**		**25**	**0.18**	**2.6E-7**
2	41		59	25	0.19	5.6E-7
3	20	80		25	0.20	3.1E-7
4	20		80	25	0.23	4.3E-7
5		100		2.5	0.39	2.0E-6
6			100	2.5	0.31	2.3E-6

Acknowledgments
The author would like to acknowledge advisers, Dr. Mark Sidebottom and Dr. Giancarlo Corti, for their guidance and support through this process, as well as graduate student Nora Duncan. Additionally, the author would like to acknowledge the processing contribution by Heidi Burch and her team at Dupont and Ohio Space Grant Consortium for the opportunity to share this project.

References
[1] B. Hu et al., "Improved design of fused deposition modeling equipment for 3D printing of high performance PEEK parts," Mechanics of Materials, vol. 137, p. 103139, Oct. 2019, doi: 10.1016/j.mechmat.2019.103139.
[2] K. H. Gardner, B. S. Hsiao, R. R. Matheson, and B. A. Wood, "Structure, crystallization and morphology of poly (aryl ether ketone ketone)," Polymer, vol. 33, no. 12, pp. 2483–2495, Jan. 1992, doi: 10.1016/0032-3861(92)91128-O.
[3] Standard Test Method for Wear Testing with a Pin-on-Disk Apparatus, ASTM G99-17, ASTM International, Washington, D.C., USA, Nov. 14, 2023.

Active Flow Control with Plasma Actuators in Supersonic Rectangular Jets

Student Researcher: Alyssa Brucchieri

Advisor: Mo Samimy

The Ohio State University
Department of Mechanical and Aerospace Engineering

Abstract

Jets and shear layers have been extensively studied due to their broad range of applications, particularly in noise generation. Early research demonstrated that jet shear layers are unstable to perturbations over a range of frequencies, due to the Kelvin-Helmholtz instability. The growth of perturbations leads to the formation of coherent structures (CS). These structures are a primary source of jet noise, as confirmed by experimental studies. The instability in the jet shear layer, which forms between the core jet flow (at the nozzle exit velocity) and the surrounding air, is referred to as the shear layer mode (SLM). The frequency at which the instability is most amplified is tied to the shear layer's momentum thickness and the jet velocity. Another significant frequency, associated with the jet column mode (JCM), corresponds to the passage of CS around the jet's potential core.

While early studies used loudspeakers to excite instabilities in incompressible, low Reynolds number flows, our group has demonstrated the use of Localized Arc Filament Plasma Actuators (LAFPAs) to generate thermal perturbations that control high-speed, high Reynolds number flows. In supersonic jets, interactions between CS and shock cells lead to broadband shock-associated noise (BBSAN). BBSAN travels in all directions, including the upstream direction toward the nozzle. When the BBSAN reaching the nozzle lip and CS generation are phase-matched, a self-sustained feedback loop can produce screech, a high-amplitude tonal noise within the JCM. In rectangular jets, azimuthal modes at the screech frequency organize CS in the top and bottom shear layers, typically forming a single antisymmetric "flapping" mode.

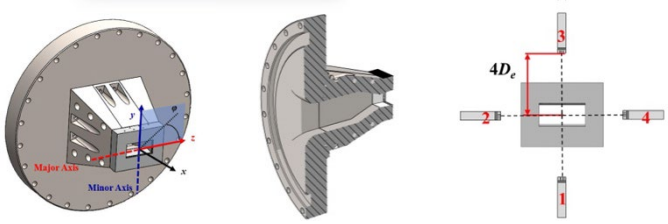
Project Objectives

Utilize LAFPAs to manipulate the development of CS in jet shear layers for control of jet screech and coupling to mitigate NF pressure fluctuations and FF noise. Additionally, the physics of the flow will naturally be explored.

Methods

This work was done at the Gas Dynamics and Turbulence Laboratory (GDTL) at the Ohio State University's Aerospace Research Center. Figure 1 shows the single rectangular supersonic jet (SRSJ) assembly, the coordinate system of the SRSJ (Fig. 1a) and the inner contour of the nozzle (Fig. 1b). The

NPR was varied from 2.77 to 3.67 ($M_j =$ 1.30 to 1.50) using a computer-controlled valve to cover flows from the overexpanded regime to the design Mach number of 1.5. The nozzle aspect ratio of the jet was 2 and the area-based equivalent diameter (De) was 19.25mm.



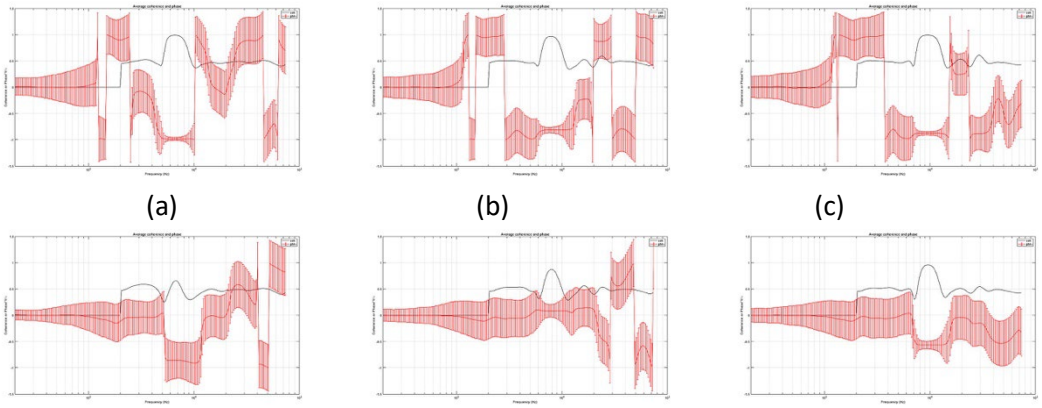
(a) (b) (c)

Figure 1: SRSJ assembly (a), nozzle inner contour (b), and NF array (c)

The 6 LAFPA's are located just upstream of the nozzle exit in boron nitride, with three on the bottom and three on the top. Each actuator channel is individually computer-controlled, granting a large variety of excitation conditions (a range of frequencies and phase delays between actuators). To imitate the natural flapping mode of the jet, all three actuators on each nozzle lip were fired simultaneously and 180° out of phase with those on the opposing lip. The other mode used in this study was the natural symmetric mode, where all six actuators were fired simultaneously. The flow and acoustic field were investigated using an NF microphone array (Figs. 1c), and the flow visualization results were collected using a planar-laser sheet imaging method. More details can be found in Hiler et. al (2025).

Results and Discussion

The Morlet wavelet coherence and phase were calculated between each microphone to assess the azimuthal mode of the jet (Fig. 2). The phase between microphones 1 and 3 across all Mj shows the natural flapping mode, confirming its natural flapping mode with what has been seen in literature (Fig. 2a-c). Between adjacent microphones moving into the overexpanded regime (Fig. 2d-f), there is an increase in coherence. This is could potentially be due to the stronger shockwaves/feedback signals or a more complicated azimuthal mode.

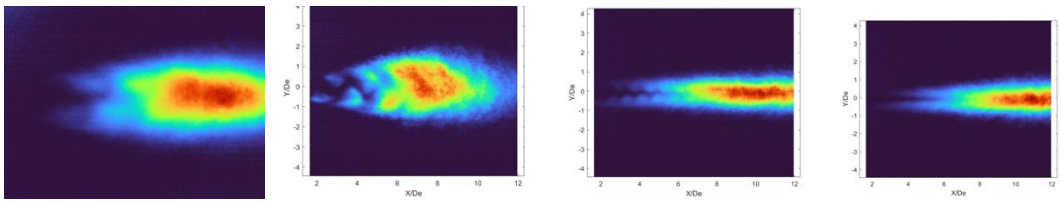


(a) (b) (c)

(d) (e) (f)

Figure 2: Baseline wavelet and coherence between microphones 1 and 3 at Mj=1.3 (a), Mj=1.4 (b), Mj=1.5 (c) and microphones 2 and 3 at Mj=1.3 (d), Mj=1.4 (e), Mj=1.5 (f)

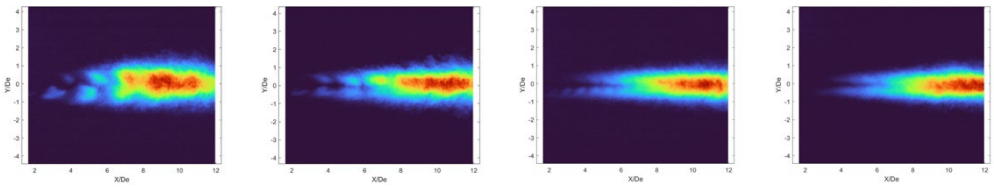
The visualization results shown are phase-averaged images generated by phase locking to either the natural screech for baseline or the LAFPA trigger for excited (Figs. 3-4). The baseline case demonstrates the alternating structures of the jet, further confirming the natural flapping mode (Fig. 3a). Exciting with the flapping mode at the natural frequency, the structures become better defined and more organized, and the flapping mode is maintained (Fig. 3b). At Ste=1.00 the structures decrease in size, the jet width decreases, and the potential core lengthens, while still demonstrating flapping mode (Fig. 3c). This trend continues at Ste=2.00 (Fig. 3d).



(a) (b) (c) (d)

Figure 3: Baseline visualization results at Mj=1.40 (a), excited flapping mode at Ste=Sts=0.38 (b), Ste=1.00 (c), and Ste=2.00 (d)

When exiting symmetric at the screech frequency, the structures are again more well-defined, and the structures do not seem to be completely out of phase or in phase (Fig. 4a). However, at Ste=0.5, the organization of the structures has now changed, appearing to be symmetric (Fig. 4b). As with the flapping excitation, the structures begin to decrease in size. This trend continues as Ste increases (Fig. 4c-d). These results show that the use of LAFPA's can change the azimuthal mode of the jet.



(a) (b) (c) (d)

Figure 4: Visualization results for excited symmetric mode at Ste=Sts=0.38 (a), Ste=0.5 (b), Ste=1.00 (c), and Ste=2.00 (d)

Acknowledgments

This work was sponsored by the Office of Naval Research (Dr. Steve Martens). The 24-25 Undergraduate STEM Scholarship provided by OSGC is greatly appreciated. Additionally, this work would not be possible without the dedication of Noah Hiler, Abhi Yarlagadda, Karli Katterle, and Nathan Webb.

References

Hiler, N., Yarlagadda, A., Katterle, K., Webb, N. J., & Samimy, M. (2025). Active control of coherent structures in an overexpanded supersonic rectangular jet. *AIAA SCITECH 2025 Forum*. https://doi.org/10.2514/6.2025-1615

Samimy, M., Webb, N., Esfahani, A., and Leahy, R., "Perturbation-Based Active Flow Control in Overexpanded to Underexpanded Supersonic Rectangular Twin Jets," Journal of Fluid Mechanics, Vol. 959, A13, March 2023. http://doi:10.1017/jfm.2023.139.

Samimy, M., Katterle, K., Leahy, R., Webb, N., Yarlagadda, A. and Hiler, N. "Active Control of Flow and Near Field Pressure Fluctuations in Heated Supersonic Rectangular Twin Jets," Journal of Fluid Mechanics, Vol. 984, p. A36, April 2024. doi:10.1017/jfm.2024.222

Development of a Device to Track Strength and Mobility Degradation of the Human Hand in Zero Gravity Environments

Student Researcher: Caleb Carlson

Advisor: Dr. Hui Shen

Ohio Northern University
Dr.Carl D Cay and H. Jane Clay Department of Mechanical Engineering

Abstract
It is known from past research that zero gravity environments, such as those that astronauts aboard the International Space Station are subject to, exhibit drastically different conditions on the human body than that of Earth's environment. In near-zero gravity environments, much of the loading that is normally due to the force of gravity is removed from the body. Force only needs to be exhibited to set objects in motion and the body does not need to counteract the constant pull of gravity. This leads to astronauts using most muscle groups less often or at less rigor than they would on Earth. Prolonged periods of no or little usage causes muscles to degrade and atrophy while strength depletes, similar to that of coma patients. Notably, ISS astronaut Scott Kelly described the difficulty readjusting to life on Earth after an almost year residency in the space station telling interviewers about the soreness and fatigue he felt after getting back and experiencing Earth's gravity again [1].

As future long-term space missions are being prepared to send humans to such places as Mars, knowing how the human body reacts to zero gravity and developing medical devices to provide care and support to astronauts is essential to the success of these missions. This project sought to research and develop a method of tracking hand strength and mobility as it changes over time in order to monitor the well-being of astronauts and ensure that the function of one of the most important parts of the human body (the hand) remains fully functional in areas where medical help is unavailable.

Objectives
In medical practice, goniometers and hand dynamometers are used to track and evaluate grip strength and mobility of the hand. These devices, especially goniometers, require training and can be impossible to use individually without the assistance of a technician. This project seeks to develop a device that will track hand mobility/range of motion and measure strength that can also be used by one person with no prior training. To guide development it is also to be noted that size, weight, and ease of disposal were evaluation metrics that determined component choices. Payload is limited when sending missions to space so smaller size and lighter weight in the device was optimal.

Methods
Initially, it was proposed to use an IMU (Inertial Measurement Unit) to tract the position of joints on the finger in all six degrees of freedom for three-dimensional space. Lines could be interpolated between joints to calculate the angles between bones in the fingers in order to perform the function of a goniometer without the need for specialized training and an extra set of hands. The problem with this sensor choice is that the IMU's were too large to be assumed as point masses and would require the user to be trained to recalibrate the system to fit to their unique hand. In this way there would not be a method which the device could be manufactured to fit universally, where the user could unpackage it and use it without calibration.

The interest of this design was the degradation of mobility over time, not necessarily the exact angle of each portion of the finger. For this reason, as well as calibration, flexible sensors (long strain gauges) were experimented with to evaluate mobility. They were anchored to a cotton glove using rubber cement and would change resistance to provide and analog single depending on the degree of deflection of the finger (see Figure 1). Bench testing of the sensor while mounted to the glove was used to separate mobility into three sections depending on the degree of deflection of the finger, these areas being: poor, fair, and good. Values for the ranges were arbitrarily set based off of analog signal value and visual degree of deflection. Further research comparing deflections with goniometer readings could create finer divisions with more robust categorial outputs.

To track pinch strength, a variable resistance force sensor was used on the thumb. This changed resistance based upon the amount of force exerted on a sufficiently small contact area from 0-20 pounds force. The user of the glove is instructed to pinch each finger against their thumb and a readout is displayed in pounds force on an LCD display.

All sensors communicated with an Arduino Uno to interpret readings and output data through an LCD. The glove was tethered to the analog input ports of the board using long leads.

Results

Mobility range was able to be tracked well using the resistance change from the flexible sensors. Divisions were written to the LCD display to tell the user whether their mobility was good, fair, or poor. The pinch strength portion of the programming did not work well. The sensor would respond to force changes but would constantly lose calibration every time the Arduino was bumped or experienced vibrations. Future work would need to address the quality of equipment used as this sensory defect would need to be addressed so that robust force outputs could be displayed to the user. Better anchoring methods would need to be developed as well. Adhering the sensors to the glove with rubber cement worked well for experimentation and development because it had a strong bond that could easily be broken to salvage and move sensors. Rubber cement is latex based which is an allergen issue for potential users. Straps were attempted to be made but ended up being extremely similar to cable ties in design, so cable ties were experimented with as sensor anchors. These did not allow for the sensor to return to match the contour of the finger after it was retracted from grip. Further development would likely incorporate a strain sensor that would need to be custom made to contain Velcro anchoring.

Figures



Figure 1: Glove with strain gauge attached.

Acknowledgements

- OSGC/NASA
- Dr. Shen –advising
- Dr. David Sawyers Jr. –managing OSGC opportunities at ONU
- Dr. Lawrence “Larry” Funke for help with sensors
- Bryan Carlson, Terri Fleming, and Alex Larese

References

[1] On Demand News, USA. *Astronaut Scott Kelly speaks about the pains of coming back to Earth. (Mar. 5, 2016).* Accessed: Sept. 12, 2024. [Online Video]. Available: https://www.youtube.com/watch?v=R5n2OaICM7g

Fatigue Behavior of a Compliant 3D printed Titanium Cervical Implant

Student Researcher: Andreas Chaffey

Advisor: Dr. Timothy Norman

Cedarville University
School of Engineering and Computer Science/Mechanical Engineering

Abstract
This research is an extension of a senior design team at Cedarville University in 2022-2023. That team developed a 3D-printed titanium cervical implant. This implant (Figure 1) was designed as a compliant mechanism to retain a degree of mobility in the neck as this implant would be repeatedly loaded and unloaded in the spine. The original team performed brief tests to verify many different properties of the implant, such as fatigue, torsion, and flexure. However, their fatigue data did not show any significant weakening of the structure at the predicted failure point. I was tasked with continuing these fatigue tests to verify their work. After performing some fatigue testing I noticed the same lack of reduction in stiffness. After consulting with my advisor, I decided to verify the yield point of the structure which had been predicted by the earlier team using an FEA model and some published data for additively manufactured Grade-23 Titanium. I performed progressively increased load compression tests to find a reduction in stiffness indicating a failure in the structure. However, my results showed an increase in the stiffness of the structure as the load increased and did not show any signs of failure at the predicted yield point. I attributed this odd behavior to the compliant structure itself which with load the geometry could be changing leading to an increase in stiffness. This would ultimately affect the S-N curve and the fatigue life I had been trying to verify as for each stress value, there would be a different stiffness. Basing our model on a strain life curve, I created a new S-N which should more properly show how the implant will act under fatigue. I believe this research helps shed some light on the behavior of compliant mechanisms under compression, especially as 3D printing makes these types of structures more affordable to manufacture.

Project Objectives
The primary objective of this project was to understand and characterize the fatigue life of a compliant cervical implant design.

Methods
Initially, I performed the fatigue testing. For this, I would choose a desired stress point on the predicted S-N plot (Figure 3). Then I would test the sample on an MTS servo-hydraulic machine with an R = 10 and a frequency of 3 Hz and pause at intervals (4-5 intervals per test) and take stiffness measurements. I would then end the test at the expected failure cycle and take a final stiffness measurement.

For the second portion of the research, I used a MARK-10 ESM303 to perform compression tests on the samples. I would load a sample to a predetermined load, starting at 200 N, and increasing by 100 N for each following test, then unload. I would then take the linear regression of the elastic portion to find a stiffness value. I then found the percent change in stiffness per 100 N of load. I then returned to a lower load value of 600N to check strain for strain hardening.

Results and Discussion

Table 1 shows that there is a distinct increase in stiffness as the maximum load is increased. However, the increase began to plateau around 700 N of load. The load-displacement curve is shown in Figure 4, where the deviation from the expected curve is obvious. It is also noteworthy that when I returned to a lower load value, the stiffness of the part was the same as the first time I loaded it. This would rule out strain hardening of the sample. Figure 5 shows a strain-life curve, which shows the effect of plastic deformation on fatigue life on a part. While the part is not plastically deforming or strain hardening, it exhibits similar traits as we increase the load, at least until we reach the point where it appears to settle again. Using this knowledge I created a hypothetical proposed S-N curve shown in Figure 6. This plot shows a transition region where the stiffness is actively increasing with load before it eventually settles at a new stiffness. This would explain why we were not experiencing failure at the point we were expecting it to be. I hope this research will help shed some light on the behavior of 3D-printed titanium compliant mechanisms under compression, especially as compliant mechanisms become more popular with the rise of 3D printing.

Figures/Charts

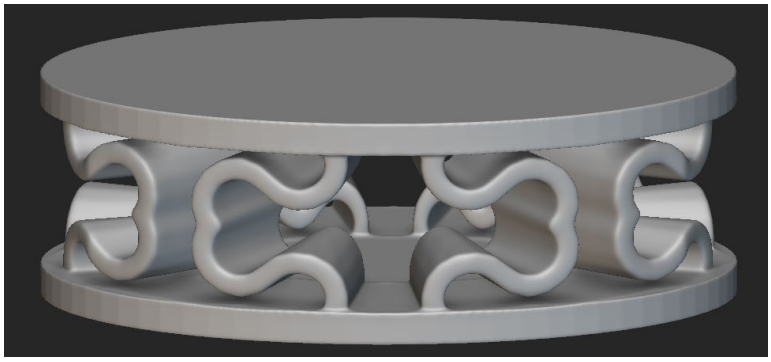


Figure 1. Cervical Implant Design



Figure 2. Cervical Implant specimen with holes for torsion tests

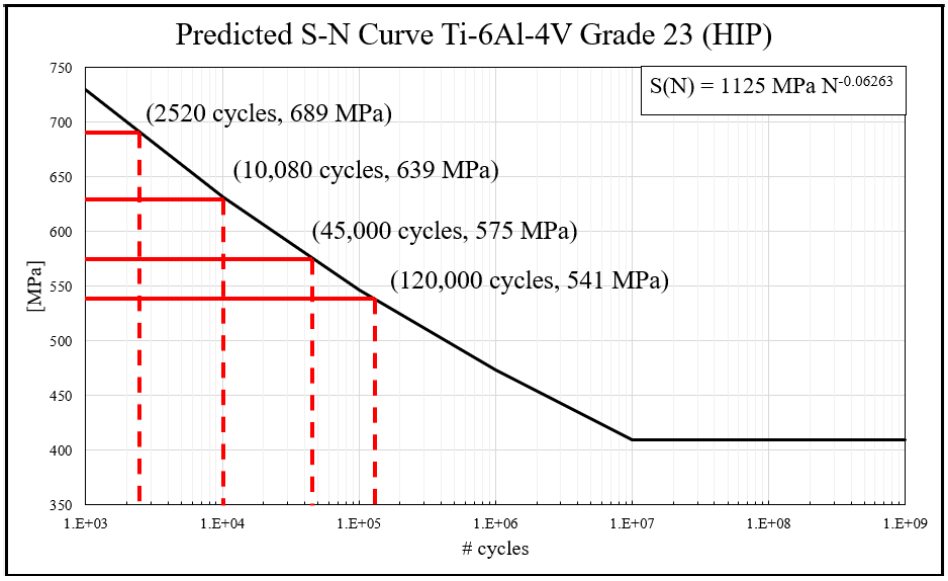


Figure 1. Predicted S-N curve from previous senior design team

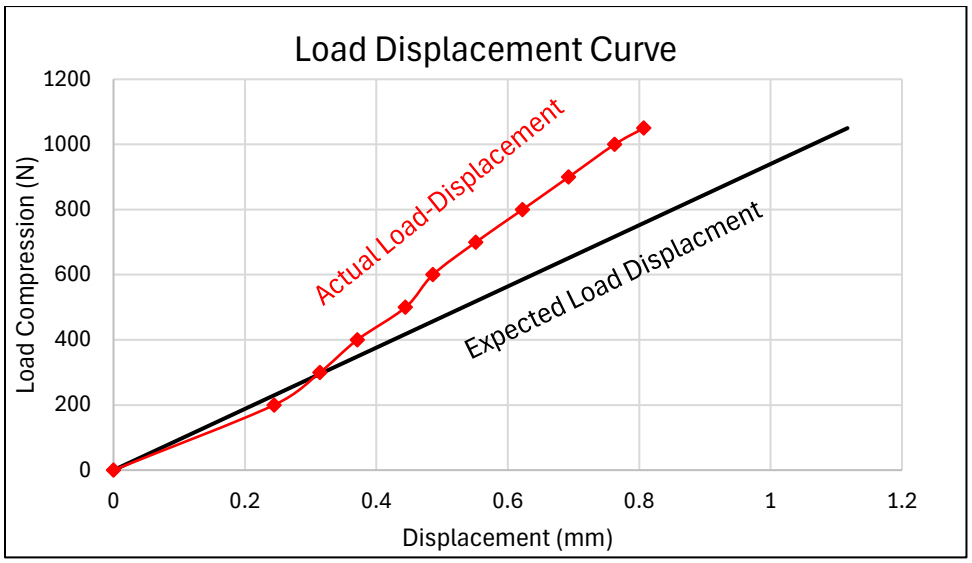


Figure 2. Load Displacement Values for the cervical implant under compression

Table 1. Data from compression tests

Load [N]	Stiffness [N/mm]	Δ% in stiffness per 100N
200	**818**	
300	**955**	**16.7**
400	**1078**	**12.9**
500	**1125**	**4.4**
600	**1234**	**9.7**
700	**1269**	**2.9**
800	**1285**	**1.2**
900	**1299**	**1.1**
1000	**1311**	**0.9**
1100	**1322**	**0.8**

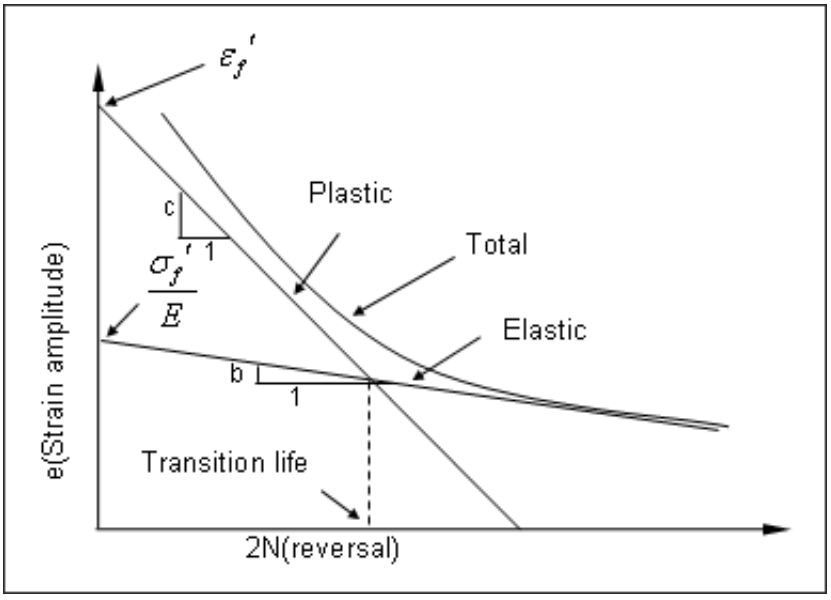


Figure 3. Strain-Life plot

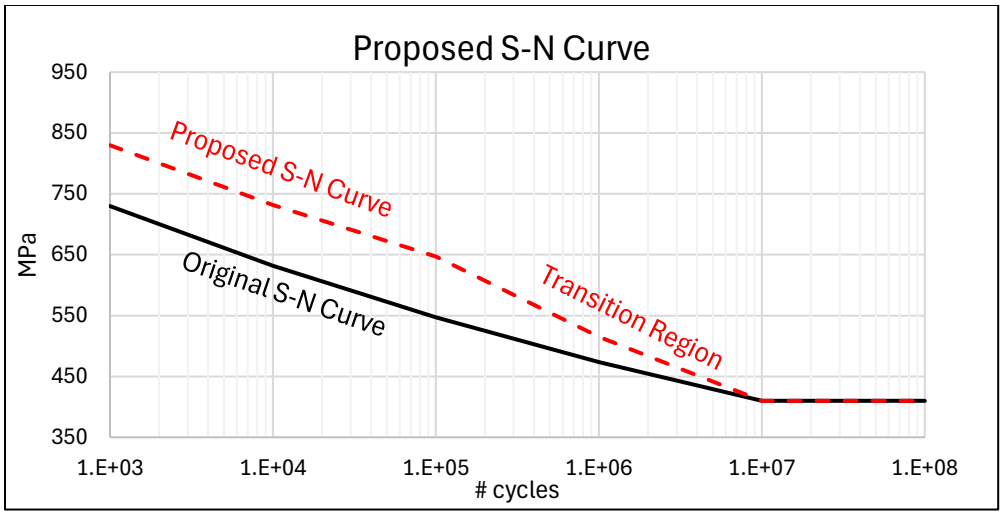


Figure 4. Proposed S-N curve with original curve underneath

Acknowledgments

I would like to thank the 2022-2023 3D Printed Spinal Disc Replacement Team as my research would've been impossible without them as well as my advisor, Dr. Timothy Norman, who has been amazing and helped guide me on much of my work. I would also like to thank Dr. Robert Chasnov, for helping facilitate this opportunity, and of course, the OSGC for funding and giving me this opportunity.

References

"3D Printed Spinal Disc Replacement" by N. Aust, B. Hulbert, J. Beckmann, A. Hunziker, S. Waayenberg, 2023, Cedarville University.

Strain-life (EN) Approach. (2025). Altair.com. https://doi.org/reference_nfg_x1y_z4b

Nanocomposite Fabric Lactate Sensor

Student Researcher: Lisa Chambers

Advisor: Dr. Chelsea Monty-Bromer

Cleveland State University
Chemical Engineering

Abstract

This work focuses on the development of a wearable fabric sensor using novel nanocomposite materials. Currently, there is no established method for noninvasive and continuous monitoring of lactate levels during exercise. This sensor will facilitate the gathering and analysis of sweat biomarkers, specifically lactate, furnishing insights into human health and performance monitoring. Lactate was selected as the analyte of interest to measure the muscular exertion of the participant, and the material to be developed will provide real-time health assessment and performance optimization. Excess lactate can cause cramping, fatigue, and diminished performance in athletes during anaerobic glucose metabolism in exercise. The nanocomposite sensors are to be validated thoroughly via an IRB-approved on-body lab testing, which will provide feedback to the design to be used for further development.

Project Objectives

The nanocomposite sensors are to be validated thoroughly via an IRB-approved on-body lab testing, which will provide feedback to the design to be used for further development. Participants will cycle for 60 minutes and sweat samples will be collected with sterile gauze adhered to the skin using Tegaderm. We aim to test 30 subjects for validation of the wearable fabric sensor. After testing, the gauze is centrifuged and analyzed for the lactate concentration using the gold standard laboratory technique, HPLC.

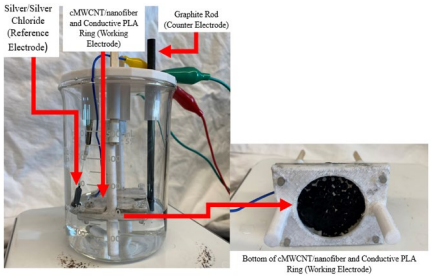
Methods

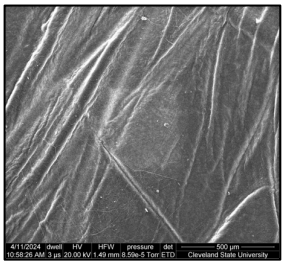
Electrospinning is a process that involves applying a high voltage to a polymer to create nanofiber fabrics. For this sensor, nylon is the polymer that provides a base. The fabric is then cut into sensors and treated via vacuum filtration with an aqueous dispersion of carboxylic acid functionalized multi-walled carbon nanotubes (MWCNTs). These lactate sensing materials were characterized via SEM to determine the morphology of the nanocomposite sensor material. MWCNTs are used because they provide binding sites for the enzyme, lactate oxidase. The active layer of the sensor is synthesized by electropolymerization using lactate oxidase, phosphate buffer solution (PBS), pyrrole, and a second aqueous dispersion of carboxylic acid functionalized MWCNTs. Lactate oxidase and pyrrole both catalyze the reaction of lactate oxidizing. This is important because the binding of lactate, when detected from sweat, will create a conformational change in the lactate oxidase enzyme. This enzymatic reaction will affect the electrochemical response and can be measured to calculate the concentration of lactate. Electrochemical properties were evaluated through cyclic voltammetry (CV) of the sensor's response to synthetic sweat solutions containing lactate. Concentrations in sweat typically range from 10 mM to 70 mM lactate, so this range was used to create a calibration curve. These solutions additionally contain common components found in sweat such as glucose, potassium, calcium, and sodium to simulate realistic results. CV shows the intermediates of the oxidation and reduction reactions of lactate as it reacts with the pyrrole and lactate oxidase.

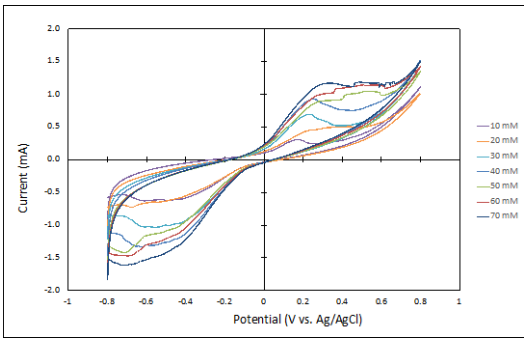
Results and Discussion

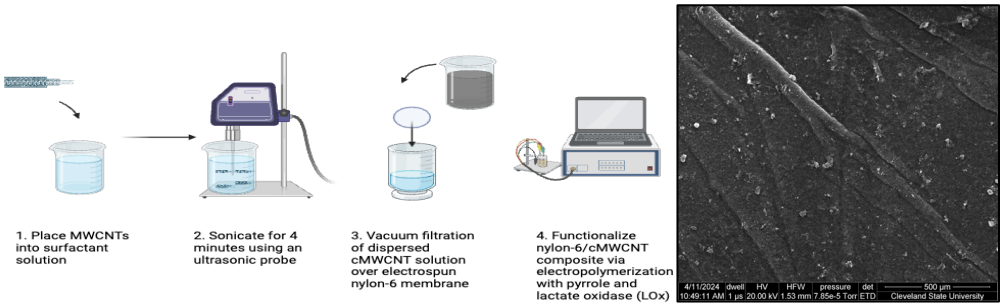
Experimental data has shown that the concentration of lactate in lab-made synthetic sweat solutions directly affects the electrochemical response current at a constant potential. To verify the accuracy of this method for determining concentration, high power liquid chromatography (HPLC) is also used to measure the concentration of lactate in each sample.

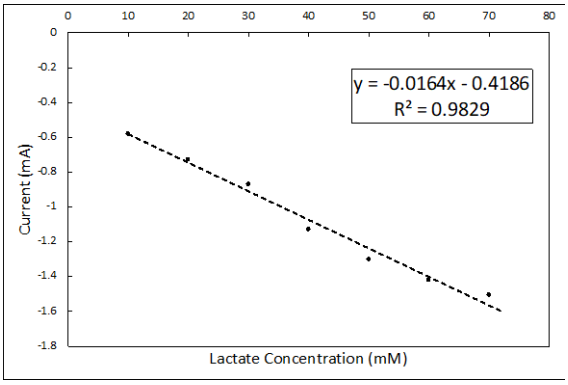
Figures/Charts

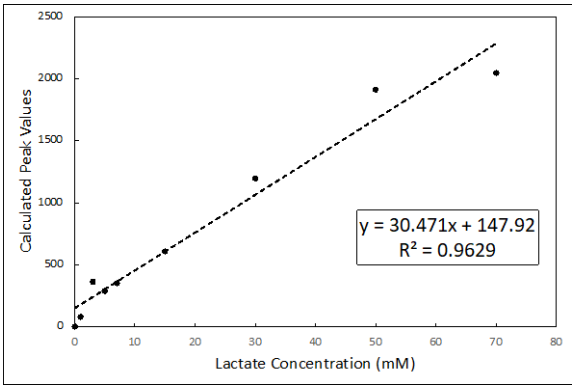












Acknowledgments

Thank you to the Ohio Space Grant Consortium for funding this research and Dr. Monty-Bromer for her mentorship on this project.

References

Bilbao, E., Garate, O., Rodríguez Campos, T., Roberti, M., Mass, M., Lozano, A., Longinotti, G., Monsalve, L., & Ybarra, G. (2023). Electrochemical Sweat Sensors. Chemosensors, 11(4), 244. https://doi.org/10.3390/chemosensors11040244.

Ohkuwa, T., Tsukamoto, K., Yamai, K., Itoh, H., Yamazaki, Y., & Tsuda, T. (2009). The Relationship between Exercise Intensity and Lactate Concentration on the Skin Surface. International Journal of Biomedical Science: IJBS, 5(1), 23–27. https://www.ncbi.nlm.nih.gov/pmc/articles/PMC3614747/

Rabinowitz, J. D., & Enerbäck, S. (2020). Lactate: The Ugly Duckling of Energy Metabolism. Nature Metabolism, 2(7), 566–571. https://doi.org/10.1038/s42255-020-0243-4

Green Energy Storage Utilizing High Pressure Air Storage Vessels

Student Researcher: Emma Core

Advisor: Dr. Matthew Franchetti

University of Toledo
Civil Engineering

Abstract

Having grown up in a family of engineers on a farm in northwest Ohio, I have witnessed the needless consumption of productive farmland for the development of wind and solar fields. While most people understand the need for a migration away from fossil fuels and thus toward green sustainable energy, we must find a way to utilize land that is already out of production to harvest green energy and save the farmland for food production. A constantly increasing world population completely depends on that premise, but inherent reliability problems exist with this type of green energy when the sun is not shining and/or the wind is not blowing. Additionally, current strategies require large scale concentrations of wind turbines and/or solar panels to access the electric grid for distribution, which puts farmland at risk. I believe this problem can be solved with the development of a much smaller scale clean dependable energy storage system that is replicable. Such a system would allow the energy to be consumed in the area where it is generated and not at the expense of farmland needed for food production. This type of system lends itself to the use of highway medians, parking lots, yards, buildings, and the like for the production and storage of green energy.

One such system could consist of small to medium scale energy storage systems consisting of electric powered air compressors to convert green energy into compressed air and store it in high pressure vessels in the area where it is generated. Pneumatic generators can then convert the compressed air back into electricity when needed and thus create a constant, clean, sustainable green energy source. This project consists of the research and engineering calculations needed to analyze available underutilized real estate for the production of green energy and determine the feasibility and scalability of utilizing high pressure air storage vessels for localized green energy storage and consumption.

Project Objectives

My project objectives consist of the research and engineering calculations needed to analyze available underutilized real estate for the production of green energy and determine the feasibility and scalability of utilizing high pressure air storage vessels for localized green energy storage and consumption.

Methodology

My methods for the project included general calculations for land available for green energy by utilizing the two major highways that run through Allen County Ohio. These calculations allowed me to determine how many acres of land was available and ultimately how many homes could be powered per year by using the energy created by solar panels on the amount of land calculated. I then designed a very basic high-pressure air storage system and researched how efficient and how economical the unit would be to determine how feasible and scalable the unit would be.

Results and Discussion

My results cover the total highway median acreage along I-75 and U.S. 30 in Allen Couty Ohio, and how many homes this lands use of solar panels could power. My results also include the estimated efficiency of a high-pressure air storage system.

U.S. 30:

- Width Varies (200'-300') = 250' average
- Length = 24 miles = 126,720' ±
- Pavement Width = 42' ± / land (2 lanes)
- Total Pavement Width = 84' ±
- Median Width = 48' ±
- Non-Median & Non-Pavement Width = 118' ±
- Assuming 50% of Non-Median & Non-Pavement Width Available for Solar Production
- Area Available for Solar = 59' x 126,720' = 7,476,480 S.F. = 172 acres

I-75:

- Width Varies (200'-250') = 225' average
- Length = 23.5 miles = 124,080' ±
- Pavement Width = 41' ± / land (2 lanes)
- Total Pavement Width = 82' ±
- Median Width = 41' ±
- Non-Median & Non-Pavement Width = 102' ±
- Assuming 50% of Non-Median & Non-Pavement Width Available for Solar Production
- Area Available for Solar = 51' x 124,080' = 6,328,080 S.F. = 145 acres

Potential for Generation of Electricity

- Energy Output = 400 megawatt-hours (MWh) per acre of solar panels
- Home Energy Consumption = 106 MWh of electricity per house per year on average
- Potential Homes Powered = 400 MWh/ac. ÷ 10/6 MWh/hs./yr. = 37.7 homes per year per acre solar
- Potential Homes Powered (U.S. 30 & I-75 in Allen County, Ohio) = 37.7 hs./yr./ac. X (172 ac. + 145 ac.) = 6,484 homes per year

Efficiency of High Pressure Air Storage Systems:

- Practical Compressor Efficiency = 80%
- Pneumatic Small Power Generation Efficiency = 75%
- Estimated System Efficiency = 0.80 x 0.75 = 60%
- Estimated Energy Loss = 40%

Conclusion

To conclude, the availability of underutilized real estate for the production of green energy is hugely significant. Areas that could be utilized include Commerical/Industrial/Agricultural Rooftops for solar; parking areas shaded with solar; residential rooftop solar; Commerical/Industrial/Agricultural sidewalls with solar; and as was researched in this project, public highway corridor solar. The underutilized portions of the U.S. 30 & I-75 corridors in Allen County, Ohio alone can power 6,484 homes.

Utilizing high pressure air storage vessels is not feasible due to energy inefficiency caused by an unacceptable level of energy loss through the system. This being an estimated 40% loss. The scalability of high pressure air storage is very high, but inconsequential due to the feasibility problems as discussed. Feasibility could be achieved if we find a way to harness and utilize the heat energy produced by the compressor and the cooling created by the release of the compressed air during the operation of the pneumatic generator.

References

www.sungoldsolar.us; www.sciencedirect.com; Peters et. al., 2002; www.sciencedirect.com

Sustainable Aviation Fuel Production from Plastic and Food Waste on Bifunctional Catalysts

Student Researcher: Kamryn Culp

Advisor: Dr. Linxiao Chen

University of Akron
Department of Chemical, Biomolecular, and Corrosion Engineering | Chemical Engineering

Abstract
Catalytic hydrocracking was studied as a chemical recycling method for converting mixed plastic, polypropylene (PP) and polyvinyl chloride (PVC), and fatty acid food waste, stearic acid, into sustainable aviation fuel-range (SAF) hydrocarbons. Addressing plastic pollution, food waste, and aviation-related CO_2 emissions, bifunctional Ni- and Pt-based catalysts supported on Al_2O_3 and TiO_2 were evaluated under hydrogen pressure in a Parr batch reactor. The inclusion of PVC, often regarded as a catalyst poison due to chlorine content, was examined at 1 wt% and 5 wt% to assess catalyst tolerance and performance. Reaction rates, conversion, and product selectivity were analyzed using gas chromatography. Results show that Ni/TiO_2 outperformed other catalysts for polymer reactions, maintaining high activity and achieving up to 38.4% selectivity toward C_8-C_{16} SAF range with 5 wt% PVC, due to the strong chlorine affinity of the TiO_2 support which mitigates catalyst deactivation and enhances acidity. Pt/TiO_2 hydrocracked stearic acid chains into desired aviation fuel range under harsher conditions of temperature and runtime of 320 °C and 24 h to produce 3.9% SAF selectivity. The work demonstrates the feasibility of using mixed plastic and food waste feedstocks for SAF production, offering a dual solution to waste management and sustainable fuel synthesis.

Project Objective
To assess the relationship between mixed plastic chemical recycling and food waste via catalytic hydrocracking on bifunctional catalysts with a selectivity towards aviation fuel.

Methods
Materials
Polypropylene (CAS-No: 9003-07-0), polyvinyl chloride (CAS-No: 9002-86-2), and stearic acid (CAS-No: 57-11-4) from Sigma-Aldrich Corporation (St. Louis, MO, USA) were used as a reactant. Octacosane (CAS-No: 630-02-4) from Sigma-Aldrich Corporation was used as an internal standard for fatty acid reactions. Nickel(II) nitrate hexahydrate (CAS-No: 13478-00-7) from Sigma-Aldrich and tetraamineplatinum(II) nitrate (CAS-No: 20634-12-2) from ThermoFisher Scientific (Ward Hill, MA, USA) were used for the catalyst metal precursor. Aluminum oxide (MW: 101.96 g/mol, CAS-No: 1344-28-1) from Sigma-Aldrich Corporation and titanium oxide (CAS-No: 13463-67-7) from US Research Nanomaterials, Inc. (Houston, TX, USA) were used for catalyst support.
Catalyst Preparation
The bifunctional catalysts were created with a salt precursor and metal support using the wet impregnation method. The precursors of nickel(II) nitrate hexahydrate and tetraammine platinum (III) nitrate were weighed to 60 mg and added to a beaker with 2 g of metal support of either TiO_2 or Al_2O_3 for the respective catalysts. 20 mL of distilled water was added and the contents were continuously stirred for three hours on a stir plate to ensure proper dispersion.

The solution was dried on a hot plate at 120 °C for a minimum of 6 hours. The dried contents were ground in a mortar and pestle, transferred to a crucible, and calcined in the muffle furnace at 400 °C. The catalysts

were then reduced by being transferred to a boat crucible and inserted into a tube furnace, where hydrogen was continuously flowed at 50 SCFM at 250 °C for 3 hours. The synthesis procedure yielded metal (Ni or Pt) nanoparticles dispersed on the oxide support.

Reaction Procedure

A small vial was loaded with 0.05 g of catalyst and 0.5 g of polypropylene to perform a "clean" polymer reaction, with PP only as the substrate free of PVC impurities. For reactions involving PVC, the appropriate amount of PVC was added to achieve the desired concentrations of 1 wt% or 5 wt% in total substrate weight and charged with 30 bar of H_2. Stearic acid reactions used 0.2 g stearic acid, 20 mg catalyst, and 20 mg internal standard outside the vial and charged to 40 bar of H_2. The vial was then placed into a Parr batch reactor (model 2430HC2), and the reactor lid was secured with clamps. The reactor was purged with hydrogen gas multiple times, pressurized, and subsequently heated to 250 °C for polymer reactions and 300-320 °C for fatty acid reactions. The run time varied from 2-24 hours depending on the reaction. Upon completion, the reactor was quenched with ice water, and the resulting gas and liquid products were collected and analyzed.

Product Analysis

The gas products were collected using a Tedlar bag and were analyzed twice in a gas chromatograph (GC, Agilent 6890N), with a carrier gas of He, to ensure consistency in gaseous product results. The liquid product was collected using an ethyl acetate solvent where the products were filtered and analyzed in a different GC (Agilent 6890N) with a carrier gas of He.

Results and Discussion

Polymer Reactions

The liquid-phase GC results for the Ni/TiO_2 catalyst with 0 wt% PVC were analyzed to represent the product distribution from polymer hydrocracking of a clean reaction shown in Figure 1. The resulting chromatogram displays a range of peaks corresponding to various hydrocarbon compounds from C_{12}-C_{20}, with peak intensity indicating relative quantity. The broad distribution of peaks is indicative of branched hydrocarbon products, a favorable trait for aviation fuel applications due to their enhanced combustion characteristics and higher energy density compared to linear paraffins typically found in gasoline [7]. Figure 2 shows the carbon mole product distribution for each carbon number from the GC data provided in Figure 5. The orange bars indicate liquid product in the fuel range of C_8-C_{16} for kerosene SAF with a 42.6% selectivity.

Figure 7 illustrates the reaction rate, calculated as the apparent rate of disappearance of polymers, as a function of catalyst type with increasing concentrations of PVC. Error bars denote the standard deviations from two replicate experiments conducted at 0 wt% PVC, establishing a baseline for comparison prior to the introduction of PVC impurity. For both Ni/Al_2O_3 and Pt/Al_2O_3 catalysts, a decrease in reaction rate was observed upon the addition of 1 wt% PVC. This decline is attributed to the chlorine released from PVC preferentially binding to the active metal sites rather than the Al_2O_3 support, resulting in catalyst deactivation. Previous studies have shown that increasing chloride ion coverage on the Al_2O_3 surface leads to a shift in preferred adsorption sites from aluminum coordination sites to oxygen sites. This transition corresponds to a reduction in the chloride-surface binding strength, indicating a weakened interaction with the oxide layer and a higher likelihood for chloride to interact directly with the metal active site [1]. Due to this observed susceptibility of the Al_2O_3 support to chlorine-induced deactivation, additional experiments at 5 wt% PVC were not pursued.

The TiO_2-supported catalysts, Ni/TiO_2 and Pt/TiO_2, exhibited an increase in reaction rate with the addition of both 1 wt% and 5 wt% PVC. This trend is interpreted as that the TiO_2 support has a higher affinity for chloride ions, effectively preventing the deactivation of the metal active sites. The adsorption of chlorine onto the TiO_2 support was known to enhance the acidity of the catalyst due to the activity increase in Brønsted acid signals with the presence of chlorine [4], which is responsible for the observed increase in reaction rate with rising PVC concentrations. Previous studies have demonstrated that the behavior of TiO_2 supports is temperature-dependent, primarily due to the desorption of chlorine atoms from titanium coordination sites at elevated temperatures. This desorption is further promoted by competitive adsorption of oxygen species, which displace chlorine atoms from the titanium surface, thereby facilitating chlorine migration from the support to the active metal phase [3].

All catalysts demonstrated increased selectivity toward the SAF range with rising PVC concentrations, which is attributed to enhanced catalyst acidity resulting from chlorine adsorption. Despite this trend, Ni/Al_2O_3 and Pt/Al_2O_3 experienced active site deactivation due to chlorine binding directly to the metal rather than the support. Pt/TiO_2 exhibited an unexpected decline in SAF-range selectivity, likely due to contamination within the reactor hood, as evidenced by a notable increase in C_{28} product formation detailed in the appendix Figure 21. In contrast, Ni/TiO_2 maintained a consistent increase in selectivity without signs of deactivation. Overall, Ni-based catalysts outperformed their Pt counterparts, highlighting Ni/TiO_2 as the most effective system for targeting the aviation fuel range in mixed plastic hydrocracking.

Fatty Acid Reactions

The chromatographic analysis shown in Figure 5 reveals a pronounced peak at 27.5 minutes, corresponding to C_{17} hydrocarbons, consistent with literature reports [9] indicating that C_{17} is a dominant product in the hydrocracking of stearic acid. Minor peaks corresponding to C_{15} and C_{16} were also observed, and their formation was influenced by catalyst type, reaction temperature, and runtime, which were varied to optimize product distribution. To assess catalytic performance, conversions were calculated for all four catalysts, specifically targeting the aviation fuel carbon range (C_8–C_{16}). As shown in Figure 6, Pt/TiO_2 demonstrated the highest conversion, indicating better catalytic efficiency toward fuel-range alkanes compared to other catalysts. Subsequent reactions conducted at an elevated temperature of 320 °C with Pt/TiO_2 resulted in a greater yield within the target fuel range, albeit with low overall selectivity (<1%). Extending the reaction time to 24 h significantly enhanced chain scission, improving selectivity to 4% toward sustainable aviation fuel.

Product distributions from stearic acid hydrocracking are illustrated in Figures 7 and 8, with Figure 8 specifically isolating compounds in the kerosene-range fraction. Under standard conditions (300 °C, 2 h), Ni/Al_2O_3 and Ni/TiO_2 failed to produce measurable quantities of C_8–C_{16} hydrocarbons. In contrast, Pt/TiO_2, under intensified thermal and temporal conditions, facilitated greater hydrocracking to as low as C_{12}, producing 0.34 carbon mmol of product. Although SAF-range selectivity remained limited, these results suggest that reaction severity of temperature and duration can enhance yield within the desired carbon range.

While hydrocracking of stearic acid with bifunctional catalysts like Pt/TiO_2 demonstrates potential for SAF production, the low selectivity and need for harsh conditions highlight a need for further process optimization. Future work could explore the conversion of food waste-derived lipids as a viable feedstock for SAF, leveraging similar catalytic pathways to enable sustainable fuel generation from organic waste sources.

Figures/Charts

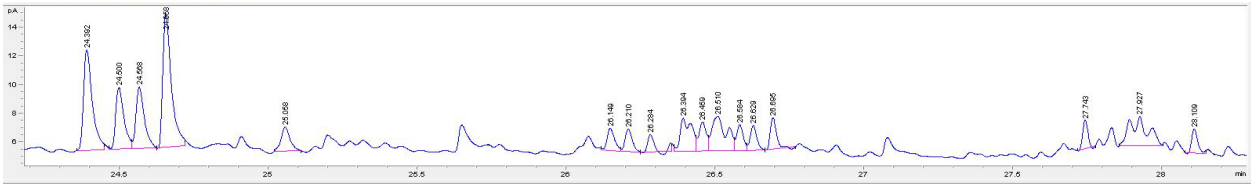


Figure 1 Portrays a sample of a liquid GC product chromatogram of Ni/TiO_2 from time of 24 to 28.5 minutes for the carbon range of C12-C20.

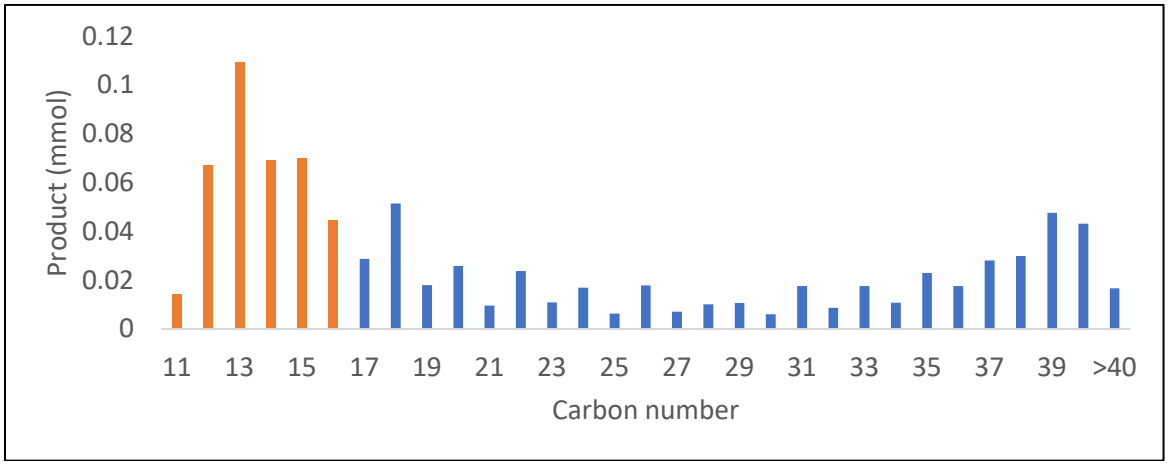


Figure 2 Depicts the liquid product distribution for Ni/TiO_2 with 0 wt% PVC. The orange products represent a 42.6% selectivity the desired kerosene SAF carbon range of C_8-C_{16}.

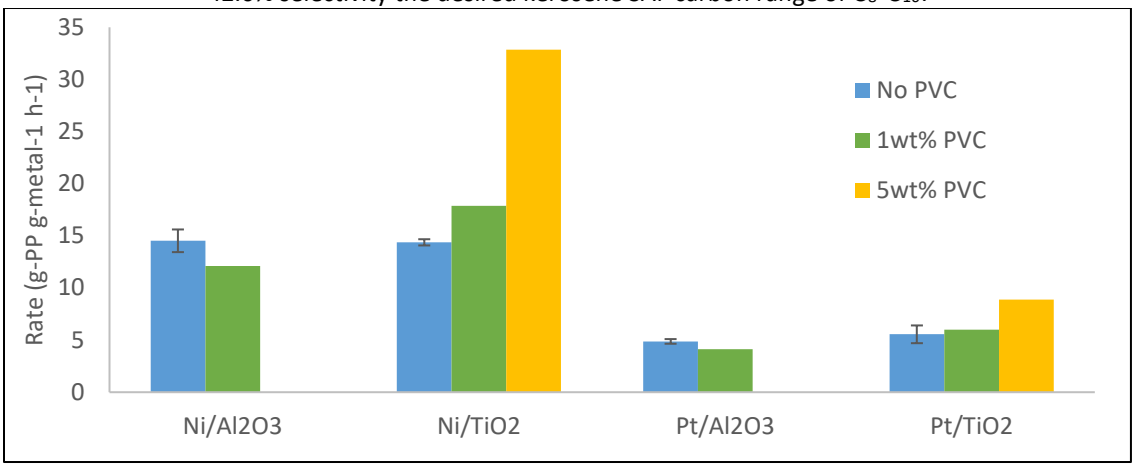


Figure 3 Displays rate as a function of catalyst with increasing amount of PVC. Ni/Al_2O_3 and Pt/Al_2O_3 were not ran with 5 wt% PVC due to the rate decreasing with 1 wt% added.

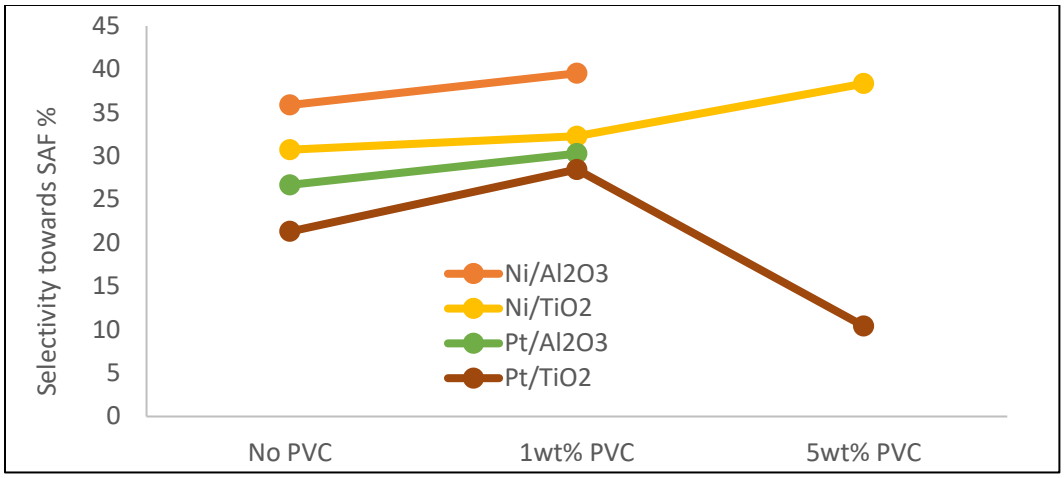


Figure 4 Presents the selectivity toward SAF range of C_8-C_{16} with increasing levels of PVC. Ni/Al_2O_3 and Pt/Al_2O_3 showed increasing selectivity, but had a decreasing rate so additional reactions were not ran.

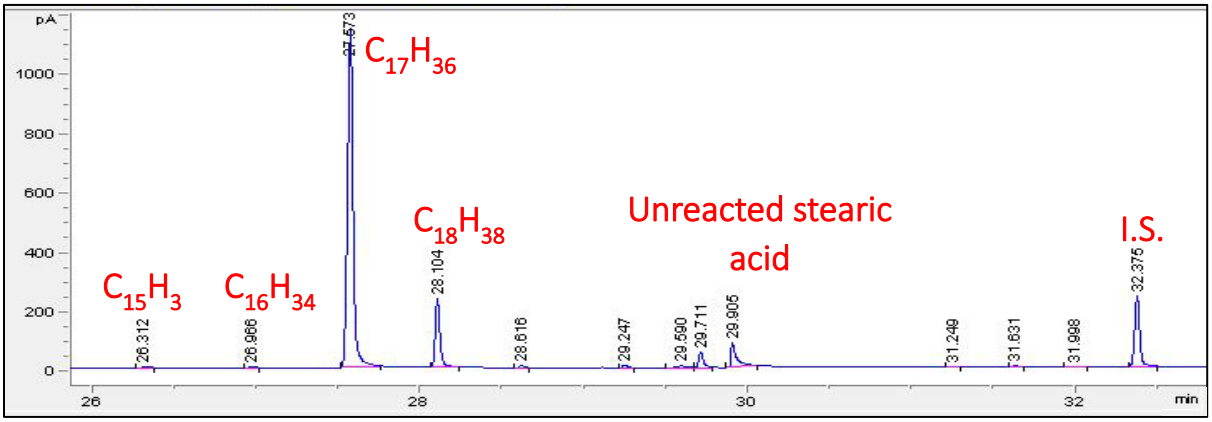


Figure 5 Shows the Pt/Al_2O_3 liquid data results from the GC where a large peak is shown for $C1_7$ indicating stearic acid cracking, but within the desired aviation fuel range of C_8-C_{16}.

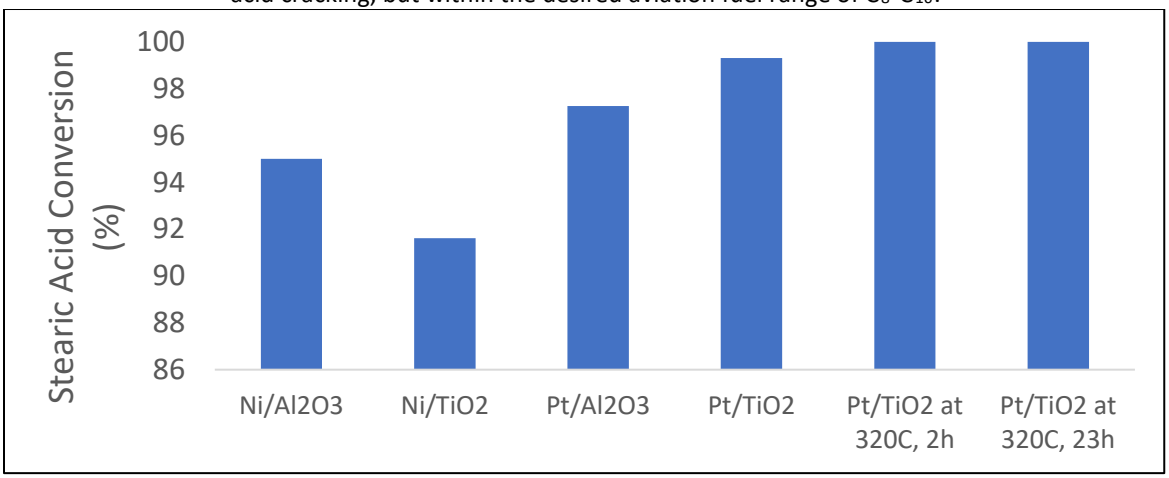


Figure 6 Depicts the reactant conversion using the four catalysts under the conditions of 0.2 g stearic acid, 20 mg catalyst, 20 mg internal standard, 300 °C, 40 bar H_2 until harsher conditions were used for Pt/TiO_2 to achieve full conversion and greater aviation fuel selectivity.

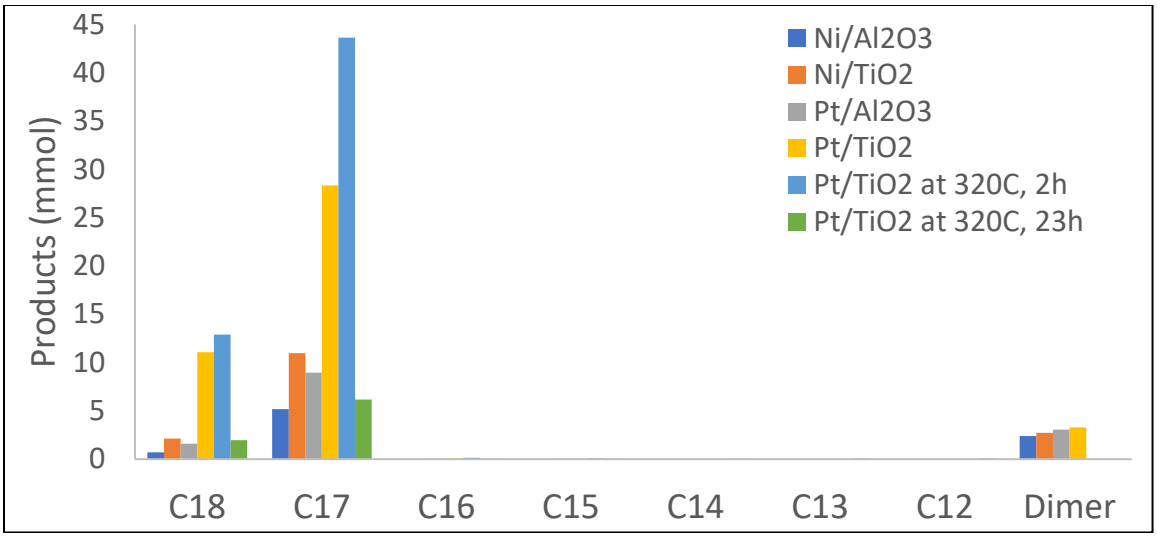


Figure 7 Displays the product distribution for the fatty acid reactions showing large distribution for C_{17}, C_{18}, and a side product of dimer formation.

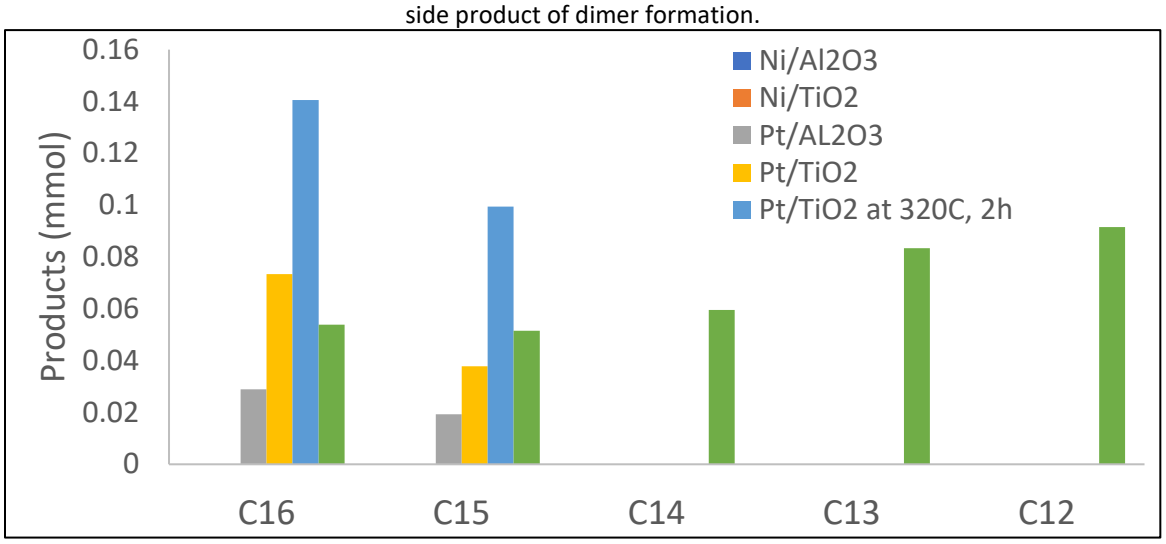


Figure 8 Shows the product distribution for the aviation fuel range from Figure 7 where a longer runtime and greater temperature of Pt/TiO_2 achieved greater selectivity in the fuel range, with no dimer product and significantly less C_{17} compared to the other reactions.

Acknowledgements

I would like to express my deepest gratitude to the Ohio Space Grant Consortium for the support and opportunity to further my research. I would also like to thank Dr. Chen, the University of Akron, and to my fellow graduate and undergrad research colleagues.

References

[1] Chuan-Hui Zhang, Min Liu, Ying Jin, Dong-Bai Sun, The corrosive influence of chloride ions preference adsorption on α-Al2O3 (0001) surface, Applied Surface Science, Volume 347, 2015, Pages 386-391, ISSN 0169-4332, https://doi.org/10.1016/j.apsusc.2015.04.088.

[2] *Food waste in America in 2025: Statistics & Facts: RTS*. Recycle Track Systems. (n.d.). https://www.rts.com/resources/guides/food-waste-america/#:~:text=The%20Facts%20About%20Food%20Waste%20*%20Americans,percent%20of%20the%20entire%20US%20food%20supply.

[3] Inderwildi OR, Kraft M. Adsorption, diffusion and desorption of chlorine on and from rutile TiO2{110}: a theoretical investigation. Chemphyschem. 2007 Feb 19;8(3):444-51. doi: 10.1002/cphc.200600653. PMID: 17226874.

[4] Junling Lu, Kathryn M. Kosuda, Richard P. Van Duyne, and Peter C. Stair
The Journal of Physical Chemistry C 2009 *113* (28), 12412-12418
DOI: 10.1021/jp902200c

[5] Shrirame, B. S., & Maity, S. K. (2025b). Sustainable aviation fuel range branched alkanes via hydrodeoxygenation of furfural-derived trifurylmethane over mesoporous NIW-zro2 composite catalysts. *Biomass and Bioenergy*, *196*. https://doi.org/10.1016/j.biombioe.2025.107759

[6] TotalEnergies. (2019, June 20). *Fuels in Aviation and Shipping*. Fuels – Consumption of airplanes and boats | Planète Energies. https://www.planete-energies.com/en/media/article/fuels-aviation-andshipping#:~:text=The%20aviation%20industry%20represents%207.8,of%20global%20final%20consumption1.

[7] U.S. Department of Energy. (n.d.). *Sustainable Aviation Fuel*. Alternative Fuels Data Center: Sustainable Aviation Fuel. https://afdc.energy.gov/fuels/sustainable-aviation-fuel.

[8] Wojnowska-Baryła, I.; Bernat, K.; Zaborowska, M. Plastic Waste Degradation in Landfill Conditions: The Problem with Microplastics, and Their Direct and Indirect Environmental Effects. *Int. J. Environ. Res. Public Health* 2022, *19*, 13223. https://doi.org/10.3390/ijerph192013223.

[9] Wu, J., Shi, J., Fu, J. *et al.* Catalytic Decarboxylation of Fatty Acids to Aviation Fuels over Nickel Supported on Activated Carbon. *Sci Rep* 6, 27820 (2016). https://doi.org/10.1038/srep2782

[10] Yayun Zhang, Dengle Duan, Hanwu Lei, Elmar Villota, Roger Ruan, Jet fuel production from waste plastics via catalytic pyrolysis with activated carbons, Applied Energy, Volume 251, 2019, 113337, ISSN 0306-2619, https://doi.org/10.1016/j.apenergy.2019.113337.

Raspberry PI Pico RP2040 Drone

Student Researcher: Dylan Damiano

Advisor: Dr. Augustus Morris

Central State University
Computer Science

Abstract
Building a drone oriented around a Raspberry Pi Pico [5], featuring an RP2040 based microcontroller can introduce numerous opportunities (see Figure 1). The scope of this project is to include low-cost, replaceable hardware components to make modular, versatile drones, which can be adapted, made open-source, and reconfigured by other users for various applications relating to but not limited to hobbyist activities, research, and work. Radio communication will be carried out either via Long Range Radio *(LoRa)* or RFM690-series packet-radios– which are intended to pull data from ground-based sensors and aerial sensors mounted on deployed devices and be further relayed to a backend web-client, capable of interpreting structured bytes, permitting for remove operation, and downstream processing featuring the use of USB-to-Transistor to Transistor Logic *(TTL)* devices.

Project Objectives
Throughout the duration of the project, we aimed to have a flying drone, modular, and remotely-operate drone via Hyper Text Transfer Protocol Secure *(HTTPS)* locally on a web browser by the end of the timeframe. There were plans on having camera modules (OV5640 or HM01B0) on the drone, however given limited time and limited number IO pins by the time this came around, implementation was to be postponed until a later date. Every device is intended to relay packets from one another via RFM69 with USB being implemented on the user's devices to receive signals from the RFM69HCW radio network, along with device identifiers in future implementations.

Methods
There were hours of soldering, reorganizing or replacing wires, and troubleshooting hardware components that were communicating via Inter-Integrated Circuit *(I2C)*, Serial Peripheral Interface *(SPI)*, and Universally Asynchronous Receive and Transmit *(UART)*. Given the nature of the motors selected, Dshot [1, 6] was an inexcusable design requirement, but there were two feasible ways to implement this, first being through Programmable IO Assembly *(PIOASM)*, second being through third-party library—ultimately the third-party library being selected [4]. For ease-of-implementation and ease-of-design, Python was selected to permit quick prototyping. There were initial issues with setting up Micro Python, so Circuit Python was chosen in place of the earlier. There are plans to migrate from Python to C++ once everything is proven to be interoperable.

Results and Discussion
Currently, the desired goals of low-cost and flying were not achieved as of now. However, the desired results regarding transfer of information between point-to-point and displaying the sensor data to a locally hosted NextJS-based webpage using USB-to-TTL devices after data transfer through RFM69 radio were successful—albeit quite slow given that the utilized library was a 'best-effort' [2]. An implementation featuring the RFM69 and USB-to-TTL device can be found in Figure 2. Initially, there were plans to utilize Wi-Fi or Bluetooth instead of RFM69 packet-radios [3], but this would have been ineffective, given the ranges of both technologies [7].

In regard to the RFM69 packet-radio, the structures for the payloads are designed from a practical perspective to ensure support for varying devices, with embedded identifications to identify the originating device, and the type of decoding that will be necessary (see Figure 3).

Moving forward, additional work done regarding allocation of Input and Output pins will need to be done, along with the possibility of reorganizing the layout of hardware modules, the programming for the drone can be done without bumping parts out of place—without causing damage as well. Longterm, it could possibly be more feasible *(and cost effective)* to purchase an existing drone, and modify it, as airframes are infrequently modified in the aerospace industry as well to suit needs.

Figures/Charts

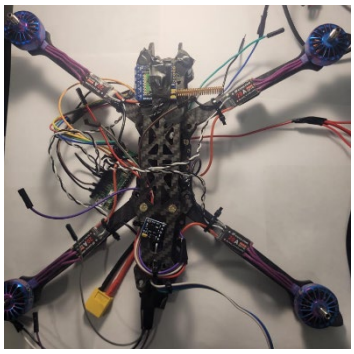


Figure 1 *Current Drone Build*

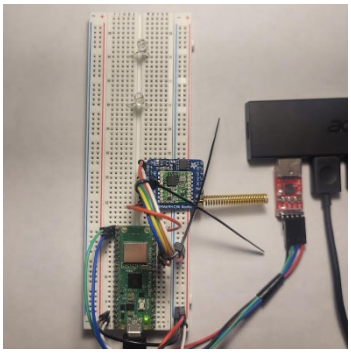


Figure 2 *Ground Module RX*

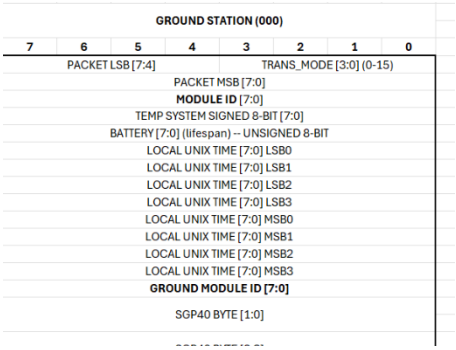


Figure 3 *Ground Module Dataframe*

Acknowledgments

1. Central State University for providing students with grants to assist my project, and that of other students
2. OSGC for offering of scholarships, participation in a larger consortium and collegiate body.

References

[1] Abdelrahman, H. (2021). Software Integration of Electronic Speed Controller (ESC) for an Unmanned Aerial Robot. University of Twente. https://essay.utwente.nl/87630/.
[2] Adafruit. (2025). Adafruit CircuitPython RFM69. https://github.com/adafruit/
[3] Diz-Bugarin, J., Rodriguez-Fernandez, J. (2024). Digital Radio Communications Module for Learning Applications and Remote Sensing. IEEE Xplore. 10.1109
[4] Dupont, J. (2023). DShotPIO. GitHub. https://github.com/jrddupont
[5] Raspberry Pi Foundation. (2025). Pico-series Microcontrollers. Raspberry Pi. https://www.raspberrypi.com/documentation/microcontrollers/pico-series.html
[6] Team Betaflight. (2025). DSHOT. Betaflight. https://betaflight.com/docs/development/dshot
[7] Qazi, S., Khawaja, B. A., & Farooq, Q. U. (2022). IoT-equipped and AI-enabled next-generation smart agriculture: A critical review, current challenges and future trends**.** *IEEE Xplore*, 21219-21235.

Maximizing Solar Capture: Comparison Between Fixed and Tracking Systems

Student Researchers: Jeremiah Daubon & Stephon Thomas

Advisor: Dr. Augustus Morris

Central State University
Department of Manufacturing Engineering

Abstract
This project explores the efficiency, performance, and cost implications of fixed solar systems versus single-axis tracking systems, focusing on the vertical-axis tracking design that moves east-to-west to refine energy capture. By comparing these two solar technologies, the project aims to determine which system provides better energy output, storage, and long-term viability. Through rigorous data collection and testing in real-world conditions, including varying weather and geographical factors, this study evaluates the effectiveness of both systems. The research incorporates a multidisciplinary approach, combining mechanical design, electrical engineering, and programming, using Arduino components to control the tracking system's servos and sensors. In addition, the project assesses the cost-effectiveness, societal impact, and environmental benefits of these systems, emphasizing their potential to reduce reliance on fossil fuels and contribute to global sustainability goals. The findings are expected to offer valuable insights into optimizing solar energy solutions, enhancing accessibility, and promoting energy independence, while offering guidance for future renewable energy projects. The use of 3D printing for manufacturing components further reduces costs and supports sustainable practices, ensuring that solar technology is both economically feasible and environmentally responsible.

Project Objectives
The main goals of this research were to compare energy output between fixed and single axis tracking solar systems and evaluate their cost-effectiveness, long-term viability, and environmental impact. We aimed to assess their performance in real-world conditions and propose extensions for future research, including dual axis tracking alternatives.

The main objective of this research is to compare the energy output between fixed and single axis tracking solar systems while evaluating their cost-effectiveness, long-term viability, and environmental impact. The study aims to assess the performance of both systems under real-world conditions, identifying potential improvements and proposing extensions for future research, such as dual axis tracking alternatives. A key focus is to evaluate performance variations across different weather conditions, analyzing how factors such as cloud cover and seasonal changes affect energy yield. Additionally, the research investigates the impact of energy storage, assessing how differences in energy output influence battery efficiency and overall system reliability. The power consumption of the tracking system is also analyzed to determine whether the energy gained justifies the energy spent. Another crucial aspect is the scalability and practicality of implementing tracking systems in small-scale and large-scale applications. Furthermore, the study explores optimization strategies for tracking algorithms, comparing LDR-based tracking with pre-programmed sun position tracking for efficiency gains. Durability and maintenance requirements are also considered, examining long-term system wear and upkeep costs. Finally, an economic feasibility study is conducted to assess the return on investment (ROI) of both fixed and tracking systems by evaluating installation, operational, and maintenance costs over their lifespan.

Methods

To achieve these objectives, we designed and constructed both fixed and vertical single-axis tracking solar systems. Voltage, current, and power were measured under various sunlight conditions over a two-week period. Arduino Nano microcontrollers were used to control servos and log data using a SD card module. The systems were tested on Jenkins Roof and MPC Field in Wilberforce, OH, three times a week for four hours a day. Materials were sourced affordably, and 3D printing was used to fabricate custom parts and mounts, reducing material costs and enhancing design adaptability.

Results and Discussion

The tracking system consistently outperformed the fixed panel in terms of energy output. Despite the higher initial costs, the increased efficiency of the tracking system makes it a viable long-term investment, especially for users in high-sunlight regions. The fixed panel, while cost-effective and low maintenance, provided less energy overall. Arduino-based control and sensor integration enabled effective autonomous operation. Weather fluctuations slightly affected results, but the tracking system proved more resilient and adaptable under varying conditions.

Data analysis also revealed that the best window for energy capture was between 11 AM and 3 PM, consistent with expected solar radiation peaks. The use of 3D-printed components reduced material costs, and custom design features allowed for better integration and durability. These findings support the viability of single-axis trackers as practical energy solutions for modern renewable infrastructure.

Acknowledgments

We extend our deepest gratitude to Dr. Augustus Morris for his invaluable mentorship and guidance throughout our research journey. We are especially thankful to Dr. Abayomi Ajayi-Majebi and Dr. Mahmoud Abdallah for their input, encouragement, and continued support. We also thank Central State University for providing the tools, resources, and space necessary to carry out our work. Special appreciation goes to the Ohio Space Grant Consortium for awarding us the scholarship and the incredible opportunity to showcase our research.

References

Team, S. (2024). Dual Axis Tracker: Definition, Types and How it Works. Solar Compare.

Team, S. (2024). Single Axis Solar Tracker: Definition, How it Works, Importance, and Types. Solar Compare.

Racharla, S., & Rajan, K. Solar Tracking System – A Review. International Journal of Sustainable Engineering.

Exosun. Elevating the Future for Solar.

De Rooij, D. (2023). Single Axis Trackers. Sinovoltaics.

Lane, C. What is a Solar Tracker and is it Worth the Investment? Solar Reviews.

Ramasamy, V., et al. (2022). U.S. Solar PV System and Energy Storage Cost Benchmarks: Q1 2022.

De Ávila, E. M. (2016). Artificial Recurrent Neural Networks for PV Grid Control.

Green, L. (2016). 15 Million Degrees: A Journey to the Centre of the Sun.

Ottman, J. A., et al. (2006). Avoiding Green Marketing Myopia. Environment Science and Policy.

The Energy Produced by an IEC Class 1 Wind Turbine

Student Researcher: Lincoln DeHaven

Advisor: Dr. James Menart

Wright State University
Mechanical and Materials Engineering/Mechanical Engineering

Abstract
In 2023 wind energy was 10.2% of the total utility scale electricity produced in the United States [find source for this]. This shows that wind energy is a vital source of energy for the economy of the United States and as such it is important to understand different aspects of wind energy. This work sought to evaluate different characteristics of wind energy and the capturing of this energy with a wind turbine. Raw wind speed data from Eaton, Ohio, along with a wind turbine power curve from AWS Truewind was used to understand these concepts. This study sought to change two different design parameters of wind energy: the location of the wind farm and the height at which the wind turbine is placed. This study saw the evaluation of how changing the standard deviation of a given wind set and scaling the wind speed relative to a change in height effected energy production. It was seen that over the ranges studied that the standard deviation saw a factor of 4 difference which resulted in half of the energy being produced. This study also saw that as the height of the turbine increases; the wind speed will increase resulting in a difference of energy being produced. It was seen that a 36% increase in energy produced resulted from only a 1 meter per second increase of wind speed.

Project Objectives
This work seeks to evaluate different characteristics of wind energy and the capturing of this energy with a wind turbine using a MATLAB Script. By this evaluation into wind energy this work also seeks to increase public knowledge of wind energy and why the development of renewable and clean energy is important. The expression of the importance of wind energy as an abundant and inexhaustible source of energy needs to be known and understood.

Methods
This evaluation of wind energy characteristics and the capturing of this energy was understood using MATLAB and Engineering Equation Solver (EES) for the calculations. The calculations done during this evaluation were focused on the raw wind data taken in Eaton Ohio at 100 meters elevation. The raw wind data was provided from my advisor through an external source. The wind speed data was taken every five minutes over an entire year, this allows for yearly estimations for wind resource and energy production from a wind turbine to be determined. When looking at the wind resource and the energy produced by the wind turbine *Wind Energy Explained: Theory, Design and Application, Second Edition* by Manwell et. al was referenced.

Manwell et al. provided equations in chapter 2 for the wind resource along with turbine production that were used. For the evaluation of the wind resource the energy density was evaluated to see the amount of energy within one square foot of wind at 100 meters. This equation for energy density can also be used to look at month by month energy density depending on the data inserted. The energy density equation is the energy density $\left(\frac{\bar{E}}{A}\right)$ equal to one half the air density (ρ) multiplied by the the time increment (Δt) and the summation of all the wind speeds (U) cubed [2]. This equation states that the energy in the wind

is directly proportional to the wind speed cubed assuming air density as a constant and can be seen in Equation 1.

$$\frac{\bar{E}}{A} = \frac{1}{2}\rho\Delta t \sum_{i=1}^{N} U_i^3 \tag{1}$$

When looking at the yearly energy production of a wind turbine, a similar equation is used to calculate the energy density for the year. To calculate the energy produced by a wind turbine, a wind turbine power curve is needed. The wind turbine power curve for these evaluations was taken from a report by AWS Truewind and is the IEC Class 1 curve that was selected. The curve developed by AWS Truewind was done by taking three actual power curves that were normalized and then rescaled to a rated capacity of 2 MW [3] and is available in Figure 1. Due to this, the swept area of the wind turbines that were used is not available to compare the energy in the wind of the swept area to the energy produced by the wind turbine. To determine the energy produced by the turbine in Eaton, Ohio the energy (E_w) is equal to the power generated by the wind turbine as a function of wind speed $\left(P_w(Ui)\right)$ multiplied by the time increment and can be seen in Equation 2.

$$E_w = \sum_{i=1}^{N} P_w(U_i)\Delta t \tag{2}$$

Equations 1 and 2 give values for the yearly energy density of the wind along with the yearly production of energy from a given wind turbine power curve. However, this study wanted to look at how characteristics of turbine design or wind farm site location could affect the resulting energy production. Looking at the difference in turbine design, the height of the hub was changed by a factor of one half and a factor of one and a half. These factors place the height of the hub at 50 and 150 meters along with the given 100 meters. The wind speed of the wind varies with the atmospheric boundary layer that is roughly about a kilometer in size. This means that the velocity of the wind inside the boundary layer can be scaled assuming a no slip condition relative to the measured value. The power law profile was selected over the logarithmic profile (log law) as the log law profile is dependent upon the surface roughness. The power law profile can be seen in Equation 3.

$$\frac{U(z)}{U(z_r)} = \left(\frac{z}{z_r}\right)^{\alpha} \tag{3}$$

Equation 3 states that the desired wind speed is equal to the measured wind speed times the new height (z) divided by the old height (z_r) all to the power law exponent alpha. An assumption of the power law exponent being equal to one seventh, for flows over a flat plate [4]. This assumption, that was used as the equation for the power law exponent involved the surface roughness which when considering earth is a very crude assumption depending on the site. This pushed the use of one seventh for the power law coefficient which for this evaluation which all parties involved were in agreement.

Another engineering design parameter that can be made with wind energy is the site location of the wind turbine. To vary the sites for this evaluation different wind data sets could be used but for these calculations the standard deviation of the wind was changed. Establishing the background forabout the distribution of wind can be done using two different methods, Rayleigh or Weibull distributions [2]. Rayleigh and Weibull distributions are commonly referred to as ‘skew’ distributions in which they are always greater than zero [2]. The Weibull distribution was chosen due to the two parameters as opposed to Rayleigh’s one parameter; this allows for a better prediction of the wind regimes [2]. To fit the Weibull

distribution, the "Statics and Machine Learning Toolbox" in MATLAB was used. This allows for the shape parameters c and k to be determined.

From the shape parameters of c and k the standard deviation can be determined using Equation 4 for the standard deviation given by Maxwell et al. [2]. This equation gives the characteristic of the wind that was changed during these calculations to artificially simulate a different site location for energy production. In this study the standard deviations were changed by factors of 0.3, 0.5, 0.7, and 1.25. After the change of standard deviation to determine the two shape parameters for the Weibull distribution, a second equation or rather another assumption to the calculation is needed. An assumption that the total energy in the wind would remain constant to see the impact that the distribution would have on energy produced. The total energy in the wind is given in Equation 5, and for Equations 4 & 5 (Γ) is the gamma function. EES was used for a trial-and-error solution due to the strength and ease of use compared to the trial-and-error solvers in MATLAB or Excel.

$$\sigma_u^2 = c^2\Gamma^2\left(1+\frac{1}{k}\right)\left[\frac{\Gamma\left(1+\frac{2}{k}\right)}{\Gamma^2\left(1+\frac{1}{k}\right)}-1\right] \tag{4}$$

$$\overline{U^3} = c^3\Gamma\left(1+\frac{3}{k}\right) \tag{5}$$

Results and Discussion

Figure 1 shows the raw wind speed of Eaton, Ohio over an entire year. It can be seen in this data that it is very sporadic and not a consistent speed over time. Due to this variability in wind speed over time, use of each raw wind speed rather than an average data for calculations is important. From the calculations over the year of data taken in Eaton, Ohio at 100 meters, there was $3500\ \frac{kW\cdot hr}{m^2}$ of energy in the wind for this year. This energy can be harnessed using IEC Class 1 wind turbine power curve in Figure 2. This wind turbine has a cut-in speed and a cut-out speed. The cut-in speed determines the minimum amount of speed that the wind must be flowing to turn the wind turbine. The cut-out speed determines the fastest speed that the IEC Class 1 can remain functional without taking damage.

The cut-in speed is four meters per second and the cut-out speed is 25 meters per second. The IEC Class 1 wind turbine when placed at the site in Eaton, Ohio over a year will produce $5910\ MW\cdot hr$ of utility scale electricity. In the interest of the production of wind energy due to different engineering choices was studied. One parameter studied was the site that the wind turbine is placed, and the effects of different standard deviations was evaluated. Over the range of standard deviations seen in Table 1 when keeping the energy in the wind constant, the energy produced was dependent on the standard deviation. The highest standard deviation that was studied shows the energy produced being $4240\ MW\cdot hr$ of electrical energy. This was a loss from the unchanged standard deviation where the wind turbine produced $5910\ MW\cdot hr$ of electrical energy.

When trending the standard deviation into a smaller distribution range this greatly increases the energy produced by the wind turbine. When the standard deviation became 1.0624 meters per second the energy produced by the turbine was $8020\ MW\cdot hr$ of electrical energy. The reasons for the drastic changes can be viewed in Figure 4. As the standard deviation became lower to keep the energy of the wind a constant, the Weibull distribution shifted towards the right. This shift caused more of the wind to be within a range that would turn the turbine. Over the range of the standard deviations studied, the energy produced showed that a factor of about four difference in the standard deviation caused the energy produced to be halved.

Another engineering parameter studied for a wind turbine is the height at which the hub of the wind turbine is placed. This study took the given 100 meter height and changed the wind data to reflect the speed at 50 and 150 meters to study the effects of energy production due to the height of the turbine. The average wind speed for the site at 50, 100, and 150 meters is 6.43, 7.10, and 7.52 meters per second respectively. At 50, 100, and 150 meters the energy produced by the IEC Class 1 wind turbine is 4820, 5910, and $6570\ MW \cdot hr$ respectively. The energy production increase over the studied ranges is 36%. With the proportionality of the wind energy being dependent on the wind speed cubed, a one meter per second wind speed difference over the ranges studied had a noticeable effect on the energy produced.

During this study MATLAB and Engineering Equation Solver were used to study different characteristics of wind energy and the capturing of this wind energy using a wind turbine. From the two cases that were evaluated it was determined that over the ranges of standard deviations studied that a factor of four difference in the standard deviation causes the produced energy to be about half to total energy. In addition, increasing the height of the wind turbine hub directly causes a difference in the energy produced because the energy in the wind is relative to the wind speed cubed. The data showed that over the ranges studied one meter per second an increase in the average wind speed caused the energy produced to increase by 36%.

Figures/Charts

Turbine Hub Height (m)	Average Wind Speed (m/s)	Standard Deviation (m/s)	Total Energy Produced $(MWhr)$
50	6.43	3.22	4820
100	7.10	3.56	5910
150	7.52	3.77	6570

Standard Deviation (m/s)	Energy Produced $(MWhr)$
1.0624	8020
1.7705	7780
2.4787	7250
3.5413	5910
4.4275	4240

Table 1 & 2: Wind Characteristics and Energy Variations with Height of Wind Turbine Hub (Left), Energy Variations with Standard Deviation of Raw Wind Data (Right).

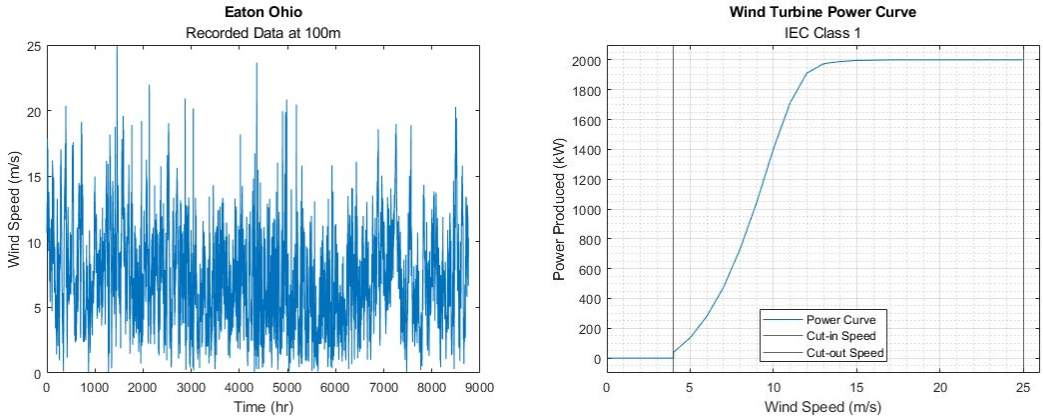


Figure 1 & 2: Raw Wind Data in Eaton Ohio over a year (Left), Composite power curve for IEC Class 1 wind turbine at standard air density (Right).

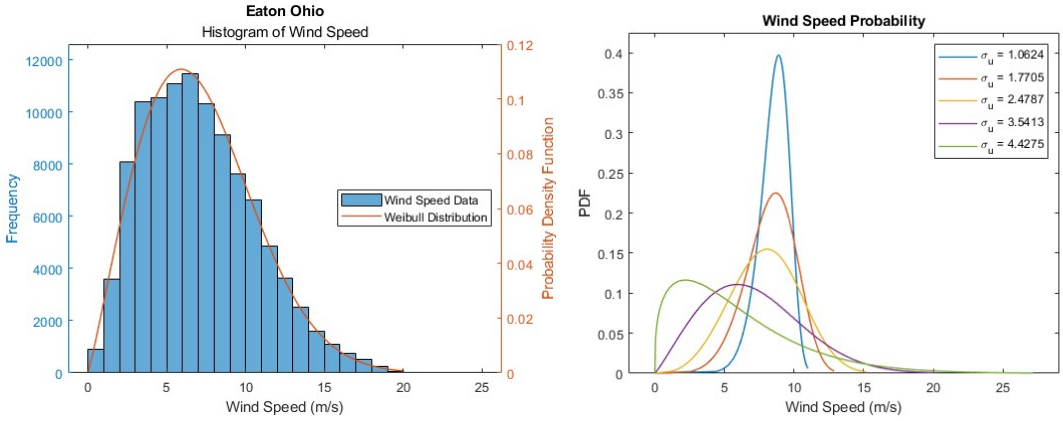


Figure 3 & 4: Histogram and Weibull Distribution of Raw Data in Eaton Ohio over a year (Left), Weibull Distribution of Different Simulated Sites (Right).

Acknowledgments

I would like to thank the Ohio Space Grant Consortium (OSGC) for the funding for this project along with my advisor Dr. James Menart for his expertise in wind power and energy production using a wind turbine. I would also like to thank my campus representative for his support and interaction with (OGSC) to get the funding for students.

References

[1] U.S. Energy Information Administration, "How much carbon dioxide is produced when different fuels are burned?," *U.S. Energy Information Administration (EIA)*, 20 Nov. 2023. [Online]. Available: https://www.eia.gov/tools/faqs/faq.php?id=427&t=3 [Accessed: 18-Apr-2025].

[2] Manwell, J. F., McGowan, J. G., and Rogers, A. L., *Wind Energy Explained: Theory, Design and Application*, 2nd ed., Wiley, Chichester, U.K., 2009.

[3] Brower, M., *Development of Eastern Regional Wind Resource and Wind Plant Output Datasets: March 3, 2008 – March 31, 2010*, National Renewable Energy Laboratory, Golden, CO, Dec. 2009. Report No. NREL/SR-550-46764. DOI: https://doi.org/10.2172/970342.

[4] Schlichting, H., *Boundary Layer Theory*, 6th ed., McGraw-Hill, New York, 1968

Analysis of Observations to find Period Change in RRL Variable Stars

Student Researcher: Nicholas Doughman

Advisor: Andrew Layden

Bowling Green State University
Physics

Abstract
Available observations of the globular cluster NGC 6171, or M107, made in a publication from Arellano Ferro et al., were shown to contain four known RR Lyrae (RRL) radially pulsating stars among around 24 total observed RRLs with discovered changes in period of their oscillating magnitude. By refining the raw photographic CCD observational data previously made of the RR Lyrae variables in M107, as well as by adding, refining and correcting more recent digital data from ZTF, ASAS-SN, PROMPT, and the BGSU observatory, the goal of this project will be to process RRL observational plots into plots of 'observed times of max light' v. 'calculated times' (O-C) to determine the stability of each known RRL's period over time. Witnessing confident data supporting the changing period of a sample star allows us as observers to tangibly represent the aging of these stars, as it suggests alterations in the dynamics within the star associated with movement or "aging" across the horizontal branch as helium is fused in stellar cores. This would provide among the smallest reasonably time-scaled methods of observation of stellar evolution, not requiring hundreds of years of similarly precise and regular observation.

Project Objectives
The primary objective of this research is to sort through observational data compiled of the 24 sample RRL variables from the collective previous observers' databases, to verify previously determined values for the period of luminosity oscillation, and to use the pared down and modified datasets to create O-C plots representing the possibility of each RRL exhibiting a changing period.

The secondary objective is to continue including more recent data with older 20th century photographic observational data to continue to verify the accuracy of the original data and to further support or refute the determination if any RRL variables from the sample group exhibit a changing or non-changing period

Methods
The first step of this research began contrarily to the norm with data analysis of archived observational data of previous teams from the early 20th century to the early 2000s. This began by going through the compiled data from the first to the latest dates of recorded observation for each star, and manually searching for likely outliers not reasonably fitted to the generated light curves folded to each star's period. A Linux supported algorithm intended to help trace the best-fit trends of each plot would reflect the sinusoidal or sawtooth curve exhibited by RRLc and RRLa-b stars respectively, which both facilitated locating outliers and highlighted the significance each erroneous data point had on the collective and by extension our assumptions on the period values.

Once the process of data refinement was complete and verified with separate light curves of each star the "new" data set was used to determine a plot of the observed values for each cycle of oscillation against the predicted or "calculated" values, for each cycle of oscillation from the start of observations to the present

The final process necessary for our research was to take the coefficient value calculated from any quadratics shown from samples of period-changing stars, and to input it into a determined formula intended to represent a qualitative value for the rate of change of the stars' period

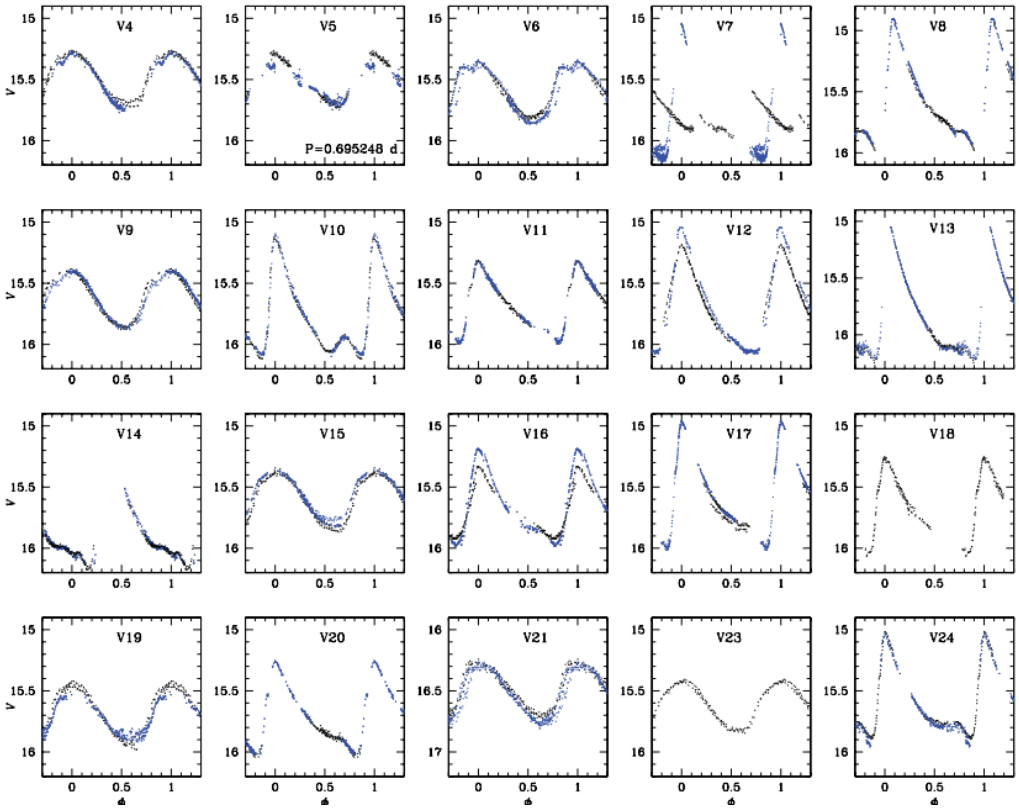
Results and Discussion

Of the time of this submission, data produced for 2 sampled stars, designated V05 and V08, had shown a strong and possible chance respectively of displaying a change in period. With varying degrees of scattering across their composite data points, manually biasing our algorithm between linear and quadratic trend lines had shown greater accuracy with the latter, making our A_2 coefficient non-zero and subsequently our value β, representing numerically the value of the rate of period change.

Addition of more contemporary data from our own surveys as well as in conjunction from yearly observations made by the ZTF, PROMPT, and ASAS-SN continued to support the probability of these sample stars displaying period change, and over the course of the next several years or remainder of the current decade continued observational data will be collected to develop a more complete and extensive picture, for the purpose of refining β, A_2, and period values in the near future.

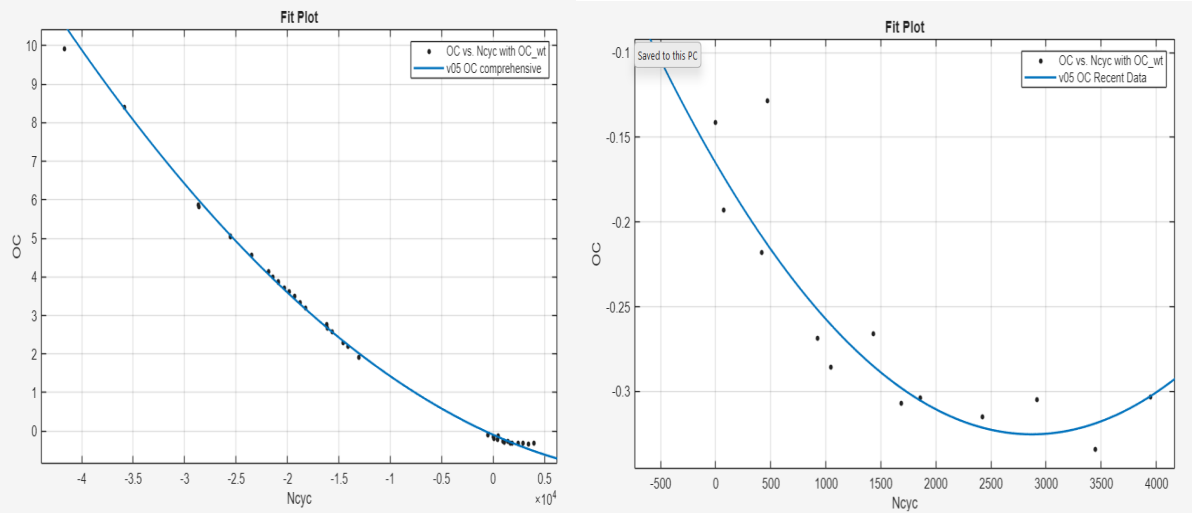
Figures/Charts (If Applicable)

Fig. 1



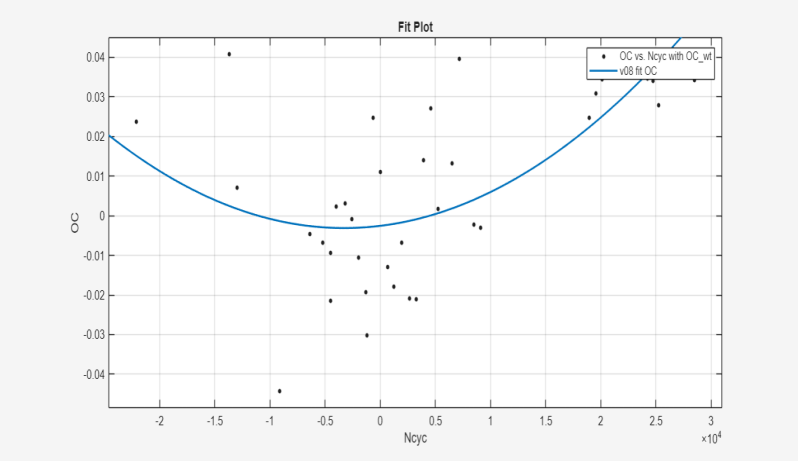
Light curves devised from existing period values for each RRL sample star. Notice some values do not seem to display that their used periods were accurate to the star's actual period

Fig. 2



Initial comprehensive O-C plot for V05 (left) and isolated recent data from 2019-present (right) data, both exhibiting levels of quadratic change suggesting period change

Fig. 3



O-C plot from comprehensive data of V08, as compared to V05 much more scattering is present, however data to the right of the figure added recently better supports a more quadratic trend

Acknowledgments

I would like to express my deepest gratitude to my mentor Dr. Andrew Layden for allowing me the opportunity to contribute to this very extensive research project, as well as my colleague Kathrine Douglas for her collaboration and aid along the way. I would also like to thank OSGC for allowing me the opportunity to present my findings to a wider audience.

References

1. Arellano Ferro, A., Rosenzweig, P., Luna, A., Deras, D., Muneer, S., Giridhar, S., & Michel, R. (2018). Period changes in the RR Lyrae stars of NGC 6171 (M107). *Astronomische Nachrichten, 339*(2–3), 158–167. https://doi.org/10.1002/asna.201813409
2. Catelan, M., & Smith, H. A. (2015). *Pulsating stars*. Wiley-VCH.

How Period of RR Lyrae Stars in M107 Have Changed

Student Researcher: Katherine Douglas

Advisor: Andrew Layden

Bowling Green State University
Physics & Astronomy

Abstract
In my astronomy research, I see how periods of RR Lyrae variable stars can change in the globular cluster, M107. A paper by A. Arellano Ferro et. al (2018, 'AF18'), published in 2018 showed how some variable stars in M107 have changing periods. AF18 collected data from 1935-1994 as well as 2015-2017, my research expands on this data. There are 24 RR Lyrae stars of interest in M107 that we continued to get data for from the Zwicky Transient Facility, (ZTF), a wide-field automated survey that consistently collects data, I focused on stars V13-V24. Using the known periods from AF18, we used our code to find good fitting light curves for each separate year of collected data. With this, we added new data to previous *O-C* curves to see how the periods of different variable stars are changing. The shape of the curve depicts how the period may be changing over time. Some stars have an increasing period while others have a decreasing period, and most are stable stars that don't have a change in period. With accurate data over a long period of time, these period-changing stars can help us better understand horizontal-branch evolution models for variable stars.

Project Objectives
The main objective of this project is to see how RR Lyrae variable stars may be changing in their periods by analyzing their phased light curves and *O-C* curves (where *O*-C is Observed minus Calculated times).

Methods
Data Mining: Known RA and Dec. values showing the locations for each star, were inputted into the ZTF database. Data was collected from their 2024 release. These files were then used to make light curves of each star.

Making Light Curves: The data files were added to a computer program and made into light curves. The data files included the star's magnitudes, the time of each observation, etc.. The AF18 period for each star was used to phase the data, giving the phased light curve shape. While making the phased light curves, occasional outliers were noted and later removed, resulting in the final light curve that either showed an RRab or RRc shape. The peak of each curve had an epoch value, or the time of maximum brightness, which was recorded to be used as the observed value, "*O*", for the *O-C* curves.

Making *O-C* Curves: *O-C* curves used the epoch values from the phased light curves, and a calculated value, "*C*", by using the star's period. This calculated value showed where the future times of maximum light would be for the star. New *O-C* data points were made and added to the previous data from AF18. These graphs were made in MATLAB where a line of best fit was added, and its coefficient values were recorded.

Results and Discussion
The *O-C* curves showed how the star's period may be changing over time based on the shape of the graph. Linear horizontal trends showed the star was a non-period changing star, with a correct AF18 period. Linear sloped trends showed the same, but the period could be corrected by adding the slope coefficient. Parabolic shapes showed the star had a steady period change with either an increase or decreasing period

based on if the parabola was concave up or down respectively. Two linear trends showed an abrupt period change in the star. Four stars were primarily studied for the results.
V18: Linear star with a corrected period compared to AF18. Less scatter, and slightly slanted due to zoomed in data.

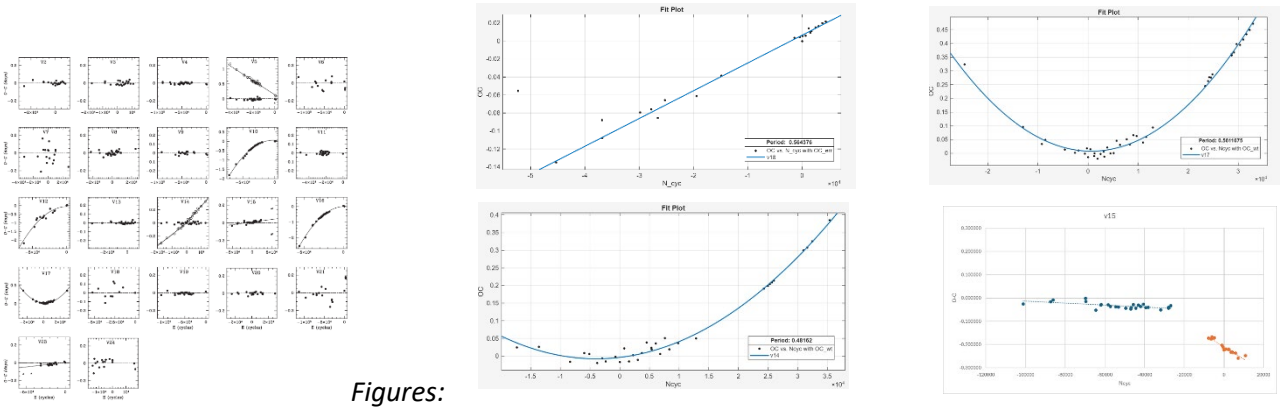
V17: Steady period changing star. Our recent data confirms and refines its parabolic shape.

V14: Steady period changing star. New data shows it could be a parabolic *O-C* curve, rather than an abrupt change as AF18 hypothesized.

V15: Abrupt period changing star. New data shows an abrupt change with two linear trends. One discrepant point from AF18 was confirmed to be going negative rather than positive.

Overall, this new data further confirms and refines the behavior of these stars, and more data in the next 10-20 years will continue to enhance our understanding of these variable stars and their evolution.

Figures/Charts



Figures: Far left) AF18's full O-C curve list. From 4, top left) Our V18 O-C curve. Top right) Our V17 O-C curve. Bottom left) Our V14 O-C curve. Bottom right) Our V15 O-C curve.

Acknowledgments
Thank you to my advisor Dr. Layden for guiding me with my research. Thank you, Nicholas Doughman, my research partner who did the other half of the stars in our globular cluster. Finally, thank you to OSGC for funding my college tuition so I can continue my research and my degree at Bowling Green State University.

References
Arellano Ferro, A., Rosenzweig, P., Luna, A., Deras, D., Muneer, S., Giridhar, S., & Michel, R. (2018). Period changes in the RR Lyrae stars of NGC 6171 (M107). *Astronomische Nachrichten*, *339*(2-3), 158–167.

Impact of Chemical Composition on the Mechanical Performance of a 3D-Printable Self-Healing Elastomer

Student Researcher: Robert "Max" Drexler

Advisor: Robert L. Lowe

University of Dayton

Department of Mechanical and Aerospace Engineering

Abstract

The development of **self-healing** elastomers for **soft robotics** is occurring at an increasingly rapid pace due to the need for resilient materials that are capable of **autonomously repairing minor damage** without human intervention. Compared to conventional *rigid* robots, *soft* robots leverage compliant elastomeric materials to enable *safe interactions with humans* and *on-the-fly adaptability to different physical environments*. Recently, the development of self-healing elastomers that are also **3D printable** has paved the way for creating parts with complex geometries and fine features (such as cavities and overhangs) that could not be achieved with traditional polymer casting processes. Similar exciting developments have been unfolding in the field of **stretchable electronics**, an emerging area of research focused on creating *soft, stretchable, and thin electronic circuits* using elastomeric materials. When embedded in a soft robot, sensors and stretchable circuitry enable **soft robotic systems that can sense and react to their environments**. ***Combining 3D-printed autonomously self-healing elastomers with stretchable circuitry and sensing presents a compelling opportunity for next-generation soft robotics with embedded resilient electronics.***

Project Objectives

Developed as a breakthrough material solution through a collaborative effort between the BAMS Lab, the University of Dayton Research Institute (UDRI), the Air Force Research Laboratory (AFRL), and the Massachusetts Institute of Technology (MIT), "BeckOHflex" is an **ultra-stretchable, self-healing elastomer** capable of **near-instantaneous self-healing in ambient, room-temperature conditions** [1]. Using a Bayesian Optimization Platform, the project is focused on intelligently navigating the design space of BeckOHflex, with a specific focus on virgin toughness, virgin hardness, and self-healed toughness. Aided by an EDBO+ optimization platform, the goal of the project is to determine a Pareto frontier (bounded design space) for BeckOHflex, highlighting the effects of chemical composition on mechanical properties (hardness and toughness) and self-healing efficiency, all in a rapid, high-throughput manner. *This design space will prove instrumental in developing substrates suitable for stretchable electronic applications.*

Methods

A Shore 00 analog durometer was used to measure the hardness of the "virgin," undamaged samples prior to tensile testing. Each sample's hardness was measured at three separate locations (each end and in the center of the gage), recorded after 15 s of contact, and then averaged. To determine the toughness of each "virgin" specimen, uniaxial tension testing was performed on an Instron 3365 universal testing machine equipped with a 2-kN load cell for force measurement. Crosshead displacement was measured by an integrated Instron LVDT. Tests were performed at a displacement rate of 50 mm/min, with up to 5 psi of pneumatic grip pressure. Engineering stress was calculated as measured force divided by original cross-sectional area, while engineering strain was calculated as measured crosshead displacement divided by grip-to-grip distance. Toughness was calculated as the area under the engineering stress-strain curve through numerical integration, with the toughness for each formulation reported as the mean of 4 to 6 different samples. To assess self-healing efficiency, virgin test specimens were cut horizontally across the center of their gage section with a clean razor blade and allowed to rest for 5 min. Afterwards, each end

of the specimen was placed back together under nominal manual pressure and allowed to self-heal for 5 min under ambient conditions. Post-healing uniaxial tension testing was then performed in the same manner as with the virgin samples. Self-healing efficiency was then calculated by dividing the average toughness of the self-healed samples by the average toughness of the virgin samples.

Results and Discussion

In total, 15 different formulations were synthesized, cured, and tested to begin populating the design space [**Figure 1**] with a few key trends emerging. First, virgin toughness generally increases with higher levels of acrylate (HDDA) [**Figure 2a**]. Second, self-healing efficiency is highest when there is a higher concentration of chain-transfer agent (thiol) [**Figure 2b**]. Third, hardness seems to have a direct correlation with percent volume of acrylate [**Figure 2c**]. With 15 different experimental formulations tested, the design space is approximately 50% through its initial experimental search. As more data is collected, a clearer Pareto frontier will allow for better insight into the effect of chemical composition on mechanical properties (hardness, toughness) and self-healing efficiency. From there, specific chemical compositions of BeckOHflex can be further investigated and tested to better understand its potential for stretchable electronic applications.

Figures

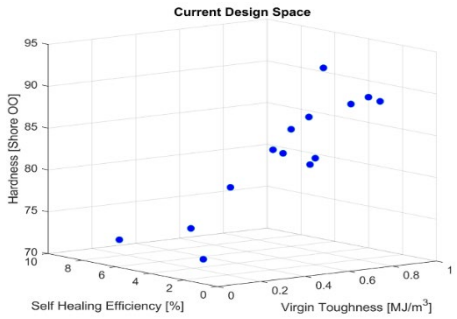


Figure 1*: Current design space based on 15 formulations of BeckOHflex*

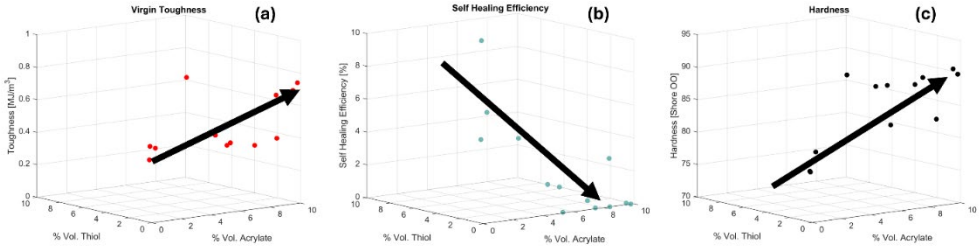


Figure 2*: Objectives of BeckOHflex campaign plotted against %vol of chemical precursors*

Acknowledgments

RMD and RLL would like to acknowledge support and guidance from AFRL, UDRI, and BlueHalo.

References

[1] Beckett, Joseph G., et al. “3D-Printable Elastomers for Real-Time Autonomous Self-Healing in Soft Devices.” *ACS Materials Letters* 7.1 (2024): 123-132.

Investigating Pulsed Flow for Efficient Cryogenic Chilldown

Student Researcher: Rahul Dulani

Advisor: Dr. Chirag Kharangate

Case Western Reserve University
Mechanical Engineering

Abstract
Cryogenic fluid management in space systems is critical due to the limited availability of propellant in microgravity environments. T he current experimental setup uses a two-way ball valve that allows continuous flow of cryogenic propellant through a tube to simulate and measure chilldown behavior. To enhance efficiency and reduce propellant consumption, our research aims to implement and test a pulsed flow system using a three-way ball valve. While data from continuous flow experiments have been collected and analyzed, the pulsed flow configuration has been designed but not yet tested. Based on previous results from NASA colleagues, pulsed flow with a 3-second period and a 10% duty cycle is expected to offer significant propellant savings while maintaining effective chilldown performance. T his research contributes to optimizing cryogenic fluid management strategies for future space missions.

Project Objectives
- Evaluate the thermal performance of continuous flow chilldown using a two-way valve.
- Design and implement a pulsed flow system using a three-way ball valve.
- Compare the thermal and propellant efficiency of pulsed versus continuous flow.
- Assess potential propellant savings while maintaining acceptable chilldown time.

Methods
- **Continuous Flow Setup**: Experiments were conducted using a two-way ball valve providing uninterrupted cryogen flow through a coated tube. Temperature sensors recorded data during chilldown.
- **Pulsed Flow System Design**: A three-way ball valve was installed, allowing redirection of flow between the tube and the propellant reservoir. The valve is controlled via a relay interfaced with LabVIEW, powered by a 24V DC supply and standard AC wall outlet.
- **Control Mechanism**: LabVIEW software was used to program a 3-second pulse cycle with a 10% duty cycle, enabling the system to alternate between energized (flow to tube) and deenergized (flow redirected to reservoir) states.
- **Expected Outcome**: Based on NASA data, a 4L coated tube using this pulsed cycle provides optimal propellant savings with a modest increase in chilldown time.

Results and Discussion
Experiments with the continuous flow setup have been completed and temperature data has been gathered. Analysis is ongoing. Experiments using the pulsed flow setup have not yet been conductged at the time of this report.

Future Work
- Conduct pulsed flow chilldown experiments in the current lab setup.
- Analyze and compare thermal data and propellant consumption between continuous and pulsed configurations.
- Optimize control parameters such as duty cycle and pulse duration for various tube geometries and coatings.

Acknowledgments
I would like to thank Anuraag Muniraj and Jayachandran K. Narayanan for their assistance in data gathering. I would also like to thank Dr. Chirag Kharangate for his guidance and for providing access to laboratory resources, and the Case Department of Mechanical Engineering for help in obtaining experimental data and figures.

References
Hartwig J, Chung JN, Dong J, Han B, Wang H, Darr S, Taliaferro M, Jain S, Doherty M. Nitrogen flow boiling and chilldown experiments in microgravity using pulse flow and low-thermally conductive coatings. NPJ Microgravity. 2022 Aug 9;8(1):33. doi: 10.1038/s41526-022-00220-9. PMID: 35945252; PMCID: PMC9363417

Ethanol-Induced Neural Activity in Male vs Female Rats

Student Researcher: Julie Dunlap

Advisor: Dr. Clare Mathes

Baldwin Wallace University
Department of Neuroscience

Abstract
The goal of this study was to determine if systemic ethanol administration induces neural activity in brain regions in female rats differently than it does in male rats. Most of the studies reviewed used exclusively male rats (Chang et al., 1995, Criado et al. 2000, Herring et al., 2004, Saalfield et al., 2019, Segovia et al., 2013) and this project aimed to determine if alcohol's impact is different in female rats. This is a problem because the prevalence of alcohol use disorder is increasing in women (White et al., 2015), yet women are underrepresented in basic research. This experiment may be used as preliminary research for future studies in the behavioral neuroscience lab at BW that will focus specifically on female rats.

Project Objectives
We hypothesized that the brains of male and female rats would process alcohol similarly, thus both sexes could be used in future research without concern of confounding sex differences. If there would be alcohol-induced sex differences at a neural level, this could provide information leading to different treatments between men and women with alcohol use disorder.

Methods
During the first phase of this study, a group of female rats (n=8) and a group of male rats (n=8) were exposed to saline injections before the experiment to acclimate them to the injection so that the stress of the large injection on experiment day did not influence our data. On experiment day, the group of female and group of male rats were either exposed to a concentration of ethanol (20% at 12.5 ml/kg ip, n=4/sex) or saline (n=4/sex). Two hours after the injection, the rats were euthanized and perfused, after which their brains were collected. The brains were sliced and stained through a process known as immunohistochemistry. We evaluated neural activity (as shown by the expression of Fos protein) in brain regions that are part of the limbic system, which processes information and guides behavior based on reward. These brain regions included the central nucleus and basolateral nucleus of the amygdala, the lateral hypothalamus, the lateral septum, and the nucleus accumbens. The data were *qualitatively* analyzed to determine if there were differences in Fos levels induced by ethanol between female and male rats.

The second phase of this study involved replicating the experiment to increase the sample size of this study. The third phase involved *quantitatively* scoring the Lateral Septum, specifically. To do this, I took images of the Lateral Septum in each rat from the replicate study. Quantitative analysis was done through the software ImageJ, which allowed human bias and error to be removed when determining Fos counts. Data was analyzed from both phases to determine if there were any significant differences between male and female subjects in the Lateral Septum.

Results and Discussion
We expected to see significantly more Fos in brain reward regions in at least the male rats that were injected with ethanol compared to those injected with saline, based on the literature reviewed. Unfortunately, we found that ethanol injection did not reliably induce Fos in the Lateral Septum when the data were analyzed (Figure 2) or when the male and female data were combined (Figure 2). Thus, we were unable to assess sex differences due to failure to replicate ethanol-induced Fos in male rats. We likely did

not replicate previous findings due to our procedure and potential stress on the animals on the experiment day. The rats went through acclimation to handling and injections before experiment day, but they may have still gone through too much stress on experiment day, potentially affecting our data. Going forward, we may use immunofluorescence instead of immunohistochemistry to stain our tissue, allowing for thinner slices, less background noise, and easier labels to show neural activity.

Figures

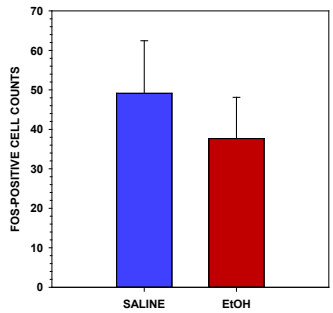


Figure 1. Ethanol did not induce Fos in the Lateral Septum.

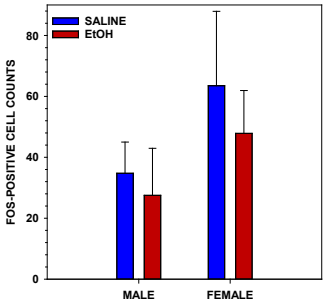


Figure 2. Ethanol did not induce Fos in male nor female rats.

Acknowledgements

Funding for this project was provided by OSGC and Baldwin Wallace Neuroscience Department. I would like to thank all the students involved in the Fall 2023 and Spring 2024 NRO459: Faculty-Student Collaboration for their help in this project. I would like to thank my advisor, Dr. Clare Mathes. I would also like to thank Sydney Miller, who performed this project alongside me. I acknowledge experimental and technical assistance by Gregg DiNuoscio. I am also grateful for the animal care provided by the Neuroscience vivarium staff.

References

1. Chang SL, Patel NA, Romero AA. Activation and desensitization of Fos immunoreactivity in the rat brain following ethanol administration. Brain Res. 1995 May 8;679(1):89-98. doi: 10.1016/0006-8993(95)00210-h. PMID: 7648269.
2. Criado JR, Morales M. Acute ethanol induction of c-Fos immunoreactivity in pre-pro-enkephalin expressing neurons of the central nucleus of the amygdala. Brain Res. 2000 Apr 7;861(1):173-7. doi: 10.1016/s0006-8993(99)02468-3. PMID: 10751579.
3. Herring BE, Mayfield RD, Camp MC, Alcantara AA. Ethanol-induced Fos immunoreactivity in the extended amygdala and hypothalamus of the rat brain: focus on cholinergic interneurons of the nucleus accumbens. Alcohol Clin Exp Res. 2004 Apr;28(4):588-97. doi: 10.1097/01.alc.0000122765.58324.6d. PMID: 15100610.
4. Saalfield J, Spear L. Fos activation patterns related to acute ethanol and conditioned taste aversion in adolescent and adult rats. Alcohol. 2019 Aug;78:57-68. doi: 10.1016/j.alcohol.2019.02.004. Epub 2019 Feb 22. PMID: 30797833; PMCID: PMC6612301.
5. Segovia KN, Vontell R, López-Cruz L, Salamone JD, Correa M. c-Fos immunoreactivity in prefrontal, basal ganglia and limbic areas of the rat brain after central and peripheral administration of ethanol and its metabolite acetaldehyde. Front Behav Neurosci. 2013 May 24;7:48. doi: 10.3389/fnbeh.2013.00048. PMID: 23745109; PMCID: PMC3662884
6. White A, Castle IJ, Chen CM, Shirley M, Roach D, Hingson R. Converging patterns of alcohol use and related outcomes among females and males in the United States, 2002 to 2012. Alcoholism, clinical and experimental research. 2015. 39(9), 1712–1726. https://doi.org/10.1111/acer.12815

Impact of Brain Infusion of the Exercise-Associated Myokine, Irisin, on Sucrose Preference and Neural Activation in Male Rats

Student Researcher: Mario J. Escobar

Advisor: Dr. Clare Mathes

Baldwin Wallace University
Department of Neuroscience

Abstract
Our project's primary goal was to determine if an intracerebroventricular infusion of irisin, a muscle-derived hormone, blunted sucrose preference in male rats, in a manner similar seen in post-exercise. Previous studies have extensively elucidated a chronic moderate exercise regime capability to reduce sucrose preference and intake in both rat models and humans. Irisin has also been found to be at transiently increased levels post exercise, while other studies verified irisin able to affect brain activity, specifically the lateral hypothalamus, suggesting irisin as the mechanistic link between exercise and its effect on taste-guided behaviors, as seen in the blunting of sucrose preference. Using male rats (n = 12), we first surgically implanted cannulas targeting the lateral ventricle. After rats were fully recovered, they were infused with irisin (n = 6; 0.25 µg irisin/µL in saline), or vehicle control saline (n = 6) (total vol = 2µL). A two-bottle sucrose preference assay 30 minutes post-infusion showed no significant differences compared to their respective control group. A separate irisin infusion was done 1 week after the conclusion of the two-bottle sucrose preference assay, wherein brains were extracted and stored for future slicing, immunohistochemical staining, and data analysis for lateral hypothalamic activity.

Project Objectives
We seek to determine if ICV administration of irisin, like that of exercise, shifts sucrose preference in rats, and if irisin is the mediator between exercise and its effects on brain activity and taste-guided behaviors.

We hypothesize that a physiologically relevant (brain-wide) infusion of irisin, like that of exercise, will:

1. **Decrease** sucrose preference in rats, similar to how exercise reduces sucrose intake.
2. **Increase** FOS expression in the lateral hypothalamus, conducive to increased brain activity of the area.

Methods
Experiment 1: Stereotaxic Surgery & Sucrose Preference Assay
Rats were surgically implanted with a cannula targeting the right ventricle (AP: -0.5 mm, ML: ±1.6 mm, DV: -4.1 mm [from bregma]). We then verified cannula placement with ICV infusion of 5-thio-D-glucose (5TG) into the lateral ventricle and measured blood glucose at baseline, 45 min, and 60 min post-infusion. Cannulas were deemed functional if glucose levels increased ≥50% from baseline. Rats were later infused with 0.50 µg of irisin at a concentration of 0.25 µg irisin/µL saline, or vehicle control saline (total vol = 2 µL). A two-bottle sucrose preference test was then done to assess whether ICV irisin significantly alters sucrose preference. The timepoints for bottle weighing were at 15min, 30min, 1h, 2h, 4h, 24h, and 48h, respectively. Data analysis is still needed to be done, with a two-way repeated measures ANOVA planned to be done to compare Irisin vs Saline at multiple recorded timepoint (sig = $p < 0.05$).

Experiment 2: Irisin Infusion & Analysis of LH Activity:
Following a week after the conclusion of the two-bottle sucrose preference test, rats were once again infused with 0.5 µg of irisin at a concentration of 0.25 µg irisin/µL saline, or vehicle control saline (total vol = 2µL). 2 hr post-infusion rats were euthanized via an overdose of barbiturates, followed by transcardial perfusion of paraformaldehyde (PFA) for brain tissue fixation. We plan to coronally slice the brains (50 µm), process them for FOS immunoreactivity, mount them on gelatin-subbed slides, and cover-slipped for analysis. Brain ROI will be identified and blinded. We will use ImageJ to quantify FOS expression. Size, contrast, and roundness of FOS will be standardized and counts per defined area will be determined, following an established protocol in our lab. Fos count per defined area of LH will be compared using an independent-sample t-test (sig = $p<0.05$)

Results and Discussion

Ultimately, we seek to assess if an ICV infusion of irisin blunts sucrose preference in a manner like exercise, and if FOS positive cell counts in the LH increase. For Experiment 1, we expect the irisin group to have a significantly lower sucrose preference (see Fig. 1). Concomitantly for Experiment 2, we expect the irisin group to have significantly increased FOS-positive cell counts in the LH, supporting increased activity of the region by irisin (see Fig. 2). The expected outcomes from both experiments would support irisin's role in mediating the exercise-induced decrease in sucrose preference and increased activity in the LH observed in past literature. Future work to analyze sucrose preference data for Experiment 1 and finish the histology portion for Experiment 2 is planned to be conducted at a future date.

Figures/Charts (If Applicable)

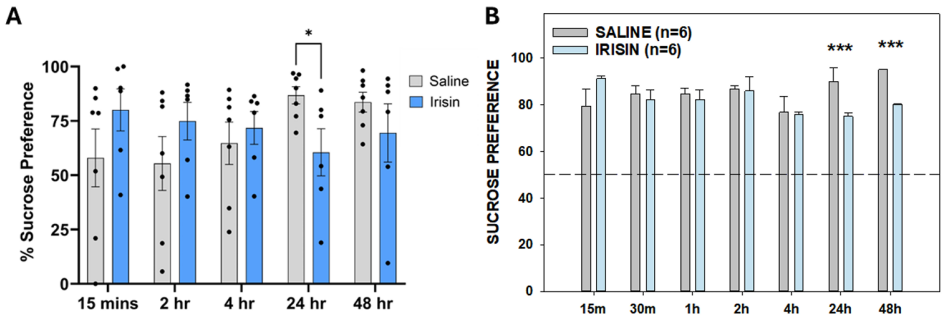


Figure 1. Effect of intracerebroventricular (ICV) irisin infusion on sucrose preference in rats.
A) Actual data from female rats (n=6 per group) showing percent sucrose preference following ICV infusion of irisin or saline across multiple time points. A significant reduction in sucrose preference was observed at 24 hours in the irisin group compared to saline ($p<0.05$). Data provided by Dr. Sarah Terrill[4].
B) *Expected outcome* of sucrose preference in male rats (n=6 per group) based on planned replication of the same protocol. Data are modeled to reflect anticipated group differences, particularly at the 24- and 48-hour time points, consistent with hypothesized behavioral effects of irisin.

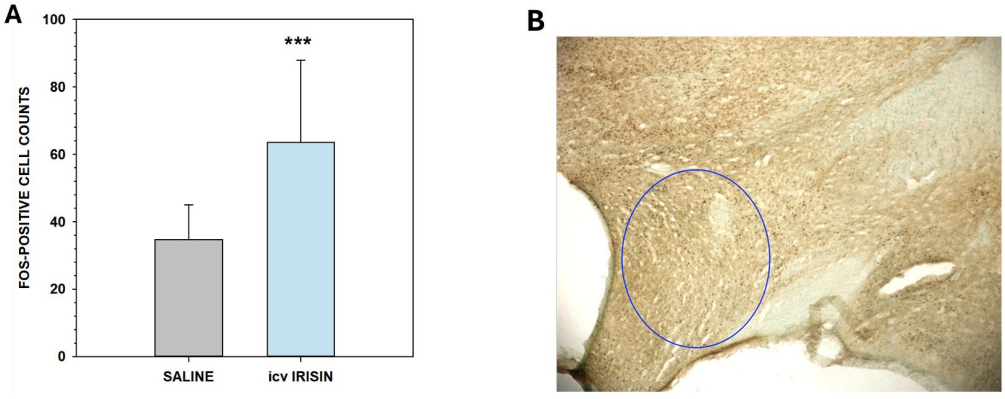


Figure 2. Expected lateral hypothalamic (LH) activity following intracerebroventricular irisin infusion.
A) *Expected results* of Fos-positive cell counts in the LH, predicting significantly elevated neural activity in the ICV irisin group compared to saline controls.
B) Representative coronal brain section highlighting the location of the LH (circled) for anatomical reference. Image provided by Sydney Miller.

Acknowledgments

We thank Dr. Sarah Terrill for providing data, Sydney Miller for assisting in postsurgical care and providing the Fos image, Kristen Sperber for providing postsurgical care, Gregg DiNuoscio for technical assistance, and the BW husbandry staff for animal care. Funding for M.E. provided in part by the Ohio Space Grant Consortium Summer Grant and Academic Year Scholarship. Poster and figures made in BioRender.

References

1. Alvarez-Monell C, Cueva E, Belda X, Armario A. Long-term exercise reduces saccharin preference and modulates corticosterone and neuropeptide mRNA levels in rats. Front Behav Neurosci. 2022;16:1017350. doi:10.3389/fnbeh.2022.1017350.
2. Rodrigues da Silva e Santos D, Gonçalves de Medeiros TG, de Jesus Gonçalves CA, Lacerda DC, de Andrade TG. Physical exercise modulates stress and anhedonia in rats: Forced swimming as a model of exercise. Sci Rep. 2024;14(1):3608. doi:10.1038/s41598-024-84391-3.
3. Bao Y, Zhang Y, Ma X, Wang C, Zhang L. Irisin: A potential hormone for the treatment of metabolic and mood disorders. Metab Brain Dis. 2022;37(2):231–246. doi:10.1007/s11011-021-00818-1.
4. Terrill S. 2025. Personal communication. Unpublished data shared with the authors, April 2025.
5. Ferrante C, Orlando G, Recinella L, Leone S, Chiavaroli A, Di Nisio C, Shohreh R, Manippa F, Ricciuti A, Vacca M, et al. 2016. Central inhibitory effects on feeding induced by the adipo-myokine irisin. European Journal of Pharmacology. 791:389–394. doi:10.1016/j.ejphar.2016.09.011.

An Investigation Into The Synthesis of Schiff Base Fullerene Complexes

Student Researcher: Love Faison

Advisor: D.R. Buffinger, PH.D.

Wilberforce University
Biology

Abstract
A study on the creation of new Schiff base fullerene complex derivatives has attracted a lot of interest due to their many uses in organic photovoltaics and other fields. Research on materials based on fullerenes has broadened since 2015 to encompass organic thermoelectrics, molecular electronics, organic electrochemical transistors, and perovskite solar cells. This study uses a Schiff base reaction, which is well known for its effectiveness in producing complex organic compounds, to synthesize a new fullerene derivative. To verify its structure and characteristics, the synthesized molecule will be thoroughly characterized using methods including NMR, IR, and UV-Vis Spectroscopy in addition to elemental analysis. If time permits, chelation experiments with transition metal ions will be performed to explore the potential of these complexes in advanced material applications. This investigation aims to contribute to the growing body of knowledge on fullerene-based materials, emphasizing their potential in emerging technologies.

Objectives
This research project has three objectives.

1. The first is to synthesize a bis-functional fullerene-Schiff Base compound. The Schiff Base substrate will be N,N'-ethylenebis(acetylacetone imine) which is referred to as H2acacen.

2. The second objective is to characterize the optoelectronic properties of the bis-functional compound using IR, NMR and optoelectronic properties.

3. The third objective is to incorporate transition metal ions such as Co+2 and Cu+2, into the Schiff Base scaffolding to ascertain the impact the metal ions have on the optoelectronic properties of the compound.

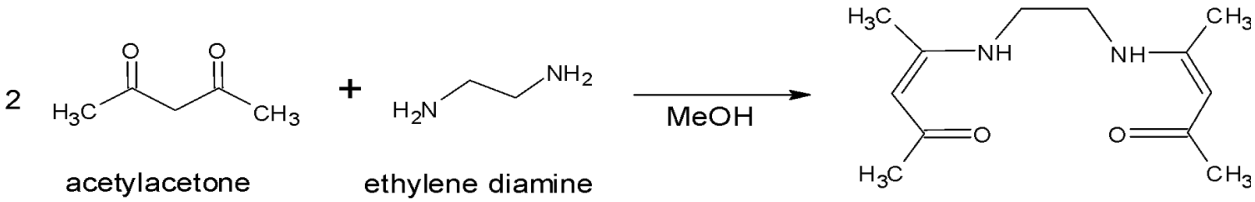
Methods
For the preparation of H2 Acacen, ethylene diamine ($C_2H_4N_2$ - 98.0%), acetylacetone ($C_5H_8O_2$ - 99.0+%) and methanol (CH_3OH - 99.9%) were purchased from Fisher Scientific and used as received. Fullerene-C60 (99.9%) was purchased from Sigma Aldrich and used as received. Iodine (I_2 - 99.8%) and 1,8-Diazabicyclo[5.4.0]undec-7-ene (DBU – 98.0+%) were purchased from Fisher Scientific and used as received. Toluene (PhMe – 99.8%) was purchased from Sigma Aldrich and used as received.

Infrared spectroscopy data was collected using a Nicolet 380 FT IR Spectrometer.

Silica Gel – 60, Thin Layer Chromatographic Plates were purchased from Fisher Scientific.

Experimental Procedure (Methods)

H2AcAcen (N,N`-ethylenebis(acetylacetone imine) was prepared using the procedure by Holm, Et. Al. (R.H. Holm, 1966) and is described below.



acetylacetone
$C_5H_8O_2$
MW: 100.13 g/mol

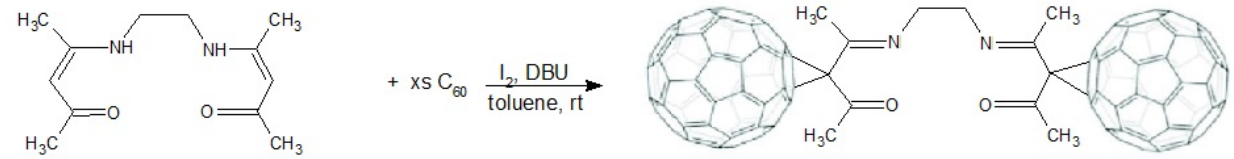
ethylene diamine
$C_2H_4N_2$
MW: 60.12 g/mol

H_2acacen
$C_{12}H_{20}N_2O_2$
MW: 224.34 g/mol

Solutions of acetylacetone (10.00g, 0.10 mol) dissolved in methanol (10.0 mL) and ethylene diamine (3.0 g, 0.05 mol) also dissolved in methanol (10.0 mL) were prepared. Both solutions were cooled in an ice bath. The ethylene diamine solution was slowly added to the acetylacetone solution with stirring. Following the addition of the ethylene diamine, the reaction was warmed to room temperature and the solvent removed nearly to dryness using a rotary evaporator. The solid was filtered using a Büchner funnel and left to dry under vacuum for a minimum of 5 minutes.

H2acacen(C60)2

The synthesis of H2acacen(C60)2 will be attempted using the following reaction scheme.



H_2acacen Fullerene

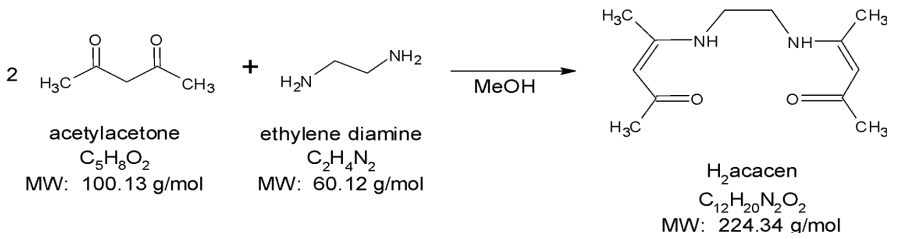
DBU (0.0041g, 0.0268 mmol) will be added to a stirred solution of H2acacen (0.0015g, 0.0067 mmol), C60 (0.010g, 0.0139 mmol), I2 (0.0019g, 0.0074 mmol) in 50 mL of toluene in a 100 mL round bottom flask adapted from a comparable material (Figueira-Duarte, et. al. 2006). The reaction will be permitted to stir at room temperature for 24 hours, and TLC analysis of reaction mixture will be used to assess product formation. The mobile phase of the will be chosen based upon the mobility of C60 and H2acacen on the TLC plates using various solvent mixtures.

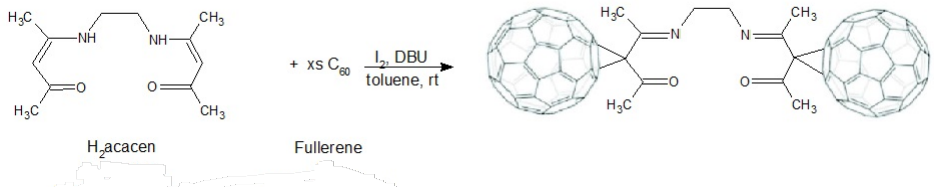
Results and Discussion

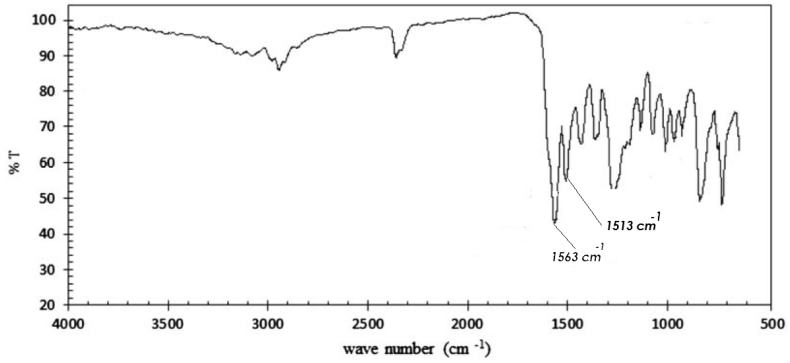
The IR spectrum confirmed that H2azacen was successfully made, matching previous studies. The Schiff Base (H2acacen) formed a colorless crystalline solid. The next step is to see if it successfully binds to fullerene and to study its electronic properties.

Now that H2acacen is confirmed, the team will finish reacting it with C60 fullerene. We will test different solvent mixtures to see which one works best. Once the Schiff Base is bound to fullerene, we'll try adding metals (like cobalt and copper) to see if they change its properties. This could lead to better materials for things like batteries, sensors, and energy storage.

Figures and Charts







Acknowledgements

I would like to express my sincere appreciation to Wilberforce University for supporting and funding this research, and to my mom for her support and guidance. Thank you to OSGC, NASA, and Ohio Aerospace Institute for the amazing experience and opportunity.

References

1 W. Yan, S. M. Seifermann, P. Pierrat and S. Brase, *Org. Biomol. Chem.*, 2015, **13**, 25-54.

2 P.J.F. Harris, *J. Carbon Research*, 2020, **6 (4)**, 71-82.

3 R.H. Holm, G. W. Everett and A. Chakravorty, *Progr. Inorg. Chem*., 1966, **7**, 83.

4 T.M. Figueira-Duarte, J. Clifford, V. Amendola, A. Gegout, J. Olivier, F. cardinal, M. Meneghetti, N. Armaroli and J. F. Nierengarten, *Chem. Commun.*, 2006, 2054-2056.

5 S. Ozkar, D. Ulku, L.T. Yildirim, N. Biricik, B. Gumgum, *J. Mol. Struc.,*2004, **688 (1-3)**, 207-211.

Custom Void Fraction Sensor

Student Researcher: Colin Fokine

Advisor: Dr. Mitch Wolff

Wright State University
College of Engineering and Computer Science

Abstract
The desire for a non-proprietary Electrical Capacitance Tomography (ECT) sensor capable of measuring void fraction led to the research, design, construction, and testing of a sensor capable of non-invasively measuring the void fraction in two-phase flow systems. A drop in capacitance across a flowing medium can be used to determine the void fraction in the system. The sensor, built using quartz tubing and copper tape electrodes, used a Silicon Labs C8051F970 for initial data acquisition and later integrated a LCR meter for higher sensitivity. The LCR meter was set to a dual measurement mode, measuring both capacitance and conductance. Initial calibration used iodized table salt to simulate a 'full' and an 'empty' reading by tilting the tube. The sensor was then tested within a system using R-134a, collecting data at three operation levels: 0W (full liquid), 750W (mixed flow), and 2000W (full vapor). Additionally, a ramped case in 100W increments from 0W to 2000W was performed to observe transient behavior. The sensor built showed a strong correlation between capacitance drop and increased void fraction. Conductance showed no correlation. Interpolation between the operation levels was used to create a calibration curve. Our sensor, as is, is effective for steady-state void fraction measurements, but is not currently suitable for high-fidelity transient measurements, as there is too much noise. An uncertainty analysis is required to determine the accuracy of the measurements.

Project Objectives
The goal of this project was to build and validate a non-proprietary and low-cost ECT sensor capable of measuring void fraction non-invasively. Additionally, this sensor would be integrated into LabVIEW for real-time data acquisition and calibration. Using these real-time measurements, a calibration curve will be established, directly displaying the correlation between capacitance and void fraction.

The development of our ECT sensor builds upon literature aimed at investigating behaviors and improving the methods of observing two-phase flow. These prior studies have provided the foundation for construction and flow behavior. This foundation informed the design, calibration, and evaluation of the custom sensor.

Zachary Carner [1] conducted a study of void fraction and quality correlation in pulsed-power thermal systems using ECT sensors. His work demonstrated the viability of the separated flow model, and more importantly, provided a framework for evaluating sensor performance under transient conditions. Hugo Canière [2] explored the use of algorithms to classify refrigerant two-phase flow patterns based on capacitance signal maps. While our goal was not to map or classify the flow, his study informed us of the physical design of our sensor. More specifically, the use of grounded guard electrodes ensures well-confined electric fields. Kathleen De Kerpel [3] investigated refrigerant flow behavior around sharp turn bends. Her design improved upon Canière's and informed our efforts to reduce the sensor profile while maintaining functionality.

Methods

The sensor was constructed using a quartz tube for visibility and to maintain a consistent inner diameter with the system used for validation. Copper tape electrodes were placed uniformly for field generation, and guard electrodes were added for field confinement and noise reduction.

An insulated 4-channel wire was used, and the unused wire was removed. The red wire was connected to the charged electrode. The ground wire was connected to the system's common ground. The other side was uncharged and treated as the measuring electrode. The sensor was then encased in a 3-D printed casing, and the empty space was filled with epoxy. The final sensor can be seen in Appendix B.

Initial testing was conducted using salt to validate the sensor's ability to detect full/empty readings. This was done using both the Silicon Labs Board and the LCR Meter.

Eventually, only the LCR meter and the sensor were integrated into a two-phase flow thermal system that used R-134a. The system was run at three power levels, 0W (full liquid), 750W (midpoint), and 2000W (full vapor). Additionally, a ramp case from 0W to 2000W was conducted at 100W steps every 30 seconds. LabVIEW was used to monitor and acquire data during tests. A commercial ECT sensor was also run, and the permittivity was measured at the same time in their proprietary software. Void fraction can be found from this measurement by subtracting the measured value from 1. The calculated value is used to create the calibration curve for void fraction estimation through interpolation between known states.

Results and Discussion

All graphical and tabled results can be requested from the author (fokine.3@wright.edu). From our sensor, capacitance decreased as power and void fraction increased. This trend remains true across static and dynamic testing. While conductance exhibited minor trends, no consistent or useful correlation was observed.

The correlation curve equation for capacitance was found to be:

$$\alpha = -3.6180e12 \times Cp + 1.4801e1$$

Equation 1: Void Fraction from Capacitance Measurement

As a result, our sensor validated this method and design for void fraction measurement. Additionally, the sensor built could measure void fraction and be integrated into laboratory software. An uncertainty analysis needs to be conducted for any laboratory use to determine accuracy. The built sensor is recommended only for non-dynamic flows, as noise leads to measurements outside of the accepted norm. This could be the result of unknown shorts in the system, or the epoxy used may have been slightly conductive. In conclusion, further investigation is needed to further refine the design and eliminate noise.

Acknowledgments

- Mitch Wolff
- Abdeel Roman
- Zach Carner
- Brian Ruggles
- Victor Tsao
- Dough Johnson
- John Horwath

References

[1] Carner, Zachary. Void Fraction and Quality Correlation Analysis Using the Separated Flow Model for Pulsed-Power Heat Loads. 2024.
[2] Canière, Hugo. “Mapping of Horizontal Refrigerant Two-Phase Flow Patterns Based on Clustering of Capacitive Sensor Signals.” International Journal of Multiphase Flow, vol. 99, 2018, pp. 173–184.
[3] De Kerpal, Kathleen. “Refrigerant Two-Phase Flow Behavior and Pressure Drop Up and Downstream of a Sharp Return Bend.” Applied Thermal Engineering, vol. 162, 2019, 114277.

All results, photographs, and tables are available upon request from the author: fokine.3@wright.edu

Investigating Tandem Propeller Performance in Multirotor Aircraft

Student Researcher: Michael Foster

Advisor: Sidaard Gunasekaran

University of Dayton
Department of Mechanical and Aerospace Engineering, Mechanical Engineering

Abstract
Strategic placement of the rotors in a non-planar configuration can improve power efficiency in multirotor aircraft. To validate this concept, a custom-built multirotor was developed to conduct flight tests based on a prior wind tunnel study at the University of Dayton. The original study, conducted in the University of Dayton Low Speed Wind Tunnel (UD-LSWT), demonstrated that a negatively staggered rotor configuration with a vertical offset of 60% of the propeller diameter (0.6 d_z) maximized power savings of individual rotors tested in tandem configuration. Flight test data confirmed improved power efficiency in negatively staggered configurations, achieving up to 18% power savings compared to a conventional configuration without vertical offset, thereby indicating the practical viability of such configurations. However, flight testing also revealed that at higher flight speeds, offsets beyond 0.2 d_z yielded diminishing returns, a trend not observed in the prior study. As a result, a 0.2 d_z offset was identified as the optimal configuration for the tested flight regime, as it balanced trade-offs between power efficiency and drag-induced performance losses. Though multirotor mass was held constant in this study, performance benefits of vertical offset are only realized if they outweigh penalties associated with increased structural mass, which is more easily mitigated in a 0.2 d_z configuration.

Project Objectives
Fixed-pitch propeller-driven multirotor aircraft are a growing endeavor throughout the aerospace industry. The shift from helicopters to multirotor aircraft for vertical takeoff and landing (VTOL) applications is driven by advances in electric motor, battery, and flight-control technologies. A common method to increase the payload of eVTOL vehicles is to add more propellers, which also helps achieve lower disk loading, thereby improving efficiency and range [1]. These eVTOL air vehicles often operate in near-edgewise flight conditions, where the rotor discs are relatively parallel to the freestream. The downstream rotors of multirotor aircraft operate within the turbulent downwash of the upstream rotors, thereby reducing efficiency due to factors such as wake interference, blade-vortex interactions, and flow unsteadiness. Consequently, rotor proximity significantly influences the magnitude of these effects.

In hover, overlapping or closely spaced rotors experience wake impingement, which alters the local inflow conditions and reduces thrust efficiency, as observed by Dingeldein [2] in wind tunnel studies on multirotor configurations. In forward flight, rotor-rotor interactions becomes more complex, often resulting in uneven loading and pitching moments that destabilize the aircraft. Otsuka et al. [3] demonstrated that such flow interference can induce pitching moments in quadrotor UAVs, while Prudden [4] investigated the broader aerodynamic implications for multirotors in forward flight. A well-established method of reducing rotor interference is to increase the horizontal spacing between upstream and downstream rotors [4, 5]. However, this approach increases the overall footprint of the aircraft, which may be disadvantageous for certain applications.
For tandem propellers, vertically offset configurations have shown potential to mitigate some wake interference effects. Cai et al. [6, 7] systematically investigated these configurations in a wind tunnel, revealing how vertical and horizontal offsets influence performance, particularly in scenarios involving staggered or overlapping propellers.

Cai et al. [6] evaluated the performance of a negatively staggered configuration, where the downstream rotor was positioned above the plane of the upstream rotor, by comparing the power consumption of tandem rotor configurations (P_t) to that of two standalone rotors (P_s) producing equivalent thrust with no rotor interference. Testing was conducted at incidence angles (θ) of 90° and 75° to represent moderate and aggressive operating ranges of multirotor aircraft in edgewise flight, respectively. At an incidence angle of 90°, an increase in vertical offset corresponded to a decrease in the power consumed across all evaluated advance ratios, indicating reduced rotor

interference. As the vertical offset increased, power consumption decreased such that with a vertical offset of $d_z = 0.6$, the difference in power consumption of the tandem rotors and two isolated rotors was negligible. Similar trends were observed at an incidence angle of 75°, although the power consumed in all configurations was less.

Consequently, the prior study suggested that power efficiency can be improved while maintaining a compact footprint of a multirotor aircraft by implementing vertical offsets to reduce rotor interference. However, the study evaluated only separately mounted tandem rotors in a wind tunnel, thereby neglecting factors such as flight stability, airframe aerodynamics, and drag introduced by the additional airframe components necessary for implementing vertical stagger. To validate the practical performance of negatively staggered configurations, a custom multirotor test platform was developed and flight tested. Unlike wind tunnel experiments on isolated rotors, flight testing of a complete multirotor aircraft enables examination of otherwise inaccessible variables and provides a more realistic assessment of vertical offset performance. Furthermore, development of a test platform advances the technology readiness level (TRL) of vertical offset configurations.

Methods

In accordance with the prior wind tunnel study at the University of Dayton [6], a custom multirotor was developed to accommodate vertical offsets of 0.0, 0.2, 0.4, and 0.6 times the propeller diameter (d_z). The multirotor was outfitted with an array of components to autonomously maintain stable flight paths, retain communication with a ground station, and record pertinent data.

Shown in Figure 1, the multirotor was powered by four KDE 2814XF-515 brushless motors paired with two-bladed 12.5” x 4.3 KDE propellers, both of which were utilized in the previous experimental studies [6, 7]. Four T-Motor F-35A electronic speed controllers (ESCs) were employed, with each ESC controlling an individual motor through DShot, a digital communication protocol. To mitigate any electrical noise passed to the ESCs from surrounding circuitry, a 35V 1000µF capacitor was placed in parallel with the DC input of each ESC. Each motor and propeller assembly, along with its respective ESC, was attached to an off-the-shelf Lumenier QAV-R carbon fiber arm. A Holybro PM07 14S Power Distribution Module was used to distribute power from the multirotor battery to all onboard electronics. The test vehicle's power source was an HRB 60C 6S 4000mAh 22.2V LiPo battery. Flight control and data acquisition were handled by a Pixhawk 6C flight controller running PX4, an open-source autopilot firmware with autonomous capabilities. The Pixhawk controlled speed, heading, and altitude of the vehicle to match predetermined flight paths. During flight, data on attitude, speed, total power consumption, and individual rotor rotational velocity were recorded at a rate of at least 4 Hz. The relatively low sampling rate was due to the processing constraints of the Pixhawk flight controller.

Since the addition of a vertical offset shifts the center of mass of the multirotor aircraft aft, an in-house-built balance-checking device was constructed, and the aircraft’s battery was strategically positioned to counterbalance the additional weight introduced by the vertical offset. Since the addition of a vertical offset alters the mass of the multirotor, an array of custom 3D-printed supplementary weights were used to keep the multirotor weight constant between vertical offset configurations. The weight of the aircraft across all configurations was 2460 g ± 6 g, accounting for slight variations in battery weights, as multiple HRB 60C 6S 4000mAh 22.2V batteries were used during testing.

Flight testing was conducted to compare the power consumption of the multirotor with a vertical offset to a baseline configuration without vertical offset. The tests utilized GPS-controlled flight paths programmed in QGroundControl software to maintain stable speed, heading, and altitude. This procedure ensured controlled flight paths with repeatable velocities and altitudes throughout testing.

During testing, the mass was kept constant, both with vertical offset and the baseline configuration. Although the benefits of a vertical offset are realized only if they outweigh the drawbacks of the increased weight required to implement it, the flight testing had two primary objectives. The first was to validate the results of the previous study using flight test data [6], and the second was to determine whether stable edgewise flight could be achieved with a

vertical offset. The corresponding test matrix is shown in Table 1. As determined by the previous study [6], power consumption decreases as a function of longitudinal offset (d_y). For this reason, a longitudinal rotor offset of 1.20 times the propeller diameter was selected, constrained by fuselage manufacturing limitations. A range of vertical offsets(d_z) between 0 and 0.6, in increments of 0.2, were chosen to compare the potential power savings of different configurations. Forward flight speeds of 3, 6, 9, and 12 m/s were selected to achieve varying velocities and vehicle incidence angles.

Flight tests were conducted at dawn under calm wind conditions to minimize statistical variance in collected data. A representative flight path is shown in Figure 2. The flight path included takeoff, acceleration, cruise, deceleration, and landing, as depicted in the figure. For each test case, the multirotor accelerated, cruised, decelerated, and rotated heading by 180° six times before landing. For each configuration, three "down-and-back" paths were conducted to reduce statistical variation, resulting in six effective runs per case. For each case the three runs with the lowest power consumption that met flight stability requirements were selected for analysis. A ground-based anemometer was positioned at the endpoint of the flight path to measure wind direction and speed throughout each run. During all test runs, ambient wind speed and direction were logged at a frequency of 1 Hz.

This study focuses on the power consumption of a multirotor during steady edgewise flight, characterized by steady-state velocity, altitude, and heading. Consequently, all flight segments recorded by the flight controller, besides cruise conditions, were systematically excluded from analysis. To minimize human error, a custom MATLAB script was developed to identify and isolate flight segments meeting the steady-state criteria. The script analyzed flight test logs for all six runs of each configuration. First, a speed threshold was applied to identify "cruise" segments where the speed remained within ±0.5 m/s of the target value. Each identified segment was evaluated to ensure altitude stability within a 2-meter range. Runs failing to meet this criterion were excluded from further analysis. The remaining runs for each configuration were then assessed to determine the three with the lowest average power consumption, which were selected for inclusion in the results presented in this paper.

Results and Discussion

Figure 3 illustrates the instantaneous wind speed and direction for all selected test runs, with the multirotor's flight path heading overlaid. As shown, the wind direction generally aligns with the flight path, acting either as a headwind or tailwind depending on the specific test run's flight direction. Among all multirotor speeds, the 6 m/s test runs exhibit the largest variation in wind direction and the greatest deviation from the flight path heading. The wide spread of data points indicates gusty conditions, although crosswinds remain calm, with gusts never exceeding 3.5 m/s. In contrast, the 12 m/s test runs show two distinct groupings of wind direction, one from the East and one from the West, each with a small spread. These groupings suggest gusts with 180° heading changes, which could momentarily push the multirotor off its flight path as it reacts to these changes. Despite these variations, wind conditions remained calm across all test runs. This indicates that statistical variations due to ambient conditions were minimal, enabling consistent and repeatable data for attitude, flight speed, and altitude.

Across all runs selected for analysis, multirotor speed, altitude, and pitch remained stable. Specifically, the median sampled multirotor speed closely aligned with the target speed in each case, indicating that the vehicle achieved the desired cruise velocity with a high degree of accuracy. When each recorded speed was plotted as a box-and-whisker plot, narrow notches around each median recorded speed was observed, suggesting consistent and repeatable speed control. When measured altitude data for each flight speed was represented as a box-and-whisker plot, it was observed that the multirotor maintained a stable median altitude, ranging between 14.95 and 15.25 meters AGL, depending on the tested flight speed. For each speed, the altitude variation from the average never exceeded 0.6 meters, approximately $\pm$4%. The 6 m/s test cases exhibited the largest IQR, indicating greater altitude variability during those tests. As expected, regardless of the vertical offset configuration, the multirotor pitch angle became more negative as flight speed increased, reflecting the larger downward-pitch angles required to maintain stable cruise flight at higher speeds. At low flight speeds of 3 and 6 m/s, the pitch angle remained relatively constant across all vertical offsets. At speeds of 9 m/s and 12 m/s, the pitch angle increased in magnitude as vertical offset increased. This variation in pitch with vertical offset may result from an increase in drag correlating with the increase in frontal

area of the multirotor due to rear-rotor offsets or from the shift of the vehicle's center of gravity along the +z-axis (CG in x and y axes remained the same for all cases) caused by the offsets-stilts used for the rear rotors.

The consistency in multirotor attitude, flight speed, and altitude data across all test cases confirms that the aircraft maintained stable edgewise flight regardless of vertical offset. Additionally, this uniformity validates the comparison of power consumption across all cases. The power consumption for the three selected runs of each test case was averaged and plotted against flight speed, as shown in Figure 4.

Across all vertical offsets, power consumption decreases with increasing flight speed, indicating improved rotor efficiency, until a flight speed of 9 m/s, where efficiency begins to decline significantly. The results demonstrate that the power consumption benefits of a vertical offset are evident across all tested flight speeds and become more pronounced at higher speeds. The confidence in these benefits is supported by the relatively small error bars for each test case. However, for vertical offsets of 0 and 0.2 d_z at 9 m/s, the error bars are slightly larger than average, likely due to ambient conditions during those specific runs. At a flight speed of 3 m/s, the decrease in power consumption with increasing vertical offset is minimal. Additionally, at this same flight speed, an offset of 0.6 d_z was found to increase the power consumption of the multirotor compared to the configuration without any vertical offset. This increase in power consumption was consistently observed across multiple test runs conducted on different flight-test days, making it unlikely that the result was due to testing error. Instead, this outlier may be attributed to a possible harmonic interaction or increased drag caused by the vertical offset geometry, which outweighs the benefit of reduced rotor interaction at such a low cruise speed.

The average power consumption was normalized as a percentage difference from the baseline configuration with a vertical offset of 0.0 d_z, as shown in Figure 5. Generally, the percent change in power consumption increased with velocity, indicating that while vertical offsets improve efficiency across all tested flight speeds, the benefits become more pronounced at higher speeds. This trend may be attributed to the increase in pitch angle correlated with higher flight speeds, where the rear rotors experience greater downwash from the front rotors in the absence of a vertical offset. Additionally, flight test data for an offset of 0.2 d_z shows the most uniform trendline of increased power savings compared to the 0.4 and 0.6 d_z configurations, which exhibit more erratic trends. Across the offset cases of 0.2, 0.4, and 0.6 d_z, the power savings remain relatively consistent with each other. This suggests that while introducing a vertical offset of 0.2 d_z significantly improves power savings, further increasing the offset yields diminishing returns. At a flight speed of 12 m/s, the maximum power savings compared to the baseline was 18%, achieved with an offset of 0.4 d_z. At the same speed, offset configurations of 0.2 and 0.6 d_z both achieved power savings of approximately 15%. In the previous study, it was observed that power savings generally increased with vertical offset across flight speeds. However, in this case, the reduced power savings for the 0.6 offset compared to the 0.4 offset may be attributed to testing errors, increased drag from the additional components required to offset the rear rotors, or harmonic interactions, particularly given the flexibility of the multirotor airframe. The power consumption data also shows a notable increase in power savings starting at an offset of 0.2 d_z. This suggests that beyond an offset of 0.2 d_z, further reductions in power consumption are minimal. The diminishing returns on power savings may result from increased drag due to vertical offset geometry or aeroelastic interactions leading to harmonics and higher data uncertainty.

The insights gained from flight testing a functional multirotor with negatively staggered rotor configuration offer a more complete assessment of offset-induced performance benefits. Furthermore, the performance benefits of vertical offset validate the prior wind tunnel study in the UD-LSWT. The findings of this research effort confirm the feasibility of negatively staggered tandem rotor configurations and extend them to real-world applications, offering a balance between efficiency and compact design.

Figures/Charts

Table 1. Preliminary Test Matrix for Multirotor Performance with Set Mass and Varying Vertical Offset

Propeller	Horizontal Offset (d_y)	Vertical Offset (d_z)	Flight Speed (m/s)	Runs per Configuration	Run Length (m)	Mass (g)
KDE – CF125	1.20	0, 0.2, 0.4, 0.6	3, 6, 9, 12	6	304.44	2455

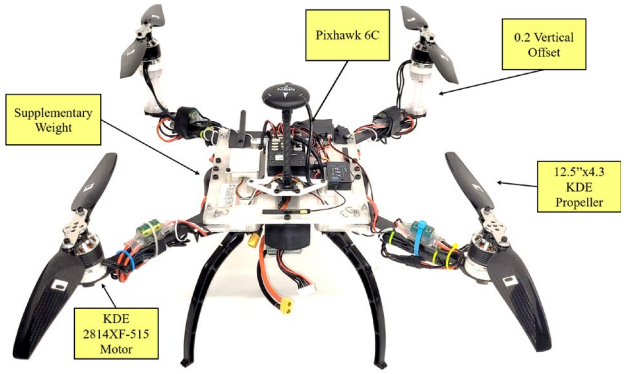


Figure 1. Front View of Multirotor with 0.2 d_z Vertical Offset

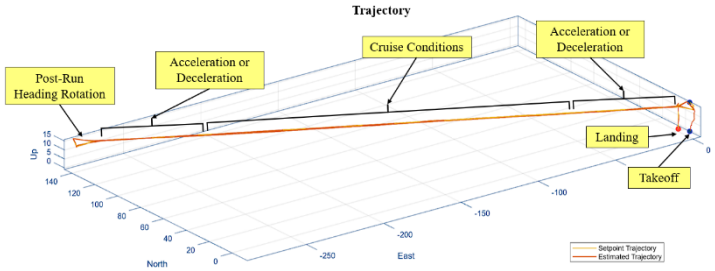


Figure 2. Representative Flight Path

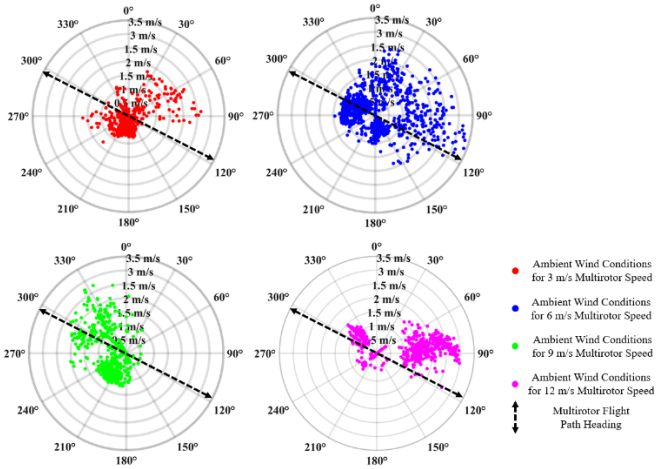


Figure 3. Ambient Wind Conditions and Flight Path for all Test Cases

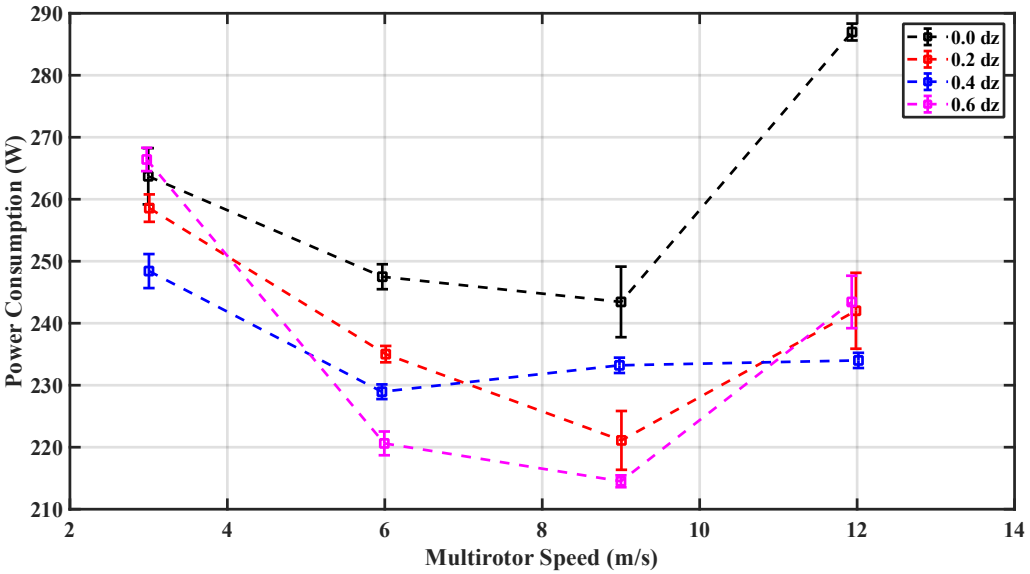


Figure 4. Power Consumption of all Test Runs for all Flight Speeds

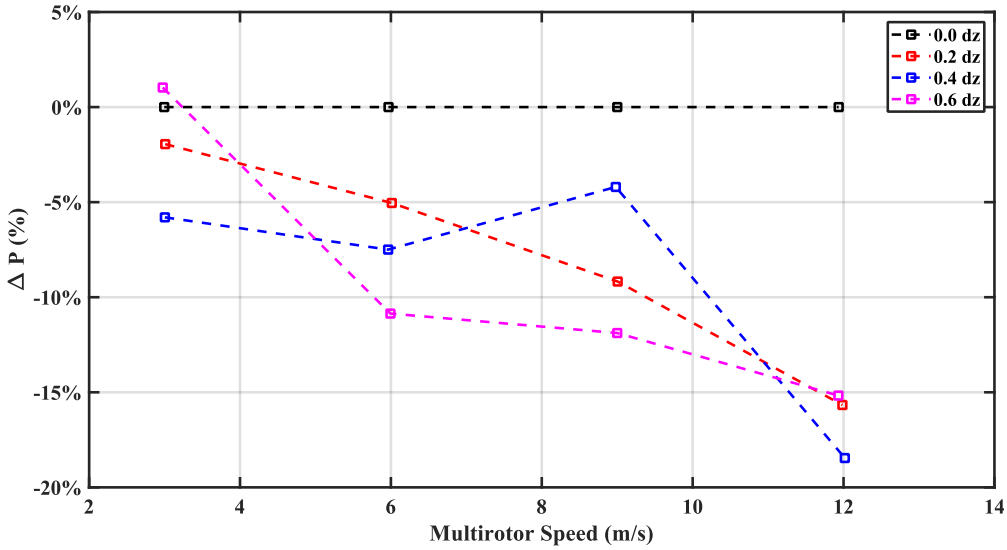


Figure 5. Change in Power Consumption with Vertical Offset for all Flight Speeds

Acknowledgments

This report incorporates content from the previously published SciTech 2025 Forum paper titled "Flight Test Validation of Tandem Propeller Performance with Vertical Offset" and University of Dayton Honors Thesis manuscript titled "Investigating Tandem Propeller Performance in Multirotor Aircraft." The author was the primary contributor to the research and writing of the conference paper and the thesis manuscript. The author gratefully acknowledges the collaborative contributions of University of Dayton undergraduate student Jessica DeMoor, graduate student Jielong Cai, and Associate Professor Dr. Sidaard Gunasekaran in the development of prior work. Generative AI was utilized in limited capacity to refine phrasing throughout this document. All technical content, including test plans, data analysis, and conclusions, was developed independently by the author.

References

[1] Leishman, J. G., “Principles of Helicopter Aerodynamics”, Cambridge University Press, 2006.

[2] Dingeldein, R. C., “Wind Tunnel Studies of the Performance of Multirotor Configurations,” NACA TN 3236, August 1954

[3] Otsuka, H., and Nagatani, K., “Pitching moment caused by rotor flow interference on a small quad-rotor unmanned aerial vehicle in a uniform flow,” in Transactions of the Japan Society for Aeronautical and Space Sciences, 2018, vol. 61, no. 2, pp. 87–96.

[4] Prudden, S. L., “Rotor Aerodynamic Interaction effect for multirotor unmanned aircraft system in forward flight” Ph.D. Thesis, RMIT University, Australia, September 2020

[5] Cai, J., Gunasekaran, S., and OL, M. V., “Vertically Offset Overlapping Propellers in Tandem Configuration”, AIAA SciTech 2023, National Harbor, MD, January 2023, AIAA 2023-2464.

[6] Cai, J., Gunasekaran, S., and OL, M., V., “Investigation of Positively Staggered Vertically Offset Propellers in Tandem”, AIAA SciTech 2024, Orlando, FL, January 2024, AIAA 2024-1510.

[7] Cai, J., “Changes in Propeller Performance Due to Rotor and Ceiling Proximity in Forward Flight” Ph.D. Dissertation, University of Dayton, May 2024.

Reinforcing Airport Safety by Automating the Retrieval of Elevation Data for Flight Simulation Software.

Student Researcher: Kavanaugh Frank

Advisor: Chad Mourning

Ohio University
Computer Science

Abstract

Safety is a critical priority for both airports and the aircraft that operate within them, and there is flight simulation software to aid in safety processes. The Ohio University Glideslope Model (OUGS), which predicts glide slope system performance in non-uniform terrain, and Ohio University NAVAID Performance Prediction Model (OUNPPM), which simulates localizer, glide slope, and VHF omnidirectional ranging (VOR) system behavior [1] are an example of such software. To support the performance and accuracy of these simulations, software has been developed to automate the retrieval and importation of elevation data from Digital Elevation Models (DEMs) hosted by the United States Geological Survey (USGS) [2]. The Terrain Extraction Automator (TEA) replaces the former manual process by the user and expedites the creation of simulations and reduces the possibility of human error. Elevation data is sourced from the USGS's National Map in the form of Geographic Tagged Image File Format (GeoTIFF) files, which encodes elevation data as raster grids, where each pixel represents the elevation at that geographic location. Data is then transformed to match the requirements of the modelling software and imported directly for us in the generation of 3D terrain models of the user specified airport.

Project Objectives

The objective of the Terrain Extraction Automator (TEA) is to streamline and accelerate the process of building 3D terrain models of specific airports used in flight inspection modelling software by automating the collection, transformation, and integration of elevation data hosted publicly by the United States Geological Survey (USGS) [2]. With the reduction of manual calculations and input, TEA enhances the accuracy and efficiency of the Ohio University Glideslope (OUGS) and Ohio University Performance Prediction Model (OUNPPM) in their efforts for fast, reliable, and accurate models for airport recertification with accurate terrain models.

Methods

The collection of the digital elevation models (DEM) is performed by an independent process, a web scraper, that sends requests to United States Geological Survey (USGS) [2] endpoints and downloads the available DEMs.

Users interact with menus within the modeling software to specify the geographic location. This includes defining a bounding box using an upper-left and lower-right latitude/longitude pair, setting the number of lateral and longitudinal sample points, and finally entering the latitude, longitude, and altitude of the glideslope, as well as the runway's heading.

The data then is transformed to match aviation standards, reduce the overall size of the elevation dataset, and allow the user to focus on specified airports. The first step is to reduce the overall dataset to only cover the elevation of the bounding box. Next, the dataset will be interpolated to reduce the number of points but keep comparable quality of the data. The modelling software has a limit of 30 by 30 data points for a single 3D terrain. The interpolated data now represents the airport in latitude/longitude (geodetic) but will need to be converted to the avionics standard of Earth Centered, Earth fixed (ECEF) which

represents the elevation points relative to the center of the Earth. A translation basis is created to convert the elevation from being relative to the center of the Earth, to the glideslope's geographic location in the local tangent plane. Lastly using the provided heading of the airport, the dataset is rotated to a true north heading center it for the modelling software. After the transformation of the data, it is sent to OUGS and/or OUNPPM to be used in the generation of accurate 3D terrain models.

Results and Discussion

TEA produces an interpolated representation of elevation for a specified airport that is formatted for the modeling software and utilized to generate 3D terrains. TEA's process for $9 * 10^4$data points, or 300 by 300, takes 7.83 seconds and results in data 5.21 MB in size; the process for $2.25 * 10^4$, or 150 by 150, data points takes 2.15 seconds and results in data 1.3 MB in size, with both datasets representing the same geographical area and maintaining comparable quality due to the application of bilinear interpolation to the dataset to reduce computational time and total size of dataset given to the modelling software as shown in Figure 1.

Figures/Charts

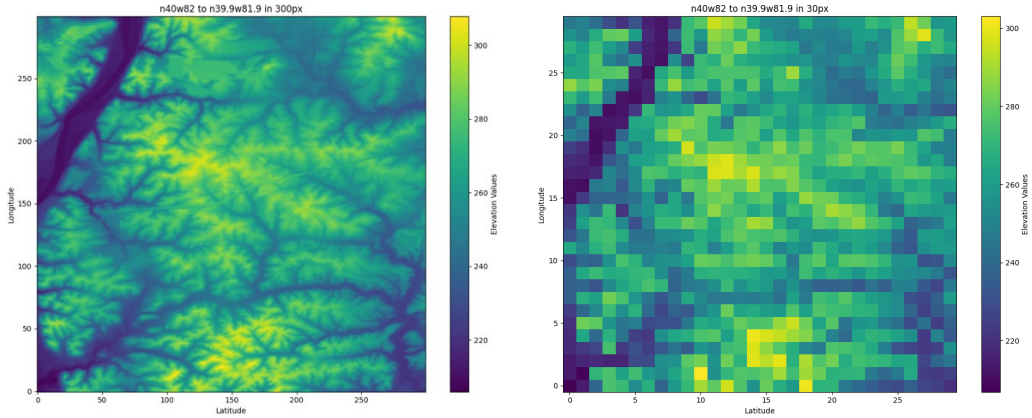


Figure 1. Scatter plot of the elevation points for the bounding box N40.0W82.0 to N39.9W41.9 at a resolution of 300x300 pixels and 150x150 pixels.

Acknowledgments

I would like to acknowledge and thank my advisor Dr. Chad Mourning as well as the EECS department at Ohio University, and the Ohio Space Grant Consortium (OSGC) for opportunity to work on this project. Additional work on this project was funded the Federal Aviation Administration.

References

[1] Dean B. Gesch, Gayla A. Evans, Michael J. Oimoen, and Samantha Arundel. The National Elevation Dataset. Earth Resources Observation and Science (EROS) Center, USGS Publications Warehouse, 2018. Index ID 70201572.

[2] C. Mourning and S. Odunaiya. Dynamic Antenna Pattern Visualization for Aviation Safety Incorporating Multipath and Situational Awareness. In Advances in Visual Computing: 16th International Symposium, ISVC 2021, Virtual Event, 2021

Electrostatic Effects on Turbine Deposition

Student Researcher: Kyle Frith

Advisor: Dr. Jeffrey P. Bons

The Ohio State University
Engineering Physics

Abstract
Gas turbine engines are at risk of ingesting sand and dust particles. Effects from ingested particles include erosion of compressor and fan blades, deposition on surfaces leading to reduced aerodynamic efficiency, and contamination of coolant flow which may result in blocked cooling passages. These effects reduce the life of a gas turbine and can cause components to fail without proper maintenance. It is also known that aircraft acquire electrostatic charge from frictional rubbing with the atmosphere. This project will examine how the acquired charge of an aircraft affects deposition on relevant gas turbine engine surfaces.

Project Objectives
Previous research has indicated that electrostatics may play a role in the adhesion mechanism for dust particles in gas-turbine engines cooling flows [1]. Current research at The Ohio State University Aerospace Research Center (OSUARC) has supported that for an impinging jet on a relevant turbine metal surface, applied charge on the surface does influence particle adhesion. The objective of this project was to expand this research by simulating turbine cooling flow through a test article that mimics a double walled cooling architecture with an applied charge to support the parallel research of impinging jet flows.

Methods
The test consisted of a test piece that replicates the double wall cooling circuit found in turbine nozzle guide vanes. A cylindrical test article with a cooling hole pattern representative of the leading edge of a nozzle guide vane along with an impingement insert was adapted to fit the Effusion Cooling Deposition Facility (ECDF) at the OSUARC. The test article was previously used by Whitaker et al. to study the effects of particle loading, size, and flow temperature [2] as well as surface temperature [3] on deposition in turbine vane leading edge cooling geometries. The test article impingement insert is constructed of stainless-steel with 38 rows of 15 (570 total), 0.635 mm diameter holes and the effusion exterior is constructed of Inconel 601 with 10 rows of 0.457 mm diameter holes (219 total). It should be noted that unlike typical nozzle guide vanes, the film holes on the cylinder eject normal to the surface. For electrostatic testing voltage was applied to the effusion exterior via a high voltage generator. Because the insert and effusion shell have a common contact point at the flow entrance, charge distributes evenly on the exterior and interior of the test article.

The ECDF consists of a heated flow with entrained dust delivered to the test article exhausting into a heated kiln. Dust was delivered to the test article via 811 k (1000°F) heated flow while the kiln temperature was set to the same temperature to prevent temperature fluctuations for the duration of the test. Six tests were run, two at each voltage condition of +5 kV, 0kV, and -5 kV. The breakdown voltage of the air at the test temperature limited the maximum value of applied charge. Voltage greater than 5 kV would cause the test article to discharge and current would flow through the experiment.

Throughout the duration of the test the pressure ratio (PR) across the test article was held constant at 1.03, a relevant cooling flow PR. PR is given by

$$PR = \frac{P_{cyl}}{P_{amb}} \quad (1)$$

Where P_{cyl} is the measured pressure in the test article and P_{amb} is the recorded ambient temperature in the facility. The particle sizes delivered were 0-5 µm diameter Arizona Road Dust (ARD). As the flow blockage increases, the experiment is designed to automatically adjust a mass flow controller via a Labview program to keep the PR constant. Consequently, the mass flow must decrease if temperature is also constant. Mass flow reduction is given by

$$MFR = \frac{\dot{m}_i - \dot{m}_c}{\dot{m}_i} * 100 \quad (2)$$

MFR was monitored for each test. Dust delivery was stopped once MFR reached 25%. After each test blockage per gram (BPG) was calculated and capture efficiency (η) for the impingement insert, effusion exterior, and combined capture efficiencies were calculated. BPG and η were calculated from equations 4 and 5

$$BPG = \frac{MFR}{m_{del}} \quad (4)$$

$$\eta = \frac{m_{dep}}{m_{del}} \quad (5)$$

where m_{del} is the delivered mass to the test article and m_{dep} is the mass that was collected from the test article. BPG is a measure of how aggressive blockage development was over the length of the test while capture efficiency measures how much mass accumulates on the relevant measured component.

In addition to high-speed engine-like experiments, six low-speed vertical drop experiments were conducted with the same ARD dust dropped into a vertical cylindrical pipe and an angled cylindrical pipe. Applied voltages consisted of +10 kV, 0 kV, and -10kV. Voltage was doubled in this case to intensify the effects from the applied voltage and observe them more readily. A 90 cm aluminum tube was placed vertically and dust was brushed through a sieve over the entrance to the tube for a period of 5 minutes in order to tribocharge the particles. In both the impinging jet and ECDF experiments the particles pass down the length of the experiment and have a chance to exchange charge with the walls of the experiment piping and each other; brushing the dust through the sieve mimics this tribocharging phenomena.

The vertical drop is designed to measure trajectory deflection of the particles as the travel down the length of the tube with respect to applied voltage. Eight tests were conducted at +10 kV, -10 kV, and 0 kV. A 90 cm angled to 10° was also utilized in six tests with the same 5-minute brushing period. The angled drop is designed to measure the effects of electrostatics on the adhesion to the inner surface of the tube as voltage is varied. Capture efficiencies were calculated to determine if any sensitivity to applied voltage existed. Results were compared to those of the high-speed experiments. A simulation of the interior electric field was performed using Ansys Maxwell to further understand any observed effects.

Results and Discussion

From figure 1, MFR displayed no sensitivity to effect of applying a charge to the test article. The resulting rates of MFR (indicated by the slope) for the +5 kV tests and the -5 kV tests were bounded by the no voltage case. Similar results occurred for BPG (figure 2) which displayed no sensitivity to the applied charges. Capture efficiency results (figure 3) were negligible.

Low-speed experiments were conducted to further validate the results from the high-speed engine-like experiments and the simulation. Figure 4 presents these results. Capture efficiencies were all under 3% which is within experimental error. No effect from the applied voltage was recorded which agrees with the high-speed experiment.

Figure 5 demonstrates the expected electric field of the air volume inside the flow as it enters the cylinder. From conductor theory [4], because the charge is distributed equally on the interior of the test piece the resulting electric field is expected to be zero. At the entrance path to the flow however charges do collect and result in some fringing fields at the entrance to the cylinder. Due to the electrostatic adaptations made to the test article, these fields were suppressed. The results of the simulation and the experimental results are in agreement.

With the cylindrical double walled cooling test article, no influence of electrostatics was observed in the capture efficiency or blockage data. Subsequent low-speed vertical drop tests with a cylindrical pipe validate that no effect of electrostatics on particle trajectory or adhesion is observed.

Figures/Charts

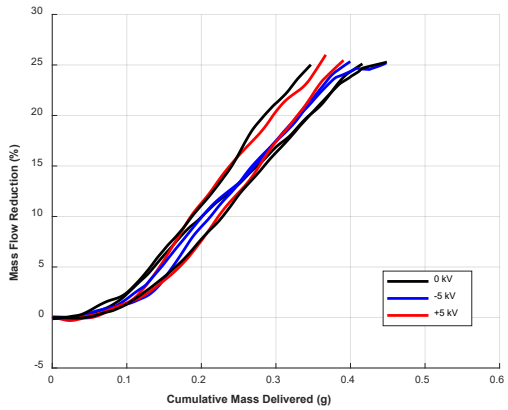


Figure 1. Mass Flow Reduction Vs. Cumulative Mass Delivered.

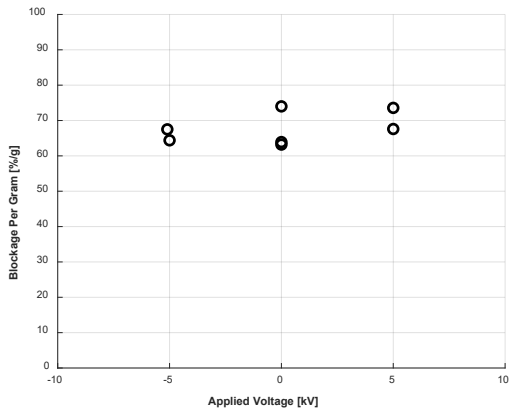


Figure 2. Blockage Per Gram Vs. Applied Voltage.

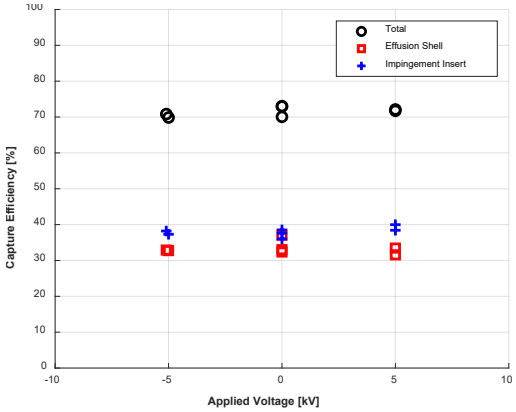


Figure 3. Capture Efficiency Vs. Applied Voltage, High-speed.

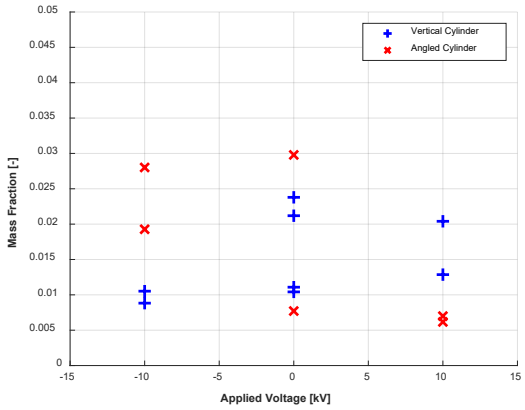


Figure 4. Capture Efficiency Vs Voltage, Low-speed.

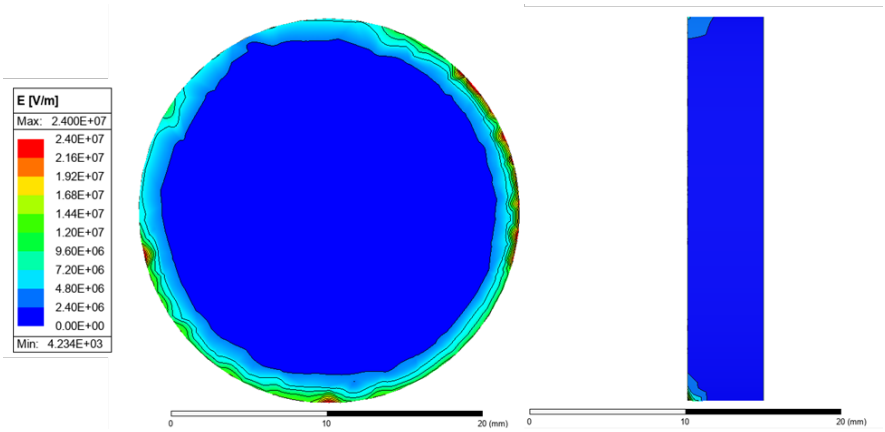


Figure 5. Simulation of Air Volume Inside Test Article.

Acknowledgments

I would like to thank Dr. Jeffrey Bons for his valuable guidance on this project and Tanner Sabau for the opportunity to contribute to his research and the insights and support he provided throughout the project. In addition, I would like to thank Josh Gueth for his assistance and help with machining parts necessary for adaptation of the prior test article to the new electrostatic testing. Lastly, I would like to thank the OSGC for their continued support of my research and the opportunity to continue my work.

References

[1] Raj, R., S. Moskowitz., 1984, "Experimental Studies of Deposition by Electrostatic Charge on Turbine Blades." ASME, 84-GT-159.

[2] Whitaker, S. M., Peterson, B., Miller, A. F., and Bons, J. P., 2016, "The Effect of Particle Loading, Size, and Temperature on Deposition in a Vane Leading Edge Impingement Cooling Geometry," presented at the ASME Turbo Expo 2016 in Seoul, South Korea, June 13-17, 2016. Paper #GT2016-57413

[3] Whitaker, S. M., Lundgreen, R. K., and Bons, J. P., 2017. "Effects of Metal Surface Temperature on Deposition Induced Flow Blockage in a Vane Leading Edge Cooling Geometry," presented at the ASME Turbo Expo 2017 in Charlotte, SC, June 26-30, 2017, (GT2017-64946).

[4] Griffiths, D. J., 1999, Introduction to Electrodynamics, Upper Saddle River, NJ, Prentice-Hall, 1999.

Testing Satellite Dynamics and Control Using Robotics Technology in the Lab Environment

Student Researcher: Gianni Gaetano

Advisor: Ou Ma

University of Cincinnati
Department of Aerospace Engineering and Engineering Mechanics

Abstract

Space debris and defunct satellites pose increasing challenges for space operations, necessitating advanced robotic solutions for In-Space Servicing, Assembly and Manufacturing (ISAM). This research investigates the dynamics and control strategies required for robotic systems to effectively interact with tumbling satellites in space environments. Using a collaborative robotic arm, we have developed a laboratory-based simulator that accurately replicates the three-dimensional gyroscopic dynamics of tumbling spacecraft. The simulator accepts initial body angles and rates as inputs to model the complex motion patterns of defunct satellites, enabling thorough testing of control algorithms in a controlled environment.

Our research demonstrates successful implementation of the simulation platform, providing a foundation for developing robust control strategies for space robotics applications. The ability to accurately simulate tumbling dynamics in a laboratory setting represents a significant step forward in testing and validating capture mechanisms and control algorithms before deployment in space. This work will contribute to the broader field of space robotics by supporting the advancement of satellite capture and manipulation techniques. The findings from this research will support the development of more effective ISAM solutions, ultimately contributing to the sustainability and safety of future space operations.

Project Objectives

The primary objective of this research is to develop and validate a laboratory-scale hardware-in-the-loop (HIL) simulator capable of accurately reproducing the three-axis tumbling motion characteristic of uncooperative satellites. The developed testbed aims to address the critical need for reliable and precise ground-based validation of autonomous spacecraft rendezvous, proximity operations, and capture (RPOC) technologies essential for In-Space Servicing, Assembly, and Manufacturing (ISAM). To achieve this overarching goal, the project outlines the following specific objectives:

1. **Simulator Development**: Design and implement a tumbling satellite simulator using a collaborative 6-degree-of-freedom robotic arm (FANUC CR-35iA) capable of precise three-axis rotation. The simulator incorporates gyroscopic dynamics modeled through Euler's rigid-body equations of motion, executed within a MATLAB/Simulink simulation environment.
2. **System Integration**: Establish robust integration between simulation software and hardware components, ensuring real-time actuation of the robotic arm based on computed satellite dynamics. This objective encompasses designing suitable electrical and mechanical control architectures for seamless data exchange and actuation.
3. **Experimental Validation**: Conduct a rigorous validation campaign leveraging a Vicon optical motion-capture system to quantify simulator accuracy. Validation efforts specifically target evaluating discrepancies between the commanded Simulink trajectory and the robot-executed physical motion in terms of Euler angles, angular velocities, and center-of-mass positioning.
4. **Performance Quantification**: Determine quantitative error metrics, including maximum angular errors, average angular deviations, standard deviation of angular tracking errors, and center-of-

mass positional accuracy. These metrics will inform the reliability of the HIL simulator in replicating realistic satellite tumbling behaviors within acceptable error thresholds.

5. **Expansion of Capabilities**: Outline future enhancements to incorporate closed-loop operations, including physical interaction and external perturbations, thereby enabling comprehensive validation of advanced capture and manipulation strategies necessary for operationally relevant ISAM scenarios.

By successfully meeting these objectives, the project aims to provide an accurate, versatile, and reliable experimental platform that significantly advances the state-of-the-art in ground-based testing of autonomous satellite capture and servicing technologies.

Methods

The experimental setup comprises a FANUC CR-35iA collaborative robotic arm utilized to replicate the tumbling motion of a satellite. Euler's rigid-body equations of motion are solved using Simulink to generate real-time control signals for the robot. Integration between Simulink and the robotic arm is achieved via a custom electrical and mechanical control system, enabling precise synchronization of simulation and physical movements. Simulation verification was done by solving Euler's ridged-body equations numerically. Validation experiments employ a Vicon motion-capture system to record actual robotic motion, allowing detailed error analysis against the intended simulation trajectories.

Results and Discussion

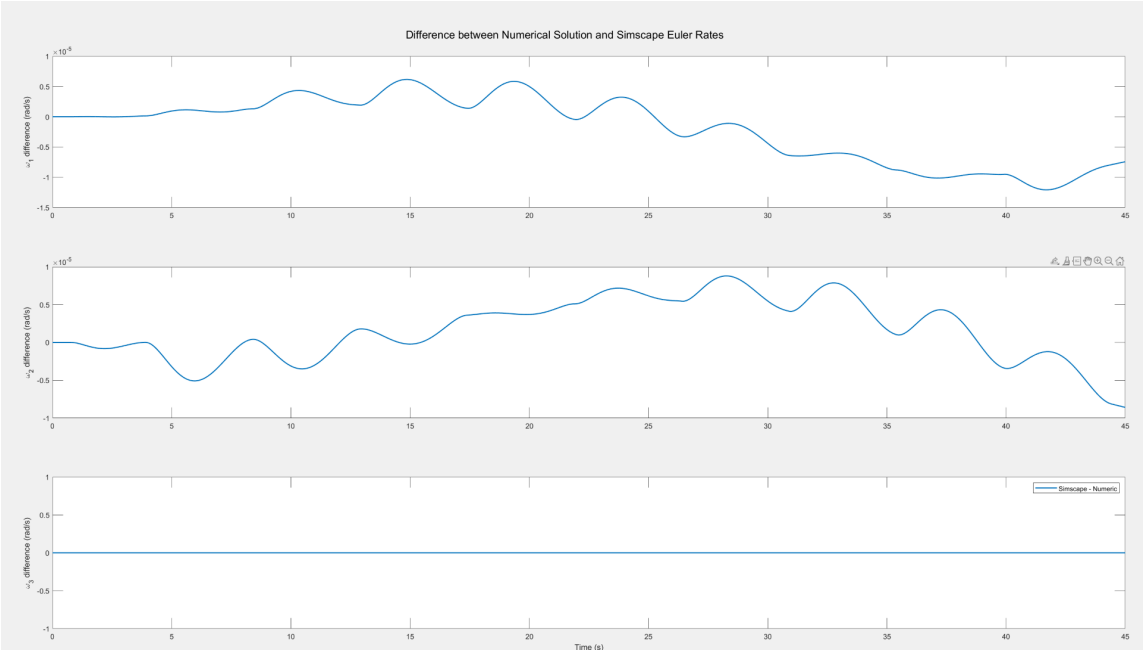
Validation results demonstrated high fidelity between the Simulink-modeled satellite dynamics and the physical motion executed by the robotic arm. Maximum angular errors observed during the validation experiments ranged from approximately 2.17° to 2.44°, with average angular deviations maintained between 0.96° and 1.21°. The standard deviation for angular tracking errors was consistently between 0.39° and 0.45°. Additionally, positional accuracy at the satellite center-of-mass (COM) exhibited a standard deviation of 1.72 mm, with a maximum error of 4.78 mm.

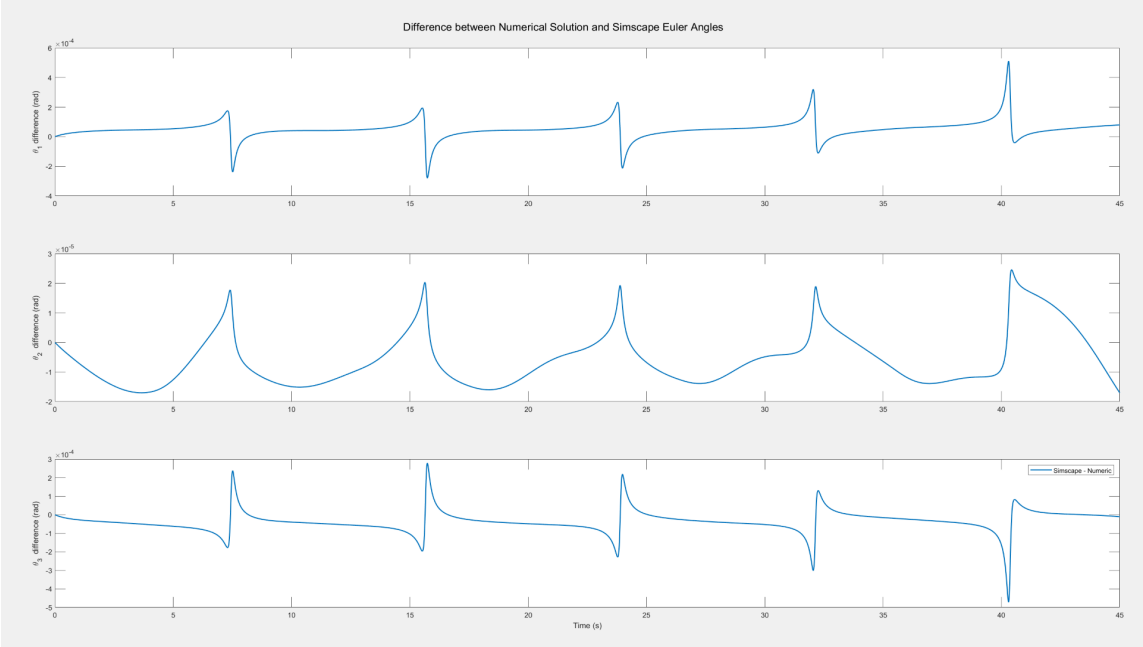
These performance metrics indicate robust simulation-to-hardware translation, essential for confidently using the HIL simulator in RPOC mission planning and testing scenarios. Minor discrepancies observed in both angles and angular rates, with residuals less than 9×10^{-6} deg/s, highlight the precision achievable with careful system calibration and integration.

The accuracy demonstrated by the current setup validates its effectiveness for ground-based testing and significantly reduces risks associated with in-orbit servicing operations. Future work aims to further enhance this fidelity by incorporating closed-loop feedback control, simulating direct physical interactions, and testing advanced manipulation strategies under dynamic operational conditions.

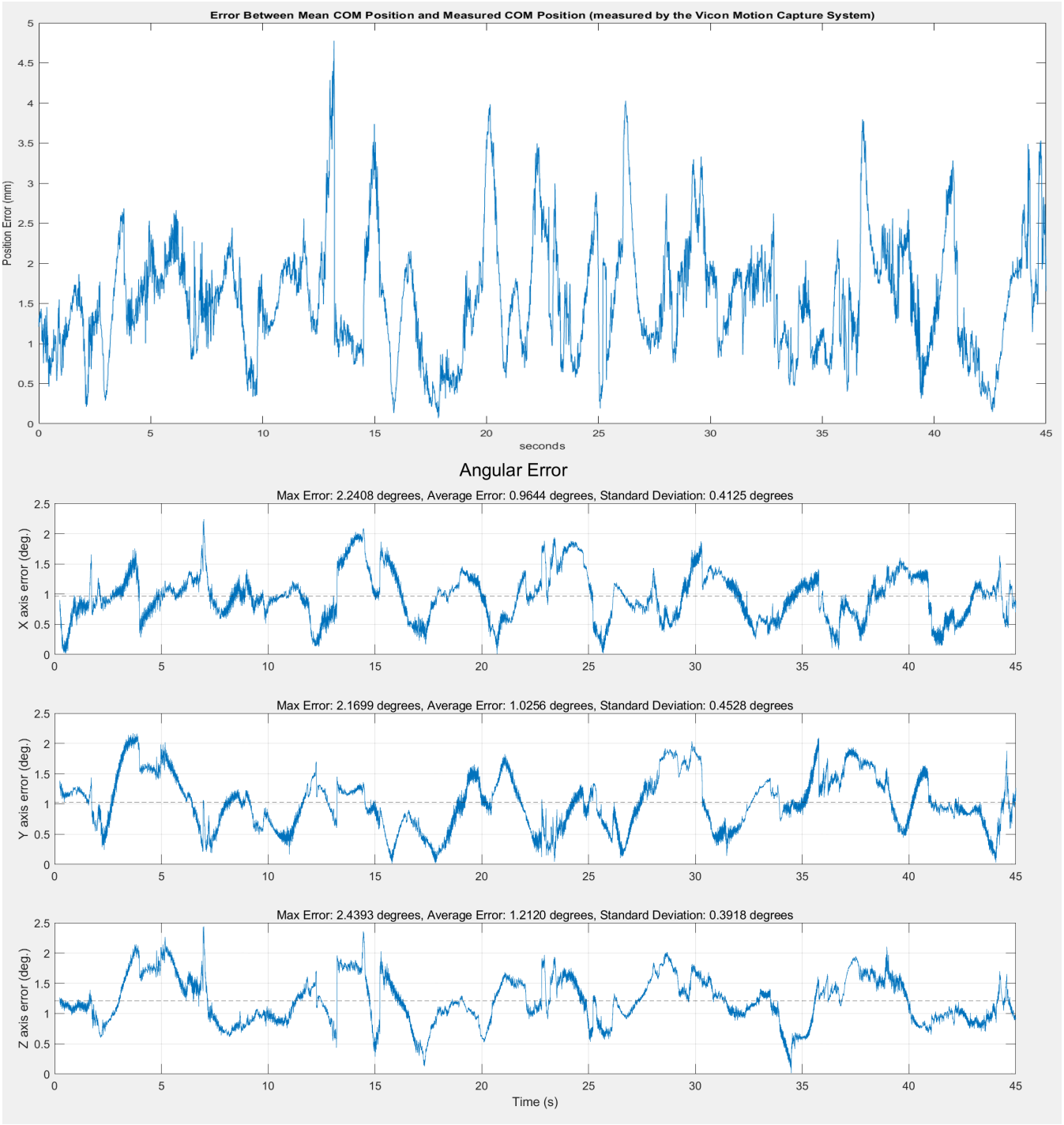
Figures/Charts

Simulation verification:





Accuracy validation:



Acknowledgments

Thank you to Dr. Ma, OSGC, and AFRL for enabling my research on this topic.

Development of Material Characterization Procedures for Aerospace Alloys

Student Researcher: John (JD) Gillum

Advisor: Dr. Daniel Young

Wright State University
Department of Mechanical and Material Engineering, Material Science and Engineering B.S.

Abstract
The development of material characterization procedures for aerospace applications is crucial for ensuring the reliability and performance of advanced alloys in critical components. This research focuses on developing comprehensive materials characterization procedure that incorporates hot compression testing to assess the mechanical properties of materials under high-temperature conditions. Hot compression testing provides valuable insights into the deformation mechanisms of materials, simulating the extreme thermal and mechanical environments encountered in aerospace applications. This procedure will specifically be applied to better understand the behavior of additively manufactured Inconel 718, a high-performance nickel-based superalloy commonly used in aerospace engines and structural components. Additive manufacturing techniques, such as Laser Powder Bed Fusion (LPBF), enable the creation of advanced design features, including voids, which can result in unique behaviors needed in aerospace environments such as expected creep exposure and vibrational dampening from powders. By integrating advanced characterization techniques, this research aims to deepen our understanding of aerospace alloys' behavior, enabling more effective material selection, process optimization, and quality control for aerospace applications.

Project Objectives
This paper initiates the development of material characterization procedures for additively manufactured parts designed with powder-filled cavities, specifically for aerospace applications. The research focuses on evaluating the mechanical properties and structural characteristics of two key materials, Inconel 718 and Stainless Steel 316, using Scanning Electron Microscopy (SEM) and hot compression testing. By understanding these materials' behavior in such specialized structures, these tests would provide critical insights into their performance under operational conditions in aerospace environments.

Methods
Laser Powder Bed Fusion (LPBF) was conducted at Wright State University using an Open Additive Panda Printer, which is capable of printing with either Inconel 718 or Stainless Steel 316. For the purposes of this study, however, all samples were fabricated with Inconel 718. Figure 1 illustrates the printer's operation, where powdered metal is melted across a powder bed and selectively fused by a laser. The sample of interest is a cylindrical part with a centrally located spherical cavity filled with metal powder. An internal cross-sectional view of the part is shown in Figure 2.
Microscopy was performed using both optical and Scanning Electron Microscopy (SEM) techniques to examine the macro and microstructural characteristics of the cavity. Several aspects were investigated to develop sample preparation methods that minimize disruption during cross-sectional analysis: internal surface finish, powder configuration, and the sintered core. To preserve the integrity of the internal surface finish, a low-speed diamond saw was used to cut the sample, preventing fracture of the sintered particles at the surface. For examining the packing of unsintered powder, a minimally invasive technique was employed: a small hole was drilled to allow vacuum-assisted injection of a two-part epoxy, which helped preserve the shape and configuration of the powder particles. For sintered samples, a 12-hour sintering process at 1,200°C was conducted. While no successful method was identified to maintain

cohesion between the sintered core and the original part, optical characterization of the two-phase structure was still performed to pair with further testing.

Hot compression testing involved three key components to thoroughly investigate the material's behavior under extreme loads. To heat the sample efficiently, an Ultra Flex Ultra-Heat SMT Induction Heater was employed, though its use limited test specimen sizing to a 1” tall by 0.5” diameter. As a result, a large load cell was required to perform the tests. For both safety and practical testing without a furnace-heated sample, a με thermometer CTLM-2M-2H pyrometer was mounted on the test frame to measure the sample's external temperature during testing.

Results and Discussion

The internal surface characteristics were analyzed through the gentle removal of powder. As shown in Figure 3, the particles maintain their spherical shape without deformation, despite the residual heat from sintering or the impact from colliding loose particles. While the use of post-processing techniques to achieve uniform surface roughness is unlikely, there is still potential to improve sintering parameters to enhance predictability and, potentially, mechanical performance.

Figure 4 presents an unetched metallographic sample with particles embedded in epoxy, allowing for analysis of properties such as particle size and distribution. This provides insight into how the particles interact after manufacturing. Current analysis of these images, using software like ImageJ, allows for the quantitative assessment of powder characteristics, including size and distribution. However, a challenge remains in accurately identifying powders embedded within the polymer matrix.

Future research will aim to explore the microstructure of the particles, potentially using electron backscatter detection. This could be facilitated by developing processes to chemically or electrically etch the sample, ensuring the particles remain embedded in the matrix. While sintering was briefly examined, this area remains underexplored due to project constraints. Hypotheses regarding sintering include exploring how the vibrational response differs between larger powders and micro-sized particles, as well as identifying potential phase transformations under varying temperature or pressure conditions. These aspects were not fully investigated but represent opportunities for future research.

Initial elevated temperature compression testing required calibration of the setup described in the methods section. A feedback loop was necessary to ensure that the external temperature was consistent with the internal temperature, especially given the use of magnetically induced heating via alternating current. To better understand the temperature distribution, an initial thermal profile test was conducted to compare the external and internal temperatures, with the aim of determining the additional steps needed to accurately characterize aerospace alloys.

Figure 5 illustrates a temperature ramp comparing readings from an internal K-type thermocouple and a pyrometer, which measures at a minimum emissivity of 0.1. This low emissivity may influence the temperature readings detected by the infrared sensors. As expected, there is an initial spread in the measurements, with the pyrometer's minimum detection temperature of 385°C contributing to a difference of approximately 200°C between 2 and 6 minutes. This spread grows to nearly 500°C as the induction heater approaches its maximum power output.

Further calibration testing will be conducted after the submission of this report. This will include repeating the same temperature ramp test, as well as isothermal holds at various material emissivities for both Inconel 718 and Stainless Steel 316, to optimize performance. In accordance with recommendations from the pyrometer manufacturer, Micro-Epsilon, these tests will be performed with an emissivity range of 0.1 to 0.2 for Inconel 718 to determine the optimal procedure [2]. Once this step is completed, hot compression testing will occur to determine advanced material properties of aerospace alloys.

In conclusion, the analysis of void characteristics and thermal testing has provided valuable insights into the behavior of powder filled cavities and has room for much more discovery. The results show that the particles maintain their spherical shape, suggesting that sintering parameters could be optimized to improve mechanical performance. While challenges remain in accurately identifying embedded powders, further research will focus on refining imaging techniques and exploring particle microstructure. Thermal profile testing also highlighted temperature discrepancies, necessitating additional calibration for accurate characterization of aerospace alloys. Moving forward, further calibration, isothermal testing, and hot compression testing will help optimize performance and advance the understanding of material properties.

Figures & Tables

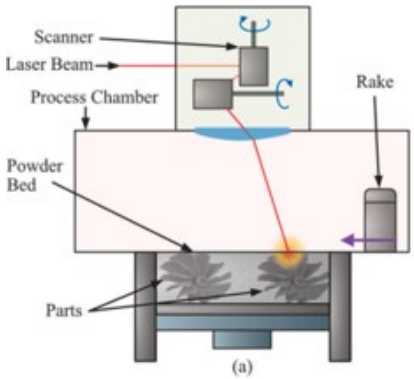


Figure 1: Diagram of Laser Powder Bed Fusion Printer

Source: [1]

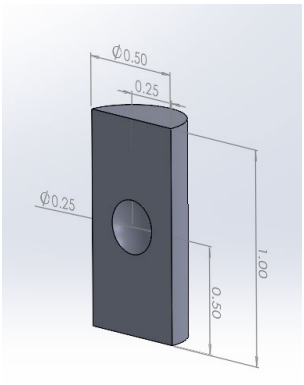


Figure 2: Cross Section Model of Designed Cavity Sample

Source: Author

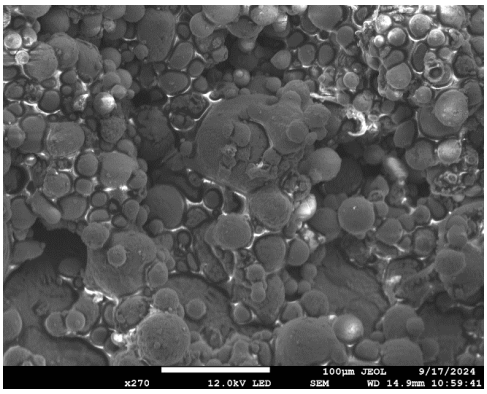


Figure 3: SEM Image of Cavity Surface Finish (270x)

Source: Author

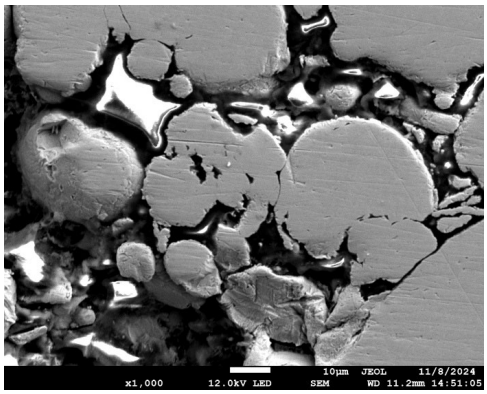


Figure 4: SEM Image of Cavity Powder Configuration (1000x)

Source: Author

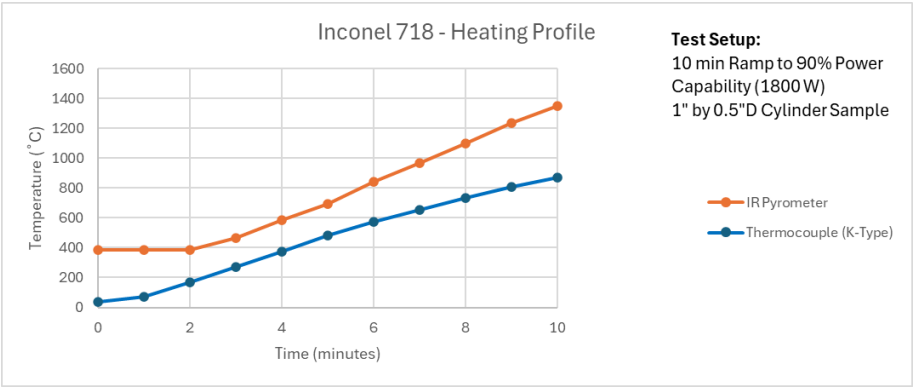


Figure 5: Thermal Measurement Study of Inconel 718

Source: Author

Acknowledgments

I am deeply grateful to the Ohio Space Grant Consortium for the opportunity to pursue research that aligns not only with my academic interests but also with my passion for materials science. I would also

like to extend my sincere thanks to the individuals who guided and supported me throughout this project: Dr. Daniel Young, Dr. Mitch Wolff, Doug Yost, Showmik Ahsan, and Vignesh Asam.

References

[1] Sanchez, Salomé, et al. “Powder bed fusion of nickel-based Superalloys: A Review.” *International Journal of Machine Tools and Manufacture*, vol. 165, June 2021, p. 103729, https://doi.org/10.1016/j.ijmachtools.2021.103729.

[2] Micro-Epsilon, “Thermometer CTL.” *Micro-Epsilon*, www.micro-epsilon.com/fileadmin/download/manuals/man- thermoMETER-CTL--en.pdf. Accessed 7 Apr. 2025.

Early-Life Ingestion of a Low-Calorie Sweetener Decreases the Number of Taste Pores of the Fungiform Papillae on the Anterior Tongue of Male Rats

Student Researcher: Emily Gilman

Advisor: Clare Mathes

Baldwin Wallace University
Department of Biology, Geology & Neuroscience

Abstract
This study investigated the long-term effects of early-life exposure to low-calorie sweeteners (LCS). Tongue tissue was collected and stained to analyze fungiform papillae taste pore number and morphology. Results revealed that LCS-exposed rats had significantly fewer total taste pores compared to controls. These findings suggest that early-life LCS exposure may reduce the overall expression of taste pores, supporting the hypothesis that LCS consumption during development reprograms the gustatory system. This is a step towards investigating the behavioral changes seen in previous studies, which warrants further investigation and may help guide people in their choice to use low-calorie sweeteners.

Project Objectives
This study focused on the impact of the regular consumption of low-calorie sweeteners (LCS) during juvenile-adolescence development on the gustatory anatomy of fungiform papillae on the anterior tongue. Low-calorie sweeteners (LCS) are increasingly used as an alternative to sugar because they provide sweet taste with fewer or no calories. Research suggests that the habitual consumption of an LCS during early development, directly and indirectly, influences taste preferences and motivated behaviors regarding sugars and that LCSs reduce the expression of sweet receptor genes in rats as adults (6). However, there is a gap in research regarding whether this reduced gene expression caused by LCS impacts the anatomical structure of the taste pores themselves, which may impact the functioning of the taste bud housed within, causing changes in taste preferences and motivated behavior seen in the research. This research is needed to gain a better understanding of the long-term consequences of LCS consumption during early development. This question is important because, in the United States, the prevalence of obesity, especially in children, has become a growing concern (2, 4). One study conducted in 2019 found that an estimated one-third of the population worldwide qualifies as being overweight or obese (3). This study pertains to this social issue as it furthers our understanding of how the gustatory tract is impacted by low-calorie sweeteners. In this study, we assessed whether early-life exposure to low-calorie sweeteners influences the number and structure of anterior tongue taste pores later in life in a rat model. We hypothesized that there would be fewer taste buds and higher levels of taste pore denervation in the rats exposed to low-calorie sweeteners when compared to the control group.

Methods
Twelve male Sprague Dawley rats were used in this study. On postnatal day (PND) 26, male Sprague Dawley rats were single-housed and divided into two experimental groups. The experimental group (n=7) received a daily dose of the low-calorie sweetener Acesulfame potassium (Ace-K, 0.1 % at 15 ml/kg) alongside water and their normal chow diet from post-natal day 26-77 and remained on only chow and water through post-natal day 210. The control group (n=5) received only chow and water throughout. The rats were euthanized and transcardially perfused to fix tongue tissue on PND 210. The dorsal aspect of the tongue anterior to the intramolar eminence was removed from the underlying tissue, using various scraping tools. I carried out a decision analytics session to determine the best staining protocol, which I standardized for the experimental tissue. After staining with 0.5% methylene blue, each tissue sample was flattened between two microscope slides to be observed.

The slides were blinded, and photographs of the tongue anterior to the intermolar eminence were taken in a serpentine grid pattern at 4x magnification. These pictures were then analyzed to determine pore characterization. Pores were deemed innervated (INV) when the pore appeared as a dark dot fully surrounded by clear, concentric rings. These rings were followed by a darker indentation before the epithelial surface at the outside edges (5). Pores were deemed denervated (DNV) if the inner rim was discernible but the pore did not appear as a dark spot or with no clear concentric rings or outer indentation before the epithelial surface (5). The difference in the number of total, innervated, and

denervated pores between the two groups (LSC & CTRL) was analyzed via an independent samples t-test. Differences were considered statistically significant when $p<0.05$.

Results and Discussion

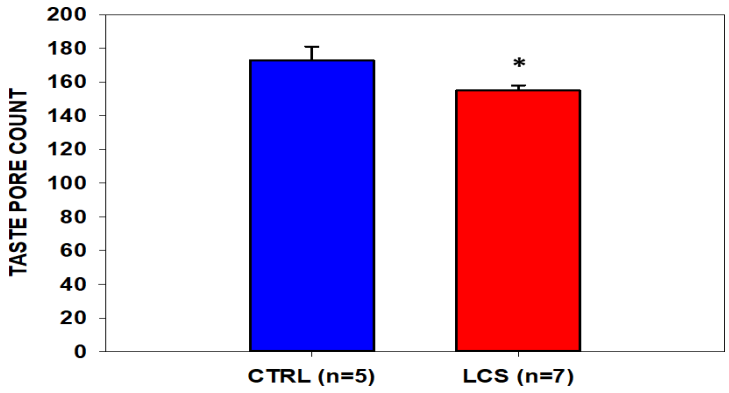


Figure 1. Rats that ingested low-calorie sweetener (LCS) early in life had fewer total taste pores than unexposed controls (CNTL; A; $(t(10)=2.3, p=0.044)$.

Using an independent samples t-test, we found that rats exposed to early-life LCS had fewer fungiform papillae taste pores on the anterior tongue than the control group. However, the number of innervated and denervated pores did not differ between groups. This suggests that early-life experience with LCS may not cause taste buds to be denervated, but that there are simply fewer expressed in general. This data correlates with prior research indicating that early-life LCS decreases the expression of taste pores in the circumvallate of the posterior tongue (6). Overall, this supports that early-life low-calorie sweeteners reprogram the gustatory axis in a way that persists into later life. This is a step towards investigating the behavioral changes seen in previous studies, which warrants further investigation and may help guide people in their choice to use low-calorie sweeteners.

Acknowledgments

We acknowledge scholarship support of Emily Gilman by the Ohio Space Grant Consortium. We thank Dr. Yada Treesukosol for guidance on anterior tongue staining.

References

1. Alvarez-Monell, A.; Subias-Gusils, A.; Mariné-Casadó, R.; Belda, X.; Gagliano, H.; Pozo, O.J.; Boqué, N.; Caimari, A.; Armario, A.; Solanas, M.; et al. Restricted cafeteria feeding and treadmill exercise improved body composition, metabolic profile and exploratory behavior in obese male rats. Sci. Rep. 2023, 12, 19545
2. Cawley, J., Biener, A., Meyerhoefer, C., Ding, Y., Zvenyach, T., Smolarz, B. G., & Ramasamy, A. (2021). Direct medical costs of obesity in the United States and the most populous states. Journal of Managed Care & Specialty Pharmacy, 27(3), 10.18553/jmcp.2021.20410. https://doi.org/10.18553/jmcp.2021.20410
3. Chooi, Y. C., Ding, C., & Magkos, F. (2019). The epidemiology of obesity. Metabolism, 92, 6-10. https://doi.org/10.1016/j.metabol.2018.09.005
4. Iyun, O. B., Okobi, O. E., Nwachukwu, E. U., Miranda, W., Osemwegie, N. O., Igbadumhe, R., Olawoye, A., Oragui, C. C., & Osagwu, N. A. (2024). Analyzing Obesity Trends in American Children and Adolescents: Comprehensive Examination Using the National Center for Health Statistics (NCHS) Database. Cureus, 16(6), e61825. https://doi.org/10.7759/cureus.61825
5. Mistretta CM, Liu HX, Gaffield W, MacCallum DK. Cyclopamine and jervine in embryonic rat tongue cultures demonstrate a role for Shh signaling in taste papilla development and patterning: fungiform papillae double in number and form in novel locations in dorsal lingual epithelium. Dev Biol. 2003 Feb 1;254(1):1-18.
6. Parks, J. D., & Whitehead, M. C. (1998). Scanning electron microscopy of denervated tastebuds in hamster: Morphology of fungiform taste pores. The Anatomical Record, 251(1), 250-239.
7. Mathes, C. M., Terrill, S. J., P., J., Chometton, S., Witt, M. J., Mendiratta, G., Gilman, E. G., Hartswick, D. R., Anderson, B. M., & Schier, L. A. (2025). Neurobehavioral plasticity in the rodent gustatory system induced by regular consumption of a low-calorie sweetener

ECT Sensor Generation and L2-Norm Based Flow Regime Analysis

Student Researcher: Liam Hackett

Advisor: Zach Carner

Wright State University
Department of Mechanical and Materials Engineering

Abstract
An important aspect of two-phase flow research revolves around the ability to accurately measure void fraction within the system. Currently, there is not a satisfactory approach to this in a manner that does not require proprietary components. The work of De Kerpel and Caniere showed promising results as they explored the development of a custom capacitance sensor. The sensor used a non-proprietary, semi-conductor, type setup to determine the permittivity of a given flow. These results will be expanded in this research to optimize the sensor design and calibration. The major contribution of this research will be the use of an industrial Electrical Capacitance Tomography (ECT) sensor to help calibrate the custom sensor. The previous researchers did not have such technology to validate their sensor. Furthermore, additional research utilizing this sensor will expand into two phase flow identification through a neural network application. Previously, Dr. Abdeel Roman used statistical analysis of the permittivity probability density function to train a neural network to predict the flow regime. This research will expand into the development of a neural network model based off image analysis of the tomogram using the L-2 Norm statistic. This approach seeks to develop an accurate way to determine flow regime based upon the tomogram generated by the ECT sensor.

Project Objectives
The objective of this research is to develop a neural network system capable of accurately identifying an unknown flow regime with little error. This network will be made by combining two individual flow regime identification neural networks, one that makes use of a statistical analysis of the tomograms data, and one that makes use of an image analysis of the tomogram itself. Once both networks have been developed with each being capable of making accurate guesses of unknown flow regimes the individual networks will be combined to develop a high accuracy flow regime classification neural network. A method of accurately identifying the current state and flow regime of a two-phase flow is highly desirable within thermal management systems because as long as the fluid remains two-phase the temperature and the pressure of the system will remain constant. Therefore, if the flow regime of the two-phase flow is always known the system can be controlled accordingly so that the fluid remains two-phase. As long as the fluid is two-phase large amounts of heat can be applied to the system with little change in temperature and pressure.

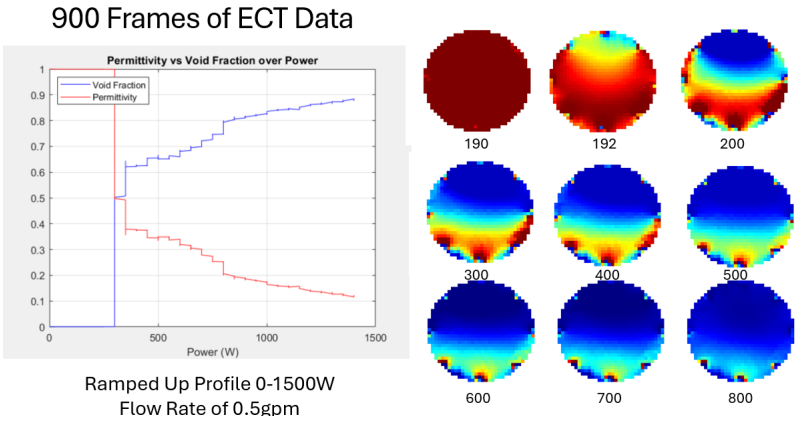
Methods
Data will be collected via a two-phase flow heat exchanger system. The system is made up of a positive displacement pump which will push the liquid refrigerant through the pipeline into a cold plate heat exchanger. The cold plate will be supplied with power so that the liquid refrigerant will partially evaporate through the cold plate. This two-phase refrigerant flow will then move through the Electrical Capacitance Tomography (ECT) sensor which will collect tomograms of fluid permittivity taking roughly 14 tomograms a second. After moving through the ECT sensor the refrigerant will go through a condenser returning it to the state at which the refrigerant entered the pump. Using the ECT data collected two flow regime identification methods are to be developed. The first is a statistical analysis of tomograms normalized

permittivity and center of gravity. From these quantities the probability density function, skewness, kurtosis and variance of the data is collected. Using all these values a neural network is trained with known flow regime tomograms to identify an unknown flow regime based on these statistical quantities. The other analysis is an image analysis of the tomogram itself. This analysis will make use of MATLAB's Deep Learning Toolbox and associated image classification neural networks to analyze the distribution and color of tomogram pixels to make a guess of the flow regime. After both methods have been developed individually, they are to be combined into a single neural network to develop a network with a high accuracy flow regime prediction.

Results and Discussion

Currently, few substantial results have been determined as neither network has been successfully developed. However, it has been determined that a single tomogram is not enough to accurately identify the flow regime of the system. Since two-phase flow fluctuates heavily between vapor and liquid, especially for higher permittivity flow regimes such as bubbly flow, a single tomogram may only reflect a portion of the flow regime. Therefore, a set of tomograms is to be used in the statistical analysis neural network and image analysis neural network for identifying individual flow regimes.

Figures/Charts



Ramped Up Profile 0-1500W
Flow Rate of 0.5gpm

Acknowledgments

- Dr. Mitch Wolff – Wright State
- Dr. Abdeel Roman – AFRL
- Zach Carner – AFRL

References

Roman, Abdeel J., et al. "Flow pattern identification of horizontal two-phase refrigerant flow using neural networks." *International Communications in Heat and Mass Transfer* 71 (2016): 254-264.

Truster, Nicholas. *Studies of Mechanically-Pumped Two-Phase Loops Under Pulsed Evaporator Heat Loads*. Diss. University of Dayton, 2024.

Carner, Zachary Joseph. *Void Fraction and Quality Correlation Analysis Using the Separated Flow Model for Pulsed-Power Heat Loads*. MS thesis. Wright State University, 2024.

Power and Thermal Management Systems in Aviation

Student Researcher: Anna Hagan

Advisor: Dr. Mitch Wolff

Wright State University
Mechanical Engineering

Abstract

As aviation technology continues to advance and become increasingly complex, power and thermal management systems have become more intricate and critical to the function of aircraft. With the increasing integration of advanced electrical systems on board, such as those supporting navigation, communication, and other vital functions, the amount of heat generated has risen significantly. This excess heat, if not carefully managed, poses a risk to both the mission's success and the overall safety of the aircraft. Instead of allowing this heat to be discarded as waste, which could compromise the survivability of the aircraft, it can be repurposed in innovative ways. Capturing this excess heat to power a generator and create energy reserves could provide a valuable resource to be utilized during times of peak energy demand, such as during high-load phases of flight or in emergencies, ensuring the aircraft has an additional source of power when it's most needed. Power and thermal management systems improve energy efficiency and enhance the reliability of modern aircraft systems.

Project Objectives

It is important to build a strong understanding of a topic before completing complex projects in that field. This project has the objective of furthering the students understanding in the field of power and thermal management systems for the student to design a project in the future.

Results and Discussion

As the technology onboard planes advances, the electrical demand has drastically increased. Navigation systems, communications, engine control, environmental controls, modern avionics, and more are commonplace in most planes. The additional load leads to a high energy demand and consequently leads to a large amount of heat being put off by all the new technology. Enter the Power and Thermal Management System (PTMS), a way to manage the additional heat and simultaneously increase the efficiency of the aircraft. A power and thermal management system is responsible for managing the heat put off by an aircraft and repurposing it so that it is increasing the efficiency of the aircraft. It is also responsible for preventing the excess heat from becoming a liability to the safety and survivability of the plane. Air force aviation typically has different energy requirements throughout its mission. This means that at certain points the aircraft will have a much higher energy demand and therefore become very hot very quickly compared to the steadier portions of its flight. The PTMS simultaneously provides energy through generators powered by redirected energy and manages the heat put off during the times of high demand.

Acknowledgments

A special thank you to Dr. Mitch Wolff.

References

Bodie, M., Russell, G., McCarthy, K., Lucus, E., Zumberge, J., & Wolff, M. (n.d.). *Thermal analysis of an integrated aircraft model*. PC Krause and Associates, Inc.; Air Force Research Laboratory.

Walters, E., Amrhein, M., O'Connell, T., Iden, S., Lamm, P., Yerkes, K., Wolff, M., McCarthy, K., Raczkowski, B., Wells, J., Borger, W., & Wampler, B. (2010). Invent modeling, simulation, analysis and Optimization. *48th AIAA Aerospace Sciences Meeting Including the New Horizons Forum and Aerospace Exposition*. https://doi.org/10.2514/6.2010-287

Differential microRNA Expression in Freeze-Tolerant Frogs during the Freeze Response

Student Researcher: Abigail Hall

Advisor: Dr. Kaleb Pauley

Cedarville University
Department of Science and Mathematics/Molecular Biology

Abstract
Several species of frogs use freeze-tolerance, in which the frogs freeze 42-65% of the water in their bodies, to survive the winter (Ingelson-Filpula & Storey, 2022). To survive this frozen state, these frogs downregulate nonessential genes and processes to conserve ATP (Ingelson-Filpula & Storey, 2022). Many regulatory mechanisms are required to perform this transition, including gene inhibition via microRNA, or miRNA (Rehman & Storey, 2024). MiRNAs are small non-coding RNAs that can prevent the translation of specific mRNA transcripts (Biggar et al., 2009). The liver is the center of metabolism (Hadj-Moussa et al., 2024), so this study focuses on the expression of miRNA in the liver of freeze-tolerant frogs.

In this study, I isolate and measure miRNA from the liver tissue of frogs before, during, or after freezing. This study examines two species of frogs: the Spring Peeper (*Pseudacris crucifer*), which is freeze-tolerant (Layne Jr. & Rice, 2003), and the Blanchard's Cricket Frog (*Acris blanchardi*), which hibernates instead of freezing (Swanson & Burdick, 2010) as a control.

My research indicates that miR-181a, miR-206, and miR-101 are all upregulated during freezing and that miR-206 is especially upregulated during both freezing and thawing in the liver tissue of both Spring Peepers and Blanchard's Cricket Frogs. However, these results are not statistically significant, and further research is needed to confirm or deny the differential expression of these miRNAs in these specific frogs during the freeze response.

Project Objectives

- Determine the difference in expression levels of specific miRNA transcripts in the liver of the Spring Peeper (*Pseudacris crucifer*) and the Blanchard's Cricket Frog (*Acris blanchardi*) during the freeze response.

Methods

Frog Collection and Preparation (performed by Dr. Michael Mendel at Cedarville University)

Spring peepers (*Pseudacris crucifer*) were collected from vernal ponds in Warren, Clark and Greene counties, in Ohio during mid-March 2020 and 2021. Blanchard's cricket frogs (*Acris blanchardi*) were obtained from streamsides in Greene County in late September 2020 and 2021. The frogs were placed in 42 x 26 x 32 cm acrylic terrariums with metal screen tops. The terrariums contained artificial plastic vegetation for climbing surfaces, and Petri dishes with spring water for drinking; moss, leaves, gravel, sand and water covered the bottom. The terrariums were placed in an outbuilding in Greene County that replicated the light, temperature, and humidity of the surrounding natural environment. The frogs were fed every two days with *Gryllodes sigillatus* (banded cricket), *Drosophila melanogaster* (common fruit fly) and wild small, wild invertebrates captured by netting. In the last week of November, the frogs were no longer fed. The frogs were then placed individually into 22 x 15 x 9 cm transparent plastic containers with perforated lids and a wet paper towel on the bottom. These containers were then placed in a Percival

Model LT41VL programmable incubator. The incubator photoperiod was set to follow the seasonal changes for Greene County; the temperature oscillated from 10°C to 2°C on a 24-hour basis.

In the second week of December, the temperature was set at 4°C. The frogs remained at 4°C (the acclimation temperature) for 25 d, after which one third of the frogs were placed into liquid nitrogen and then stored at -80°C. For the remaining frogs, the incubator temperature was lowered 1 C° day-1 (ca 0.04°C h-1). This rate of incubator temperature change was similar to that used by do Amaral et. al. (2018) for *D. chrysocelis* and Costanzo et al. (2015) for *Lithobates sylvaticus*. The incubator temperature continued to decline until it reached -3°C. As the temperature dropped below -1.5° C, ice chips (Breville food processor) were added to the area surrounding the frog to help initiate freezing. Frogs were monitored to determine the timeframe in which they froze. After all frogs had been frozen for at least 48 h, half of these frogs were placed in liquid nitrogen and stored at -80°C. The temperature was then increased 1°C day-1 (ca 0.04°C h-1) to 4°C. Frogs remained at 4°C for 48 h, and were examined for signs of recovery (including "righting reflex"within 2 s after being positioned on their dorsum). These frogs were then placed in liquid nitrogen and stored at -80°C.

Frog Dissection (performed by Elias Ng at Cedarville University)

During each lysis preparation, the frog sample was taken from the -80°C storage freezer and dissected quickly to minimize RNA degradation. Liver tissue was extracted from each specimen. Dissection was performed on an iced aluminum plate under a dissecting microscope. Stainless steel forceps, scissors, and scalpels were used to open and extract tissue from the specimens. The tools were regularly soaked in 70% ethanol throughout the dissections. Once harvested, the liver tissue was transferred to a microcentrifuge tube containing RNAlater™ solution. This microcentrifuge tube was placed in an iced aluminum temperature block, without being centrifuged. Rather, it was transferred to a 4°C refrigerator, where it was kept overnight. On the next day, each sample was transferred to the -80°C freezer for storage.

miRNA Isolation

miRNA from frozen samples of tissue from the liver of each frog was isolated according to the *mirVana™* kit protocol (*mirVana™*, 2011). Each specimen fell into one of three categories based on when they were dissected: hibernation, frozen, and post-freezing. Eight Spring Peepers from each harvest (n=24) and three Blanchard's Cricket Frogs from each harvest (n=9) were analyzed. Approximately 10 volumes per tissue mass of Lysis/Binding Buffer were added to the sample, and the lysate was vortexed, centrifuged at 10,000 rpm for 1 minute, and homogenized with a cell pestle (*mirVana™*, 2011). The lysate was then vortexed, centrifuged, and homogenized once more in the same manner. Approximately 1/10 lysate volume of miRNA Homogenate Additive was added, and the samples were incubated on ice for 10 minutes (*mirVana™*, 2011). After the incubation, approximately 1 volume equal to the lysate volume of Acid-Phenol:Chloroform was added to the sample (*mirVana™*, 2011). The samples were vortexed for 30-60 seconds and centrifuged at 13,200 rpm until a colorless supernatant was yielded (*mirVana™*, 2011). This supernatant containing miRNA was collected and combined with 1.25 volumes of molecular grade ethanol (*mirVana™*, 2011). Up to 700 µL of this solution was transferred into a collection tube onto a filter cartridge, and the samples were centrifuged at 10,000 rpm for approximately 15 seconds (*mirVana™*, 2011). The flow-through was discarded and this step was repeated until all of the ethanol-miRNA solution had been run through the filter (*mirVana™*, 2011).

Three wash steps followed using 700 µL miRNA Wash Solution 1 and 2 x 500 µL Wash Solution 2/3 (*mirVana™*, 2011). In each of these wash steps, the wash solution was added to the filter, the samples were centrifuged at 10,000 rpm for 15 seconds, and the flow-through was discarded (*mirVana™*, 2011). After the third wash step, the samples were centrifuged at 10,000 rpm for 30 seconds to dry the filter

(*mirVana™*, 2011). The filters from each sample were transferred to fresh collection tubes and 100 µL of Elution Solution pre-heated to 95°C was added to the filters (*mirVana™*, 2011). The samples were then centrifuged at 10,000 rpm for 15 seconds to elute the miRNA out of the filter and into the bottom of the collection tube (*mirVana™*, 2011). Finally, the samples were tested for concentration and purity using a biophotometer (*mirVana™*, 2011).

RT-qPCR

After the miRNA samples were isolated, reverse transcription was performed according to the RT-qPCR protocol from the *SYBR Green PCR Master Mix and SYBR Green RT-PCR Reagents Kit* (2011) with modifications made by Dr. Kaleb Pauley. For each set of reverse transcription reactions, one sample from each of the three categories was tested (Pauley, 2009). The miRNA samples were first tested for concentration and purity, even if they had already been tested (Pauley, 2009). Any samples that reported absolute values that were too high to be displayed were diluted with nuclease-free water and tested again (Pauley, 2009). Samples were diluted to 10 ng/µL for reverse transcription, and one miRNA sample from each harvest was treated at a time (Pauley, 2009). A reverse transcription master mix was prepared using the following reagents: 7.5 µL10x RT buffer, 1.0 µL 25x dNTP mix, 15.0 µL 10x RT microRNA primer, 5.0 µL Multiscribe Reverse Transcriptase, 1.0 µL RNase inhibitor, and 20.0 µL Nuclease-free water (Pauley, 2009).

Four sets of reverse transcription master mix were prepared, one for each primer (U6 snRNA, miR-181a, miR-206, and miR-101). U6 snRNA was used as an endogenous control to which the expression levels of the miRNAs would be compared. After mixing these reagents, the master mix tubes were briefly centrifuged (~10 sec) at 10,000 rpm. 10 µL of the reverse transcription master mix was combined with 5 µL of the diluted miRNA in PCR tubes (Pauley, 2009). The PCR tubes were then run in a thermocycler according to the microRNA protocol below (Pauley, 2009):

1. 16 °C for 30 min
2. 42 °C for 30 min
3. 85 °C for 5 min
4. Hold at 4 °C

After the reverse transcription was performed, the cDNA produced was analyzed using qPCR. A qPCR mix was prepared using the following reagents: 50.0 µL qPCR master mix, 5.0 µL Target primer, and 35.0 µL Nuclease-free water (Pauley, 2009).

After combining these reagents, 8.0 µL of this mix was combined with 2.0 µL cDNA in a PCR tube, and each sample was run in triplicate in a thermocycler using the Comparative Ct fast PCR protocol as outlined below (Pauley, 2009):

1. Stage 1: 1x
    a. 95 °C for 20 sec
2. Stage 2: 40x
    a. 95 °C for 1 sec
    b. 60 °C for 20 sec

Statistical Analysis

Based on the Ct values, the expression of each miRNA relative to the corresponding expression in the hibernation sample was calculated for each frozen and post-freeze sample. These relative expression

values were then used to perform a two-tailed, unpaired T-test and calculate a p-value to determine significance at the 0.05 confidence level.

Results and Discussion

Spring Peepers

The results of this study showed that in the freeze-tolerant Spring Peepers (Layne Jr. & Rice, 2003), miR-181a expression was increased both during and after freezing relative to hibernation levels (Figure 1). The same was true for miR-206, in which the increase in expression was more pronounced than that of miR-181a (Figure 1). Finally, miR-101 expression increased during freezing but decreased after freezing relative to hibernation levels (Figure 1).

Blanchard's Cricket Frogs

The results of this study showed that in the Blanchard's Cricket Frogs, which are not freeze-tolerant (Swanson & Burdick, 2010), miR-181a expression was increased both during and after freezing relative to hibernation levels (Figure 2). The same was true for both miR-206 and miR-101, with miR-101 having the most pronounced increase during freezing and miR-206 having the most pronounced increase after freezing (Figure 2).

Discussion

The results of this study show a marked increase in miR-206 expression both during and after freezing in both species of frogs, indicating that it is an integral factor for the freeze response (Figures 1&2). This miRNA has previously been associated with suppressing cell proliferation (Liu et al., 2020), which would make its upregulation ideal for the freeze response, during which energy and resources must be conserved. However, the p-values calculated from the results are greater than the 0.05 significance cutoff, so the results are not statistically significant (Tables 1&2). Therefore, more research is needed to confirm or deny the role of miR-206 in the freeze response.

Additionally, there is an increase in both miR-181a and miR-101 during freezing, especially in the Blanchard's Cricket Frogs (Figures 1&2). It is unclear why these miRNAs show such a pronounced increase in expression in the Blanchard's Cricket Frogs compared to the Spring Peepers, but it is possible that this difference in expression levels is due to the fact that the Blanchard's Cricket Frogs are not freeze-tolerant (Swanson & Burdick, 2010). miR-181a is associated with downregulating the NF-κB pathway (Kozloski et al., 2016), and miR-101 inhibits the protein STMN1 (Zhu et al., 2018). Both NF-κB and STMN1 promote cell proliferation, so the upregulation of their respective miRNAs results in less cell growth and division. This is useful for the freeze response for the same reasons that miR-206 upregulation would be beneficial. However, these results are not statistically significant, so more research is needed to reach a firm conclusion (Tables 1&2).

Figures/Charts

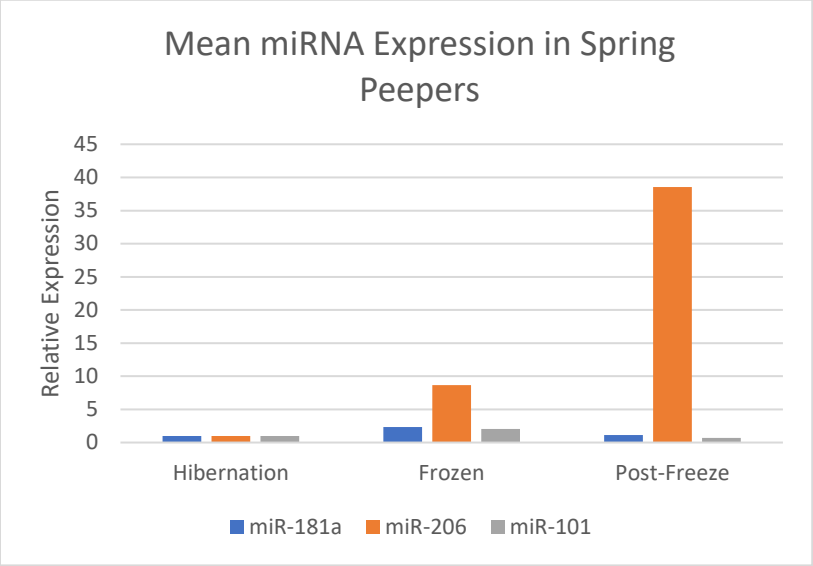


Figure 1. Mean miRNA Expression in Spring Peepers

	miR-181a	**miR-206**	**miR-101**
Hibernation vs Frozen	0.1439	0.1397	0.2229
Hibernation vs Post-Freeze	0.7654	0.2081	0.164
Frozen vs Post-Freeze	0.2232	0.3814	0.1382

Table 1. p-values for miRNA expression in Spring Peepers

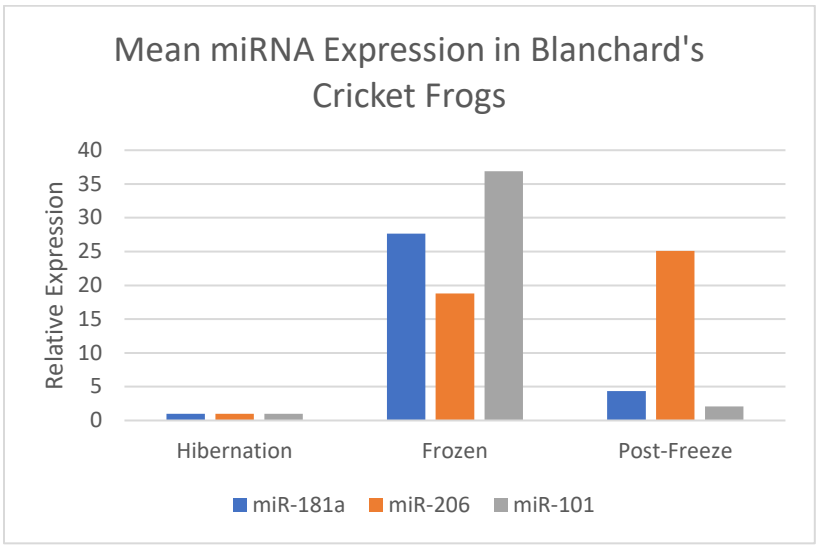


Figure 2. Mean miRNA Expression in Blanchard's Cricket Frogs

	miR-181a	**miR-206**	**miR-101**
Hibernation vs Frozen	0.1423	0.3519	0.2646
Hibernation vs Post-Freeze	0.3487	0.1575	0.4771
Frozen vs Post-Freeze	0.1943	0.7884	0.2773

Table 2. p-values for miRNA Expression in Blanchard's Cricket Frogs

Author Contributions

Dr. Michael Mendel wrote and performed the protocol for the "Frog Collection and Preparation" section of this study, and Elias Ng wrote and performed the protocol for the "Frog Dissection" section.

Acknowledgments

I would like to thank mirVANA™ miRNA isolation kit for supplying the reagents for the miRNA isolation and the SYBR Green PCR Master Mix and SYBR Green RT-PCR Reagents Kit for supplying the reagents for the qPCR. I would also like to thank Dr. Michael Mendel for directing this project and providing the frogs, as well as my advisor, Dr. Kaleb Pauley, for instructing and overseeing my miRNA isolation and analysis. Finally, I would like to thank Elias Ng for dissecting the frogs.

References

Biggar, K. K., Dubuc, A., & Storey, K. (2009). MicroRNA regulation below zero: Differential expression of miRNA-21 and miRNA-16 during freezing in wood frogs. *Cryobiology*, *59*(3), 317-321. https://doi.org/10.1016/j.cryobiol.2009.08.009

Costanzo, J. P., Reynolds, A. M., do Amaral, M. C. F., Rosendale, A. J., & Jr.Lee, R. E. (2015). Cryoprotectants and Extreme Freeze Tolerance in a Subarctic Population of the Wood Frog. *PLoS ONE*, *10*(2), 1–23. https://doi.org/10.1371/journal.pone.0117234

do Amaral MCF, Frisbie J, Goldstein DL, & Krane CM. (2018). The cryoprotectant system of Cope's gray treefrog, Dryophytes chrysoscelis: responses to cold acclimation, freezing, and thawing. *Journal of Comparative Physiology. B, Biochemical, Systemic, and Environmental Physiology*, *188*(4), 611–621. https://doi.org/10.1007/s00360-018-1153-6

Hadj-Moussa, H., Ingelson-Filpula, W. A., & Storey, K. B. (2024). Biogenesis and regulation of the freeze–thaw responsive microRNA fingerprint in hepatic tissue of *Rana sylvatica*. *DNA*, *4*(4), 380-396. https://doi.org/10.3390/dna4040027

Ingelson-Filpula, W. A., & Storey, K. B. (2022). MicroRNA biogenesis proteins follow tissue-dependent expression during freezing in *Dryophytes versicolor*. *Journal of Comparative Physiology B: Biochemical, Systems, and Environmental Physiology*, *192*(5), 611-622. https://doi.org/10.1007/s00360-022-01444-7

Kozloski, G. A., Jiang, X., Bhatt, S., Ruiz, J., Vega, F., Shaknovich, R., Melnick, A., & Lossos, I. S. (2016). miR-181a negatively regulates NF-κB signaling and affects activated B-cell-like diffuse large B-cell lymphoma pathogenesis. *Blood*, *127*(23), 2856–2866. https://doi.org/10.1182/blood-2015-11-680462

Layne Jr., J. R., & Rice, M. E. (2003). Postfreeze locomotion performance in wood frogs (*Rana sylvatica*) and spring peepers (*Pseudacris crucifer*). *Canadian Journal of Zoology*, *81*(12), 2061–2065. https://doi.org/10.1139/z03-202

Liu, C., Li, J., Wang, W., Zhong, X., Xu, F., & Lu, J. (2020). miR-206 inhibits liver cancer stem cell expansion by regulating EGFR expression. *Cell Cycle*, *19*(10), 1077–1088. https://doi.org/10.1080/15384101.2020.1739808

mirVanaTM miRNA isolation kit (2011). Life Technologies Corporation.

Pauley, K. (2009). *miRNA RT-PCR Protocol* [Unpublished protocol, adapted from the *SYBR Green* kit protocol]. Department of Oral Biology, College of Dentistry, University of Florida

Rehman, S., & Storey, K. B. (2024). Small RNA and freeze survival: The cryoprotective functions of microRNA in the frozen muscle tissue of the grey tree frog. *Metabolites*, *14*(7), 387-399. https://doi.org/10.3390/metabo14070387

Swanson, D. L., & Burdick, S. L. (2010). Overwintering physiology and hibernacula microclimates of Blanchard's Cricket Frogs at their northwestern range boundary. *Copeia*, *2010*(2), 247–253. https://doi.org/10.1643/CP-09-121

SYBR Green PCR Master Mix and SYBR Green RT-PCR Reagents Kit (2011). Life Technologies Corporation.

Zhu, L., Chen, Y., Nie, K., Xiao, Y., & Yu, H. (2018). MiR-101 inhibits cell proliferation and invasion of pancreatic cancer through targeting STMN1. *Cancer Biomarkers*, *23*(2), 301–309. https://doi.org/10.3233/CBM-181675

Controlled Deflection of a Subsonic, Axisymmetric Jet Using Plasma Actuators

Student Researcher: Zain Hamid

Advisor: Dr. Nathan Webb

The Ohio State University
Mechanical & Aerospace Engineering

Abstract

Thrust vectoring is the controlled deflection of a jet to change the angle of thrust generated from the exhaust nozzle. Current thrust vectoring methods include heavy, mechanical nozzles with many complexities to allow greater maneuverability and short or vertical take-off/landing capabilities. Coanda-based thrust vectoring is another method of effectively controlling jet deflection which uses a fixed geometry "reaction surface" and a substantial amount of bleed air relative to the primary mass flow. This is a major drawback in application. This research examines the use of azimuthally evenly distributed localized arc-filament plasma actuators (LAFPAs) and a reaction surface, curved away from the jet axis, to control the deflection of a subsonic, axisymmetric jet. LAFPAs have demonstrated the ability to control the mixing and entrainment characteristics of various flows using thermal perturbations to target the Kelvin-Helmholtz instability in flows with free shear layers. Excitation frequency (pulsing frequency of the LAFPAs) sweeps were completed at $\boldsymbol{M_J}$ = 0.48 and 0.9 using an array of static pressure taps fixed in the reaction surface to examine the control authority at various frequencies. The results showed the LAFPAs' ability to create static pressure asymmetry towards and away from the azimuthal center of the active group of LAFPAs. The observed trends show lower frequencies increasing suction downstream of the active LAFPAs while higher frequencies increase suction on the opposing side of the jet. Streamwise PIV results confirmed the measured static pressure asymmetries correspond to jet deflection. Asymmetry has been observed in the baseline flow and determining the effect of the baseline asymmetry on the control authority of the LAFPA's is of interest. Current work includes investigating the effect of various reaction surface geometries to maximize the thrust vectoring capabilities of this active flow control method.

Project Objectives

Thrust vectoring is the controlled deflection of a jet to change the angle of thrust from the exhaust nozzle which enables hyper-maneuverability and short or vertical takeoff/landing. Localized Arc-Filament Plasma Actuators (LAFPAs) repeatedly strike a low-power arc between pin electrodes. The drawbacks seen in current thrust vectoring methods such as complexity, weight, and bleed air requirements are eliminated using LAFPA control authority due to its light weight, low power input, and fixed geometry. Azimuthally evenly distributed LAFPAs and a nozzle outlet surface, termed a "reaction surface", curved away from the jet axis have demonstrated the ability to control mixing and entrainment characteristics of various flows using Coherent Structures (CS). The LAFPAs target the Kelvin-Helmholtz instability using thermal perturbations in free shear layers, inducing the formation of CS. Altering the pulse frequency, termed "excitation frequency", varies the size and spacing of the CS resulting in various effects of control. Low excitation frequencies have resulted in higher suction towards the active group of LAFPAs while high excitation frequencies have resulted in higher suction on the opposite side of the jet from the active group of LAFPAs. The effect of asymmetric static pressure distributions while the LAFPAs are inactive will be investigated. While the LAFPAs are inactive, the static pressure distribution around the jet is not perfectly symmetric due to small manufacturing imperfections and/or imperfect connections between nozzle extensions. The effect of asymmetric static pressure distributions on the control authority will be examined by analyzing various static pressure asymmetries while the LAFPAs are inactive and then analyzing the corresponding static pressure distributions when the LAFPAs are active. Understanding the

effect of various baseline static pressure asymmetries will provide further knowledge on the physics of this control method and may lend insight into reaction surface geometric parameters that are appropriate for applications.

Methods

The capabilities and control of the LAFPAs has been implemented in a blowdown facility at the Gas Dynamics and Turbine Laboratory at the Ohio State University's Aerospace Research Center. The ability to precisely control the jet stagnation pressure to maintain the nozzle pressure ratio allowed for experimentation at both Mach 0.48 and 0.9 to examine the effect of two subsonic Mach numbers on the LAFPAs' control authority. An existing boron nitride nozzle extension was used on a 25.4 mm diameter, axisymmetric, converging nozzle to house the LAFPA pin electrodes. The nozzle extension has a 6.5 mm long constant-diameter section with the LAFPA pin electrodes housed in a 1 mm wide by 0.5 mm deep groove (to shield and stabilize the arc) located 0.5 mm upstream from the end of the extension. The nozzle extension houses 8 pairs of pin electrodes azimuthally distributed around its circumference. Each LAFPA consists of a pair of 1 mm diameter tungsten pin electrodes with a center-to-center separation of 3.8 mm. The reaction surface extension was mounted to the nozzle extension and the backward facing step is created from the difference in diameter between these extensions. The reaction surface is 3D printed in-house to be parallel to the jet axis at its furthest point upstream and curves radially outward with a constant radius of curvature as it extends downstream. The reaction surface creates a step height of 1 mm with a radius of curvature of 73mm (outlet angle of 15°). The reaction surface includes 12 azimuthally distributed static pressure taps (perpendicular to reaction surface) located 13.3 mm downstream of the step. The nozzle extension and reaction surface assembly can be seen in Figure 1. An existing Scanivalve DSA 3217 16-channel pressure transducer (+/- .05% full-scale long-term accuracy) was used to collect static pressure distributions from the reaction surface which has been proven to quantify jet deflection. The pressure transducer was operated using an in-house developed LabVIEW code. Each static pressure measurement was an average of 50 points recorded at a rate of 10 Hz. An in-house built power supply drove each actuator supplying a periodic 8 kV potential across pin electrodes.

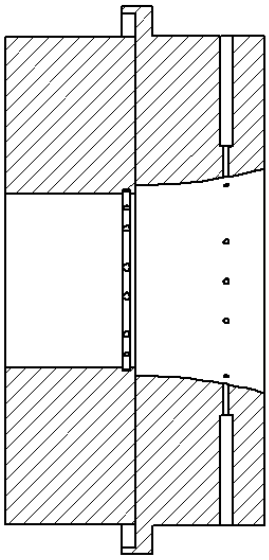


Figure 1: Boron Nitride nozzle extension with 3D printed reaction surface. Side view (flow left-to-right) of actuators, static pressure taps, and reaction surface contour.

To analyze the effects that the baseline asymmetry have on LAFPA control authority, the baseline asymmetry of the nozzle geometry must first be recorded. The baseline asymmetry is found by acquiring static pressure measurements of the jet when the LAFPAs are not excited. This baseline asymmetry is likely due to geometric imperfections and gives a good idea on the natural jet deflection angle without LAFPA control authority. To find the baseline asymmetry direction, a magnitude vector is created from each individual static pressure tap measurement and is summed into a resultant vector. This resultant vector shows the natural, slight deflection of the jet and is termed," baseline asymmetry vector". The alignment of the baseline asymmetry vector and the active group of LAFPAs is hypothesized to influence the LAFPAs' ability to control the flow. To test this, the static pressure measurements towards and away from the active group of LAFPAs were recorded across the full range of excitation frequencies for two cases. The first case is when the center of the active LAFPA group is aligned with the baseline asymmetry vector and the second case is when the center of the active LAFPA group is aligned 180 degrees azimuthally from the baseline asymmetry vector. When excited cases are collected, the active group of LAFPAs include a group of 3 adjacent LAFPAs being fired at the same frequency on one side of the jet.

Results and Discussion

The LAFPAs' control authority was primarily assessed using static pressure measurements obtained at various excitation frequencies. Figures 2 and 3 display the pressure asymmetry for a range of excitation frequencies from 1-83.33 kHz for M_j = 0.48 and 0.9. The definition of pressure asymmetry is such that a positive value indicates the net suction on the jet is directed toward the center of excitation (CE, the azimuthal location of the center of the active group of LAFPAs) while a negative value indicates the net suction is directed opposite the CE (OCE, 180° from the CE).

Figure 2 displays the pressure asymmetry for the full range of excitation frequencies for M_j = 0.48 and 0.9 when the baseline asymmetry vector is aligned with the CE (case 1). The LAFPAs demonstrate the ability to attach the flow to the reaction surface towards the CE effectively at low frequencies (1-20 kHz). The LAFPAs do not demonstrate the ability to effectively detach the flow from the reaction surface towards the CE and direct it towards the OCE, which is expected at higher frequencies. The baseline asymmetry vector signifies that there is higher flow entrainment in the direction of this vector and therefore greater suction. When the baseline asymmetry vector is aligned with the CE, it is intuitive that attaching the flow towards the CE by entraining more mass flow is effective because the natural entrainment already creates suction towards the CE. It also makes sense that detaching the flow from the reaction surface towards the CE (using high frequency excitation) is not as effective because increasing the excitation frequency decreases the entrainment towards the CE which is difficult when fighting the natural entrainment shown by the baseline asymmetry vector. This difficulty may also stem from an apparent lower-level baseline entrainment observed OCE.

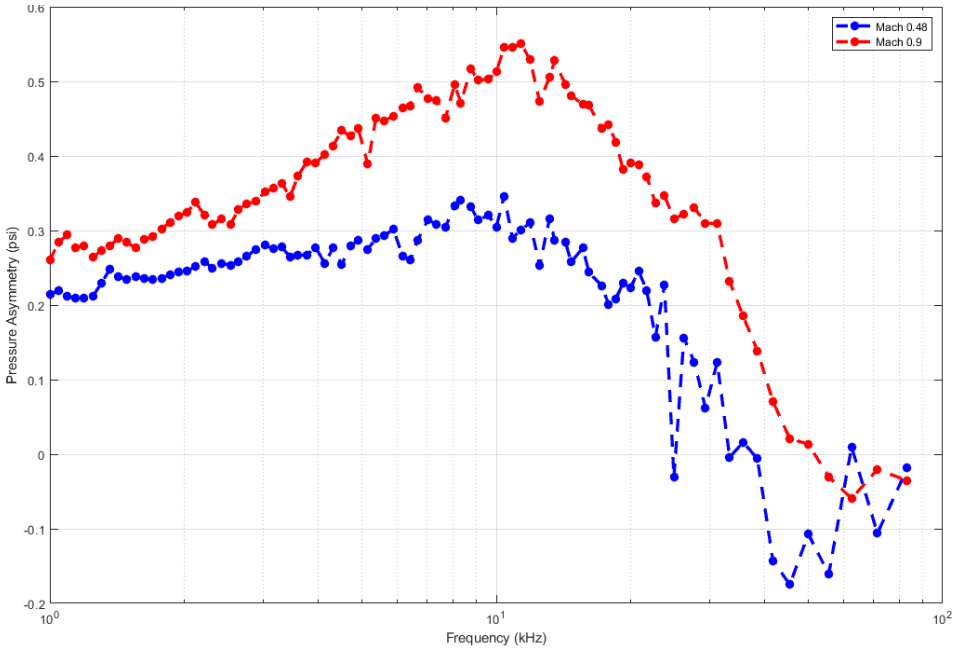


Figure 2: Full frequency sweep static pressure measurements for case 1 (active group of LAFPAs aligned with baseline asymmetry vector).

Similarly, Figure 3 displays the pressure asymmetry for the full range of excitation frequencies for M_j = 0.48 and 0.9 when the baseline asymmetry vector is aligned with OCE (case 2). In this case, the effects of the baseline asymmetry appear to be opposite of the effects seen in the first case. The effectiveness of attaching the flow to the reaction surface towards the CE is much lower than the effectiveness of detaching the flow from the reaction surface towards the CE. This is likely due to the natural entrainment shown by the baseline asymmetry vector pulling the flow away from the entrainment created through LAFPA control. This results in the flow to detach from the reaction surface towards the CE and be pulled towards the reaction surface OCE. When the baseline asymmetry vector is aligned OCE, the LAFPA control is fighting the natural entrainment at low frequencies which results in less effectiveness than detaching the flow at higher frequencies when the LAFPA control is working with the natural entrainment shown by the baseline asymmetry vector.

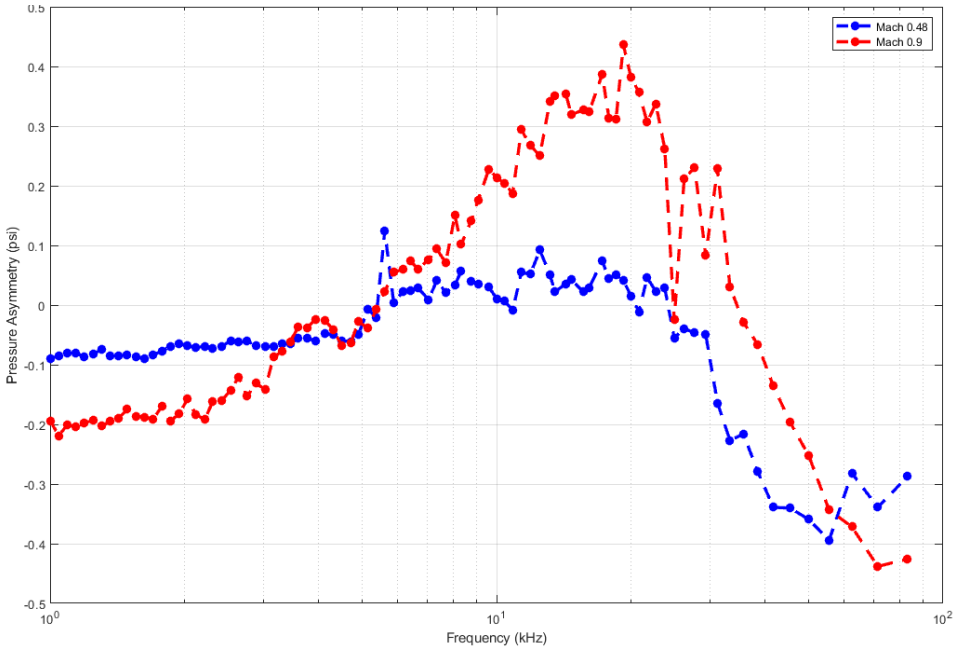


Figure 3: Full frequency sweep static pressure measurements for case 2 (active group of LAFPAs aligned opposite baseline asymmetry vector).

In conclusion, the baseline asymmetry investigation agreed with the hypothesis showing that the alignment of the baseline asymmetry vector relative to the active group of LAFPAs does influence the LAFPAs control authority. If the baseline asymmetry vector is aligned with the active group of LAFPAs (CE), attachment-based control at low frequencies has a bigger effect while detachment-based control at high frequencies has a smaller effect. The effects are opposite if the baseline asymmetry vector is aligned opposite the center of the active group of LAFPAs (OCE). The effect of the LAFPAs is either stronger or weaker depending on if the coherent structures created by the LAFPAs are deflecting the flow in the same direction as the baseline asymmetry vector or the opposing direction. This implies that the active group of LAFPAs must be chosen carefully and consistently based on the baseline asymmetry vector of the current rection surface geometry because the effects of control can be skewed in the direction of this baseline asymmetry vector. It also implies that the baseline asymmetry must be eliminated when used in application. Future work involves an investigation into the effect of different reaction surface geometries. This includes analyzing the effects on control authority by varying the step height and reaction surface length.

Acknowledgments

The support of this work by the Office of Naval Research through Drs. David González and Leighton Myers is greatly appreciated. Support by the Ohio Space Grant Consortium of Alex Barnhouse through a fellowship, and Zain Hamid through an undergraduate research scholarship is also gratefully acknowledged.

References

[1] Gill, K. The Development of Coflow Fluidic Thrust Vectoring Systems. Dissertation. University of Manchester, Manchester, UK, 2008.

[2] González, D., Gaitonde, D., and Lewis, M. “Large-Eddy Simulation of Plasma-Based Asymmetric Control of Supersonic Round Jets.” International Journal of Computational Fluid Dynamics, Vol. 29, Nos. 3–5, 2015, pp. 240–256. https://doi.org/10.1080/10618562.2015.1053877.

[3] Samimy, M., Webb, N., and Crawley, M. “Excitation of Free Shear-Layer Instabilities for High-Speed Flow Control.” AIAA Journal, Vol. 56, No. 5, 2018, pp. 1770–1791. https://doi.org/10.2514/1.J056610.

[4] Warsop, C., and Crowther, W. J., “Fluidic Flow Control Effectors for Flight Control,” AIAA Journal, Vol. 56, No. 10, 2018, pp. 3808–3824. https://doi.org/10.2514/1.J056787

Using Martian Meteorites to Interpret Future Gamma-Ray and Neutron Data of Phobos

Student Researcher: Adrienne Hammontree

Advisor: Dr. Andrew Beck

Petroleum Engineering & Geology Department
Marietta College

Abstract
The Mars-moon Exploration with GAmma rays and NEutrons (MEGANE) instrument aboard the Martian Moons eXploration (MMX) spacecraft will travel to Phobos, the larger of the two martian moons, to take elemental measurements of the surface. Led by the Japan Aerospace Exploration Agency (JAXA), MMX aims to determine the origin of the martian moons (giant impact vs. captured asteroid) via sample return and orbital measurements of Phobos. MEGANE (orbital gamma ray and neutron detector) data interpretation can be improved by a robust geochemical library of martian meteorites. In this study, we compiled bulk chemical analyses of various martian meteorites in order to calculate gamma ray and neutron measurable ranges for different martian petrographic groups. We employed efforts to ensure chemistries were representative of whole rock composition and applied statistical thresholds to identify outliers in any petrologic group, which were then removed from the dataset. In total, we ended with a dataset of 51 unique petrologies which represents about 17% of the martian meteorite clan.

Project Objectives
We aimed to compile a series of martian meteorite bulk chemistries that will be used for data comparison once we get measurements of Phobos' composition within the next couple of years.

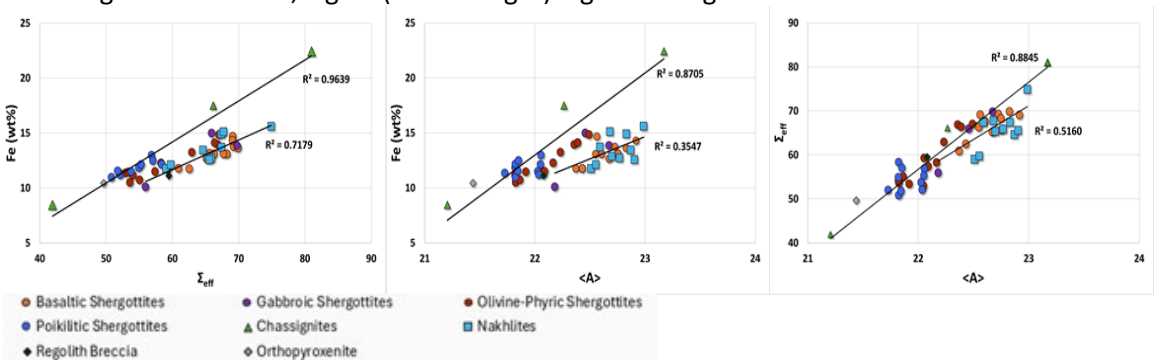
Methods
We followed methods described in Beck et al. (2015) (gamma ray and neutrons in HEDs) and applied them to the martian meteorite clan. We collected bulk chemistry data of different martian meteorite groups; shergottites, nakhlites, and chassignites, as well as a single orthopyroxenite (ALH 84001) and a polymict regolith breccia (NWA 7475). The shergottites were then subdivided petrologically due to their large quantity and variations in composition. Elemental data from 190 splits of various meteorites were averaged to ensure final chemistries were representative of each whole meteorite; 72% of the meteorites had data from two or more splits averaged together. 69 meteorites were analyzed in this study, of which 4 were excluded due to their lack of specific element data (i.e. Si, Fe), leaving 65. Paired meteorites were grouped together and averaged to better represent whole samples. This resulted in 51 unique martian meteorites in the dataset. This represents about 17% of the martian meteorite clan (Meteoritical Bulletin Database as of December 2024), as compared to Beck et al. (2015)'s similar study with the HEDs (they compiled 22% of the clan). Macroscopic thermal neutron absorption cross-section (Σeff) and average atomic mass (<A>) were calculated from Prettyman et al. (2013). Both Σeff and <A> are measurements that MEGANE will take of Phobos along with an elemental suite including H, O, Na, Mg, Si, K, Cl, Ca, Fe, Th, and U.

Results and Discussion
The chassignites show widely variable values in and both Σeff and <A> measurables, as well as Fe and Mg (Mg not shown here) (Figs. 1, 2, and 3). This is mainly due to the differences in olivine composition (Fe_2SiO_4 vs. Mg_2SiO_4), which composes ≥ 90 vol% of the chassignites. The olivine composition for each chassignite are as follows: Chassigny-$Fo_{67.64\text{-}68.40}$, NWA 2737-$Fo_{77.58\text{-}78.84}$, NWA 8694-$Fo_{53.19\text{-}54.25}$ (Hewins et

al., 2020). They also contain a much lower Si content than other martian petrologies making them appear more similar to chondritic compositions. If Phobos' formation is similar to Earth's moon, mainly being composed of mantle material, then understanding these ultramafic/dunitic compositions represented best by the chassignites will prove to be important in future data interpretation. Within the martian petrologies, there are two noticeable trends in <A> and Σeff corresponding to compositions dominant in olivine and orthopyroxene (opx) and those of plagioclase and clinopyroxene (cpx) (Figs. 1, 2, and 3). Trend 1 (top line in Figs. 1-3), which represents olivine and opx, includes the chassignites, poikilitic shergottites, and the single orthopyroxenite ALH84001. Trend 2 (bottom line in Figs. 1-3), which represents plagioclase and cpx, includes the nakhlites, basaltic shergottites, and gabbroic shergottites. The olivine-phyric shergottites were not included in either one of these groups due to them being a porphyritic mix of both groupings (Udry et al., 2020). This can be seen by them falling in between our two trendlines in figs. 1 & 2.

Figures/Charts

Fig. 1. (top left) Fe wt% vs macroscopic thermal neutron absorption cross-section., Fig. 2. (top right) Fe wt% vs average atomic mass., Fig. 3. (bottom left) Macroscopic thermal neutron absorption cross-section vs average atomic mass., Fig. 4. (bottom right) legend for figs. 1-3.



Acknowledgments

We would like to thank the MMX/ MEGANE Team for their collaboration on this project. We'd also like to thank the Marietta College Investigative Studies Program as well as the Marietta College Petroleum Engineering & Geology Department for their support throughout this study.

References

(1) Beck, A.W., Lawrence, D.J., Peplowski, P.N., Prettyman, T.H., McCoy, T.J., McSween, H.Y., Jr, Toplis, M.J. and Yamashita, N., (2015), Using HED meteorites to interpret neutron and gamma-ray data from asteroid 4 Vesta. Meteorit Planet Sci, 50, 1311-1337. (2) Hewins, R.H., Humayun, M., Barrat, J.-A., Zanda, B., Lorand, J.-P., Pont, S., Assayag, N., Cartigny, P., Yang, S., Sautter, V., (2020), Northwest Africa 8694, a ferroan chassignite: Bridging the gap between nakhlites and chassignites. Geochim. Cosmochim. Acta 282, 201–226. (3) Lawrence, D.J., Peplowski, P.N., Beck, A.W., Burks, M.T., Chabot, N.L., Cully, M.J., Elphic, R.C., Ernst, C.M., Fix, S., Goldsten, J.O., Hoffer, E.M., Kusano, H., Murchie, S.L., Schratz, B.C., Usui, T., Yokley, Z.W., (2019), Measuring the elemental composition of phobos: The mars-moon exploration with GAmma rays and NEutrons (MEGANE) investigation for the Martian Moons eXploration (MMX) Mission. Earth and Space Science, 6, 2605–2623. (4) Prettyman, T.H., Mittlefehldt, D.W., Yamashita, N., Beck, A.W., Feldman, W.C., Hendricks, J.S., Lawrence, D.J., McCoy, T.J., McSween, H.Y., Peplowski, P.N., Reedy, R.C., Toplis, M.J., Le Corre, L., Mizzon, H., Reddy, V., Titus, T.N., Raymond, C.A. and Russell, C.T., (2013), Neutron absorption constraints on the composition of 4 Vesta. Meteorit Planet Sci, 48, 2211-2236. (5) Udry, A., Howarth, G. H., Herd, C. D. K., Day, J. M. D., Lapen, T. J., & Filiberto, J., (2020), What Martian meteorites reveal about the interior and surface of Mars. Journal of Geophysical Research: Planets, 125

Robotic Terrain Traversal: Comparative Review of Legs and Wheels

Student Researcher: Joseph Hefler

Advisor: Dr. Rui Liu

Kent State University
College of Aeronautics and Engineering / Aerospace Engineering

Abstract
This research compares dynamic legged robot systems and wheeled rovers, focusing on AI-driven path planning and human-robot interaction to improve planetary exploration on rugged terrain. While wheeled rovers like NASA's Spirit and Curiosity have worked well on Martian terrain, their movement is limited on steep or uneven areas. Dynamic legged robots, modeled after biological movement, offer better adaptability and stability in tough environments. This project looks at how both systems perform using AI-based simulations and explores tools like NASA's AEGIS for autonomous navigation. The study identifies trade-offs in control, efficiency, and mission reliability between different types of mobility systems and suggests ways to combine their strengths.

Project Objectives
The main goal of this study is to compare legged and wheeled robotic movement systems for use in planetary exploration. It examines how current wheeled rovers, like NASA's Curiosity and Perseverance, handle rough ground and the problems caused by fixed wheel structures—like worn treads, getting stuck, and using too much energy on rocky surfaces. The study also looks into legged systems by analyzing their mechanical design, movement types, and ability to handle uneven terrain.

Even though full simulations were not completed due to technical issues, research from past studies was used to analyze mobility, terrain handling, and autonomous decision-making. AI tools were also explored for possible use in terrain mapping and avoiding obstacles. The goal is to use what was learned to help develop stronger, more flexible robots that can support long-term missions in harsh environments.

Methods
To evaluate how different robotic systems perform in planetary exploration scenarios, this project aimed to use ROS2 (Robot Operating System 2) and Gazebo to simulate movement across terrains To see how different robotic systems perform on difficult surfaces, the project used ROS2 and Gazebo to simulate movement across Mars-like terrain. ROS2 managed control of the robot joints and sensor data, while Gazebo simulated how the robots moved and reacted to the environment.

The simulations were set up to test different ways of moving. For hexapod robots, the focus was on walking styles like tripod, wave, and ripple gaits. These were picked because they are useful for walking on rough terrain and offer a balance of stability and energy use. Wheeled robots were also tested using basic movement as a comparison.

To create accurate robot models, URDF files were used to define the robot's shape, joints, and sensors. RViz and TF tools helped check that everything was placed and connected correctly. RViz let us see the robot's parts and movements in a 3D view, and TF managed the positions of each part during the simulation.

Despite the setup, several problems kept the simulations from running completely. Some software components didn't work well together, and the computer hardware wasn't strong enough to keep the simulations running smoothly.

To help fill in the gaps, past studies were used. Xu et al. (2019) created a model of a climbing hexapod robot and showed that keeping the robot's center of mass inside the support area helps it stay balanced. This showed how legged robots can handle steep or vertical terrain. Chakraborty and Ghosal (2004) looked at how wheeled robots move on bumpy ground and explained how the shape of the wheels and the ground affects their grip. Their work helped explain why wheeled robots sometimes struggle on soft or uneven terrain.

By combining these studies, the project compared how well each robot type could move, handle terrain changes, and stay under control. This helped lay the foundation for future robots that use both legs and wheels.

Results and Discussion

Although direct simulations were not completed due to technical challenges, insights from existing studies offer valuable perspectives on the comparative performance of legged and wheeled robotic systems in planetary exploration scenarios.

Xu et al. (2019) developed a kinematic model for a wall-climbing hexapod robot using the Denavit-Hartenberg method. Their analysis emphasized the importance of maintaining the robot's center of mass within the support polygon to ensure stability, especially when navigating vertical surfaces. This paper explains the potential of hexapod robots to maintain stability in complex terrains, which is crucial for planetary exploration where uneven and unpredictable surfaces are common.

Legged robots, such as Boston Dynamics' BigDog, have shown improved adaptability in challenging environments. These platforms can climb slopes over 35°, step over large obstacles, and maintain traction on deformable surfaces like snow or sand. The dynamic limb control in these robots allows for active adjustment of posture and gait using sensor feedback, enabling them to maintain balance and adapt to terrain changes effectively. Many are also capable of self-adjusting after falls, adding to their resilience in unpredictable environments.

Chakraborty and Ghosal (2004) analyzed the kinematics of wheeled mobile robots on uneven terrain, accounting for wheel-ground interactions and non-holonomic constraints. Their model provides a framework for understanding the limitations of wheeled systems in rough environments, particularly regarding their ability to maintain traction and stability.

Wheeled systems like NASA's Curiosity rover, equipped with rocker-bogie suspension, perform efficiently on terrain by passively keeping ground contact. However, their performance declines on loose or steep surfaces. For example, Curiosity experienced significant wheel slip and immobilization on a 31° slope of soft soil, despite being rated for 45°. Additionally, its slow speed (~0.14 km/h) limits quick terrain coverage, which can be a disadvantage in time-sensitive exploration missions.

The comparative analysis indicates that while wheeled robots are effective on relatively smooth and stable terrains, their adaptability is limited when facing steep, uneven, or soft surfaces. In contrast, legged robots, particularly hexapods, offer enhanced mobility and stability in such challenging conditions. Their ability to actively adjust limb movements allows them to navigate obstacles and maintain balance more effectively than wheeled counterparts.

Advanced navigation algorithms like A* offer significant promise for enhancing the autonomy of both legged and wheeled robotic systems. When integrated with Multiple Input Multiple Output (MIMO) systems, which process multiple sensor and actuator data streams in real time, A* enables dynamic path planning and effective obstacle avoidance. This integration is crucial for operating in unpredictable extraterrestrial environments, where real-time decision-making and adaptability are essential.

Based on these findings, legged robots like hexapods show promise for future planetary missions, especially in areas where wheels are less effective. Their ability to adapt to different terrain makes them well suited for exploring slopes, caves, or unstable surfaces that rovers typically avoid. With better terrain coverage, these robots could reach places that might hold signs of preserved organic materials. They may also be used to support sample collection in more difficult areas, expanding our ability to study planetary geology and possibly uncover clues about past life. In future missions, these systems could help scout new regions, help astronauts, or perform scientific tasks in risky or unexplored areas. As mobility and autonomy continue to improve, legged robots could play a key role in the next generation of exploration on the Moon, Mars, and other planets.

Acknowledgments
I would like to thank Dr. Rui Liu and the Cognitive Robotics and AI (CRAI) Lab at Kent State University for their support and guidance throughout this research. I also thank the College of Aeronautics and Engineering for providing additional resources that made this project possible. Additional, thanks to Weston Suhadolnik for his contributions to the research.

References

Xu, X., et al. (2019). Research on Kinematics and Stability of a Bionic Wall-Climbing Hexapod Robot. *Journal of Robotics*. https://pmc.ncbi.nlm.nih.gov/articles/PMC6466939/

Chakraborty, N., & Ghosal, A. (2004). Kinematics of wheeled mobile robots on uneven terrain. *Mechanism and Machine Theory*, 39(12), 1273-1287. https://www.researchgate.net/publication/222676779_Kinematics_of_wheeled_mobile_robots_on_uneven_terrain

RobotsGuide. (n.d.). *BigDog*. https://robotsguide.com/robots/bigdog

Jet Propulsion Laboratory. (2021, March 3). *NASA's self-driving Perseverance Mars rover takes the wheel*. https://www.jpl.nasa.gov/news/nasas-self-driving-perseverance-mars-rover-takes-the-wheel/

NASA. (n.d.). *Curiosity wheel wear*. https://llis.nasa.gov/lesson/22401

Tang, C., & Li, Y. (2023). Legged robot advances, technologies, and applications. *Robotics and Autonomous Systems, 162*, 104280. https://www.sciencedirect.com/science/article/abs/pii/S0952197624015768

Zhang, J., & Wang, Y. (2021b). Multiple-input multiple-output (MIMO) in 6G communications. *ScienceDirect*. https://www.sciencedirect.com/science/article/pii/S2772671123002711

The Role of KFB in Gravitropism

Student Researcher: Elyse D. Hensley

Advisor: Dr. Sarah Wyatt

Ohio University
Department of Environmental and Plant Biology

Abstract
The Wyatt Lab studies the biochemical components of a plant's gravity response to better understand gravitropic pathways. In the BRIC-20 spaceflight experiment, we identified 968 genes that were differentially regulated in 3-day-old etiolated *Arabidopsis thaliana* seedlings in spaceflight, compared to ground control replicates (Kruse et al., 2020). A group of proteins that function in the ubiquitin proteasome system (UPS), E3 ligases, were differentially expressed. E3 ligases are involved in the pathway that labels molecules for degradation in the cell. One of these E3 ligases was investigated in this thesis: Kelch domain-containing F-box protein (AT1G23390, *KFB*). KFB was identified to have a possible role in gravitropism through reorientation experiments conducted on Earth. This is being investigated through experimentation with *kfb* and chalcone synthase (AT5G13930, *CHS*) mutants. CHS is a substrate of KFB, meaning it is labelled for degradation by KFB. Two kfb mutant lines, *kfb-1* and *kfb*-2, and one chs mutant line, *chs-1*, were studied in this project and compared to the wild type ecotype, Columbia (Col-0). Root curvature and gravity persistent signaling (GPS) experiments were used to compare the mutant gravitropic phenotype with the wild type phenotype. The *kfb* mutants were also analyzed through disorientation on 3D clinostats. A novel clinostat protocol was developed for this experiment. These findings will further the knowledge on plant gravitropism which aims to improve our ability to grow plants in space as a source of food to support long-term spaceflight missions.

Project Objectives
The goal of this project is to determine the roles of KFB and CHS in *A. thaliana* gravitropism. The first objective is to characterize root and shoot curvature differences between Arabidopsis wild-type plants, *kfb* mutants, and *chs* mutants. The second objective is to develop a protocol on 3D clinostats to characterize plant responses to simulated microgravity.

Methods
Recombinant *A. thaliana* seeds were obtained from the Arabidopsis Biological Resource Center (ABRC), containing a tDNA insertion within the transcribed region of *KFB* or *CHS*. These knockout lines were grown and bred to homozygosity, confirmed by DNA extraction and PCR. Plants homozygous for the insertion were then used for experimentation. Three knockout lines, *kfb-1*, *kfb-2*, and *chs-1*, were studied in this project and compared to the wild type ecotype Col-0. Root curvature experiments are conducted by reorienting 7-day-old *A. thaliana* seedlings, turning them 135° (Figure 1A). Over 10 hours, their response to the new gravity vector is measured, comparing *kfb-1* and *kfb-2* to Col-0 (Figure 1B) and comparing *chs-1* to Col-0 (Figure 1C). GPS experiments are conducted by placing mature, 8 to 10 cm tall, *A. thaliana* plants on their side in the fridge for an hour, then placing them upright at room temperature (Figure 2A). Over two hours, their response to the old gravity vector is measured, comparing all mutant lines to Col-0 (Figure 2B). Recovery and response to the current gravity vector is also observed in this timeframe. Clinostat disorientation experiments are conducted by placing 7-day-old *A. thaliana* seedlings in a 3D clinostat and constantly rotating them leftwards at 1.5 RPM and forwards at 3.83 RPM (Figure 3A). Over 10 hours, their root response to clinorotation is measured, comparing *kfb-1* and *kfb-2* to Col-0. (Figure 3B). Type III

ANOVAs were conducted on the GPS, clinostat disorientation, and *kfb* root curvature measurements (p-value < 0.05). A Student's t-test was conducted on the *chs* root curvature measurements (p-value < 0.05).

Results and Discussion

For the root curvature experiment, there were no significant differences between *kfb-1*, *kfb-2*, and Col-0 at any time point (Figure 1B), but there were significant differences between *chs-1* and Col-0 at time points 4 through 10 (Figure 1C). These results indicate that CHS plays a role in root gravitropism, but that KFB does not. For the GPS experiment, there were no significant differences between *kfb-1*, *kfb-2*, and Col-0 at any time point (Figure 2B), but there were significant differences between *chs-1* and Col-0 at time points 60 through 120 (Figure 2B). These results indicate that CHS plays a role in stem gravitropism, but that KFB does not. For the clinostat disorientation experiment, there were significant differences between *kfb-1* and *kfb-2*, when compared to the Col-0 at time points 4 through 10 (Figure 3B). These results indicate that KFB might play a role in root gravitropism during constant reorientation or in an altered gravity environment.

Figures

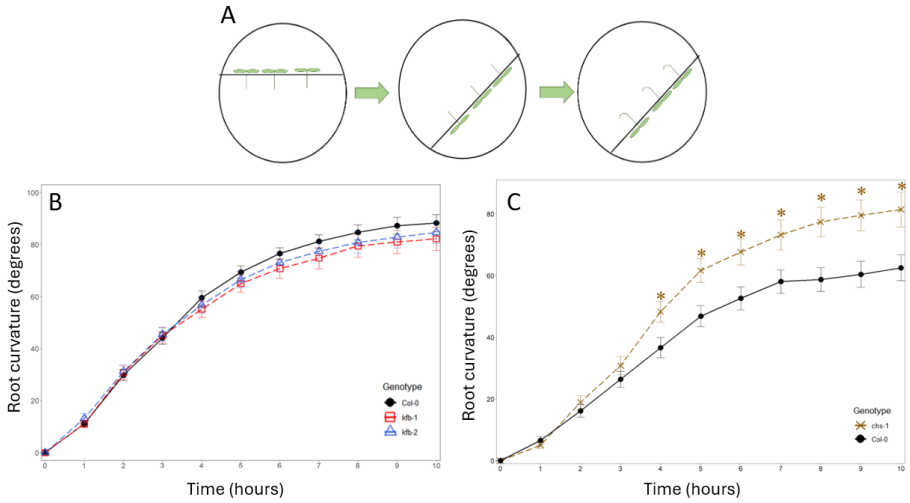


Figure 1. Root curvature setup and results. Stars indicate significance from the wild type (p-value < 0.05).

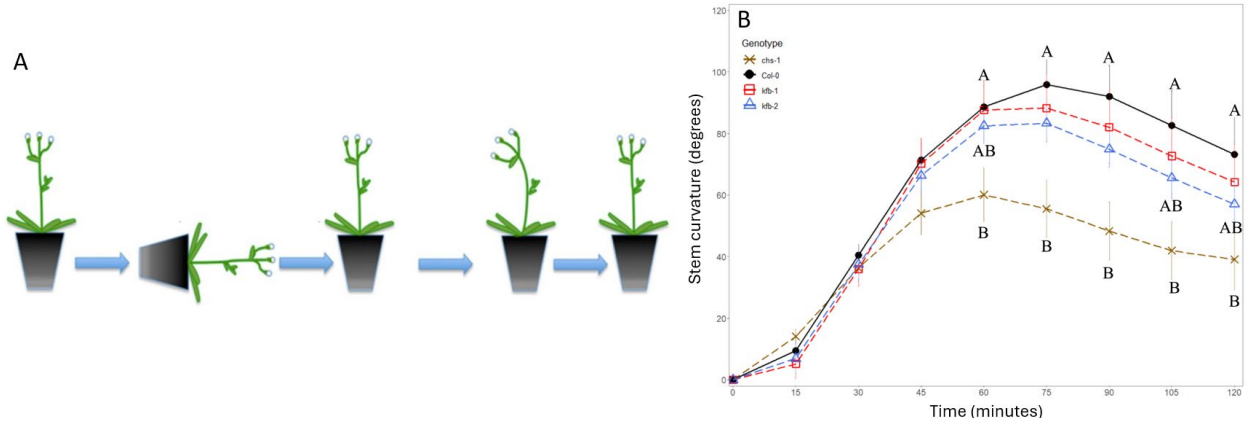


Figure 2. GPS setup and results. Letters indicate significant differences between groups (p-value < 0.05).

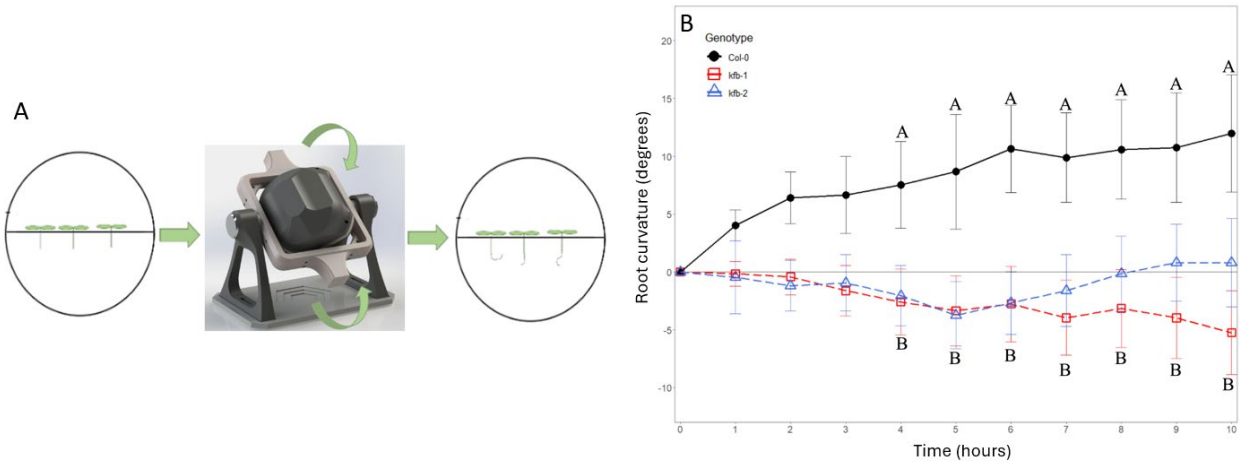


Figure 3. Clinostat disorientation setup and results. Letters indicate significant differences between groups (p-value < 0.05).

Acknowledgments

I would like to thank the Ohio Space Grant Consortium and Ohio University for funding this project. I would also like to thank my advisor Dr. Sarah Wyatt and lab members Samantha Fedoush, Emma Canaday, and Victoria Swiler for their guidance during this project.

References

Kruse, C. P., Meyers, A. D., Basu, P., Hutchinson, S., Luesse, D. R., & Wyatt, S. E. (2020). Spaceflight induces novel regulatory responses in Arabidopsis seedling as revealed by combined proteomic and transcriptomic analyses. *BMC Plant Biology*, *20*(1). https://doi.org/10.1186/s12870-020-02392-6

Reliable Power Conversion for Space Applications

Student Researcher: Claire Hopfensperger

Advisor: Dr. Mark Scott

Miami University
Electrical and Computer Engineering Department/Computer Engineering & Electrical Engineering

Abstract
Power electronics are essential to space innovations, supporting critical functions such as power conversion, conditioning, and management. Due to the complex and dynamic behavior of power electronics, reliable tools and methods for simulation, health monitoring, and failure prediction are not currently widely available. By determining when power electronics will fail, we can balance the expensive costs of frequent component replacement against the risks of unexpected failures. One health monitoring method being explored in the current research space is using a digital twin, or simulated version of a system, for failure detection and prediction. This research aims to design and fabricate a compact, accessible, and scalable printed circuit board (PCB) that consolidates a previously developed digital twin-based multi-part system for power electronics health monitoring and failure prediction. The condensed PCB was designed with Altium Designer to fit and interact with a Raspberry Pi 3, enabling adjustable and scalable operation.

Project Objectives
The objective of my research is to condense a previously developed digital twin-based health monitoring system to one PCB, which interacts with a Raspberry Pi 3 as a Raspberry Pi HAT ("Hardware Attached on Top"), to reduce the size of the system while increasing the scalability and ease of use. My research is the next step in prototyping a health monitoring and failure prediction system.

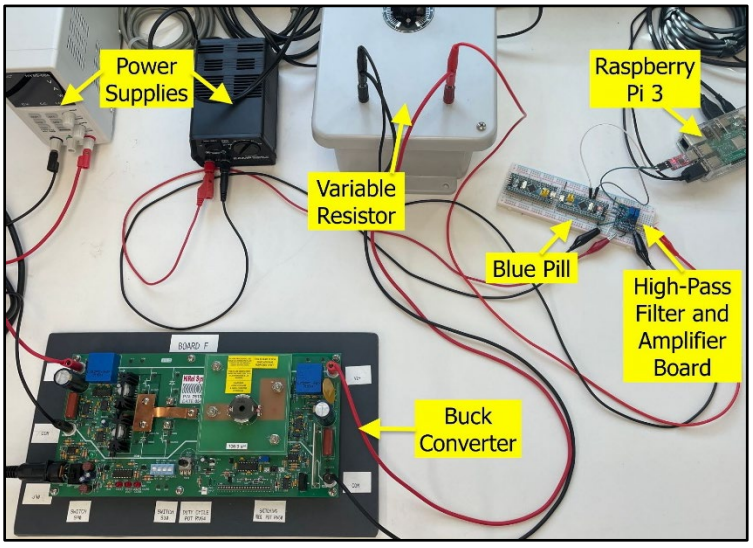


Fig. 1: Original System Setup

A Miami University 2023-2024 senior capstone group developed this previous system (Fig. 1) that monitors the health of a capacitor within a Buck converter, a commonly used power converter.

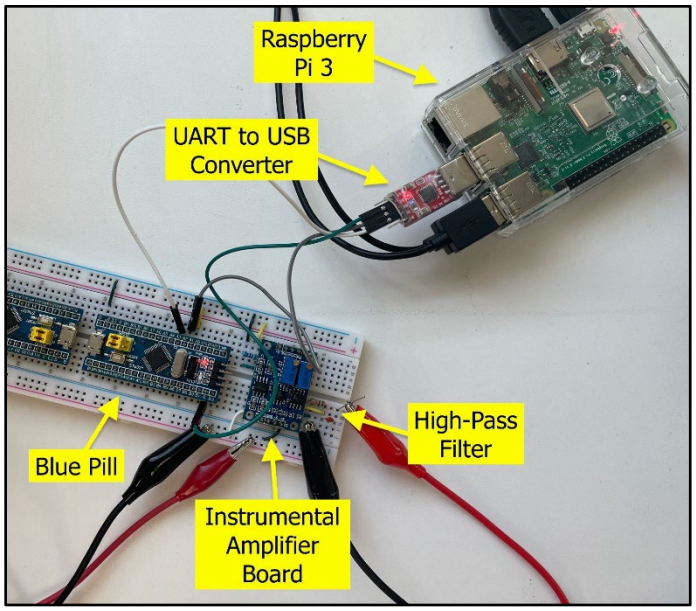


Fig. 2: Original system setup sub-section including high-pass filter, instrumental amplifier board, Blue Pill, UART to USB converter, and Raspberry Pi 3.

The previous system consists of a high-pass filter, an instrumental amplifier board [1], and an STM32 microcontroller (called a "Blue Pill") [2]. These three components are connected on a breadboard and then connected to a Raspberry Pi 3 via a UART to USB converter (Fig. 2). The high-pass filter removes the DC offset from the Buck converter capacitor ripple voltage signal so that the amplifier can read it, the amplifier board amplifies the signal so it can be sampled, and the Blue Pill samples the signal with its analog-to-digital converter (ADC) and then transfers it to the Raspberry Pi via UART communication for analysis.

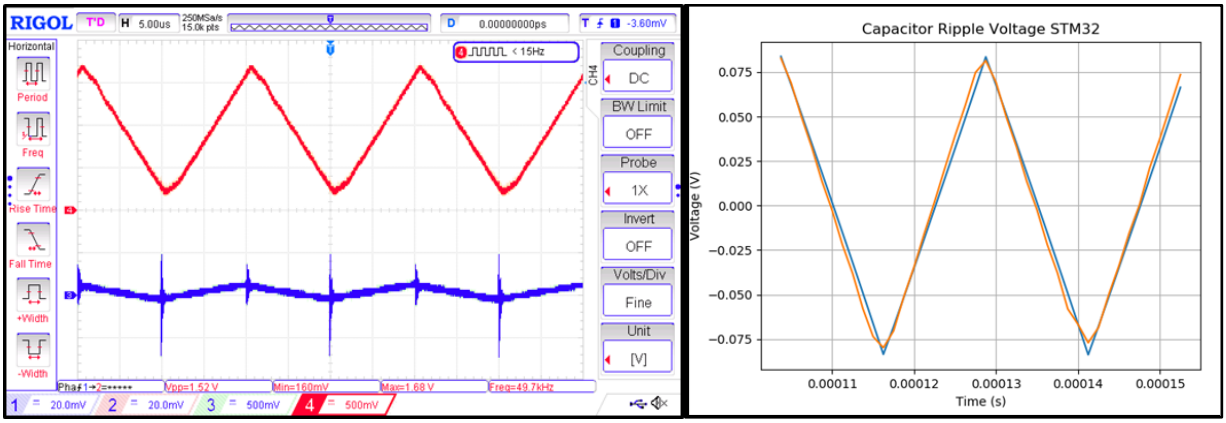


Fig. 3: Left: Oscilloscope capture of capacitor voltage with no DC offset (blue) and amplified capacitor voltage (red). Right: Raspberry Pi plot of measured capacitor voltage (orange) and simulated capacitor voltage (blue).

On the Raspberry Pi, via a Python script, the sampled signal is plotted against the ideal capacitor ripple voltage model (the "digital dwin") (Fig. 3), which was also developed by the 2023-2024 senior capstone group, so visual comparison can be used to determine if the capacitor is in good health or failing. The health of the capacitor is determined based on the shape difference of the ripple voltage signals; if the sampled ripple voltage is much larger or offset from the simulated ripple voltage, then the capacitor's

equivalent series resistance has increased or its capacitance has decreased, meaning the capacitor has aged.

Methods

First, to determine how the system could be condensed to a single PCB, I needed to understand how the previous system worked and what the expected outcome should look like. Upon breaking the system down and learning each part's purpose and functionality, I made several small adjustments to the original system to ensure the Raspberry Pi HAT PCB system would be achievable. Before, the amplifier board and Blue Pill were externally powered, but I determined that they could be powered with the 5 V and 3.3 V sources, respectively, from the Raspberry Pi. I also discovered that by reconfiguring the Raspberry Pi to enable UART communication, I could eliminate the need for the UART to USB converter and connect the Blue Pill directly to the Raspberry Pi's UART transmit/receive general purpose input/output (GPIO) pins.

Then, I started designing my Raspberry Pi HAT PCB. I used Altium Designer for the circuit design and PCB layout process. The PCB circuit would include the high-pass filter, the amplifier board components, GPIO header pins to attach the Blue Pill to the top of the PCB, and GPIO header pins to attach the PCB to the Raspberry Pi.

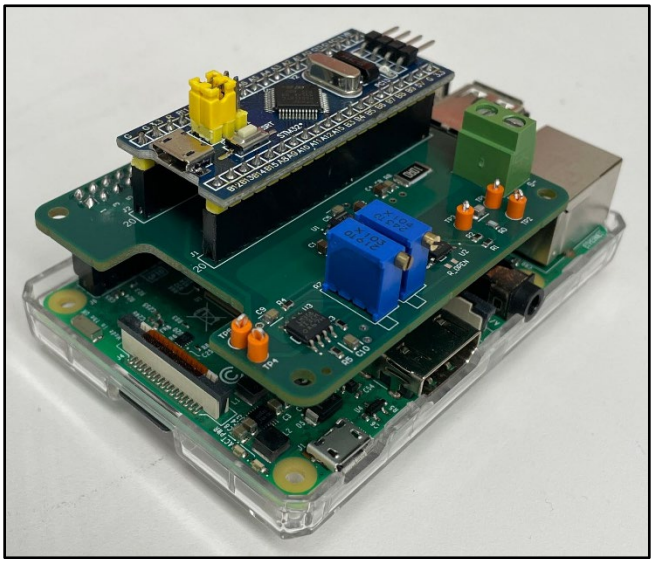


Fig. 4: Raspberry Pi HAT plugged into Raspberry Pi with Blue Pill attached on top.

Next, I ordered the PCB for fabrication and assembly through JLCPCB.com. Throughout the layout process, I ensured that the majority of my components were available through JLCPCB so that I could receive the PCB mostly assembled. Some components were not available through JPCPCB, though, so I hand-soldered those remaining components onto the PCB once it arrived and then integrated the Raspberry Pi HAT with the Blue Pill and Raspberry Pi (Fig. 4).

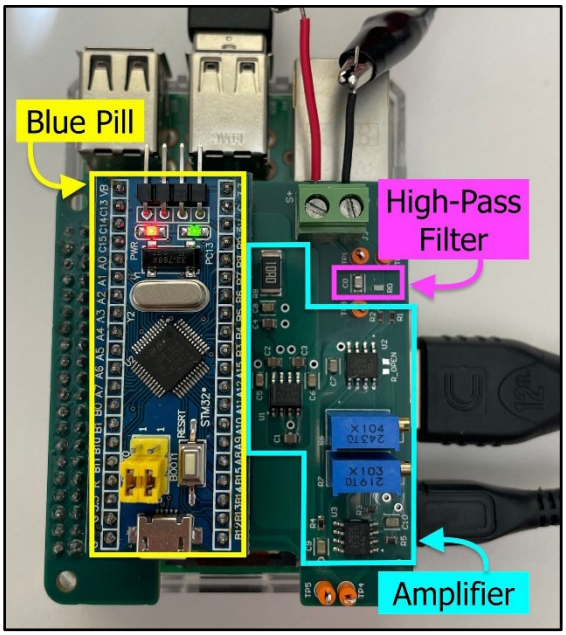


Fig. 5: New system setup sub-section showing the high-pass filter, amplifier, and Blue Pill on the Raspberry Pi HAT atop the Raspberry Pi.

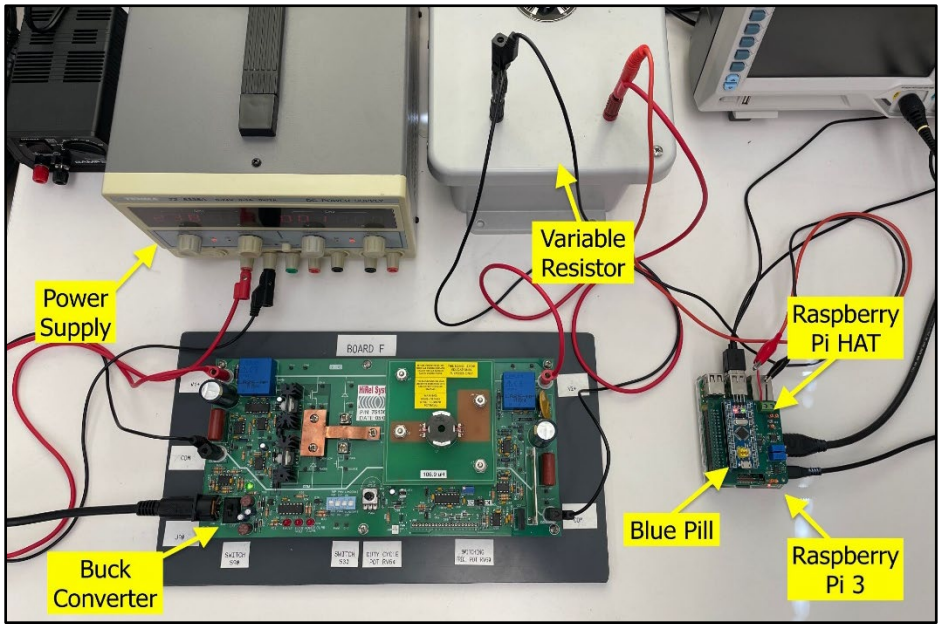


Fig. 6: New system setup.

Finally, I set up the new system (Fig. 5, 6) and tested the Raspberry Pi HAT to ensure proper functionality.

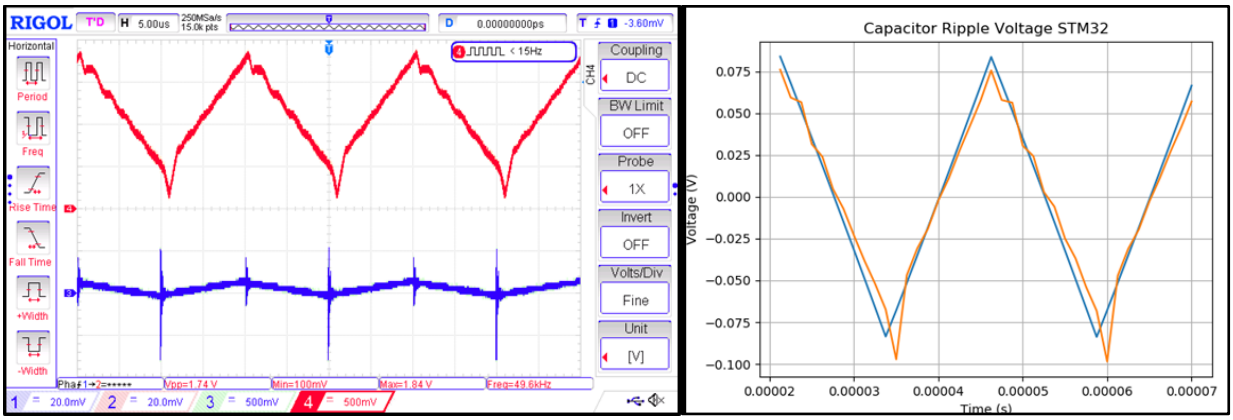


Fig. 7: Left: Oscilloscope capture of capacitor voltage with no DC offset (blue) and amplified capacitor voltage (red). Right: Raspberry Pi plot of measured capacitor voltage (orange) and simulated capacitor voltage (blue).

Luckily, the HAT worked as intended on the first try (Fig. 7)! Because the testing process was shorter than anticipated, I also implemented pseudo-live sampling. I adjusted the Raspberry Pi Python script to repeatedly trigger the Blue Pill to sample the capacitor voltage and send the data to the Raspberry Pi for data plotting. The sampling does not update instantaneously, but the repeated sampling offers a better idea of how the capacitor voltage acts over a short time period rather than a singular snapshot of its behavior.

Results and Discussion

The Raspberry Pi HAT system was successful in recreating the expected outcome of the original system (Fig. 3), with slightly more noise than the original system (seen in the peaks and dips of the measured signal) (Fig. 7). After investigating this difference with my advisor, we decided that the PCB system is more reliably sampling the capacitor voltage due to its secure connections in the PCB versus the breadboard setup, and the imperfect test setup introduces noise into the system, as seen in the measurements. Or, the additional noise is due to some artifact that came with the new system that we have not yet discovered in our investigation.

The PCB's adjustability and scalability come from the two potentiometers included in the circuitry (Fig. 5). The 100 kΩ potentiometer (labeled "104") adjusts the amplifier gain of the signal, and the 10 kΩ potentiometer (labeled "103") adjusts the amplifier offset of the signal. By adjusting these two potentiometers, the user can line up the measured capacitor voltage with the simulated capacitor voltage for easier visual comparison. It is with these adjustable aspects of the Raspberry Pi HAT along with the programmability of the Blue Pill and Raspberry Pi that we hope to be able to extend the use of this health monitoring system to more than just a capacitor in a Buck converter.

This research has a lot of room for future work and advancements. First, the pseudo-live sampling could be improved to get the sampling as close to live as possible. Achieving live sampling would allow for a more accurate representation of the signal in real time. Second, doubling the Blue Pill sample rate would allow for more detailed sampling of the capacitor voltage, which, in turn, draws a more detailed graph of the voltage on the Raspberry Pi. The more detailed graphs would enable a more accurate and reliable visual comparison between the sampled voltage and the simulated voltage for health monitoring. Third, testing the entire health monitoring system with different power systems and components that require health monitoring would expand the known ability of the health monitoring system. To test different power systems, though, more digital twin models of these power systems would need to be developed, which in and of itself is an important research topic.

NASA had developed a similar health monitoring system called the Inductive Monitoring System (IMS) [1]. IMS is a data-driven anomaly detection system. It extracts "models of normal system operation from archived data," which it gathers during its learning process by taking measurements of the system during normal operation [1]. Then, during IMS's monitoring process, the system "reads and normalizes real-time or archived data values" and attempts to fit it to the model [1]. If any of the data parameters are outside of the expected values decided by the model, IMS reports that behavior, and as the parameters stray further from the expected values, the system alerts the user to a potential anomaly [1]. This anomaly detection system is similar to my research's health monitoring system as it compares a model of the system under test to the measured values of the system under test. My research strives to remove the need for the hardware that is used to measure the normally operating system by replacing it with the digital twin version of the system. Since sensors and other hardware can have failure rates of their own, removing the need for them could result in more reliable health monitoring and, eventually, failure prediction.

For more detailed information on my research process and test results, please visit my GitHub repository at [2].

Acknowledgments

I would like to thank the Ohio Space Grant Consortium (OSGC) for enabling me to conduct this research and present my findings at the OSGC Student Research Symposium at the Ohio Aerospace Institute in Cleveland, Ohio. I also thank the 2023-2024 Miami University senior capstone group, Alecea Grosjean, Ethan Barnes, and Jimmy Roach, who developed the digital twin model and health monitoring system upon which I based my research. Lastly, I would like to express my gratitude to my research advisor, Dr. Mark Scott, for the guidance, support, and expertise he offered me throughout this entire research process.

References

[1] D. L. Iverson, R. Martin, M, Schwabacher, L. Spirkovska, W. Taylor, R. Mackey, J. P. Castle, and V. Baskaran. "General Purpose Data-Driven System Monitoring for Space Operations." in *Journal of Aerospace Computing, Information, and Communication*, Volume 9, No. 2, Oct. 2012. [Online]. Available: https://c3.ndc.nasa.gov/dashlink/static/media/publication/IMS_JACIC.pdf

[2] clairehopfensperger. "OSGC_Research_Virtual_Twinning." GitHub. [Online]. Available: https://github.com/clairehopfensperger/OSGC_Research_Virtual_Twinning

Plastic Waste to Energy via Chemical Reactions in Multiphase Environments

Student Researcher: Sania Imran

Advisor: Dr. Jorge E. Gatica

Cleveland State University
Department of Chemical and Biomedical Engineering

Abstract

More than 250 million metric tons of municipal waste are produced by Americans each year. Most of this waste is either unrecyclable, incinerated, or placed in landfills. With the adverse effects caused by incinerators, and landfills reaching maximum capacity, finding a solution to this ever-growing problem has become more apparent than ever. The concern from scientists and engineers has grown, and solutions and better alternatives to current waste management practices have become increasingly needed.

One such solution is waste gasification, a process that breaks down carbon-based materials into synthetic gas (syngas). This process has advantages over traditional procedures such as incineration, as it requires a much lower temperature and produces fewer by-products, thus leading to a lower energy footprint.

At Cleveland State University, a catalytic gasification process is being investigated in a low-to-medium temperature and high-pressure reactor. The goal for this research project is to resolve the fluid dynamics of a multi-phase reacting environment where waste substrates are converted to syngas with the aid of solid catalysts.

Project Objectives

Addressing the challenges of waste management in space exploration requires the development of innovative, cost-effective, and sustainable solutions. One promising approach is catalytic gasification, a process that can transform space waste into valuable resources like methane (CH_4) and oxygen (O_2). These resources could play a crucial role in supporting long-duration missions beyond Low Earth Orbit (LEO).

Indeed, exploring waste-to-energy processes can help reduce our reliance on Earth-based resupply missions. These technologies not only potentially mitigates the impact associated with such missions (by not generating debris) but also promote in-situ resource utilization (ISRU) strategies.

Furthermore, the innovations conceptualized for space waste management can also be applied to ground-based initiatives. Implementing these solutions in terrestrial applications could significantly address the growing waste crisis and hold the potential to power local communities, offering a dual benefit of improving sustainability both in space and on our planet.

Methods

This study explores the gasification of various waste types of the primary polymers under investigation are polyethylene and cellulose, both of which are significant components of municipal and space waste. Polyethylene is found in many plastic products, while cellulose appears in paper and wood. These two materials behave differently during gasification, polyethylene melts at reaction temperatures, whereas cellulose remains solid, influencing how they react and break down.

Proof-of-concept experiments have been successfully carried out in a high-pressure laboratory reactor operating at constant temperatures between 300-350 °C, and pressures range from 1200 to 2500 psig. The catalysts tested were ruthenium (Ru) and platinum (Pt) supported on aluminum oxide (Al_2O_3). Bi-metallic alternatives are currently under investigation.

Discussion and Future Goals

This study aims to model and analyze heterogeneous gasification by examining mixing, particle dynamics, and transport phenomena during the decomposition of solid substrates. A key focus will be the simulation of the gasification of solid substrates in a high-pressure stirred reactor using finite-element-based computational fluid dynamics (CFD) software to gain insights into the complex interactions governing the process. This study will help characterize the fluid dynamics and mixing parameters to optimize chemical reactions and material transport, ensuring efficient conversion of biomass into synthetic gas. Furthermore, this strategy will lay out the foundation to scale up the process from batch to continuous gasification, providing a framework for industrial implementation and advancing the feasibility of sustainable biomass utilization.

Acknowledgments

Support for this project was provided by the Washkewicz College of Engineering at CSU, the Ohio Space Grant Consortium (OSGC), and the Department of Chemical and Biomedical Engineering.

References

1. Cartland Glover, G.M. and J.J. Fitzpatrick "Modelling vortex formation in an unbaffled stirred tank reactors," Chem Eng. J., 127, 11-12 (2007)
2. Nagata, S. "Mixing: principles and applications," Wiley, New York (1975)
3. Busciglio, A., F. Grisafi, F. Scargialia, and A. Brucato "On vortex shape in unbaffled stirred vessels as measured by digital image analysis," pp. 49-54 in Proceedings of the 14th European Conference on Mixing, Warszaw, Poland (September 2012)
4. Tillo, A. "Will Plastics Recycling Meet its Deadline?" C&E News, 99 (37), October (2021).
5. Reyes, K.M., N. Plentovich, M.J. Lang, and J.E. Gatica "Catalytic Gasification of
6. Polyethylene As an in-Situ Resource Utilization (ISRU) Alternative," 2020 National AIChE Annual Meeting, November 16-20 (2020).
7. Lang. M.J. and J.E. Gatica "Catalytic Gasification - a Critical Analysis of the Water-Gas-Shift Reaction on Ru and Pt-based Catalysts," International Journal of Chemical Reactor Engineering, In Preparation (2024).
8. Lange, E.M., B. DeMattia, and J.E. Gatica "Catalytic Gasification - a Critical Analysis of Carbon Dioxide Methanation on a Ru/A1203 Catalyst," Int. J. Chem. React. Eng., (2018).
9. Santiago-Maldonado, E., J. Captain, R. Devor, and J. Gleaton, "Creating Methane from Plastic: Recycling at a Lunar Outpost," AIAA 2010-1551, 48th AIAA Aerospace Sciences Meeting, Orlando, FL (January 2010).
10. Sener, C.; Wesley, T. S.; Alba-Rubio, A. C.; Kumbhalkar, M. D.; Hakim, S. H.; Ribeiro, F.H.; Miller, J. T.; Dumesic, J. A., "PtMo Bimetallic Catalysts Synthesized by Controlled Surface Reactions for Water Gas Shift," ACS Catalysis 6 (2), 1334-1344 (2016).
1. Wheeler, C., A. Jhalani, E. J. Klein, S.Tummala,, and L. D. Schmidt "The water-gas-shift reaction at short contact times," Catalysis J., 223, 191-199 (2004).
2. Zamani, A.H. and S.J.M Rosid "Enhanced low temperature reaction for the CO2 methanation over Ru-promoted Cu/M on alumina support catalyst using double reactor system, " Taiwan Inst. of Chem. Eng. J., ms. # JTICE-D-18-01923 (2020).

Transforming Radar Manufacturing Through Automation

Student Researcher: Jeremy Jackson

Advisor: Dr. Mahmoud Abdallah

Central State University
Manufacturing Engineering

Abstract
Can a Fanuc robot replace the human labor of placing radar chips into an Electronically Scanned Array?

This project focuses on designing and implementing an automated robotic system using a FANUC industrial robot to replicate the assembly process of radar systems, specifically the precise placement of radar chips onto a circuit board or assembly fixture. Radar systems are critical components in industries such as automotive (for advanced driver-assistance systems), telecommunications, and aerospace, where precision and reliability are essential. The goal of this project is to create a fully automated process that demonstrates the potential of robotics in high- precision manufacturing. The system consists of a FANUC robot programmed to execute precise motions required for the placement of radar chips. The robot is equipped with a gripper end capable of handling delicate radar chips without causing damage or misalignment. The process begins with the robot picking up radar chips from a supply station, identifying the target positions using the vision system, and then placing the chips onto the assembly with sub- millimeter accuracy. The project incorporates elements of robotics, programming, and system integration to simulate a realistic manufacturing environment. A significant portion of the work involves developing the robot's motion control sequences, calibrating the machine vision system, and designing an efficient workflow to optimize placement speed and precision. By automating the radar chip placement process, this project demonstrates how robotics can address challenges in high-precision assembly, such as human error, inefficiencies, and variability in production.

Project Objectives
The objectives of this project is to replicate the process of a human building a radar. This project will allow for a robot to manufacture a radar with using human labor.

Methods
Visuals based off sensors – Sensors will be coded to tell the robot where to place the card chips. (Image process)
Orientation based of X-Y Plane- The engineer will manually create a X-Y plane for the robot to work in. Everything will be based on coordinates.
Manual Jogging- An engineer moves the robot each step of the way. This requires the most work input.

Results and Discussion
In conclusion, it was found successful that a robot can replace the human labor of manufacturing a radar component. The robot accurately and precisely completed the program multiple times. This program should be used in indutry in oder to streamline the manufacturing process of radars in aircraft. This was a successful project, and the researcher is grateful for the funding and support of the Ohio Space Grant Program.

Figures/Charts (If Applicable)

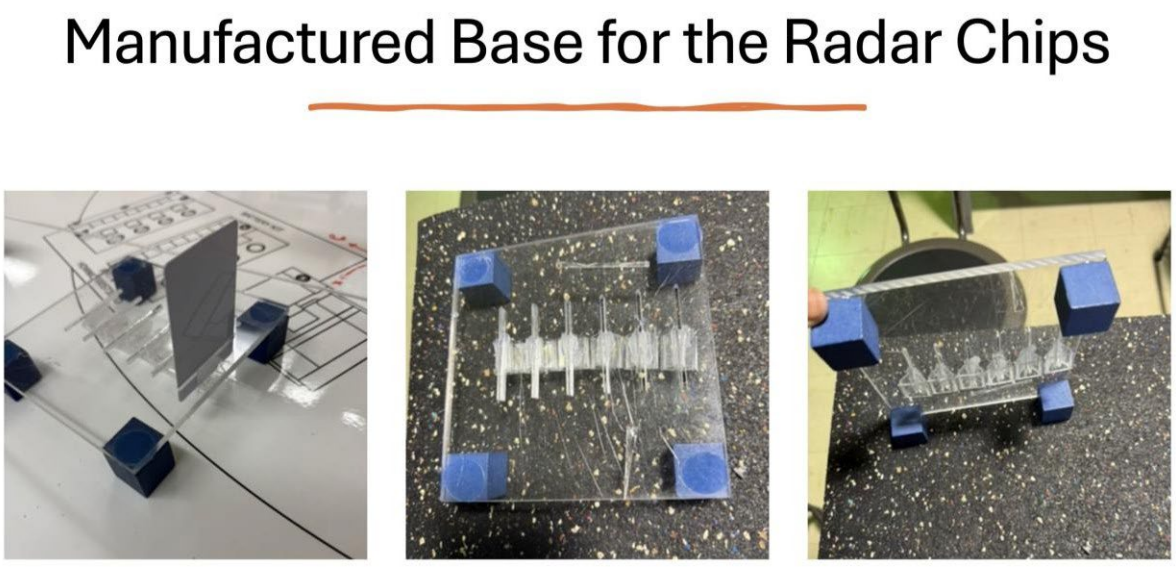


Figure 1: Base

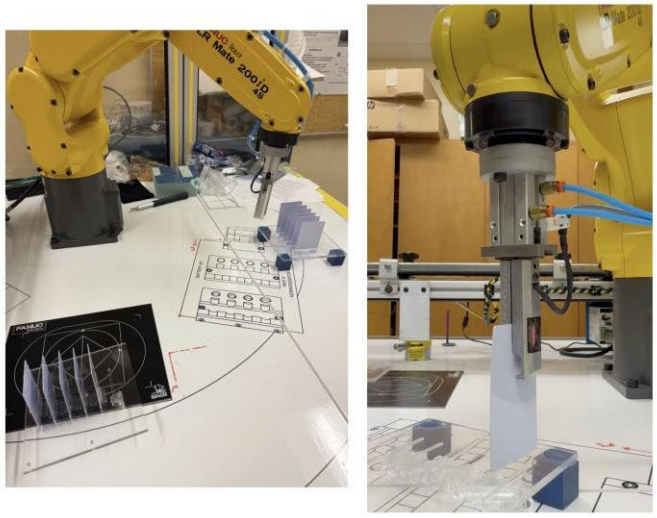


Figure 2: Robot placing chips

References

- "AN/APG-81 Active Electronically Scanned Array (AESA)." *Northrop Grumman*, www.northropgrumman.com/what-we-do/air/an-apg-81-active-electronically-scanned-array-aesa-fire-control-radar. Accessed 22 Oct. 2024.
- Laird, Robbin. "Northrop Grumman Delivers 500th AN/APG-81 AESA Radar for F-35." *Second Line of Defense*, 9 Nov. 2019, sldinfo.com/2019/11/northrop-grumman- delivers-500th-an-apg-81-aesa-radar-for-f-35/.
- "APG-81." *Wikipedia*, Wikimedia Foundation, 27 Dec. 2008, en.wikipedia.org/wiki/AN/APG-81.

Enhancing Quadrotor Autonomy Using ROS2-Based Control Algorithms

Student Researcher: Kevin Johnston

Advisor: Krishna B. Kidambi, Ph.D.

University of Dayton
School of Engineering/Mechanical Engineering

Abstract

In the evolving landscape of unmanned aerial vehicles (UAVs), the autonomy and stability of quadrotors are crucial, especially in critical applications such as search and rescue missions and surveillance. This research focuses on the development and implementation of planning and control algorithms within the Robot Operating System (ROS2) framework. Initial work focused on developing Proportional-Integral-Derivative (PID) control algorithm in a realistic simulated environmental conditions, incorporating the effects of sensor noise. Following successful simulations, the study transitioned to real-world testing, validating the effectiveness of the proposed solutions in ROS2. The work conducted has not only demonstrated the practical utility of these algorithms in both simulated and real-world environments but has also laid the groundwork for more advanced applications in aerial robotics. The successful integration of ROS2 has opened up new avenues for modularity and scalability, critical for the ongoing evolution of autonomous drone technology.

Motivation

Quadrotors are not only engineering marvels but also powerful tools with the potential to profoundly impact society. Their compact size, agility, and versatility make them uniquely suited to perform tasks in environments that are dangerous or difficult for humans to access. Figure 1 illustrates a wide range of real-world applications for quadrotor drones, including search and rescue, mapping, infrastructure inspection, agriculture, and aerial manipulation [1].

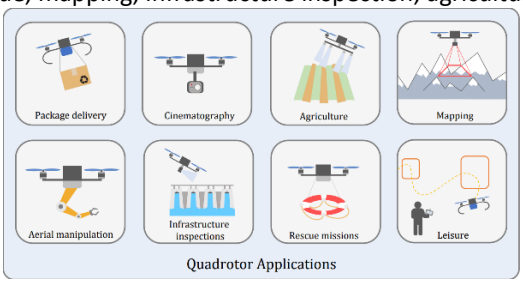


Figure 1: Overview of common quadrotor applications [1].

One particularly compelling use case is disaster response. In the aftermath of structural collapses—such as the Champlain Towers South condominium collapse in Surfside, Florida—searching for survivors becomes a race against time. Figure 2 shows the devastating result of this event, where unstable debris made traditional search-and-rescue operations extremely hazardous. In such cases, deploying drones equipped with cameras or thermal sensors can allow rescuers to safely explore compromised structures, locate trapped individuals, and deliver crucial supplies.



Figure 2: Champlain Towers South collapse in Surfside, Florida (2021). Drone-based inspection can aid in search and rescue efforts in such disasters. Image source: BBC [2].

These examples highlight the urgency and importance of improving drone autonomy and control robustness. With the right control systems, drones can safely navigate cluttered and unpredictable environments, reducing risk to human life while accelerating mission success. This research seeks to make such missions more reliable through the development and evaluation of robust control algorithms in ROS2.

Introduction

The advancement of autonomous systems has ushered in a new era of technological innovation, with unmanned aerial vehicles (UAVs) playing a pivotal role across both civilian and military domains. Among the various UAV configurations, quadrotors have emerged as a particularly attractive platform due to their mechanical simplicity, vertical take-off and landing (VTOL) capabilities, and agile maneuverability. Their applications now span from aerial photography and package delivery to environmental monitoring and life-critical missions such as search and rescue.

Achieving precise and stable flight in dynamic environments requires the development and implementation of robust control algorithms. Over the years, researchers have explored a spectrum of control techniques including adaptive control [3], robust control [4], and model predictive control (MPC) [5], each offering trade-offs between performance, complexity, and robustness. More recently, feedback methods such as Incremental Nonlinear Dynamic Inversion (INDI) have gained traction for their ability to handle model uncertainties and external disturbances in real-time [6].

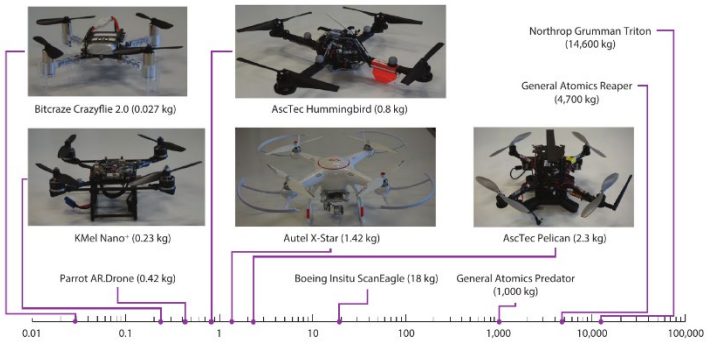


Figure 3: Size and weight comparison of various quadrotor platforms [7]. This work focuses on the Bitcraze Crazyflie 2.0, a 27-gram research-grade micro-UAV.

To support the development of advanced control systems, the open-source Robot Operating System (ROS) has become foundational in UAV research. ROS2, the latest iteration, enables more modular, distributed, and real-time implementations. It splits robotic functionality into individual software modules called nodes, which can communicate by publishing and subscribing to topics. This node-based structure allows researchers to decouple tasks such as vision, navigation, and control, as illustrated in Figure 4.

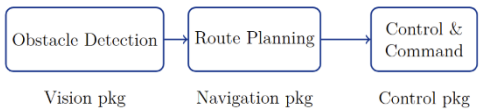


Figure 4: Example ROS2 architecture separating UAV perception, planning, and control. Adapted from Open Robotics documentation [8].

This research investigates the use of ROS2 for the Bitcraze Crazyflie 2.0 platform, focusing on developing and testing control algorithms capable of stable and precise trajectory tracking. The system architecture was implemented using a ROS2 framework to interface simulated and real-world flight data, with custom nodes dedicated to trajectory generation, feedback control, and data logging. Both Proportional-Integral-Derivative (PID) and Incremental

Nonlinear Dynamic Inversion (INDI) control strategies were developed and evaluated, with INDI showing improved performance in dynamic environments. These contributions position the work at the intersection of control theory and practical robotics, laying the groundwork for future integration of SLAM and cooperative drone behavior.

Mathematical Model

Quadrotors are aerial vehicles equipped with four rotors mounted equidistantly around a central body. These rotors produce lift and torque that, when differentially modulated, allow the vehicle to move in six degrees of freedom. The spatial configuration and motion of a quadrotor are most effectively described using two coordinate systems: an inertial frame and a body-fixed frame. The inertial frame *I* = {e1, e2, e3} is a stationary, global coordinate system often aligned with Earth. The body-fixed frame *B* = {b1, b2, b3} is attached to the center of mass of the quadrotor and moves and rotates with it. Position vectors such as [x, y, z]T a are defined in the inertial frame, while orientations and angular velocities are more conveniently defined in the body frame.

Figure 5 shows the quadrotor geometry and the relationship between these two coordinate systems. Each rotor is located at a fixed distance *L* from the vehicle's center. The front and back rotors typically rotate counterclockwise, while the left and right rotors rotate clockwise, inducing moments about the roll (ϕ), pitch (θ), and yaw (ψ) axes.

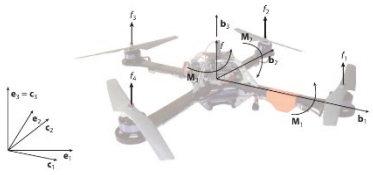


Figure 4: Quadrotor geometry and coordinate systems: Inertial frame *I* is fixed to the world, while body frame *B* moves with the drone [7].

To determine the orientation of the quadrotor in 3D space, rotation matrices are used to map vectors between coordinate systems. These matrices represent sequential rotations about the principal axes and are defined as [7]:

$$R_x(\phi) = \begin{bmatrix} 1 & 0 & 0 \\ 0 & \cos\phi & \sin\phi \\ 0 & -\sin\phi & \cos\phi \end{bmatrix}, \quad R_y(\theta) = \begin{bmatrix} \cos\theta & 0 & -\sin\theta \\ 0 & 1 & 0 \\ \sin\theta & 0 & \cos\theta \end{bmatrix}, \quad R_z(\psi) = \begin{bmatrix} \cos\psi & \sin\psi & 0 \\ -\sin\psi & \cos\psi & 0 \\ 0 & 0 & 1 \end{bmatrix}$$

The combined rotation matrix from body frame to inertial frame is obtained by the R = Rz (ψ)Ry(θ)Rx(ϕ), assuming a ZYX Euler angle convention. This transformation enables the conversion of control inputs—computed in the body frame—into position changes in the inertial frame.

Quadrotor Dynamics

The motion of a quadrotor is governed by a complex set of nonlinear, coupled differential equations that arise from Newton-Euler mechanics. These dynamics result from the balance of gravitational forces, rotor-generated thrust, body torques, and external disturbances. Unlike fully actuated systems, quadrotors are inherently underactuated: although they move in six degrees of freedom (DoF), they are controlled through only four independent inputs (the thrusts from each of the four rotors).

Quadrotor Dynamics - Equations of Motion

To describe the dynamics of a quadrotor, we define the state of the vehicle using position xQ ∈ R3, velocity x'Q ∈ R3, orientation R ∈ SO(3) (the rotation matrix from body to inertial frame), and angular velocity Ω ∈ R3 in the body frame.

The full state vector is therefore given by:

$$\mathbf{x} = \begin{bmatrix} \mathbf{x}_Q^\top & \dot{\mathbf{x}}_Q^\top & \mathrm{vec}(R)^\top & \boldsymbol{\Omega}^\top \end{bmatrix}^\top$$

The continuous-time dynamics of the system can be expressed as [7]:

$$\dot{\mathbf{x}} = \begin{bmatrix} \dot{\mathbf{x}}_Q \\ \frac{f}{m} R\mathbf{e}_3 - g\mathbf{e}_3 \\ R\hat{\mathbf{\Omega}} \\ J^{-1}\left(\mathbf{M} - \mathbf{\Omega} \times J\mathbf{\Omega}\right) \end{bmatrix}$$

Here: m is the mass of the quadrotor, g is gravitational acceleration, f is total thrust (in body frame), J is the inertia matrix in body frame, M is the control torque vector, Ω_hat denotes the skew-symmetric matrix of angular velocity. This formulation separates translational and rotational dynamics and aligns with the special Euclidean group SE(3) representation common in modern UAV literature.

Quadrotor Dynamics - Force and Torque Mapping

The forces and torques acting on the vehicle originate from the four propellers, each located at a distance L from the center of mass. The relationship between the individual rotor thrusts f_i and the net force and moments can be expressed as:

$$\begin{bmatrix} f \\ M_x \\ M_y \\ M_z \end{bmatrix} = \begin{bmatrix} 1 & 1 & 1 & 1 \\ 0 & L & 0 & -L \\ -L & 0 & L & 0 \\ -\mu & \mu & -\mu & \mu \end{bmatrix} \begin{bmatrix} f_1 \\ f_2 \\ f_3 \\ f_4 \end{bmatrix}$$

This transformation matrix maps the thrust values from each rotor into a total upward thrust f and torques Mx, My, Mz about the roll, pitch, and yaw axes, respectively. The term μ denotes the drag-to-lift ratio which determines how each rotor's spin contributes to the yawing moment.

Quadrotor Dynamics – Control-to-Motion Pipeline

Figure 6 summarizes the pipeline from control inputs (i.e., U1, U2, U3, U4) to motor thrusts, and ultimately to system acceleration and orientation. Rotor speeds influence both translational and rotational states, which in turn affect the vehicle's trajectory in space.

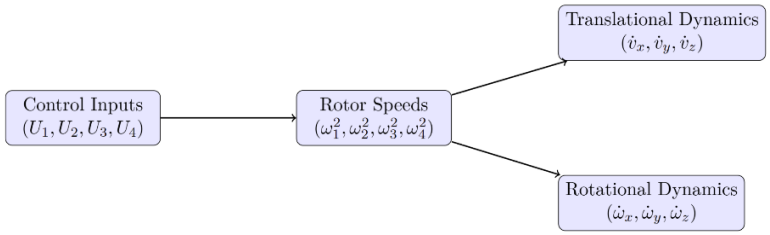


Figure 6: From control inputs to motion: rotor speeds govern both translational and rotational dynamics.

Quadrotor Dynamics – Sensor Considerations and Feedback

To estimate the current state of the vehicle for feedback control, onboard sensors such as inertial measurement units (IMUs), gyroscopes, and accelerometers are utilized. IMUs provide data about the drone's angular velocities and accelerations, while additional sensors such as optical flow or UWB modules are used for velocity and position estimation. These measurements are fused through algorithms such as the Extended Kalman Filter (EKF) to estimate the full state vector **X** in real time.

Control Model

During the operation of unmanned aerial vehicles (UAVs), handling the unpredictability and noise of real-world conditions is crucial. The effectiveness of a quadrotor's control system depends not only on the underlying controller but also on its ability to estimate system states accurately. Filters such as the Complementary Filter [9] and the Extended Kalman Filter (EKF) [10] are essential for fusing noisy sensor data from onboard sources such as IMUs, accelerometers, gyroscopes, and optical flow sensors. The Complementary Filter provides a computationally

efficient means of combining high-frequency and low-frequency sensor signals to produce reliable state estimates. The EKF, though more computationally intensive, is highly effective in nonlinear systems and dynamically adjusts state estimates based on model predictions and real-time sensor feedback.

To regulate quadrotor motion, feedback controllers are employed to minimize the error between the desired trajectory and the actual flight path. This feedback loop is illustrated in Figure 7, where the error signal e(t) is processed by the controller to generate control inputs that drive the system toward the reference state.

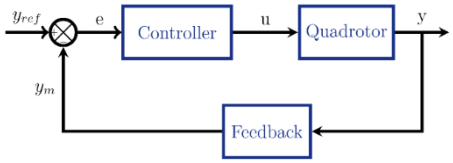


Figure 7: PID feedback loop for quadrotor control.

The quadrotor's position is determined using LocoNodes, a UWB-based indoor localization system. Once the target position and yaw angle are defined, the system computes desired roll and pitch values. These orientation commands are then translated into motor inputs that control lift and orientation through a cascade of inner and outer-loop controllers.

Control Algorithms: PID and INDI

The Proportional-Integral-Derivative (PID) controller has long been a standard in robotics due to its simplicity and effectiveness under nominal conditions. It computes the control signal u(t) as:

$$u(t) = K_p e(t) + K_i \int_0^t e(\tau)\, d\tau + K_d \frac{de(t)}{dt}$$

While PID performs adequately for many systems, its reliance on predefined gain tuning and its susceptibility to disturbances make it less ideal for rapidly changing environments. To address these limitations, Incremental Nonlinear Dynamic Inversion (INDI) has emerged as a more robust control strategy [6]. INDI adapts to disturbances in real-time using measured state deltas: $\delta u = -\mathbf{A}^{-1}\left(\mathbf{B}\delta x + \mathbf{C}\right)$

Here, δu represents the change in control input, while δx reflects changes in system state. Matrices A, B, and C are derived from linearizations of the system dynamics. This approach enhances performance under uncertainties and minimizes reliance on accurate system modeling.

Experimental Platform

The experiments conducted in this research utilized the Bitcraze Crazyflie 2.1, a lightweight and highly modular nano-quadcopter platform. The Crazyflie is open-source and designed specifically for indoor environments, making it ideal for academic and robotics research. As shown in Figure 8, the Crazyflie features a compact form factor and supports stackable sensor decks, allowing researchers to customize the hardware for various autonomous navigation and control tasks.

One of the platform's key advantages is its compatibility with real-time telemetry, onboard computation, and localization systems such as ultra-wideband (UWB). The Crazyflie integrates seamlessly with ROS2 through community-maintained packages, enabling efficient communication between software nodes and real-world flight systems. Its safe operation indoors, robustness in experimentation, and ease of reconfiguration make it especially suitable for iterative control algorithm development and swarm robotics applications.



Figure 8: Crazyflie 2.1 Nano Quadcopter platform [11].

To support the flight control and localization required for this research, several sensor modules were deployed. These include the Flow Deck v2 for optical flow-based velocity estimation, the Loco Positioning Deck for UWB-based localization, the Multi-Ranger Deck for distance sensing, and the AI Deck for onboard neural processing. Figure 9 provides a visual overview of the hardware components used. The final testing area was constructed with fixed positioning nodes distributed throughout a flight enclosure, enabling precise spatial tracking during all flight experiments.

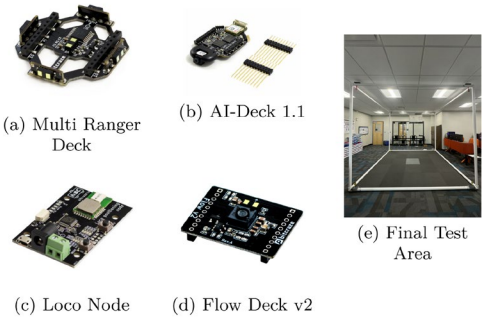


Figure 9: Sensor and localization hardware modules used in experimentation. The right column shows the final test area with all components integrated.

Simulation and Experimental Results - Trajectory Generation and Simulation Environment

To evaluate the control strategies developed in this project, various reference trajectories were first generated using custom Python scripts. These included circle, figure-eight, square, lawnmower, and helix trajectories. These flight paths were selected to stress different aspects of control and stability, such as sustained turns, abrupt transitions, and vertical climb maneuvers. Initial testing of these trajectories was conducted in a simulation environment without ROS2, allowing for rapid iteration and visualization of the flight paths. Figure 10 displays a representative set of these simulated trajectories, which were later used as benchmarks for both ROS2-based simulation and physical experiments.

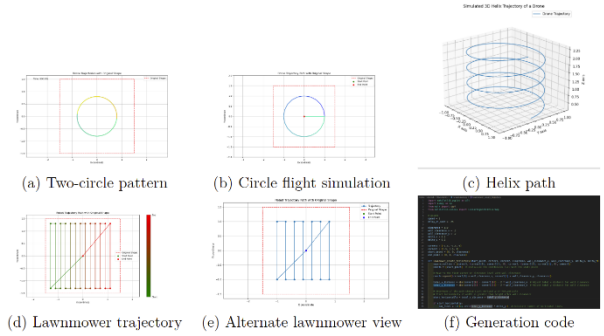


Figure 10: Simulated trajectory patterns generated without ROS2.

Simulation and Experimental Results - Simulation Using ROS2 and RViz2

After verifying the trajectories and controller performance in the basic simulation, the project transitioned to a ROS2-based simulation pipeline. This phase utilized Gazebo and RViz2 to emulate quadrotor behavior in a more realistic environment. Nodes were structured to reflect modular ROS2 architecture, allowing for simulation of flight control, trajectory tracking, and sensor fusion within a distributed system.

The CrazySim toolchain [12] was used to enable software-in-the-loop simulation with the Crazyflie platform. This allowed researchers to visualize drone behavior before flight execution and validate the interaction of ROS2 packages. Figure 11 shows ROS2 terminals running the controller stack alongside the corresponding RViz2 flight visualization.

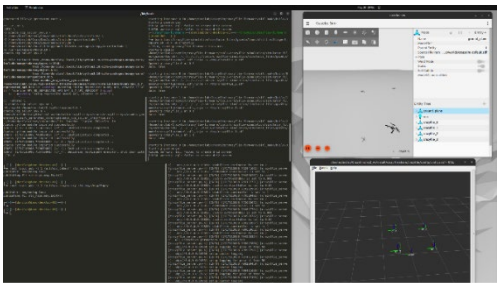


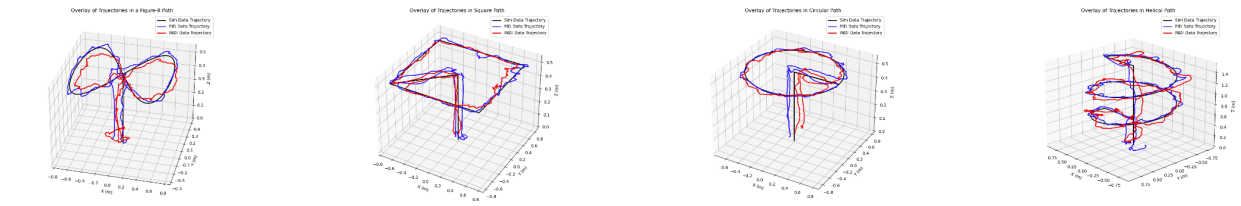
Figure 11: Terminals executing ROS2 flight stack and visual simulation of drone trajectory in RViz2 [12].

This ROS2-based simulation workflow enabled modular debugging and streamlined the transition to hardware experiments, ensuring that the same codebase used in simulation could be reused for physical deployment with minimal adjustments.

Simulation and Experimental Results - Experimental Flight Tests and Controller Comparison

Upon successful simulation, the system was tested on a real quadrotor in a controlled lab environment using the Bitcraze Crazyflie platform. The same trajectories used in simulation were uploaded to the drone and executed using both PID and INDI control architectures. Flight logs were collected in real time and visualized in three dimensions for evaluation against simulated trajectories.

Figure 12 illustrates the actual flight paths compared to the planned references. The data visualizations show: Black: Reference simulation trajectory; Blue: Trajectory tracked using PID control; Red: Trajectory tracked using INDI control.



(a) Figure-eight (b) Square (c) Circle (d) Helix

Figure 12: Flight trajectory comparisons for various paths: (a) figure-eight, (b) square, (c) circle, and (d) helix.

In each case, the INDI controller produced tighter adherence to the reference path, particularly in the presence of disturbances or sensor delay. The PID controller, while effective, tended to overshoot corners and exhibited increased steady-state error in dynamic trajectories such as the helix.

A qualitative demonstration of the helix flight is shown in Figure 13, with a link to the full flight video provided in the footnote.



Figure 13: Snapshot from helix trajectory experiment. See Full Video Here

Simulation and Experimental Results – Discussion

The results indicate that the PID controller performs well in simple and symmetric flight paths but suffers from lag and overshoot in more dynamic conditions. INDI, by contrast, adapts to model discrepancies in real time using incremental feedback, offering improved robustness and trajectory tracking in complex maneuvers. Moreover, the consistency between simulated and experimental results validates the effectiveness of the ROS2 architecture and highlights the seamless transition between virtual and physical environments. This modularity and realism make ROS2-based pipelines highly favorable for continued research in swarm robotics, collaborative exploration, and adaptive control. Future experiments will quantify trajectory error using metrics such as Mean Squared Error (MSE) and expand testing to larger fleets of quadrotors. The goal is to evaluate control algorithms not only by precision but also by scalability and resilience in unpredictable environments.

Acknowledgments

This research was supported by multiple academic initiatives and funding sources, including the University of Dayton Summer Undergraduate Research Experience (SURE) Program, the Berry Summer Thesis Institute (BSTI), the University of Dayton Honors Program, and the Ohio Space Grant Consortium (OSGC). I would especially like to thank Dr. Krishna Bhavithavya Kidambi and Dr. Nicholas M. Stiffler for their continued mentorship, guidance, and technical insight throughout this project. Their support has been instrumental in both the development and execution of this research. I am also deeply grateful to my peers in the DaRC-ARMS Laboratory at the University of Dayton for their collaboration, encouragement, and constructive feedback throughout the research process.

References

[1] E. Carvalho, Neural learning for efficient quadrotor flight control. PhD thesis, Université Grenoble Alpes, 2023.
[2] BBC News, “Miami building collapse: What happened at the surfside condo?,” 2021. Accessed: 2025-04-16.
[3] N. Koksal, H. An, and B. Fidan, “Backstepping-based adaptive control of a quadrotor uav with guaranteed tracking performance,” ISA transactions, vol. 105, pp. 98–110, 2020.
[4] K. B. Kidambi, C. Fermüller, Y. Aloimonos, and H. Xu, “Robust nonlinear control-based trajectory tracking for quadrotors under uncertainty,” IEEE Control Systems Letters, vol. 5, no. 6, pp. 2042–2047, 2020.
[5] C. Greatwood and A. G. Richards, “Reinforcement learning and model predictive control for robust embedded quadrotor guidance and control,” Autonomous Robots, vol. 43, pp. 1681–1693, 2019.
[6] E. Smeur, Q. Chu, and G. de Croon, “Incremental nonlinear dynamic inversion for attitude control of micro air vehicles,” The International Journal of Robotics Research, vol. 35, no. 10, pp. 1155–1173, 2016.
[7] S. Tang and V. Kumar, “Autonomous flight,” Annual Review of Control, Robotics, and Autonomous Systems, vol. 1, no. 1, pp. 29–52, 2018.
[8] Open Robotics, “ROS 2 Documentation.” https://docs.ros.org/en/humble/index.html, 2024. Accessed: 2025-04-16.
[9] J. Wu, Z. Zhou, H. Fourati, R. Li, and M. Liu, “Generalized linear quaternion comple-mentary filter for attitude estimation from multisensor observations: An optimization approach,” IEEE Transactions on Automation Science and Engineering, vol. 16, no. 3, pp. 1330–1343, 2019.
[10] A. Kaba and E. Kıyak, “Optimizing a kalman filter with an evolutionary algorithm for nonlinear quadrotor attitude dynamics,” Journal of Computational Science, vol. 39, p. 101051, 2020.
[11] K. McGuire, “Crazyflie summer project with ROS2 and mapping,” 2022. Accessed: 2024-06-12.
[12] C. Llanes, Z. Kakish, K. Williams, and S. Coogan, “Crazysim: A software-in-the-loop simulator for the crazyflie nano quadrotor,” in Int. Conf. Rob. Aut, 2024.

Spiking Neural Networks utilizing Deep Learning for Space Domain Awareness

Student Researcher: Kaleb Keichel

Advisor: Dr. Jundong Liu

Ohio University
Computer Science

Abstract
The complex issue of space domain awareness (SDA) is one often tackled with traditional, AI based means and/or ground-based detection systems. It is an issue with many vested stakeholders, and the scenarios oftentimes provided create great limitations on potential solutions. Most namely, power consumption and rapid classification constraints. By researching and developing event-based solutions, both major constraints can be solved with one elegant solution. A solution that is capable of being produced without much more additional training, as they utilize packages similar to popular to those used in popular solutions. The research conducted here specifically addresses the classification of these spiking neural networks through developing non-neuromorphic hardware, to be implemented on the neuromorphic hardware in the future. Once constructed, these models can easily be translated onto the preferred hardware for energy efficiency. Through my research, we were able to establish that even non-event-based datasets can be converted easily and effectively for use by using popular AI packages such as SNNTorch, a variant of the popular PyTorch, further showcasing the elegance of the solution.

Project Objectives
The United States conducts Space Domain Awareness (SDA) to monitor artificial objects in Earth's orbit, a capability that is critical for both commercial and military space operations. However, current systems predominantly rely on ground-based data processing, which limits real-time applications and autonomous decision-making in space operations.

Throughout my time as a senior scholar for OSGC, my goal has been to improve SDA by leveraging cutting-edge neuromorphic computing technologies (a human brain-inspired hardware and software design paradigm) to enable advanced on-the-fly data processing. This project focused on one primary objective: developing real-time solutions for image recognition and object detection. It is important to note that I will now focus on my other main objective throughout my work as an OSGC fellow, where I will be applying these solutions to detect and track Resident Space Objects (RSOs) within the SDA framework. To achieve this, I designed spiking neural networks (SNNs) capable of processing signals in real time for target detection and tracking and eventually will employ event-based vision cameras.

The progression of this project helps lay the foundation for future deployment in SDA tasks, enabling real-time RSO catalog updates and object tracking using on-orbit sensors. This effort aligned with the objectives of NASA's Aeronautics Research Mission Directorate (ARMD), Space Technology Mission Directorate (STMD), Science Mission Directorate (SMD), and Space Operation Mission Directorate (SOMD).

The detection, tracking, identification, and cataloging of space objects is referred to as Space Domain Awareness. Current SDA in the United States relies heavily on ground-based systems, which face coverage gaps due to geographic limitations, data transmission challenges, and hardware constraints, prompting the need for space-based SDA solutions to enable real-time object detection and tracking using on-orbit sensor networks.

Dynamic Vision Sensor (DVS), or event camera [2], could provide an ideal solution for this task. Unlike the traditional cameras, where frames are captured at a fixed rate, a DVS only responds to changes in brightness in its field of view, qualified as an event. DVS sensors have low latency, high dynamic range and low power consumption, making it ideal for high-speed motion tracking. Connecting DVS with spiking neural networks (SNNs) [3] would maximize the advantage of the asynchronous nature and the energy efficiency of the overall system. In this project, I aim to develop a transformative approach to SDA by taking advantage of the remarkable capabilities of event-based vision sensors and neuromorphic computing on SNNs.

The DVS, event cameras, and other neuromorphic computing solutions all revolve around the idea of recreating the human neuron for computations. The human brain works incredibly efficiently on as little as 20W [4], which is much better compared to traditional computing solutions. While it will take a significant amount of time before reaching that level of efficiency, we can create simulated versions of this. This is the thought behind utilizing event-based hardware, such as neuromorphic solutions. This, in turn, allows us to create AI models such as SNNs to benefit from this increased efficiency. These solutions can be further simulated in traditional, Von Neumann architecture for translation later. This idea can be perfected by potentially fitting new or existing structures in orbit with neuromorphic sensors. This will allow them to be fitted with event-based AI models and therefore reap the benefits of a highly efficient and reliable working solution.

Methods

To ensure the practicality of this solution, only popular and/or variants of popular, well-known packages and programming languages were used. As Python 3 has become the staple of machine learning, this language was chosen as many others already have experience in this. Furthermore, by utilizing popular packages such as NumPy and pandas, little retraining would need to be used when it comes to fully implementing and adjusting on the end user scale. Finally, the bulk of the work is done using a variant of the popular machine learning Python package PyTorch known as SNNTorch. This package is developed by the original PyTorch developers and allows for easy integration into most codebases.

While it is possible to develop full datasets using neuromorphic hardware as described earlier, it is much more feasible to translate traditional datasets for proof-of-concept purposes. This is mostly due to the large financial constraint that comes alongside developing sophisticated datasets that cover as much variation as a real sensor would need to rely on. While our research lab did not have direct access to SDA related datasets, the math and relative structure of these would remain the same, so we used traditional computer vision datasets. The most notable would be a translated version of MNIST, a dataset created utilizing a series of hand drawn digits, and a conversion of the popular CIFAR-10 dataset, which consists of 60000 32x32 color images in 10 classes, with 6000 images per class [10].

At our OHIO Learning and Intelligent Systems Lab (LiSL), a series of SNN-based machine learning solutions have been developed [3, 4, 5, 6, 7, 8]. I successfully implemented an N-MNIST Digit Classification system using Intel Lava. Figure 1 shows a screenshot of the network's output after processing the video shown on the left. Each dot on the right represents a spike generated by the network's output, which consists of 10 choices —one for each digit from 0 to 9. The image clearly depicts a "0" (barring the noise at the end of the datapoint), and the graph shows that most spikes occur in the network output correspond to the digit 0, which is a correct recognition of the input. This dataset was preloaded with most of my research deals with translating and generating the event-based datasets for proof-of-concept purposes.

During the development of the SNN, several distinctive decisions had to be made to increase effectiveness. For starters, one major limitation is simplifying the complexity of the human neuron in its

classification of an event. When a neuron “spikes”, it creates a complex and difficult to recreate voltage spikes. From here, we can simplify by creating two states: 0 for no event and 1 for an event detection. The issue with this approach can be seen in the derivative, which is required in the backward pass for training purposes. This generates a “dead neuron” problem, where the set doesn’t work as intended. This can be mitigated through a variety of ways, but the way chosen for this project was to utilize pooling and a specific optimizer. This allowed for the back pass for training not to result in a linear output, where the distinctions can be seen in figure 2.

The main dataset used was the popular N-MNIST dataset. A variety of different forms of this dataset was utilized. Using Python 3 packages such as tonic, it is possible to preload event-based implementations of this dataset, as previously mentioned. This was used as an initial proof of concept for the SNN developed. For the practicality of implementing existing, non-neuromorphic datasets, I opted to generate event-based data from the original MNIST dataset [9]. The results are shown in figure 3. This was the primary dataset utilized; however, due to some hardware constraints, training could not fully converge in a reasonable amount of time. For the fellowship research that will be conducted from fall of 2025 to the spring of 2026, this will not be an issue.

The specific spiking neural network created was a convolutional one. Traditional convolutional neural networks (CNN’s) are incredibly useful in the field of computer vision. As I was utilizing a dataset that was originally a traditional computer vision set, I created a SCNN for the purpose of classification. Other models were utilized, but this specific implementation was generated with the SCNN. The specifics of the model are shown in figure 4. While this may seem to be a simple CNN implementation, this architecture was chosen to allow for the model to converge quicker, as the NMNIST set is known for being an easier set to train on. If a more advanced dataset was used, for example one in the field of space domain awareness, a more advanced model would have been created.

Results and Discussion

Throughout the training of the SCNN, near “optimal” accuracy was achieved. By using a computer with Nvidian GeForce Titan X, 12GM**,** I was able to achieve 98% accuracy. This was rather impressive given the limited computing power. An example classification can be seen in figure 5. This generated a myriad of accurate classifications, with varying degrees of noise. Further tests will be implemented to showcase the effectiveness and robustness of this approach.

For future implementations, starting in the summer, more space-related datasets will be utilized on hardware that is better equipped to handle the training cost. The next dataset that will be testing on is the Event-Based Space Situational Awareness (EBSSA) Dataset [13] and the Event_Based-Space_Imaging-Speed_Dataset [14]. Other datasets will be utilized in the meantime [11][12]. These datasets are much more complicated when compared to MNMIST, as their dimensions are a lot larger. Additionally, while this does not apply to SDA, as this has no instances of space debris or other related objects, it fits the problem set better and provides better proof of concept.

Furthermore, we will be implementing these onto neuromorphic computers, which will then be measured to detect the extent of effectiveness and efficiency. These initially will be implemented on systems such as Intel Lohi 2 or non-neuromorphic hardware such as Field Programmable Gate Arrays. There may be some accuracy lost in the conversion, but further training on the actual hardware should mitigate this risk.

Figures/Charts

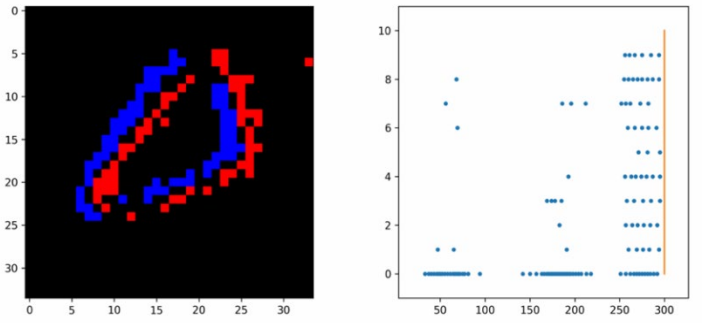


Figure 1: Illustration of a frame of the event MNIST dataset (left) and the classification result (right). The input is correctly recognized as a "0".

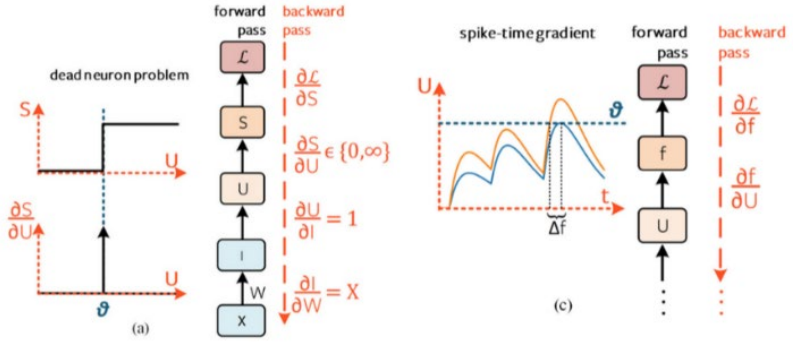


Figure 2: Illustration of the dead neuron problem and the solution utilized in this project.

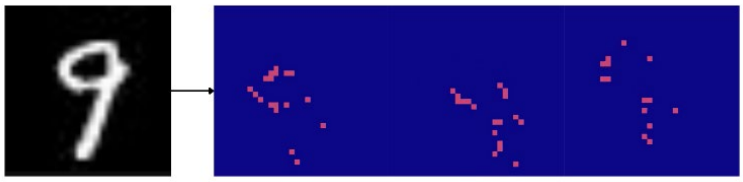


Figure 3: Example translation between the traditional MNIST value (class 9) and the spiking set. The frames are captured at the 1s, 5s, and 10s mark.

```
----------------------------------------------------------------
        Layer (type)               Output Shape         Param #
================================================================
            Conv2d-1           [-1, 12, 30, 30]             612
             Leaky-2  [[-1, 12, 15, 15], [-1, 12, 15, 15]]
            Conv2d-3           [-1, 64, 11, 11]          19,264
             Leaky-4  [[-1, 64, 5, 5], [-1, 64, 5, 5]]
            Linear-5                 [-1, 10]          16,010
             Leaky-6       [[-1, 10], [-1, 10]]               0
================================================================
Total params: 35,886
Trainable params: 35,886
Non-trainable params: 0
----------------------------------------------------------------
Input size (MB): 0.01
Forward/backward pass size (MB): 75.01
Params size (MB): 0.14
Estimated Total Size (MB): 75.15
----------------------------------------------------------------
```

Figure 4: Rough formatting of the SCNN utilized in training on the N-MNIST dataset.

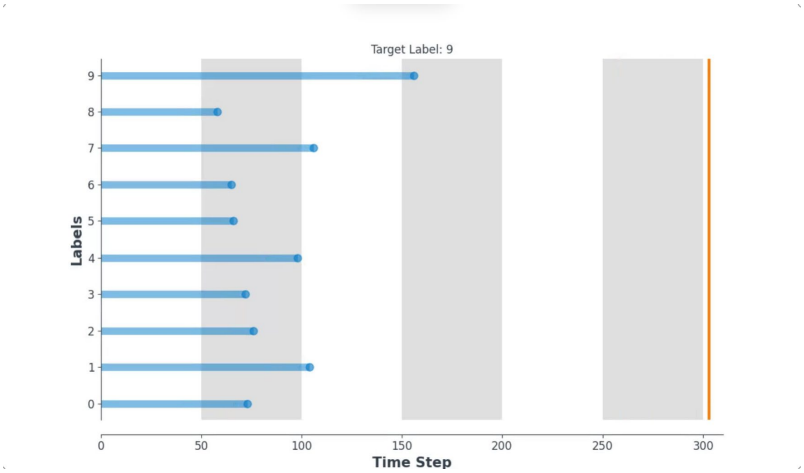


Figure 5: Classification of the target class 9. As you can see, it correctly classifies the data.

Acknowledgments

I'd like to personally thank OSGC for giving me this tremendous opportunity to pursue my dream of performing cutting edge research that has a positive impact on our society. I've always dreamed of working on computer science research, and being able to do so for OSGC and being affiliated with NASA is a tremendous dream come true. I'd also like to thank my advisor, Dr. Jundong Liu, for molding me into the researcher and programmer I am today. He saw potential in me and allowed me to become the best version of myself. Finally, I'd like to thank the OHIO Learning and Intelligent Systems Lab (LiSL), as they have all provided me with a great opportunity and excellent help. I've built connections there that will go a long way in my future life and career.

References

[1]Intel Loihi 2 Technology: https://www.intel.com/content/www/us/en/research/neuromorphiccomputing-loihi-2-technology-brief.html

[2] Event camera: https://en.wikipedia.org/wiki/Event_camera

[3] Smith, Colton. C. (2021). The evaluation of current spiking neural network conversion methods in radar data (Master's thesis, Ohio University).

[4] Di Caterina, G., Zhang, M., & Liu, J. (2024). Theoretical advances and practical applications of spiking neural networks. Frontiers in Neuroscience, 18, 1406502 [link].

[5] Baltes, M., Abujahar, Yue, Y., T., Smith, C. D., Liu, J. (2023). Joint ANN-SNN Co-training for Object Localization and Image Segmentation. IEEE Interntional Conference on Acoustics, Speech, and Signal Processing (ICASSP'23) [pdf].

[6] Yue, Y., Baltes, M., Abuhajar, N., ... & Liu, J. (2023). Spiking neural networks fine-tuning for brain image segmentation. Frontiers in Neuroscience, 17. [pdf].

[7] Yue, Y., Baltes, M., Abujahar, N., Sun, T., Smith, C. D., Bihl, T., & Liu, J. (2023). Hybrid Spiking Neural Network Fine-tuning for Hippocampus Segmentation. IEEE International Symposium on Biomedical Imaging (ISBI'23) [pdf].

[8] Eshraghian, J. K., Ward, M., Neftci, E. O., Wang, X., Lenz, G., Dwivedi, G., ... & Lu, W. D. (2023). Training spiking neural networks using lessons from deep learning. Proceedings of the IEEE.

[9] N-MNIST dataset: Orchard, G.; Cohen, G.; Jayawant, A.; and Thakor, N. “Converting Static Image Datasets to Spiking Neuromorphic Datasets Using Saccades", Frontiers in Neuroscience, vol.9, no.437, Oct. 2015 (open access Frontiers link).

[10] Li, Hongmin; Liu, Hanchao; Ji, Xiangyang; Li, Guoqi; Shi, Luping (2017). "CIFAR10-DVS: An Event-Stream Dataset for Object Classification". Frontiers in Neuroscience. 11: 309.

[11] Redmon, J., Divvala, S., Girshick, R., & Farhadi, A. (2016). You only look once: Unified, real-time object detection. In Proceedings of the IEEE conference on computer vision and pattern recognition (pp. 779-788).

[12] Prophesee: Automotive Megapixel Event-Based Dataset: https://www.prophesee.ai/2020/11/24/automotive-megapixel-event-based-dataset/

[13] Event-based Space Situation Awareness (EBSSA) dataset: https://www.westernsydney.edu.au/icns/resources/reproducible_research3/publication_support_materials2/space_imaging

[14] Event-based Space Imaging Slew Speed Star dataset: https://github.com/NicRalph213/ICNS_NORALPH_Event_Based-Space_Imaging-Speed_Dataset

Waste to Energy – Reaction Engineering & Sustainability

Student Researcher: Brooke Kennedy

Advisor: Jorge Gatica

Cleveland State University
Chemical Engineering

Abstract
Americans produce over 250 million tons of waste annually, with most discarded materials left unrecycled, incinerated, or sent to landfills. As landfills reach capacity and incineration poses environmental and energy challenges, the need for efficient waste management and resource recovery has drawn global attention from engineers and scientists. One promising alternative is waste gasification, a process that converts carbon-based materials into synthetic gas. The Chemical Reaction Engineering Laboratory has been exploring catalytic processes as a low-temperature approach to gasifying solid waste. This method, known as Wet-Thermal Catalytic Oxidation (WTCO), operates at significantly lower temperatures (300-350°C) compared to conventional incineration (which exceeds 1000°C), reducing energy consumption and environmental impact. Among the common plastic components in municipal waste are polyethylene, cellulose, and nylon. The catalytic gasification of cellulose presents unique challenges. Unlike low-melting-point materials like polyethylene, cellulose remains in the solid phase, creating a heterogeneous reaction environment. This system consists of solid catalyst particles, cellulose particles, and oxygen in both liquid and gas phases, making effective interaction between these elements essential. Achieving this requires a detailed fluid dynamics (CFD) characterization of the particulate system, which is explored in the following section.

Project Objectives
Modeling and experimental analysis of heterogeneous gasification are aimed at characterizing mixing, particle dynamics, and transport phenomena associated with decomposing (gasifying) solid substrates. The desired outcomes/goals are as follows:

- Model the waste gasification process of cellulose in a pressure stirred reactor using a finite element based CFD software (COMSOL).
- Characterize the fluid dynamics and determine the mixing parameters to optimize chemical reaction and transport phenomena.
- Characterize catalytic gasification dynamics for cellulose particles. Including sample collection and characterization through gas chromatography, and thermal analysis.
- Scale up the process from batch to continuous gasification.

Methods
To learn the COMSOL software, a simple sudden expansion model was created using a COMSOL tutorial. The flow velocity profile was studied, and data was exported to EXCEL. This data was then interpolated in the radial direction to get a complete velocity profile. This complete velocity profile is needed in order to accurately predict where a catalyst particle would go if placed in this flow field. This interpolation was done in MATLAB. After getting a complete model for the sudden expansion situation, a model was developed for a stirred tank reactor similar to the one in Professor Gatica's lab. The Eddy diffusivity forces were found at different gravities and rotation rates. Then, catalyst particles were added into the CSTR model at various diameter lengths to model the difference in particle trajectories.

Results and Discussion

The sudden expansion model yielded a complete particle tracing model, using the information that at radius equal to zero, the velocity is equal to the inlet velocity, and the velocity at the wall is zero. The points in-between along the radius were interpolated from certain points that were generated by the COMSOL software. For the stirred tank reactor, this approach couldn't be replicated due to the rotation forces. Multiple eddy diffusivity graphs were generated at different gravities, and not many differences were observed. This is because the force due to gravity that is exerted on a particle is overcome by the greater force exerted by the rotation in the reactor. The same study was done with changing the rotation rate of the stirrer in the tank and no differences were observed with rpms from 50-400. Then, particle tracing was added to the model with a cellulose catalyst. As the particle size changes, the particle trajectory will change as well due to the weight of the particle changing. Particle trajectory graphs were generated for particle sizes of 0.01 m, 0.02m, 0.04 m, 0.06 m, and 0.1 m with a tank that has a total diameter of 1 m. The most optimal particle trajectory that was observed was for the largest particle because minimal particles ended up stuck at the bottom. If the catalyst particles get stuck at the bottom of the reactor, the reaction will not be as efficient.

Figures/Charts

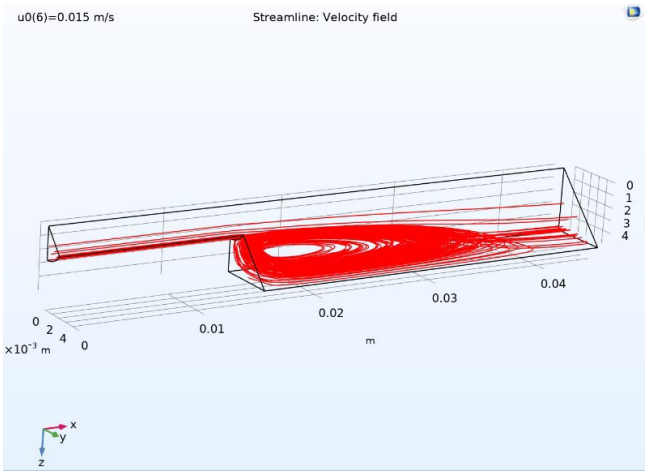


Figure 1: Sudden Expansion Flow Field

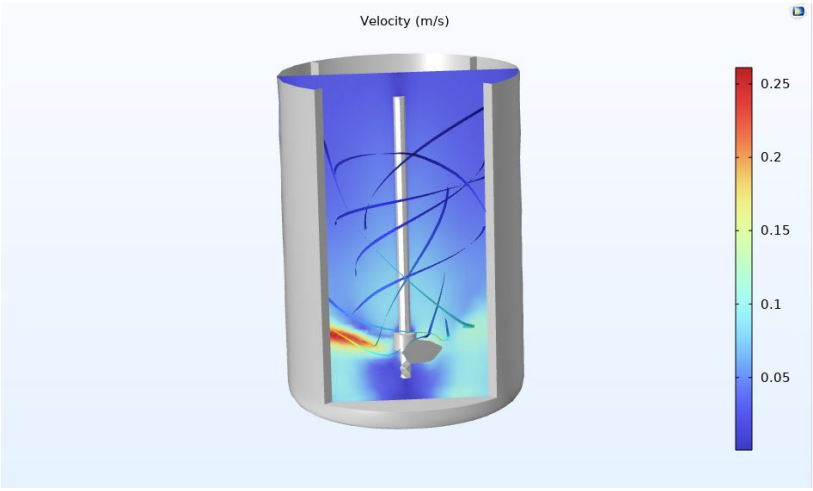


Figure 2: Stirred Tank Reactor Flow Field

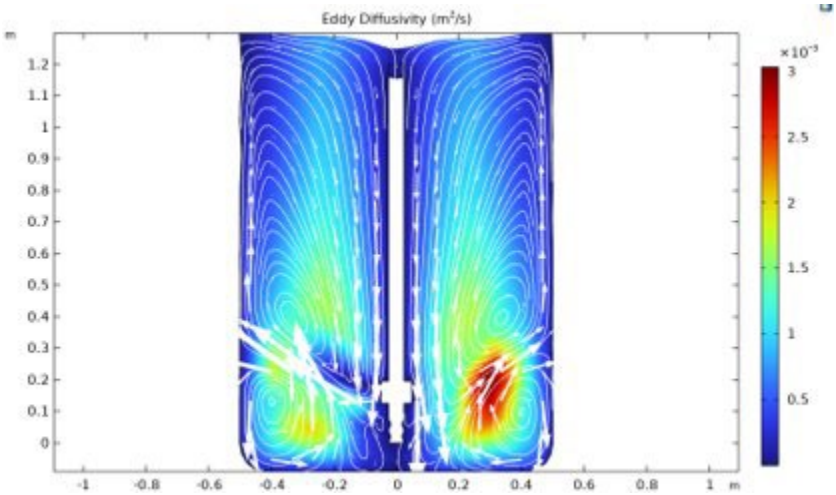


Figure 3: Eddy Diffusivity Currents of CSTR at 50 rpm

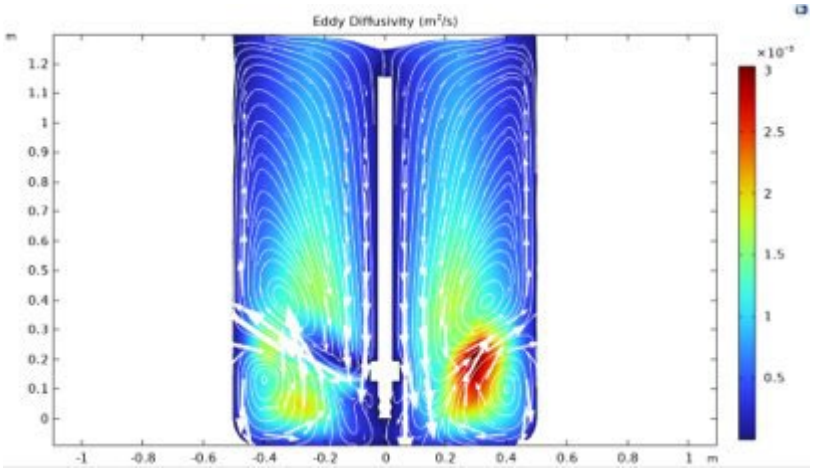


Figure 4: Eddy Diffusivity Currents of a CSTR at 100 rpm

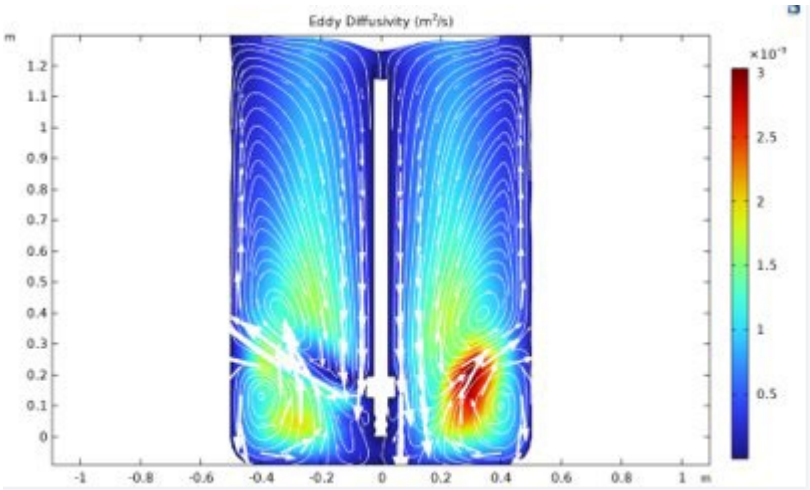


Figure 5: Eddy Diffusivity Currents of a CSTR at 200 rpm

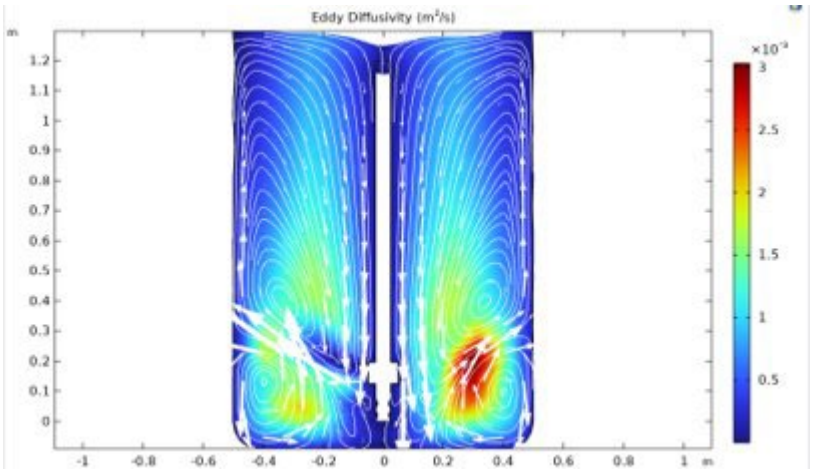


Figure 6: Eddy Diffusivity Currents of a CSTR at 400 rpm

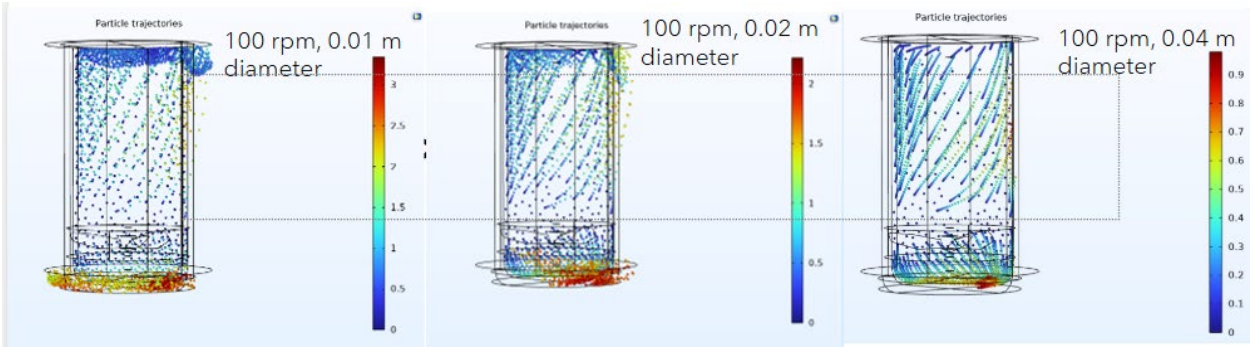


Figure 7: Particle Trajectories at Conditions Labeled

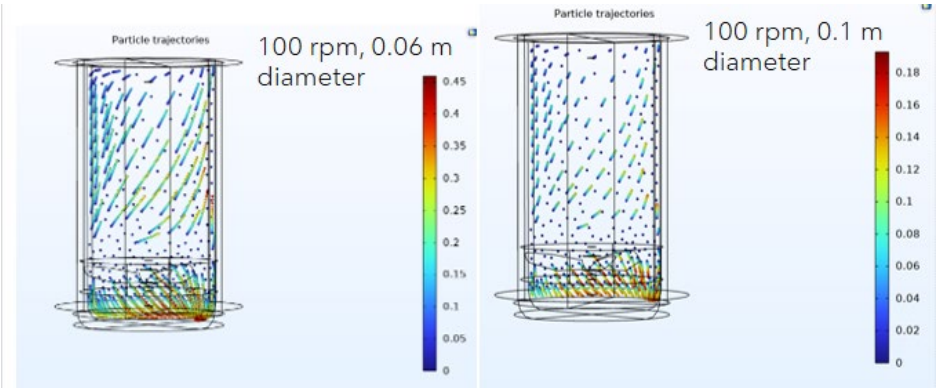


Figure 8: Particle Trajectories at Conditions Labeled

Acknowledgments
Thank you to the OSGC for providing the scholarship and ability to conduct this research. I gained a lot of valuable experience in project management and communication with my advisor. Thank you to Dr. Jorge Gatica for guiding me, dedicating time to meeting with me and answering all my questions. Thank you to Cleveland State University for the funding and lab space, as well as letting undergraduate students gain experience in research.

References

1. Cartland Glover, G.M. and J.J. Fitzpatrick "Modelling vortex formation in an unbaffled stirred tank reactors," Chem Eng. J., 127, 11-12 (2007)
2. Nagata, S. "Mixing: principles and applications," Wiley, New York (1975)
3. Busciglio, A., F. Grisafi, F. Scargialia, and A. Brucato "On vortex shape in unbaffled stirred vessels as measured by digital image analysis," pp. 49-54 in Proceedings of the 14th European Conference on Mixing, Warszaw, Poland (September 2012)
4. Tillo, A. "Will Plastics Recycling Meet its Deadline?" C&E News, 99 (37), October (2021).
5. Reyes, K.M., N. Plentovich, M.J. Lang, and J.E. Gatica "Catalytic Gasification of Polyethylene As an in-Situ Resource Utilization (ISRU) Alternative," 2020 National AIChE Annual Meeting, November16-20 (2020).
6. Lang. M.J. and J.E. Gatica "Catalytic Gasification – a Critical Analysis of the Water-GasShift Reaction on Ru and Pt-based Catalysts," International Journal of Chemical Reactor Engineering, In Preparation (2024).
7. Lange, E.M., B. DeMattia, and J.E. Gatica "Catalytic Gasification – a Critical Analysis of Carbon Dioxide Methanation on a Ru/Al2O3 Catalyst," Int. J. Chem. React. Eng., (2018).
8. Santiago-Maldonado, E., J. Captain, R. Devor, and J. Gleaton, "Creating Methane from Plastic: Recycling at a Lunar Outpost," AIAA 2010-1551, 48th AIAA Aerospace Sciences Meeting, Orlando, FL (January 2010).
9. Sener, C.; Wesley, T. S.; Alba-Rubio, A. C.; Kumbhalkar, M. D.; Hakim, S. H.; Ribeiro, F. H.; Miller, J. T.; Dumesic, J. A., "PtMo Bimetallic Catalysts Synthesized by Controlled Surface Reactions for Water Gas Shift," ACS Catalysis 6 (2), 1334-1344 (2016).
10. Wheeler, C., A. Jhalani, E. J. Klein, S. Tummala,, and L. D. Schmidt "The water–gas-shift reaction at short contact times," Catalysis J., 223, 191–199 (2004).
11. Zamani, A.H. and S.J.M Rosid "Enhanced low temperature reaction for the CO2 methanation over Ru-promoted Cu/Mn on alumina support catalyst using double reactor system, " Taiwan Inst. of Chem. Eng. J., ms. # JTICE-D-18-01923 (2020).

Metal Organic Frameworks for Precious Metal Sensors

Student Researcher: George E. Kerg

Advisor: Dr. Douglas Genna

Youngstown State University
Chemistry

Abstract
This research was focused on the synthesis of a metal organic framework (MOF) that was capable of precious metal adsorption. The synthesis was carried out on UiO-67 and two derivatives. The MOFs were characterized by using PXRD. The samples were tested for adsorption using ICP-MS after being exposed to the diluted standardized samples for 24 hours. The higher functionalized UiO-67 derivative had a lower adsorption across each concentration investigated in this study when compared to the lower functionalized UiO-67.

Project Objectives
The objective of this research was to successfully synthesize a MOF that was capable of sensing precious metals. While obtaining this objective, another goal was set which was to determine if pyridyl functional groups on the MOF linkers had any significant effect on the adsorption of the metals.

MOF selection was critical as both linker and metal may play a role in the adsorption. For this reason, an aluminum-MOF was first synthesized. Aluminum does not have a high affinity for many functional groups so it was hypothesized that there would be insignificant competition between the metal centers of the MOFs and the functional groups of the linker. This would allow more functional groups to be available to coordinate with the precious metals instead of the framework of the MOF. Another reason that the Al-MOF was selected was its thermal stability and its stability in water. Both of these meant that the MOF could be stored without decomposing due to environmental factors. The synthesis, however, proved too challenging for the time constraints of this project.

UiO-67 was the second MOF selected for this project. UiO-67 has previously been studied and employed in the lab in which this project was conducted which made it an ideal candidate because of the simple solvothermal synthesis, easily identified structure, and its organic linkers that contained biphenyl-dicarboxylic acid (BPDC). This organic linker contains two phenyl rings that do not contribute to the coordination of the metal centers of the MOF. This is ideal as these π electrons could then coordinate to the precious metals.

Two more derivatives of UiO-67 were then synthesized; one containing a monopyridyl linker, 6-(4-dicarboxylic) nicotinic acid, and the other containing a dipyridyl linker, bis-pyridyl-dinicotinic acid. The purpose of this was to observe if there was a trend as more pyridyl functional groups were introduced to the MOF, if the absorption would be affected. The null hypothesis was that the absorption of Pd, as was used in this research, would increase as the functionality of the linkers increased since Pd has a high affinity for nitrogen.

Methods
The first objective of this research was to synthesize a MOF. To do this, a simple procedure was followed for a known synthesis. The first step would be to dissolve the metal in the DMF and HCl premixed solution. Then, the linker would be dissolved in DMF and added to the metal solution. The solution was sonicated for 20 minutes and then placed in the oven at 80 °C. The solution was taken out of the oven after 24 hours

and centrifuged at 5,000 rpm for 5 minutes. The mother liquor was decanted and fresh DMF was used to wash the MOF. The MOF was washed two more times and centrifuged between each wash, replacing the DMF each time for a total of three washes. After the third wash with DMF, the MOF was washed in a similar process twice in 100% ethanol. Following the second ethanol wash the supernatant was decanted one final time and placed on high vacuum for 24 hours to dry.

Once dry, the MOF was analyzed with PXRD to confirm the structure and TGA to determine the water retained in the MOF from the moisture in the air.

To test the adsorption capability of each MOF, three solutions of 100, 10, and 1 ppm Pd made from a 1000 ppm standard were made. The MOF was weighed out in triplicate for each solution for a total of nine samples. The standards that were to be added to the MOFs were analyzed using ICP to determine a starting concentration. The samples containing the Pd standard were then added to the MOFs. After 24 hours of the MOF being exposed to the sample, the supernatant was decanted using a hypodermic needle and filtered through a 35 µm filter into a centrifuge tube. The supernatant was then analyzed using ICP-MS.

Results and Discussion

The calculations were made as follows:

1.) $\frac{\text{Initial ppm} - \text{Final ppm}}{1000} * \frac{1 \text{ mol}}{106.42 \text{ g}}$ = mmol Pd Adsorbed

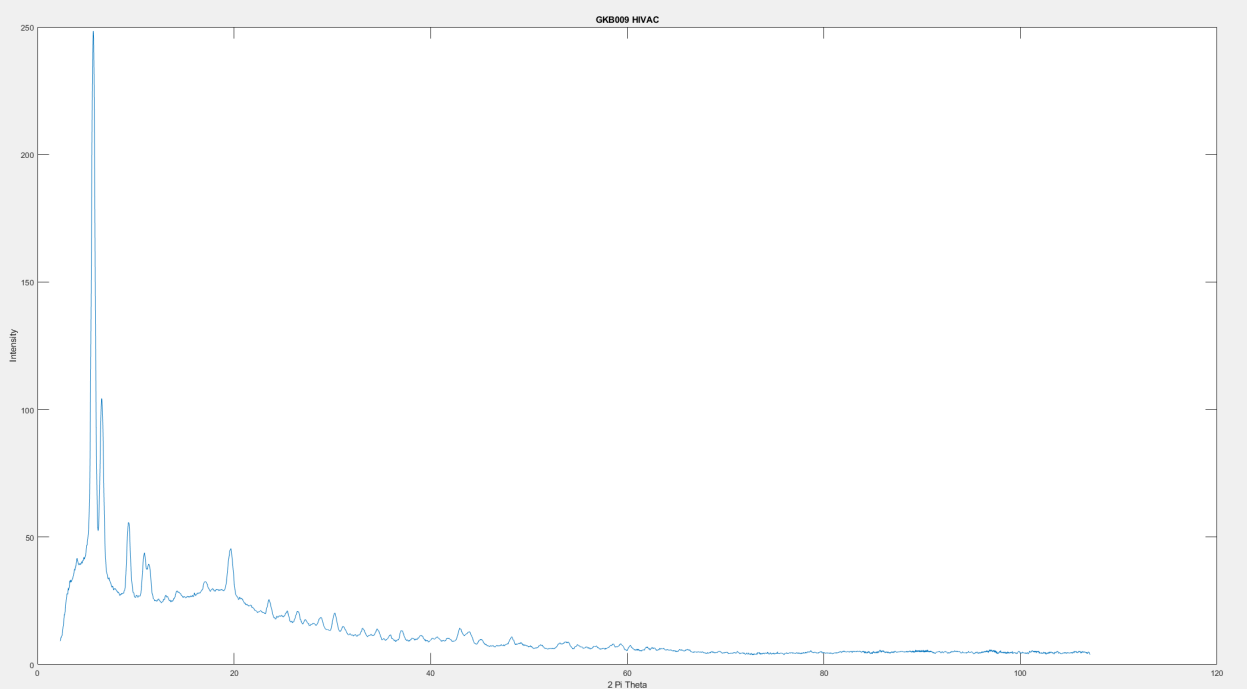
2.) $\frac{\text{Mass of MOF (g)}}{\text{Molar Mass of MOF } (\frac{\text{g}}{\text{mol}})} * \frac{6 \text{ Linkers}}{1 \text{ MOF}}$ *1000 = mmol Linker

3.) Final Answer Reported in $\frac{\text{mmol Pd Adsorbed}}{\text{mmol Linker}}$

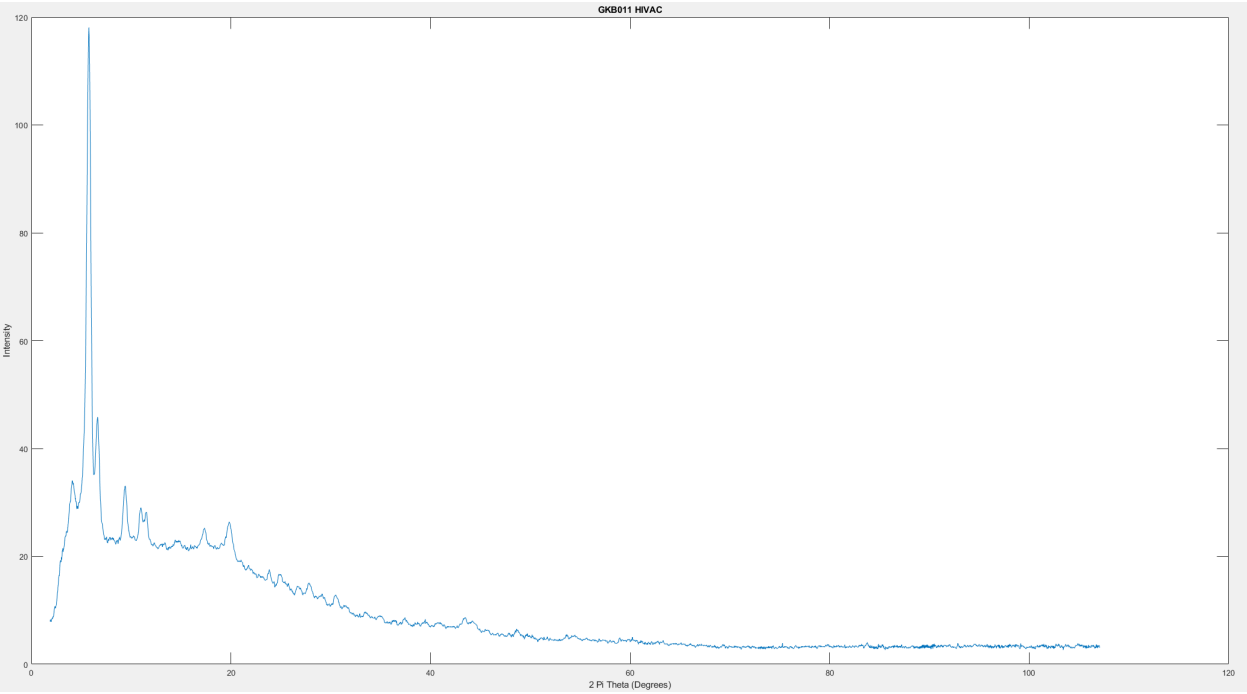
Overall, each successful MOF that was synthesized and successfully analyzed through ICP-MS was capable of sensing up to 1 ppm Pd. This was concluded as there was a difference that was detected above the limit of detection of the instrument used. Furthermore, the less functionalized MOF (GKB013; 6-(4-carboxyphenyl) nicotinic acid) had a higher affinity for the Pd than the higher functionalized MOF (GKB009, GKB011; BPYDC). This rejects the null hypothesis that was made in the beginning of the research.

Another observation that was made from the results was that it was clear that the MOFs in each trial were not fully saturated. This is to say that there were some linkers that were not coordinated to Pd, although Pd remained in the solution. This was evident as the higher the concentration of the sample, the higher the adsorption of the MOF.

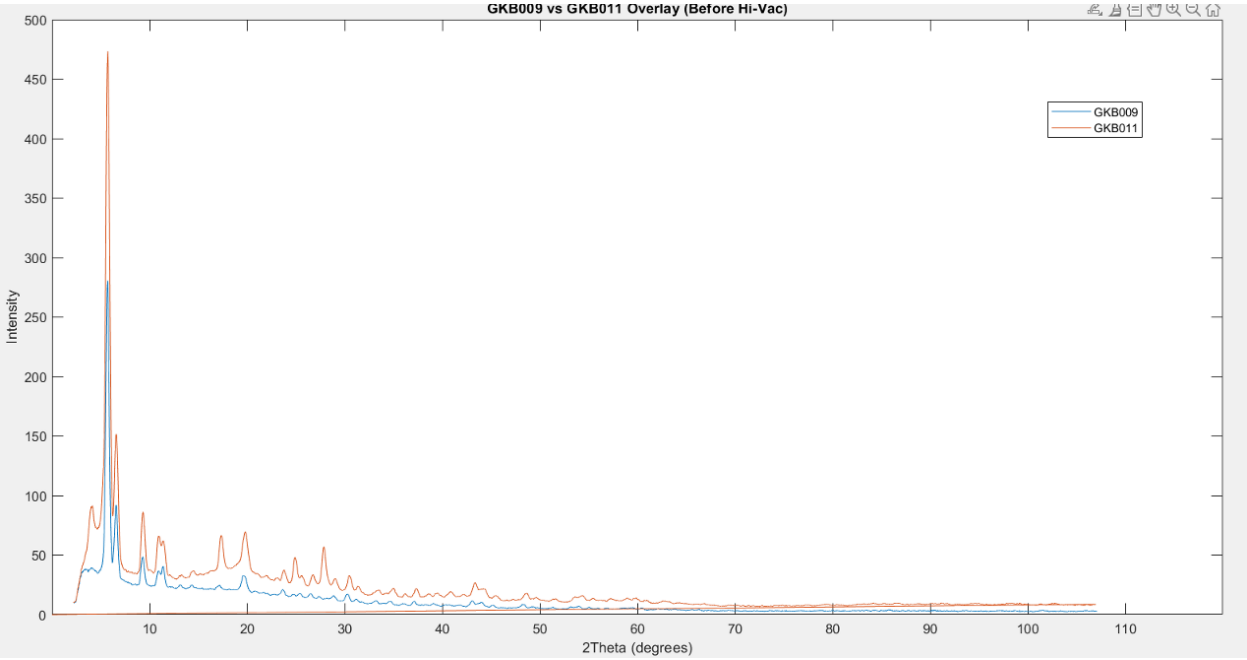
Figures/Charts



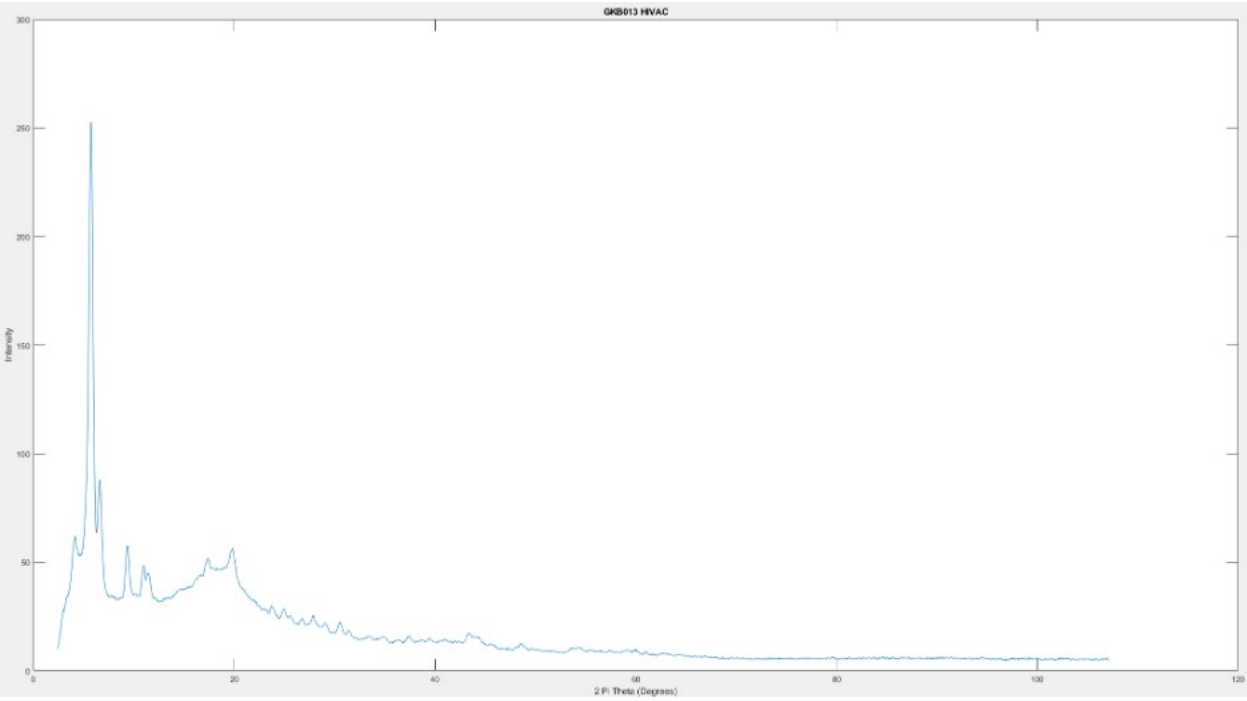
PXRD of GKB009 (BPYDC)



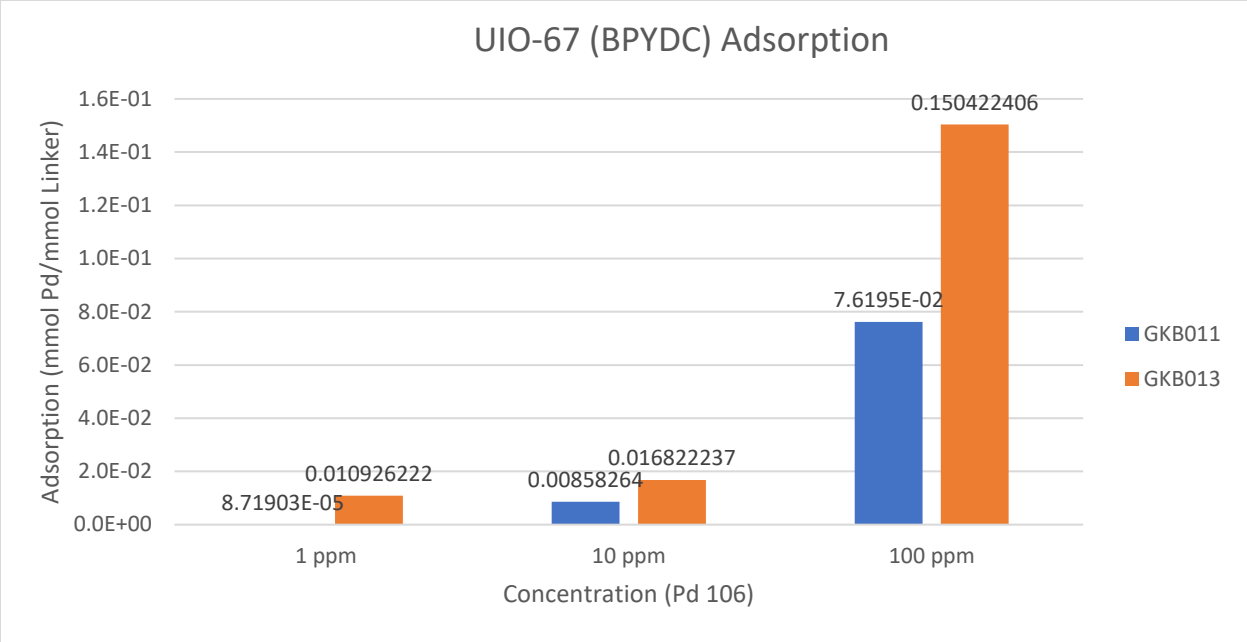
PXRD of GKB011 (BPYDC)



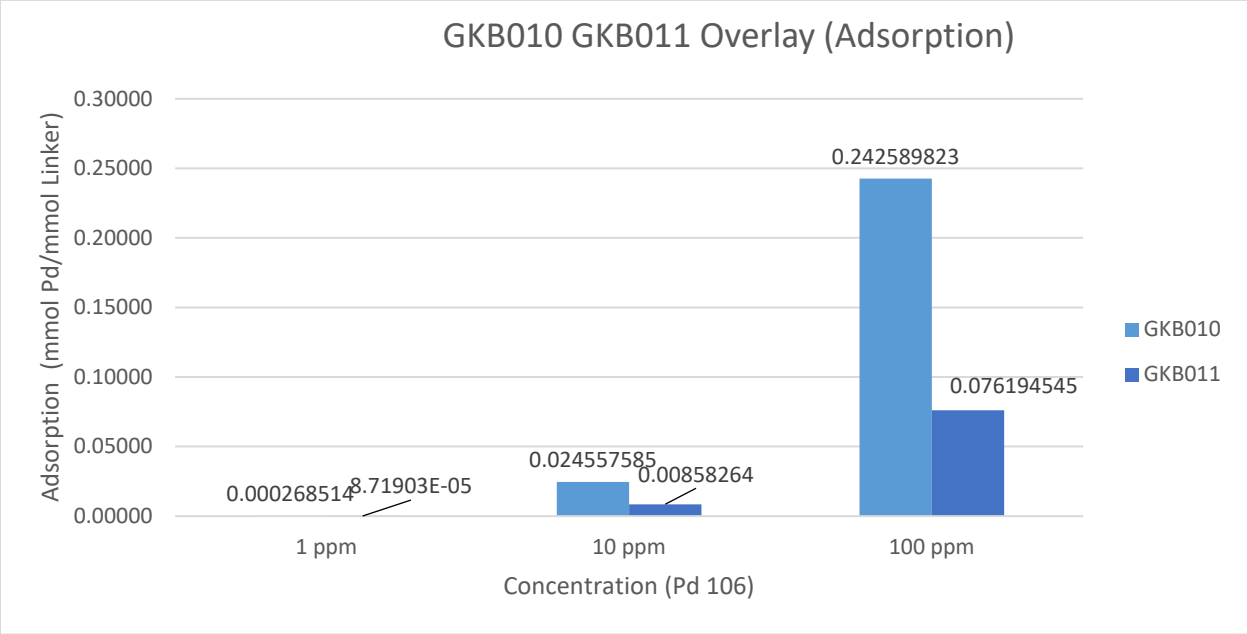
PXRD Overlay of GKB009 and GKB011



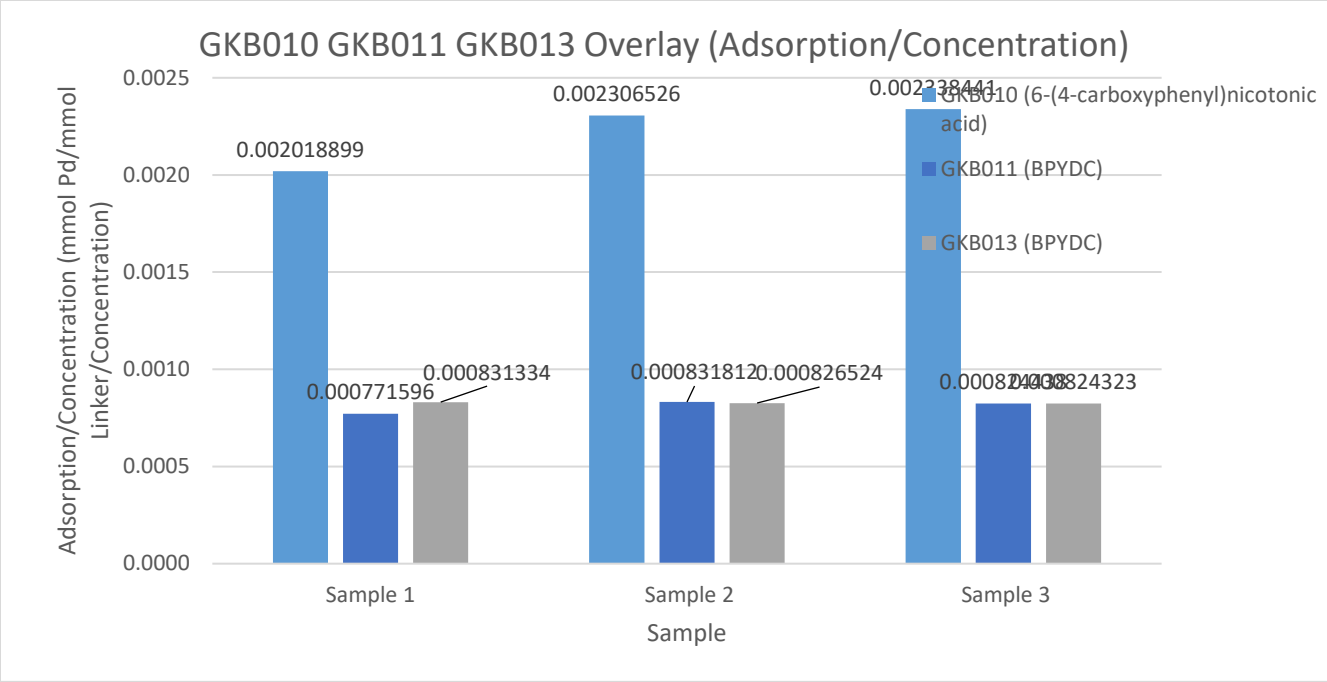
PXRD of GKB013 (6-(4-dicarboxyphenyl) nicotinic acid)



Adsorption Results of UiO-67 (BPYDC)



Adsorption Overlay Results of UiO-67 (BPYDC and 6-(4-dicarboxyphenyl) nicotinic acid))



Adsorption Overlay Results of UiO-67 (BPYDC and 6-(4-dicarboxyphenyl) nicotinic acid)) as function of Concentration

Acknowledgments

First off, Ohio Space Grant Consortium Undergraduate STEM Scholarship. I also would like to thank Dr. Douglas Genna, my project advisor, for this research. His guidance was invaluable during my time working on this project. Finally, I would like to thank my coworkers in the lab for always helping me out whenever I had questions or needed advice on my experiments.

References

1.) Genna, D. T. *Chem. Commun.* **2020**, *56* (2), 237–240

2.) Nobar, S. N. *J. Environ. Chem. Eng.* ***2021****, 9 (1), 104790*

3.) Zhao, Y. Zou; R. *ACS Mater. Lett.* **2020,** *2* (3), 220-226

Exploring Optimal Treatment Strategies for Fractures in Microgravity Environments

Student Researcher: Nabeel Khatri

Advisor: Dr. Chris Sanford

University of Toledo
Orthopedic Surgery / Bioengineering

Abstract
The expanding interest in space exploration, including missions to the Moon, Mars, and beyond, necessitates advancements in medical care tailored to the unique challenges of microgravity. Treating bone fractures in such environments presents significant difficulties due to microgravity-induced bone density loss, fluid redistribution, and the absence of mechanical stabilization provided by gravity. Current fracture management methods in space rely on adaptations of terrestrial techniques, which require refinement for effective long-term care in extraterrestrial settings. This review synthesizes existing knowledge from peer-reviewed articles, case studies, and technical reports to identify the limitations of current approaches. It also explores countermeasures like parathyroid hormone therapy to stimulate bone growth and NASA's efforts to mitigate bone and muscle loss through exercise and pharmacological interventions. Additionally, advancements in stabilization techniques, adaptable fixation devices, and innovative methods for promoting bone healing in microgravity environments are discussed. By addressing these challenges, this research aims to propose novel solutions that improve fracture treatment and enhance astronaut safety during long-duration missions. These advancements are critical for ensuring the success of human exploration and habitation beyond Earth, paving the way for sustainable space travel.

Project Objectives
Assess current technologies and future developments in regards to fracture treatment in a microgravity environment.

Methods
Conduct an in-depth analysis of the literature for gaps in the treatment options and begin developing a solution.

Results and Discussion
Microgravity environments pose significant challenges to fracture treatment due to the physiological changes in bone structure, fluid dynamics, and mechanical stabilization. One of the most critical effects is the loss of bone density. Without the mechanical loading experienced on Earth, bones experience rapid resorption, with astronauts losing up to 1-2% of their bone mineral density per month during extended missions (Genah, 2021). This reduction weakens the bone matrix and increases the incidence of fractures. Microgravity has been found to enhance osteoclast activity while simultaneously suppressing osteoblasts, leading to an imbalance that impairs the repair mechanisms of bone tissue (Baran, 2022). Furthermore, this compromised integrity further limits the effectiveness of traditional treatment methods since the weakened bone provides less support for healing. Poor bone regeneration in microgravity environments is further contributed by the reduction in anabolic signaling pathways, such as those involving bone morphogenetic proteins (BMP). There is also a shift of bodily fluids to the upper part of the body which affects nutrient and oxygen delivery to tissues. Changes in interstitial fluid dynamics in microgravity environments disrupt the microenvironment essential for osteogenesis, further exacerbating the challenges in fracture healing (Baran, 2022). Additionally, altered fluid dynamics may impact the production and circulation of critical growth factors, such as vascular endothelial growth factor (VEGF), which is vital for angiogenesis and fracture repair (Blaber, 2014). Moreover, the redistribution of fluids increases intracranial pressure, which has been linked to systemic changes in cellular behavior, potentially influencing bone health and repair processes (Wuest, 2017). These disruptions may also interfere with the inflammatory response critical to the early stages of repair, prolonging recovery times.

The absence of gravity presents significant challenges to traditional mechanical stabilization methods used in fracture treatment. Devices like splints, casts, and external fixators rely on gravity-dependent forces to maintain

alignment and stability. In microgravity, these forces are absent, leading to difficulties in achieving and maintaining proper bone alignment (Baran, 2022). Additionally, the lack of consistent mechanical loading impairs the mechanotransduction pathways essential for bone remodeling and stabilization (Blaber, 2014). There is a need for stabilization techniques that can accommodate the unique biomechanical environment of space, such as advanced fixation devices as well as the portability of these techniques.

Conventional terrestrial techniques for fracture treatment, such as casts, splints, and fixation devices, have been adapted for potential use in space missions. However, these methods face significant limitations in microgravity. Casts and splints, which rely on gravitational forces to maintain alignment, may become ineffective without consistent loading. Similarly, external fixation devices may struggle to maintain tension and alignment in a microgravity environment. Internal fixation techniques, such as plates and screws, remain promising due to their ability to provide rigid stabilization irrespective of gravity. However, the reduced bone density may compromise the anchoring of such devices. Logistical challenges, such as limited access to surgical resources and the inability to rely on Earth-based medical support, make the development of autonomous medical systems and the training of astronauts to handle such emergencies a necessity (Scheuring, 2016).

NASA has implemented numerous strategies to reduce bone loss and enhance skeletal health during space missions. The Advanced Resistive Exercise Device (ARED), which simulates Earth-based weightlifting using vacuum cylinders to generate resistance, has been instrumental in maintaining muscle mass and bone density. Research indicates that consistent use of ARED can slow bone loss; however, it does not completely prevent it, particularly in vulnerable regions like the hips and spine, which are most affected by microgravity (Lloyd, 2023). Pharmacological interventions have also been explored as complementary measures. Bisphosphonates, widely used to treat osteoporosis on Earth, have been tested on astronauts to inhibit bone resorption. Studies suggest that these drugs can mitigate bone loss during extended missions (Rosenthal, 2024). Additionally, parathyroid hormone (PTH) analogs, administered via subcutaneous injections, have demonstrated the potential to stimulate bone formation and speed up fracture healing (Swaffield, 2018). Portable imaging technologies, such as ultrasound, have been deployed on the International Space Station (ISS) to assess bone quality and detect fractures in real time. These tools provide non-invasive evaluations, allowing for timely interventions without the need for bulky equipment (Scheuring, 2016). Dietary interventions are also being explored as part of an integrated approach to combat bone loss. Ensuring adequate intake of calcium and vitamin D is critical and works alongside exercise and pharmacological treatments to maintain bone health during missions (Lang, 2017).

NASA is exploring pharmacological therapies to combat spaceflight-induced bone loss and aid fracture recovery. Intermittent Parathyroid hormone (PTH) analogs like teriparatide, an osteoporosis medication, have the potential to stimulate osteoblast activity (Sibonga, 2024). Advanced drug delivery systems, such as nanoparticles and sustained-release formulations, are being studied to improve treatment and ensure consistent therapeutic effects in space(Zhang, 2024). NASA is also exploring sclerostin inhibitors, which block a protein that slows bone formation(Aditya, 2022). Bone Morphogenetic Protein-2 (BMP-2) is another promising pharmacological agent due to its ability to promote osteogenesis. However, studies have revealed that BMP-2 may also affect bone remodeling at non-injured skeletal sites, potentially leading to unintended systemic effects (Zamarioli, 2022). To mitigate these risks, researchers are focusing on developing controlled-release formulations and targeted delivery systems that optimize the localized effects of BMP-2. The absence of gravity presents challenges to conventional stabilization techniques. To address this, researchers are developing advanced fixation devices designed for microgravity environments. These include magnetic and self-adjusting stabilization systems that leverage non-gravitational forces to maintain bone alignment. Smart fixation devices embedded with biosensors are also being explored to provide real-time data on bone healing, allowing astronauts and mission control to monitor progress and intervene when necessary (Sibonga, 2024). Additionally, shape-memory alloys and adaptive materials that respond to environmental changes are under development to provide dynamic support and maintain proper fracture stabilization. These devices aim to offer secure, reliable fixation without relying on gravitational forces. A notable development in this field is the creation of an easy-to-use external fixator designed for hostile environments. This fixator is engineered to be operable by individuals with varying levels of medical training (Manon, 2023).

3D-printed scaffolds made from biocompatible materials like bioactive ceramics and hydrogels are being developed to support bone regeneration. These scaffolds can be printed on demand and tailored to the specific geometry of a

fracture, potentially incorporating growth factors or stem cells to accelerate healing. Recent advancements have also highlighted the potential of combining 3D-printed scaffolds with stem cell therapy to enhance bone regeneration. By integrating mesenchymal stem cells into biocompatible scaffolds, researchers have observed improved osteogenic differentiation and bone healing, offering a promising approach for treating fractures in space environments (Jemison, 2021). Collectively, these cutting-edge pharmacological, mechanical, and regenerative approaches signify a transformative shift in how fracture treatment and bone health management are addressed for long-duration space missions.

References

Aditya, S., & Rattan, A. (2021). Sclerostin inhibition: A novel target for the treatment of postmenopausal osteoporosis. *Journal of Mid-life Health*, *12*(4), 267–275. https://doi.org/10.4103/jmh.jmh_106_20

Baran, R., Wehland, M., Schulz, H., Heer, M., Infanger, M., & Grimm, D. (2022). Microgravity-Related Changes in Bone Density and Treatment Options: A Systematic review. *International Journal of Molecular Sciences*, *23*(15), 8650. https://doi.org/10.3390/ijms23158650

Blaber, E., Dvorochkin, N., Torres, M., Yousuf, R., Burns, B., Globus, R., & Almeida, E. (2014). Mechanical unloading of bone in microgravity reduces mesenchymal and hematopoietic stem cell-mediated tissue regeneration. *Stem Cell Research*, *13*(2), 181–201. https://doi.org/10.1016/j.scr.2014.05.005

Bonanni, R., Cariati, I., Marini, M., Tarantino, U., & Tancredi, V. (2023). Microgravity and musculoskeletal health: What strategies should be used for a great challenge? *Life*, *13*(7), 1423. https://doi.org/10.3390/life13071423

Genah, S., Monici, M., & Morbidelli, L. (2021). The effect of space travel on bone metabolism: Considerations on today's major challenges and advances in pharmacology. *International Journal of Molecular Sciences*, *22*(9), 4585. https://doi.org/10.3390/ijms22094585

Guzman, A. (2024, March 21). Counteracting bone and muscle loss in microgravity - NASA. *NASA*. https://www.nasa.gov/humans-in-space/counteracting-bone-and-muscle-loss-in-microgravity/

Jemison, M., & Olabisi, R. (2021). Biomaterials for human space exploration: A review of their untapped potential. *Acta Biomaterialia*, *128*, 77–99. https://doi.org/10.1016/j.actbio.2021.04.033

Lang, T., Van Loon, J. J., Bloomfield, S., Vico, L., Chopard, A., Rittweger, J., Kyparos, A., Blottner, D., Vuori, I., Gerzer, R., & Cavanagh, P. R. (2017). Towards human exploration of space: the THESEUS review series on muscle and bone research priorities. *Npj Microgravity*, *3*(1). https://doi.org/10.1038/s41526-017-0013-0

Manon, J., Pletser, V., Saint-Guillain, M., Vanderdonckt, J., Wain, C., Jacobs, J., Comein, A., Drouet, S., Meert, J., Casla, I. J. S., Cartiaux, O., & Cornu, O. (2023). An Easy-To-Use External Fixator for All Hostile Environments, from Space to War Medicine: Is It Meant for Everyone's Hands? *Journal of Clinical Medicine*, *12*(14), 4764. https://doi.org/10.3390/jcm12144764

Scheuring, R., DO, MS, RMSK, FAsMA, NASA- Johnson Space Center, Buerhle, M., NASA EPDC, Nicogossian, A., Konieczynski, D. D., Truty, M. J., Biewener, A. A., Baldwin, K., Herrick, R., McCue, S., Kertsman, E., Barnes, M., Dekorse, T., Saile, L., Sayson, J., Hargens, A., Wing, P., LeBlanc, E. A., & Smith, E. A. (2016). *Sports injuries and space injuries: Prevention and treatment*. https://ntrs.nasa.gov/api/citations/20160002368/downloads/20160002368.pdf

Sibonga, J. D., NASA Johnson Space Center, Spector, E. R., KBR, Yardley, G., KBR, Alwood, J. S., NASA Ames Research Center, Sibonga, J., NASA Johnson Space Center, NASA Glenn Research Center, KBR, KBR, KBR, KBR, KBR, & KBR. (2024). Risk of Bone Fracture due to Spaceflight-induced Changes to Bone. In *Human Research Program* [Report]. National Aeronautics and Space Administration. https://humanresearchroadmap.nasa.gov/evidence/reports/Bone%20Fracture%20Evidence%20Report_07-18-2024.pdf

Swaffield, T. P., Neviaser, A. S., & Lehnhardt, K. (2018). Fracture risk in spaceflight and potential treatment options. *Aerospace Medicine and Human Performance*, *89*(12), 1060–1067. https://doi.org/10.3357/amhp.5007.2018

Wei, F., Flowerdew, K., Kinzel, M., Perotti, L. E., Asiatico, J., Omer, M., Hovell, C., Reumers, V., & Coathup, M. J. (2022). Changes in interstitial fluid flow, mass transport and the bone cell response in microgravity and normogravity. *Bone Research*, *10*(1). https://doi.org/10.1038/s41413-022-00234-9

Wpadmin. (2019, May 28). *National Osteoporosis Month: Testing a new osteoporosis therapy on the ISS*. ISS National Lab. https://issnationallab.org/iss360/national-osteoporosis-month-testing-a-new-osteoporosis-therapy-on-the-iss/

Wuest, S. L., Stern, P., Casartelli, E., & Egli, M. (2017). Fluid Dynamics Appearing during Simulated Microgravity Using Random Positioning Machines. *PLoS ONE*, *12*(1), e0170826. https://doi.org/10.1371/journal.pone.0170826

Zamarioli, A., Adam, G., Maupin, K. A., Childress, P. J., Brinker, A., Ximenez, J. P. B., Chakraborty, N., Gautam, A., Hammamieh, R., & Kacena, M. A. (2022). Systemic effects of BMP2 treatment of fractures on non-injured skeletal sites during spaceflight. *Frontiers in Endocrinology*, *13*. https://doi.org/10.3389/fendo.2022.910901

Zhang, M., Xu, F., Cao, J., Dou, Q., Wang, J., Wang, J., Yang, L., & Chen, W. (2023). Research advances of nanomaterials for the acceleration of fracture healing. *Bioactive Materials*, *31*, 368–394. https://doi.org/10.1016/j.bioactmat.2023.08.016

Analysis of Real-Gas Effects in The Ohio State University Large Area Reflected Shock (LARS) Tunnel

Student Researcher: Henry Kitchen

Advisors: Dr. Jesse Little and Dr. Nathan Webb

The Ohio State University
Aerospace Engineering

Abstract

The objective of this research is to estimate operational envelopes for the LARS facility with inclusion of real-gas effects. For speeds below Mach 5, these envelopes can be calculated using calorically perfect gas equations, meaning the specific heat capacity is considered constant. However, for hypersonic flows, temperatures increase such that vibrational effects cannot be neglected. This means that the specific heat capacity becomes a function of temperature. These vibrational effects take energy out of the flow, causing the calorically perfect gas equations to lose their accuracy. Flows with these vibrational effects are described as calorically imperfect—the thermally perfect, calorically imperfect conditions make up the 'real-gas effects' of hypersonic flows. This study involves implementing real-gas equations, using numerical methods, to update existing calorically perfect operational envelopes. This investigation will generate more accurate operational envelopes for the LARS facility and ultimately define its overall hypersonic research capability.

Project Objectives

The primary goal of this research project is to improve the estimation of the LARS facility's operational envelopes by incorporating real-gas effects into the current perfect gas envelope model, enabling a more accurate characterization of the facility's experimental testing limits.

Methods

The original program that calculated operational envelopes for the LARS facility (developed in MATLAB®) took initial limits for the tube temperature, gas composition, and test section Mach number to generate perfect gas performance envelopes. The implementation of real-gas equations originated from the *NACA 1135 Report* [2] which outlines real-gas equations in terms of temperature-varying specific heats. These equations were swapped with the original perfect gas equations, but as a result of the non-constant specific heats, numerical methods had to be implemented in order to calculate pre/post shock states in the shock tube in addition to test section flow variables. This process occurred across the finely discretized range of initial conditions that were further processed to remove conditions that would exceed shock tube pressure ratings, oxygen liquefaction conditions, and other states that would not be optimal to use for experimental testing.

Further, a companion shock tunnel calculator was similarly adapted by carrying through a similar set of calculations to define shock properties and flow variables at discrete initial conditions. This tool has the additional capability of quickly defining the available conditions of the flow given user-specified flow variables. Used alongside the operational envelopes of the facility, conditions for potential testing runs can be quickly calculated at a greater accuracy compared to their perfect gas counterparts.

Results and Discussion

The real-gas operational envelopes for the LARS facility are calculated and compared to the corresponding perfect gas envelopes in the figures below. This reduction in envelope was the expected result since it is indicative of the vibrational effects of real-gases that take energy out of the temperature of the flow. Since those effects are not taken into consideration in the perfect gas equations, they are shown to

overestimate the flow conditions. It's also apparent that, as test section Mach number increases, these effects are exacerbated. This is why, for plots that include facility performance-enhancements that increase test section Mach number, such as heated shock tubes, Helium as a driver gas, and new throats, the differences between the real-gas and perfect gas plots also increase.

Figures

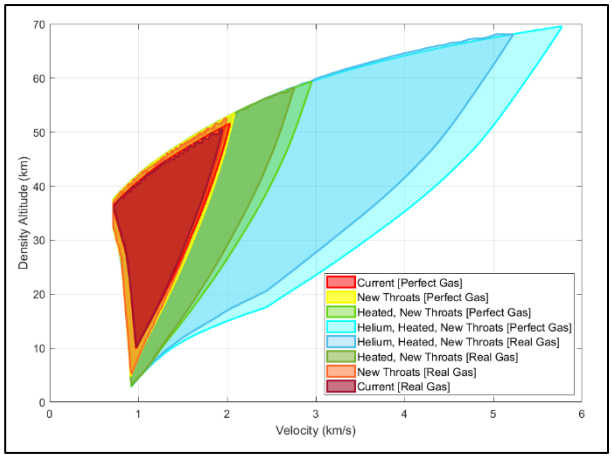


Figure 1. Real-Gas Effects on Density Altitude and Test Section Velocities

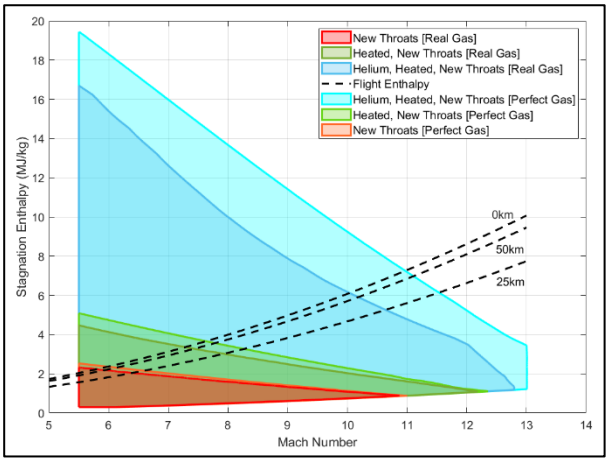


Figure 2. Real-Gas Effects on Stagnation Enthalpy and Mach Number

Acknowledgments

I thank both of my advisors, Dr. Jesse Little and Dr. Nathan Webb, for their invaluable guidance, support, and mentorship throughout the duration of this project. I also thank the Ohio Space Grant Consortium for the opportunity to pursue this research project and for their commitment to engage students in STEM research.

References

[1] Pope, A. and Goin, K. (1965) 'Real Gas Effects', in High-Speed Wind Tunnel Testing. John Wiley & Sons, Inc., pp. 21–27.

[2] Ames Research Staff (1953) Equations, Tables, and Charts for Compressible Flow. rep. National Advisory Committee for Aeronautics, pp. 14–16.

[3] Anderson, J. (2021) 'Chapter 7', in Modern Compressible Flow: With Historical Perspective. 4th edn. McGraw-Hill Education, pp. 261–302.

Design, Modeling, and Analysis of Molded Pulp Packaging Using Siemens NX Software

Student Researcher: Suraju Lawal

Advisor: Dr. Augustus Morris

Central State University
Manufacturing Engineering

Abstract

The "Pulp Packaging Structure Design Project for Quality Assurance" is an innovative engineering senior design project that focuses on developing a quasi-honeycomb pulp packaging structure utilizing advanced computer-aided design (CAD) tools, specifically the NX Unigraphics engineering design system. The primary objective of this project is to create a sustainable, durable, and cost-effective packaging solution that meets high-quality assurance standards while adhering to environmental sustainability principles.

Pulp packaging is an eco-friendly alternative to traditional plastic-based materials due to its biodegradability and recyclability. However, maintaining structural integrity and minimizing material usage are critical challenges. This project aims to address these issues by leveraging the quasi-honeycomb design concept, renowned for its lightweight yet strong structural properties. The honeycomb-inspired geometry is optimized to distribute loads evenly and resist deformation during handling, storage, and transportation.

Project Objectives

The objective of this project is to design and develop an innovative pulp packaging structure that maximizes quality assurance through enhanced structural integrity and sustainability. Leveraging advanced engineering principles and tools, this project seeks to create a quasi-honeycomb packaging design that balances strength, durability, and material efficiency.

This senior design project will utilize Siemens NX-Unigraphics, a cutting-edge engineering design platform, to model, simulate, and analyze the proposed packaging solution. The quasi-honeycomb design will be engineered to improve load-bearing capacity, shock absorption, and overall performance during storage and transportation. By employing geometric optimization techniques, the design will reduce material usage without compromising functionality, aligning with modern sustainability goals.

Methods

Optimization Method

1. Define Project Objectives and Constraints

The primary objective is to optimize the pulp packaging structure for quality assurance, focusing on achieving high strength-to-weight ratio, cost-effectiveness, sustainability, and manufacturability. Constraints include material availability, compliance with environmental standards, compatibility with production processes, and ensuring minimal deformation under compressive and impact loads.

2. Material Selection and Analysis

Select appropriate materials, such as recycled pulp fibers, and analyze their mechanical properties, including tensile strength, elasticity, and durability. Utilize simulation tools in NX-Unigraphics to evaluate material performance under various conditions, ensuring sustainability and functionality.

3. Design Parameter Identification

Identify critical design parameters, including cell wall thickness, honeycomb cell dimensions, and overall geometry. Incorporate these parameters into the quasi-honeycomb design to ensure structural integrity and efficient material usage.

4. Generate Initial Design Concepts

Develop initial design concepts using NX-Unigraphics. Employ parametric modeling to create multiple iterations of quasi-honeycomb structures with varying geometric configurations. Use the software's optimization module to define baseline designs.

5. Finite Element Analysis (FEA)

Perform FEA simulations to evaluate the structural behavior of designs under load conditions, including compression, vibration, and impact. Analyze stress distribution, deformation, and failure points to refine the design iteratively.

6. Optimization Algorithms

Use topology optimization to identify material distribution and remove unnecessary mass. Implement design of experiments (DOE) techniques to systematically vary parameters and evaluate their effects on performance metrics. Employ genetic algorithms or other advanced optimization techniques in NX-Unigraphics to explore the design space and achieve optimal configurations.

7. Manufacturing Feasibility Assessment

Assess manufacturability using NX-Unigraphics' manufacturing simulation tools. Ensure the design aligns with pulp molding processes, including mold flow and cycle times, and minimizes waste. Evaluate tooling costs and scalability for mass production.

8. Prototype Development and Testing

Fabricate prototypes of the optimized design for real-world testing. Conduct physical tests to validate computational results, including compression, drop, and impact tests. Refine the design based on test feedback.

9. Iterative Optimization

Integrate prototype testing results into the design loop, iterating on geometry, material properties, and manufacturing processes. Finalize the design after multiple iterations converge on an optimal solution.

10. Documentation and Quality Assurance

Document the optimization process and final design specifications. Create quality assurance guidelines for production, ensuring the design meets strength, sustainability, and cost requirements. Use NX-Unigraphics' tools to generate technical drawings and assembly instructions for implementation.

Results and Discussion

The project focused on the design, modeling, and analysis of molded pulp packaging using Siemens NX software. The final design successfully met the functional requirements of product protection,

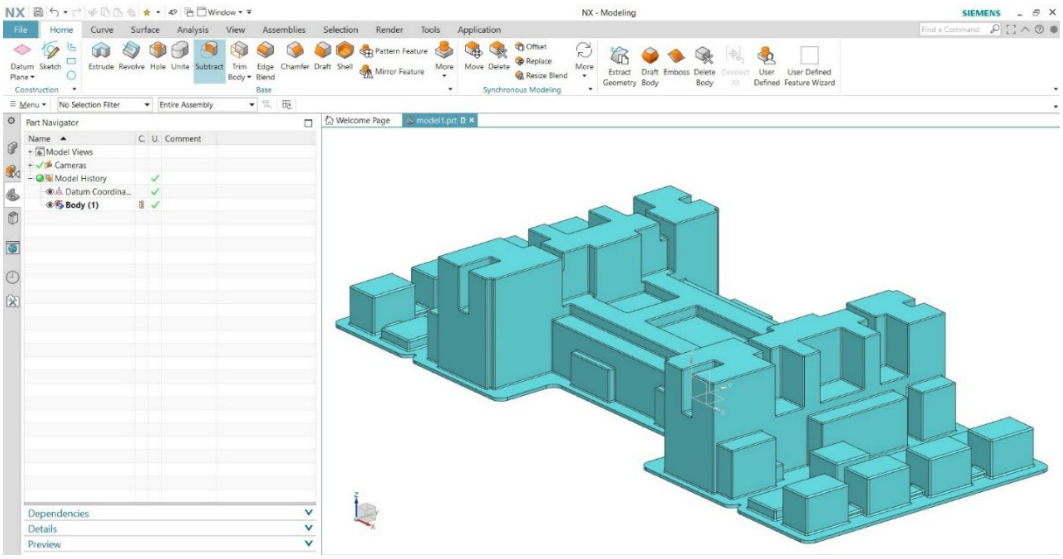
sustainability, and manufacturability. The 3D model was developed using Siemens NX, considering material properties and geometric constraints relevant to molded pulp.

The finite element analysis (FEA) conducted within Siemens NX revealed critical insights into the structural behavior of the packaging under different loading conditions. Stress distribution and deformation patterns were observed when simulating drop and compression tests, showing that the design effectively absorbed impact energy while maintaining its integrity. The maximum stress values remained within acceptable limits for molded pulp materials, indicating the packaging's reliability in practical applications.

Additionally, the design showed potential for material optimization, with minimal waste and efficient support structures. The results highlighted that the molded pulp packaging not only met environmental standards but also demonstrated robustness comparable to conventional plastic packaging.

Overall, the combination of CAD modeling and FEA in Siemens NX provided a comprehensive understanding of both the visual and functional performance of the packaging. The design process validated the use of molded pulp as a sustainable alternative in the packaging industry, supporting further research and development in eco-friendly materials.

Figures/Charts







Acknowledgments

I would like to express my sincere gratitude to all those who have supported and guided me throughout the course of this design project titled *"Design, Modeling, and Analysis of Molded Pulp Packaging Using Siemens NX Software."*

First and foremost, I am deeply thankful to my project supervisor, Dr. Augustus Morris, for his invaluable guidance, encouragement, and insightful feedback at every stage of this project. His expertise in design and analysis using Siemens NX played a critical role in shaping the direction and quality of this work.

I extend my appreciation to the faculty and staff of the Manufacturing Engineering, Central State University, for providing access to necessary resources and facilities, as well as creating an environment conducive to learning and innovation.

I am also grateful to my peers and friends for their continuous support, collaboration, and helpful discussions, which significantly contributed to the completion of this project.

Finally, I would like to thank my family for their constant encouragement, patience, and motivation throughout the duration of this project. Their unwavering belief in my abilities has been a source of strength and inspiration.

This project has been an enriching experience, and I am truly thankful to everyone who played a part in its successful completion.

References

1. **Cao, Y., & Zhang, X. (2017).** *Molded pulp packaging: Analysis, design, and application.* Journal of Packaging Technology and Research, 1(1), 1-12.
    - A comprehensive review of the design and analysis methodologies for molded pulp packaging.
2. **Thiel, C. A., & Murren, S. L. (2016).** *Finite element analysis in molded pulp design.* International Journal of Engineering Simulation, 33(5), 367-374.
    - Discusses the application of finite element analysis (FEA) in the design of molded pulp products using engineering tools like NX.
3. **Müller, R., & Meyer, F. (2015).** *Optimizing molded pulp packaging with computer-aided design tools.* Journal of Packaging Science and Technology, 4(2), 49-55.
    - Explores the role of CAD systems, including NX, in optimizing the design of molded pulp packaging.

Advanced Thermal Management for Military Aircraft

Student Researcher: Nathan Lewan

Advisor: Mitch Wolff

Wright State University
Mechanical and Materials Engineer/Mechanical Engineering

Abstract
Advancements in aircraft systems and supporting equipment have resulted in high thermal loads within new generations of military aircraft without allocating the space requirements that would traditionally be needed for additional cooling. Therefore, the necessity arises of creating more efficient thermal management systems to increase the cooling capabilities of the aircraft. Heat exchangers play a critical role in these systems and operate by transferring energy from a higher potential medium to a lower one. Conventional heat exchanger design has been governed by manufacturability, but with recent improvements in additive manufacturing, conformable triply periodic minimal surface heat exchangers, which are additively manufactured heat exchangers (AMHX) are now feasible. This work presents a computational fluid dynamics (CFD) study over a AMHX created in nTopology software. The bulk of this process included importing geometry to ANSYS Fluent, setting up boundary conditions for varying tests, meshing, and finally the solution. As this project is solely numerical, results were compared to existing research and test data to provide a rough order-of-magnitude analysis for validation. This research is designed to serve as a basis for which future CFD studies can be compared to as well as improve upon exiting methods for this type of analysis.

Project Objectives
The objective of this project is twofold. The first is to create a realistic model of the AMHX by utilizing computational fluid dynamics. In doing so, performance metrics such as the Nusselt number, convection coefficient, and pressure loss can be found for the model. The second objective arises from the result of the first, which is to streamline the process of creating geometry within nTop and exporting over to Fluent, along with testing different setups within Fluent which allow for rapid optimization of the heat exchanger for a given application.

The heat exchanger chosen for this analysis is shown below in figure 1a. This model was created at the Air Force Institute of Technology (AFIT), by John Brewer, Stephen Richter, and Tanner Barber, by utilizing the geometry software nTop. As shown below in the figure, the heat exchanger is shaped in a way that it can be conformal to its surroundings, allowing for more flexibility within a given aircraft system. Also shown below in figure 1b is the fluid paths for the hot and cold fluid, as denoted by the red and blue color, respectively. The fluid domain in this figure does not include the wall thickness nor the baffles, which prevent the fluid paths from intersecting at the inlets and outlets. This is the reason for the small gap on all four entrance and exit regions, as well as the gap between the main interface of both fluid domains.

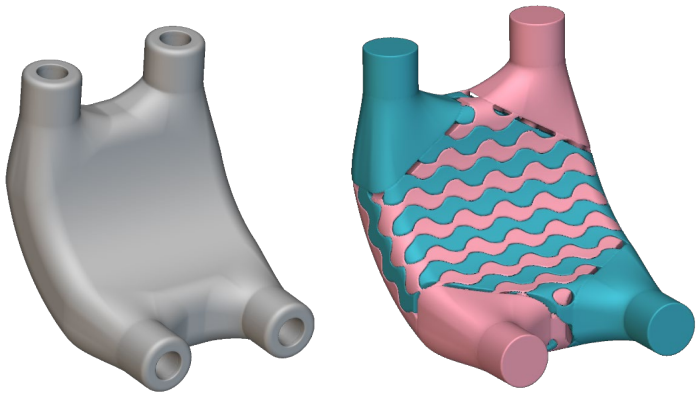


Figure 1: (a) Additively manufactured heat exchanger shell and (b) both flow paths

Methods

One of the major challenges in this analysis was exporting the geometry from nTop – the software utilized to design the AMHX, into Fluent. Ansys fluent is a commercial finite volume-based solver that allows for many variations when it comes to solution methodology. Fluent offers many different modeling approaches, including Reynolds Averaged Navier Stokes (RANS), Large Eddy Simulation (LES), and Scale Adaptive Simulation (SAS), with a wide variety of turbulence models to choose from [1]. The default approach is RANS, by which the highest order of accuracy offered is second order, typically paired with an upwind scheme. Fluent offers both pressure and density-based methods, by which the pressure-based method conserves mass for the pressure governing equation [2]. Many different options for problem setup are also available, including steady state/transient analysis, implicit/explicit schemes, and coupled/segregated approaches. This difficulty for this project stemmed mainly from the already well-known issue of CFD which is geometry. If the geometry of a model has slight issues, larger ones will arise when meshing and later solving the given problem. The more complex geometry in this scenario further amplifies this problem.

The geometry created in nTop is defined as an implicit model, meaning that it is created by mathematical equations as opposed to the traditional CAD method of boundary representation (BREP). The BREP method describes geometry in terms of surfaces and interfaces, as traditionally seen in a CAD software. The implicit method is advantageous due to it's ability to quickly generate the geometry for a given change or update, however, it does come with challenges.

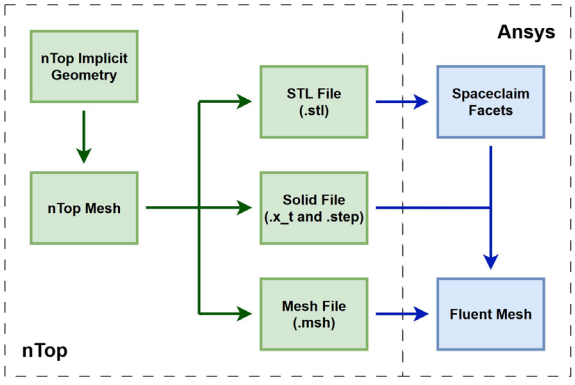


Figure 2: Methods for geometry file conversion from nTop to Ansys

The major challenge associated with the implicit geometry within nTop is the need for a meshable file format such as a STL or Parasolid, which are the traditional file types used for CFD analyses. As shown above in figure 2, three main file conversion types were explored: STL, solid file, and mesh file. The STL file was the first explored. This method was feasible, however, was only attempted for very simplified geometries. This method also required additional steps of cleaning up individual faces, which was carried out by using Ansys Spaceclaim. This proved not be feasible at more complex geometries, such as the heat exchanger given above in figure 1. Conversion to a step file was attempted next and also proved to be challenging due to meshing faces together that were intended to be separate, making an accurate CFD simulation difficult. The final method explored and successfully tested was to utilize a special feature within nTop, allowing for a mesh geometry file to be generated. With this method, boundary condition locations such as inlets and outlets were selected within nTop and imported into Fluent with the mesh file.

Another issue that was present was that the interface between the hot and cold fluid gave many errors when both were meshed together, meaning, the hot and cold fluid meshes should having matching elements in which the data from the analysis can be transferred through/interpolated. This is critical for obtaining good results. Due to issues with meshing the interface between the hot and cold fluid in fluent, only the hot side was modeled, as shown in figure 3 below.

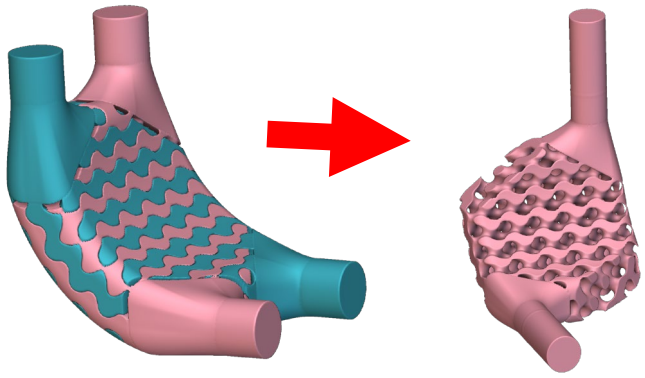


Figure 3: CFD model simplification – only hot fluid path

For this project the setup consisted of a second-order upwind scheme. A velocity inlet boundary condition was used, and the temperature and velocity were specified to be 323K 1.70 m/s, respectively. These parameters were chosen as they were the upper limits for the experimental testing skid which will be utilized to test the heat exchanger in the future. An interface temperature, modeled as a solid wall temperature, was specified to be 278 K, allowing for a negative heat transfer into the fluid. Lastly, an outlet pressure boundary condition was used and set to be 0 psig, used for finding the pressure loss across the heat exchanger.

The outcome of the CFD analysis was to find the following parameters: the average convective heat transfer coefficient h, the outlet temperature, and the pressure loss across the heat exchanger. Results were then verified using a grid independence study.

Results and Discussion

The post processing capabilities over the CFD analysis are endless, and thus, only a few different figures were disused below. The solution verification to ensure that a realistic solution was created was a contour plot of pressures within the heat exchanger. The result was found to be:

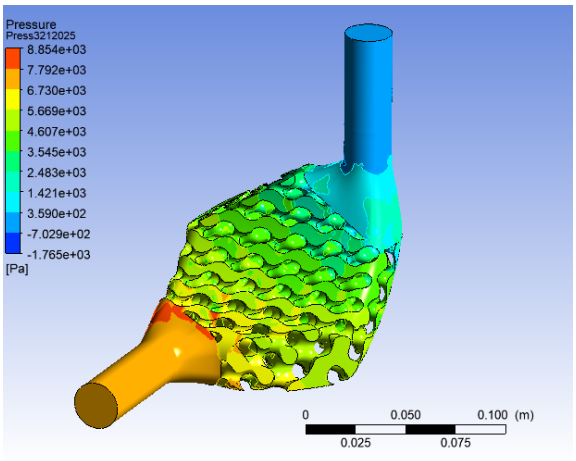


Figure 4: CFD model results – pressure contour plot

As shown above in figure 4, the pressure contour plot of the hot fluid path seems reasonable, having a higher pressure on the inlet side with a downstream gradient. Other parameters to characterize the heat transfer within the heat exchanger were then also found. To further validate the model, a grid indpence study was then found. The results of this study are given in table 1 below.

# Cells	y+	h (W/m^2*k)	Tout (K)	ΔP (Pa)
630k	6.374	11389	316.72	6869
1.5M	4.979	12623	316.12	7198
2.6M	4.754	12894	316.01	7421
4.7M	4.521	13123	315.84	7567

Table 1: CFD model results – grid independence study

As shown in the table above, as the number of cells was increased, the parameters converged to a value. The results of this study were taken from the analysis with the largest number of cells, 4.7 million. All of the thermal and hydraulic parameters of interest converged to values with a less than 2% difference on the final mesh refinement. The heat transfer coefficient, h, converged to a final value of 13,123 W/m^2*k. The outlet temperature converged to 315.84 K, a very reasonable temperature for this setup. Finally, the pressure loss was found to be 7,567 Pa. It should be noted that for this study, the y+ value remained below five for the final three iterations, the upper limit for what is necessary for good results.

Future work will be conducted experimentally testing the heat exchanger to compare to these results and setup more CFD studies to compare to these results as well as make predictions for future tests.

Acknowledgments
A special thank you to Abdeel Roman, Zach Carner, Mitch Wolff, and Jacob Spark for their invaluable guidance and assistance throughout the project. I would also like to thank my company, PCKA, for the opportunity to gain experience with hands-on testing of heat exchangers, which lead me into this project.

References

[1] Menter, F.R., R. Lechner, and A. Matyushenko. "Best Practice: RANS Turbulence Modeling in Ansys CFD." Presented at Ansys Germany GmbH. Accessed April 3, 2025. https://www.ansys.com/content/dam/amp/2022/march/quick-request/Best%20Practice%20RANS%20Turbulence%20Modeling%20in%20Ansys%20CFD.pdf.

[2] "What Are Pressure-Based Solver vs. Density-Based Solver in FLUENT?" Ansys Innovation Space, January 25, 2023. https://innovationspace.ansys.com/knowledge/forums/topic/what-are-pressure-based-solver-vs-density-based-solver-in-fluent/.

Suppressing Two-Phase Flow Instabilities Utilizing a Hardware-in-the-Loop Approach

Student Researcher: Nathan Lynn

Advisor: Dr. Mitch Wolff

Wright State University
Mechanical Engineering

Abstract
Two-phase pumped loop systems are renowned for their ability to reject large quantities of heat without substantial temperature change. However, a major challenge of these systems is introduced by instabilities. The objective of this research is to investigate the feasibility of using active flow controls in a hardware-in-the-loop (HIL) approach to mitigate these instabilities. The project involves implementing communication between hardware components, such as the Speedgoat Data Acquisition System, motor controller, power supply, chiller, thermocouples, and pressure transducers. The Simscape software library within Simulink will then be used to create a thermal model that accurately represents the system. To validate the system, an aircraft model will be created to simulate sample heat loads corresponding to mission profiles, with loads coming from the engine, sensors, electronics, and other essential equipment. Tests will be conducted to apply these heat loads to the experimental system, and results will be recorded using a Speedgoat Data Acquisition System. This hardware-in-the-loop test setup will be capable of applying sample mission profiles to a benchtop test skid, ensuring effective simulation and data collection for future system evaluations and instability mitigation research.

Project Objectives
The objective of this project is to develop an active control method to mitigate two-phase flow instabilities. This will be achieved through a Hardware-in-the-Loop (HIL) benchtop experiment designed to simulate dynamic aircraft heat loads. Utilizing Simscape models and a Speedgoat Data Acquisition System, the project further aims to demonstrate the feasibility of two-phase pumped loop refrigerant systems operating under aircraft conditions, with the goal of eventual integration into real aircraft platforms.

Methods
The benchtop experiment of two-phase refrigerant flow will be established. A two-phase fluid model will be created using Simulink and Simscape's Two-Phase Fluid Toolbox, which includes components such as pumps, reservoirs, pipes, heat exchangers, and more. The model will then be validated against the physical benchtop system. Once the model and benchtop demonstrate consistent behavior, they will be integrated via a Speedgoat Data Acquisition System, enabling real-time communication between the simulation and hardware components, including a heat load, condenser, thermocouples, pressure transducers, and additional instruments. After enough characterize instability identifying data is collected, pressure-based control strategies will be applied to mitigate unstable two-phase flow behavior.

Results and Discussion
The Simulink model is nearly complete, pending minor fidelity enhancements. Experimental results were not obtained for this project due to shifting priorities and limited resource allocation.

Figures/Charts

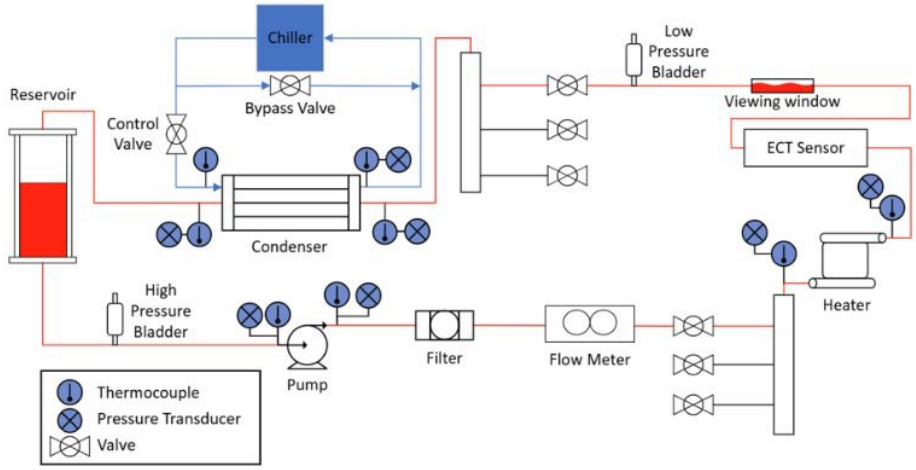


Figure 1: Schematic of two-phase hardware-in-the-loop system. Red represents refrigerant and blue represents chilled water.

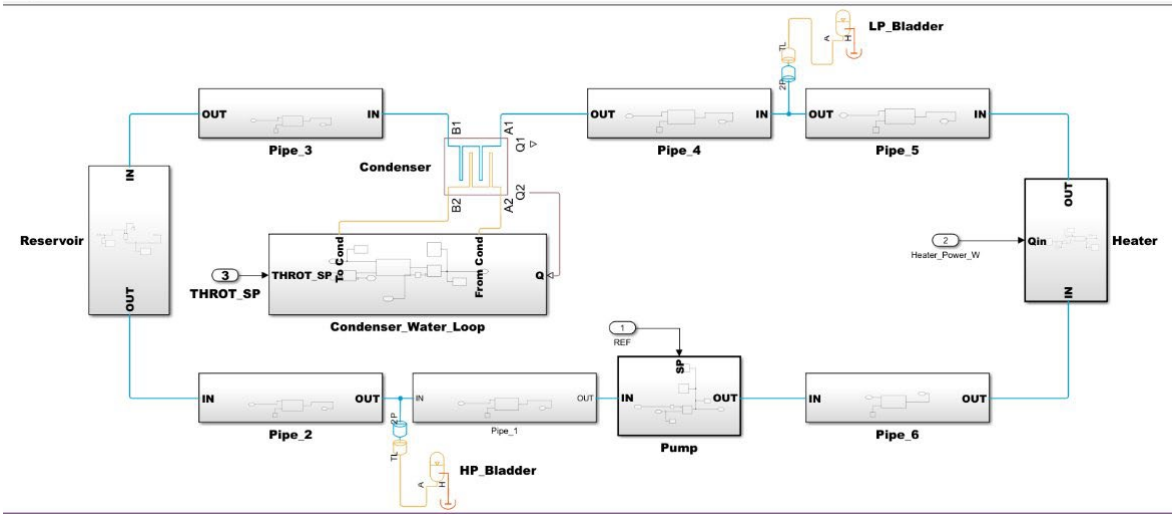


Figure 2: Simulink Model of Benchtop using Simscape Components.

Acknowledgments

This research was supported by the Ohio Space Grant Consortium (OSGC), the Air Force Research Laboratory (AFRL) (Dr. Abdeel Roman and Zach Carner, M.S.), and Wright State University (Dr. Mitch Wolff). Their contributions to research funding, project guidance, and facility access are gratefully acknowledged.

References (IEE)

[1] MathWorks, “MathWorks - Makers of MATLAB and Simulink,” *Mathworks.com*, 2019.

https://www.mathworks.com/

Smart Material Actuated Flap

Student Researcher: James Lyons

Advisor: Dr. Nicholas Garafolo

The University of Akron
Department of Mechanical Engineering, B.S.M.E

Abstract
The objective of this research project is to develop and evaluate a torsional Shape Memory Alloy (SMA) actuated flap mechanism for micro air vehicles (MAVs). SMA actuation will be considered as an alternative to conventional electromechanical mechanisms. This study investigates the feasibility of SMA-driven flap systems under MAV-representative conditions, emphasizing flap actuation, lift generation, and mechanical simplicity, and power requirements.

The actuator system employs Nitinol wire activated via Joule heating, with closed-loop, temperature-controlled power delivery. Two primary prototypes were constructed: a benchtop test model for actuator characterization and a wind tunnel test model integrated with a sting-mount interface for aerodynamic evaluation. Iterative shape training experiments were conducted to achieve the shape memory effect, with eventual success attained using a simple, at-home method.

The wind tunnel testing displayed successful actuation of the flap, achieving the target deflection angle and increasing lift by 13%. However, the power demands and offboard electronics and controls highlight the current limitations for MAVs.

While the SMA-actuated flap demonstrated mechanical feasibility and aerodynamic efficacy, tradeoffs in power efficiency and control precision remain significant. These findings support the continued exploration of SMA-based actuation for morphing structures and high-lift systems, especially where simplicity, compact form factor, and infrequent actuation are prioritized.

Project Objectives
The primary objective of this project is to develop a torsional Shape Memory Alloy (SMA) actuated flap mechanism for use in micro air vehicle (MAV) systems and assess its potential as an alternative to traditional electromechanical actuation. The project aims to deliver a mechanically simple, aerodynamically efficient solution that provides sufficient lift augmentation during critical flight maneuvers such as takeoff and landing.

To achieve this, several key benchmarks and performance requirements were identified based on the MAV use case, SMA material behavior, and user safety. The actuator was constrained within the airfoil envelope to preserve aerodynamic efficiency. A 15° downward deflection target was set with a required return to a neutral position within a 30–45 second cycle for use in infrequent high-lift scenarios like landing and takeoff. A thermocouple-controlled feedback loop was specified to prevent overheating of the SMA wire during Joule heating. Accordingly, the materials used must withstand high thermal loads and electrically isolate key components. For the preliminary design of 7” flaps, 11.5 oz-in of torque is needed to overcome aerodynamic forces and maintain structural stiffness during dynamic loading.
The project deliverables are structured to incrementally validate the design through both mechanical and aerodynamic testing. These include: a validated shape training process to achieve the desired actuation

behavior in SMA wire, a benchtop test model to characterize actuator performance through torque generation and power draw, and a wind tunnel test model to evaluate flap-induced lift enhancement under MAV-representative flight conditions.

Given the unique safety challenges posed by high-temperature SMA heating and active mechanical actuation, the design process incorporated robust precautions to mitigate electrical, thermal, and pinch hazards. Through these objectives, the project seeks to not only demonstrate the functionality of SMA-based flap actuation but also to critically assess its practicality and performance within the operational constraints of MAV applications

Methods

Hinge Actuator Concept

The actuator concept for this project is derived from the torsional hinge architecture developed at TU Delft. The design utilizes antagonistic Shape Memory Alloy (SMA) and Superelastic (SE) elements to enable reversible actuation. Dr. Qiang Liu and Dr. K.M.B. Jansen from the original research group generously provided design insights and fabrication guidance, which built upon my earlier prototype developed under the Ohio Space Grant Consortium Junior Scholar award.

The final hinge configuration integrates a Joule-heated SMA wire, which activates upon heating by recovering from an “S” shape to a “U” shape—resulting in flap deflection. The opposing SE wire, which retains an “S” shape at room temperature, passively restores the flap to its neutral position as the SMA cools. This bidirectional system eliminates the need for mechanical linkages or return springs.

Shape Memory Actuation and Shape Training

A major challenge was the shape training of SMA wire to exhibit reliable shape memory behavior. Multiple trials were conducted using both conventional furnace treatments and alternative aging methods:

- 550°C for 30 minutes, water quench
- 450°C for 30 minutes, water quench
- 475°C for 1 hour, water quench
- 575°C for 45 minutes, air cooling, aged at 400°C for 1 hour
- 520°C aging for 2 hours

Despite these varied conditions, all samples exhibited only the superelastic effect, not the desired shape memory behavior. Additionally, attempts to train the SMA wire using Joule heating within a rigid casing were unsuccessful due to uneven heating and wire constraint issues.

A successful shape training procedure was developed using manual tools. The wire was bent into shape using pliers, held in a paraffin candle flame for ~20 seconds, and then rapidly quenched in water. This method reliably locked in the “U” shape for the SMA wire, which subsequently demonstrated repeatable actuation under Joule heating.

Experimental Setup and Actuator Characterization

To verify actuator performance, the SMA wire was restrained to a wooden test rig and connected to a benchtop power supply. A known weight was suspended from a calibrated moment arm to measure torque, while electrical parameters were adjusted to initiate actuation. The peak observed values were 8

oz-in (4.9 N·cm) of torque at a power draw of 2.2–2.64 W (0.6 V at 3.66–4 A). These results confirmed that the actuator could meet the estimated torque requirement for the flap under simulated flight conditions.

Wing and Hinge Fabrication

The test wing features a 14" span and 11.75" chord with a Clark Y airfoil with selected for compatibility with a concurrent simulation effort by another researcher. The model was fabricated primarily from 3D printed components. The Main Body was a single piece of polycarbonate achieved using a soluble support material and the 5" flaps and print-in-place hinge mechanism were printed from ABS. The "male" hinge components have 45° tapered cones that align geometrically similar cones shaped voids on the "female" hinge components with 0.3 mm offset to ensure smooth actuation and self-alignment.

Hinge and Electrical Integration

The hinge modules were inserted into designated cutouts and fastened using M2 screws. Steel surgical tubing was added to isolate and protect the SMA and SE wires. Electrical leads were soldered onto the SMA elements, and thermocouples were affixed using Kapton tape. Silicone wiring was routed through the wing structure to the sting-mount area for external connection.

Control System Design

An initial benchtop setup used manual current-limited power delivery. The final test setup employed a software-controlled Joule heating system. The main power is provided by a 15A 120VAC to 24VDC supply which feeds two 24VDC current and voltage limited switch-mode converters. The outputs are then routed through two solid-state relays (SSR) that are triggered by 5V logic signals from a raspberry pi.

Temperature Feedback Loop

Type K thermocouples are routed through an analog-to-digital converter to provide temperature feedback to the controller. The python program provides independent relay control to each element based on the user-defined Set Point (SP) and Overtemperature (OT) thresholds. The system enabled thermal management and safety shutdown in the event of overheating, ensuring that the model was not damaged during testing.

Aerodynamic Load Verification

Finite Element Analysis (FEA) was performed in SolidWorks to evaluate the structural integrity of the test model under 50 mph, 0° AoA wind tunnel conditions. The resulting Reynolds number of 470,000, estimated C_L of 0.4 yielded a calculated lift force of ~5.5 lbf (with 1.75 lbf net upward load). For a worst-case estimate, 5.5 lbf was used which yielded a maximum von Mises Stress: 2.32 MPa at the sting mount, well below the 63 MPa yield strength of polycarbonate.

Wind Tunnel Testing

The completed model was mounted into the sting interface of the University of Akron Aerolab Subsonic Educational Wind Tunnel. Initial trials began with still-air cycling and gradually increased to the target flow speed of 50 mph. The trial performance was satisfactory with 15° flap deflection achieved, a successful return to neutral position, and minimal flutter at full deflection. The wind tunnel's visual interface allowed for real-time monitoring of airspeed, pitch angle, normal force, and pitching moment throughout the test cycle, which will be discussed next.

Results and Discussion

The final wind tunnel trial demonstrated the functionality of the smart material actuated flap under MAV-representative conditions. The flap reached the target deflection angle and returned to its neutral position within 40 seconds, meeting the specified actuation cycle time. The recorded aerodynamic data, shown in Figure 1, provided clear performance trends. The peak lift observed was 6.27 lbf, a 13% increase over the baseline lift of 5.53 lbf with the flap in the neutral position. However, this improvement in lift was accompanied by an increase in drag 0.11 lbf to 0.22 lbf during peak deflection.

The prototype demonstrated integration of the SMA actuator into the airfoil structure without protruding beyond the envelope, preserving aerodynamic form, however the external power and controls did not meet this requirement. The system's materials resisted the applied thermal and electrical loads throughout operation. The closed loop thermal control system functioned as intended to prevent overheating of the SMA element.

The largest challenge of this project was shape training the SMA wire. Despite initial failures in a lab setting, an at-home approach ultimately succeeded. The final procedure of manual shaping over a candle flame followed by water quenching produced a wire that reliably exhibited the shape memory effect under Joule heating. While the actuator achieved the mechanical and aerodynamic performance goals, its applicability to MAVs is constrained by several practical limitations. The system consumed approximately 3 watts of power per flap, a stark contrast to the ~0.4 watts typically required by conventional 9g servo motors. This inefficiency, coupled with imprecise response and offboard power and controls, currently limits the feasibility of this SMA approach for onboard MAV use. Additionally, minor flutter was observed, indicating the need for further improvements in hinge stiffness to ensure stability under dynamic flow conditions.

Overall, the project successfully demonstrated a mechanically simple, thermally controlled flap system using shape memory alloy actuation. While the concept shows promise in controlled environments and specific applications requiring infrequent actuation, major development is needed to optimize energy efficiency, actuation precision, and dynamic stability.

Figures/Charts

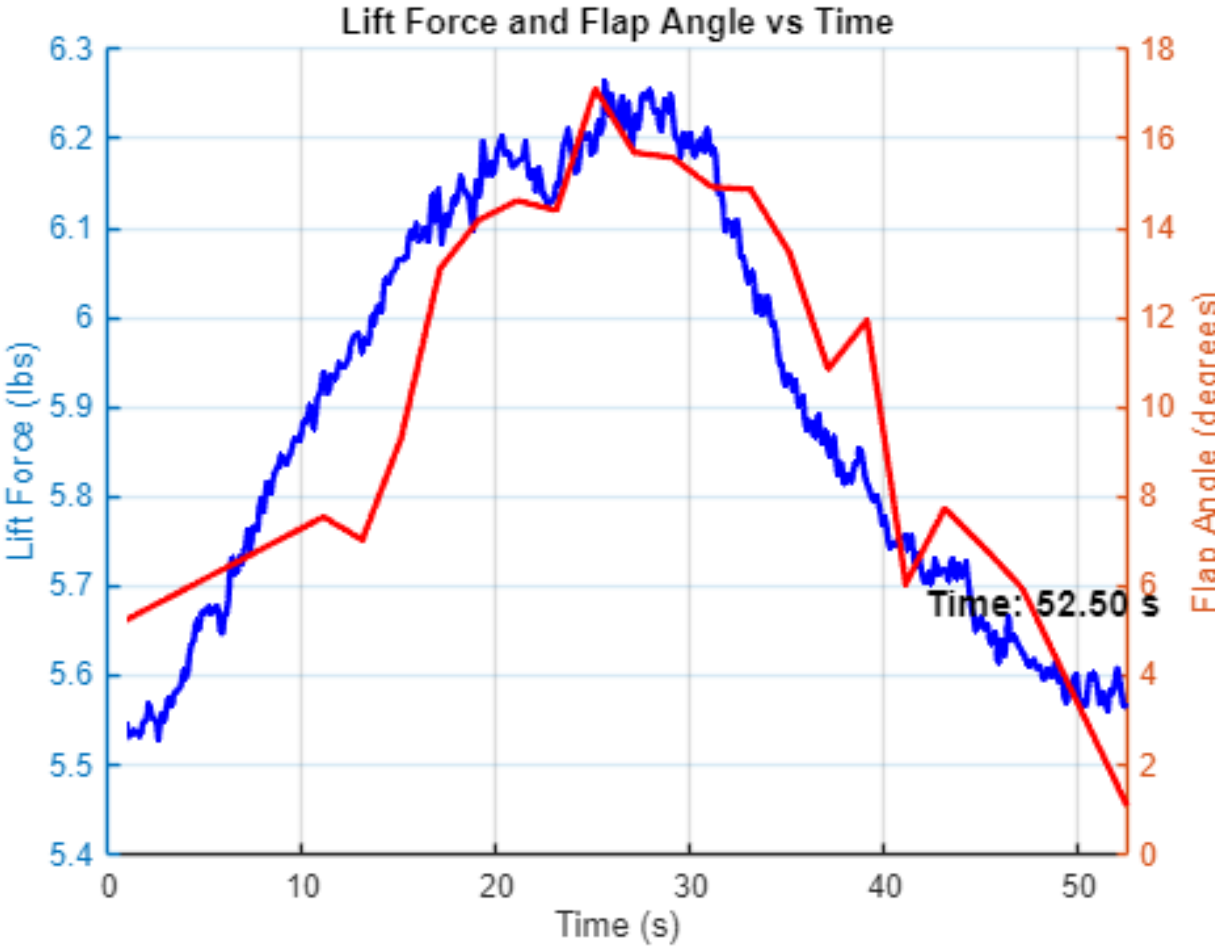


Figure 1: 50 Mph Trial Lift Force and Flap Angle vs. Time

Acknowledgments

Thank you to my advisor for 3 years of OSGC research, Dr. Garafolo and UA's OSGC Coordinator Dr. Julie Zhao for the opportunity and continued support. Thank you to Dr. Jennifer Lillard, an additional advisor and reader, for her expertise and laboratory support for shape training process development. My utmost gratitude to my industry-advisor Gustavo Hrycyna for his guidance and to UA faculty Bill Wenzel (Engineering Tech. / Machinist), Aaron Trexler (Senior Engineering Tech.), and Eric Pfiffner (Senior Engineering Tech.) for their continued manufacturing and testing support.

I also appreciate Qiang Liu, Ph.D of Delft University of Technolog for supporting my implementation of his novel torsional SMA hinge design by providing permission, sample materials, and process guidance to replicate his work.

References

Bertin, J. J., & Cummings, R. M. (2022). Aerodynamics for engineers (8th ed.). Cambridge University Press. ISBN: 978-0-13-2832288-5.

Dieter, G. E., & Schmidt, L. C. (2013). Engineering design (5th ed.). McGraw-Hill.

Haughn, K. P., Gamble, L. L., & Inman, D. J. (2018). Horizontal planform morphing tail for an avian inspired UAV using shape memory alloys. Proceedings of the ASME 2018 Conference on Smart Materials, Adaptive Structures and Intelligent Systems, Volume 2. https://doi.org/10.1115/SMASIS2018-7986

Hutapea, P., Kim, J., Guion, A., Hanna, C., & Heulitt, N. (2008). Development of a smart wing. Aircraft Engineering and Aerospace Technology, 80(4), 439–444. https://doi.org/10.1108/00022660810882791

Karagiannis, D., Stamatelos, D., Spathopoulos, T., Solomou, A., Machairas, T., Chrysohoidis, N., Saravanos, D., & Kappatos, V. (2014). Airfoil morphing based on SMA actuation technology. Aircraft Engineering and Aerospace Technology, 86(4), 295–306. https://doi.org/10.1108/AEAT-10-2012-0194

Liu, Q., Ghodrat, S., & Jansen, K. M. B. (2024a). Design and modelling of a reversible shape memory alloy torsion hinge actuator. Materials & Design, 237, 112590. https://doi.org/10.1016/j.matdes.2023.112590

Liu, Q., Ghodrat, S., & Jansen, K. M. B. (2024b). Mimosa: Modular self-folding hinges kit for creating shape-changing objects. Proceedings of the Eighteenth International Conference on Tangible, Embedded, and Embodied Interaction, 1–13. https://doi.org/10.1145/3623509.3633381

McHugh, G. R. (2016). An experimental investigation in the mitigation of flutter oscillation using shape memory alloys [Master's thesis, University of Akron]. OhioLINK Electronic Theses and Dissertations Center. http://rave.ohiolink.edu/etdc/view?acc_num=akron1479119992818089

Sansone, M., Ameduri, S., Concilio, A., & Cestino, E. (2022). Understanding shape memory alloy torsional actuators: From the conceptual to the preliminary design. Actuators, 11(3), 81. https://doi.org/10.3390/act11030081

Numerical Modeling of Helium-Neon Mixtures for Cryogenic Reverse Brayton Cycle Applications

Student Researcher: Joseph Lyons

Advisor: Dr. Maryam Younessi

Cleveland State University
Mechanical Engineering

Abstract
Long-duration space missions require efficient storage of cryogenic propellants. This study models helium-neon mixtures as working fluids in a reverse Brayton cycle cryocooler to determine optimal compositions for cryogenic applications. Using REFPROP data and Excel-based modeling, the thermodynamic performance of pure and mixed helium-neon fluids was evaluated over a range of low temperatures. Results show that pure neon offers the best efficiency and lowest work input for Reverse Brayton Cycles above 40 K, while mixtures offer performance advantages across broader temperature ranges.

Project Objectives
The primary objectives of this project were to model the thermodynamic behavior of helium-neon mixtures in a reverse Brayton cycle, evaluate the impact of mixture composition on net work input, minimum pressure ratio, and second-law efficiency, and determine the optimal working fluid for cryogenic cooling applications in space.

Methods
The reverse Brayton cycle was simulated using a model consisting of four components: a compressor, a turbine, and two heat exchangers. Helium-neon mixtures were evaluated at varying mole fractions, including pure helium, pure neon, and 70/30, 50/50, and 30/70 neon-helium combinations. The REFPROP database provided fluid property data, while Microsoft Excel was used to perform calculations based on thermodynamic equations derived from the first and second laws of thermodynamics. Each fluid composition was analyzed at temperatures ranging from 120 K to 40 K. However, modeling mixtures below 40 K was limited by the inability of REFPROP to compute convergent solutions.

Key performance metrics included net work input, minimum pressure ratio, and second-law efficiency. Net work input was calculated as the work required by the compressor minus the work produced by the turbine. Minimum pressure ratio was determined based on the compressor outlet pressure necessary to sustain cooling, while second-law efficiency was derived from the comparison between actual and ideal (Carnot) efficiency. These values were determined using Excel-based numerical solutions tailored to each mixture and temperature.

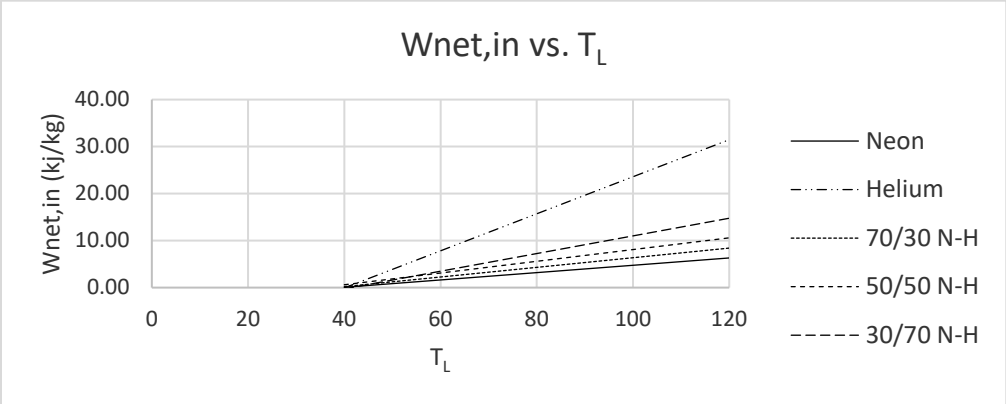
Results and Discussion
Pure neon demonstrated the lowest net work input among all tested fluids, establishing it as the most efficient working fluid for reverse Brayton cycle operation at temperatures above 40 K. Helium, by contrast, exhibited the highest work input requirements, indicating that its application should be limited to scenarios requiring extremely low temperatures.

The pressure ratio results were relatively consistent across all fluid compositions, although neon-containing mixtures showed minor advantages in terms of reduced mechanical demands. These modest differences can contribute to improved system reliability and extended component lifespans by alleviating stress on mechanical parts such as compressors and turbines.

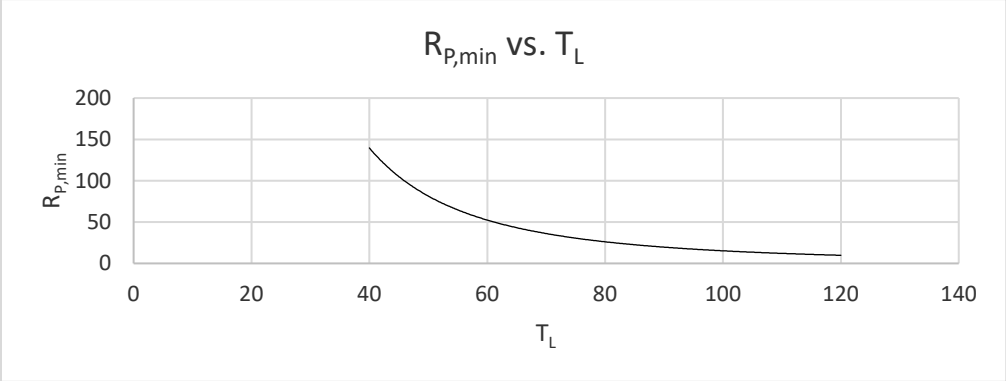
Second-law efficiency improved as the temperature of the low-temperature reservoir decreased. This trend reflects the reduced irreversibilities present in the system at lower operating temperatures. Overall, these findings support the use of neon at and above 40 K and demonstrates the potential of mixtures for enhancing the efficiency and reliability of cryocooler systems below 40 K.

Figures/Charts

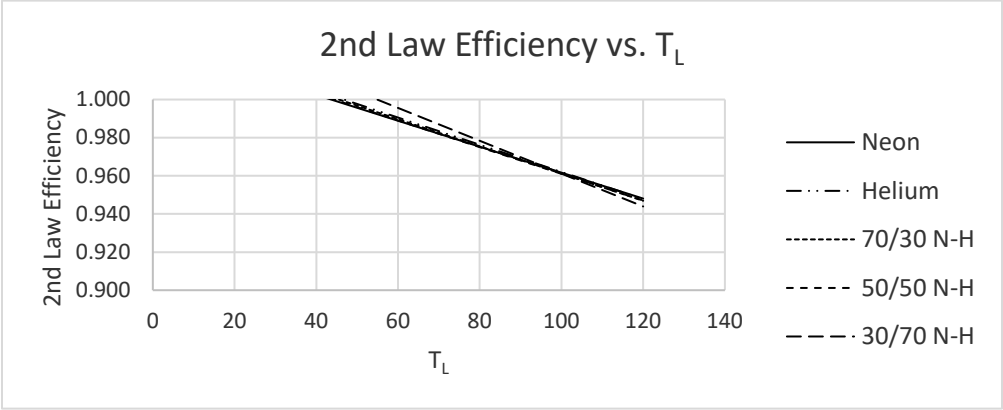
Graph 1: Net Work Input vs. Temperature (TL)



Graph 2: Minimum Pressure Ratio vs. Temperature (TL)



Graph 3: Second Law Efficiency vs. Temperature (TL)



Acknowledgments
I would like to thank Dr. Maryam Younessi for her mentorship throughout the course of this project. Appreciation is also extended to the NASA Ohio Space Grant Consortium for their support and funding of this research.

References

[1] Guzik, M. C., and Tomsik, T. M., “An Active Broad Area Cooling Model of a Cryogenic Propellant Tank with a Single-Stage Reverse Turbo-Brayton Cycle Cryocooler,” TFAWS Proceedings, NASA Glenn Research Center, 2011.
[2] Nugent, B. T., Grotenrath, R. J., and Johnson, W. L., “20 Watt 20 Kelvin Reverse Turbo-Brayton Cycle Cryocooler Testing and Applications,” NASA Glenn Research Center Technical Report, 2020.
[3] Plachta, D. W., Feller, J. R., and Guzik, M. C., “In-Space Cryogenic Propellant Storage Applications for a 20 W at 20 K Cryocooler,” Cryocoolers 19, Boulder, CO, 2016, pp. 88–94.
[4] NASA Glenn Research Center, “Mixed Gas Refrigerant Study for Integrating Cryocoolers with Large Cryogenic Tanks,” NGFFP Research Topics, NASA, 2024

Cybersecurity Measures for Hybrid Satellite Networks to Prevent Cyberattacks

Student Researcher: LyDel Madden

Advisor: Dr. Deok Hee Nam

Wilberforce University
Computer Science

Abstract
Hybrid satellite networks, which integrate satellite communication with terrestrial infrastructures, introduce both advanced capabilities and complex cybersecurity challenges. This project proposes a comprehensive cybersecurity framework designed to safeguard such hybrid systems from evolving cyber threats. The approach employs a multi-layered defense strategy, including the implementation of robust encryption protocols, strict access controls, and the strategic deployment of firewalls and Intrusion Detection and Prevention Systems (IDPS). It also highlights the necessity of proactive patch management, network segmentation, and continuous monitoring to detect and respond to threats in real-time. Key to this framework is the emphasis on human factors: cybersecurity awareness training for personnel and the enforcement of rigorous vendor security standards. Additionally, the project underscores the importance of well-defined incident response and disaster recovery plans to ensure business continuity and minimize the impact of security breaches.

By integrating these measures, the proposed framework aims to enhance the integrity, confidentiality, and availability of data and services across hybrid satellite-terrestrial networks.

Project Objectives
To effectively address cybersecurity threats in hybrid satellite networks (HSNs), this project will initiate a comprehensive threat analysis aimed at identifying and evaluating cyber risks across satellite communication systems. These threats will be classified into categories such as signal-based attacks (e.g., jamming and spoofing), data breaches, malware intrusions, and AI-driven cyberattacks that exploit automation for advanced, targeted breaches.

An in-depth review of real-world cyber incidents involving satellite networks will be conducted to understand attack methodologies, system vulnerabilities, and adversarial tactics. Threat vectors will be mapped across the key components of HSNs: the space segment (satellites and onboard payloads), the ground segment (control centers and communication gateways), and the user segment (end-user terminals and mobile devices). This structured mapping will support a thorough risk assessment and guide the development of precise and adaptive security strategies.

Building upon this analysis, the project will develop a multi-layered cybersecurity framework tailored to the complex architecture of HSNs. This framework will include advanced communication protections such as post-quantum encryption and quantum key distribution (QKD) to ensure secure, tamper-proof data exchange. AI-powered threat monitoring will be implemented for real-time detection of anomalies, while Zero Trust Architecture (ZTA) will provide strict access controls and continuous identity verification to prevent unauthorized access.

In addition, Software-Defined Networking (SDN) will be utilized to enable dynamic, threat-aware adjustments to network defenses. Security policies will be established for satellite-to-ground and inter-

satellite communications, safeguarding data integrity and confidentiality at all stages. Finally, the project will outline best practices for embedding cybersecurity into every phase of the HSN lifecycle—from system design and launch to operation and maintenance ensuring that security is not an afterthought, but a core element of satellite network resilience.

Methods

To ensure the cybersecurity of hybrid satellite networks (HSNs) against sophisticated cyber threats, this project is divided into four critical phases: Threat Analysis and Risk Assessment, Security Framework Design, Simulation and Testing, and Deployment with Continuous Monitoring. Each phase is designed to systematically identify vulnerabilities, implement advanced security measures, and validate their effectiveness in real-world HSN environments.

The initial phase focuses on understanding past cyber incidents, analyzing vulnerabilities in current satellite communication systems, and mapping potential attack vectors across the space, ground, and user segments. This foundational research will guide the development of a comprehensive security strategy tailored to the unique challenges of HSNs.

Building on the risk assessment findings, the Security Framework Design phase will introduce a multi-layered defense strategy incorporating AI-driven intrusion detection, blockchain-based authentication, and post-quantum cryptography to mitigate security risks. These solutions will then be rigorously tested in a simulated HSN environment through penetration testing and cyberattack simulations to assess their resilience.

The final phase involves deploying security solutions within real-world satellite networks, ensuring continuous monitoring and adaptive threat detection through AI-powered analytics. By leveraging cutting-edge cybersecurity technologies, this phased approach aims to establish a resilient, self-adaptive security infrastructure capable of defending HSNs against evolving cyber threats.

Results and Discussion

The proposed cybersecurity measures for hybrid satellite networks (HSNs) demonstrate wide-ranging applicability across multiple critical sectors, reinforcing the resilience and integrity of space-based communication systems.

In the military and defense sector, the implementation of these measures is essential for securing tactical satellite systems. The integration of advanced encryption, access controls, and intrusion detection mechanisms will help prevent adversaries from intercepting, disrupting, or manipulating mission-critical communications. This protection is vital for ensuring operational superiority and maintaining the confidentiality of sensitive defense data.

Within the commercial domain, particularly in global internet and IoT connectivity, cybersecurity enhancements will safeguard major satellite internet providers such as Starlink and OneWeb. These enhancements will contribute to the reliability and security of satellite-based internet infrastructure, supporting uninterrupted connectivity and reducing vulnerabilities to cyberattacks that could affect users worldwide.

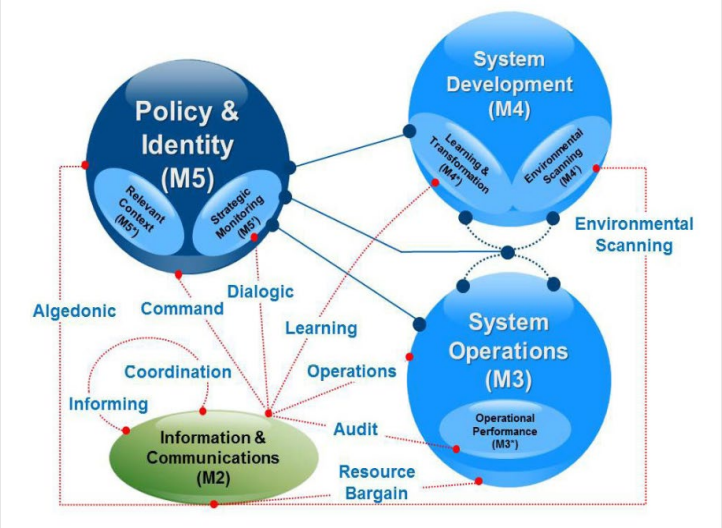
For space missions and scientific research, the deployment of robust security frameworks will protect telemetry, tracking, and control systems (TT&C) of satellites. This is critical for avoiding unauthorized

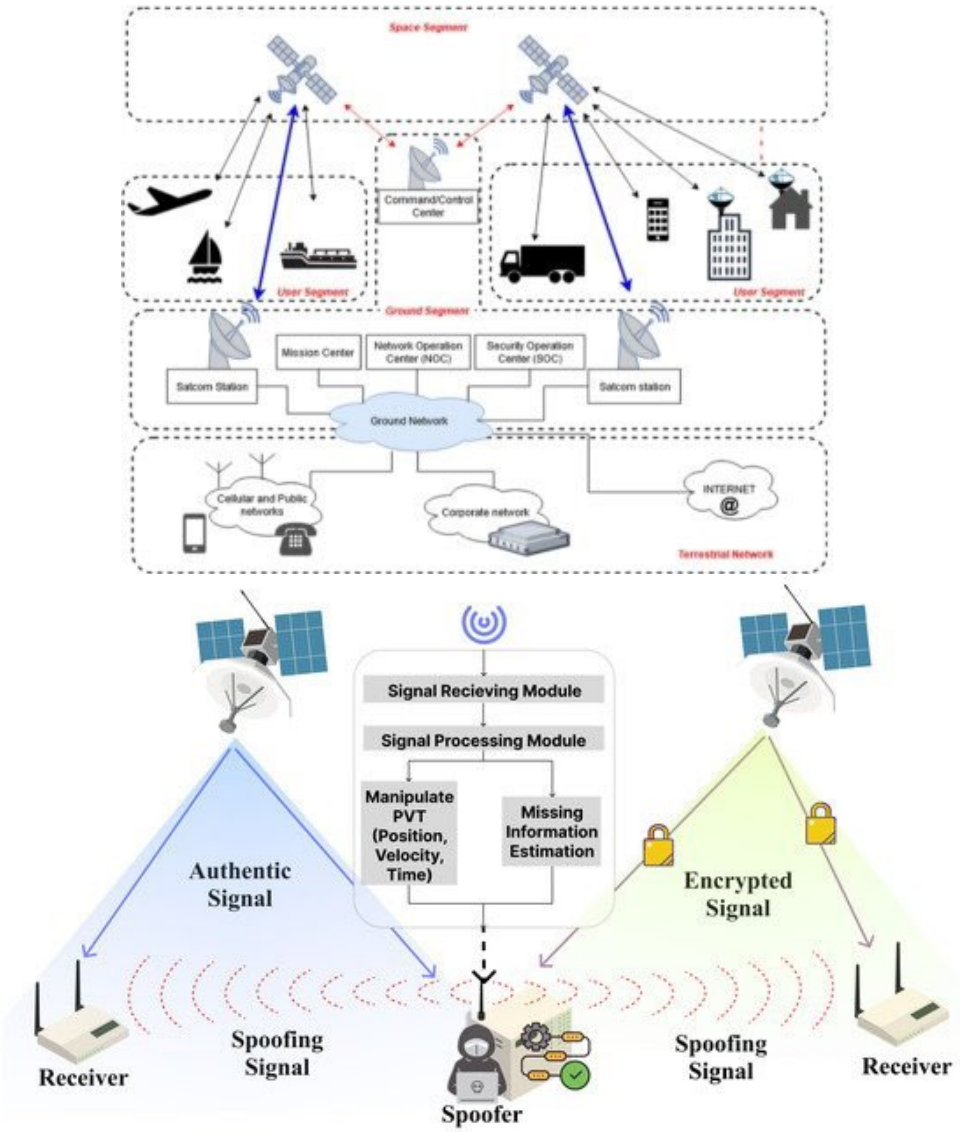
access or malicious interference that could endanger satellite operations conducted by government space agencies and private aerospace firms alike.
In the realm of disaster response and remote sensing, secure satellite networks will play a key role in preserving the integrity of real-time data used for humanitarian aid, environmental monitoring, and crisis management. Protecting satellite imagery and sensor outputs ensures that decision-makers receive accurate, tamper-free data during emergencies.

The integration of AI-driven threat detection, blockchain-based authentication, and post-quantum encryption within this cybersecurity framework offers a forward-looking solution to the evolving threat landscape. These technologies not only strengthen the defense posture of HSNs but also introduce adaptive capabilities for real-time response and self-healing network functions.

By addressing the unique vulnerabilities of hybrid satellite architectures, this project contributes to the broader goal of safeguarding critical satellite infrastructure. The findings support the creation of secure, resilient, and scalable cybersecurity solutions that can be adapted to meet the demands of both current and future satellite network environments.

Figures/Charts





Acknowledgments

Many thanks to the Ohio Space Grant Consortium for their support through the academic scholarship program. Special appreciation goes to Mr. Romero and Mr. Hale at the Ohio Aerospace Institute (OAI) for their guidance and coordination of the OSGC Program. I would also like to extend sincere thanks to Dr. Deok Nam at Wilberforce University for his mentorship and continued support throughout this project.

References

Smith, E. (2025, February 18). *Implementing cybersecurity solutions for space network protection*. CSIAC, 9(1).

Rodić, F. C., & Galletta, L. (2024). Securing SATCOM user segment: A study on cybersecurity challenges in view of IRIS2. *Computers & Security, 140*.

Gheorghe, A. V., Payne, J. C., Sisti, J., Keating, C. B., Katina, P. F., & Edmonson, W. (2023). Critical space infrastructure: A complex system governance perspective. *International Journal of Cyber Diplomacy, 4*.

NiTiHf15 Alloy: Binder Jetting for the Future

Student Researcher: Daniel Mahoney

Advisor: Dr. Mohammad Elahinia

University of Toledo
Mechanical, Industrial, and Manufacturing Engineering Department

Abstract
Binder jetting additive manufacturing (AM) is becoming a preferred method of high-temperature shape memory alloys (HTSMAs). The advancement of AM technology has vastly decreased the challenges of the formability of HTSMAs. Binder jetting allows us the opportunity for the fabrication of NiTi-based SMAs. The proper combination of HTSMA properties and AM provides a wide range of applications that other forming methods, such as machining, do not. Binder jetting AM has the advantage of not melting and solidifying, which enhances reliability and isentropic material properties. This paper investigates the optimization binder jetting of NiTiHf15 following the methodology, as a continuation, of "Process development of NiTi using binder jetting additive manufacturing: Investigation of the sintering process." [1]

Project Objectives
This study aims to optimize the Binder Jetting process for NiTiHf15 by investigating curing, debinding, and sintering stages. By refining these key factors, the research aims to improve the alloy's performance, including its transformation temperatures and shape memory properties, thereby making it more suitable for high-temperature applications.

Methods

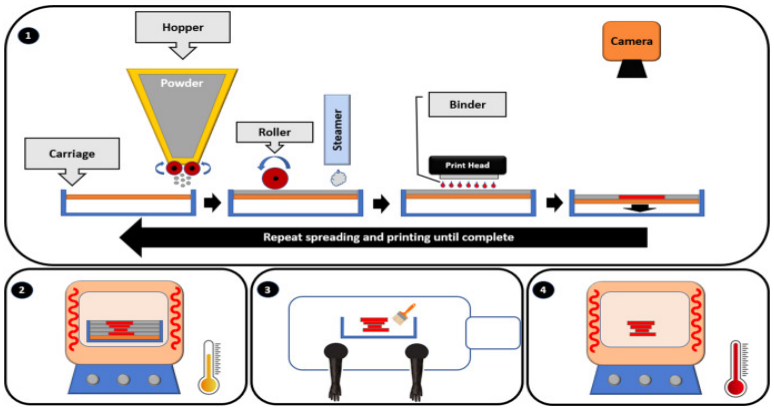


Figure 1: Overview of binder jetting process. [1]

Fig. 1 depicts the process of binder jetting AM for the fabrication of NiTiHf components. Stage (1) is the printing stage, a thin layer of NiTiHf powder is spread across the build platform and evened out with a roller. A camera is used to monitor accuracy. The print head deposits a binder on only desired areas. The print head repeats this process after each layer. Stage (2) the fresh part is cured in a furnace, hardening the binder. The part is then removed for stage (3), where the powder without binder is brushed off of the now-cured part, called de-powdering. Stage (4) has the part put in the furnace for debinding, where the binder is burned off. The part is now ready for the sintering process, causing particle coalescence and densification.

Powder Characterization

Powder with a composition of $Ni_{50}Ti_{34}Hf_{15}$ with spherical morphology was obtained from Oak Ridge National Laboratory and TLS Technik. Fine powder with particle size distribution of D10 (4.46 µm), D50 (9.46 µm), and D90 (17.51 µm), detailed in Fig. 2. Coarse powder with particle size distribution of D10 (9.61 µm), D50 (19.91 µm), and D90 (41.26 µm), detailed in Fig. 3.

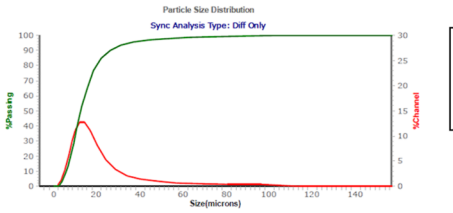


Figure 2: Particle distribution of NITiHf15 fine powder.

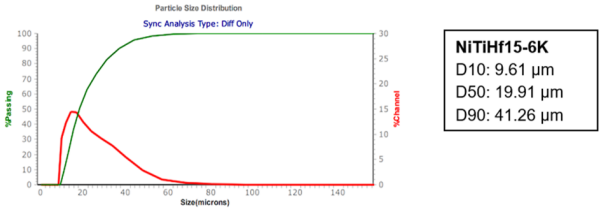


Figure 3: Particle distribution of NITiHf15 coarse powder.

A mixture of these powders was then created using a centrifugal mixer with ball bearings as an agitator, as detailed in Fig. 4. The mixture consisted of 65% fine powder and 35% coarse powder. Characterization of the new mixture showed the particle distribution of D10 (5.13 µm), D50 (14.85 µm), and D90 (25.75 µm), detailed in Fig. 5.

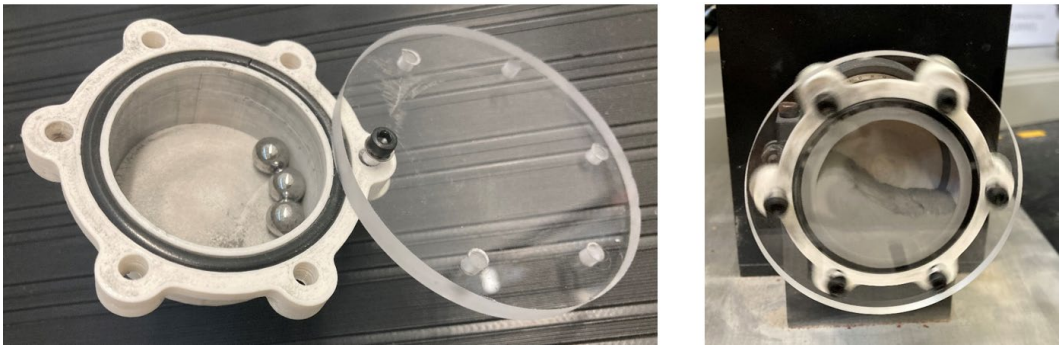


Figure 4: Centrifugal mixer with ball-bearing agitators.

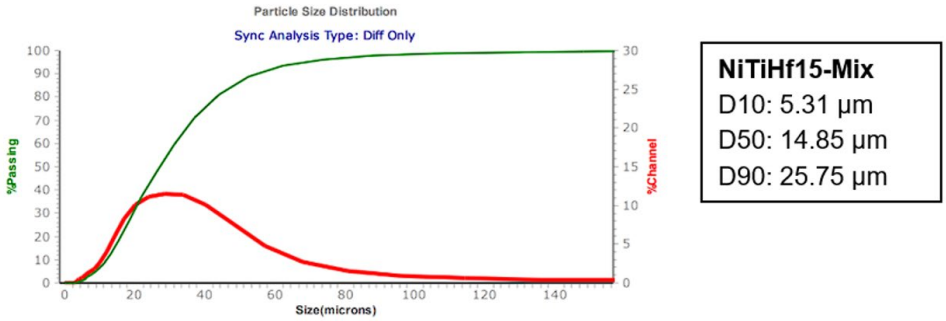


Figure 5: Particle distribution of NITiHf15 65% fine powder and 35% coarse powder mixture.

Powders were tested to obtain oxygen and carbon levels, using Elemtrac ONH-p and CS-I analyzers manufactured by ELTRA. The results for fine, coarse, and mixed powders are shown in Table 1, which the mixed powder was determined to be used in curing, debinding, and sintering optimization.

	Oxygen (wt.%)	**Carbon (wt.%)**
NiTiHf15-<20µm	0.045	0.023
NiTiHf15-6K	0.349	0.020
NiTiHf15-Mix	0.169	0.022

Table 1: Powder contaminant levels of Oxygen and Carbon.

Curing

Desktop's Metal SPJ-04 binder, composed of ammonium hydroxide and polyethyleneimines, was used for this project. The powder and binder were mixed with a saturation of 60% ($S = \frac{V_{binder}}{V_{void}}$). [1] Thermogravimetric analysis (TGA) was run on the green part to analyze the thermal decomposition of the green parts, detailed in Fig. 6. The increase in weight at 400°C shows possible oxidation at higher temperatures.

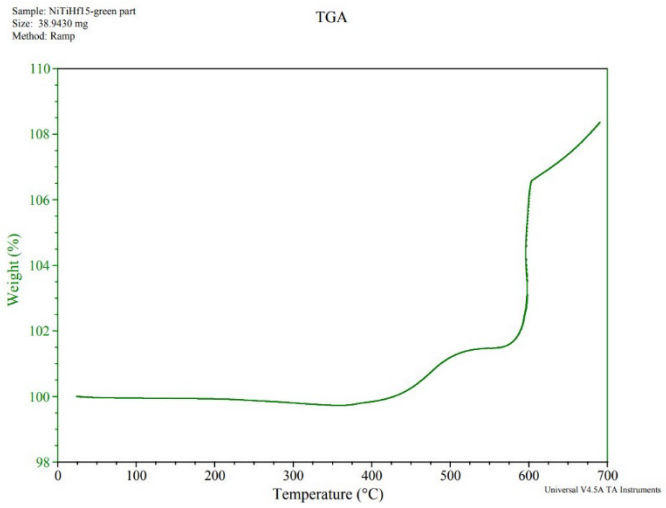


Figure 6: TGA of NiTiHf15 green part.

The curing of fresh/green parts is closely related to the known thermal properties of the binder. The binder has a decomposition temperature of 207°C. [1] The curing temperature was selected below the decomposition temperature at 165°C for 1 hour under air. The carbon and oxygen levels were then tested on the green and cured part, detailed in Table 2.

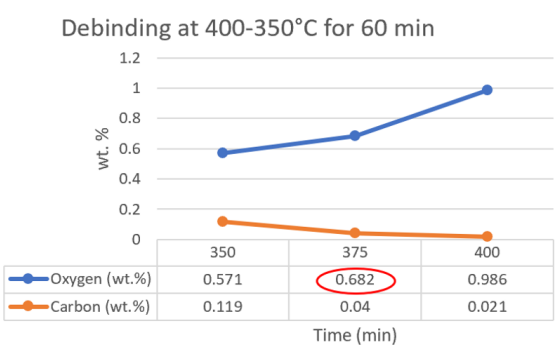
	Temperature (°C)	Soak (min)	Atmosphere	Oxygen (wt%)	Carbon (wt%)
NiTiHf15-green				0.523	0.444
Curing	165	60	Air	0.400	0.428

Table 2: Cured and green part contaminant levels.

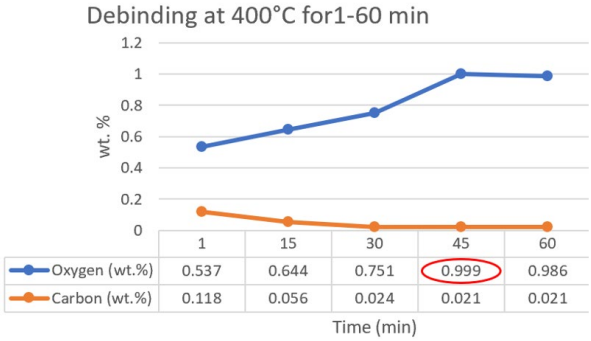
Debinding

The debinding process of the cured part was based on the TGA of the green part, which showed an increase in weight at 400°C. The cured samples were tested at 350°C, 375°C, and 400°C for 60 minutes. The cured samples were also tested at 400°C for 1–60 minutes at varying intervals. The oxygen and carbon

content of the debinded samples are detailed in Fig. 7 and Fig. 8. The final optimized debinding was 375°C for 45 minutes based on oxygen and carbon contamination levels.



	350	375	400
Oxygen (wt.%)	0.571	0.682	0.986
Carbon (wt.%)	0.119	0.04	0.021



	1	15	30	45	60
Oxygen (wt.%)	0.537	0.644	0.751	0.999	0.986
Carbon (wt.%)	0.118	0.056	0.024	0.021	0.021

Figure 7: Debinding of NiTiHf15 samples at 350°C - 400°C for 60 minutes. **Figure 8:** Debinding of NiTiHf15 samples at 400°C for 1-60 minutes.

Sintering

The debinded parts (brown parts) were placed into a tube furnace (STF-1700, Across International) under argon. The green part was positioned in a crucible with small metal pieces to protect the sample from oxidation. The samples were tested at ten different temperatures and durations. The sintering temperatures ranged from 1240°C to 1340°C for soak times between 2 hours and 8 hours. The furnace's initial heating rate was 5°C/min until it reached 900°C, followed by a brief soak; the heating rate was then reduced to 2°C/min until the final setpoint was reached. This process was implemented to prevent thermal cracks and ensure uniform heating.

The ten samples were then measured to find density using the Archimedes Method. The relative densities were then calculated by comparing the experimental densities to the density of the powder and the density of NiTiHf15, as discovered in literature [2]. The sample sintered at 1320°C for 5 hrs had the highest relative densities of 96.68% and 95.94%, as detailed in Fig. 9.

Fully Dense NiTiHf15	8.114 (Powder)	8.177 (As lit)			Relative Density	
					As 8.114	As 8.177
Temperature (C)	Time (Hr)	Weight in Air	Weight in Water	Density of Sample		
1240	5	2747.80	2326.90	6.50942	80.225%	79.606%
1290	5	2691.68	2260.46	6.22392	76.706%	76.115%
1310	2	2610.22	2165.21	5.84861	72.080%	71.525%
1310	5	2714.30	2295.28	6.45892	79.602%	78.989%
1310	8	2674.91	2285.45	6.84823	84.400%	83.750%
1315	5	2724.25	2340.18	7.07239	87.163%	86.491%
1320	5	2732.67	2385.35	7.84476	96.682%	95.937%
1320	8	2683.23	2249.11	6.16295	75.955%	75.369%
1325	5	2644.24	2305.06	7.77309	95.798%	95.060%
1340	2	2746.86	2396.51	7.81730	96.343%	95.601%

Figure 9: Density calculations of sintered samples.

Additionally, Fig. 10 displays several of the samples after sintering. As depicted by the relative density calculations, we suspect the sample at 1320°C for 5 hrs to be the optimized parameter. Fig. 10 shows the sample morphology is consistent with that expected. We see that other samples either had insufficient sintering time/temperature based on the morphology or achieved a fully melted state.

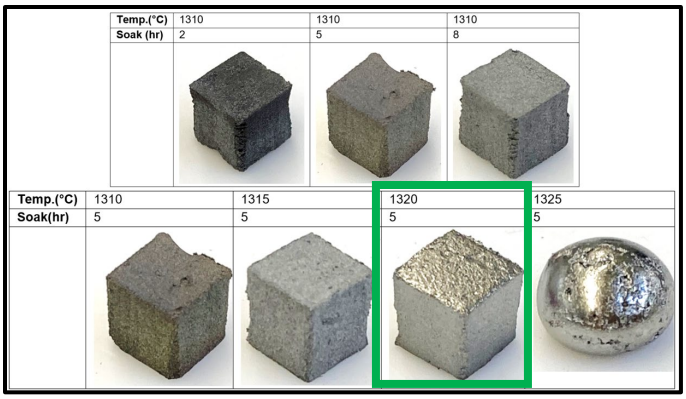


Figure 10: Sintered samples.

Results and Discussion

Half of the sintered samples were tested using Elemtrac ONH-p and CS-I analyzers to find the oxygen and carbon content, detailed in Fig. 11 and Fig. 12. Of the samples tested, the sample at 1320°C for 5 hrs had the lowest oxygen content of 0.727% and second lowest carbon content of 0.0605%.

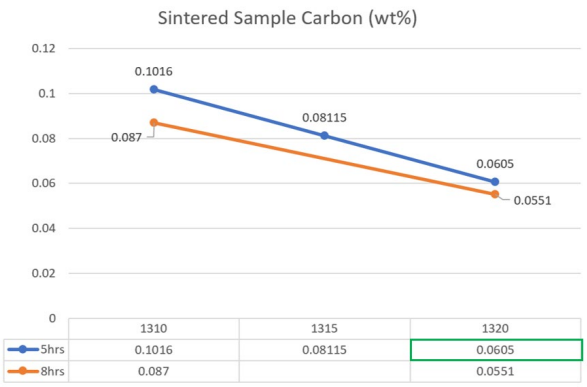


Figure 12: Carbon Levels of Sintered Samples.

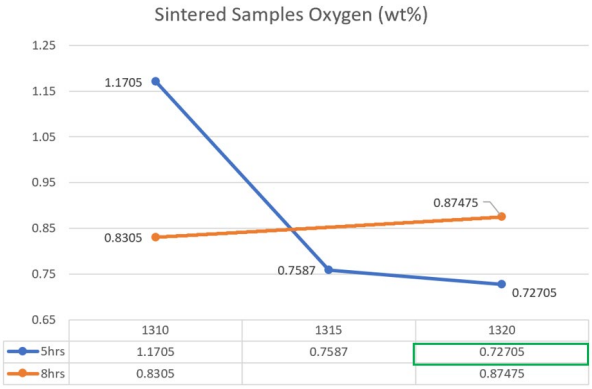


Figure 11: Oxygen Levels of Sintered Samples.

Differential Scanning Calorimetry (DSC) analysis was conducted on the same five samples. In Fig. 13, DSC revealed the sample sintered at 1320°C for 5 hrs has the largest peaks in the martensite and austinite phase, depicting the highest thermal energy exchange, allowing for the most amount of heat to be absorbed and released.

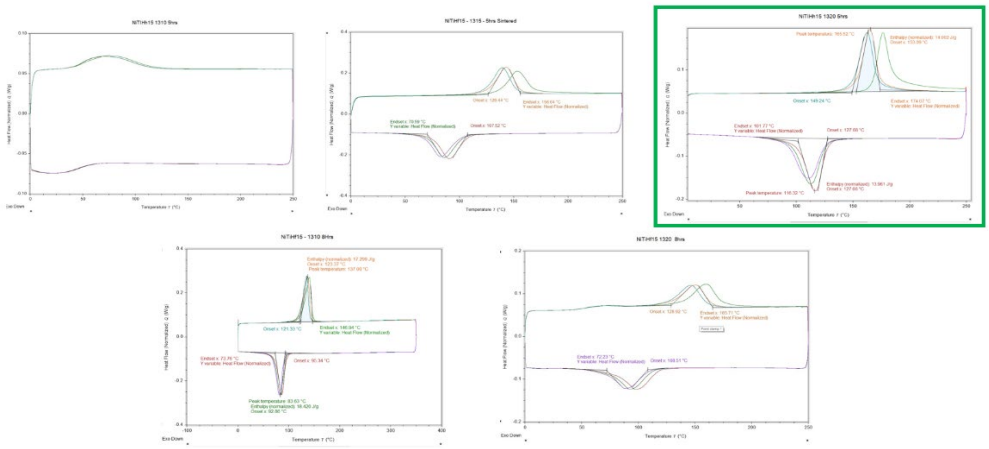


Figure 13: DSC Analysis on Sintered Samples.

The results above describe the optimized process for NiTiHf15 curing, debinding, and sintering of binder-jetted AM samples. The purpose of adding Hafnium to NiTi is to raise the transformation temperatures to allow for high-temperature applications, for example, aerospace applications. Fig. 14 depicts the comparison between the optimized NiTiHf15 sample to NiTi [1]. The NiTi at 60% saturation has a transformation temperature of -80°C to 100°C, whereas NiTiHf15 has a transformation temperature of 0°C to 250°C. This confirms the increase of transformation temperatures and the possibility for use in high-temperature applications.

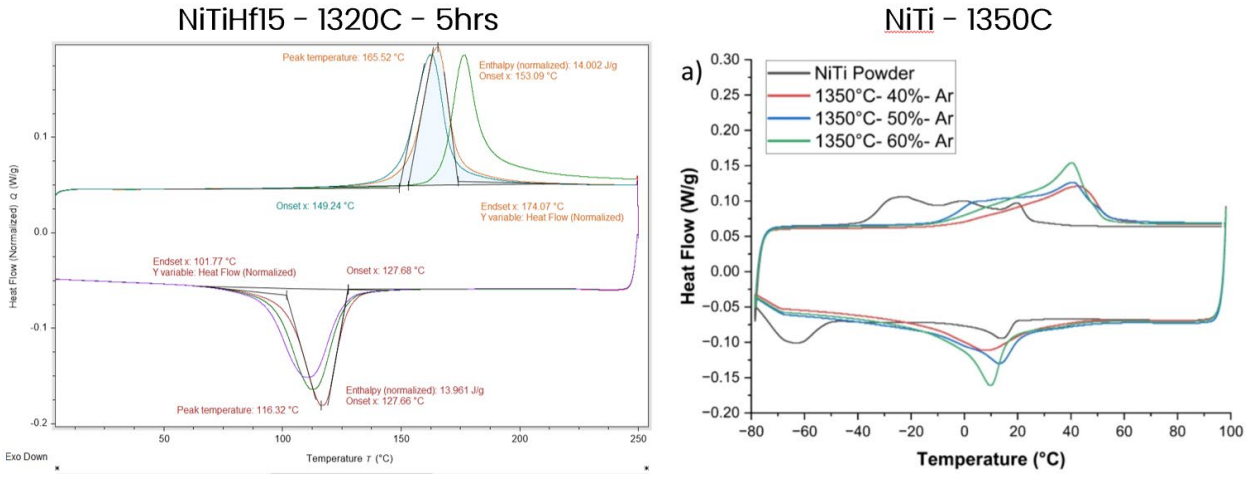


Figure 14: DSC Analysis on NiTiH15 at 1320°C for 5 hrs Vs. NiTi [1]

Acknowledgments

I am thankful to the Ohio Space Grant Consortium (OSGC), the University of Toledo, and my advisors — Dr. Mohammad Elahinia, Dr. Mohammad Pourshams, Dr. Ahu Celebi, and the rest of the research team.

References

[1] Pourshams, M., Elliott, A., Chinnasamy, C., Poorganji, B., Benafan, O., & Elahinia, M. (2024). Process development of niti using binder jetting additive manufacturing: Investigation of the sintering process. *Journal of Manufacturing Processes*, *127*, 671–682. https://doi.org/10.1016/j.jmapro.2024.08.009

[2] Wang, J., & Hu, K. (2017). Phase transformation of NiTi alloys during vacuum sintering. IOP Conference Series Materials Science and Engineering, 204, 012023–012023. https://doi.org/10.1088/1757-899x/204/1/012023

Two Phase Flow CFD Simulations on the Chilldown Process of a Vertical Upflow LN2 Line

Student Researcher: Arnav Manu

Advisor: Dr. Chirag Kharangate

Case Western Reserve University
Mechanical & Aerospace Engineering

Abstract
Cryogenic fluid management is vital for the safe storage and transfer of liquid nitrogen in aerospace, industrial, and scientific applications. Traditional thermal management strategies combine passive measures, such as multilayer insulation that minimizes heat input through reflective layers, with active cooling techniques, such as cryocoolers, to maintain cryogenic fluids near their boiling points and achieve near zero boil-off. However, during transient operations such as the chilldown process, where transfer lines or storage vessels are rapidly cooled, complex thermal phenomena, including rapid phase transitions and steep temperature gradients, introduce significant challenges. These thermodynamic dynamics can lead to rapid boil-off, thermal stresses, and system inefficiencies. This research aims to investigate how computational fluid dynamics simulations, using ANSYS, can model the chilldown process of liquid nitrogen in a vertical upflow tube. The goal of this research is to enhance the understanding of the thermal behavior during cryogenic fluid handling,resulting in the optimization of system design and operational efficiency. These advancements have the potential to improve the functionality of cryogenic systems used in both terrestrial and space applications. The study employs a mixture model to capture multiphase flow behavior and introduces spatially varying Lee coefficients to improve heat transfer predictions. Several configurations are examined.

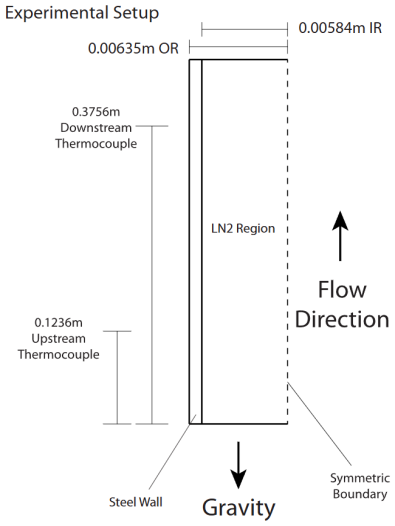
Project Objectives
To observe the discrepancies between physical experiments and CFD (using a multiphase mixture model) of upstream and downstream thermocouples. After this discrepancy has been observed, another aim is to suggest that it can be solved using a Lee coefficient function instead of a constant.

Methods
Physical data (from Dr. Jason Hartwig) is taken to construct boundary conditions in Ansys Fluent, such as inlet temperature, pressure, and mass flux. A 2D axisymmetric setup and mixture model with Lee phase change coefficient is used to model the boiling process. First, a mesh size is selected, with finer elements near the tube wall, and the Y+ is verified to be less than 1 to ensure full resolution of the boundary layer. Then, multiple trials are run on the same set of data with varying Lee coefficients as constants, and their results in the upstream and downstream thermocouples are plotted and compared against physical data.

Results and Discussion
It was consistently observed that when the Lee coefficient was adjusted to bring the upstream thermocouple into agreement with the physical data, the downstream prediction failed to match, and when the coefficient was tuned to match the downstream thermocouple, the upstream wall temperature failed to match. This behavior demonstrates that a single, constant Lee coefficient cannot simultaneously reproduce wall temperature histories at two axial locations. Making the Lee coefficient vary as a function of axial position rather than remain fixed could address this. In principle, a spatially varying coefficient could allow both thermocouples to be matched in the same simulation. In practice, however, defining such a function poses a challenge. Any downstream coefficient inferred from fitting assumes that the

upstream coefficient is correct, yet the upstream fit itself shifts when downstream data are targeted. Because the upstream thermal history directly influences downstream conditions, isolating an independent, spatially varying Lee coefficient requires a multi-point calibration strategy and may not yield a unique solution.

A separate observation concerns the dimensionality of the simulation. Two dimensional axisymmetric models produce chilldown curves that are overly smooth and fail to reproduce the characteristic inflection associated with the transition boiling phase. In contrast, three dimensional simulations accurately capture the sharp slope that signify transition boiling [1]. This comparison demonstrates that three dimensional flow structures and interfacial dynamics play a critical role in reproducing the experimentally observed chilldown behavior.



Acknowledgments
Thank you to Dr. Chirag Kharangate, Dr. Jayachandran K. Narayanan, and the Two Phase Flow and Thermal Management Lab at CWRU for facilitating this research.

References
[1] Narayanan, J. K., Kharangate, C. R., Hylton, S., Kassemi, M., Hartwig, J. W., Mackey, J. R., "Three-dimensional CFD simulations in the Film Boiling Regime during LIquid Nitrogen Chilldown Process," *American Institute of Aeronautics and Astronautics SciTech*, https://ntrs.nasa.gov/api/citations/20230017400/downloads/AIAA_SciTech%20CFD%20paper.pdf

Simulation of Variable Lunar Joint Sensing and Communications System

Student Researcher: Dimitry A. Melnikov

Advisor: Dr. Nathan Ida

The University of Akron
Electrical Engineering

Abstract
A simulation of the physical layer of a 4-antenna 802.11az MIMO communications system is developed in MATLAB. The simulation determines Channel State Information (CSI) describing simulated, transmitted, data input to a raytraced MIMO channel distorted by radio hardware. The raytraced channel is applied to three environments: an ideal line-of-sight outdoor environment, and indoor environment, and an outdoor lunar analog. Linear distance is estimated from Time of Flight (ToF), and methods of Direction of Arrival (DoA) estimation are discussed and simulated. The simulated estimates of DoA are finally compared to a real-world MIMO testbed constructed from commercial off-the-shelf (COTS) components, developed at the University of Akron. Theoretical analysis shows promising results, though real-world nonidealities discovered on the testbed demonstrate obstacles to overcome in completing the proposed navigation system.

Project Objectives
NASA's Artemis program requires precise navigation capabilities to establish the first sustained presence on the lunar surface. However, prior to the deployment of orbital navigation infrastructure around the moon, early Artemis missions will not hold the benefits of accurate radio-navigation services. Nonetheless, reliable surface navigation capabilities are needed to fulfill mission objectives. Wireless surface communications networks such as Wi-Fi or 5G networks include the ability to localize user radios with a high level of accuracy. Localization capabilities of these systems require user radio systems to connect to three or more separate base stations for multilateration. However, user radios in early Artemis missions will only have connectivity to a single base station. The motivating objective of this project is to develop theory, technique and demonstration of a localization capability for Wi-Fi radios that only require a single base station.

The proposed technique relies on two features of modern Wi-Fi and 5G radios, namely Multiple-Input-Multiple-Output (MIMO) RF front-ends, as well as Orthogonal Frequency Division Multiplexing (OFDM), which facilitates automatic channel equalization systems. In addition to improving data throughput these subsystems of Wi-Fi and 5G radios, together, provide data on the radio channel between the two ends of the radio system. This is known as the Channel State Information (CSI).

This same CSI may be employed for navigational purposes. The CSI is used to determine the Direction of Arrival (DoA) of the other radio in the link. Additional parameter estimation systems in the Wi-Fi or 5G radio determine one-way Time of Flight (ToF) of the radio waves. The location of the user radio (Customer Premises Equipment – CPE) can thereby be determined relative to a single base station. The proposed system thereby provides a navigation solution not requiring multiple base stations. The resulting addition to Wi-Fi or 5G radios leverages advanced MIMO and OFDM capabilities to enable high accuracy localization with only a single base station.

Methodology

To evaluate the proposed navigation system, a MIMO testbed was developed by a group of undergraduate students at the University of Akron, shown in **Figure 1**. The testbed was composed of a base station and user terminal, analogous to a cellular tower and a tracked consumer peripheral, respectively. To best emulate deployed hardware, the testbed was constructed exclusively with consumer-grade COTS components, on which an 802.11ac Wi-Fi network is hosted and from which CSI is extracted prior to calculating the required navigation solution.

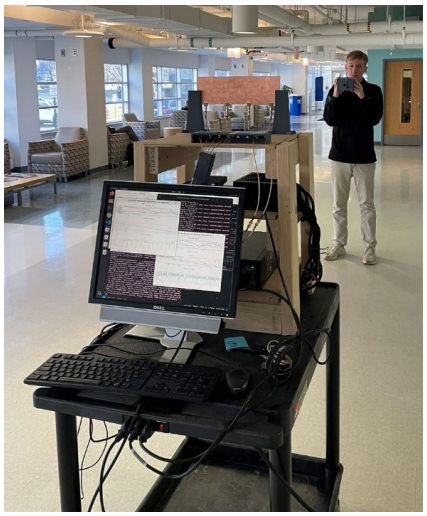


Figure 1. *The University of Akron's MIMO Testbed. (Foreground: Base Station / Cellular Tower analog; Background: Evan Bartel, University of Akron undergraduate, holding User Terminal / Customer Premises Equipment analog)*

To prepare signal processing techniques for the testbed and allow for more advanced follow-on work, a testbed simulation was developed. Developed from an elaborated combination of two separate link simulation examples provided with MATLAB R2023a, the simulation generated 802.11az waveforms, passed them through a simulated, raytraced channel, and estimated the Channel State Information (CSI) before estimating Direction of Arrival and Time of Flight.

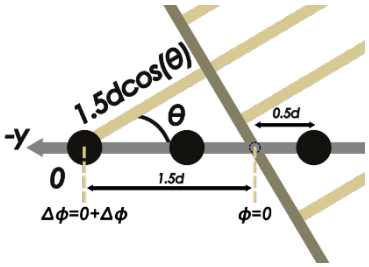


Figure 2. *Trigonometric representation of phase differences observed across elements to impinging plane wave.*

Channel State Information (CSI) models a signal's path from one transmitting antenna to another receiving antenna as a Linear Time-Invariant (LTI) system with a Magnitude and Phase. This directly translates to an impinging plane wave from a target, allowing for the application of coherent signal processing algorithms.

To determine the Direction of Arrival, the Multiple Signal Classification (MUSIC) algorithm was applied to the Uniform Line Array (ULA) steering equation. The MUSIC algorithm was chosen due to its resilience to both high-noise and -multipath environments. The antenna array on the MIMO testbed consisted of four patch antennas etched onto a copper-clad laminate at NASA Glenn Research Center (GRC). Each pair of antennas was connected to a single Network Interface Card (NIC). This array is approximated as a Uniform Line Array with isotropic radiators as seen in **Figure 2**.

Through a modified formulation presented in *Van Trees' Optimum Array Processing*, the Direction of Arrival may be naïvely determined as the following, where $\Delta\Phi$ represents the successive phase difference due to the target plane wave, k represents the wavenumber, and p_{y_n} represents the position of the nth element in the y-plane:

$$\theta = \cos^{-1}\left(\frac{\Delta\Phi}{k\Delta y}\right) = \cos^{-1}\left(\frac{\Delta\Phi}{kp_{y_n}}\right) = \cos^{-1}\left(\frac{\lambda\Delta\Phi}{2\pi p_{y_n}}\right)$$

MUSIC extends the formulation by incorporating the array manifold vector, which provides the expected complex excitation – magnitude and phase – for each element in an array with a given geometry and DOA [1]:

$$\vec{\boldsymbol{v}}(\theta) = \left[e^{-jk\vec{p}_{y_0}\cos(\theta)}, e^{-jk\vec{p}_{y_1}\cos(\theta)}, \dots, e^{-jk\vec{p}_{y_{N-1}}\cos(\theta)}\right]^T$$

For *N* elements, with *D* incident wavefronts, noise *W*, and expected element excitation *F*, the incoming CSI *H* may be modeled after [2]:

$$\begin{bmatrix} H_1 \\ H_2 \\ \vdots \\ H_N \end{bmatrix} = [v(\theta_1) \quad v(\theta_2) \quad \cdots \quad v(\theta_D)] \begin{bmatrix} F_1 \\ F_2 \\ \vdots \\ F_D \end{bmatrix} + \begin{bmatrix} W_1 \\ W_2 \\ \vdots \\ W_N \end{bmatrix}$$

$$H = V(\theta)F + W$$

The covariance matrix of the CSI is defined as:

$$R = HH^H = V(FF^H)V^H + WW^H = VPV^H + \lambda_{min}R_0, \qquad \lambda_{min} \geq 0$$

Defining the noise eigenvectors, E_N, orthogonal to the signal subspace as the eigenvectors with the smallest eigenvalues in R, MUSIC provides the likelihood of a signal to be arriving from a direction θ as:

$$P_{MUSIC}(\theta) \triangleq \frac{1}{\vec{v}(\theta)^H E_N E_N^H \vec{v}(\theta)}$$

The predicted Direction of Arrival $\hat{\theta}$ is therefore calculated to be:

$$\hat{\theta} \triangleq \arg\max_{\theta} |P_{MUSIC}(\theta)|$$

A similar process is followed for Time of Flight estimation, using MUSIC to refine the estimate, as defined by the original 802.11az MATLAB example upon which the simulation was elaborated.

To evaluate the efficacy of the proposed tracking techniques, the testbed simulation is capable of reconfiguring array geometry, signal-to-noise ratio (SNR), terrain geometry, and material characteristics. These characteristics are then fed into a shooting-and-bouncing ray tracing channel emulator, which modulates transmitted data.

To determine the Channel State Information (CSI), the simulation generates an 802.11az waveform, passes the waveform through the raytraced channel, and performs channel estimation on the altered waveform. The resulting CSI is then fed into the aforementioned tracking algorithms.

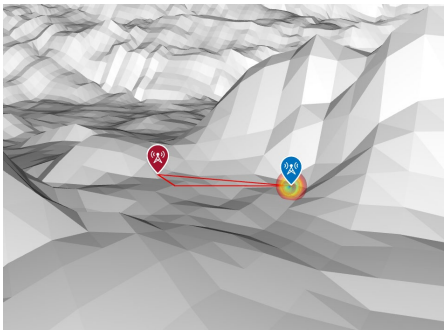


Figure 3. *Testbed simulation on lunar surface model*

Other nonidealities encountered on the MIMO testbed, such as the internal antenna switching and center frequency offsets, are applied to the altered waveform prior to channel estimation to better emulate the physical layer of the system.

The ideal Line-of-Sight scenario is simulated with no structures, and no bounces. The worst-case indoor scenario, shown in **Figure 7**, uses a model of a smaller conference room with concrete walls, with the intent of inducing significant multipath. The operational scenario – the lunar analog – uses a NASA-sourced STL model of the Moon's Copernicus crater [3] with an approximate 2x planar and 3x vertical exaggeration, modeling the lunar regolith as concrete as well. This scenario is shown in **Figure 12**. Due to the exaggerated size of the STL relative to the rest of the simulation, the bit energy to noise power spectral density (E_b/N_0) is scaled to the minimum allowable value necessary for demodulation and channel estimation.

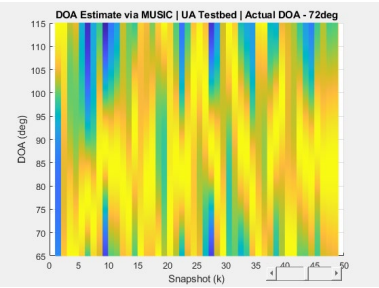


Figure 4*. DOA via MUSIC on MIMO Testbed*

Results and Discussion

The simulation provides promising results. Even in an environment with a high degree of multipath and a low operational E_b/N_0 value, **Figure 8** demonstrates that MUSIC provides a stable estimate for DOA and a tolerable ranging error. As expected, increasing the signal-to-noise ratio improves the quality of the location estimate. Though, paradoxically, can sway the Time of Flight ranging estimate. Regardless, applying the Cramér-Rao Lower Bound (CRLB) derived in Kay's *Fundamentals of Statistical Signal Processing: Detection Theory* [4], provides an expected cross-sectional accuracy of 43m (0.61°) at 2km from the target with DOA alone. **Figure 11**, as a best-case, high-SNR, line-of-sight scenario, closely approaches the CRLB – but quickly diverges when introducing noise and multipath (as seen in **Figure 9** and **Figure 8**), implying the need for more robust super-resolution algorithms to rival the performance of traditional multilateration systems.

The application and system-level evaluation of the lunar model may be said to be inclusive due to time constraints. Most publicly-available lunar terrain models are large and tricky to work with, inducing significant processing costs. Lunar propagation models are under active development, yet of great interest to NASA GRC. Nevertheless, it is possible to incorporate accurate terrain models to the simulation, and it would be further possible to integrate the MATLAB simulation with more actively-used tools, such as the Ansys Systems Tool Kit (STK), for more accurate validation.

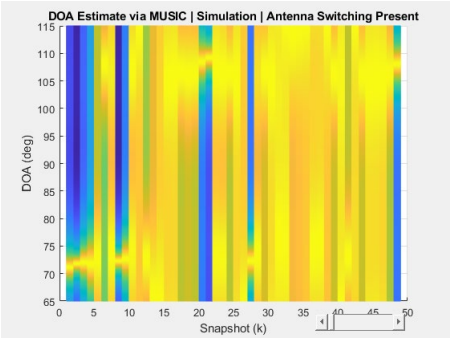


Figure 5. *Line of Sight DOA Estimate via MUSIC for 60dB Eb/No, demonstrating the effects of internal antenna switching*

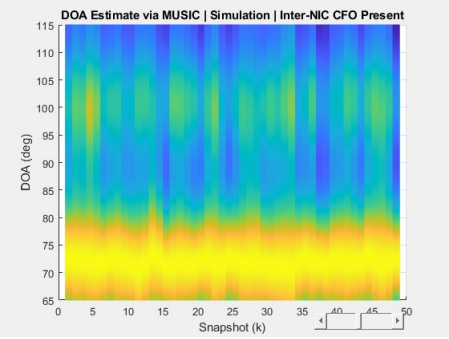


Figure 6. *Line of Sight DOA Estimate via MUSIC for 60dB Eb/No, demonstrating the effects of inter-NIC CFO*

In practice, the results on the MIMO testbed (shown in **Figure 4**) diverge significantly from the ideal, phase-coherent conditions of the simulation. Through the simulation and experimental validation, the primary issues inherent to the realized system have been found to be internal antenna switching and inter-radio center frequency offsets (CFO). As the testbed consists of two NICs, each with separate reference oscillators. The reference oscillators hold a center frequency accurate enough to communicate within the Wi-Fi standard, but not accurate enough to one another. This induces a phase gradient in the collected CSI, disrupting the measurement, as shown in **Figure 6**. On another note, as COTS hardware, the NICs internally switch their antennas seemingly randomly, and with no direct indication. Both this, shown in **Figure 5**, and the inter-NIC CFO likely combine in the CSI generation process, manifesting the distortions seen in the testbed data seen in **Figure 4**. Nevertheless, these nonidealities may be greatly reduced with relatively minor changes to hardware – either by providing reference signals, or by synchronizing the NIC reference oscillators.

Figures for Various Simulated Configurations

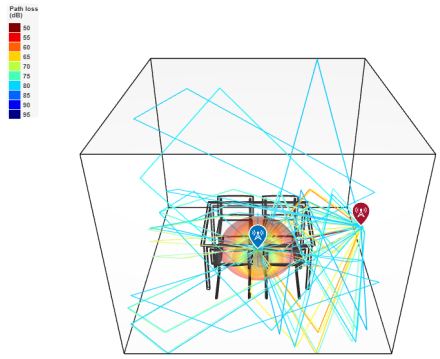


Figure 7. *Simulation Configuration for Indoor Room. Target placed 1.5m away, 105° off array parallel.*

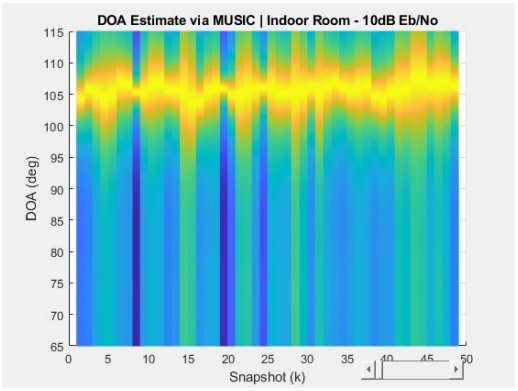


Figure 8. *Indoor DOA Estimate via MUSIC for 10dB Eb/No. Ranging Error: 7.99%*

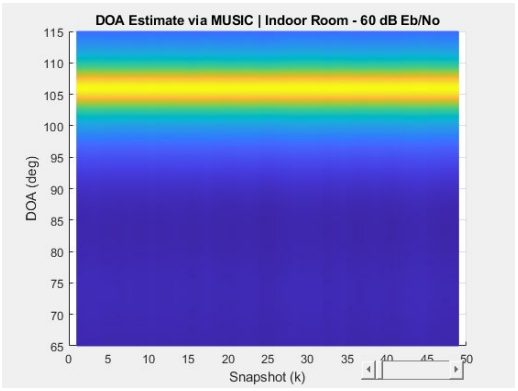


Figure 9. *Indoor DOA Estimate via MUSIC for 60dB Eb/No. Ranging Error: 23.32%*

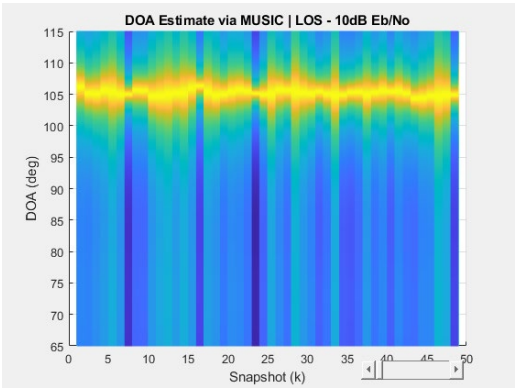


Figure 10*. Line of Sight DOA Estimate via MUSIC for 10dB Eb/No. Ranging Error: 4.15%*

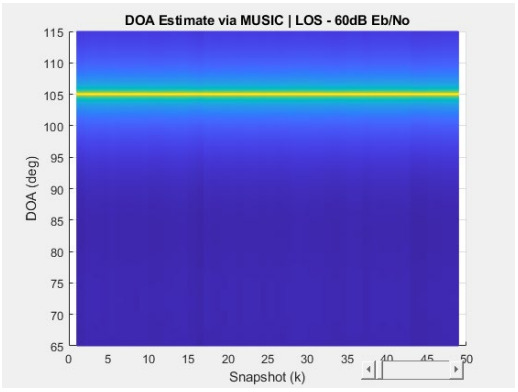


Figure 11*. Line of Sight DOA Estimate via MUSIC for 60dB Eb/No. Ranging Error: 0.32%*

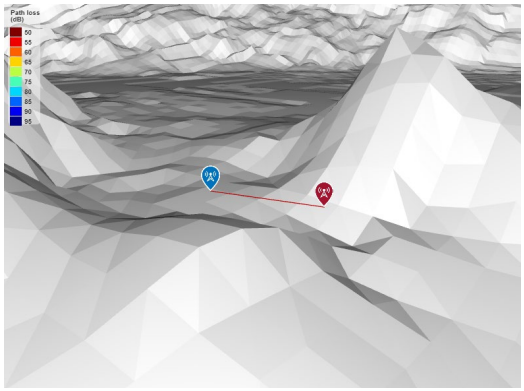


Figure 12. *Simulation Configuration for Lunar Analog. Target placed 1.5m away, 105° off array parallel.*

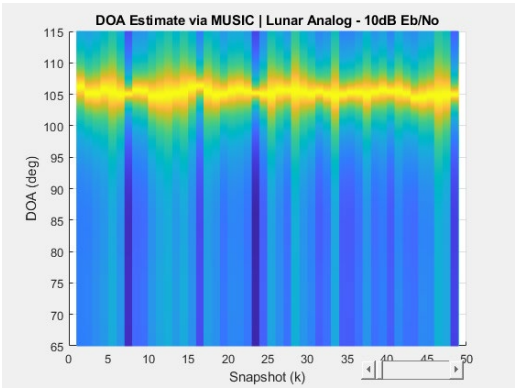


Figure 13. *Lunar Analog DOA Estimate via MUSIC for 10dB Eb/No. Ranging Error: 3.95%*

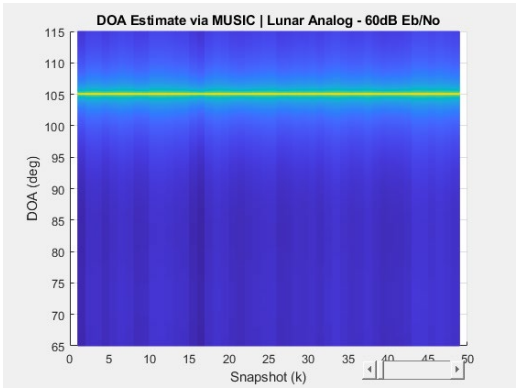


Figure 14. *Lunar Analog DOA Estimate via MUSIC for 60dB Eb/No. Ranging Error: 0.11%*

Acknowledgments & References

The author would like to give special thanks to Dr. Obed Scott Sands, Mr. Bryan Schoenholz, and Dr. James Downey for their continued support and guidance in the development of the project. The University of Akron's V.E.C.T.O.R. Testbed Development Team – including Mr. Evan Bartel, Mr. Andrew Burrier, and Mr. Goran Gjorgievski – greatly informed the creation of the discussed theoretical and observed results. The author would also like to thank the Ohio Space Grant Consortium for funding this research and the Ohio Aerospace Institute for hosting the symposium.

[1] Van Trees, H. L. (2002a). *Optimum Array Processing*. Wiley-Interscience.

[2] Schmidt, R. (1986). Multiple emitter location and signal parameter estimation. *IEEE Transactions on Antennas and Propagation*, *34*(3), 276–280. https://doi.org/10.1109/tap.1986.1143830

[3] Northeast Planetary Data Center; NASA RPIF System; Horowitz, S. S.; & Schultz, P. H. (2015, August 3). *Copernicus Crater [3D model]*. NASA 3D Resources. Relevant Mission: Lunar Orbit and Landing Approach. Retrieved October 30, 2024, from https://nasa3d.arc.nasa.gov/detail/copernicus-crater

[4] Kay, Steven M. *Fundamentals of Statistical Signal Processing: Detection Theory*. Pearson, 1998.

The Formation of Devil's Tower

Student Researcher: Ethan Miller

Advisor: Tej Gautam

Marietta College
Petroleum Engineering

Abstract
In this project I plan on talking about the formation of Devil's Tower, a famous historical monument located in Wyoming. I also plan on talking about the geological structure of Devil's Tower and the geological processes that formed this giant geological monument. I plan on talking about the composition of the monument and how it has been affected over time by the environment and climate of Wyoming as well.

Project Objectives
Determine the composition, history of formation, and cultural significance of Devil's Tower

Methods
Carefully analyzed multiple sample rocks to determine the composition of Devil's Tower and that there was a volcano there many millions of years ago.

Results and Discussion
Devils Tower was formed from a volcanic plug that was once a hot magma in a volcano. The volcano eroded over time, which is why we are left with the harder, crystalline rock from the volcanic plug.

Figures/Charts





Rock sample of Devil's Tower showcasing a mix of large crystals known as phenocrysts

Acknowledgments
I want to thank Prof. Andrew Beck for leading the field trip to the monument and Prof Tej Gautam for accompanying us on said field trip and being a great advisor for my project.

References

Prof. Beck, Prof. Gautam, and

https://www.nps.gov/deto/learn/nature/tower-formation.htm

Sex Differences in Ethanol-induced Brain Activity

Student Researcher: Sydney Miller

Advisor: Clare Mathes

Baldwin Wallace University
Department of Neuroscience

Abstract

This project's primary goal was to determine if acute ethanol administration induces neural activity in brain regions differently in male versus female rats. We would not be able to fully understand the effects of ethanol on the brain without looking at both sexes. Previous studies have focused on male rats, rather than female rats. The prevalence of alcohol use disorder is overall decreasing in the United States; however, it is increasing in women. In this study, we assessed differences in ethanol-induced neural activity in the central nucleus of the amygdala (CeC), the Lateral septum (LS), the Lateral hypothalamus (LH), and the nucleus accumbens (NuAc), which are critical in the perception and assessment of reward. To assess this, we quantified the number of cells containing Fos, a protein produced when neurons are active and can be visualized through immunohistochemistry. Male (n= 8) and female Sprague-Dawley rats (n=8) were given an intraperitoneal injection of saline or ethanol (20% at 12.5 ml/kg) and, 2 hours following the injection, euthanized via overdose of barbiturate and transcardially perfused to fix brain tissue. Coronal brain slices (80 µm) were processed for Fos immunoreactivity, mounted on gelatin-subbed slides, and counter-stained with methyl green. Images, including the structures, were taken, blinded, and Fos was quantified using ImageJ. Fos counts per area between EtOH- and saline-injected groups were analyzed via independent-sample t-test (sig = $p<0.05$). The results show significant Fos expression in the CeC ethanol group as compared to the saline group. The second phase of this study will increase the sample size (total n=32) and bring sex differences into account. Understanding if ethanol-induced Fos activation differs between male and female rats, will influence whether both sexes can be used in future experiments on this topic.

Project Objectives

With the data from phase 1, I seek to demonstrate that an ethanol injection induces Fos in rat brain reward areas to a greater extent than saline injection (regardless of rat sex). Phase 2 will double the sample size to allow for sex difference analysis. Ultimately, we seek to determine if ethanol-induced Fos activation differs between male and female rats.

Methods

Sprague-Dawley rats (n=16) were put into groups based on sex & injection type. In the days leading up to the test day, all rats were injected with first small (0.5 mL) and then large injections (3.0-6.0 mL) to limit the stress of large injections on test day. On test day, Rats were either injected with ethanol (20% at 12.5 ml/kg ip) or saline. Two hours after injection, rats were euthanized via overdose of barbiturate and transcardially perfused with paraformaldehyde, fixing the brains, which were then removed. The brains were sliced coronally on a cryostat (80 µm), and slices were processed for cFos immunoreactivity. The slices were then mounted on gelatin-subbed slides, counter-stained with methyl green, and cover-slipped. Slices representative of brain regions of interest were identified, and microscopic images were taken and then blinded for nonbiased Fos scoring. Fos immunoreactivity in each region was quantitatively scored using Image J. A protocol was used to standardize the contrast threshold, size, and circularity of Fos and provide counts per area defined. In combination with blinding the images, this automated scoring method

helped eliminate human bias while scoring. Fos counts per area between EtOH- and saline-injected groups were analyzed via independent-sample t-test (sig = $p<0.05$). Some areas could not be visualized on some brains, and the analysis did not include outliers with scores ≥3 SE from the mean.

Results and Discussion

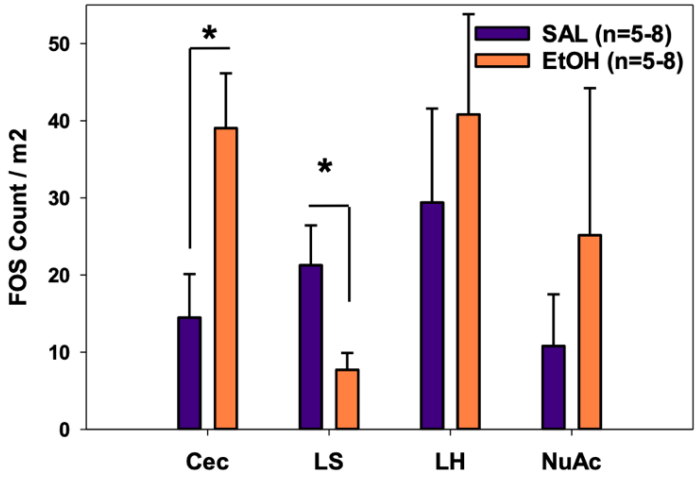


Figure 1. Two-tailed independent samples t-test with injection group as between-subject independent variables and Fos per meters squared in each region as dependent variable. CeC: t(12)=2.744, p=0.018 (EtOH>SAL), LS: t(11)=-2.265, p=0.045 (not the direction we'd expect, SAL>EtOH), LH: t(14)=1.122, p=0.281, NuAc: t(8)=0.712, p=0.497.

Ultimately, we seek to assess if ethanol-induced Fos differs between male and female animals. Understanding alcohol-related sex differences at a neural level may inform different treatments for men and women with alcohol use disorder. We show here that systemic ethanol induces Fos in the CeC to a greater extent than saline injection in a mixed-sex cohort. This was performed blinded and standardized using automated scoring equipment (ImageJ). The data from using ImageJ reflects and quantitatively supports our qualitative assessment conducted in the Spring of 2024 during a faculty-student collaborative course. We expected higher Fos in EtOH-injected rats in all brain areas based on prior literature. We failed to replicate that (and had the opposite in one case), potentially due to low sample sizes, mixed-sex groups, robust injection acclimation, and bleaching due to counterstaining. To address some of these concerns, I conducted a second phase to increase the sample size, allowing for the analysis of sex differences. During the second phase, we decreased the acclimation to injections to prevent stress. Alternate tissue slices from this phase were collected and processed without counterstaining to allow for future analysis of Fos counts without the potential of bleaching due to the methyl green counterstain.

Acknowledgments

Funding for this project was provided in part by the BW Summer Scholars Program (to SM), OSGC (to JD), the Baldwin Wallace Neuroscience Department, the Office of Graduate Studies and Research (to CMM), and John Huntington Scholarship Fund (to SM). We would like to thank all students who participated in the NRO459X: Faculty/Student Collaboration course, and a portion of these data were presented at Ovation 2024. An additional thank you to Mallory Witt and Gregg DiNuoscio for experimental and technical assistance. We also thank the Neuroscience vivarium staff for animal care.

References

Chang SL, Patel NA, Romero AA. Activation and desensitization of Fos immunoreactivity in the rat brain following ethanol administration. Brain Res. 1995 May 8;679(1):89-98. doi: 10.1016/0006-8993(95)00210-h. PMID: 7648269.

Criado JR, Morales M. Acute ethanol induction of c-Fos immunoreactivity in pre-pro-enkephalin expressing neurons of the central nucleus of the amygdala. Brain Res. 2000 Apr 7;861(1):173-7. doi: 10.1016/s0006-8993(99)02468-3. PMID: 10751579.

Herring BE, Mayfield RD, Camp MC, Alcantara AA. Ethanol-induced Fos immunoreactivity in the extended amygdala and hypothalamus of the rat brain: focus on cholinergic interneurons of the nucleus accumbens. Alcohol Clin Exp Res. 2004 Apr;28(4):588-97. doi: 10.1097/01.alc.0000122765.58324.6d. PMID: 15100610.

Saalfield J, Spear L. Fos activation patterns related to acute ethanol and conditioned taste aversion in adolescent and adult rats. Alcohol. 2019 Aug;78:57-68. doi: 10.1016/j.alcohol.2019.02.004. Epub 2019 Feb 22. PMID: 30797833; PMCID: PMC6612301.

Segovia KN, Vontell R, López-Cruz L, Salamone JD, Correa M. c-Fos immunoreactivity in prefrontal, basal ganglia and limbic areas of the rat brain after central and peripheral administration of ethanol and its metabolite acetaldehyde. Front Behav Neurosci. 2013 May 24;7:48. doi: 10.3389/fnbeh.2013.00048. PMID: 23745109; PMCID: PMC3662884

White A, Castle IJ, Chen CM, Shirley M, Roach D, Hingson R. Converging patterns of alcohol use and related outcomes among females and males in the United States, 2002 to 2012. Alcoholism, clinical and experimental research. 2015. 39(9), 1712–1726. https://doi.org/10.1111/acer.12815

Trapped Wave Resonance Tones Radiated Toward the Nozzle in a Supersonic Jet

Student Researcher: Mason Mitchell

Advisor: Dr. Mo Samimy

The Ohio State University
Department of Mechanical and Aerospace Engineering/Aerospace Engineering, B.S.

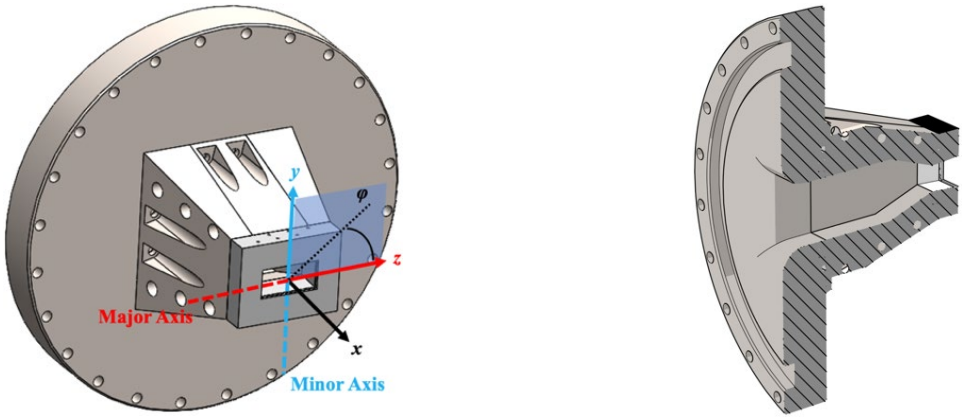
Abstract
The research project aimed to demonstrate the existence of trapped wave (TW) resonance tones in the near-field (NF) acoustic signature of a supersonic single rectangular jet (SRSJ). It is currently believed that TW are the result of a second mode of free shear layer instability with the spectral peaks of TW strictly appearing in the acoustic near-field and forward arc of the acoustic far-field. Although the appearance of TW in these regions of the acoustic field has limited documentation in existing literature, there is ongoing research on this phenomenon that has linked screech – a high amplitude resonance tone generated by supersonic jets – to the first or second harmonic of the TW fundamental frequency. The extensive literature on screech has identified a strict dependence of screech resonance with the interaction of coherent structures (CS), or wavepackets, formed within the shear layer. There are several mechanisms present within the flow field that could impact the formation and interaction process of CS, such as TW, necessary for establishing the feedback (resonance) loop of screech. In a preliminary effort to clarify the relationship between CS and TW, the SRSJ was operated in flow regimes from high subsonic to highly underexpanded operating conditions. The presented baseline results confirmed the presence of the spectral peaks of TW in the NF acoustic signature.

Project Objectives
The acoustic waves emitted from a jet exhausting into quiescent air are generated by dynamics of coherent structures (CS) that are formed within the shear layer by the Kelvin-Helmholtz instability. Under certain conditions in the flow field environment, a feedback loop could develop that reinforces the emission of an acoustic wave at a certain frequency. The persistent emission of a specific acoustic wave is known as resonance. There are several mechanisms within the flow field that impact the establishment of the feedback loop for resonance. For example, in supersonic jets, the coherent structures will interact with the shock cell structure present within the shear layer, emitting an acoustic wave each time, that could travel upstream and play a role in the establishment of the feedback loop. The presence of acoustic waves within the jet core, known as trapped waves, may also impact the feedback loop.

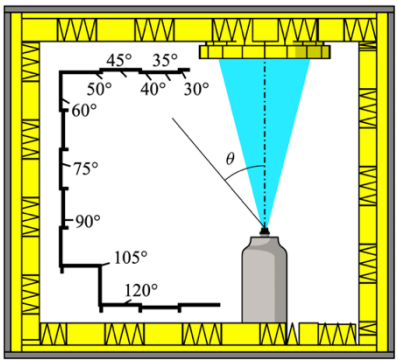
Michalke (1984) identified a second instability mode that subsequent work by Tam and Hu (1989) further distinguished into two branches contained (trapped) within the jet core. The waves associated with this second mode are known as trapped waves (TW) or guided jet waves. Towne et al. (2017) and Schmidt et al. (2017) provided clear visualizations of these TW within the jet core for a subsonic (M_J = 0.90) jet in their extensive simulation work. In recent experimental studies, the acoustic signatures of TW have been identified in the acoustic near-field (Zaman et al. (2022)) and forward arc of the acoustic far-field (Zaman et al. (2024)) for various nozzle geometries in highly subsonic to highly underexpanded operating conditions with the TW appearing as a series of distinct spectral peaks. The nature of TW has been extensively studied. However, there is no information on the potential connection between TW and coherent structures, which are responsible for entrainment between the jet and ambient air, jet mixing processes, and radiated noise in the acoustic far-field.

The primary objectives of this project are twofold. The first is to demonstrate the existence of trapped waves spectral peaks in the near-field (NF) acoustic signature of a supersonic rectangular single jet (SRSJ) with a design Mach number 1.5 exhausted from a bi-conical convergent-divergent nozzle, operating over a range of flow regimes (from overexpanded to underexpanded). The second is to identify target frequencies at which to implement active flow control with Localized Arc Filament Plasma Actuators (LAFPAs) to explore the relationship between coherent structures and trapped waves. The results acquired through this project will complement and advance current interests within the aeroacoustics research community. It also has the potential to provide insights on techniques for the mitigation of acoustic structural loads on military aircraft and cabin noise in commercial aircraft.

Methods



(a) *(b)*



(c) *(d)* *(e)*

Figure 1: SRSJ assembly (a), inner contour of nozzle (b), SRSJ installed in anechoic chamber at GDTL (c), and NF azimuthal microphone array radial location (d) and axial location (e). SRSJ coordinate system, major and minor axes, and azimuthal angle (φ) are defined in (a) while the polar angle (θ) is defined in (c).

The experimental facility utilized a supersonic rectangular single jet (SRSJ) that was designed and built at the Gas Dynamics and Turbulence Laboratory (GDTL) within The Ohio State University's Aerospace Research Center. The SRSJ is bi-conic ("military-style"), rectangular, convergent-divergent nozzle with a

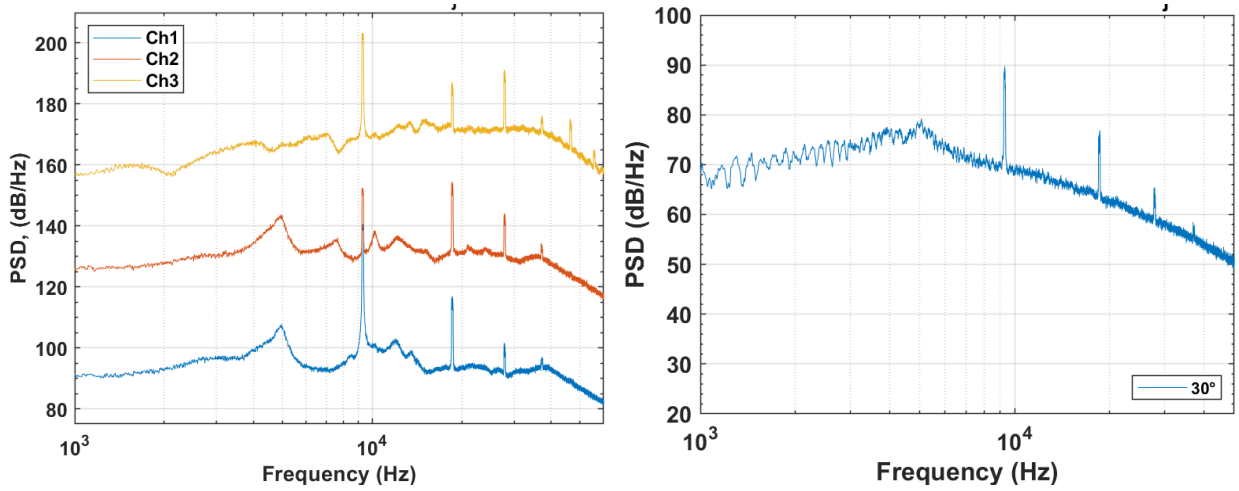
sharp throat, design Mach number of 1.5 (M_D = 1.5), and aspect ratio of 2 (AR = 2). The nozzle exit has a width (w) and height (h) of 24.13 mm and 12.07 mm, respectively, with an area-based equivalent diameter (D_e) of $2\sqrt{(w \times h)/\pi}$ =19.25 mm. The SRSJ assembly is shown in Fig. 1 with the coordinate system and major and minor axes of the SRSJ (Fig. 1a), the inner contour of the nozzle (Fig. lb), and the installation of the SRSJ within the anechoic chamber at the GDTL (Fig. 1c). The anechoic chamber has wall-to-wall dimensions of 6.2 m by 5.6 m by 3.4 m and a cutoff frequency of 160 Hz. For acoustic measurements, all reflecting surfaces within the anechoic chamber, except the nozzle's exit face, were covered with acoustic foam to avoid unwanted acoustic reflection from these surfaces. The angle, θ, measured with respect to the x-axis of the SRSJ, is the polar angle for FF acoustic measurements (Fig. 1c) and the angle, φ, measured with respect to the positive z-axis, is the azimuthal angle of the SRSJ (Fig. 1a). The y and z axes are the minor and major axes of the jet, respectively.

The flow through the SRSJ was driven by high-pressure air supplied from three, five-stage reciprocating compressors connected to two large pressure vessels with 36 m^2 total volume and a maximum pressure of 2300 psi (16 MPa). There is sufficient air flow capacity for the experiments to run unheated flow continuously. The stagnation pressure of the flow is set by a computer-controlled valve, which automatically maintains the desired nozzle pressure ratio (NPR), i.e., the ratio of jet stagnation to ambient pressure. The SRSJ was operated over a wide range of nozzle pressure ratios (NPR = 1.493 to 5.283, corresponding to fully expanded Mach number M_J = 0.78 to 1.74 in flow regimes from high subsonic to highly underexpanded. The M_J and NPR for the design conditions are 1.5 and 3.67, respectively.

The flow and acoustic fields of the SRSJ were investigated with a FF microphone array (Fig. 1c) and a NF microphone array (Fig. 1d). The FF microphone array consists of eight Brüel and Kjær $\frac{1}{4}$ in. microphones (model 4939) mounted at polar angles ranging from 30° to 120º as measured from the downstream jet axis, and they are aimed at the origin of the SRSJ coordinate system (Fig. 1a). The SRSJ assembly can be rotated to locate the FF microphone array on the plane of the SRSJ configuration's major axis ($\varphi = 0°$) or minor axis ($\varphi = 90°$). The individual microphone distances from the origin of the SRSJ range from 99D_e to 196 D_e. In these results, only the data from one FF microphone at a polar angle of 30º at a distance of 99D_e is presented. The NF microphone array consists of an azimuthal array with three Brüel and Kjær $\frac{1}{4}$ in. microphones (model 4939). The microphones were positioned at an axial location of x/D_e = 0.5 and radially (measured normal to the major axis) at r/D_e= h/2 (for microphones 1 and 2) and at the nozzle exit plane at an axial location of x/D_e = 0 and radially at r/D_e = 4 (for microphone 3). Microphones 1 and 2 locations are similar to those used by Zaman et al. (2022 & 2024) and used to examine the presence of TW. Microphone 3 provides a point of comparison to historical acoustic data of the SRSJ. The sampling frequency was 200 kHz, and 100 blocks of 32768 samples each were acquired per NPR, which results in a frequency resolution of 6.10 Hz. Prior to acquiring a set of NF acoustic data, test runs were conducted to establish the appropriate gain setting for each test case to leverage the entire dynamic range without saturating the channels. The microphones were calibrated *in-situ* at the selected gain through the use of a Brüel and Kjær (model 4231) acoustic calibrator. The gain value was set to 31.6 mV-Pa^{-1} for the FF acoustic measurements and 1 mV-Pa^{-1} for the NF acoustic measurements.

Results and Discussion

The baseline experimental results using the described SRSJ will be addressed here to investigate the presence and behavior of trapped waves across various operating conditions in a rectangular jet. The preliminary results included simultaneous NF and FF acoustic measurements of the pressure spectra collected in accordance with the techniques described above.



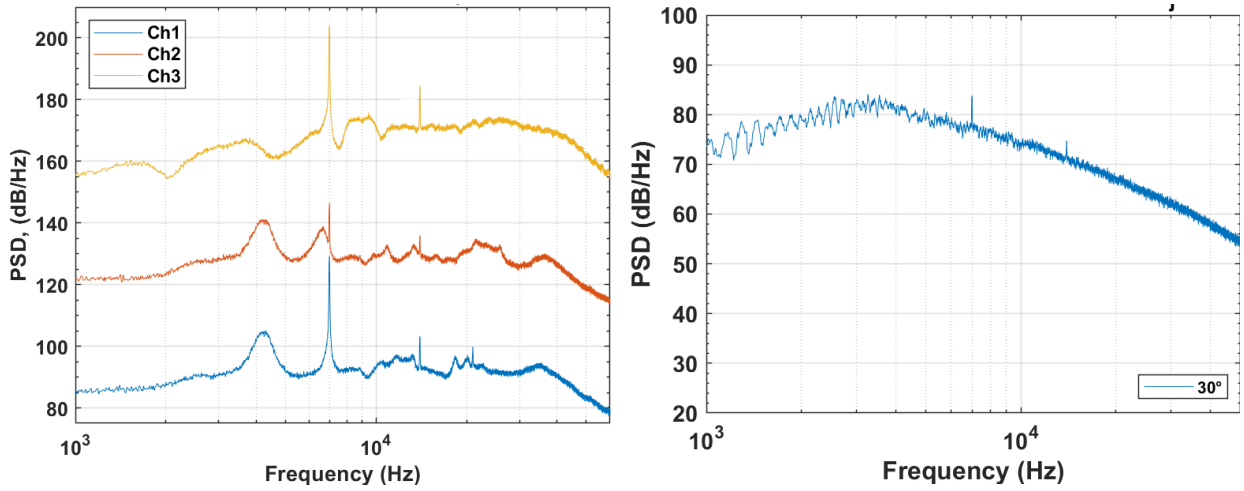
(a) *(b)*

Figure 3: NF spectra with 40 dB offset between microphone channels (a) and FF spectrum at θ = 30° (b) for the baseline M_J = 1.32 case.

The NF spectra of the three microphones is shown in Fig. 3a for a moderately overexpanded regime (M_J = 1.32) with the corresponding FF spectrum at θ = 30º shown in Fig. 3b. In both the NF and FF spectra, a distinct screech peak is observed at a frequency of 9200 Hz as well as the first and second harmonics of screech. The signature of peak turbulent mixing noise is visible as a broadband peak in the FF spectrum centered at 5000 Hz. The NF spectrum obtained using microphone 3 at the nozzle exit plane includes higher harmonics of screech not visible in the FF spectrum or NF spectra of microphones 1 and 2. However, there is a clear peak around 5000 Hz on both the NF spectra of microphones 1 (on the minor axis) and 2 (on the major axis). The first and second harmonics of this peak, along with the screech tone and its harmonics previously mentioned, are clearly shown in microphone 2 (on the major axis). On the other hand, the screech tone and its harmonics dominate the NF spectrum of microphone 1 (on the minor axis) in which only the primary tone of the trapped waves is clearly visible. In Zaman et al. (2022), multiple harmonics of the primary peak could be seen in the NF spectrum of the minor axis with the number of peaks doubling on the major axis of a rectangular jet of *AR* = 2. Zaman et al. (2022) also observed either the first or second harmonic of the primary TW peak transitioning to a screech tone when the jet started screeching. The preliminary results presented here partially corroborate the findings of Zaman et al. (2022), although there are apparent differences between them. Recall that Zaman et al. (2022) used a convergent rectangular nozzle and investigated the nature of TW in underexpanded jets while the current work used a bi-conic rectangular convergent-divergent nozzle operating in both overexpanded (Fig. 3) and underexpanded flow regimes. It is possible that these differences are connected to the nozzle geometry, flow regime, or another phenomenon.

In the nozzle design condition (M_J = M_D = 1.50) case, the noted trends in spectral profiles are maintained in the NF spectra shown in Fig. 4a with the corresponding FF spectrum at θ = 30º shown in Fig. 4b. The typical convergent-divergent nozzles used in laboratories are designed through the method of characteristics, which ensures the internal nozzle surface profile in the diverging section promotes shock-free flow through the nozzle at M_D. However, the nozzle in the current work is bi-conic. Therefore, there are weak shock waves originating from the sharp throat region, and thus screech tones, even at the design

Mach number. The screech peak is again clearly visible in both the NF and FF spectra, but the screech peak in the FF spectrum is quite weak in this case. As expected, the screech frequencies for the fundamental and first harmonic of screech have decreased with the increase in M_J, consistent with the results in the literature (Samimy et al. (2023)). There is a spectral peak again observed below the screech fundamental in the NF spectra of microphones 1 and 2, which has decreased in frequency with the increase in M_J, and this is consistent with the results reported in Zaman et al. (2022). However, this spectral peak is not as well-defined as in the overexpanded regime. If this peak is a signature of the TW, the screech frequency is not exactly the same as the first harmonic of the TW observed on the major axis.



(a) *(b)*

Figure 4: NF spectra with 40 dB offset between microphone channels (a) and FF spectrum at θ=30° (b) for the baseline M_J = 1.50 case.

The staggered spectra of the NF acoustic signature for Microphone 1 and Microphone 2 are shown in Fig. 5a,c and Fig. 5b,d, respectively, across the whole range of operating conditions (Fig. 5a,b) and strongly overexpanded operating conditions (Fig. 5c,d). The screech peak, which can be identified as the large amplitude event in the shown acoustic signatures, shifts to lower frequencies with successive increases in M_J. The broader peak, occurring at a lower frequency, that accompanies screech displays this same trend. However, the TW spectral peaks are more difficult to discern in staggered spectra of Fig. 5a,b due to their smaller amplitude nature. Fig. 5c,d displays the lower frequency band for several strongly overexpanded cases to further scrutinize the acoustic signature for TW. There are spectral peaks at 4900 Hz and 7100 Hz in the acoustic signatures of Microphone 1 (Fig. 5c), but only the spectral peak at 7100 Hz can be found in that of Microphone 2 (Fig. 5d). In addition, these identified spectral peaks did not appear in the FF spectrum (not shown), which signifies these are TW spectral peaks. The number of TW spectral peaks observed on the minor axis is twice that observed on the major axis for M_J = 0.88 and M_J = 0.91. For these cases, the number of tones differs by a factor of the rectangular nozzle's *AR*.

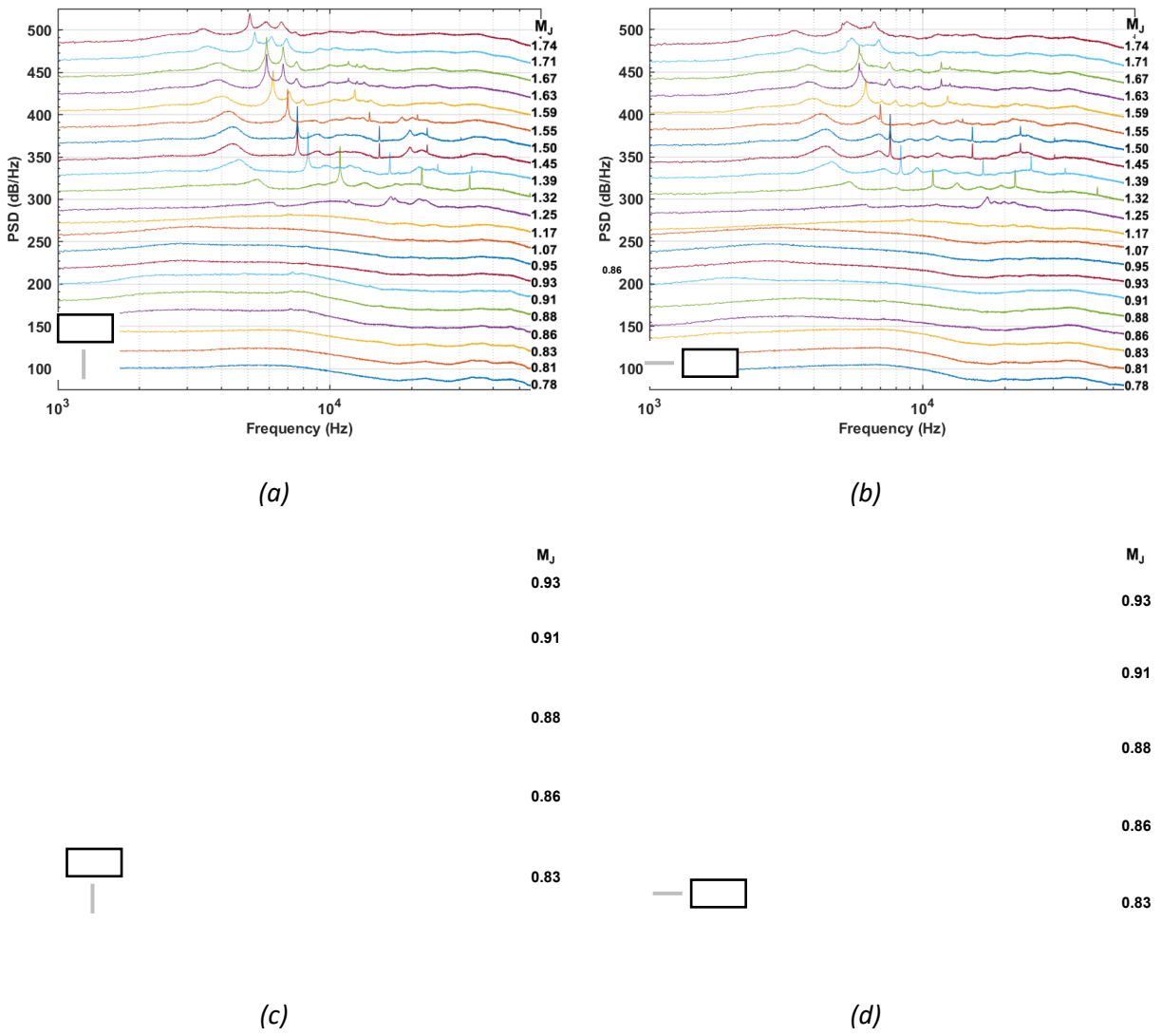


Figure 5: NF staggered spectra with 20 dB offset between spectra for Microphone 1 (on minor axis) (a,c) and Microphone 2 (on major axis) (b,d). The values of M_J for each acoustic signature are indicated along the side for the whole range of operating conditions in the top row (a,b) and only the strongly overexpanded operating conditions in the bottom row (c,d).

The baseline experimental results have confirmed the presence of TW spectral peaks across a range of operating conditions, from high subsonic to highly underexpanded, in the SRSJ shown in Fig. 1a. The presented trends of the TW corroborate the findings from the literature on this acoustic phenomenon. First, the number of tones observed on the minor axis is higher than those on the major axis by a factor of the nozzle's *AR*. Second, the TW spectral peaks shift to lower frequencies with increasing M_J. Third, the transition from a trapped wave to screech remains unclear.

The future work on this project will present more detailed baseline results on trapped waves for the SRSJ shown in Fig. 1a and investigate the effects of excitation on the acoustic signatures measured by the FF microphone array (Fig. 1c) and NF microphone array (Figs. 1d and 1e). The NF microphones will be used to demonstrate the existence of trapped waves in the SRSJ before implementing a method for active flow

control known as Localized Arc Filament Plasa Actuators (LAFPAs). In addition, the NF array will highlight the effect of excitation on spectra and tonal components in the NF while the FF array will evaluate the effectiveness of excitation on reducing the directional radiated FF noise of the SRSJ. The jet will again be operated across a range of NPRs from the overexpanded to the underexpanded flow regime to ensure detailed baseline and control results. For each NPR, the LAFPAs will be used to control the jet over a broad excitation frequency range to further investigate the physical relationship between coherent structures and trapped waves. There will be additional experimental tools, such as focused schlieren, utilized to further assess the effects of active control of CS on the TW beyond the acoustic signatures.

Acknowledgements

The support of this research by the Office of Naval Research, under grant number N00014-22-1-2227, with Dr. Steve Martens as well as an Ohio Space Grant Consortium scholarship for Mason Mitchell is gratefully appreciated. The author extends a special thanks to Abhi Yarlagadda, Noah Hiler, and Alyssa Brucchieri for their help in the collection of acoustic measurements.

References

Michalke, A., "Survey on Jet Instability Theory," *Progress in Aerospace Sciences,* Vol. 21, 1984, pp.159-199.

Samimy, M., Webb, N., Esfahani, A., and Leahy, R., "Perturbation-Based Active Flow Control in Overexpanded to Underexpanded Supersonic Rectangular Twin Jets," Journal of Fluid Mechanics, Vol. 959, A13, March 2023. http://doi:10.1017/jfm.2023.139.

Schmidt, O., Towne, A., Colonius, T., Cavalieri, A., Jordan, P., Brès, G.A., "Wavepackets and Trapped Acoustic Modes in a Turbulent Jet: Coherent Structure Eduction and Global Stability," *Journal of Fluid Mechanics,* Vol. 825, 2017, pp.1153-1181. https://doi.org/10.1017/jfm.2017.407.

Tam, C., Hu, F., "On the Three Families of Instability Waves of High-Speed Jets." *Journal of Fluid Mechanics*, Vol. 201, 1989, pp.447–483. https://doi.org/10.1017/S002211208900100X.

Towne, A., Cavalieri, A.V.G., Jordan, P., Colonius, T., Schmidt, O., Jaunet, V., Brès, G.A., "Acoustic Resonance in the Potential Core of Subsonic Jets," *Journal of Fluid Mechanics*, Vol. 825, 2017, pp.1113-1152. doi:10.1017/jfm.2017.346.

Zaman, K.B.M.Q., Fagan, A.F., Upadhyay, P., "Pressure Fluctuations due to 'Trapped Waves' in the Initial Region of Compressible Jets," *Journal of Fluid Mechanics,* Vol. 931, 2022. doi:10.1017/jfm.2021.954.

Zaman, K.B.M.Q., Bridges, J., Upadhyay, P., Brown, C., "'Trapped Wave' Resonance Tones Radiated in the Forward Arc of High-Speed Jets," NASA/TM-20240009873, 2024.

Design of a Force Transmission System Within a Real-Time Apogee Control System on a High-Powered Model Rocket.

Student Researcher: Seth Mitchell

Advisor: Dr. Joe Miller

Cedarville University
School of Engineering and Computer Science

Abstract
As part of the Cedarville University Mechanical Engineering Senior Design Capstone Course, a high-powered model rocket was designed for the NASA Artemis Student Launch Challenge. For the first time, airbrakes are integrated as a secondary experimental payload to dynamically alter the altitude of the rocket during flight using real-time data. The airbrakes consist of flaps actuated using a crank slider mechanism with a near-constant angular velocity ratio. The mechanical force transmission system was analyzed rigorously using computational (Computational Fluid Dynamics and Finite Element Analysis), analytical, and experimental techniques to determine both internal and external forces on the system. A lockup friction study was conducted for a Polyethylene Terephthalate Glycol collar on a carbon fiber rod to determine the coefficient of friction of this combination of materials. The controls system uses a probabilistic state space model, and the controller runs a Raspberry Pi Pico to control apogee. Full-scale tests are planned to validate the integrated system performance before final rocket delivery.

Project Objectives
The rocket altitude needs dynamically altered during flight. The solution is the secondary experimental payload called airbrakes (AB). Airbrakes control velocity in flight by inserting a control surface into an airstream to increase coefficient of drag. This is sort of like pumping a car's brakes, but it is one dimension in the air. The AB has seven success criteria as seen in AB.S.1-AB.S.7:

- AB.S.1 Confirmation of AB deployment during launch.
- AB.S.2 AB were stowed within ±2 seconds of apogee.
- AB.S.3 Rocket apogee achieved within ±25 feet of target altitude.
- AB.S.4 Confirmation of drag flaps actuation in the onboard camera.
- AB.S.5 The drag flaps should be located no further than 2 inches behind the CP to ensure aerodynamic stability.
- AB.S.6 No components of the system shall experience mechanical failure during any stage of flight.
- AB.S.7 No electrical brownout or blackouts shall occur.

Methods
The airbrakes are composed of three subsystems. First, the mechanical system is the physical actuation system. Second, the electrical system gives life to the mechanical system. Third, the controller is the brain of the operation, giving direction to the system while in use. The design process for the mechanical system was composed of six major steps.

1. Crank slider motion velocity analysis for a constant angular velocity ratio.
2. External fluid force analysis of the flaps.
3. Internal pin force analysis.
4. Kinematic analysis of lockup friction in the slider anchor.
5. Mechanical design and of FEA of the slider anchor.
6. Experimental testing.

The component names will be expounded upon for understanding within the context of the subsystem, but the subsystem with all components named can be seen in Figure 6. Overall, the process was to create a force transmission system which could jettison a control surface into the air and slow down the rocket, design a mechanical system which could take the force of this system, and then test the system mechanically and electrically.

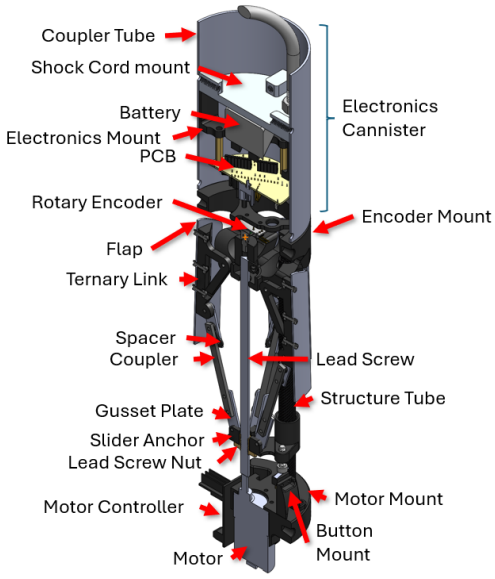


Figure 1. The final design of the airbrakes with names of all components.

Before any design took place, a preliminary design was drawn up based on the use case. This similarity between the initial design and the final design can be seen through its use of flap deployment, motor positioning, structure tube usage, lead screw crank slider, coupler links, and vent holes. This initial design drawing can be seen in Figure 2.

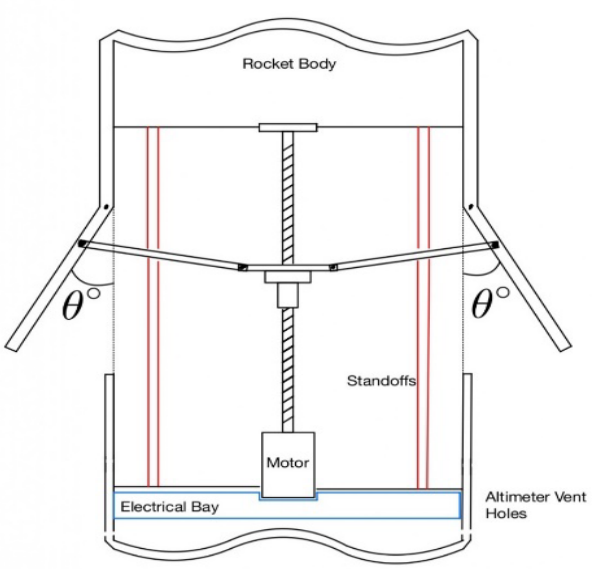


Figure 2. Drawing of preliminary airbrakes design.

To analyze and confirm the type of drag surface, a CFD model was tested in SOLIDWORKS. This CFD model was a comparative analysis of an arbitrary rocket with no breaks, blade brakes, and flap brakes as seen in Table 1. Since the highest amount of drag force was desired, the flap brakes were chosen as seen in Figure 6.7.2a. The number of flaps was in question, and because of force distribution is equal with two and four flaps, this was desired (as seen in Figure 2b). To determine the quantity of flaps, a comparative CFD analysis tested two, three, and four flaps. Overall, four flaps brakes were chosen for the drag surface.

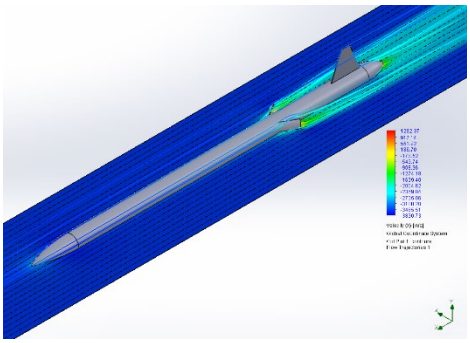


Figure 2a. Chosen airbrakes flap style in CFD.

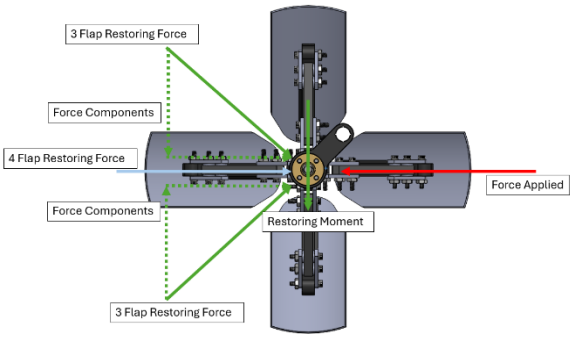


Figure 2b. Explanation of flap number using force vectors.

Table 1. Airbrakes flap style choice table. It compares the style of brakes with the amount of drag force they create.

Model Name	Drag Force [lb]
No Brakes	3.0
Blade Brakes	3.2
Flap Brakes	6.0

To create the force transmission system a kinematic analysis was conducted to determine the dynamics of the system. Figure 3a shows the first attempt where the pivot point of the system is on the airframe, the motion is created by a crank slider, and the flap is on the output link. This was not desirable because, as shown in Figure 4, the motion did not have a constant angular velocity ratio. A constant angular velocity ratio was the ideal output for this analysis because it allowed the flap to move upward linearly with the linear motion of the motor. Thus, as the motor controlled the system, it would not drastically, but gradually, change the position of the flap as it moved up and down the slider.

Therefore, to change the angular velocity ratio from 3:1 to 2:1 through the crank slider motion, an offset was introduced to the anchor point as seen in Figure 3b. The velocity ratio of each mechanism using graphical velocity methods at different positions. As seen in Figure 4, the angular velocity ratio of the revised mechanism was greatly improved to 2:1 throughout nearly the whole motion. As a bonus, the minimum transmission angle was $48.39°$, which means that the mechanism will never be close to toggle. Unfortunately, because of practical constraints, the kinematics of the system changed which made the design have a higher angular velocity ratio at the beginning (2:1) than at the end (1:1).

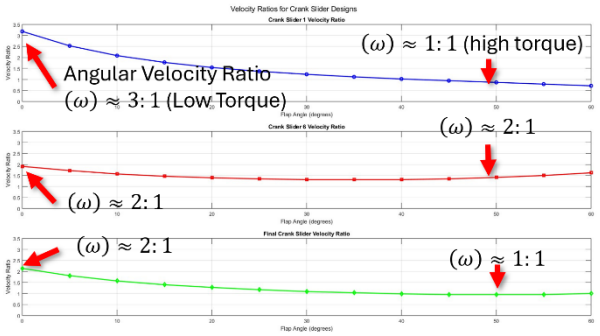


Figure 4. Comparative kinematic analysis of first design, updated design, and final design.

After this kinematic analysis, a fluid force analysis was conducted on the flaps (the first component of the force transmission system). A base line analysis was conducted earlier in the project using the newtons flat plate method which determined that each flap would receive approximately $6.85\,\frac{lb}{flap}$. This does not account for the wind speed decreasing as the flap angle increases, so another analysis was conducted later in the project (after airbrakes construction and testing) which determined a more accurate force profile over each flap as a function of both velocity and flap angle. This can be seen in Table 3. Still, because this information did not come into the project until late, the following analysis is presented as calculated with the base line answer.

Table 3. The most up to date force on flaps as a function of flap angle and velocity.

Angle	Drap Force Per Flap [lb]	Velocity [ft/s]
13.75	0.9024	577.05
27.5	2.3766	549.55
41.25	3.3797	518.52
55	3.6059	485.34

The next point in the force transmission system is the coupler from the flaps. The couplers are part of the mechanical system that can be seen in Figure 5. The gusset plates were analyzed as part of the coupler using the aluminum 6061 plate in double sheer technique. The screw (4-40 oxide steel) of the gusset plate would fail at $9.8150 \cdot 10^4[psi]$, but given the safety factor of two at an applied force of $6.85\,\frac{lb}{flap}$ the applied stress in the screw was $803.96\,[psi]$, thus the screw would not fail. Because the gusset plate was assumed to be under compression, the gusset plate was assumed to fail in bearing, so to avoid failure in bearing it needed to be $0.001318\,[in]$. This thickness is not practical, so it was thickened up for manufacturability to $\frac{1}{32}\,[in]$. The math for the mechanical design and kinematic analysis can be seen in the MATLAB code in Appendix A.1

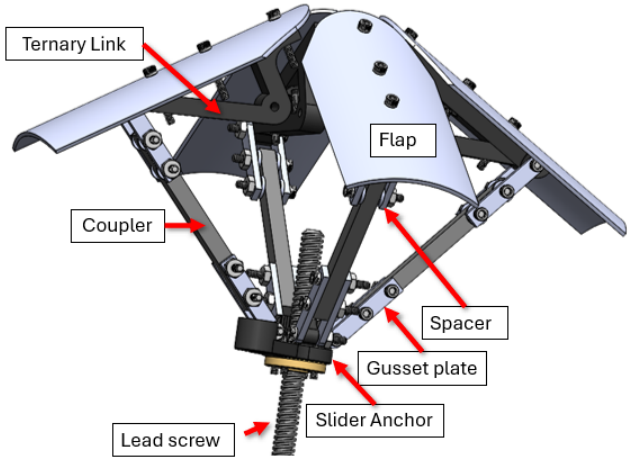


Figure 5. Airbrakes mechanical system.

The coupler was then tested in INSTRON machine, and experienced fiber reinforce anisotropic delamination in the carbon fiber pultruded rod. The coupler was connected to the machine in compression and experienced a compressive failure strength of $258\,[lb]$ which is about 19 times stronger than the expected force. This test 1. Verifies the coupler design by outperforming the needed force, and 2. Validates the calculations done because the calculations said the coupler would be 23 times stronger than needed and since the carbon fiber rod broke first it proves the calculations make sense.

The final point of the force transmission system is the slider anchor. It was designed using FEA where the coupler was assumed to be in compression on the slider anchor. For unique design and quick prototyping, the slider anchor was 3D printed. The maximum stress applied to the lug of the slider anchor is $1246[psi]$ which is much less than the ultimate compressive strength PETG at $8402.26[psi]$ (Figure 6). Thus, this meets the criterium for a safety factor of two. Unfortunately, the slider anchor lug failed in tension, which was not the assumption. The component was redesigned with thicker lugs and 3D printed from aluminum.

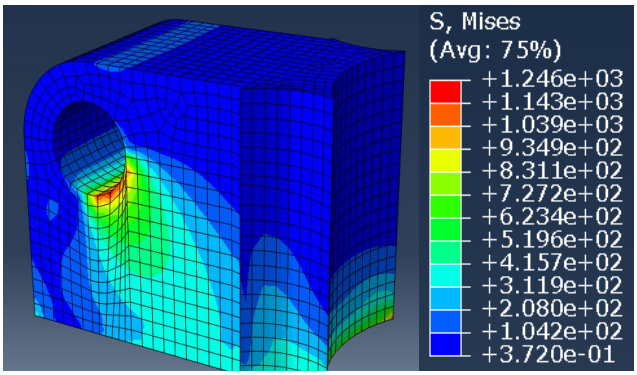


Figure 6. FEM of the loaded slider anchor lug.

The slider anchor needed a kinematic analysis for slider lockup friction. To determine the proportions of the slider anchor collar to avoid friction lockup a combination of analytical and experimental methods was used. First, static coefficient of friction (μ) was solved analytically using the static equilibrium equation. Then using the value found online for μ, a balance of the ratio between the critical dimensions of the collar drove the design. Once the first iteration was tested the critical dimensions were optimized (made smaller) to be practical until the smallest coefficient of friction was used that wouldn't cause lockup. The final coefficient of friction between PETG and carbon fiber was determined to be 0.3968 and where $\mu = \frac{dy}{dx_3}$. The airbrakes mechanical system was tested under load (Figure 7). The expected load of $3.6\ [lbs]$ was used for this test since it commenced after the final CFD calculations took place. To give the mechanism a performance margin of approximately 1.25, a load of $4.5\ \left[\frac{lbs}{flap}\right]$ was lifted in 2.1 seconds. This was accomplished by adding rubber bands to the springs to add more resistance to the flaps.

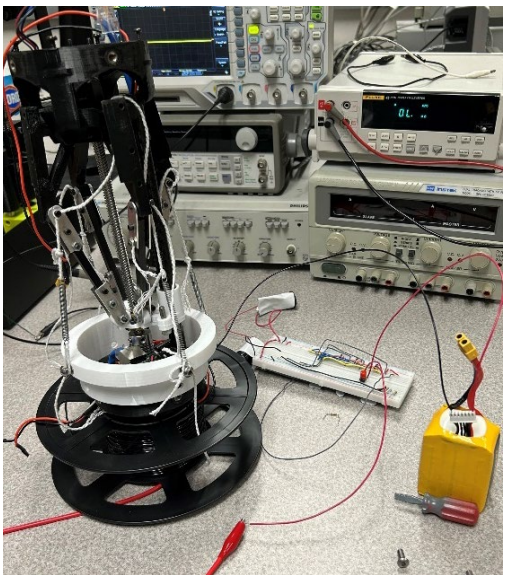


Figure 7. Final AB mechanism test setup.

The airbrakes consisted of more than a mechanical system, it incorporated an electrical and control structure. The electrical system was made up of a raspberry pi pico, SD card, a pressure sensor, an accelerometer, buck converter, speaker, end stop button, rotary encoder, 24V motor, and battery. The sensors are present to take in data and determine the state. The raspberry pi is the microcontroller of the system and handles all data, state logic, and decision making in flight. The buck converter reduces the voltage from the battery. The rotary encoder, motor, and button give the mechanical system life by turning it with the motor, tracking it with the encoder, and detecting the stop position with the button. The software of this system is handled by the ECE team of the SLI.

Results and Discussion

The airbrakes consisted of more than mechanical, but that was the focus of this research. Figure 8 shows the mechanical system actuating during the Vehicle Demonstration Flight and Payload Demonstration Flight. The control system did not work as expected, but the mechanical worked exactly as intended and brought the rocket to the apogee predicted by the P controller within an accuracy of 10 ft.

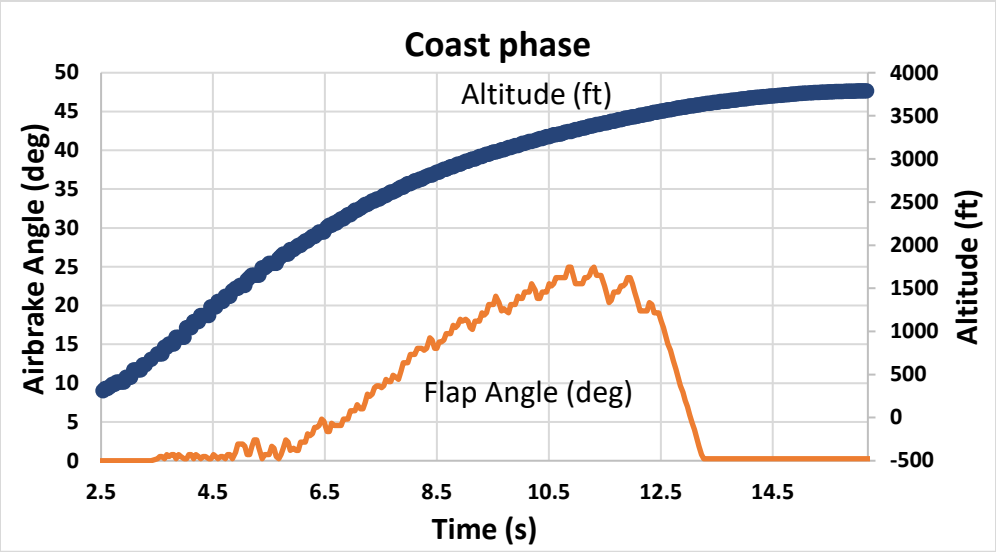


Figure 8. Flight data from VDF/PDF.

Acknowledgments

Dr. Clint Kohl, Dr. Thomas Ward, Dr. Joe Miller, Grant Parker, Daniel Hogsed, Joseph Copeland, Elisa Schmitt, Jack Kealen, Jesse DePalmo, Jackson Maley, Rebekah Porter, Kenneth Lee III, Arkin Solomon.

References

American Institute of Aeronautics and Astronautics. (2015). *S-120A: Section public review and co-ballot draft*. Retrieved October 25, 2024, from https://www.aiaa.org/docs/default-source/uploadedfiles/publications/standards/s-120a-sec-public-review-andco-ballot-draft.pdf?sfvrsn=ac4256aa_0.

Arduino. (2021). *Arduino® Nano*. https://docs.arduino.cc/resources/datasheets/A000005-datasheet.pdf

Athanasios P. Iliopoulos a, a, b, AbstractThe mechanical properties of the glass-epoxy composite material known as "G-10, Dasgupta, A., Lamberson, L., NEMA Standards Publication No LI 1-1998, 60893-3-1, I. I. S., MIL-I-24768, Zherlitsyn, S., Watt, T., Challita, A., Ravi-Chandar, K., Mechanical, E., & Shindo, Y. (2015, December 17). *Determination of anisotropic mechanical properties of G-10 composite via direct strain imaging*. Polymer Testing. https://www.sciencedirect.com/science/article/pii/S0142941815301094

Davies, M. (2021, September 16). *What Is the Density of PETG & How Does It Affect 3D Printing? - 3D Print Beast*. 3D Print Beast. https://www.3dprintbeast.com/petg-density/

Direcn. (2024). *ZYTD520 6V-12V-24V 10 RPM 37mm Geared DC Motor*. Https://Www.direnc.net/. https://www.direnc.net/zytd520-6v-12v-24v-10rpm-37mm-reduktorlu-dc-motor-en

DragonPlate. (2019). *What Is Carbon Fiber? | DragonPlate*. Dragonplate.com. https://dragonplate.com/what-is-carbon-fiber

Embedded, M. (2024). *Gearbox DC motor 12v ZYTD520*. Microscale Embedded. https://www.microscale.net/products/gearbox-dc-motor-12v-zytd520

Engineering Toolbox. (2004). *Metals and alloys - densities*. Engineeringtoolbox.com. https://www.engineeringtoolbox.com/metal-alloys-densities-d_50.html

Hartcher-O'Brien, J., Evers, J., & Tempelman, E. (2019). Surface roughness of 3D printed materials: Comparing physical measurements and human perception. *Materials Today Communications*, *19*, 300–305. https://doi.org/10.1016/j.mtcomm.2019.01.008

NAR. (2024). *Kevlar*. National Association of Rocketry. https://www.nar.org/educational-resources/model-rocket-building-techniques/kevlar/.

Norton, R. L. (2009). *Kinematics and dynamics of machinery*. McGraw Hill.

Performance Composites. (2009, July). *Mechanical Properties of Carbon Fibre Composite Materials*. Www.performance-Composites.com. https://www.performance-composites.com/carbonfibre/mechanicalproperties_2.asp

Philhower III, E. F. (2023, March 18). *Arduino-Pico*. GitHub. https://github.com/earlephilhower/arduino-pico

Plastics, T. (n.d.). *Pultruded carbon rods & tubes*. TAP Plastics. Retrieved October 25, 2024, from https://www.tapplastics.com/image/pdf/Pultruded_Carbon_Rods__Tubes.pdf

Ries, E. (2011). *The Lean Startup*. Portfolio Penguin.

Shojaie-bahaabad, M., Bozorg, M., Najafizadeh, M., & Cavaliere, P. (2024). Ultra high temperature ceramic coatings in thermal protection systems (TPS). Ceramics International, 50(7), Part A. https://www.sciencedirect.com/science/article/pii/S0272884223043080

The Engineering ToolBox. (2003). *Young's Modulus - Tensile and Yield Strength for common Materials*. Engineeringtoolbox.com; Engineering Toolbox. https://www.engineeringtoolbox.com/young-modulus-d_417.html

Singh, S., & Gupta, P. K. (2022). Investigations on tensile and flexural properties of wheat straw fibre reinforced polymer composite. *Advances in Materials and Processing Technologies*, 1–19. https://doi.org/10.1080/2374068x.2022.2153523

Zhang, D., & Huang, Y. (2021). Influence of surface roughness and bondline thickness on the bonding performance of epoxy adhesive joints on mild steel substrates. *Progress in Organic Coatings*, *153*, 106135. https://doi.org/10.1016/j.porgcoat.2021.106135

Restoration of a Hypersonic Wind Tunnel System

Student Researcher: Lincoln Montunnas

Advisor: Dr. Jesse Little

The Ohio State University
Department of Mechanical and Aerospace Engineering / Aerospace Engineering

Abstract
The Ohio State University (OSU) Aerospace Research Center (ARC) has a long history of working with high-speed wind tunnels. Several facilities were created in the past that have gone unused for many years. One such facility was a mid-scale hypersonic wind tunnel. This wind tunnel received supply air from an electric heating apparatus. Restoring this facility, with a focus on the electric heater, could be useful for performing long-duration tests that complement an existing large-scale impulse facility at the ARC.

Due to the time elapsed since its construction, documentation on the wind tunnel's design and capabilities is limited. By reviewing research conducted using the facility, it is possible to estimate the system's maximum capabilities. From this, viable testing conditions can be calculated where the heater could be used as a supply. Furthermore, the entire wind-tunnel system has been evaluated for overall sizing. Estimations have been performed to determine how long the wind tunnel system could run based on a provided vacuum chamber size and pressure. Once this is evaluated, the heater will be inspected for damage and returned to an operational state, where it will be used for supplying heated air to the mid-scale long duration hypersonic wind tunnel facility.

Project Objectives
The objective of the project is to determine the feasibility of repurposing existing equipment for use in a hypersonic wind tunnel. The purpose of utilizing this equipment will be to supplement the current large wind tunnel facilities with a smaller alternative that can produce longer run times. The maximum operational limits of the equipment should be determined, as well as what flight conditions the system can create.

Methods
The first step of the project was to source and review any literature covering the design and operation of the wind tunnel system. This was done by searching online OSU libraries as well as physical documentation located at the ARC. Once the existing literature had been reviewed, the collected data was used to calculate and plot performance envelopes detailing the capabilities of the system. Furthermore, the literature was used to tabulate information detailing the materials and design limitations of the air heater. All performance characteristics were calculated from Mach 2 to 14, and all computational scripts were written in MATLAB.

Results and Discussion
For all performance calculations, it was assumed that the heater and tunnel system could be supplied with dry air, and that any mass flow rate can be provided. The tunnel was assumed to have a nozzle that does not limit the overall capabilities of the system, and the diffuser was modelled as a normal shock at the exit of the test section. Real gas effects were not considered in this analysis.

Before conducting any analysis, material data was collected for the heating system, as well as maximum operational parameters. The operational limits of the tunnel were determined to be a maximum air

temperature of 1500 Kelvin, a maximum internal pressure of 27.5 megapascals, and a minimum flow rate requirement of 0.47 kilograms per second. Furthermore, it was determined that the internal wiring of the heater was created using Kanthal A-1 wire supported by alumina rods. The insulative material was FiberFrax, a type of ceramic fiber [1]. Obtaining the specific materials used is useful in case the heater is currently damaged or sustains damage in operation, as it will allow for matching material to be ordered for repair.

The first performance characteristic calculated was the range of possible density altitude the system could achieve at various Mach numbers. This envelope was calculated by first establishing a minimum temperature (based on the liquefaction of oxygen) and a maximum temperature (determined by the limits of the supply air heater). From the temperature span, a maximum and minimum density were calculated at each Mach number, resulting in Figure 1 shown below. The densities and corresponding altitudes were provided by the United States Standard Atmosphere [2]. This was done for both blowdown to atmospheric and blowdown to vacuum conditions. The vacuum system can provide pressures as low as 70 pascals (0.01 psi). The results suggest that the heater can provide flow well into the hypersonic regime at a large span of density altitudes. However, if the tunnel is exhausting to atmospheric pressure, it will not be able to operate higher than Mach 8.6 without liquefaction occurring. In blowdown to vacuum, the heater could supply air to all speeds in the Mach number range, with decreasing ability to operate at multiple density altitudes as the Mach number is increased.

The same process was used to calculate a range of total specific enthalpy and Reynolds numbers per meter. The results are shown below in Figures 2 and 3. Both results can be used to compare the capabilities of a tunnel supplied by this air heater to current tunnels at the OSU ARC. Finally, the run time of a tunnel using various test section diameters was calculated. The results of this calculation are shown below in Figure 4. The estimates suggest that if the tunnel was restored to operating condition, it could be capable of providing run times ranging from 10 to 160 seconds. However, these times were calculated assuming ideal scenarios and not accounting for engineering challenges in the design. In reality, a run time of 160 seconds at the required Mach 14 would pose significant structural and heating challenges and would likely not be possible. However, run times of even 20 seconds would be significantly longer than the existing OSU hypersonic tunnel and many other facilities around the country, suggesting that a tunnel of this nature could be very useful.

Figures

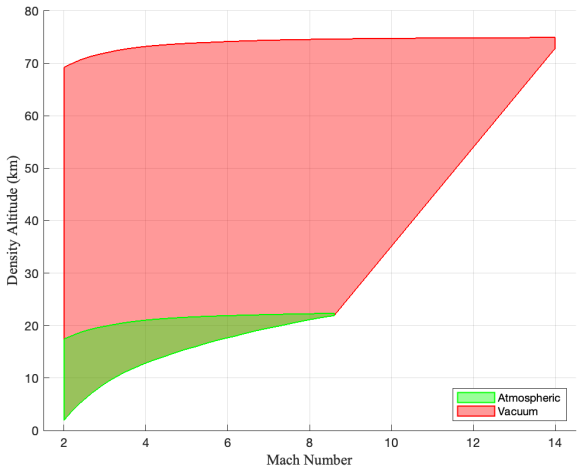


Figure 1: Estimation of what density altitudes can be created at each velocity. The performance is plotted for both blowdown to vacuum (in red) and blowdown to atmospheric (in green).

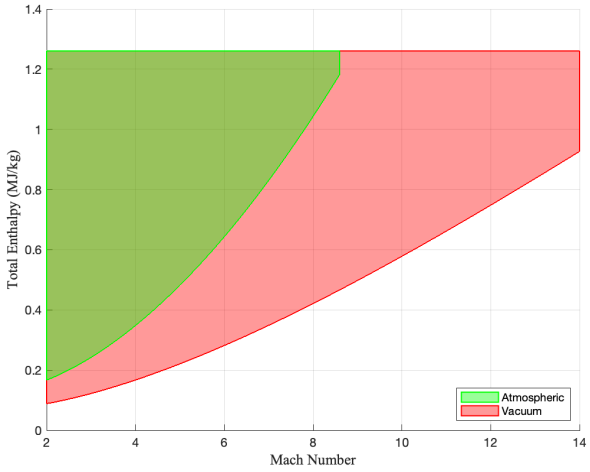


Figure 2: The range of total enthalpies that can be produced based on the operating limits of the heater.

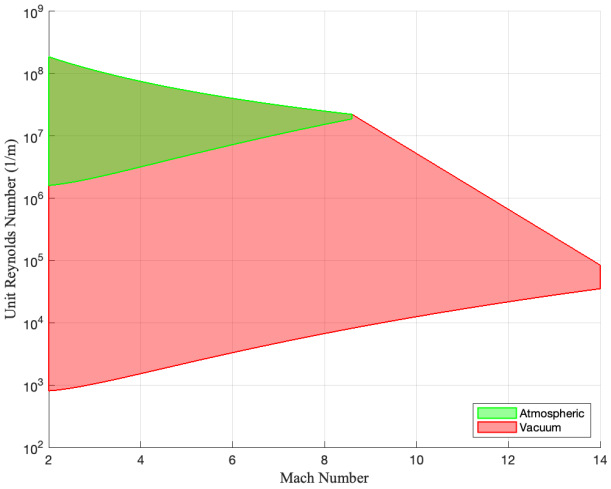


Figure 3: The range of unit Reynolds Numbers based on the capabilities of the heater.

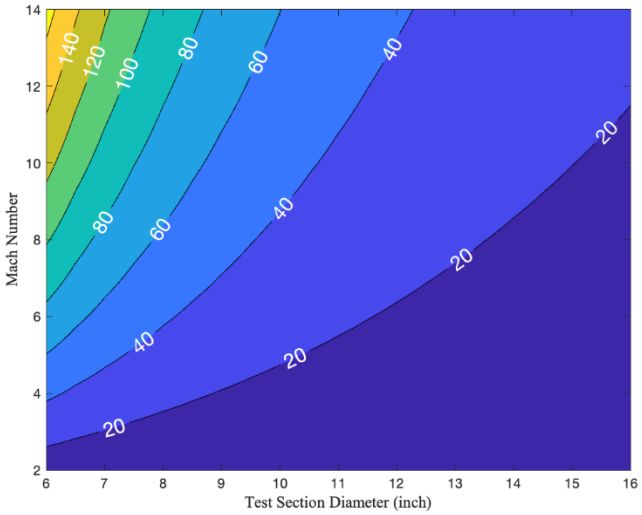


Figure 4: The estimated run time (in seconds) based on a given test section diameter and desired flow velocity.

Acknowledgments

I would like to thank Dr. Jesse Little and Dr. Nathan Webb for the guidance they provided during this project. I would also like to thank the Ohio Space Grant Consortium for providing the opportunity to present and complete this work.

References

[1] J. Lee and G. L. Von Eschen, "PRELIMINARY STUDIES, DESIGN AND THEORY, FOR THE OHIO STATE UNIVERSITY HYPERSONIC WIND TUNNEL," Aug. 1956.

[2] National, G., "U.S. standard atmosphere (1976)", Planetary and Space Science, vol. 40, no. 4, 1992. doi:10.1016/0032-0633(92)90203-Z.

Artificial Neural Network Models to Predict the Response to Capture These Super-elastic Load-unload Cycles

Student Researcher: Madisyn Moore

Advisor: Dr. Josiah Owusu-Danquah

Cleveland State University
College of Engineering, Civil Engineering

Abstract

Over the past years, several high temperature SMAs have been developed by NASA Glenn Research Center (NASA GRC) to design aerospace actuation components. In their application process, the actuator conforms to different shapes for each heating and cooling cycle under an applied bias stress. It is important to assess evolutionary behavior, i.e., changes in the stress-strain-temperature responses as these materials undergo hundreds to thousands of cycles. Mostly, such stress-strain-temperature characterization has been obtained through experiments that may be supplemented with predictive finite element constitutive models. For cases where it is important to study different SMA compositions, and material performance at thousands of cycles, most of the currently available models are not applicable. The objective of this research is to demonstrate why Artificial Neural Network (ANN) models are most suitable in predicting the cyclic, non-linear shape memory behavior of high-temperature SMAs, i.e., NiTiPd, and NiTiHf alloys, used to design aerospace and aeronautic structural components.

Project Objectives

- Improve my written and speaking communication skills
- Build upon previously learned knowledge of computational modeling and simulation tools
- Expand my understanding of the relationship between multifunctional material properties and their effect on structures
- Enhance my preparation for graduate school by learning basic skills of conducting research

Methods

This study involved conducting thorough literature reviews, critically analyzing data, and drawing conclusions based on evidence. Literature reviews aimed to find various articles and information related to the proposed research topic focusing on superelastic shape memory alloys. The literature review also explored novel applications of Shape Memory Alloys (SMAs), with an emphasis on their superelastic behavior. From this review, it was understood that superelasticity is a property exhibited by SMAs, describing the degree to which they are able to return to their original state they have been subjected to deformation. As part of the research study, we also looked at the various types of computational modeling, to determine the most suitable one that can be used to demonstrate the superelasticity behavior during the load and unload mechanical cycles.

Results and Discussion

The term smart material describes the ability of a material to exhibit unique or advanced functionalities beyond those observed in conventional materials. Shape memory materials belong to the class of smart materials because they can react to or change their shape in response to an environment or stimuli [1]. In general, we have two types of the memory materials, i.e., the shape memory alloys (SMAs) and shape memory polymers (SMPs). The most common type of the SMAs is the Nickel-Titanium based alloys. These materials exhibit several unique properties, but the feature that has much application in several

engineering devices is the superelastic behavior. Superelastic behavior show the relationship between stress and strain when SMAs are subjected to loading and unloading and their ability to return to their original shape [5]. In actuation applications, where the material must undergo several cycles, analysis of the response curve during each loading and unloading cycles gives insight to the number of cycles mechanical loading frequency before permanent deformation occurs. The degree of superelasticity is dependent on the number of cycles, load magnitude, and recoverable strain; the more cycles SMAs can withstand before failure indicates the higher amount of superelasticity [4]. An emphasis on functional fatigue and behaviors is considered to understand how the material is changing, specifically for the case of the commercially available SMAs Nickel-Titanium alloy.

Although superelastic behaviors provide useful functionalities, these responses are highly nonlinear [3]. Therefore, tracking the response whilst understanding the transformation is more complex. Capturing the superelasticity behavior is complex due to being nonlinear, unpredictable, and not having 100% certainty on the number of cycles it can withstand under the variable stresses, loading rates, etc. Modeling is an important aspect to study the behavior of SMAs. Typically, the numerical models can capture the experimentally observed responses but lose their accuracy over extensive loading conditions and with more complex structures. In the case of needing to predict the behavior for high cycle rate for loading and unloading, a more viable model is an Artificial Neural Network (ANN).

Artificial Neural Networks are a subsection of deep learning. What makes ANN so attractive is its ability to mimic, capture and predict SMA responses even under hundreds of cycles [7]. ANN is inspired by the biological neuron functions that were adapted for programming and technological advancement [3]. ANNs model the cells of the nervous system and humans major processing units to simulate actions of the nervous system in the brain [3]. ANN is an equipped model capable of handling more complex systems. Superelasticity behavior is nonlinear, therefore ANN is the most preferred option to capture such nonlinearities under cyclic load conditions.

Acknowledgments
Thank you to my advisor Dr. Josiah Owusu-Danquah, Cleveland State University, and The Ohio Space Grant Consortium for their invaluable guidance, support and encouragement throughout the course of this research.

References
[1]. Qader, Ibrahim & Kök, Mediha & Dagdelen, Fethi & Aydogdu, Yildirim. (2019). A Review of Smart Materials Researches and Applications. El-Cezeri Fen ve Mühendislik Dergisi. 6. 755-788. 10.31202/ecjse.562177.
[2]. Paulo Silva Lobo, João Almeida, Lúıs Guerreiro, Shape Memory Alloys Behaviour: A Review, Procedia Engineering, Volume 114,2015, Pages 776-783,
[3]. Hmede, R., Chapelle, F., & Lapusta, Y. (2022). Review of Neural Network Modeling of Shape Memory Alloys. *Sensors*, *22*(15), 5610. https://doi.org/10.3390/s22155610
[4]. Church, N. L., et al. "Functional fatigue during superelastic load cycling of Ti2448 (Ti-24Nb-4Zr-8Sn, wt%)." *Materialia* 28 (2023): 101719.
[5]. Vaidyanathan, R., Bourke, M.A.M. & Dunand, D.C. Texture, strain, and phase-fraction measurements during mechanical cycling in superelastic NiTi. *Metall Mater Trans A* **32**, 777–786 (2001)
[6]. Alshannag MJ, Alqarni AS, Higazey MM. Superelastic Nickel-Titanium (NiTi)-Based Smart Alloys for Enhancing the Performance of Concrete Structures. Materials (Basel). 2023 Jun 12;16(12):4333. doi: 10.3390/ma16124333. PMID: 37374517; PMCID: PMC10301377
[7] Owusu-Danquah, J. S., Bseiso, A., & Allena, S. (2022). Artificial neural network models to predict the responses of 55NiTi shape memory alloy under stress and thermal cycles. Neural computing and Applications, 1-14.

Effects of Freezing on Insulin Regulation of Intracellular Solute Concentrations in the Freeze Tolerant Spring Peeper (genus Pseudacris)

Student Researcher: Elias Ng

Advisor: Michael Mendel, Heather Kuruvilla

Cedarville University
School of Science and Math/Molecular Biology

Abstract

Man's exploration of harsh environments has often been informed by phenomena observed in animals. A prime example is the cryobiology (the study of life in cold, harsh conditions) of certain North American frog species. In this case, scientists have observed members of the frog genera Dryophytes, Pseudacris, and Rana, among others, which survive harsh North American winters. In the winter, these frogs undergo a frozen state, during which their body tissues and fluids freeze. Once spring arrives with warmer temperatures, these frogs are then able to re-emerge apparently unharmed by the process. Various studies have been conducted to explain the molecular pathways that lead to this amazing ability. Authors such as Storey and Storey have cited glucose and the associated insulin-glucagon pathway as an important cryoprotectant strategy for certain freeze-tolerant species in frogs such as wood frogs and leopard frogs. This study will specifically analyze the presence of the insulin signaling pathway in species of genus Pseudacris. To accomplish this, specimens of freeze-tolerant Pseudacris species were incubated, euthanized at different stages of entering into their frozen state, and preserved at -80 C so that their proteins could later be extracted and analyzed. Specimens from non-freeze tolerant species were also prepared in similar fashion, in order that their proteins could be compared to the freeze-tolerant species. The proteins extracted from these specimens were then analyzed using ELISA and western blot testing to characterize the proteins and compare insulin content between the extracts from these frogs.

Project Objectives

This project aimed to compare the relative insulin concentrations between the two frog species analyzed (*Pseudacris crucifer* and *Acris blanchardi*) and also between specimens subjected to three treatments (euthanizing before hibernation state, during hibernation state, and after coming out of hibernation state). The goal was to determine if there were any significant trends or differences between the species or treatments.

Methods

Protein lysate samples were prepared from skeletal muscle tissue of the *Pseudacris crucifer* specimens as well as *Acris blanchardi* specimens. These lysate samples were tested for insulin concentration using ELISA protein assays with a horseradish peroxidase-bound secondary antibody. Each frog lysate sample was added in either duplicate or triplicate to the ELISA plate, and the relative fluorescence of each sample well was measured using a fluorimeter. The relative fluorescence levels were used as indicators of relative protein abundance. Two western blotting tests were also performed using protein lysate from a green frog (*Lithobates clamitanes*). These tests were meant to confirm both the presence of insulin and that the ELISA antibody was effectively binding insulin.

Results and Discussion

The ELISAs were inconclusive due to several limiting factors. The array of protein bands observed on the Western blot suggest that the primary antibody participated in nonspecific binding (the bands observed did not match the molecular weight of the insulin protein). Overall, nonspecific binding and/or failure of antibody to bind antigen likely masked significant trends in insulin abundance between samples. In addition, the inconsistencies in the standard curves between the different ELISAs made it difficult to compare the relative fluorescence values between different ELISA trials. The insulin concentrations did not follow a linear progression and in the second trial, some of the samples showed negative fluorescence values, suggesting protein degradation.

While the hypothesis was not supported, there was also not enough data to conclusively deny it. This experiment showed that direct protein analysis was not sufficient to directly detect insulin levels, due in part to troubles with the insulin standard curve and nonspecific binding of the primary antibody. An alternative method of analysis, such as quantifying the levels of microRNAs encoding for insulin production may be more accurate and precise.

Figures/Charts

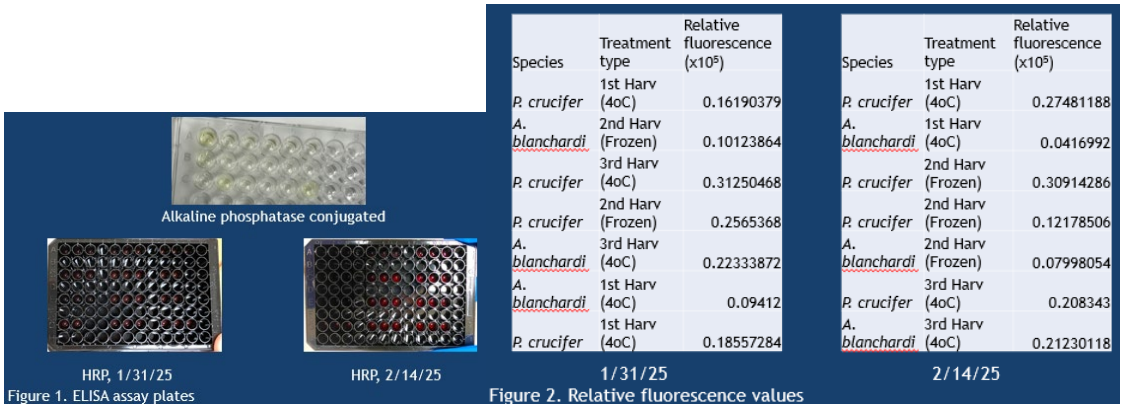


Figure 1. ELISA assay plates

Species	Treatment type	Relative fluorescence (x10⁵)
P. crucifer	1st Harv (4oC)	0.16190379
A. blanchardi	2nd Harv (Frozen)	0.10123864
P. crucifer	3rd Harv (4oC)	0.31250468
P. crucifer	2nd Harv (Frozen)	0.2565368
A. blanchardi	3rd Harv (4oC)	0.22333872
A. blanchardi	1st Harv (4oC)	0.09412
P. crucifer	1st Harv (4oC)	0.18557284

1/31/25

Species	Treatment type	Relative fluorescence (x10⁵)
P. crucifer	1st Harv (4oC)	0.27481188
A. blanchardi	1st Harv (4oC)	0.0416992
P. crucifer	2nd Harv (Frozen)	0.30914286
P. crucifer	2nd Harv (Frozen)	0.12178506
A. blanchardi	2nd Harv (Frozen)	0.07998054
P. crucifer	3rd Harv (4oC)	0.208343
A. blanchardi	3rd Harv (4oC)	0.21230118

2/14/25

Figure 2. Relative fluorescence values

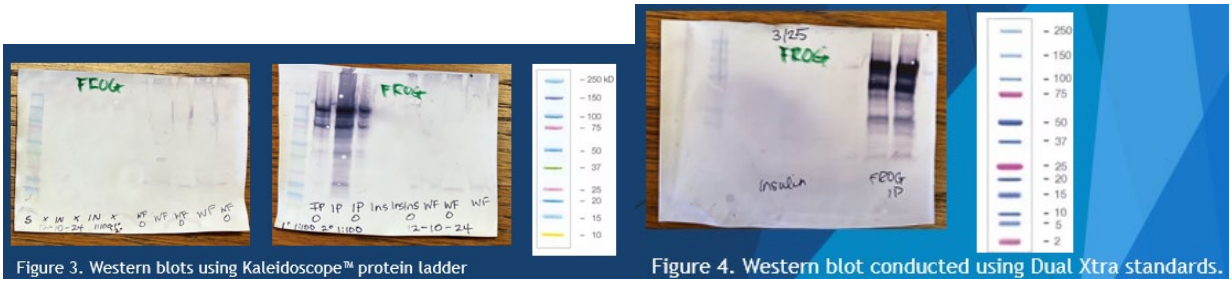


Figure 3. Western blots using Kaleidoscope™ protein ladder

Figure 4. Western blot conducted using Dual Xtra standards.

Acknowledgments

I am grateful to my advisors, Dr. Michael Mendel and Dr. Heather Kuruvilla for all their help and input on this project. I am also grateful to the Ohio Space Grant Consortium for providing the scholarship which allowed me to conduct this research and also to Dr. Robert Chasnov, who helped facilitate this scholarship opportunity.

References

Storey, K. B. & Storey, J. M. (2017). Molecular Physiology of Freeze Tolerance in Vertebrates. *Physiological Reviews, 97*(2), 623-665. doi: 10.1152/physrev.00016.2016

Design of Haptic Actuators using Smart Materials for Virtual Reality Applications

Student Researcher: Jack Nomina

Advisor: Dr. Jeong-Hoi Koo

Miami University
Department of Mechanical and Manufacturing Engineering

Abstract
This research is centered on two important technological concepts: haptic systems and smart materials. Haptic systems are methods to receive tactile feedback from digital electronic systems, like how a cell phone vibrates upon a notification's appearance. Smart materials are generally defined as materials that have been designed to respond in a certain predictable way to an external stimulus. The question posed by this research is simple: how can smart materials be implemented to create improved haptic feedback systems? Currently, this research is being conducted by testing the responsiveness of Electro-Rheological (ER) Fluid (a smart material liquid that becomes more viscous as it is exposed to an electric field) to different stimuli. ER Fluid is a dark brown petroleum-based liquid smart material, consisting of a base as well as many small particles. When exposed to an electric field, the particles in ER fluid will align in the direction of the field, providing tactile resistance, which has the potential to be used to create haptic sensations. There is an increasing demand for vibrotactile feedback in various modern industries. Sensory information improves user experience, and can even be essential for some users with sensory impairments.

Project Objectives
The objective of this research is simple: to design and fabricate flexible haptic modules that can provide variable resistance to depression using ER Fluid stimulated by varying input voltages.

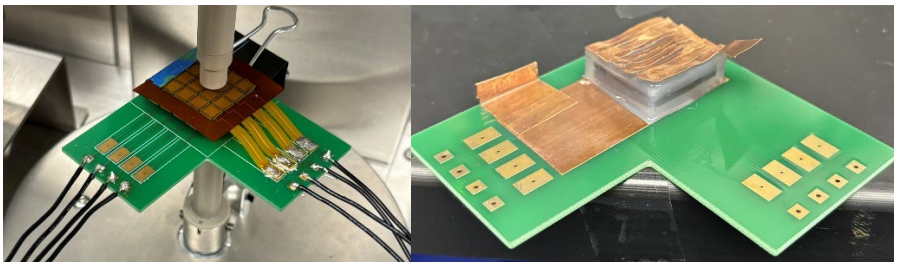
Methods
Flexible haptic modules were designed to consist of elastomers made using EcoFLEX© 30 Resin. Each module was fabricated in 2 parts using molds. Dimensions for the module were determined by the student researcher and Dr. Koo to minimize size while allowing for fluid activation. Once modules were fabricated, A Dynamic Mechanical Analyzer (DMA) was used to perform depression tests on the completed prototypes. Tests were performed with indentations of 1mm and 2mm for various input voltages, with an indentation speed of 1mm/s. Following testing, data for normal force (g) and indentation distance (mm) was collected, then MATLAB was used to process this data. For this round of testing, 2 different types of haptic modules were considered, with the key difference between the two being the type of electrode used to generate their electric field. The first module tested used a wire mesh electrode, while the second used a copper tape electrode.

Results and Discussion
Between the two modules tested, only one displayed any type of electric field activation. The mesh electrode failed to display any differentiation between different voltage inputs, meaning that the ER Fluid inside the module failed to activate. There are many possible reasons for this, however the first hypothesis explored was that the mesh electrode did not provide significant enough coverage to generate a strong electric field. The next module tested, the copper electrode, alleviates this with more consistent coverage of the module. The copper electrode module did display some differentiation between tests, however not

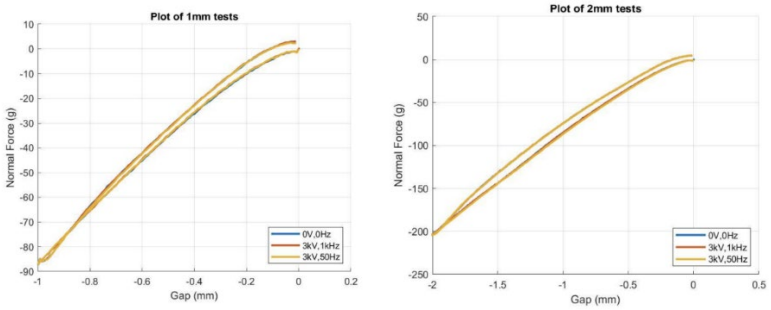
in the way that was expected. The expected outcome for fluid activation was that more force would be required in order to depress the module the same distance. What happened instead is that there was some damping present, but no change in required force. This means that the fluid did activate to some extent with different voltage inputs, however since the desired results were not achieved, more modules should be fabricated and tested in the future. Possible next steps to take include fabricating a less flexible module (in case the bending of the electrode is disrupting the electric field) or fabricating a thicker module (in case the amount of fluid present is not enough to sufficiently stiffen the module).

Figures/Charts

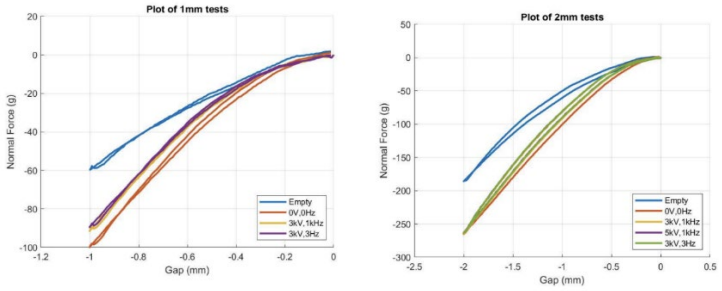
Images of Mesh (left) and Copper Tape (Right) Electrode Modules



Plots of 1mm and 2mm tests for Mesh Electrode Module



Plots of 1mm and 2mm tests of Copper Tape Electrode Module



Acknowledgments

I would like to acknowledge Dr. Jeong-Hoi Koo and Dr. Tae-Hyeon Yang for their guidance and support throughout this research process.

Experimental Investigation of PRANDTL-D3C Near-Wake

Student Researcher: Julian Pabon

Advisor: Sidaard Gunasekaran

University Of Dayton
School of Engineering/Mechanical Engineering

Abstract

The disappearance of the tip vortex in the near wake of a wing challenges conventional aerodynamic theories and presents new opportunities for drag reduction. Recent computational studies suggested that the PRANDTL-D3C wing—a swept, multi-element, and tapered wing with a bell-shaped lift distribution—exhibits this tip vortex disappearance. The current study explores the wake topology underlying this claim experimentally and numerically. Force-based and Particle Image Velocimetry (PIV) investigations were conducted on a 1:11 half-span scaled model of the PRANDTL-D3C wing to characterize the wake at various angles of attack. All experiments were performed in the University of Dayton Low Speed Wind Tunnel (UD-LSWT) using an open-jet test section configuration. Streamwise PIV was conducted at a chord-based Reynolds number of 185,000 across different spanwise stations to characterize the near-wake momentum deficit, and the non-planar wake formation. The experimental results showed a strong correlation between the wake velocity momentum deficit profiles and the FlightStream® panel method simulations, confirming reduced momentum deficit drag near the wingtips and higher aerodynamic efficiency compared to an elliptical lift distribution without a span increase at the design condition. Additionally, the analysis demonstrated that the near wake at this angle of attack lacks evidence of a trailing vortex, providing experimental validation of the computational predictions. However, to conclusively confirm the absence of the vortex, cross-stream PIV measurements are required to capture the full three-dimensional wake structure.

Project Objectives

The PRANDTL-D3C wing, based on Ludwig Prandtl's 1933 theory [1], can, under certain conditions enhance aircraft efficiency and facilitate coordinated turns without the need for rudder through its bell-shaped lift distribution. However, it is important to note that these advantages require a 22.5% increase in wingspan compared to wings with an elliptical lift distribution. For wings without an extended span (or with a span constraint), the elliptical lift distribution remains the optimal choice at the design C_L, which is mostly targeted at the cruise condition. In an elliptically loaded wing, the lift distribution gradient approaches infinity at the wingtip to satisfy zero circulation, resulting in strong tip vortex formation [2]. A marked discontinuity exists between the upwash and downwash at the wingtip, indicative of a strong vortex. However, with the bell-shaped lift distribution, due to the shift of the center of lift inboard of the wing, the wingtips are lightly loaded, which can result in a near zero-lift distribution gradient at the wingtips. This is evidenced by the smooth transition between the upwash and downwash, occurring inboard of the wing and producing a "wing vortex" rather than a wingtip vortex. The presence of a wing vortex has been confirmed through flight tests [3] and wind tunnel tests [4] across a range of operating conditions. Overall, the goal of this project is to experimentally verify and characterize the wake signature of the PRANDTL-D3C model

Methods

All experiments were conducted in the University of Dayton's Low Speed Wind Tunnel (UD-LSWT) using its open-jet test section configuration. The tunnel is an open return type and has a 16:1 contraction ratio, six anti-turbulence screens, and a 0.762 m by 0.762 m open-jet test section. The effective length of the test section is 0.183 m. A 1.128 m by 1.128 m collector gathers the expanded air into the diffuser. A pitot tube is connected to a Siemens QBM-3230-U5D analog pressure transducer to measure the freestream velocity during the experiments. A TSI T600 Micromanometer was used to calibrate the pressure transducer, and an NI-USB-6259 DAQ was used to collect the pressure transducer data at the same sampling rate as the F/T transducer.

A 1:11 scaled model of the PRANDTL-D3C wing was fabricated using 3D printing. The wing's dimensions and twist distribution were obtained from [3] and [5]. The model has a 25-inch span and a mean aerodynamic chord of 3.5 inches and was tested at a Reynolds number of 185,000. Images of the experimental setup are shown in Figure 1. The wing model was mounted to a rotary stage and an ATI Gamma F/T balance assembly. The sensor's calibrated

uncertainty was 1.25% for the Y-axis, which measures the wing's normal force, and 0.75% for the X-axis, which measures the wing's axial force. A 0.914 m x 1.829 m splitter plate enabled half-span model testing of the wing.

Streamwise Particle Image Velocimetry (PIV) was conducted downstream of the trailing edge to capture the wake at various locations along the span, as shown in Figure 2a. Due to the sweep angle of the model the captured field of view (FOV) is located at different downstream distances from the wing trailing edge. The distance from the trailing edge is furthest at the root showing a more developed wake. The experiment utilized a ViCount smoke machine to seed the wind tunnel with particles. A Quantel ND-YAG dual-pulse laser (Quantel Twin CFR 300), in combination with a plano-concave lens and a mirror, was used to produce a laser sheet that illuminated a streamwise plane. The laser and an Imperx B2021 camera with a 100 mm lens were triggered simultaneously using a Quantum Composer pulse generator. The PIV setup in the UD-LSWT is shown in Figure 2b. The time delay between laser pulses was set to achieve an 8 to 10-pixel particle displacement in the free shear layer. For each run, 1,000 image pairs were captured and processed using Fluere [12]. Two iterations were performed in the DPIV processing: the first iteration used 64-pixel interrogation windows, and the second iteration used 32-pixel interrogation windows. All components were mounted on an optical bench supported by a linear rail to allow for spanwise translation.

Eleven different spanwise stations were interrogated, with refined spacings between the interrogation planes closer to the wingtip. The field of view (FOV) was consistent for the first eight regions. Since the wing model has a 5° dihedral, the FOV for the spanwise stations closer to the root had to be lowered in the Z-direction and was made slightly larger than the outboard FOV. The Reynolds number was maintained at 185,000 for all cases, and PIV was conducted at each spanwise station at six different angles of attack. Note that α_Wing in Table 1 is defined as the angle of attack at the root chord of the wing, consistent with the nomenclature used by Hammer and Garmann [5].

FlightStream® [6] was used to numerically investigate the same model geometries tested in the wind tunnel to obtain the surface pressure distribution on the PRANDTL-D3C wing. FlightStream® includes two main types of potential flow solvers: a pressure-based solver and a vorticity solver. The pressure-based solver, which utilizes the pressure fields on the model geometry to determine the aerodynamic loads, is used in the present study. A combination of source and sink panels, along with doublet panels on the trailing edge, is employed to provide a solution for the pressure-based potential flow solver. For the current study, the pressure-based solver was selected based on its good agreement with the wind tunnel experimental results in our previous studies [8–11]. The boundary layer is assumed to be fully turbulent, with viscous coupling enabled. The surface mesh of the wing and the splitter plate in FlightStream® is shown in Figure 3. The wing platform has a structured mesh with 120 node points spanwise and 80 node points chordwise on both the upper and lower surfaces. The chordwise mesh also has a dual-side growth rate of 1.05 to better resolve the leading and trailing edge geometry. Additionally, a splitter plate of the same size as the one used in the wind tunnel experiment is included in the model to better represent the actual experimental conditions (minus the boundary layer growth and interaction). The splitter plate has 60 node points from side to side and 120 node points downstream.

Results and Discussion

The aerodynamic coefficients comparing results from experiments, FlightStream® simulations, and findings from Hammer and Garmann [5] are shown in Figure 4. The C_L results show good agreement between the simulations up to the point of stall. Differences in the stall angle of attack may be attributed to variations in Reynolds numbers between the simulations conducted by Hammer and Garmann (Re = 300,000) and the experiments performed at the UD-LSWT (Re = 185,000). The drag coefficients from the various methods also show good agreement, with the highest drag observed in the experiments, as expected. Since the FlightStream® results closely align with the experimental data, they can be utilized to visualize the wake rollup process.

The near-wake simulation results are compared between Hammer and Garmann [5] and FlightStream® at an 8° angle of attack, as shown in Figure 5. Both simulations indicate that no trailing vortices are present at this angle of attack, which appears to be a unique feature of the PRANDTL-D3C wing's bell-shaped lift distribution. The absence of trailing vortices suggests reduced drag. The mitigation of strong wingtip vortices observed in elliptically loaded wings can be attributed to shifting the lift distribution inboard and reducing the loading at the wingtips Furthermore, as illustrated in Figure 5c, the 8° angle of attack corresponds to the point of maximum aerodynamic efficiency (L/D), as evidenced by all three investigation methods (experiment, FlightStream®, and RANS). The variations in the maximum L/D

between different cases are attributable to slight differences in predicting C_D, as shown in Figure 4b. Nevertheless, the correlation between the angle of attack with no trailing vortices and maximum L/D provides insight into the optimal aerodynamic efficiency of the PRANDTL-D3C design. However, the factors underlying the disappearance of the wingtip vortex at this angle of attack remain experimentally unproven and the associated aerodynamic features leading to this condition are yet undescribed in the literature. Addressing this gap is one of the research objectives of the current study

The delayed wake rollup process observed by Ranjan and Ansell [7] can also be replicated by FlightStream®, which operates based on the panel method. The delayed wake rollup is observed in the wake of the Prandtl-D at an 8° angle of attack. According to the FlightStream® simulations, one full rotation of the trailing vortex occurs at approximately 100 x/c, which aligns well with the results published by Ranjan and Ansell [7].

A streamwise average of the drag coefficient was determined along the span to analyze the changes with angle of attack using different normalizations, as shown in Figure 6. The differences in normalization techniques highlight the sensitivity of drag distribution to chord length variations. Figure 6a shows the drag normalized by $\bar{c}$, and Figure 6b shows the drag coefficient normalized by the local chord. Normalizing by the local chord (Figure 6b) appears less effective in capturing momentum deficit changes due to the varying chord lengths across the span, while the global chord normalization in Figure 6a better reflects drag trends. However, all cases display a nonlinear drag distribution, mirroring the downwash characteristics associated with the bell-shaped lift distribution. This finding is consistent with Hammer and Garmann's [5] study and reflects the downwash distribution associated with the bell-shaped lift distribution.

At $\alpha_{Wing} = 0°$, the location of minimum drag is positioned at $y/(b/2) = 0.4$. Increasing the angle of attack shifts the location of minimum drag further toward the wingtip, which could be correlated to the movement of the wing vortex. As α_{Wing} increases, the drag coefficient also rises at all span locations, except at 8° and 10°, where a reduction in drag starting from 60% of the span is observed. This trend is particularly evident in Figure 6c, which shows the drag coefficient normalized by the 0° case. Figure 6c also reveals that the increase in drag is uniform at 2° across all span locations; however, this increase becomes nonlinear after 4°, with a higher increment in drag observed closer to the root.

The normalized W component of velocity in the wake of the wing is shown in Figure 7 for each of the angles of attack tested. The same spanwise stations of $\alpha_{Local} = 0°$, and $|\alpha_{Local}|_{Max}$ are included here, along with the spanwise location where $W/U_\infty = 0$, indicating the transition from downwash to upwash. It is hypothesized that under certain conditions a vortex forms at the spanwise location where $W/U_\infty = 0$. However, cross-stream PIV needs to be conducted to identify under what set of conditions are necessary for this to occur. Starting with the inboard segments of the wing, as the angle of attack increases, the blue region of downwash increases from a moderate magnitude within the first quarter span at 0° to a more intense magnitude at 10° that further extends along the span. The location and proximity of $\alpha_{Local} = 0°$ do not appear to impact the transition from downwash to upwash, as these locations become increasingly distant from each other between 4° and 8°, suggesting a strong three-dimensional velocity component responsible for their separation at these angles of attack.

The location of $W/U_\infty = 0$ shifts gradually outboard from 0° to 8° and then makes a large jump from 8° to 10°, likely due to the nonlinear twist, which changes at a greater rate around $y/\bar{c} = 0.7$. As the upwash moves toward the outboard wing section, the magnitude of the vertical velocity increases to a maximum of $W/U_\infty = 0.1$, indicating very intense upwash at 10°. At 8°, approximately one-third of the wingspan produces upwash, while the remaining two-thirds generate downwash in the inboard segments. The tip region shows a strengthened area of upwash, but not as intense as at 10°, where there is a noticeable increase in upwash intensity near the tip.

The PIV data was used to generate isosurfaces of the W velocity, while the FlightStream® data was used to create long-form streamlines in the wing's wake, extending up to 40 chord lengths downstream. Together, in Figure 8, this overlay of data shows a relationship between the near-wake velocity measurements and the far-wake vortex rollup at $\sim 40\ x/\bar{c}$ if such a superposition can be entertained. The alignment between the PIV isosurfaces and the spanwise location of upwash growth with the downstream wake rollup of the FlightStream® streamlines is in good agreement. It should be noted that the rear view of the wake streamlines represented in Figure 8 is more than 40 chord lengths away and for most angles of attack, one full rollup of the vortex is not complete. Nevertheless, the formation of

upwash appears to play a critical role in the inboard movement of the wingtip vortex, indicating that the bell-shaped lift distribution effectively influences downstream vortex positioning. A dedicated cross-stream PIV study is needed to fully understand the extent to which the lift distribution, angle of attack, and associated upwash profiles play a role in the development and location of the wing vortex.

The W velocity data from the current study's PIV is compared to the Hammer and Garmann simulations [5]. There is strong agreement between the two with respect to the formation of an upwash region near the tip of the wing, which decreases as the angle of attack increases. Additionally, the growth of a downwash region near the inboard section of the wing is prominent in both data sets, with this region expanding as the angle of attack increases. Notably, the general trends in the global wake profile observed in the PIV data are captured by the RANS simulations, showing relatively similar regions of upwash and downwash behavior and magnitude across the span. This agreement builds confidence that the RANS simulations are accurately capturing trends in the wake flow field and can be used to further explore changes to the geometry and their impact on the wake profile.

Figures/Charts

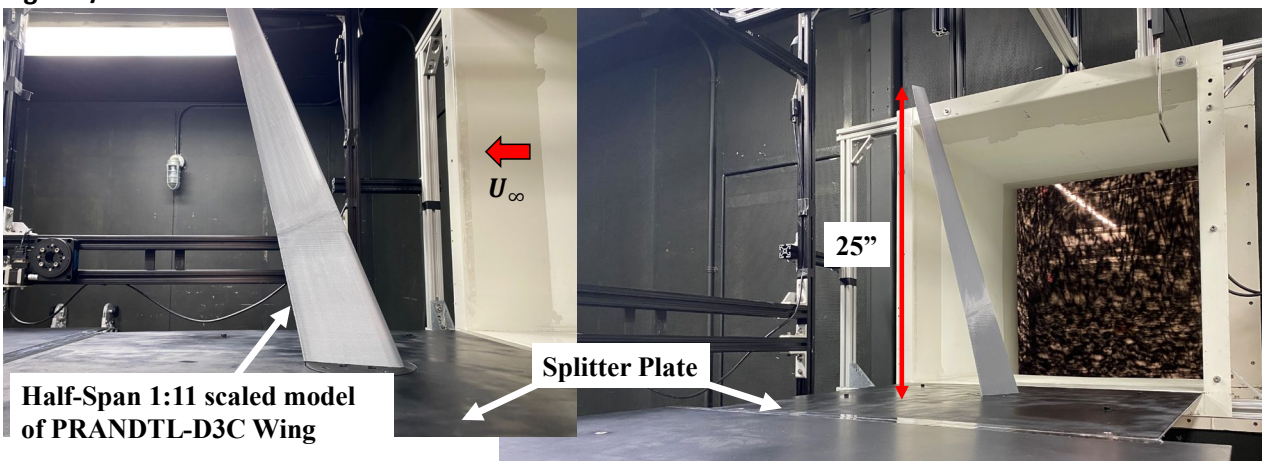


Figure 1 Force-based experimental setup of scaled PRANDTL-D3C model at the University of Dayton Low Speed Wind Tunnel

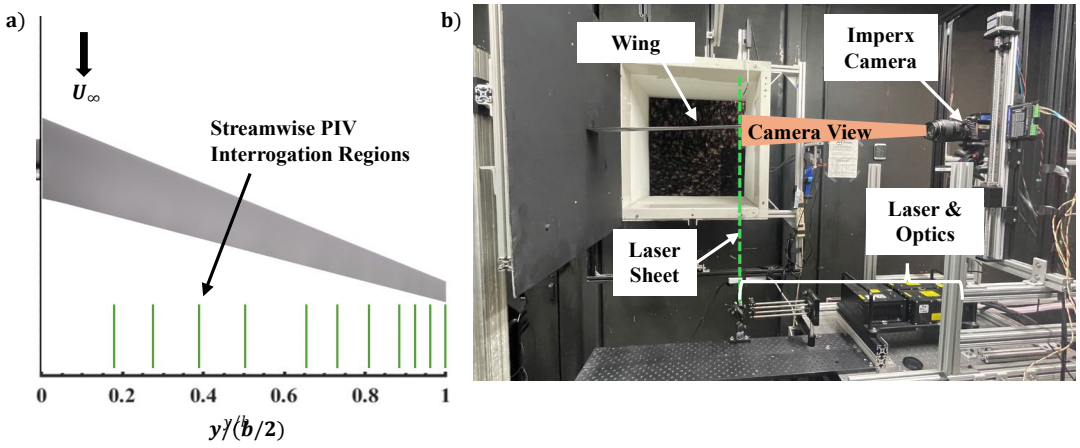


Figure 2 a) Local Y location of PIV planes along the spanwise direction b) PIV setup in the UD-LSWT

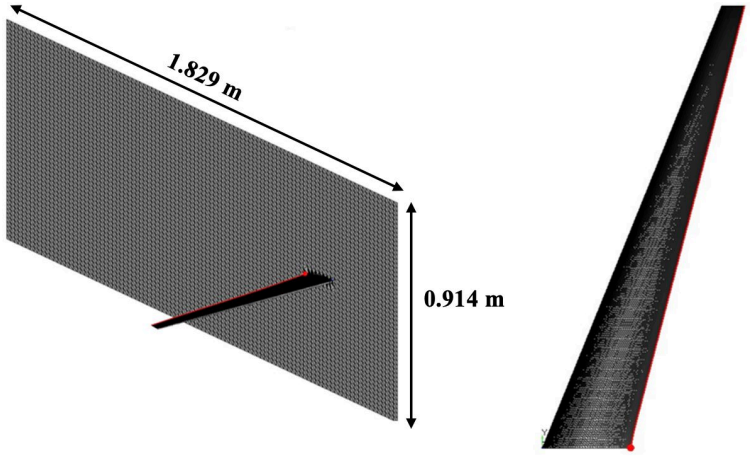


Figure 3 Surface Mesh in FlightStream® for a) Isometric View of the Wing & Splitter Plate and b) Top View of the Wing

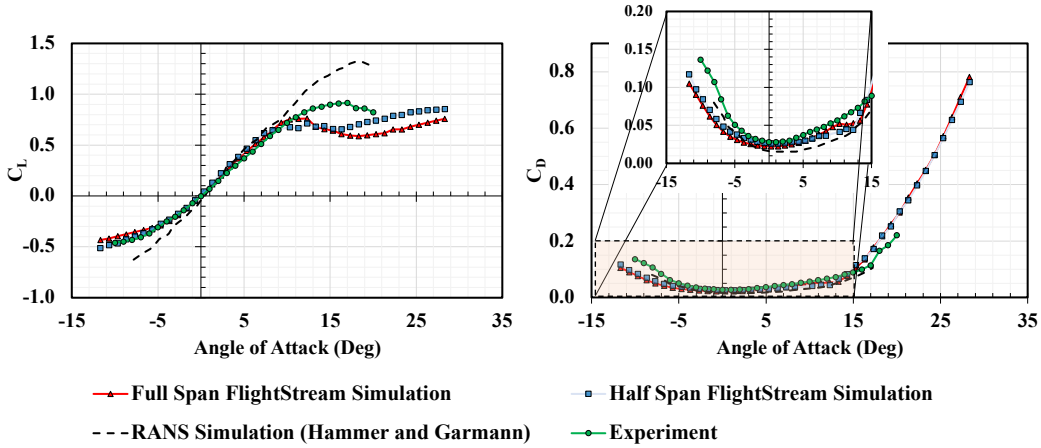


Figure 4 Comparisons of Coefficient of lift and coefficient of drag as a function of angle of attack among experiments, FlightStream® simulations and RANS simulation from [5]

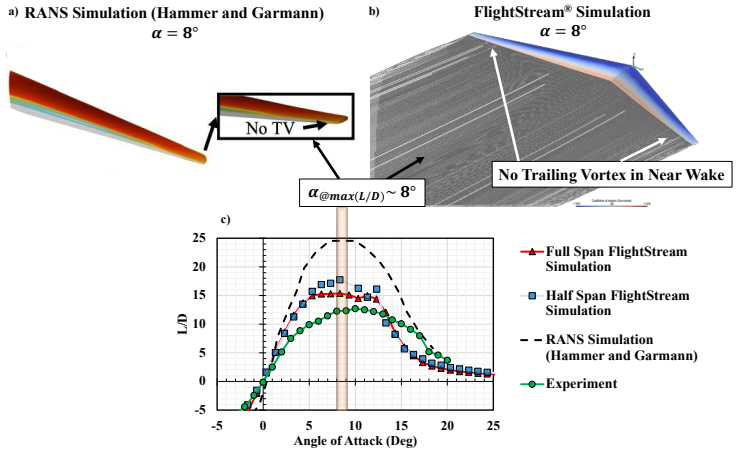


Figure 5 Simulation results a) from Hammer and Garmann [5] b) FlightStream® of PRANDTL-D3C wing at 8° angle of attack. c) Variation of aerodynamic efficiency as a function of angle of attack from FlightStream®, experiments, and RANS simulation from Hammer and Garmann [5]

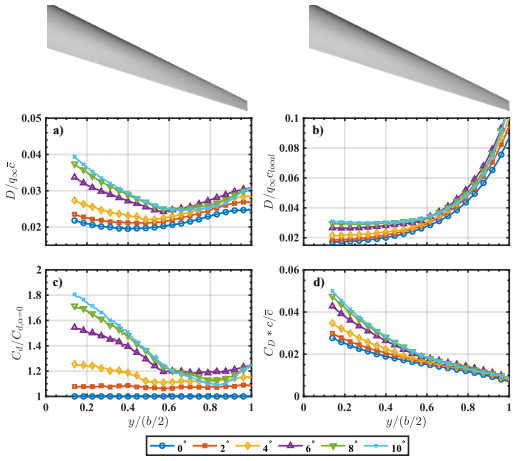


Figure 6 a) Drag coefficient along the wingspan normalized by a) MAC, b) local chord, c) Drag coefficient normlized by drag coefficient at $\alpha = 0$ at different α_{Wing}, and d) $\bar{c}/c$.

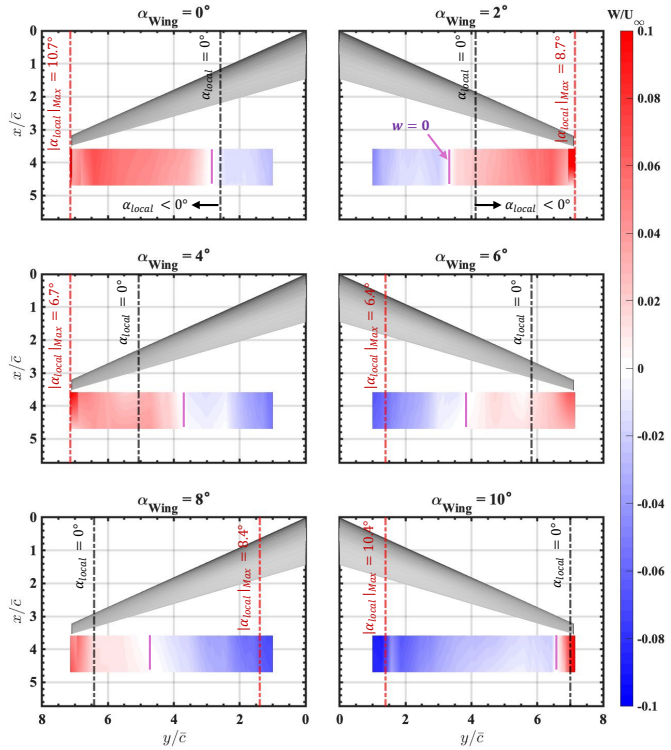


Figure 7 Variation of W/U_∞ velocity on the wake centerline curvature along the wingspan at different α_{Wing}

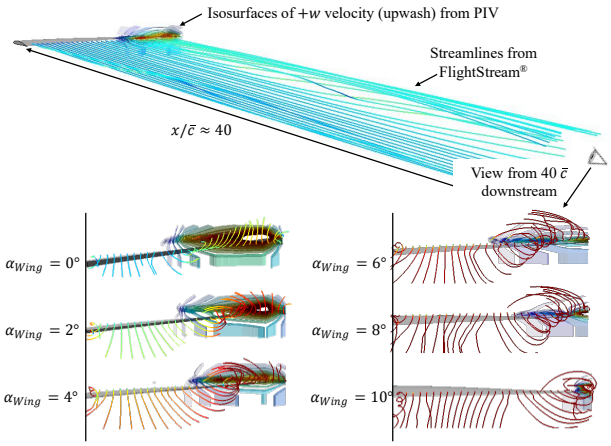


Figure 8 Overlay of +W velocity contours from PIV and wake streamlines from FlightStream at different α_{Wing}

Acknowledgments

The authors would like to thank OSGC for supporting the creation of the work presented as well as Grace Schreyer, Michael Mongin, and Aaron Altman who helped to complete the study.

References

[1] Prandtl, L. "Über Tragflügel Kleinsten Induzierten Widerstandes." Zeitschrift für Flugtecknik und Motorluftschiffahrt 24 (1933): 556–561.

[2] Bragado-Aldana, Estela, Mudassir Lone, and Atif Riaz. "On Wings with Non-Elliptic Lift Distributions." In Proceedings of the International Council of the Aeronautical Sciences (ICAS), 2021.

[3] Bowers, A. H., O. J. Murillo, B. Eslinger, and C. Gelzer. "On Wings of the Minimum Induced Drag: Spanload Implications for Aircraft and Birds." Technical report, NASA Armstrong Flight Research Center, Edwards, 2016.

[4] Zelenka, Bradley J., Erik D. Olson, and Xiaofeng Liu. "Prandtl-D Qualitative and Quantitative Wind Tunnel Tests." In AIAA SCITECH 2022 Forum, 0545. 2022.

[5] Hammer, R., and Daniel J. Garmann. "Wake-Structure of the Prandtl-D." In AIAA AVIATION 2023 Forum, 4003. 2023.

[6] DAR Corporation. "FlightStream." Accessed November 13, 2024. https://www.darcorp.com/flightstream-aerodynamics-software/.

[7] Ranjan, Prateek, and Phillip J. Ansell. "Computational Analysis of Vortex Wakes Without Near-Field Rollup Characteristics." Journal of Aircraft 55, no. 5 (2018): 2008–2021. https://doi.org/10.2514/1.C034870

[8] Pabon, Julian A., Xinyu Gao, Jielong Cai, and Sidaard Gunasekaran. "Experimental Investigation of a Novel Morphing Wing Design." In AIAA SCITECH 2024 Forum, 1349. 2024.

[9] Gogidze, George J., Sidaard Gunasekaran, and Jielong Cai. "Effect of Propeller Incidence Angle on Wing Embedded Propeller Configuration in Forward Flight." In AIAA SCITECH 2023 Forum, 2284. 2023.

[10] Jestus, Nevin, Sidaard Gunasekaran, Michael P. Mongin, and Aaron Altman. "Aerodynamic Characterization of Wing-Wing Interactions for Distributed Lift Applications." In AIAA SCITECH 2023 Forum, 0030. 2023.

[11] Cai, Jielong, Caiden Guzman, Emma Schutter, and Sidaard Gunasekaran. "On the Linear Superposition of Wing and Propeller Performance in a Wing Embedded Propeller System." In AIAA SCITECH 2024 Forum, 1511. 2024.

[12] Lynch, K. P. "Fluere for Particle Image Velocimetry: User Manual." (2011).

Plasma Induced Thrust Vectoring of Subsonic Axisymmetric Jets

Student Researcher: Jinit Patel

Advisor: Dr. Nathan Webb

The Ohio State University
Department of Mechanical and Aerospace Engineering

Abstract

This research explores the use of localized arc-filament plasma actuators (LAFPAs) for thrust vectoring in subsonic, axisymmetric jets. Unlike traditional thrust vectoring methods, which require secondary jets or complex nozzle geometries, LAFPAs induce thermal perturbations that excite the Kelvin-Helmholtz instability within the jet shear layer, forming vorticial coherent structures (CS). This study investigates the effect of excitation frequency on jet deflection at Mach numbers of 0.48 and 0.9, using static pressure measurements and Particle Image Velocimetry (PIV) to validate and visualize the flow.

Project Objectives

The primary goal of this research is to assess the effect of excitation frequency on jet deflection at jet Mach numbers of 0.48 and 0.9. This is achieved through static pressure measurements and Particle Image Velocimetry (PIV) to confirm deflection and visualize the flow. A key objective is also to understand the underlying physics and mechanisms behind the coherent structures induced by LAFPA actuation. Additionally, the study aims to characterize the frequency-dependent deflection of the jet using Strouhal number analysis.

Methods

The research involves a subsonic axisymmetric jet operating at Mach numbers of 0.48 and 0.9. Localized arc-filament plasma actuators (LAFPAs) are used to induce thermal perturbations within the jet shear layer, exciting the Kelvin-Helmholtz instability. To measure the effects, static pressure measurements are taken to confirm jet deflection, and Particle Image Velocimetry (PIV) is employed to visualize and analyze the flow. The effect of excitation frequency on jet deflection is assessed by characterizing the flow using Strouhal number analysis.

Results and Discussion

The results show that LAFPA excitation led to a significant change in pressure asymmetry within the jet. These findings were confirmed by PIV data, which illustrated that LAFPA actuation altered the flow attachment to the reaction surface, enhancing control authority over the jet. The study also found that excitation frequency plays a critical role in jet deflection, with different frequencies resulting in varying levels of deflection at different Mach numbers. The successful manipulation of jet deflection through LAFPA actuation demonstrated the potential for this technology to improve thrust vectoring performance, particularly in subsonic applications. In conclusion, LAFPAs provide a promising, low-power alternative to traditional thrust vectoring methods, offering increased control authority without the need for complex nozzle geometries or secondary flow jets.

Figures/Charts

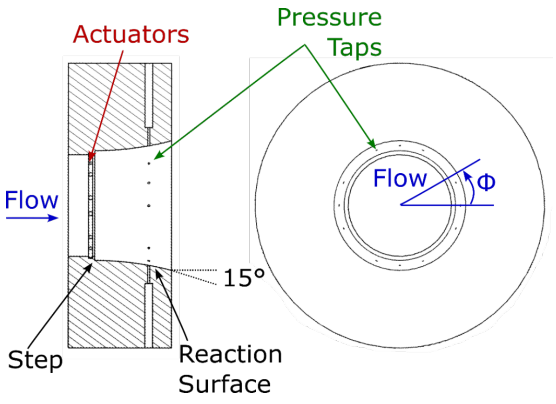


Figure 3

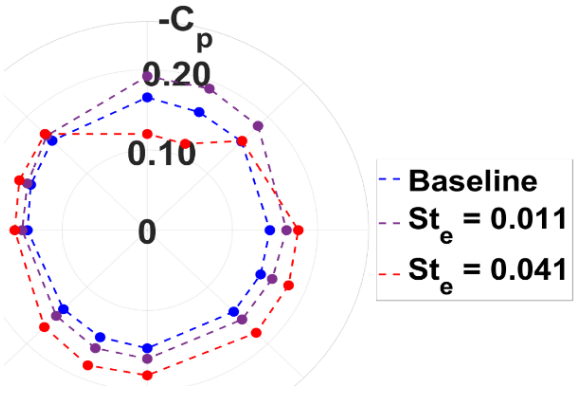


Figure 4

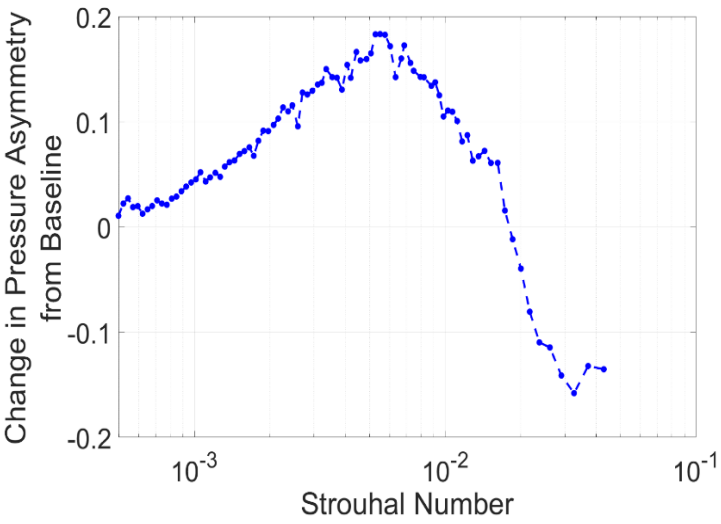


Figure 5

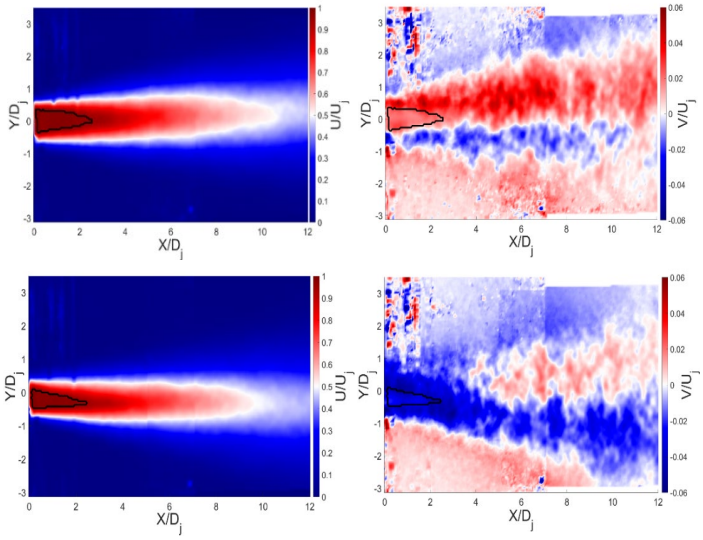


Figure 6

Figure 3 presents the reaction surface nozzle geometry. Figure 4 depicts static pressure profiles for ABC and DBC at M_j = 0.48. Figure 5 shows the pressure asymmetry change from baseline versus excitation frequency. Figure 6 provides the streamwise PIV data for M_j = 0.48, with subfigures 6a and 6b comparing the baseline case with the DBC case.

Acknowledgments

I would like to express my sincere gratitude to my advisor, Dr. Nathan Webb, and my lab group for all their guidance and support throughout this project. I also extend my thanks to the Ohio State University Aerospace Research Center (ARC) for providing the necessary resources and facilities to enable this research. This project would not have been possible without the generous financial support from the Office of Naval Research (ONR), particularly Drs. David González and Leighton Myers, and the Ohio Space Grant Consortium (OSGC).

References

1. Mills, A. J., Barnhouse, A., Cartwright, E., and Webb, N. J., “Controlled Deflection of a Subsonic, Axisymmetric Jet using Plasma Actuators,” AIAA 2024-3544, Session: Flow Control Devices and Applications, 2024. https://doi.org/10.2514/6.2024-3544

2. Warsop, C., and Crowther, W. J., “Fluidic Flow Control Effectors for Flight Control,” AIAA Journal, Vol. 56, No. 10, 2018, pp. 3808–3824. https://doi.org/10.2514/1.J056787

Key Discoveries Leading to the Hypothesis that Earth once had a Ring

Student Researcher: Kira Paul

Advisor: Dr. Daniel Holm

Kent State University
Earth Science Department

Earth's Ancient Ring System Uncovered

All large planets in our Solar System have rings and Mars may have had a ring in the past. Tomkins et al. (2024) recently suggested that Earth also once had a chondrite ring system during the Ordovician period, starting 466 million years ago. The key discoveries leading to their startling hypothesis, published over the past 25 years, including a high flux of Devonian meteorites, preserved in primarily low latitudes, together with extraterrestrial elemental identifiers are summarized here. The equally remarkable potential consequences of a temporary ring that collapsed onto earth are also noted, including significant global cooling, mass extinction, and a late Ordovician biodiversification event known as the Global Ordovician Biodiversification event (GOBE) that led to a staggering increase in biodiversity of marine life and an increase in biocomplexity (Schmitz et al., 2008). The line of discoveries starts with Schmitz et al. (2001) who's team documented 'a rain of Early Ordovician ordinary chondritic meteorites in Lower Ordovician (480 Ma) marine limestone in southern Sweden'. Subsequent discoveries include geographic expansion of similar aged meteorites, and additional analyses including geochemistry of chromite grains, oxygen isotopes measurements, and cosmic-ray age determinations. Before 1992, so few fossil meteorites (only half a dozen) were documented that some investigators argued that meteorites did not fall before the late Quaternary. Other meteorite investigators counterargued that fossil meteorites in the ancient rock record may have been altered and therefore not readily recognized.

Project Objectives

In this project we explore the hypothesis that the Earth once had an ancient ring system, that not only left physical evidence but had an impact on the Earth's atmosphere. The objective of this project is to synthesize and highlight supporting evidence related to events surrounding the Mid-Ordovician. While touching base on the possible triggers of the Great Ordovician Biodiversification Event after the parent body breakup of the L-chondrite parent body. Overall, we wanted to share the incredible connections between events and evidence discovered and shared by researchers.

Methods

The methods used for the project were research based through scientific publications.

Results and Discussion

It's suggested that due to the influx of meteor impacts in the Ordovician they triggered the GOBE and the Hirnantian Icehouse period. Bed-by-bed studies were conducted from Baltoscandian and China focusing on the diversification and expansion of brachiopod and cystoids. Bed-by-bed studies were supported by oxygen and osmium isotopes as well as invertebrate fossil discoveries (Schmitz and others, 2008). Evidence of impacts around the equatorial band triggering seismic and tsunami activity corresponding to nearby megabreccia deposits. Researchers use tectonic plate reconstructions to figure out where craters were located when they first formed. There were 21 impact craters from the Ordovician impact spike and all impacts were located within an equatorial band (≤30° latitude), despite 70% of the exposed crust lying outside this range. The MER21 model shows the locations of 21 chondrite impact craters formed between 467 and 450 Ma during the Ordovician period clustered within an equatorial band. The tectonic plate reconstruction MER21 model allows for researchers to piece back together where L chondrite impact craters originally formed in the Ordovician period. Approximately 70% of the exposed crust during the Ordovician period doesn't have any impact craters. Researchers believe that younger craters are more subjected to being within the confined boundaries or the palaeoequator. While older chondrite impact structures would waiver more in paleolatitude. Out of the 21 craters, 14 craters were found to have similar age probabilities ranging ≥ 0.5 within the 467–450 Ma time frame (Tomkins and others, 2024). The 14 craters were preserved in old continental crust and show connections to paleolatitude band distributions. The evidence from continuously similar ancient paleolatitude

L chondrite impact sites suggests that Earth a chondrite ring system. The frequent impacts likely disrupted shallow to deep marine environments and changed ecological systems. Climate conditions reaching chilling temperatures during 463 to 444 Ma also correlate to changes in biota that are more resistant to global temperatures changes.

Figures/Charts

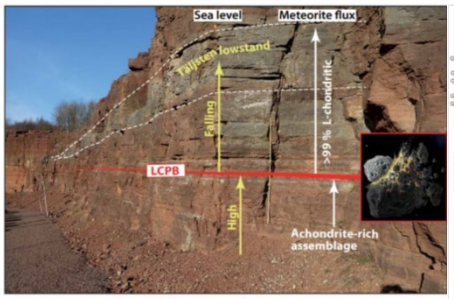


Fig. 11. The mid-Ordovician Hällekis section in southern Sweden. The red line corresponds to the time of the breakup of the LCPB in the asteroid belt. At this level, bioclastic limestone fragments begins to increase, indicating onset of a gradual sea level fall that culminates with Täljsten low-stand deposit traceable around the globe (Schmitz and others, 2019).

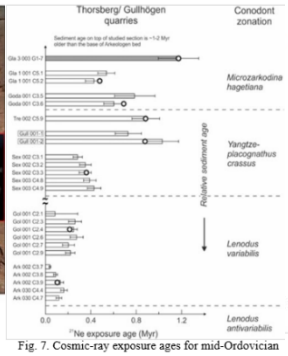


Fig. 7. Cosmic-ray exposure ages for mid-Ordovician fossil meteorites (Schmitz and others, 2014).

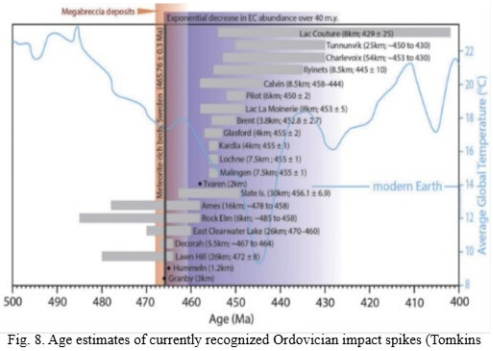


Fig. 8. Age estimates of currently recognized Ordovician impact spikes (Tomkins and others, 2024).

Acknowledgments

I would like to thank OSGC, the Ohio Space Grant Consortium, for providing funding for this research. This project would not have been possible without the OSGC scholarship award and the guidance of KSU's highly esteemed geology advisor, Dr. Daniel Holm.

References

Schmitz and others, 2001, A rain of ordinary chondritic meteorites in the early Ordovician. Earth and Planetary Science Letters 194, 1-15. Fig. 2, 3, and 4.

Heck and others, 2004, Fast delivery of meteorites to Earth after major asteroid collision. Nature, 430, 323-325.

Heck and others, 2008, Noble gases in fossil micrometeorites and meteorites...Meteoritics & Planetary Science 43, 517-528. Fig. 5.

Schmitz and others, 2008, Asteroid breakup linked to the Great Ordovician Biodiversification Event. Nature Geosciences.

Heck and others, 2010, A single asteroidal source...Geochimica et Cosmochimica Acta, DOI 10.1016/jgca.2009.10.027. Fig. 1 and 6.

Schmitz and others, 2014. A Fossil Winonaite-like Meteorite in Ordovician Limestone: A Piece of the Impactor That Broke up the L-chondrite Parent Body? Earth and Planetary Science Letters, 400, 145–152. Fig. 7.

Schmitz and others, 2016, A new type of solar-system material recovered from Ordovician marine limestone. Nature Communications, DOI: 10.1038/ncomms11851.

Schmitz and others, 2019, An extraterrestrial trigger for the mid-Ordovician ice age:....Science Advances, 5, eaax4184. Fig. 11.

Tomkins and others, 2024, Evidence suggesting that earth had a ring in the Ordovician. Earth and Planetary Science Letters 646, 118991. Fig. 8, 9, and 10.

Pilot Weather Awareness: A 3D Augmented Reality Approach

Student Researcher: Brady Phelps

Advisor: Dr. Chad Mourning

Ohio University
Advanced Computing

Abstract
Weather is one of the most critical factors influencing flight paths, flight safety, and overall aviation operations. While modern tools like FIS-B and ForeFlight provide valuable 2D weather data during flight, they can lack the spatial depth and clarity needed for rapid decision-making. In contrast, 3D weather visualizations offer enhanced depth perception, immersion, and situational understanding. This work introduces a novel 3D weather visualization system leveraging augmented reality (AR) to improve pilot situational awareness and enhance flight safety. The system integrates real-time data from the National Oceanic and Atmospheric Administration's High-Resolution Rapid Refresh (HRRR) system to generate dynamic 3D weather models. These models are displayed through an AR headset, offering pilots an interactive, real-time visualization of weather conditions directly within the cockpit. By allowing pilots to see and interpret complex weather systems in three dimensions, this immersive experience significantly enhances in-flight decision-making. The system has been developed and tested in controlled, simulated environments, establishing a solid foundation for future real-world deployment and operational use.

Project Objectives
Weather-related incidents continue to pose significant risks to aviation safety. According to the Federal Aviation Administration (FAA), the majority of weather-related crashes are fatal [1], and weather continues to be one of top reasons for plane crashes [2]. This project aims to address these challenges by developing a 3D weather visualization system that leverages augmented reality (AR) technology to enhance pilot situational awareness in real-time flight environments.

The core objectives of this project are:

- To design and implement a 3D AR-based weather visualization platform that delivers real-time, spatially immersive weather data directly to pilots.
- To explore the feasibility of integrating live meteorological data into an AR headset for interactive in-flight use.

Background
To address these dangers, the FAA has launched initiatives such as the Weather Technology in the Cockpit (WTIC) program. WTIC seeks to develop weather service recommendations for cockpit weather information and its presentation, cockpit weather technology, and pilot weather training [3]. The overarching goal of the program is to reduce weather-related risk by creating safer and more informative cockpit environments. This initiative highlights the need for continued research into effective mid-flight weather visualization systems.
For up-to-date weather analysis, pilots currently depend on a several systems designed to deliver real-time weather data and ensure informed decision-making throughout all phases of flight. Among the most widely used tools are the Automated Weather Observing System (AWOS) and the Automated Surface Observing System (ASOS), which provide continuous and automated weather observations at airports across the country. These systems deliver critical information such as wind speed and direction, visibility,

temperature, dew point, and barometric pressure, helping pilots assess local weather conditions during pre-flight planning and just prior to takeoff [4]. Complementing these systems is the Automated Terminal Information System (ATIS), which transmits audio broadcasts of weather and airport information over designated radio frequencies. These broadcasts include data on active runways, available approaches, and relevant Notices to Air Missions (NOTAMs), along with updated meteorological conditions. ATIS plays a vital role in reducing radio frequency congestion and providing pilots with continuous access to essential operational and weather details at controlled airports [5]. In addition to ground-based systems, pilots utilize Flight Information Services–Broadcast (FIS-B) technology, a service enabled through Automatic Dependent Surveillance–Broadcast (ADS-B). FIS-B provides weather and aeronautical information in-flight, including METARs, TAFs, NEXRAD radar imagery, AIRMETs, SIGMETs, and TFRs.

One of the most popular tools for in-flight weather awareness is ForeFlight, a mobile electronic flight bag application. ForeFlight consolidates weather data from multiple sources, including ADS-B, satellite (XM Weather), and cellular networks. While the cellular connection enables data updates on the ground or in low-altitude airspace, it is often unreliable or unavailable at cruising altitudes. ForeFlight presents weather data through a 2D map interface, allowing pilots to view precipitation, wind patterns, cloud coverage, turbulence, and more in real time [6]. Moreover, regulatory requirements mandate that all pressurized, passenger-carrying aircraft be equipped with airborne weather radar, as outlined by the International Civil Aviation Organization (ICAO) [7]. These radars are essential for detecting convective weather, including thunderstorms and turbulence, ahead of the aircraft's flight path.

While these traditional and modern systems play an essential role in enhancing flight safety, they largely rely on 2D representations of weather data. These representations, though effective for certain tasks, are limited. As a result, there is growing interest in exploring 3D weather visualization tools that can provide a more informative and intuitive understanding of weather phenomena in flight.

This research seeks to address these limitations by developing and evaluating a novel 3D weather visualization system that leverages augmented reality (AR) to enhance situational awareness during flight. Furthermore, work on this project was presented at AIAA SciTech 2025 [8].

Methods

i. Data

Real-time, high-fidelity weather data is essential for effective in-flight visualization. For this application, we rely on the HRRR model provided by NOAA via the NOMADS interface [9]. The HRRR model provides hourly forecasts with updates every 15 minutes and a spatial resolution of approximately 3 kilometers. This fine temporal and spatial granularity make it ideal for real-time applications. These forecasts include key variables for understanding atmospheric conditions, such as temperature, wind, and pressure. To deliver this data efficiently, the application queries weather information in real time through the Low Altitude Weather Network (LAWN) API. This server reconciles HRRR model forecasts with proprietary observational data collected from LAWN's network of ground-based sensors [10]. Once retrieved, this data is used to dynamically populate the 3D spatial environment within the application with ground temperature information. An overview of this architecture can be seen in Figure 1.

Real-time visibility data, such as fog and cloud coverage, is a planned enhancement for future iterations. Initial efforts used Worley noise to simulate realistic volumetric patterns for low-visibility regions [11]. Visibility isosurfaces are computed with a threshold of 3 miles, aligning with Visual Flight Rules (VFR) minimums [12], offering a meaningful safety context for pilots operating under VFR.

ii. Software

The application is developed using the AftrBurner engine [13], a 3D game engine utilized in other Ohio University research projects, such as the Ohio University NAVAID Performance Prediction Model (OUNPPM) [14]. AftrBurner's modular architecture allows for simple integration of existing projects, enabling this project to build upon prior work and support future expansion. This proved especially valuable, as the system incorporates earlier developments in virtual reality heatmap visualization (see Figure 2) [15]. For rendering, AftrBurner utilizes OpenGL, a popular open-source graphics AP. Throughout this work, we integrated OpenGL with OpenXR for XR (extended reality) support. OpenXR, a cross-platform interface maintained by the Khronos Group. This integration allows the application to run on a range of XR devices with minimal modification.

During runtime, once atmospheric data is retrieved, the AftrBurner engine renders each frame and passes it to the OpenXR compositor. The compositor handles tasks such as stereoscopic rendering, lens distortion correction, and head tracking synchronization. This ensures an immersive, distortion-free augmented experience suitable for in-flight use.

iii. Hardware

The application is currently being testing on the Meta Quest Pro. The Quest Pro supports advanced features such as hand tracking, eye tracking, and voice input, allowing for future expansions to the interface, such as pinch selection or command-based interactions. Thanks to OpenXR support, the application is not hardware-locked; future testing will explore compatibility with alternative XR headsets and even mobile devices. This hardware-agnostic design ensures that the application can be tailored to different aircraft environments and pilot preferences. While headsets like the Quest Pro offer many immersive capabilities, alternative options, such as see-through head-up displays (HUDs), AR glasses, or mobile devices, may ultimately provide a less intrusive solution for in-flight use.

Results and Discussion

The final implementation allows users to view and interact with real-time 3D weather data within a virtual/simulated environment. Although this system is ultimately intended for use within aircraft cockpits, in-flight testing is not currently authorized. As a result, a simulated virtual environment was developed to evaluate the application in a controlled context. Upon launch, users are placed in a blank virtual scene with mouse-based navigation. The user interface allows selection from predefined geographic environments, including regions in Ohio, Colorado, California, Michigan, and Texas. Once a location is chosen, the system queries the LAWN API for real-time HRRR data, processes temperature and terrain layers, and generates a heatmap overlay on the rendered 3D environment. These overlays are displayed using a color gradient where red representing warmer regions and blue indicating cooler zones, providing immediate visual insight into temperature dynamics of a desired location as seen in Figure 3 and Figure 4.

Moving forward, several enhancements are planned to transition the system toward real-world aviation use:

- Hardware Alternatives: While the current implementation runs on the Meta Quest Pro (and other OpenXR compatible headsets), future versions will target less intrusive hardware, such as optical AR glasses (e.g., Google Glass [16], Meta's new Orion glasses [17]), that may be more suitable for in-cockpit use.
- Expanded Information Visualization: Real-time visibility data, such as fog and cloud cover, is a high-priority addition. Integrating this will provide a more comprehensive view of flight-critical weather conditions. Currently we utilize Worley noise to simulate some of these conditions, but in the future, there is room to blend these with the HRRR data.

- Field Testing and Certification: To transition from simulation to operational use, the application must undergo rigorous testing and evolution to attain certification for in-flight deployment.
- Scientific Potential: Beyond operational benefits, this tool opens new avenues for atmospheric research by enabling real-time, immersive visualization of 3D weather data mid-flight.

Figures/Charts

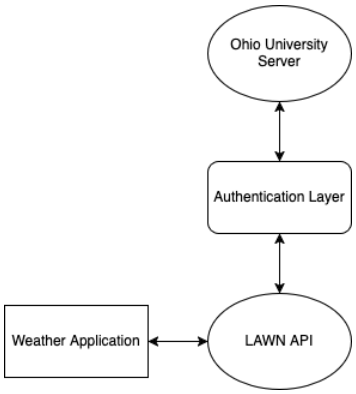


Figure 1. The weather data retrieval process architecture.

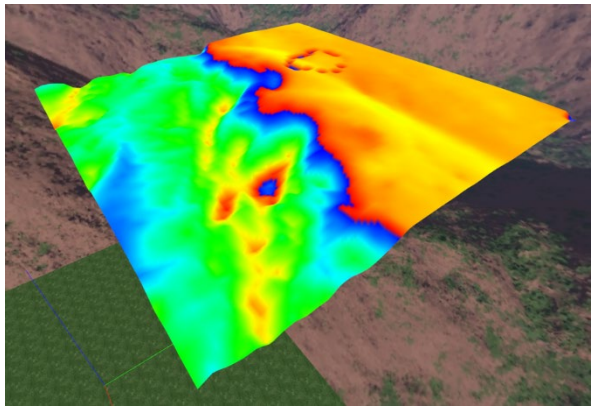


Figure 2. Initial terrain data rendered with a temperature heatmap.

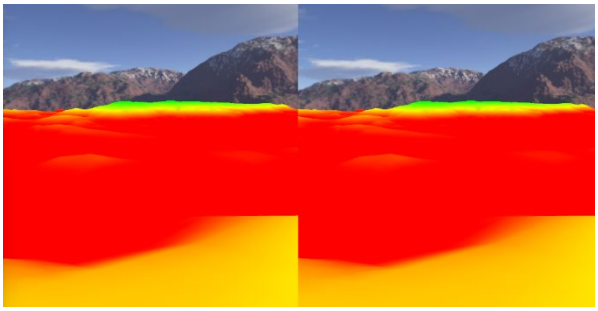


Figure 3. Image taken from the point-of-view of a simulated pilot flying low to the horizon in California. The image on the left and right represent the images for the left and right eye.

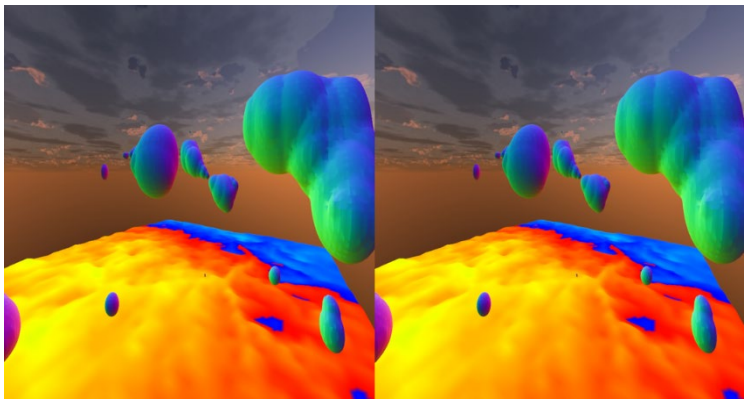


Figure 4. Aerial point-of-view of a pilot flying over Athens, Ohio. Simulated cloud coverage can be seen, along with warmer forest brushing up against the cooler Hocking River.

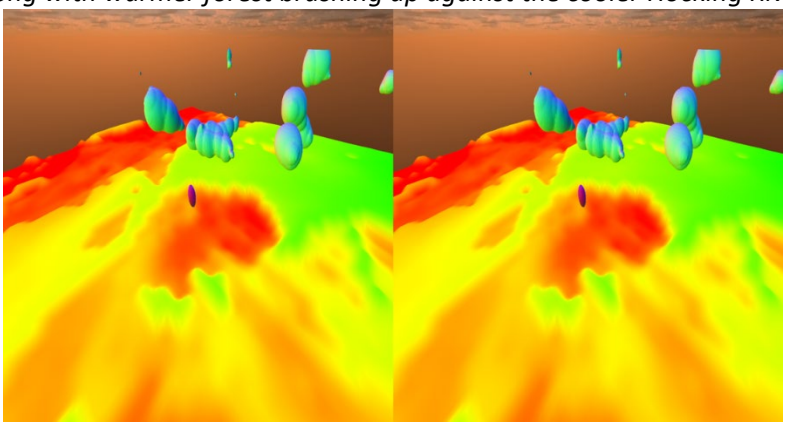


Figure 5. Aerial point-of-view over an arid Colorado environment. Light cloud coverage also featured.

Acknowledgments

Special thank you to the Ohio Space Grant Consortium for funding this project.

References

[1] F. A. Administration, "General Aviation Safety," 2024. [Online]. Available: https://www.faa.gov/newsroom/general-aviation-safety?newsId=21274.

[2] F. A. Administration, "Aviation Safety Information Analysis and Sharing (ASIAS)," 2024. [Online]. Available: https://www.asias.faa.gov/apex/f?p=100:1:::NO:::.

[3] F. A. Administration, "Weather Technology in the Cockpit (WTIC)," 2024. [Online]. Available: https://www.faa.gov/nextgen/programs/weather/wtic.

[4] N. C. f. E. I. (NCEI), "Automated Surface/Weather Observing Systems (ASOS/AWOS)," 2024. [Online]. Available: https://www.ncei.noaa.gov/products/land-based-station/automated-surface-weather-observing-systems.

[5] F. A. Administration, "Air Traffic Control Order JO 7110.65," 2023. [Online]. Available: https://www.faa.gov/air_traffic/publications/atpubs/atc_html/chap2_section_9.html.

[6] ForeFlight, "How can I get updated weather in flight?," 2024. [Online]. Available: https://support.foreflight.com/hc/en-us/articles/202977639-How-can-I-get-updated-weather-in-flight.

[7] I. C. A. Organization, "Operation of Aircraft, Part I - International Commercial Air Transport," 2018. [Online]. Available: https://ffac.ch/wp-content/uploads/2020/09/ICAO-Annex-6-Operation-of-Aircraft-Part-I-International-commercial-air-transport.pdf.

[8] B. Phelps and C. Mourning, "3D Real-Time Augmented Reality Weather Visualizations for Aircraft Safety During Flight Authors Brady M Phelps, Chad Mourning Publication date 2025 Book AIAA SCITECH 2025 Forum Pages 2293 Description Weather significantly influences aviation, dictating fl," in *AIAA SciTech 2025 Forum*, Orlando, 2025.

[9] N. C. f. E. Prediction, "High-Resolution Rapid Refresh (HRRR," NOAA Earth System Research Laboratory, [Online]. Available: https://rapidrefresh.noaa.gov/hrrr/. [Accessed 2024].

[10] D. Wright, C. Mourning, J. Murray, T. Albin, C. Young and E. Krimins, "Weather Visibility Sensor Network: Platform Characterization," in *2023 IEEE International Conference on Omni-layer Intelligent Systems (COINS)*, 2023.

[11] S. Worley, "Cellular Textures," in *Proceedings of the 23rd Annual Conference on Computer Graphics and Interactive Techniques*, 1996.

[12] F. A. A. (FAA), "VFR Weather Minimums," [Online]. Available: https://www.faasafety.gov/files/gslac/courses/content/25/185/vfr%20weather%20minimums.pdf. [Accessed 2024].

[13] S. Nykl, C. Mourning, M. Leitch, D. Chelberg, T. Franklin and C. Liu, "An overview of the STEAMiE educational game engine," in *IEEE 38th Annual Frontiers in Education Conference*, 2008.

[14] C. Mourning and S. Odunaiya, "Dynamic Antenna Pattern Visualization for Aviation Safety Incorporating Multipath and Situational Awareness," *Advances in Visual Computing,* 2021.

[15] G. Sarakadam, *Low Altitude Weather Network API with Real-Time HRRR Chunks and Sensor Data Integration,* Unpublished Master's Project Report, 2024.

[16] Google Inc., "Google Glass," 2013. [Online]. Available: https://www.google.com/glass/start/.

[17] Meta Platforms, Inc., "Meta Orion," 2024. [Online]. Available: https://about.fb.com/news/2024/09/introducing-orion-our-first-true-augmented-reality-glasses/.

Applying a Multi-Level Structure to High-Precision Priority Encoders

Student Researcher: Maxwell Phillips

Advisors: Dr. Firas Hassan, Dr. Ahmed Ammar

Ohio Northern University
Electrical and Computer Engineering and Computer Science Department

Abstract
Priority encoders are a traditionally expensive hardware component, particularly at high input precisions (above 1024 bits). Due to this cost, they are often avoided, but could be leveraged to improve the performance of or provide an alternative method for various operations and algorithms, such as high-precision integer arithmetic. In this work, we introduce a generalized method for constructing high-precision priority encoders by dividing them into multiple levels. This builds upon our previous work which introduced the idea of the two-level priority encoder. We extend this concept to three levels using two different techniques (cascading and composition) and comment on further generalization. Finally, we provide insights on hardware complexity and delay in relation to input size.

Project Objectives
This work builds on the central hardware component utilized in [1] and [2], and provides a complement to [3], extending the techniques used in that work from decoders to priority encoders. More generally, the purpose of this line of research is to provide building blocks for hardware acceleration of encryption at high input precisions. The priority encoder discussed in this work has numerous applications, particularly related to and within this domain. High input precisions are necessary due to the continually increasing power of computers, which are more and more easily able to decrypt larger encryption keys. For example, the minimum RSA key size recommended by the NIST is 2048 bits, with 3072 bits preferred [4]. However, to accommodate such large data, the hardware must be more and more complex. Thus, the primary goal of this work is to reduce the complexity, and by extension both power and cost, of the priority encoder, allowing more efficient usage of it in encryption applications.

Methods

A digital encoder is a logic circuit that takes a number of input wires n (where n is a power of 2), and converts them into $\log_2 n$ outputs. In a normal encoder, only one input may be high (active, or having a value of 1) at a time. A priority encoder (PE) is an advanced version of the digital encoder which can handle more than one active input. Each input is given a priority according to its equivalent numerical place value. The priority encoder takes an input x and provides an output $\lfloor \log_2 x \rfloor$. This is also the numeric index of the most significant high bit (MSHB) of the input. An example of a 4:2 priority encoder is shown in Figure 1.

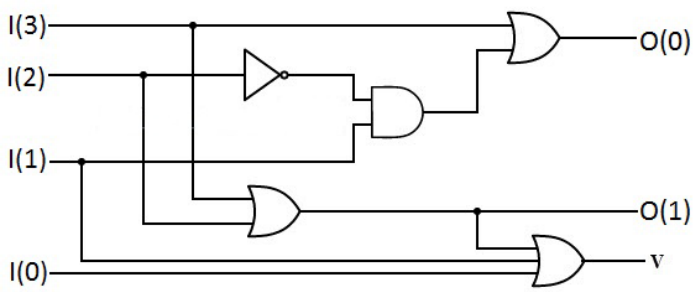


Figure 1: 4:2 Priority Encoder [5].

Furthermore, an example table of inputs and outputs is given in Figure 2.

The priority encoder has been long considered an expensive circuit. The chief reason for this is due to its poor scalability when implemented in the traditional single-level manner. Refer to Figure 1 for an example of a 4:2 PE. Figure 3 shows an 8:3 PE, and Figure 4 shows a 16:4 PE. From these simple examples it is clear that the complexity of the hardware grows rapidly with increasing input size. In general, it is difficult to convert numerous inputs to substantially fewer inputs, and in this case the number of inputs literally grows exponentially as output size increments.

Input	Output
1111 (15)	11 (3)
1110 (14)	11 (3)
⋮	⋮
1000 (8)	11 (3)
0111 (7)	10 (2)
0110 (6)	10 (2)
⋮	⋮
0010 (2)	01 (1)
0001 (1)	00 (0)

Figure 2: Sample outputs of 4:2 PE.

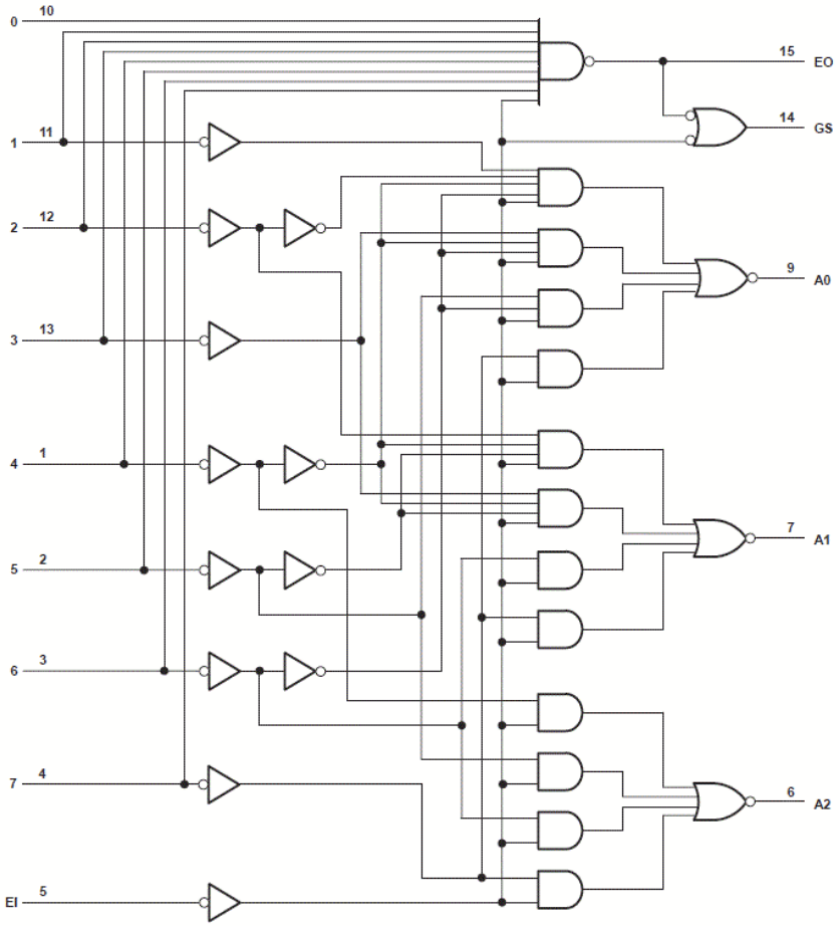


Figure 3: Example of 8:3 PE [6].

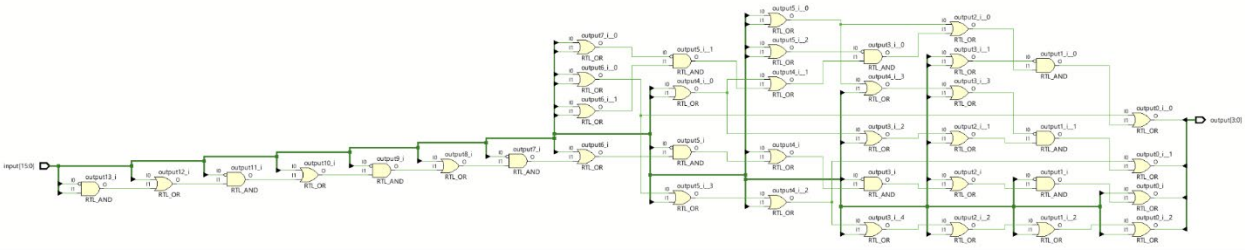


Figure 4: Example of 16:4 PE.

The two-level priority encoder (2LPE), introduced in [2] and shown in Figure 5, begins to solve this problem. The 2LPE functions as follows. First, the input is divided into multiple "bit slices" via a number of OR gates k. Each OR gate is q bits wide. Note that $k \times q = n$. The outputs of the OR gates form the inputs to the "coarse" PE. The output of the coarse PE reveals which bit slice contains the MSHB. This value is then taken by the multiplexer as its select signal. In this way, the bit slice containing the MSHB is provided to the "fine" PE, which in turn finds the location of the MSHB within the bit slice. By concatenating the outputs of the coarse and fine PE, the final result is obtained.

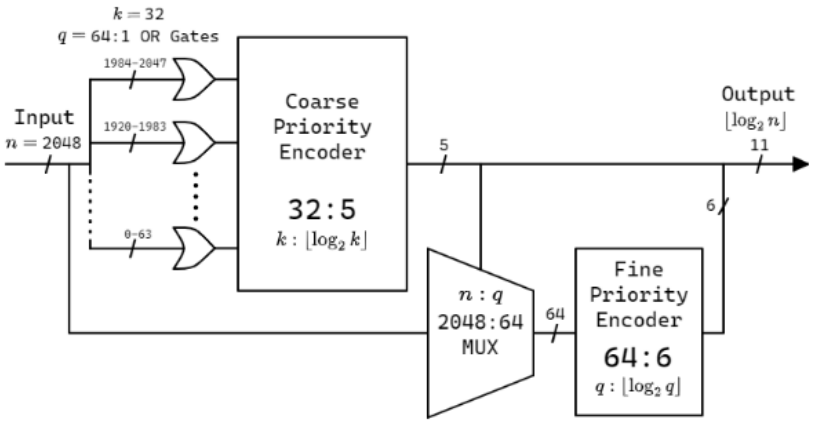


Figure 5: A Block Diagram for a 2048-bit 2LPE.

We present two methods for generalizing the two-level priority encoder to three or more levels: 1. "composition," and 2. "cascading" or "chaining."

In the "composition" method, shown in Figure 6, the coarse and fine PEs in the 2LPE are themselves 2LPEs. This structure is more clearly visualized at a high level via Figure 7, which shows a tree diagram illustrating the three levels composing the device.

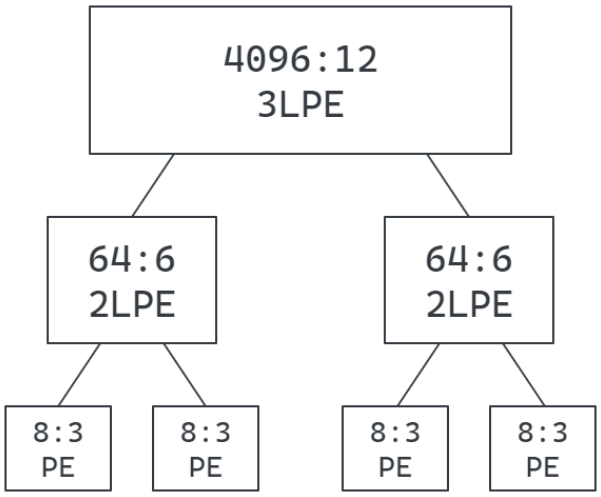


Figure 7: 4096:12 PE tree diagram.

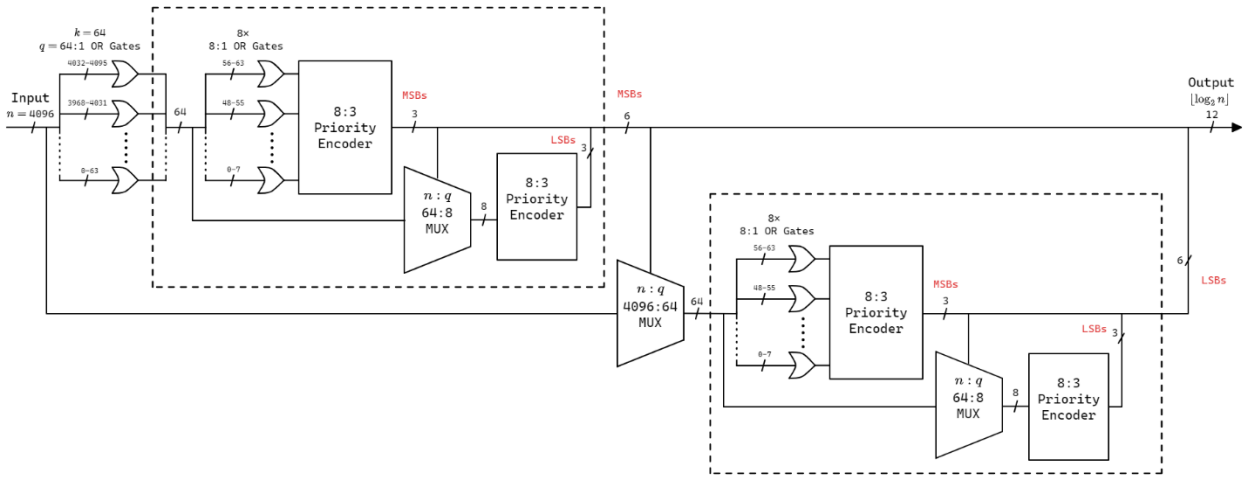


Figure 6: Composition method for 4096:12 3LPE.

The “cascading” or “chaining” method is shown in Figure 8. The easiest way to visualize this method is as if another set of multiplexer and smaller PE are added around the original 2LPE, and the sizes are redefined appropriately.

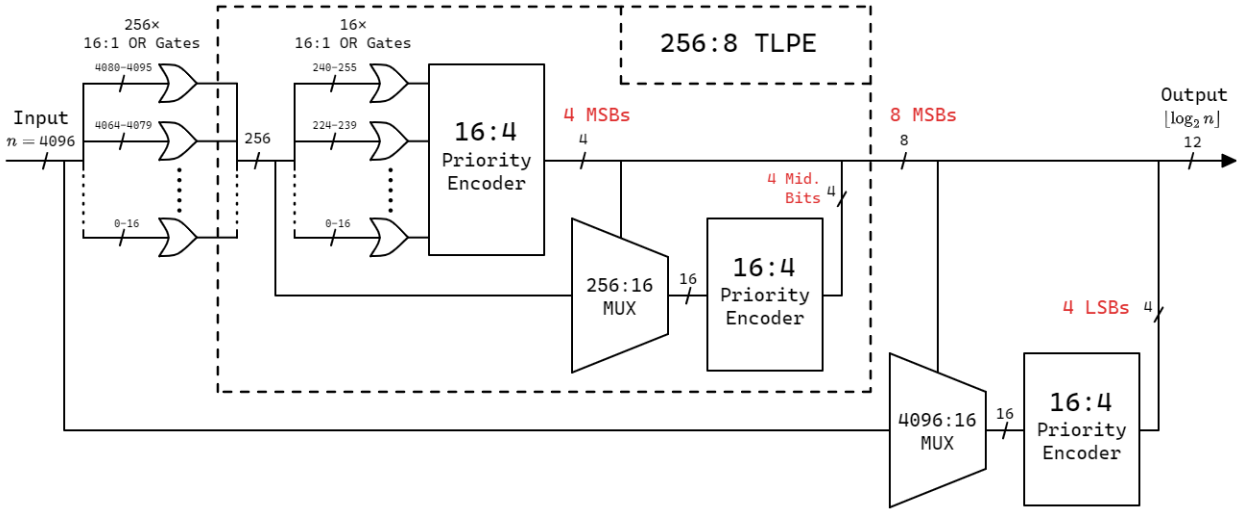


Figure 8: Cascading method for 4096:12 3LPE.

Results and Discussion

Our first major finding was that the 2LPE cuts complexity in half, but correspondingly doubles delay. This type of complexity-delay tradeoff is not uncommon. For synthesis on FPGA, past 64 Kib (65536 bits) the single-level priority encoder is no longer synthesizable. However, looking at the trends in Figure 9, we

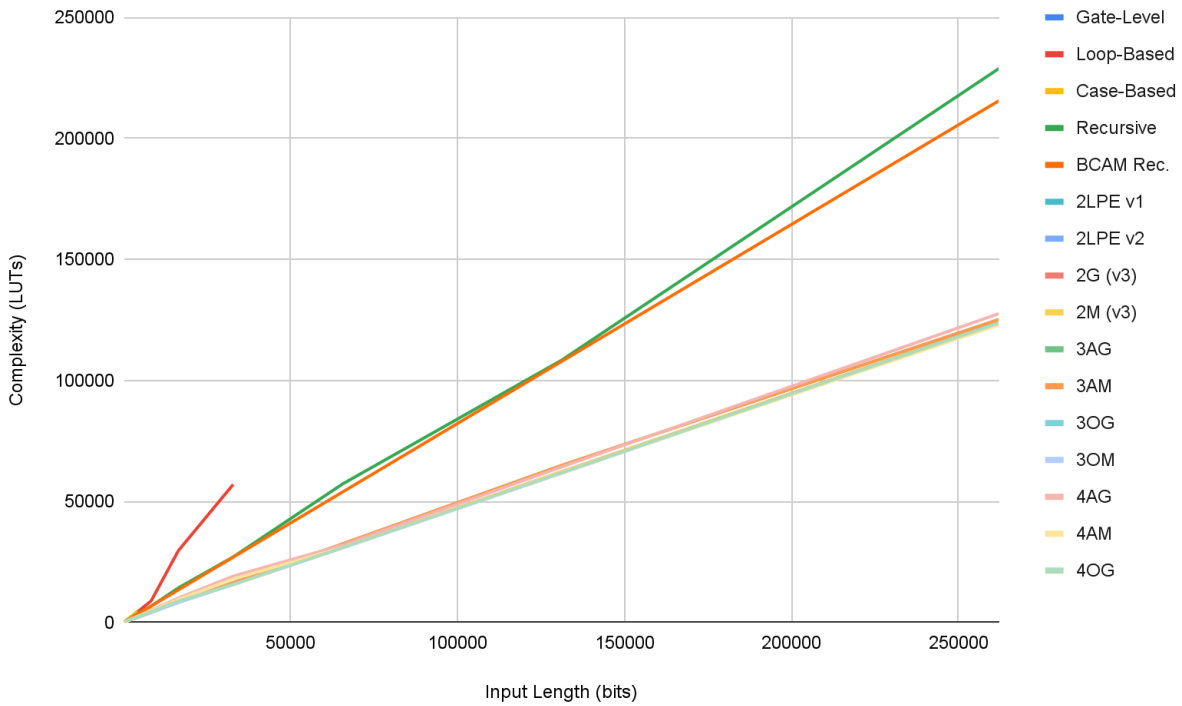


Figure 9: Complexity comparison among PE construction methods.

can see that the correlation between input size and lookup tables (LUTs) required is nearly 1:1. In Figure 9 we also compare our methods against a recursive design found in [7] (the orange line) and our recreation of that design (green). More curiously, moving from two levels to three levels does not provide another drop in complexity as we initially expected. In a future work we will expand our analysis to include ASIC technologies (transistor-level) as well as more in-depth delay evaluation.

Acknowledgments
Thanks to OSGC and by extension NASA for funding this research and hosting the recent research symposium which I presented at. Special thanks to my advisors, Dr. Firas Hassan and Dr. Ahmed Ammar.

References
[1] M. Phillips, F. Hassan, A. Ammar, and N. Hagerdorn, "Leveraging a Novel Two-Level Priority Encoder for High-Precision Integer Multiplication," in the Proceedings of the IEEE 66th International Midwest Symposium on Circuits and Systems, 2023, pp. 1118–1122.
[2] A. Ammar, F. Hassan, and H. Drennen, "High-Precision Priority Encoder Based Integer Division Algorithm," in the Proceedings of the IEEE 64th International Midwest Symposium on Circuits and Systems, 2021, pp. 494–497.

[3] M. Phillips, A. Ammar, and F. Hassan, "A Generalized Multi-Level Structure for High-Precision Binary Decoders," in the Proceedings of the IEEE 67th International Midwest Symposium on Circuits and Systems, 2024, pp. 42–46.

[4] H. Ferraiolo and A. Regenscheid, "Cryptographic Algorithms and Key Sizes for Personal Identity Verification," csrc.nist.gov, July 2024. Available: https://csrc.nist.gov/pubs/sp/800/78/5/final.

[5] Nitianabhigyan, "A 4-2 Priority Encoder," licensed CC BY-SA 4.0. Available: https://commons.wikimedia.org/w/index.php?curid=58418050.

[6] Texas Instruments, "SNx4HC148 8-Line to 3-Line Priority Encoders," April 2004. Available: https://www.ti.com/lit/ds/scls109h/scls109h.pdf

[7] A. M. S. Abdelhadi and G. G. F. Lemieux, "Deep and narrow binary content-addressable memories using FPGA-based BRAMs," in 2014 International Conference on Field-Programmable Technology (FPT), 2014, pp. 318–321.

Oil and Gas Logistics

Student Researcher: Alex Posey

Advisor: Dave Freeman

Marietta College
Petroleum Engineering, Geology

Abstract
The oil and gas industry, much like NASA's logistics for rockets and heavy machinery, relies heavily on complex logistical operations. This sector reaps numerous benefits from streamlined logistics, including reduced emissions, lower downtime, minimized wear and tear on both machinery and infrastructure, cost efficiency, and decreased Health, Safety, and Environmental (HSE) risks. These advantages emphasize the critical role of optimized logistical strategies in enhancing operational efficiency, safety, and environmental sustainability within the industry. By addressing these logistical challenges effectively, the oil and gas sector continues to advance its performance and sustainability.

Project Objectives
My project aims to exam the logistics of transporting materials to well pads and attempt to optimize these processes to increase efficiency. The main aim will be to see if several smaller loads would be more efficient than one larger load. The secondary aim will be to examine ways to improve loading density of these shipments to further increase efficiency.

Methodology
I thoroughly reviewed and considered the various methods to simplify and improve the logistics of the oil and gas industry. I compiled all of this research to the most concentrated and relevant methods/processes.

Results and Discussion
Efficiency in logistics and shipping can be significantly improved by adopting smarter equipment, optimizing routes, and using concentrated forms of chemicals. Utilizing advanced technologies like coil tubing or wireline units for drill outs and sandbox units for frac sand can streamline operations and enhance performance. Additionally, the use of plastic pallets not only reduces logistics costs but also increases load density, maximizing space and efficiency. Route optimization plays a crucial role as well, leading to fewer fuel deliveries and reduced individual shipments through increased load density. Shipping chemicals in concentrated forms further enhances logistical efficiency by allowing fewer shipments while increasing load capacity, ultimately saving costs and resources. These strategies together highlight the potential for more sustainable and effective logistics systems.

Acknowledgments
I would like to acknowledge and thank Dave Freeman and Andrew Beck.

References
1) Al Suwaiei, Fahad, Al Husayni, Musab, AlGhamdi, Saeed, and Mohammed Kanwi. "The Transformation of Shipping & Transport Material to Polymer-Based Products. A Case Study of Wooden-To-Plastic Pallets." Paper presented at the AMPP Middle East Corrosion Conference and Exhibition, Manama, Kingdom of Bahrain, November 2023.

2) Comer, Alan , and Olivier Alferez. "Composite Plug Milling via Wireline Reduces HSE Risks and Logistics on Location." Paper presented at the SPE Eastern Regional Meeting, Charleston, West Virginia, USA, October 2019. doi: https://doi.org/10.2118/196584-MS

3) Barnes, J. R., Regalado, D. Perez, Crom, L. A., Doll, M. J., King, T. E., Covin, D. Y., Crawford, J. N., and P. J. Kunkeler. "Large Scale EOR Projects: Cutting Costs on Surfactant Supply Logistics." Paper presented at the SPE EOR Conference at Oil and Gas West Asia, Muscat, Oman, March 2018. doi: https://doi.org/10.2118/190453-MS

4) Mitschanek, Mathias , Thonhauser, Gerhard , and Michael Prohaska. "Modeling Transportation Logistics, Water Use, and Surface Footprint for Shale Gas Field Developments." Paper presented at the SPE/EAGE European Unconventional Resources Conference and Exhibition, Vienna, Austria, February 2014. doi: https://doi.org/10.2118/167697-MS

A Systematic Review Of Telemedicine Based On Perception And Interaction

Student Researcher: Anthony Quear

Advisor: Sang-Eun Song, PhD

The University of Akron
Department of Mechanical Engineering

Abstract
This systematic review explores telemedicine through the lens of perception and interaction, assessing its impact on healthcare accessibility, patient-provider communication, and overall user satisfaction. By analyzing relevant literature, key insights emerge regarding telemedicine's benefits and challenges, highlighting areas for improvement in technology and user experience.

Project Objectives
Telemedicine is a wide field that is essential for reaching patients in remote and underserved areas all over the world. By nature, this field is heavily reliant on enabling technologies that facilitate remote perception, communication and interaction. The unique challenges the conception and implementation of these technologies present have given rise to an interdisciplinary field of healthcare and engineering.

Some relevant technologies of note include skin stretch interfaces, which aim to improve accuracy through a novel form of haptic feedback (1). Predictive mixed reality displays enhance surgical visualization by addressing latency issues and filling in gaps with predicted visual updates (2–4). Recreation for remote palpitation involves the use of pneumatic systems to replicate tissue physical properties, allowing for accurate remote palpitation (5–7). General networking remains a significant challenge in telemedicine, as haptic systems require less than 1ms latency, while audio and video can tolerate slightly higher delays (8).

Methods A systematic search was executed on PubMed and IEEE Xplore using the following keywords: (telemedicine or telesurgery) and (visual or vision or perception or interaction) and (3D or touch or body sound or auscultation or palpation) and (remote) NOT (review). Articles were excluded from this initial search based on the following criteria: (1) were not related to telemedicine or a technology that could directly benefit telemedicine; (2) were not related to human perception nor interaction. Results of the search that met inclusion criteria were organized into four categories: Haptic Methods, Visual Methods, Auditory Methods, and Data-Driven Diagnostic Techniques. Some articles present a technology that has focus in more than one category, these were touched upon in each relevant category.

Results and Discussion
The search provided a window into the current state of telemedical technologies ranging from haptic feedback interfaces for telepalpation to mixed reality systems for surgical telementoring and AI-driven image-based diagnostics in wound care categorization.

References
1. Thai MT, Hoang TT, Phan PT, Lovell NH, Do TN. Soft microtubule muscle-driven 3-axis skin-stretch haptic devices. IEEE Access [Internet]. 2020 [cited 2024 Feb 9];8:157878–91. Available from: https://ieeexplore.ieee.org/document/9178739
2. Farhang S, Foruzan AH, Chen YW. A real-Time stable volumetric Mass-Spring Model based on a multi-scale mesh representation. 2016 23rd Iranian Conference on Biomedical Engineering and 2016 1st International Iranian Conference on Biomedical Engineering, ICBME 2016. 2017 Mar 30;165–9.

3. Šarić M, Russo M, Kraljević L, Meter D. Extended Reality Telemedicine Collaboration System Using Patient Avatar Based on 3D Body Pose Estimation. Sensors (Basel) [Internet]. 2023 Dec 20 [cited 2024 Feb 9];24(1):27. Available from: http://www.ncbi.nlm.nih.gov/pubmed/38202889
4. Richter F, Zhang Y, Zhi Y, Orosco RK, Yip MC. Augmented reality predictive displays to help mitigate the effects of delayed telesurgery. Proc IEEE Int Conf Robot Autom. 2019 May 1;2019-May:444–50.
5. Costi L, Iida F. Multi-silicone bilateral soft physical twin as an alternative to traditional user interfaces for remote palpation: a comparative study. Sci Rep [Internet]. 2023 Dec 27 [cited 2024 Feb 9];13(1):23014. Available from: http://www.ncbi.nlm.nih.gov/pubmed/38155254
6. Kim K. Haptic augmented skin surface generation toward telepalpation from a mobile skin image. Skin Research and Technology. 2018 May 1;24(2):203–12.
7. Filippeschi A, Brizzi F, Ruffaldi E, Jacinto JM, Avizzano CA. Encountered-type haptic interface for virtual interaction with real objects based on implicit surface haptic rendering for remote palpation. IEEE International Conference on Intelligent Robots and Systems. 2015 Dec 11;2015-December:5904–9.
8. Senk S, Ulbricht M, Tsokalo I, Rischke J, Li SC, Speidel S, et al. Healing Hands: The Tactile Internet in Future Tele-Healthcare. Sensors. 2022 Feb 1;22(4).

Electromagnetic Traversal Robot Neural Network-Based Localization Method

Student Researcher: John Radey

Advisor: Dr. David Sawyer

Ohio Northern University
Mechanical Engineering

Abstract
Maintenance of spacecraft, such as the International Space Station, currently relies on astronaut-conducted spacewalks, which are both time-consuming and hazardous. Satellites, in contrast, are often decommissioned when maintenance is required, as in-orbit servicing remains technically and economically challenging. This research investigates a neural network-based localization method for an Electromagnetic Traversal Robot (EmTR) designed for autonomous servicing of space structures. The EmTR uses electromagnets for mobility and relies on Hall effect sensors embedded in its smart pads to detect magnetic foot positions. A convolutional neural network (CNN) was trained to infer the robot's 2D position from sensor readings, enabling precise localization without external vision. Experimental results demonstrate the feasibility of this approach, supporting its potential application in extending spacecraft operational life through autonomous maintenance and inspection tasks.

Introduction
Maintenance of in-orbit space assets is costly and time-consuming. On the International Space Station (ISS), astronauts conduct spacewalks for many repair tasks, which are inherently dangerous and can last several hours [1]. To reduce this burden, the ISS uses large, custom-built robotic systems that assist with or autonomously perform basic operations [2].

In contrast, satellites are rarely serviced. Most low Earth orbit (LEO) satellites are deorbited to burn up in the atmosphere, while geosynchronous satellites are relocated to graveyard orbits at the end of their operational life [3]. A few exceptions exist, such as the Hubble Space Telescope, which was maintained through space shuttle missions [4], and the Mission Extension Vehicle (MEV), which successfully docked with and extended a satellite's operation in 2020 [5]. However, these cases are uncommon due to the complexity and cost involved.

These examples highlight the high operational and financial demands of space maintenance, whether through replacement launches, crewed missions, or specialized robotic platforms. This project proposes a neural network-based localization method for an electromagnet-based extravehicular mobile robot. Such a system could be deployed on spacecraft or satellites to extend mission lifespans and reduce the need for direct human intervention.

Objective
The objective of this project is to design, prototype, and test a neural network (NN)-based smart pad equipped with embedded Hall effect sensors. The smart pad will output 2D location data of a magnet placed on its surface, enabling precise localization of an electromagnet-based extravehicular mobile robot.

Methodology

A series of experiments were conducted to model the relationship between Hall effect sensor outputs and the position of an electromagnet. The initial experiment used a single analog Hall effect sensor mounted beneath an 18-gauge cold-rolled steel plate. Voltage readings were recorded while the magnet was positioned at various known locations in both the x and y directions to identify spatial correlations.

Subsequent experiments expanded the setup to include four Hall effect sensors arranged beneath the same steel plate. To minimize magnetic interference, holes were drilled in the steel directly above each sensor. A dataset was generated by moving the electromagnet across the plate to known positions and recording the corresponding sensor outputs. The resulting dataset contained approximately 3,000 samples, each with four Hall sensor inputs and associated (x, y) position labels.

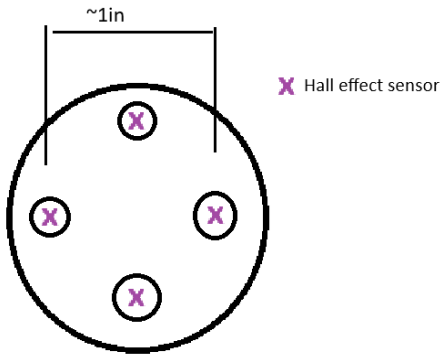


Figure 1: Diagram of smart pad with Hall effect sensor placements.

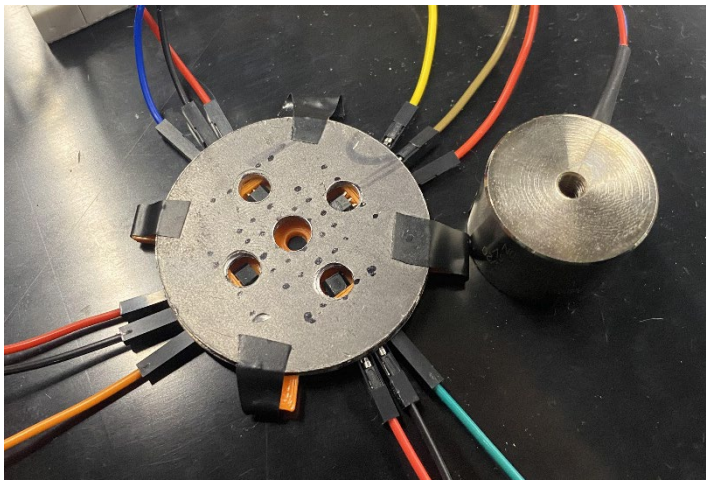


Figure 2: Assembled smart pad test setup.

The model architecture was a four-layer convolutional neural network (CNN), selected to manage the high dimensionality of the sensor data. Hyperparameters for the initial model where tuned by trial and error while the hyperparameters for the final model were tuned using a grid search over the following

parameters: optimizer, number of neurons, dropout rate, activation function, batch size, number of epochs, and L1/L2 regularization coefficients. The final model used an 80/20 training-validation split and was trained using the mean absolute error (MAE) as the loss function. The input layer accepted four values (one from each sensor), and the output layer produced a two-dimensional vector representing x and y coordinates.

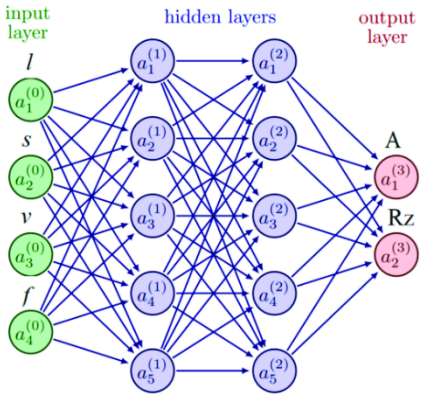


Figure 3: Convolutional neural network diagram [6].

Results

An initial observation from the experiments was that the output data from the hall effect sensors had a highly nonlinear relationship with the magnet location. A sample of this data can be seen in Figure 4 below.

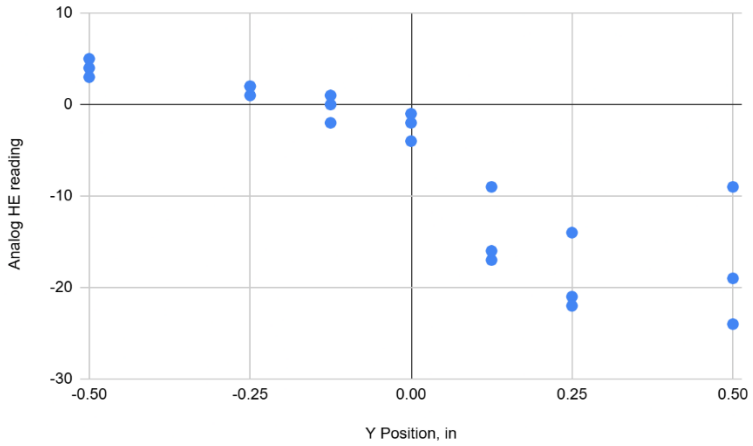


Figure 4: Hall effect output data sample.

This result was a driving factor towards developing a neural network model. The initial CNN developed was a convolutional neural network with the following parameters seen below in Table 1.

Table 1: Table of initial CNN parameters.

Parameter	Value
Optimizer	adam
Neurons	128
Dropout	0.2

Activation Fcn	tanh
Batch Size	8
Epochs	200
L1	0.0001
L2	0.01

Figure 5 below shows the training and validation loss of this model across the training epochs. It can be seen that the model shows little signs of overfitting and converges at a mean absolute error of 0.221in.

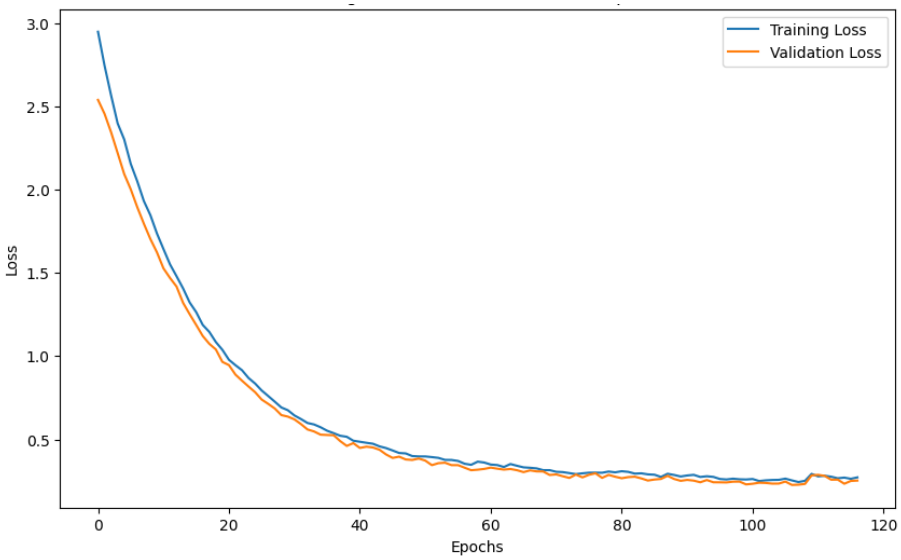


Figure 5: Training and validation loss of initial model.

The grid search performed took roughly 3 days to run and found the best model was comprised of the parameters found below in Table 2.

Table 2: Table of grid search parameters.

Parameter	**Value**
Optimizer	Rmsprop
Neurons	64
Dropout	0.2
Activation Fcn	relu
Batch Size	8
Epochs	100
L1	0.0001
L2	0.01

The mean absolute error of this model was 0.183in, Figure 6 below shows that the training and validation loss converges and shows little signs of overfitting.

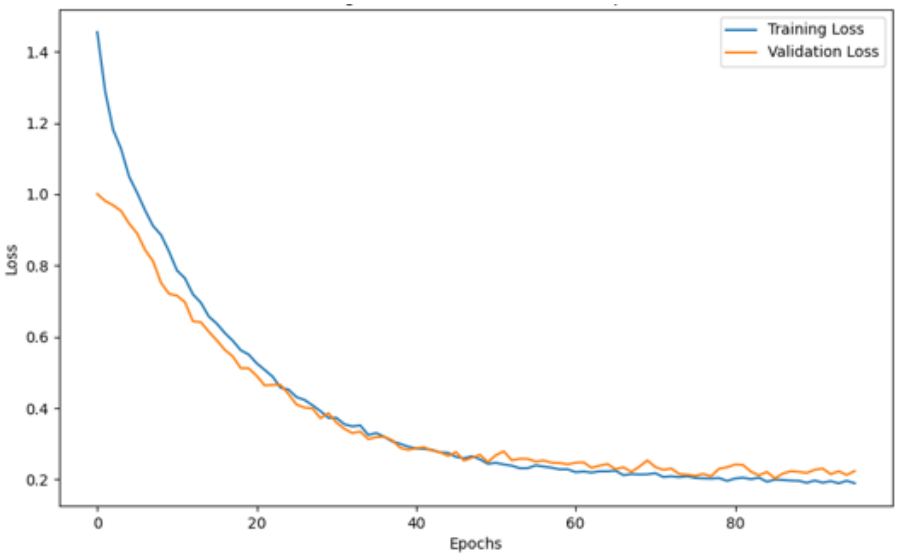


Figure 6: Training and validation loss of final model.

Conclusion

The results of this study demonstrate that neural network-based localization using Hall effect sensors is a viable approach for electromagnet-based mobile robots. The final model, optimized via grid search, achieved a mean absolute error of 0.182 inches. Considering the test platform's 2-inch traversal diameter, this error represents a reasonably accurate prediction given the system's simplicity and sensor count.

While promising, the current results are limited by the relatively small dataset (~3,000 samples). Expanding the dataset is expected to improve model performance and generalization. Additionally, since the current model showed minimal signs of overfitting, future work should explore deeper or more complex neural network architectures to further enhance accuracy. This approach has the potential to enable embedded, low-cost localization for autonomous robotic systems operating on constrained or structure-bound surfaces, such as spacecraft exteriors.

References

[1] NASA, "Spacewalks (Extravehicular Activities or EVAs)," *NASA*, 2023. [Online]. Available: https://www.nasa.gov/mission_pages/station/spacewalks/. [Accessed: 18-Apr-2025].

[2] NASA, "Dextre at Work," *NASA Image and Video Library*. [Online]. Available: https://www.nasa.gov/image-article/dextre-work. [Accessed: 18-Apr-2025].

[3] European Space Agency (ESA), "End-of-life Disposal of Satellites," *ESA*. [Online]. Available: https://www.esa.int/Enabling_Support/Preparing_for_the_Future/Discovery_and_Preparation/End-of-life_disposal_of_satellites. [Accessed: 18-Apr-2025].

[4] NASA, "Missions to Hubble," *NASA Science – Hubble Space Telescope*. [Online]. Available: https://science.nasa.gov/mission/hubble/observatory/missions-to-hubble/. [Accessed: 18-Apr-2025].

[5] Northrop Grumman, "Northrop Grumman Expands Satellite Life Extension Services," *Newsroom*. [Online]. Available: https://news.northropgrumman.com/file/northrop-grumman-expands-satellite-life-extension-services?action=. [Accessed: 18-Apr-2025].

[6] M. Amini, M. Ghadimi, M. Asadollahi-Yazdi, and M. Sadeghi, “Studying the Factors Affecting Tool Vibration and Surface Quality during Turning through 3D Cutting Simulation and Machine Learning Model,” *ResearchGate*, Fig. 6. [Online]. Available: https://www.researchgate.net/figure/Neural-network-with-four-inputs-and-2-outputs_fig6_370697709. [Accessed: 27-Mar-2025].

The Exploration and Construction of a Bacterial Fuel Cell

Student Researcher: Caely Ressler

Advisor: Paul Penko

Baldwin Wallace University
Engineering

Abstract
This project explores the development of a bacterial fuel cell (BFC) to generate electrical energy using local lake water. A prototype was constructed using carbon tubing, copper mesh, and a proton exchange membrane, and tested with water from Coe Lake in Berea, Ohio. Two trials demonstrated measurable power output, validating the concept. However, energy output declined over time, prompting redesign efforts. The study supports the potential of BFCs for sustainable energy solutions in real world applications, such as wastewater treatment plants and breweries.

Project Objectives
The main objectives of this research project were to design and construct a functioning bacterial fuel cell, test its ability to generate electricity using naturally occurring bacteria in local lake water, and evaluate its potential scalability as a sustainable energy source. Additionally, the project aimed to identify areas of improvement for future designs, especially in creating a vertical prototype that can function effectively in an open-water environment.

Methods
The prototype bacterial fuel cell, seen in Figure 1, was constructed using a PVC shell for the main body. Inside, carbon tubing served as the anode while a copper screen acted as the cathode. A proton exchange membrane (PEM) separated the two chambers, allowing protons to pass while electrons traveled through an external circuit. Initially, the device was designed to allow solutions to be poured in from the top, making it primarily suitable for benchtop testing.

The BFC produces energy through a five-step process. First, bacteria near the anode decomposes organic matter, freeing electrons and H+ ions using the electron transport chain. Then, the free electrons flow from the bacteria to the anode, with assistance from a mediator molecule. Next, the electrons flow through a wire from the anode to the cathode, generating electrical current. As this is happening, the free H+ ions flow to the cathode through a semi-permeable membrane, referred to in this report at the PEM. This process is driven by the electro-chemical gradient resulting from a high concentration of H+ ions near the anode. Finally, the electrons, now at the cathode, combine with oxygen and the free H+ ions to form H_2O.

For field testing, water was collected from Coe Lake in Berea, Ohio. The water was poured into the fuel cell to activate naturally occurring bacteria. In the first trial, a multimeter was connected directly to the fuel cell to measure the voltage output over a period of three days. This test aimed to verify that Coe Lake water could support electricity generation. In the second trial, a 55-ohm resistor was added in series with the multimeter. Voltage measurements were taken over two days, and power output was calculated using the recorded voltage and known resistance.

Results and Discussion

In Trial 1, the primary goal was to determine whether environmental bacteria in Coe Lake water could generate electricity. The voltage peaked at 16.748 millivolts, with an initial spike followed by a gradual decline, as seen in Figure 2. This indicated that the bacteria were actively producing electrons at first but lost efficiency as conditions in the fuel cell changed, likely due to the depletion of organic matter or bacterial die-off.

Trial 2 involved more advanced testing by adding resistance to the circuit, which allowed both voltage and power output to be measured. The peak voltage reached 116.3 millivolts, and the maximum power output recorded was 0.24 milliwatts, as seen in Figures 3 and 4. Similar to the first trial, power output steadily decreased over the testing period. These results confirmed the BFC's ability to generate power but also highlighted its limitations in sustaining output over time.

The declining performance in both trials suggests that the fuel cell needs a continuous supply of nutrients or more robust bacterial populations to maintain energy generation. It also underscores the importance of refining the internal environment of the cell to support long-term bacterial activity. These findings informed the decision to redesign the prototype, leading to the development of a new vertical model.

The new design aims to address the limitations observed in earlier trials. It features a vertically oriented structure with an open-bottom design, as seen in Figure 5. This allows for natural water exchange when placed in lakes or ponds. This setup is expected to support continuous bacterial activity by providing a steady influx of fresh organic material. Future testing will explore the energy output of this vertical design and assess its potential for long-term deployment in natural water bodies.

Figures/Charts

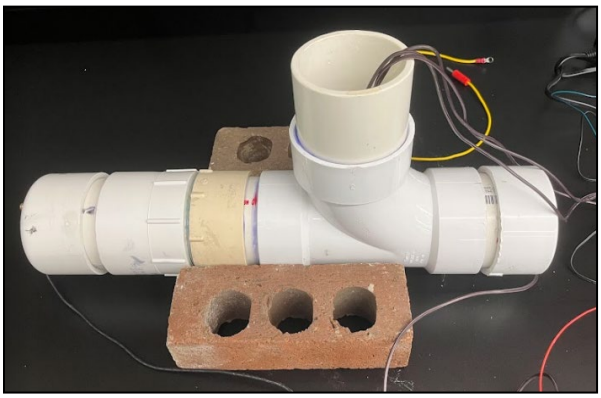


Figure 1: Prototype Bacterial Fuel Cell on which testing was conducted

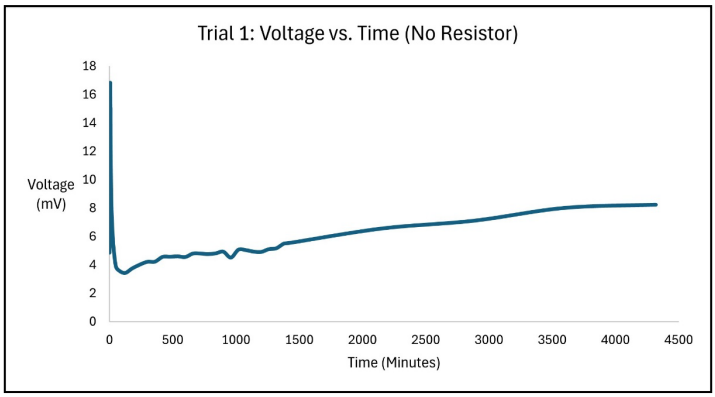


Figure 2: Trial 1 Voltage Results

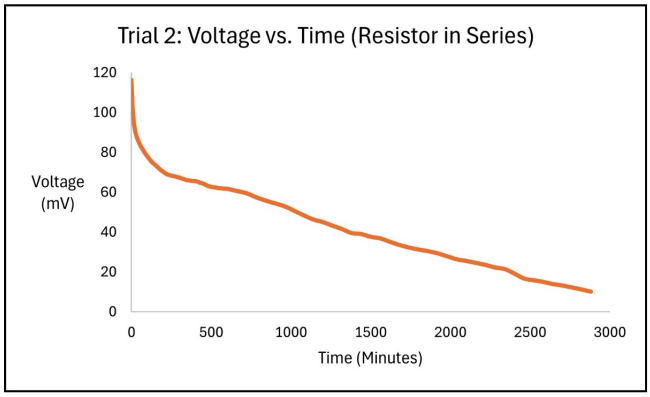


Figure 3: Trial 2 Voltage Results

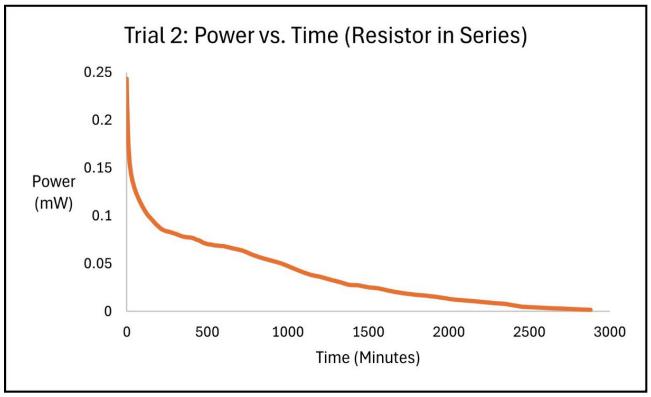


Figure 4: Trial 2 Power Results

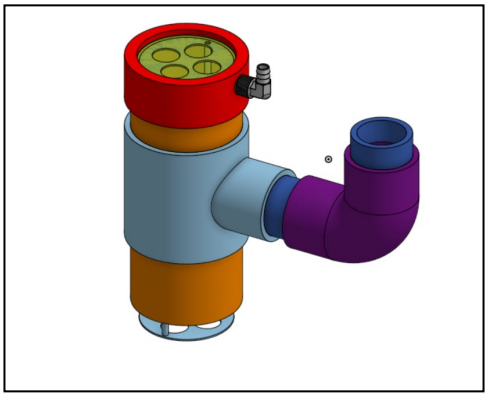


Figure 5: Redesigned Prototype CAD, highlighting vertical orientation.

Acknowledgments
Special thanks to Professor Paul Penko of the Baldwin Wallace University Engineering Department for his guidance and mentorship throughout the project. Additional appreciation goes to Martin Flores for his

assistance in the fabrication lab, as well as to previous students who contributed to early versions of the bacterial fuel cell.

References

Ali, H.Y., Rushdi, S.A. & Alhameedi, H.A. Microbial Fuel Cells: Their Shapes, Designs, and Transportation Methods (Mini Review). Russ J Appl Chem 97, 183–197 (2024). https://doi.org/10.1134/S1070427224010142

De Gaetano, Antonio. (2015). Bachelor's Thesis conference at University of Naples " Parthenope".

Erfan Abbasian Hamedani, Ali Abasalt, S. Talebi, “Application of microbial fuel cells in wastewater treatment and green energy production: A comprehensive review of technology fundamentals and challenges.” Fuel, Volume 370, 2024, 131855, ISSN 0016-2361, https://doi.org/10.1016/j.fuel.2024.131855.

Mercer, Justin. “Microbial Fuel Cells: Generating Power from Waste.” USC Viterbi School of Engineering, 12 Nov. 2017, illumin.usc.edu/microbial-fuel-cells-generating-power-from-waste/.

“MFCS - Basic Information.” FABE, 2024, fabe.osu.edu/mfcfacts.

Researchfeatures. “Scaling up Microbial Fuel Cells to Clean Wastewater and Produce Electricity.” Research Features, 8 Nov. 2023, researchfeatures.com/scaling-microbial-fuel-cells-mfcs-clean-wastewater-produce-electricity/.

Roy, Hridoy et al. “Microbial Fuel Cell Construction Features and Application for Sustainable Wastewater Treatment.” Membranes vol. 13,5 490. 30 Apr. 2023, https://doi.org/10.3390/membranes13050490

Sarma, Pranab & Mohanty, Kaustubha. (2019). An Insight into Plant Microbial Fuel Cells. 10.1002/9781119611103.ch8.

Schröder, U. Discover the possibilities: microbial bioelectrochemical systems and the revival of a 100-year–old discovery. J Solid State Electrochem 15, 1481–1486 (2011). https://doi.org/10.1007/s10008-011-1395-7

Sokhee P. Jung, Soumya Pandit, Chapter 3.1 - Important Factors Influencing Microbial Fuel Cell Performance, Editor(s): S. Venkata Mohan, Sunita Varjani, Ashok Pandey, In Biomass, Biofuels and Biochemicals, Microbial Electrochemical Technology, Elsevier, 2019, Pages 377-406, ISBN 9780444640529, https://doi.org/10.1016/B978-0-444-64052-9.00015-7.

Vishwanathan, A S. “Microbial fuel cells: a comprehensive review for beginners.” 3 Biotech vol. 11,5 (2021): 248. https://doi.org/10.1007/s13205-021-02802-y.

Walter, X.A., Gajda, I., Forbes, S. et al. Scaling-up of a novel, simplified MFC stack based on a self-stratifying urine column. Biotechnol Biofuels 9, 93 (2016). https://doi.org/10.1186/s13068-016-0504-3

Wang, J.; Ren, K.; Zhu, Y.; Huang, J.; Liu, S. “A Review of Recent Advances in Microbial Fuel Cells: Preparation, Operation, and Application.” BioTech 2022, 11, 44. https://doi.org/10.3390/biotech11040044

Design and Fabrication of Dual-Sided Laser Induced Graphene Microheaters for Biomedical Applications

Student Researcher: Collin Richards

Advisor: Dr. Byung-Wook Park

Youngstown State University
Chemical Engineering

Abstract
This project explores the design and fabrication of a novel dual-sided Laser Induced Graphene (LIG) microheater system for biomedical applications. Using direct laser writing on polyimide (PI) films, conductive LIG patterns were created and characterized for thermal performance. A dual-sided geometry was proposed, featuring a LIG heater on one side and a copper-electroplated thermal spreader on the reverse. This configuration enhances heat distribution while maintaining flexibility and low power consumption, offering potential for wearable transdermal drug delivery and wound care devices.

Project Objectives
This research aims to develop flexible, dual-sided LIG-based microheaters for biomedical devices such as transdermal patches and wound dressings. A key goal is to upscale heating area while maintaining uniform thermal distribution and low power use. However, increasing surface area and electrode spacing raises electrical resistance, which increases power demands. To address this, LIG formation parameters—laser power, speed, and pulse density—were optimized for high conductivity.

Multiple heater geometries (solid, meander, lines, mesh) were tested to identify layouts offering optimal resistance, heat uniformity, and fabrication ease. A dual-sided architecture was introduced with copper electrodeposition on the reverse PI surface. This electrically isolated copper layer acts as a passive heat spreader—improving heat distribution without increasing power draw. Through laser parameter tuning, geometry optimization, and dual-layer integration, the project targets scalable, energy-efficient heaters for next-gen biomedical applications.

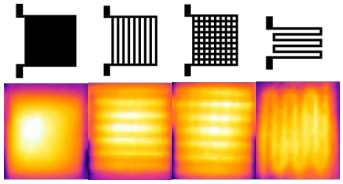
Methods
Laser Induced Graphene (LIG) patterns were fabricated by irradiating commercial polyimide films using a CO_2 laser engraver. To ensure high conductivity and material integrity, a systematic power and speed optimization assay was conducted. Laser power was varied between 3.2–4.8 W, and scanning speeds were adjusted from 8–60 mm/s to determine optimal parameters for consistent LIG formation. The resulting graphene was characterized microscopically and electrically to assess conductivity, pattern uniformity, and surface morphology. Once optimal conditions were established, multiple heater geometries (solid, meander, lines, and mesh designs) were patterned and evaluated for their electrothermal performance.

Following LIG formation, copper was electrodeposited onto the reverse side of the polyimide substrate to create a passive thermal spreader. This process was carried out in an aqueous copper sulfate solution using a two-electrode system. An electrodeposition assay was performed by varying current density (0.125–0.325 mA/mm^2) and plating duration (from 1 to 20 minutes) to determine the ideal combination for uniform copper coverage without delamination or overplating. The dual-sided structure, LIG on one side for Joule heating, and copper on the opposite side for enhanced thermal conduction—was then assembled and tested. Electrical resistance was measured using a digital multimeter, while a FLIR infrared camera was used to capture thermal

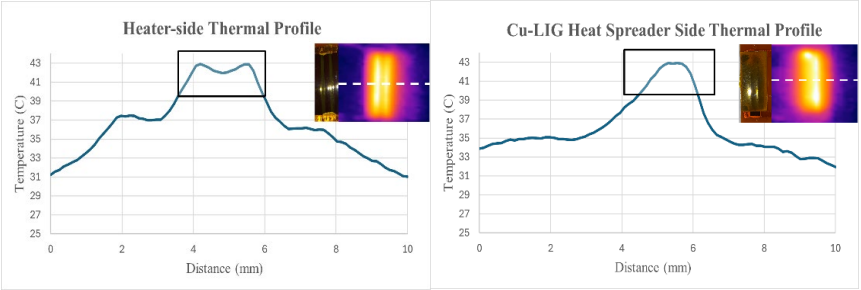
profiles under low-voltage (0–5V) conditions, enabling comparative analysis of heating rates, uniformity, and heat dissipation efficiency.

Results and Discussion

Four LIG heater geometries—solid, lines, mesh, and meander—were tested with fixed LIG area and 2 mm gaps to support scalable designs. Resistance, power use, and thermal behavior were measured at 4V. The solid design had lowest resistance and fastest heating but showed thermal hotspots. Meander geometry had high resistance, limiting its practical heating capability. The lines design offered the largest area with balanced resistance and uniform heating—supporting both scalability and performance.



Copper electrodeposition on the opposite side of the polyimide improved thermal uniformity across all designs. Although electrically isolated, the copper layer acted as a heat spreader, reducing hotspots and enhancing lateral conduction. Optimal plating conditions (0.225–0.275 mA/mm² for 15–20 minutes) produced uniform coverage without compromising flexibility. This dual-sided design effectively addressed heating inefficiencies, making it well-suited for scalable, low-power biomedical applications.



Acknowledgments

Special thanks to Dr. Byung-Wook Park and Pari Dhungana for guidance and characterization assistance, and to the Ohio Space Grant Consortium and Youngstown State University for financially supporting this research opportunity.

References

[1] Jeroish, Z.E. *et al.,* Microheater: material, design, fabrication, temperature control, and applications—a role in COVID-19, *Biomed Microdevices,* 2022, 24, 3.

[2] Markota, A. et al., Therapeutic hyperthermia for the treatment of infection—a narrative review, *Front Physiol*, 2023, 14, 1215686.

[3] Huang, J. et al., Exploring Thermal Dynamics in Wound Healing: The Impact of Temperature and Microenvironment, *Clin Cosmet Investig Dermatol*, 2024, 17, 1251-1258.

[4] Yang, Y. et al., Fabrication of flexible microheater with tunable heating capabilities by direct laser writing and selective electrodeposition, *J Manuf Process*, 2022, 74, 88-99.

The Effects of Carbon Fibers on Mechanical and Shrinkage Properties of Ultra-High-Performance Concrete (UHPC)

Student Researcher: Aliah Rodriguez

Advisor: Dr. Srinivas Allena

Cleveland State University
Department of Civil and Environmental Engineering

Abstract
Ultra-high-performance concrete (UHPC) is an advanced cementitious composite known for its exceptional compressive and tensile strength, durability and reduced permeability. These qualities make UHPC ideal for structural applications in transportation, pre-casting, and other infrastructure systems. Traditionally, UHPC achieves its superior performance through the inclusion of steel fibers (SF), due to its behavior in bridge cracks and post-cracking behavior. However, as the construction industry continues to prioritize sustainability, cost-efficiency, and innovation, this study explores the effects of incorporating carbon fibers (CF) into UHPC as a partial or full replacement for steel fibers. Carbon fibers present unique benefits, including greater local availability, lighter weight, and enhanced corrosion resistance – masking them a potentially sustainable and economical alternative.

Project Objectives
This research focuses on evaluating how CF's influence the mechanical performance and shrinkage behavior of UHPC mixtures, with the goal of promoting durable and environmentally conscious material alternatives. Specifically, we examined changes in compressive strength, tensile strength, and drying shrinkage associated with the use of CFs at varying replacement levels. We also explored the interaction between curing conditions and fiber composition to determine optimal conditions for performance.

Methods
UHPC mixtures were prepared using ASTM-specified materials: Type 1L Portland limestone cement (PLC), Class F fly ash, silica fume, and fine sand. High-range water-reducing admixture (HRWRA) was used to maintain workable mixtures with a target flow of 8 inches. The fiber system varied between control mixtures with 100% steel fibers and those with 35%, 50%, and 75% CF replacement by square footage. Tests were conducted in accordance with ASTM standards: flow table (ASTM C1437), compressive strength (ASTM C109), aplit tensile strength (ASTM C496), and drying shrinkage (ASTM C157). Curing conditions included warm bath curing at 90°C, moist curing at 23°C, and a combination of both to simulate accelerated and standard environments.

Results and Discussion
Results revealed that increasing CF content led to a decrease in workability due to differences in fiber morphology and bonding compacity. As CF content rose, higher HRWRA dosages were required to maintain target flow levels. An optimal dosage of 16g/kg of HRWRA was identified for the 75% CF mixture, balancing flow and fiber dispersion without causing segregation.
In terms of compressive strength, a general decreasing trend was observed with higher CF replacements levels, likely due to the reduced mechanical interlock between CF's and the cementitious matrix. However, the 50% CF mixture still achieved compressive strengths near the UHPC benchmark of 17,500 psi under moist curing conditions, demonstrating that partial CF substitution is feasible without significant performance loss. Warm bath curing generally enhanced compressive strength across all mixes, likely due

to accelerated hydration, while combinations of curing methos yielded variable results based on fiber type.
The split tensile strength performance was particularly promising. The 75% CF mixture exhibited the highest strength among all mixes, exceeding even the control. This suggests that while CFS may not anchor as effectively for compressive load bearing, they excel in bridging microcracks under tensile strength. This result also reflects the improved dispersion of CFs when HRWRA is optimized, allowing for more uniform fiber reinforcement across the matrix.

Drying shrinkage results further highlighted the benefits of CF incorporation. The 50% CF mixture cured at 20°C exhibited the lowest shrinkage values, even outperforming fbe control. CFs appeared to restrain early-age dimensional changes, likely reducing the formation of shrinkage-induced microcracks. These findings indicate that CFs not only offer structural reinforcement but may also help improve long-term dimensional stability and service life.

Overall, this study supports the use of carbon fibers as a viable and sustainable alternative to steel fibers in UHPC. Partial replacement – particularly at 50% level – balances strength retention with improved shrinkage control and reduced dependence on steel. These findings contribute to broader efforts to reduce material costs, utilize locally available materials, and enhance the environmental sustainability of infrastructure materials. Future studies could expand on this work by exploring hybrid fiber systems using recycled materials, long-term durability under cyclic loading, and cost-benefit analysis for field applications. This research adds to the growing body of knowledge surrounding UHPC innovation and demonstrates new possibilities for durable, sustainable high-performance concrete in the future of infrastructure.

Preliminary Study: Minimizing the Gap between Pre-and Post-Spaceflight

Student Researcher: Caleb Scheideger

Advisor: Dr. Louis DiBerardino

Ohio Northern University
Department of Mechanical Engineering

Abstract

Long-duration space missions pose significant challenges to astronaut health, primarily due to the detrimental effects of microgravity on musculoskeletal and cardiovascular systems. This research proposal aims to address the critical gap between pre- and post-spaceflight physiological conditions, focusing on the marked decline in muscle mass, bone density, and cardiovascular function. Existing countermeasures, such as resistive exercise, are insufficient to prevent muscle atrophy and bone demineralization, highlighting the need for novel solutions. Neuromuscular Electrical Stimulation (NMES) emerges as a promising intervention, capable of eliciting muscle contractions to maintain function and mitigate atrophy. By integrating NMES into existing exercise regimens, we hypothesize enhanced efficacy in preserving lower body musculature, maintaining bone density, and supporting cardiovascular health. This proposal leverages findings from dynamometer force acquisition and bed rest studies, combined with meta-analytic insights into NMES's effectiveness in clinical settings, to optimize protocols for spaceflight application. The ultimate goal is to develop robust countermeasures ensuring astronaut health for safe interplanetary travel. Further investigations including OpenSim software modeling and predictive framework will be investigated in this research for later implementation and analysis.

Keywords: microgravity, muscle atrophy, OpenSim, electrical stimulation

Introduction

Spaceflight presents extreme challenges to human physiology. Without the constant pull of gravity, astronauts experience rapid muscular, skeletal, and cardiovascular degeneration. Studies show that within just two weeks, astronauts may lose up to 20% of their muscle mass and strength[1]. Bone density declines at a rate of 1–2% per month[1], while cardiovascular shifts result in fluid redistribution and altered cardiac output[2]. These physiological changes not only compromise in-flight performance but also pose risks during reentry and post-mission recovery.

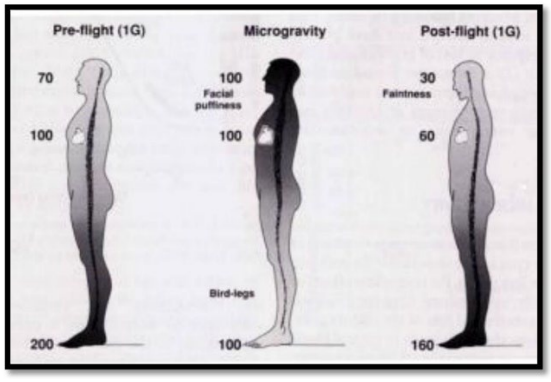


Figure 1. Fluid Shift Distribution Pre-and Post-flight[3]

Although astronauts adhere to a rigorous 2.5-hour daily exercise regimen using resistive devices, these countermeasures are often insufficient[1]. Muscle atrophy, particularly in the quadriceps and gluteal muscles, remains significant. Neuromuscular Electrical Stimulation (NMES), widely used in clinical rehabilitation for spinal cord injuries, chronic obstructive pulmonary diseases, cerebral palsy, and disuse atrophy, presents a novel tool for space medicine[4]. NMES can evoke muscle contractions through electrical pulses, thereby preserving muscle tone and delaying atrophy. Has also been investigated in mitigating bone demineralization[5].

This study proposes a muscle modeling approach that observes biomechanical modeling, muscle activity tracking via EMG, and predictive simulation in OpenSim to evaluate NMES integration[6]. The hypothesis: NMES-enhanced regimens will outperform conventional resistance training in maintaining musculoskeletal function during spaceflight.

Methods

2.1 Experimental Setup

A standing squat was performed by the test subject using a lightweight bar (negligible mass), purely for form consistency and motion reference. No significant resistance was applied during this physical trial. The primary purpose of this movement was to capture accurate joint trajectories and kinematic behavior for modeling in OpenSim.

2.2 Data Preparation and Capture

Motion capture data was recorded to extract hip, knee, and ankle trajectories utilizing OpenCap[7]. While EMG was not implemented in this phase, it is planned for future work. This motion data served as input for biomechanical simulations in OpenSim.

2.3 OpenSim Modeling

A musculoskeletal model was adapted to simulate a male subject performing a loaded standing squat. The external load (modeled as a 135lb barbell) was applied virtually in OpenSim via a force vector applied to the upper body (shoulder area). A Hill-type muscle model was used to simulate force production by primary movers including the quadriceps and gluteal muscles[8].

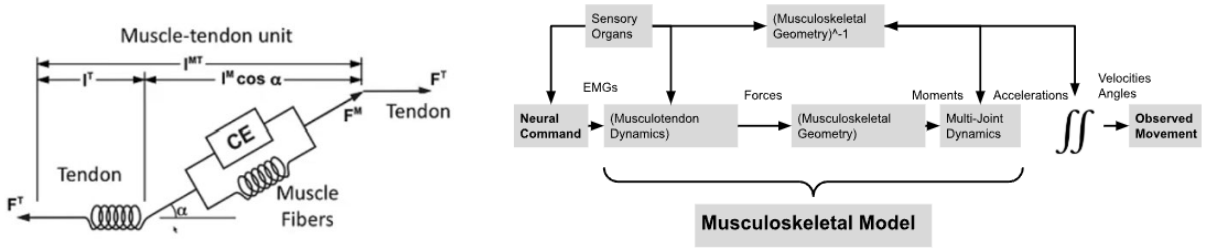


Figure 2 & 3. Hill-Type Muscle Model (Left) & OpenSim Musculoskeletal Model (Right)[7]

2.4 Simulated Conditions

The squat was simulated under both Earth gravity (−9.81 m/s²) and microgravity (0 m/s²). The modeled 135 lb bar remained constant in both simulations to allow comparison of muscle output under varying gravitational loads. Atrophy was simulated by applying an exponential decay to the maximum isometric force (F_{max}) to reflect long-duration muscle weakening.

2.5 Analytical Force Model

To evaluate the effects of atrophy on force production, an analytical model was constructed based on the Hill-type muscle model. This model estimates total muscle force across a range of normalized muscle lengths (l / l_{opt}) using Gaussian and exponential components to represent active and passive forces, respectively.

Muscle force was calculated using the following hill-type muscle model equations:

Active Force

$$F_{active}(l) = F_{max} \times \exp\left(-\left(\frac{l-l_{opt}}{0.15\times l_{opt}}\right)^2\right) \quad (1)$$

Passive Force

$$F_{passive}(l) = \begin{cases} 0 & l \le l_{opt} \\ \exp\left(k\left(l-l_{opt}\right)\right) - 1 & l > l_{opt} \end{cases} \quad (2)$$

Total Force

$$F_{total}(l) = F_{active} + F_{passive} \quad (3)$$

Attenuation (Difference Pre-and Post-Flight)

$$A(l) = F_{pre}(l) - F_{post}(l) \quad (4)$$

Where:

- l_{opt} is the optimal muscle length,
- l is the current muscle length,
- k is the stiffness constant (0.05),
- F_{max} represents maximum isometric force.

This framework allows for simulation of progressive atrophy by modifying F_{max} and shifting l_{opt} to represent remodeling effects. These force equations were used to generate force-length profiles for different stages of muscle loss (pre-flight, post-flight, extended deconditioning), as shown in Figure 4 below.

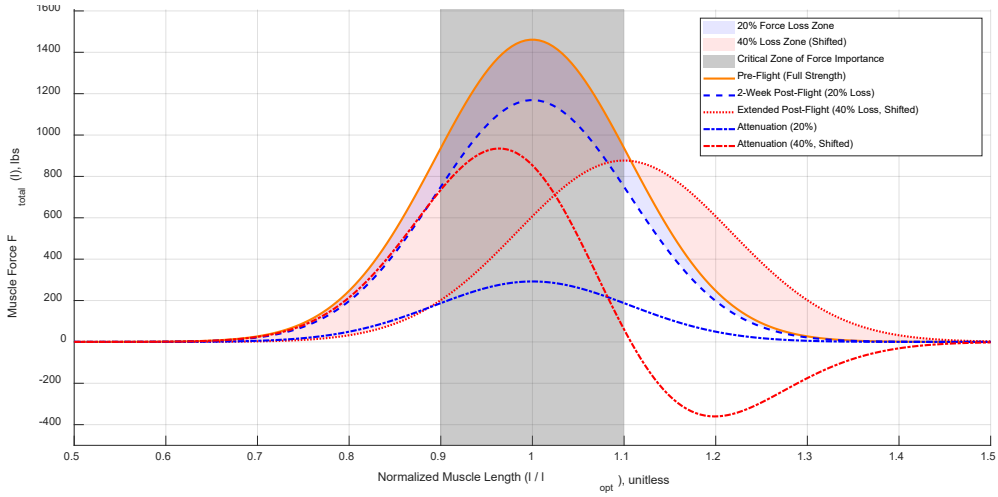


Figure 4. Muscle Force Length Curve with Highlighted Attenuation Zones

Discussion

This study utilized OpenSim to extract inverse kinematic data for a standard lower extremity squat movement under Earth gravity. Quadricep muscles were observed and directly measured through muscle fiber length ratios[9], used in scaling the model during active force contraction. The joint trajectories of the hip, knee, and ankle were used as the foundation for an analytical model, designed to approximate total contractile force output. The objective was not to simulate specific muscular activations but to establish a force-based framework capable of quantifying the gap in functional muscle output resulting from microgravity-induced atrophy.

The model emphasizes the force-length relationship of muscle-tendon units, particularly the region surrounding the normalized muscle length of l_{opt} = 1.0, where sarcomeres achieve peak overlap and thus maximal force. This critical ±10% window is biomechanically significant for lower-body functional tasks such as standing, walking, stair climbing, and squatting.

Simulation results show that with progressive atrophy (20–40% loss), there is:

- A downward shift in peak force,
- A rightward shift in the force-length curve,
- And a reduction in force production within the functional range.

These outcomes suggest that post-spaceflight muscle does not just lose strength, it also becomes less biomechanically effective at key joint angles involved in daily mobility.

Although NMES was not implemented in this study, the framework developed here creates a platform for future NMES simulation and optimization. By quantifying the theoretical force deficit across lower extremity joints, the model can be extended to determine how much external stimulation would be required—timed and scaled appropriately—to restore function within the weakened range. This provides a structured path toward implementing predictive NMES strategies for maintaining mobility in microgravity environments.

Future Work

Future phases of this research will improve predictive modeling fidelity and explore NMES as a countermeasure through the following avenues:

- Subject Expansion & Validation: Introduce more test subjects and incorporate inverse dynamics to increase model robustness.
- EMG Integration: Implement EMG to validate predicted muscle activation patterns and enhance simulation accuracy.
- Time-Based Fatigue Modeling: Apply decay functions to simulate progressive force loss in OpenSim[6].
- NMES Protocol Simulation: Test variable parameters (frequency, intensity, pulse duration, ramp times, ON/OFF cycles) to identify optimal stimulation profiles[10].
- Multi-DOF Modeling: Expand joint range of motion to include rotational and lateral degrees of freedom at the hip and knee[8].
- Force Redistribution Analysis: Study how gravitational unloading alters joint load paths and compensation strategies.
- Control System Implementation: Build feedback-based or reinforcement learning (RL) control models to adjust NMES parameters in real time based on length, torque, or fatigue states[6].

These improvements aim to develop a personalized, adaptive NMES framework capable of targeting contractile force deficits in microgravity, particularly in the critical range needed for maintaining mobility and independence. A rough sketch of the controller is as seen below.

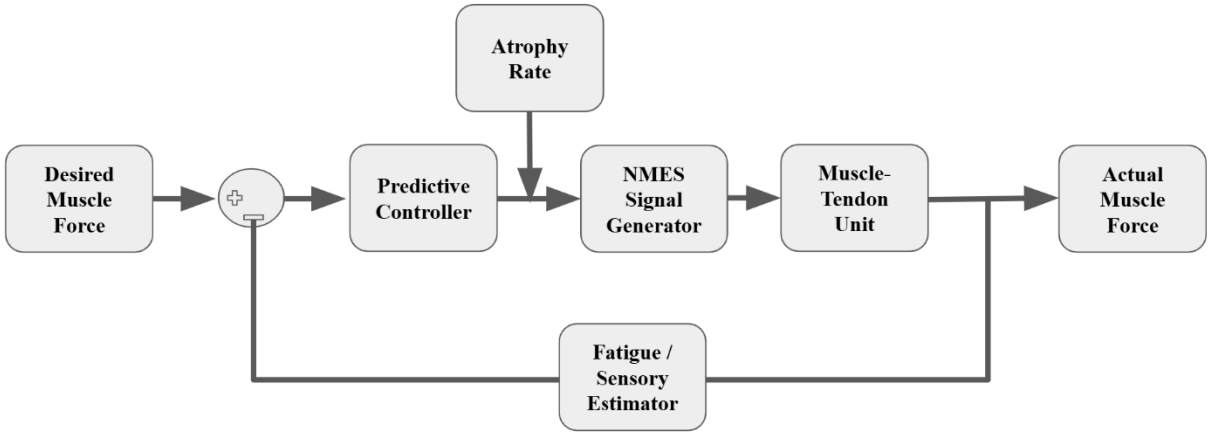


Figure 5. Closed-loop NMES controller for compensating atrophy-induced muscle force deficits. The system compares desired and actual muscle force to generate adaptive NMES stimulation based on feedback and atrophy modeling.

References

[1] Comfort P;McMahon JJ;Jones PA;Cuthbert M;Kendall K;Lake JP;Haff GG;, “Effects of spaceflight on Musculoskeletal Health: A systematic review and meta-analysis, considerations for Interplanetary Travel,” Sports medicine (Auckland, N.Z.), https://pubmed.ncbi.nlm.nih.gov/34115344/

[2] Peter Jirak, Moritz Mirna, Richard Rezar, Lukas J Motloch, Michael Lichtenauer, Jens Jordan, Stephan Binneboessel, Jens Tank, Ulrich Limper, Christian Jung, How spaceflight challenges human cardiovascular health, European Journal of Preventive Cardiology, Volume 29, Issue 10, August 2022, Pages 1399–1411, https://doi.org/10.1093/eurjpc/zwac029

[3] Alan R. Hargens, Sara Richardson, (2009) Cardiovascular adaptations, fluid shifts, and countermeasures related to space flight, Respiratory Physiology & Neurobiology, Volume 169, Supplement, Pages S30-S33, ISSN 1569-9048, 10.1016/j.resp.2009.07.005. (http://www.sciencedirect.com/science/article/pii/S1569904809001840)

[4] Nussbaum EL, Houghton P, Anthony J, Rennie S, Shay BL, Hoens AM. Neuromuscular Electrical Stimulation for Treatment of Muscle Impairment: Critical Review and Recommendations for Clinical Practice. Physiother Can. 2017;69(5):1-76. doi: 10.3138/ptc.2015-88. PMID: 29162949; PMCID: PMC5683854.

[5] Abitante, T. (2023). Evaluation of Neuromuscular Electrical Stimulation as a Bone Loss Countermeasure on a Long Duration Mars Mission (Order No. 31091570). Available from ProQuest One Academic. (3031031545). https://www.proquest.com/dissertations-theses/evaluation-neuromuscular-electrical-stimulation/docview/3031031545/se-2

[6] N. Wannawas, M. Subramanian and A. A. Faisal, "Neuromechanics-based Deep Reinforcement Learning of Neurostimulation Control in FES cycling," 2021 10th International IEEE/EMBS Conference on Neural Engineering (NER), Italy, 2021, pp. 381-384, doi: 10.1109/NER49283.2021.9441354.

[7] S. D. Uhlrich *et al.*, "OpenCap: Human movement dynamics from smartphone videos," *PLoS Comput. Biol.*, vol. 19, no. 10, Oct. 2023, Art. no. e1011462, doi: 10.1371/journal.pcbi.1011462.

[8] OpenSim, "Musculoskeletal Models Deconstructed," YouTube, Aug. 18, 2020. [Online]. Available: https://youtu.be/Kj91GXk1LXY

[9] Felix E Zajac. Muscle and tendon: properties, models, scaling, and application to biomechanics and motor control. *Critical Reviews in Biomedical Engineering*, 1989, 17 (4), pp.359-411. ⟨hal-04849267⟩

[10] Doucet, B. M., Lam, A., & Griffin, L. (2012). Neuromuscular electrical stimulation for skeletal muscle function. The Yale journal of biology and medicine, 85(2), 201–215.

Meteorites: A Petrological, Chemical and Isotopic Synthesis

Student Researcher: Abigail (Abby) Shartle
Advisor: Dr. Andrew Beck
Marietta College
Petroleum Engineering and Geology

Abstract
Chondritic meteorites can be paired based on mineralogy, chemical composition, and structure. Pairing helps identify meteorite fragments from common origins, aiding in understanding their distribution. This study evaluates previously proposed pairings, particularly focusing on R Chondrites within the PRE 95404 group. Petrographic analysis was used to test these pairings against Antarctic Meteorite Newsletter (AMN) reports.

Project Objectives
The goal of this project is to evaluate proposed pairings of chondrites and support or refute them through petrographic and compositional analysis. Criteria include indicators of parent body history, space exposure, and terrestrial weathering, with a focus on petrography and mineral composition.

Methods
Samples PRE 17271 and PRE 17272 were analyzed using petrographic microscopy and scanning electron microscopy (SEM) at Marietta College. Reported features from the AMN were compared against observed properties. These include sulfide nodules (pyrrhotite, pentlandite, magnetite), phosphate and Cu-rich lamellae, and unequilibrated clasts containing type 3.0-3.4 ordinary chondrite-like silica composition.

Results and Discussion
Initial comparisons supported the AMN-reported pairings based on petrographic features, including textural similarity and mineral composition. Type 3 clasts and mineral inclusions appeared consistent across PRE 95404 group samples. This suggests a common origin for the meteorites in the group and reinforces the validity of the pairing methodology.

Acknowledgments
Thank you to Dr. Andrew Beck for supporting my meteorite requests and research. Thanks also to NASA, NSF, ANSMET, the Smithsonian Institute, and the Antarctic Meteorite Newsletter for their resources and support. Special thanks to the faculty and staff of Marietta College for guidance and access to lab equipment.

Additional Discussion on R Chondrites
R type chondrites, also called Rumuruti chondrites, represent a distinct and rare group of meteorites, accounting for only about 0.1% of collected samples. They are noted for their high $\Delta^{17}O$ values and are classified among oxidized chondrites. R chondrites contain minimal iron and nickel minerals and may show evidence of metamorphism by aqueous fluids or may be unaltered and primitive. The samples in this study are classified as petrologic grade 3, indicating relative primitiveness. Chondrules, key components in classification, are spherical to subspherical silicate or metal-sulfide particles found within a matrix. Understanding variations within R chondrites helps us study the compositional effects of metamorphism and thermal history.

Contributions

This research contributes to the field of planetary science and meteoritics by testing and supporting current pairing schemes of R chondrites. Future efforts aim to assist ANSMET by continuing the petrographic and SEM-based pairing of meteorites, providing deeper insight into the formation of the early solar system, planetary differentiation, and meteorite classification.

References

Arizona State University, https://meteorites.asu.edu/meteorites/importance-of-meteorites

Antarctic Search for Meteorites (ANSMET), 2018, Chondrites vs. achondrites: Case Western Reserve University, https://caslabs.case.edu/ansmet/2018/01/08/chondrites-vs-achondrites/.

NASA Johnson Space Center. 2015. *Meteorite Classification and the Formation of the Solar System: NASA Technical Reports, NTRS 20150001911*, https://ntrs.nasa.gov/citations/20150001911,

Hutichinson R, 2006, Meteorities: A Petrologic, Chemical and Isotopic Synthesis, www.Cambridge.org/9780521470100

Isa, J., Rubin, A. E., Wasson, J. T., 2014, R-chondrite bulk-chemical compositions and diverse oxides: Implications for parent-body processes. Geochimica et Cosmochimica Acta, 131-151, ISSN 0016-7037, http://dx.doi.org/10.1016/j.gca.2013.09.018.

NASA Johnson Space Center. 2025. *Petrologic Description of Meteorite PRE95404: NASA Meteorite Collection*, https://curator.jsc.nasa.gov/antmet/samples/petdes.cfm?sample=PRE95404

NASA Johnson Space Center. 2025. *Petrologic Description of Meteorite PRE95411: NASA Meteorite Collection*, https://curator.jsc.nasa.gov/antmet/samples/petdes.cfm?sample=PRE95411

NASA Johnson Space Center. 2025. *Petrologic Description of Meteorite PRE17271: NASA Meteorite Collection*, https://curator.jsc.nasa.gov/antmet/samples/petdes.cfm?sample=PRE17271

NASA Johnson Space Center. 2025. *Petrologic Description of Meteorite PRE17272: NASA Meteorite Collection*, https://curator.jsc.nasa.gov/antmet/samples/petdes.cfm?sample=PRE17272

Benoit, P. H., Sears, D. W. G., Akridge, J. M. C., Bland, P. A., Berry, F. J., & Pillinger, C. T. (2000). The non-trivial problem of meteorite pairing. Meteoritics & Planetary Science, 35, 393–417.

A multi-sensor approach to monitor cropland irrigation within the Lake Erie Basin

Student Researcher: Andrew Shenal

Advisor: Dr. He Yin

Kent State University
Environmental Studies, Department of Geography

Abstract
As shifts within the climate continue to create greater weather variability and warmer temperatures across the globe, farmers are feeling a pressing need to irrigate their agriculture. Mapping irrigation within the Midwestern and Eastern US states is challenging as higher availability of water resources has created less interest and therefore less available data and regular monitoring. Despite this, existing studies reported an increasing trend in irrigation in these regions. This research aims to bridge this gap by mapping local temporal trends in the extent of irrigated land around the Lake Erie Basin. By applying existing methods of irrigation mapping using Landsat 8 and MODIS from 2014 to 2023 I evaluate the effectiveness of current mapping techniques within the region through annual irrigation maps at a 30-meter resolution. Additionally, this will allow me to understand opportunities for improving irrigation mapping within the Great Lakes region in future studies by applying new sensors.

Project Objectives
The primary objective of this project is to establish an understanding of the limitations of irrigation mapping within the Great Lakes region utilizing existing methods. Thirty-meter resolution irrigation maps will be created from 2014 to 2013 in Southeastern Michigan. Through this, researchers and policymakers can understand the direction needed for future studies such as different sensors and allocation of resources.

Methods
Using both National Land Cover Database landcover of agricultural land and the USDA Cropland Data Layer of cultivated land, a crop mask was created indicating the full extent of agricultural land within the study period from 2014 to 2023. Training data of irrigated land points for 2014-2017 was acquired through an existing irrigation mapping study from Xie and Lark in 2021, “Mapping annual irrigation from Landsat imagery and environmental variables across the conterminous United States”. For the later years, very high-resolution imagery was used to locate fields with irrigation infrastructure and higher visual greenness during the growing season. For classification, twenty variables were acquired from Landsat 8 and MODIS indices along with climate data from Daymet V4. Utilizing a random forest supervised classification model, irrigated land was classified on a yearly basis at 30m resolution. To reduce overclassification normalized irrigation frequency was calculated: normIrrFreq = (irrFreq)/(irrYrlast − irrYrfirst). Due to the need for costly irrigation infrastructure, fields are unlikely to be irrigated infrequently. Therefore, pixels with values below 0.5 were removed from the irrigated class as they are unlikely to be irrigated. Additionally, irrigated clusters too small to contain irrigation infrastructure were removed from the irrigated class.

Results and Discussion
First, the study demonstrated that the most important variables for classification were related to the greenness of the fields. In contrast, the climate variables were found to have the least importance. This is likely due to the relatively small differences in climate across the study area compared to field level differences in crop greenness. Variables related to soil moisture were also important to the random-forest classification. On initial qualitative assessment of the classification, areas with sparse clusters of

agriculture were found to be most effectively classified as irrigated. Intensely cultivated regions within the study area most often experienced overclassification. The results of this study indicate that integration with other sensors such as Sentinel-1 could provide increased effectiveness. Increased spatial and temporal resolution as well as availability of synthetic aperture radar data would expand opportunities for more variables related to soil moisture.

Acknowledgments

I would like to thank my advisor, Dr. He Yin, for his invaluable guidance and support throughout this study. I also wish to thank Dr. Yanhua Xie for generously sharing his expertise in irrigation research, and Esmaeel Adrah for his technical assistance.

References

Dewitz, J., 2023, National Land Cover Database (NLCD) 2021 Products: U.S. Geological Survey data release, https://doi.org/10.5066/P9JZ7AO3.

USDA National Agricultural Statistics Service (2015). CropScape - Cropland Data Layer. U.S. Department of Agriculture. Dataset. https://doi.org/10.15482/USDA.ADC/1227096

Xie, Y., & Lark, T. J. (2021). Mapping annual irrigation from Landsat imagery and environmental variables across the conterminous United States. Remote Sensing of Environment, 260, 112445.

Investigating Audio-Haptic Integration for Enhanced Tactile Feedback

Student Researcher: Mason Shultz

Advisor: Dr. Jeong-Hoi Koo

Miami University
Department of Mechanical Engineering

Abstract
This study explores the integration of audio and haptic signals to enhance tactile feedback through audio-haptic synthesis. The primary objective is to evaluate the potential of audio signals as a medium for referencing surface textures and interactions, with implications for applications in sensory augmentation and virtual reality. By leveraging a UR3E Universal Robot, a marker was dragged across a wooden surface at controlled speeds ranging from 25 mm/s to 100 mm/s. A microphone attached to the marker captured the surface interaction audio, which was then transmitted to a piezoelectric actuator. An accelerometer recorded the actuator's vibrations, allowing comparison between the audio and vibrational data using spectrogram analysis.

Results showed a close frequency correlation between the recorded audio signals and the actuator's vibrational feedback, indicating the feasibility of translating surface texture data into meaningful haptic responses. However, signal noise posed challenges during data collection, highlighting the need for improved audio isolation and signal processing techniques.

Future work will focus on enhancing the data collection setup to reduce interference, expanding the surface interaction database by varying surface materials and interaction pressures, and developing a functional haptic device capable of real-time signal transmission. Long-term goals include integrating this technology into immersive virtual environments, improving accessibility for visually impaired individuals, and pushing the boundaries of human-computer interaction through more nuanced tactile experiences.

This research demonstrates a novel pathway for using audio-driven haptics to replicate and communicate surface characteristics, paving the way for advanced multisensory feedback systems.

Project Objectives

The overarching goal of this project is to investigate the feasibility and effectiveness of integrating audio signals into haptic feedback systems to enhance the perception of surface textures through audio-haptic synthesis. With the implementation of synthesized audio-haptic signals, the virtual world can become a more immersive experience for all users [1].

In the real world, there are many applications for the synthesis of audio-haptic signals. For instance, the "Field of Vision" provides visually impaired sport fans with a device that allows them to follow along with games in near real-time [2]. Another application is with virtual reality. By synthesizing audio and haptic signals, users can have an immersive experience that allows them to hear, see, and feel the environment that surrounds them [3].

Methods

To evaluate the feasibility of using audio signals to replicate surface textures through haptic feedback, an experimental setup was developed utilizing robotic automation, acoustic sensing, and vibrational analysis. A prior study had been conducted in which an accelerometer was used to record vibrational frequencies between the interaction between a surface and a needle [4]. For our research, the same setup is used, except a microphone records the audio interaction, rather than acceleration.

A UR3E Universal Robot was programmed to clamp a standard marker in its grippers and move it across the surface of a wooden work table. The robot was configured to operate at constant linear speeds of 25 mm/s, 50 mm/s, 75 mm/s, and 100 mm/s to ensure controlled, repeatable motion. This allowed for systematic variation in the interaction between the marker and the table surface.

A microphone was securely attached to the marker to capture the real-time audio produced by the surface interaction. These audio signals were then recorded and stored for post-processing. Once captured, the audio data was transmitted to a piezoelectric actuator, which was used to reproduce the recorded vibrational characteristics based on the audio input.

To measure the actuator's response, an accelerometer was affixed to the actuator, capturing vibrational data as the device mimicked the original surface interaction. Both the audio and accelerometer signals were then analyzed using spectrogram analysis, a technique that displays how the frequency content of a signal varies over time. This enabled a direct comparison between the audio-generated vibrations and the original acoustic profile of the surface interaction.

This method provided a framework to assess the fidelity and accuracy of audio-driven haptic feedback, laying the foundation for further development in multisensory feedback systems.

Results and Discussion

The use of audio signals to reference surface interactions in the digital world is determined to be possible, but many improvements need to be made before the process may be implemented into physical devices. First, the physical environment in which testing takes place needs to be better controlled to eliminate excessive noise which was detected by the microphone. Testing was held inside of Miami University's machine and design lab, so outside noise from active equipment was picked up by the microphone. Additionally, the UR3E robot's joints produce detectable noise as the arm extends and contracts during tests. If most, or all, of these sources of excess noise can be eliminated from the experimental process, then more reliable conclusions can be drawn.

As shown in the figures section, multiple tests produced very interesting results. For example, the 75 mm/s test produced frequencies lower than the 50 mm/s test. Higher speed tests should produce higher frequency signals during the surface interaction, but the results here showed otherwise. We think this result may have been due to the excess low frequency noise detected by the microphone. Next, the 50 and 25 mm/s tests produced an odd break in frequency data as shown in the output plot. No specific source of interference could be identified, but we think it may be related to the surface of the work table that may only be detected at slow speeds. Finally, the 25 mm/s test produced an audio frequency plot with very, very low frequency for the first half of the test, before showcasing a data plot that was expected. Again, we believe it is somehow related to the surface interaction at a very slow rate.

Moving forward, the data collection process should be improved before further testing takes place. Once these improvements have been implemented, we hope to compile a database of surface interactions, where different variables are tested, to then draw further conclusions. For example, the force applied to the surface or the surface itself are two other variables that can be tested using the control of a UR3E robot. As successful testing is completed, we can move to recording data from events or interactions that do not need the control of a robot, such as the event of crushing a soda can in the palm of someone's hand. As a database of audio-haptic interactions is compiled, the construction of a haptic actuator device will become the new objective of the project. And finally, the implementation of this device into a virtual reality unit will be the ultimate goal.

Figures/Charts

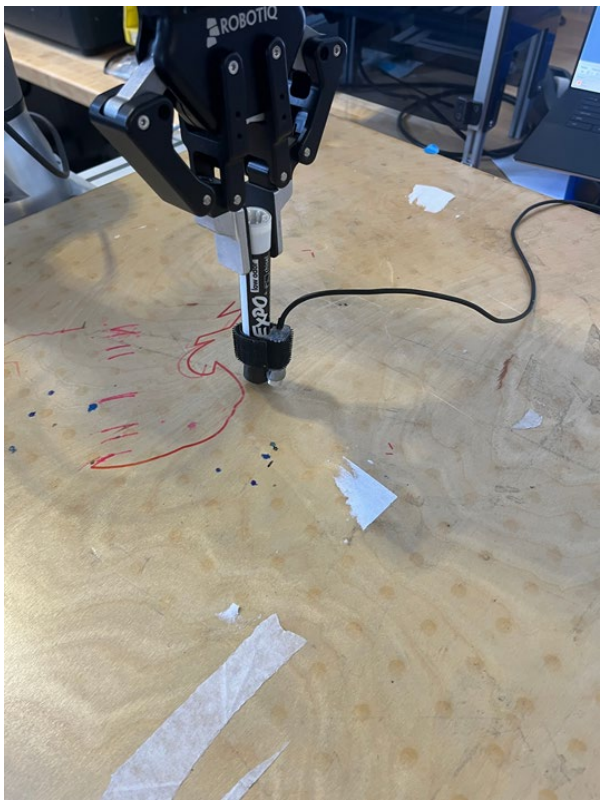


Figure 1: Visual depiction of physical setup with the robot. An EXPO marker is clamped between the robot grippers and a microphone is velcro-strapped to the marker to record the audio interaction as the marker is dragged across the wooden work table.

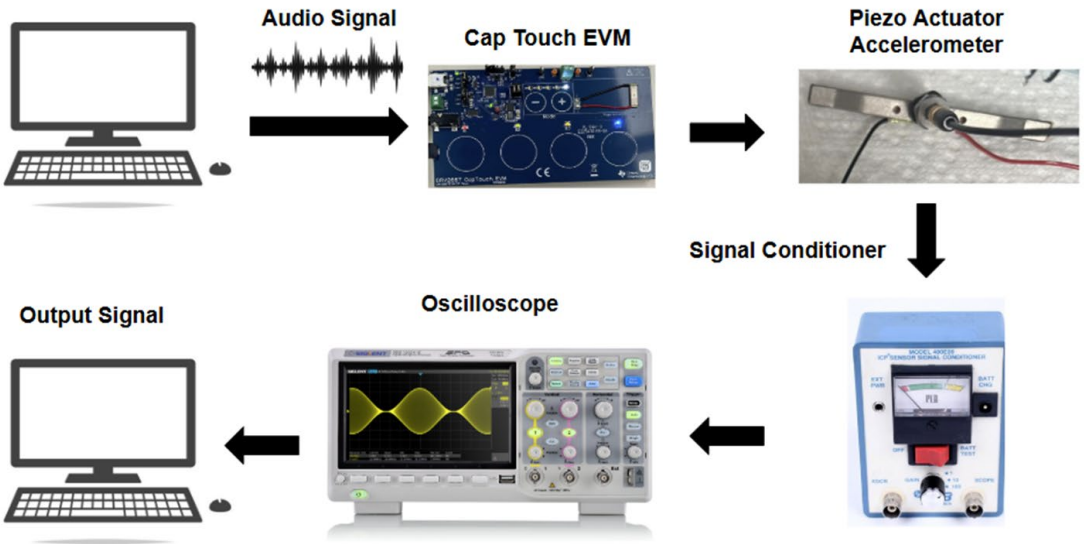


Figure 2: Visual representation of the data analysis, beginning with the transmission of an audio signal to the audio amplifier. The amplified audio signal is played through the actuator, whose acceleration is detected by the accelerometer. A signal conditioner conditions the acceleration signal before it is recorded by the oscilloscope. Finally, it is sent to MATLAB for spectrogram analysis.

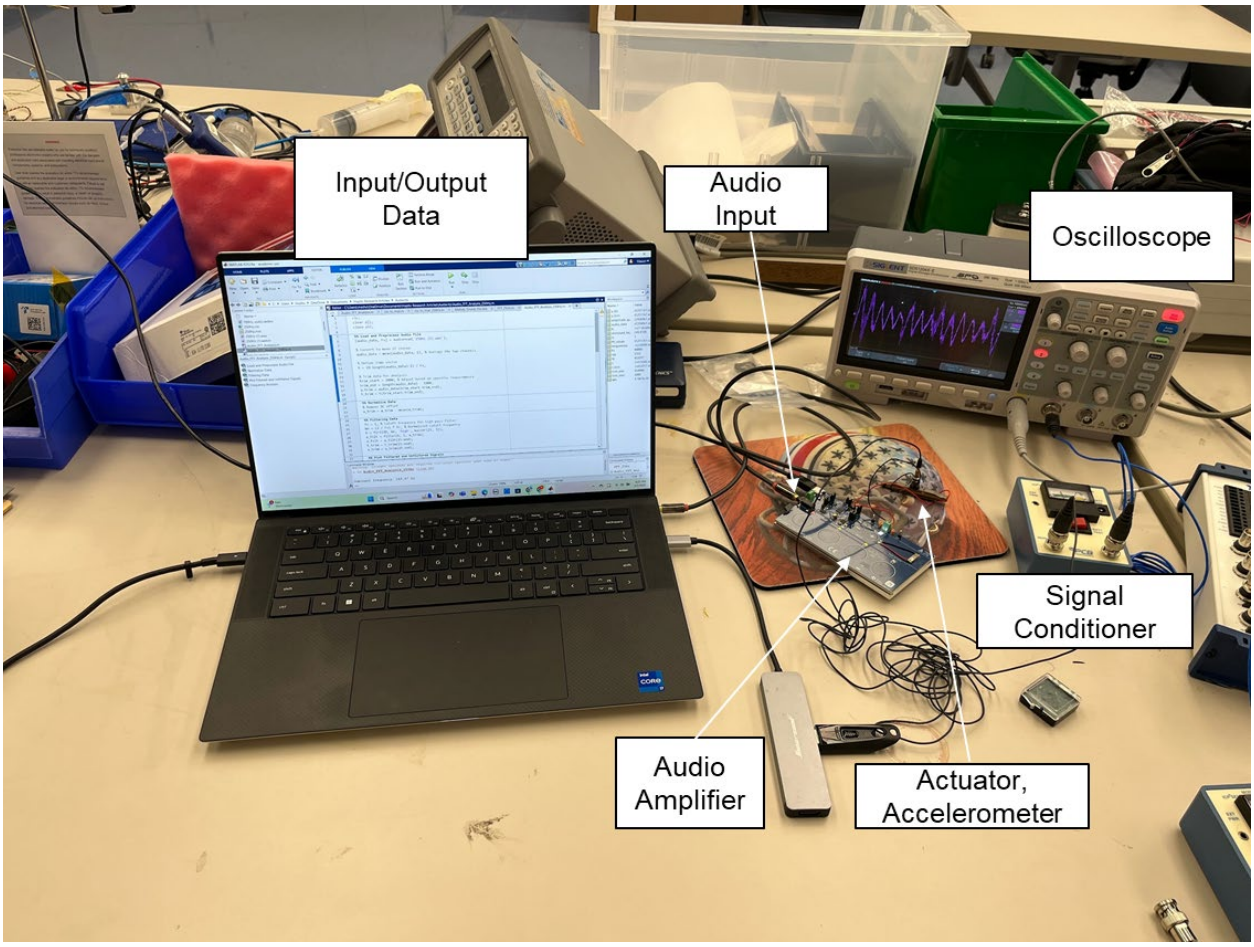


Figure 3: Figure 3 is an image of the physical setup for data analysis.

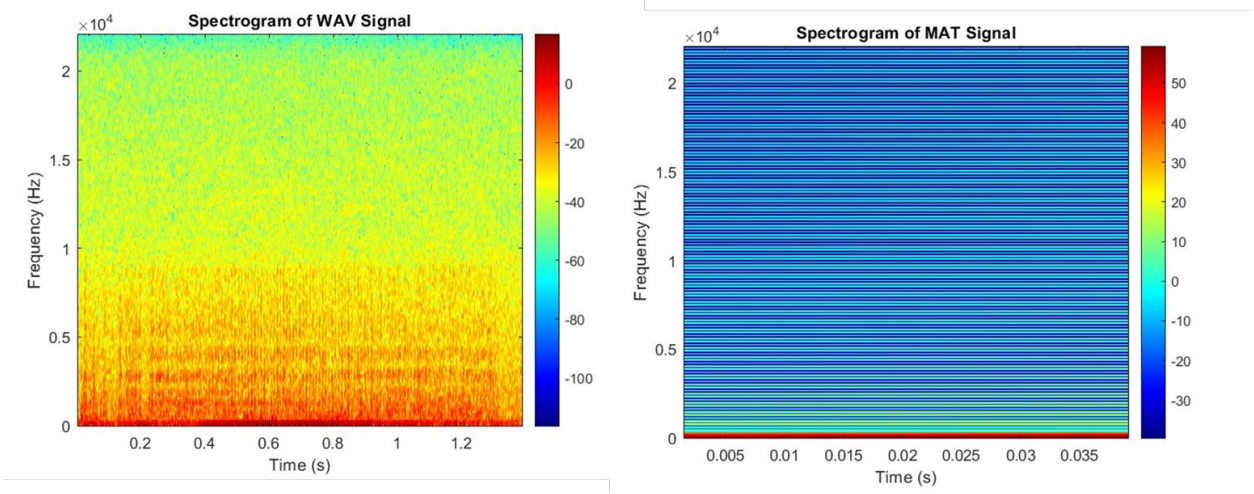


Figure 4: Spectrogram displays 100 mm/s testing.

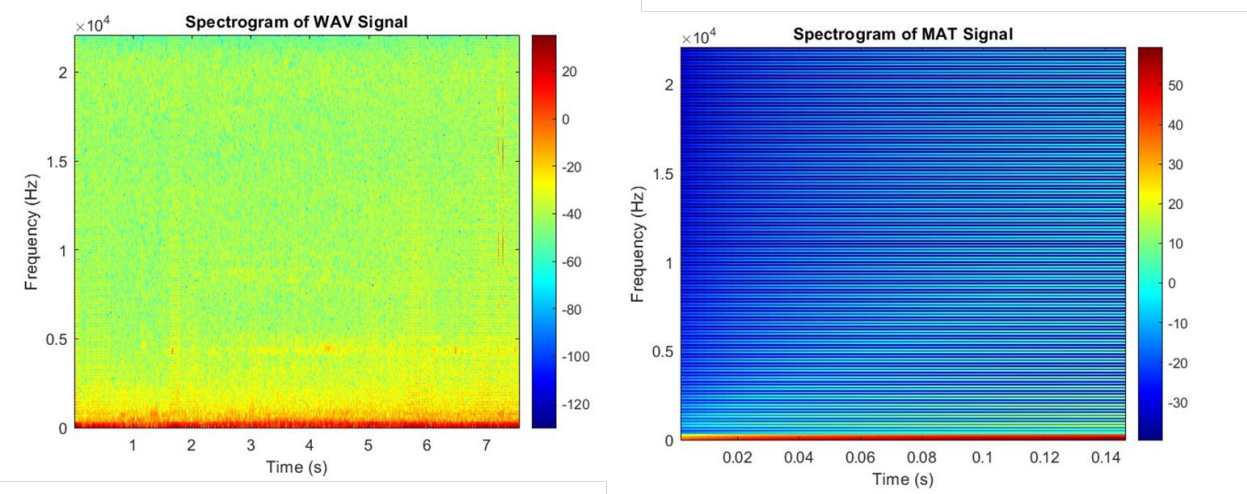


Figure 5: Spectrogram displays for 75 mm/s testing.

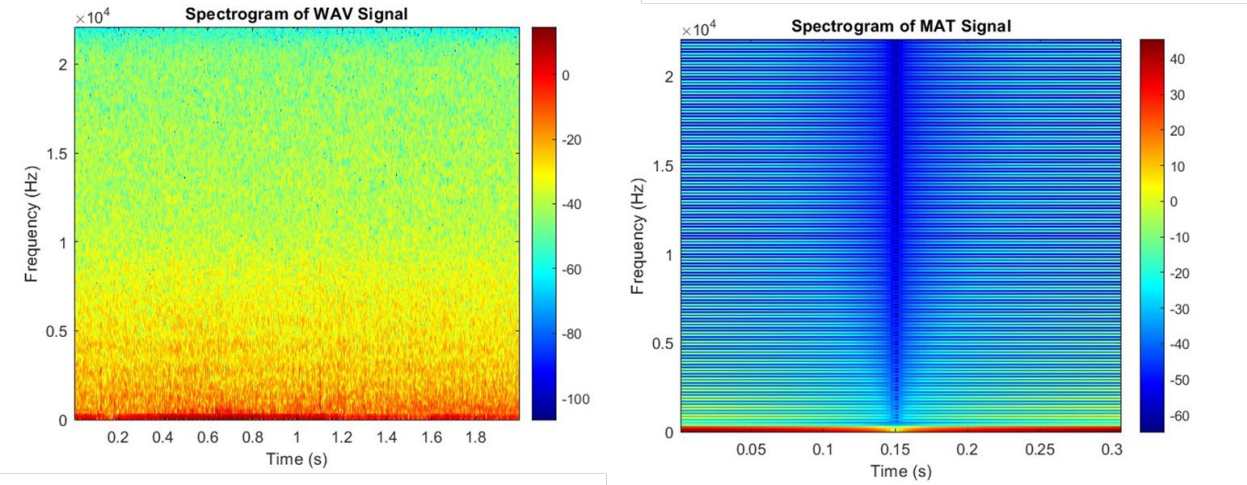


Figure 6: Spectrogram displays for 50 mm/s testing.

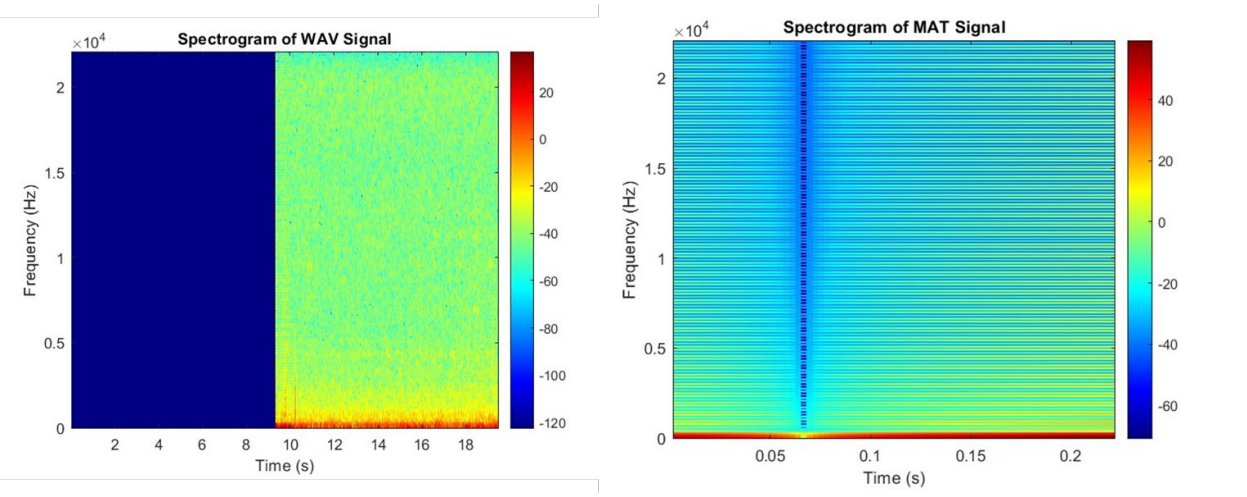


Figure 7: Spectrogram displays for 25 mm/s testing.

Acknowledgments
I would like to express my sincere gratitude to my research advisor, Dr. Jeong-Hoi Koo, for his mentorship and for providing me with the invaluable opportunity to engage in undergraduate research under his guidance over the past several years. It has been a rewarding experience to contribute to work that holds the potential to advance future virtual environments.

I would also like to extend my appreciation to the Ohio Space Grant Consortium for supporting and enabling me to present our research at the annual symposium. It was both an honor and a privilege to participate in the event and to witness the exceptional work being carried out by fellow researchers from across the state.

References
[1] Inc., Apple. "Designing Audio-Haptic Experiences - WWDC19 - Videos." Apple Developer, 5 June 2019, developer.apple.com/videos/play/wwdc2019/810/?t=0h9m59s.

[2] Bantock, Jack. "This Handheld Sensory Device Is Helping Blind Sports Fans 'feel' the Game." *CNN*, Cable News Network, 10 Oct. 2024, www.cnn.com/world/europe/field-of-vision-blind-sport-stadium-spc/index.html.

[3] Cho, Hyunsung, et al. SonoHaptics: An Audio-Haptic Cursor for Gaze-Based Object Selection in XR. Proceedings of the 37th Annual ACM Symposium on User Interface Software and Technology (UIST '24), 13–16 Oct. 2024, Pittsburgh, PA, USA. ACM, 2024, https://doi.org/10.1145/3654777.3676384.

[4] Hwang, Gui Won, et al. A Spatially Selective Electroactive-Actuating Adhesive Electronics for Multi-Object Manipulation and Adaptive Haptic Interaction (Supplementary Information). Advanced Functional Materials, 2024, https://doi.org/10.1002/adfm.202308747.

PC/104 Electrical Power Supply (EPS) Development for Space Applications

Student Researcher: Mark Stallone

Advisor: Dr. Jeffrey Balcerski

Kent State University
Aerospace Engineering

Abstract

This research project focuses on developing low-cost PC/104 printed circuit boards (PCB) for CubeSats. CubeSats often rely on expensive commercial electronics solutions, notably electrical power supply (EPS) boards and main control boards. These can cost thousands of dollars and pose a financial burden to institutions that are breaking into the CubeSat development field. This project aims to develop in-house EPS boards that reduce costs while ensuring high reliability and adaptability to most commercial systems. By selecting components with high environmental ratings, these boards can withstand the temperature changes and radiation present in LEO, ensuring a long mission lifecycle. Size constraints of the PC/104 form factor prove to be difficult to ensure redundancy and functionality in the physical limitations of the space available.

Project Objectives

Initial objectives for this research project are to develop a preliminary ground version of a CubeSat EPS board. This was achieved by first creating a PC/104 PCB template to ensure that all boards created for this project will be physically compatible with the others. Ensuring physical compatibility is crucial for successful integration of these boards as the amount of functionality and redundancy included takes up the majority of the 90 x 96 mm area of the PCB. Another objective is learning how to leverage free design tools such as Kicad and other open-source firmware to further reduce the cost to entry for the future editing of the original design files. Tackling the EPS design first provides valuable knowledge for the next board in the development process, a main control board compatible with this EPS, with the final goal of creating an ecosystem of low-cost PC/104 components. In addition to these objectives, another project goal is to begin creating a custom Kicad parts/symbols/footprints library that can be easily imported to manage the shareability of this and future projects.

Methods

The design of the circuits included in this EPS board are focused on mimicking key functionalities found on many commercial EPS solutions such as, telemetry, error code logging, inhibit systems, and low power onboard processing for control logic. Common manufacturers that are established in the commercial space include EnduroSat, AAC Clyde, and Pumpkin Space Systems; the boards available from these manufacturers were compared in aspects of price and power output capabilities in addition to their flight heritage. These boards range in price from ~$10,000 to ~$50,000 and all have previous flight heritage, most of these well out of budget for CubeSat development at smaller schools like Kent State University. One common factor between these manufacturers is a high-power output from each of their respective EPS boards, this significant power output is overkill for the intended use cases of the EPS designed for this research project. Additionally, as a result of including a high-density array of components on this board, a 6-layer stackup was chosen to offer a balance between manufacturing cost and managing signal integrity of the board. The configuration chosen is a commonly used stackup that features the layers in the following order from the top down: signal, ground, power, signal, ground, signal.

Components were selected based on their respective functionalities that were identified from each manufacturer's data sheets. Key components included battery charge integrated circuits (IC), buck converters, and a low-power microcontroller capable of handling the error and telemetry logging. The current version of the board contains 3V and 5V regulators, but future revisions will also include 12V regulators. The 3V power distribution circuits are currently triple redundant however they will be reduced to dually redundant as reliability is confirmed in future testing. Additional future work includes adding analog voltage, current, and temperature monitors to provide a wide range of telemetry from the EPS. Following these steps, the board designed in this project, the EPS-M1, will be manufactured and full ground testing will begin.

Results and Discussion

The microcontroller selected for the EPS-M1 is the STM32L462CET in the 48LQFP package. This chip was selected for its low power consumption and many favorable interfaces. This STM32 features an Arm® 32-bit Cortex®-M4 CPU with FPU and interfaces such as USB 2.0 FS, 4x I2C channels, 1x UART, 3x SPI, and 1x CAN interface. This microcontroller is used to gather the telemetry data and perform error handling for the voltage busses. This STM32 IC would be used for configuring the EPS and the code onboard will manage switching between the different voltage regulators. Future revisions of this board will include an additional flash chip for storing the telemetry in a rolling buffer, this flash will be radiation tolerant to improve the data security of the stored information.

The resulting EPS created from this research project contains critical circuits duplicated in parallel. The battery charge IC selected was the LTC4015 from Linear Technologies. This chip is a multichemistry buck battery charger that features integrated telemetry over I2C, as well as configurable controls over the I2C channel. The LTC4015 measures battery voltage, current, resistance, and temperature while also logging data on the input voltage, current and the temperature of the LTC4015 die temperature. These measurements are conducted by a digital system contained within the IC. Additional features of this chip include voltage and current limiting controls that are applicable to the input and outputs of the IC. The LTC4015 features a several configuration pins that are designated in the EPS-M1 through a configurable resistor grid. This circuit is replicated in a triple redundant design with the connections in parallel.

The 3V regulator circuits contain the Onsemi NCV891330PD33R2G chip. These regulators are connected to the USB port's 5V in addition to the battery and solar panel output for separate ground testing purposes. Each NCV regulator is capable of 3A of peak output. The NCV regulators operate at a switching frequency of 2 MHz and features the ability to switch to an included low dropout regulator for lower current draw applications. The layout of this circuit has been verified as working in other boards developed from previous research endeavors.

The 5V regulator circuits feature the TI TPS543x switching regulators that are capable of 4A peak current output. These regulators operate at a fixed 500 kHz switching frequency. The TPS regulators were selected based on the relatively low component count needed. Currently, telemetry of this system is not implemented as analog current, voltage, and temperatures are being tested in evaluation boards.

Additional features of the EPS-M1 include p-channel MOSFETs for high side power inhibit switching, as well as three connection points for external inhibits and a remove before flight pin. These features were included to ensure compliance with the University Nanosatellite Program's user guide regarding EPS inhibits. Compliance with these guidelines ensures the components are accessible to other schools attempting to break into the CubeSat development space, ensuring access to a low cost ecosystem of CubeSat components.

Schematic Overview

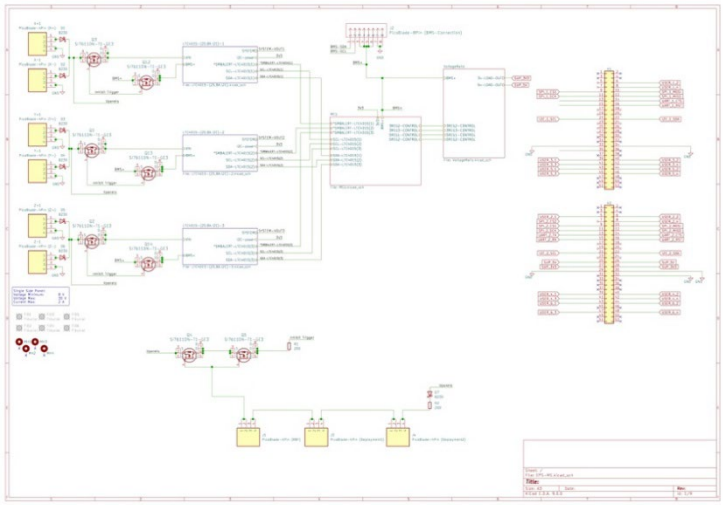


Figure 1: Schematic Overview

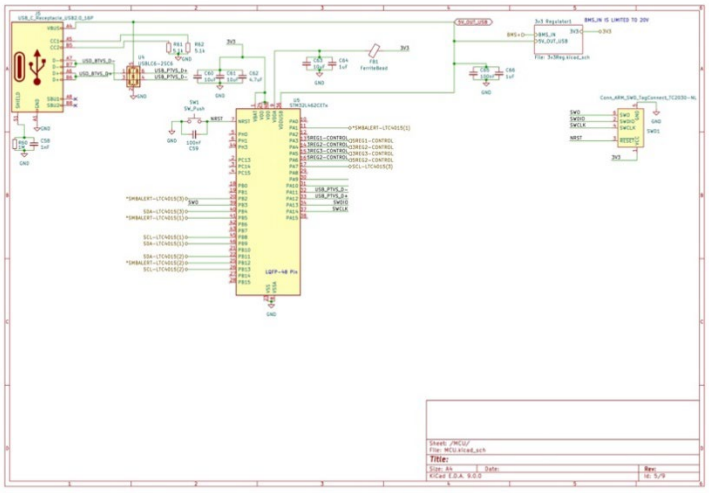


Figure 2: Microcontroller Schematic

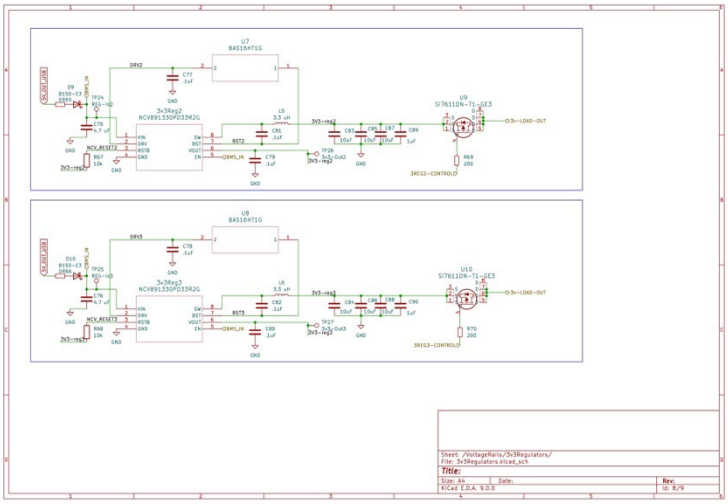


Figure 3: 3V Regulator Schematic

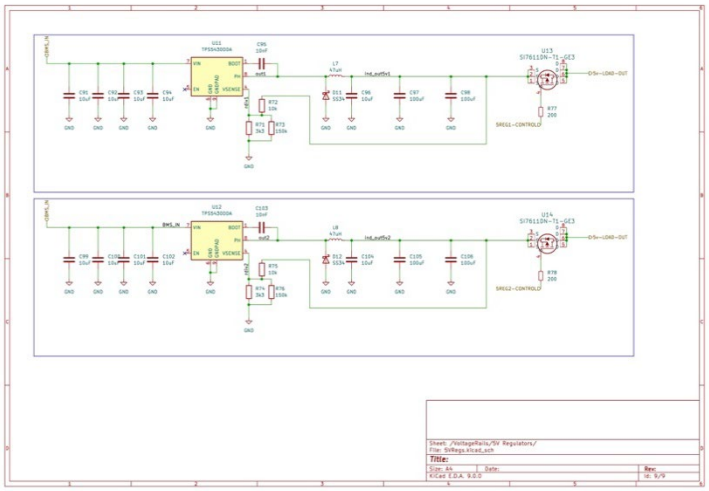


Figure 4: 5V Regulator Schematic

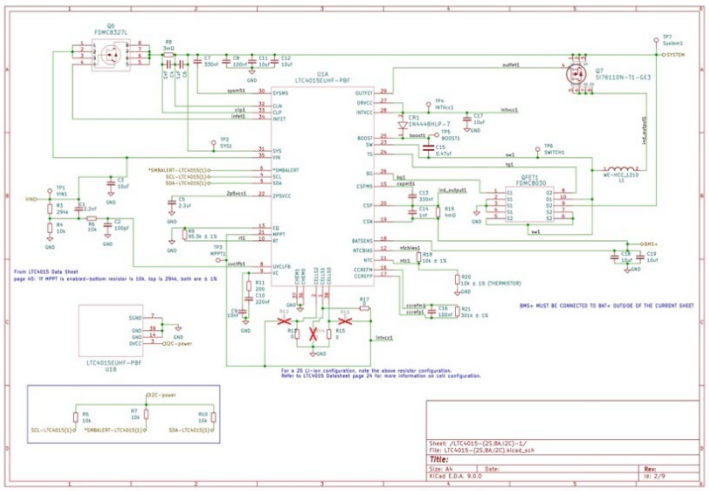


Figure 5: LTC4015 Battery Charger Schematic

The above schematics show the connections included on this board in its current revision, and shown below is a 3D rendering of the completed PCB.

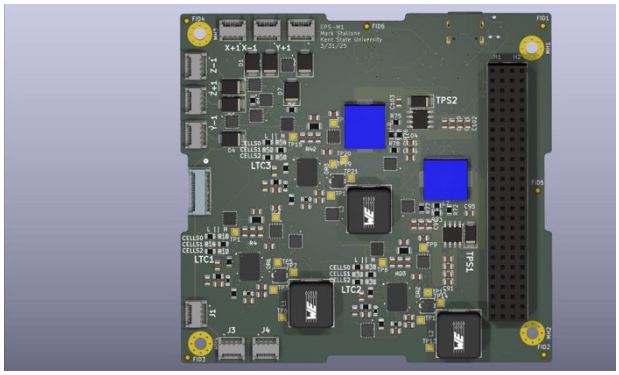


Figure 6: Top View EPS-M1

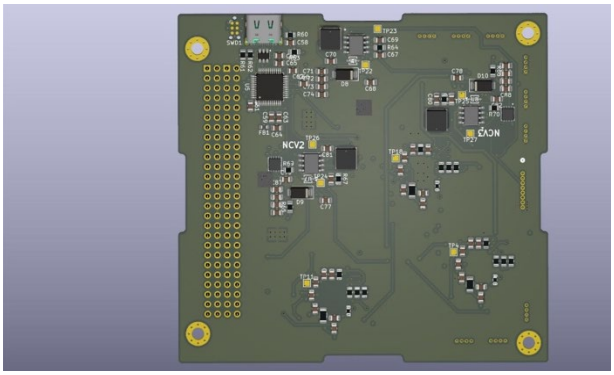


Figure 7: Bottom View EPS-M1

Acknowledgments

I would like to thank Mark Desko for sharing years of his industry experience in electrical engineering during the first stage of this project, and for his continued support as I further develop this system.

Additionally, I extend my thanks to Dr. Jeffrey Balcerski for his unwavering commitment to enabling the success of this project and the further development of a configurable CubeSat ecosystem.

References

[1] “CubeSat EPS - STARBUCK-Nano | AAC Clyde Space.” Accessed: Apr. 17, 2025. [Online]. Available: https://www.aac-clyde.space/what-we-do/space-products-components/pcdu/cubesat-eps-starbuck-nano

[2] “CubeSat EPS I Power Module,” Orbital Transports. Accessed: Apr. 17, 2025. [Online]. Available: https://catalog.orbitaltransports.com/eps-i-power-module/

[3] “High-power Multi-channel Electrical Power System Module (EPSM1),” Pumpkin, Inc. Accessed: Apr. 17, 2025. [Online]. Available: http://www.pumpkinspace.com/store/p216/High-power_Multi-channel_Electrical_Power_System_Module_%28EPSM1%29.html

[4] “LTC4015-Data Sheet.” Linear Technologies. Accessed: Apr. 12, 2025. [Online]. Available: https://www.analog.com/media/en/technical-documentation/data-sheets/4015fb.pdf

[5] “NCV891330-Data Sheet.” Accessed: Apr. 12, 2025. [Online]. Available: https://www.onsemi.com/pdf/datasheet/ncv891330-d.pdf

[6] P. Scherz and S. Monk, *Practical electronics for inventors*, Fourth Edition. New York: McGraw-Hill Education, 2016.

[7] “SI7611DN-Data Sheet.” Accessed: Apr. 12, 2025. [Online]. Available: https://www.vishay.com/docs/69939/si7611dn.pdf

[8] “STM32L462CE-Data Sheet.” Accessed: Apr. 12, 2025. [Online]. Available: https://www.st.com/resource/en/datasheet/stm32l462ce.pdf

[9] “TI TPS5430-Data Sheet.” Accessed: Apr. 12, 2025. [Online]. Available: https://www.ti.com/lit/ds/symlink/tps5430.pdf

Revolutionizing Aviation: An In-Depth Analysis of NASA's Transformative Aeronautics Concepts Project

Student Researcher: Lucas R. Stammen

Advisor: Dr. Ala Qattawi

University of Toledo
Engineering/Mechanical Engineering

Abstract
NASA's Transformative Aeronautics Concepts Project represents a step forward to the future of aviation, focusing on the development of technology that will improve aircraft efficiency, performance, and safety. NASA does so by exploring advanced propulsion systems, the use of test pilots/flight engineers, and smart materials. This aims to redefine the boundaries of current technology in the aeronautical field. This research provides an analysis of the project's goals, concepts, and impacts on the future of air travel.

Project Objectives
The main objectives of the Transformative Aeronautics Concepts project include: To rapidly improve aircraft performance, efficiency, and safety. To further advance aeronautical technology through development of novel concepts. To explore and implement the newest technology that pushes the barriers of current aviation practices.

Methods
Advanced propulsion systems are needed for enhancing the level of performance and efficiency of each aircraft. NASA's research on advanced propulsion systems includes the creation of new engine technology, such as Hybrid-electric and electric propulsion systems. The use of smart materials into aviation technology to enhance the performance, safety, and efficiency of aircraft. Smart materials, which can respond to changes in the environment such as temperature, pressure, and strain, offer significant potential for improving aircraft design and functionality. NASA is also using test pilots in their program to evaluate cutting-edge aviation technologies that aim to revolutionize air travel. These pilots play a crucial role in testing experimental aircraft and systems under real-world flight conditions. Their hands-on feedback helps engineers refine designs and ensure safety, performance, and practicality before implementing designs. By bridging the gap between theoretical ideas and actual implication, test pilots help NASA accelerate the development of next-generation, sustainable aviation solutions.

Results and Discussion
Following this project I plan to conduct further research on how test pilots from the Air Force and Navy can be more effectively utilized in NASA's Transformative Aeronautics Concepts Project. I will begin by reviewing official NASA documentation and reports related to the TACP. This includes technical papers about the testing of new equipment, press releases, and program updates available on NASA's website and through scholarly databases. I will also examine case studies and past collaborations between NASA and military test pilots to understand the roles they have played in evaluating advanced aviation technologies. Identifying the unique skill sets and experience military test pilots bring including handling high-performance aircraft and operating under extreme conditions that will help highlight how their expertise aligns with NASA's goals in experimental flight testing.

In addition, I will explore interviews, articles, and publications involving military test pilots and NASA engineers to gain insights into their past collaborations. Researching the training programs and operational environments of both Air Force and Navy test pilots will help me study how their methods and decision-making can enhance NASA's testing strategies. I also plan to reach out to subject matter experts through forums, academic networks, or even directly to institutions like the U.S. Air Force Test Pilot School and U.S. Naval Test Pilot School for more detailed information. This comprehensive approach will provide a deeper understanding of how to better integrate military test pilot expertise into NASA's transformative aeronautics initiatives.

Acknowledgements and References

- NASA. (2023). Transformative Aeronautics Concepts. Retrieved from [NASA's official website]
- Smith, J. (2022). Advances in Electric Propulsion for Aircraft. *Journal of Aerospace Technology*, 45(3), 112-129.
- Johnson, L., & Lee, A. (2021). Autonomous Flight Systems: Current Trends and Future Directions. *International Journal of Aviation*, 59(2), 55-67.
- Brown, R. (2023). The Role of Advanced Materials in Modern Aircraft Design. *Materials Science Review*, 67(4), 89-104.
- Slover, Greg. (2022). "Working As A NASA And Air Force Test Pilot." *Pathwise.io*, https://pathwise.io/podcasts/greg-slover/.

Electro-Mechanical Characterization of a Novel Self-Healing Electronic Polymer System

Student Researcher: Adin Stoller

Advisor: Dr. Robert Lowe

University of Dayton
Department of Mechanical and Aerospace Engineering/Mechanical Engineering

Abstract

The development of self-healing elastomers for soft robotics is occurring at an increasingly rapid pace due to the need for resilient materials that are capable of autonomously repairing minor damage without human intervention (similar to biological tissues). The inherent compliance, conformability, and capacity for large-strain elastic deformations enable safe interactions with humans and on-the-fly adaptability to different physical environments. Space-related applications ranging from inflatable antennas to flapping-wing aerial reconnaissance vehicles are expected to derive significant functional benefit from materials with embedded self-healing, particularly in remote and austere environments (like space) where human intervention is impractical. However, electronic payloads onboard these soft robotics systems are currently limited. To pave the way for advanced electronic control systems, innovative methods for integrating stretchable electronic components into elastomers need to be undertaken to create a new generation of "digital materials." BeckOHflex is a novel material that couples both self-healing and 3D-printability into a single elastomeric material system. A key feature of BeckOHflex is its near-instantaneous self-healing in ambient, room-temperature conditions. Liquid metal inks (such as the commercially available ELMNT ink) provide a compelling strategy to create stretchable conductive pathways (traces) on insulative BeckOHflex substrates

[**Figure 1**] to power embedded electronic payloads (e.g., sensors). ELMNT ink exhibits superior conductivity under large cyclic strains relative to other paradigms (e.g., silver nanoflake ink), making it a compelling choice for enabling next-generation "electronic polymers" with embedded self-healing.

Project Objectives

This project focuses on developing and executing an electro-mechanical test program for the proposed self-healing, highly-stretchable electronic polymer in two ways: (a) optimize the mechanical properties of BeckOHflex and (b) develop unique templates emulating simple electronic components from ELMNT ink by leveraging laser micro machining (LMM) to manufacture complex liquid metal networks. The resulting test data, collected under a variety of deformation modes, will be analyzed and integrated into material models that will enable the design, optimization, and control of a prototype soft robot, capable of sensing and interacting with its environment.

Methods

ELMNT ink traces were deposited onto 3D-printed BeckOHflex ASTM D412 type C tensile specimens to create an "electronic polymer" [**Figure 1**]. Self-healing tests were performed by cutting the specimens horizontally across the center of their gage section with a clean razor blade, manually placing the halves back into contact under nominal pressure, and allowing them to self-heal for 5 min under ambient conditions. After cutting but before self-healing, several specimens were machined with a femtosecond ultra-short pulse laser (USPL) under low and high settings. (USPL parameters such as laser power, hatch width, and scan speed were varied to understand their impact on ablation and ink activation.) Uniaxial tension testing was subsequently performed on all healed specimens following ASTM D412 on an Instron 3365 universal testing system equipped with a 2-kN load cell. Engineering stress was calculated as force (measured by the load cell) divided by the undeformed cross-sectional area, while engineering strain was calculated as crosshead displacement (measured by the integrated Instron LVDT) divided by grip-to-grip distance.

Results and Discussion

The resulting engineering stress-strain curves are shown in

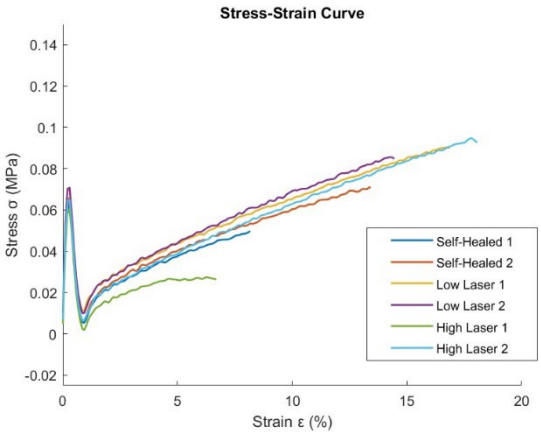


Figure 2: *Variable Self-Healing Efficiency.* Laser micro-machining upon self-healing sites can affect mechanical properties of elastomer

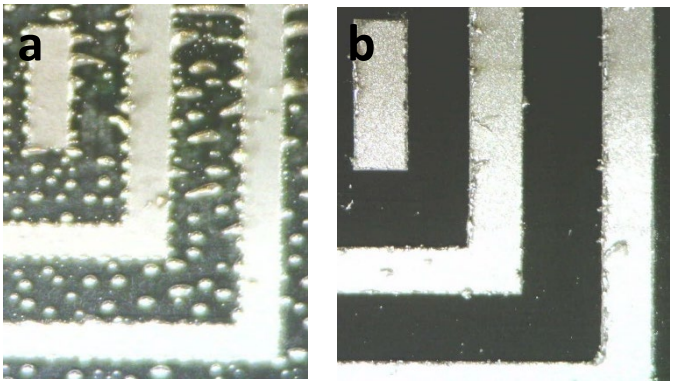


Figure 3: *Femto-Second Laser Activation.* (a) Poor laser activation parameters resulting in pooling. (b) Optimized selective ablation of ELMNT Ink traces.

Figure 2. Due to high relative humidity (75% RH) during testing, the self-healing of BeckOHflex was inconsistent and less effective than anticipated, making it difficult to assess the impact of laser micro-machining on self-healing performance. The age of the HEA (a key chemical precursor in BeckOHflex) is also a potential cause of the underperformance in self-healing. Future testing will incorporate a desiccator to maintain reliable humidity and temperature levels to normalize the testing of future samples. Optimization of laser machining profiles proved very successful. As seen in **Figure 3**, ablation areas were fully removed rather than simply pooling. Conductivity was not present in unoptimized samples as the liquid metal ink was not properly activated. By reducing scan speed and increasing hatch size, the ELMNT ink was successfully activated.

Acknowledgments

AS thanks to the Berry Summer Thesis Institute and the University of Dayton Honors Program for providing financial support and professional development opportunities during this research experience. RLL and AS gratefully acknowledge the University of Dayton Research Institute Additive Manufacturing Technology Development Group (UDRI AMTD), especially Allyson Cox, for providing technical expertise and lab assistance.

Identifying Magnetotactic Bacteria in Acid Mine Drainage

Student Researcher: Bryce Stoltz

Advisor: Dr. Courtney Wagner

Kent State University
Department of Earth Sciences/Geology B.S.

Abstract

Magnetotactic bacteria (MTB) are microscopic organisms that biomineralize magnetic particles in their cells to navigate within the water column toward the oxic-anoxic interface (OAI), a chemocline which is typically found near the water-sediment interface. MTB are abundantly found across the globe and can even live in some 'extreme' environments with pH levels ranging as low as 1 and as high as 10, and temperatures ranging from near freezing to 60 degrees Celsius. These harsh environments make MTB great analogs for extraterrestrial life and early life on Earth. For this project, water samples were taken at various parts of a stream that has been impacted by agricultural practices and, more importantly, acid mine drainage. Samples were collected along a transect, starting upstream from the acid mine drainage (where there was just agricultural impact) and finishing downstream of the acid mine drainage. This acid mine drainage is the result of coal mines that were active up to the 1970s, when they were then abandoned. Water and oxygen react with pyrite present in the mines/spoils which contribute to increased levels of dissolved heavy metals and decreased pH and dissolved oxygen levels. These conditions serve as our extraterrestrial analog environment in this study.

Water quality monitoring has been performed to track how dissolved oxygen, and pH has evolved in the samples along with changes in temperature. Moving forward, I have plans to implement light microscopy to identify MTB in the samples. Electron microscopy will then be used to further image and identify the MTB and the magnetic particles that they are biomineralizing. This will help in our understanding of potential extraterrestrial life forms and how they might record these environments.

Project Objectives

The primary objective of this project was to identify magnetotactic bacteria in an acid mine drainage setting, and to characterize them using light microscopy along with electron microscopy. The application of this is to gain a deeper understanding of magnetotactic bacteria and the environments they can inhabit, along with a potential proxy for life on Mars. Magnetotactic bacteria can be used to infer past environmental changes, by analyzing the changes in MTB in the stratigraphic column. The reason changes in MTB populations indicate environmental changes, is because different MTB thrive in difference environments. This is why modern studies of MTB are important, if we can understand what environment a particular species lives in, we can use that as an analog for previous environments when they were living.

The reason an acid mine drainage site was selected for sampling, is due to the similarities between acid mine drainage and Mars. This connection to potential life on Mars connects this idea of previous environments and to space and the NASA mission. Mars and acid mine drainage both have high amounts of heavy metals, iron oxides and sulfur. It is also inferred that the surface water of Mars would be highly acidic with a low amount of dissolved oxygen in the water, due to high amount of CO_2 in the atmosphere. This carbon dioxide would dissolve into the water and form carbonic acid. Acid mine drainage sites also have low pH levels due to the oxidation of sulfides into sulfuric acid, which releases protons into solution. Finding MTB in a harsh condition that shares traits of Mars can help us understand what kind of life could have been present. The magnetofossils formed after MTB death is also easily preserved and identified, so this would be good for preserving past environments of Mars.

Methods

The methods included in this project included sample collection, water quality measurements, magnetic separation, light microscopy and electron microscopy.

Sampling was done using plastic jars that were about 1L volume. Sample collection included filling these jars about a third of the way with sediment from the site, followed by filling the remainder of the jar with water from the site. Using a YSI water probe; ph, dissolved oxygen, and temperature were measured and recorded at each site. After samples were brought back to the lab, the YSI probe was used to monitor water quality changes that occurred in the lab setting. The resolution of this samples began as daily for the first month, then was scaled back to weekly, sampling the water quality every Monday morning.

Magnetic separation was done by using two magnets on each jar, placing them on opposite sides of the jar around the water sediment interface. The water sediment interface is often where the oxic-anoxic water in face is, and this is the environmental magnetotactic bacteria inhabit. Ensuring the magnets were placed here reduced the probability of coercing the MTB into an environment that would not allow for them to live. The magnets were also placed so that the attracting sides of the magnets would both be facing in towards the jar, meaning oppositely charged sides were placed towards the jar. This was done to create a strong magnetic field in the jar, which would then coerce the magnetotactic bacteria closer to the magnets.

After magnetic separation, I then used a pipet to draw water enriched in MTB from near the magnets, and added a water drop to a well dish. This well dish was put onto a hold, and an inverted Echo Revolve microscope was then used to image the MTB. I used a 60x oil immersion objective, and found the water drop edge. Then using a separate magnet, I coerced the MTB towards the water drop edge, holding the magnet on one side of the well dish. Using the screen record function on the iPad used for the microscope, I took videos of the MTB by moving the magnet to induce magnetotaxis.

For scanning electron microscopy, I used a pipette to draw water and sediment from near the magnets and transferred it into a smaller glass jar (about 4 fluid oz). I then used more magnets to further concentrate the MTB. I then used a pipette to add about 30 microliters of water onto a SEM stub with a sticky carbon tab on it. I then used a

desiccator to dry the samples. I then used an environmental SEM to scan the carbon tabs. The original goal was to see MTB and use electron dispersion spectroscopy to make an elemental map of the particles. This would allow us to know if the MTB were mineralizing greigite or magnetite. However, we were unable to image the MTB due to the resolution of our SEM, but we were able to identify gypsum and string-like iron oxides. This is still relevant because it allows us to have an idea of minerals precipitating from the solution, thus what ions are in solution.

Results and Discussion

Comparing the water chemistry of the AMD and pre-AMD sites, the AMD site has a lowered pH level despite the remediation efforts. The AMD water is about ten times as acidic as the pre-AMD site water. While this is not too drastic of a difference, it is still a significant difference showing the ability of MTB to live in a wide variety of conditions.

Both samples had a gradual increase in pH as time went on in the lab and the reason for this is unknown. Mineral precipitation and carbon dioxide being used up are the most likely explanations to this change.

Looking at the dissolved oxygen of both the sites, there did not appear to be too much of a difference. This is likely due to the AMD water being far from the source, and after the oxygenation of the water using the aerobic wetland remediation. Also, both samples showed a dramatic decrease in dissolved oxygen when they were brought back to the lab. This is likely due to the increase in temperature, which decreases the amount of gas that water can hold. As more time passes in the lab, there was a gradual increase in oxygen in the samples, this is likely due to the permeation of oxygen through the plastic jar along with microbial activities producing oxygen.

Magnetotactic bacteria were successfully identified in both pre-AMD impacted, and AMD impacted sites. It was observed that the AMD site had predominately spirilla form bacteria. This was not consistent throughout the research, as the first MTB identified in this sample were cocci. This raises questions of how the MTB population changed as time went on in the lab and why these changes occurred. It was also evident that cocci were the dominate morphology of the MTB in the pre-AMD site, which seemed consistent throughout time in the lab. The differences in these morphologies suggest that the MTB living in pre-AMD sites are significantly different from AMD MTB.

The identification of MTB in these different environments will aid in our understanding of previous MTB and the conditions they lived in. This can help in reconstructing a paleoclimate at points in Earth history and potentially Mars.

Next steps in this research include resampling, characterization of soil, further MTB concentration, transmission electron microscopy, genomics, and expanding to other harsh condition sites. Resampling of these sites is in interest because of the changes in MTB population as time went on in the lab. We aim to track how the morphology changes more closely and how water chemistry/soil chemistry evolves with those changes. Soil characterization will play into giving insight about what minerals are forming in the lab and how those may influence the water chemistry. This can also help us identify more similarities and differences between the mineralogy of these sites compared to Mars. Further concentrating the MTB will potentially help with SEM-EDS

data. If we can concentrate them enough, we may be able to see what types of minerals are forming in their bodies even if we cannot see the individual cells. Along with this, we aim to implement TEM in our future studies. Concentration is crucial for this step due to the narrow field of view on the machine. TEM will allow us to see the shape and size of the magnetic particles that are being biomineralized, aiding in our understanding of the differences between the MTB. Other harsh conditions are another interest due to the weak acidity associated with the current acid mine drainage site. While it was significantly more acidic that the unimpacted area, it was still relatively normal conditions. There is a particular acid mine drainage site in more central Ohio, named Yellow Creek, which has a harsher condition with more heavy metals and lower pH. This will aid in our understanding of MTB in a wider range of environments. Genomics will also be an area of focus in further research. Understanding the genetic differences between these MTB will help in our understanding of how and why they are able to live in more harsh conditions along with why they biomineralize a particular mineral composition and shape.

Figures/Charts

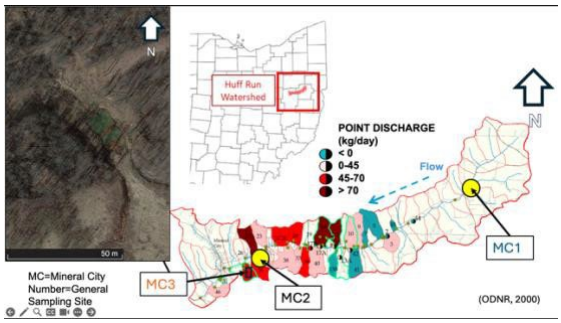


Fig. 1) Figure on the left shows the arial view of the remediation of MC3. Bottom figure is the overview of Huff Run watershed with sampling sites indicated. Colors on the map show the different discharge rates in each sub-water shed in the late 90s.

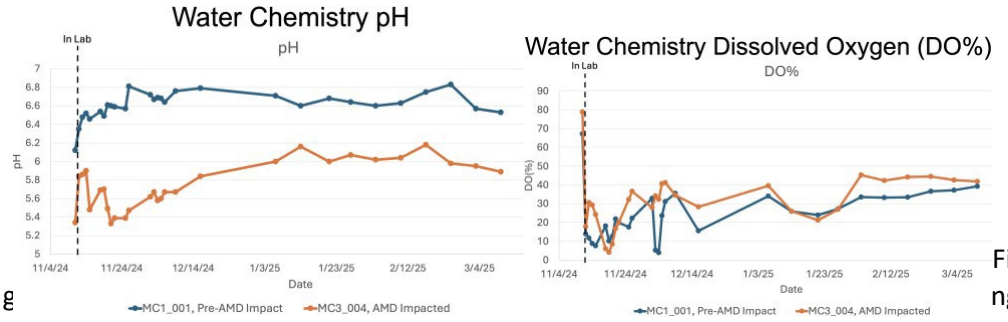


Fig 2.) Shows two nge amd impacted). Left graph shows the pH of each sample over time while right shows dissolved oxygen

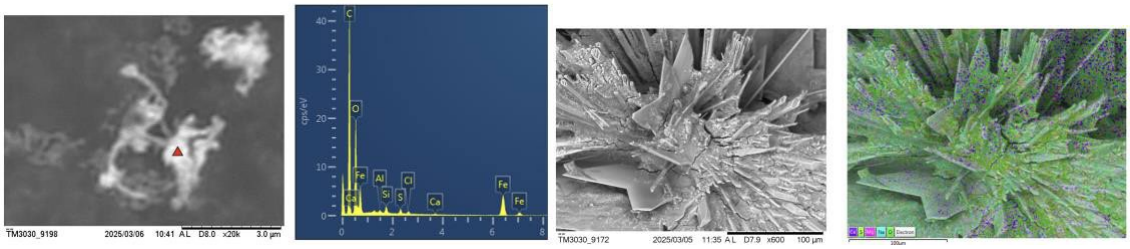


Fig. 3) Left images show SEM image of iron oxides and a corresponding element point spectrum indicated by the red triangle. Right images show SEM image of gypsum precipitate and element map. Greens show oxygen and sulfur while the purples are calcium.

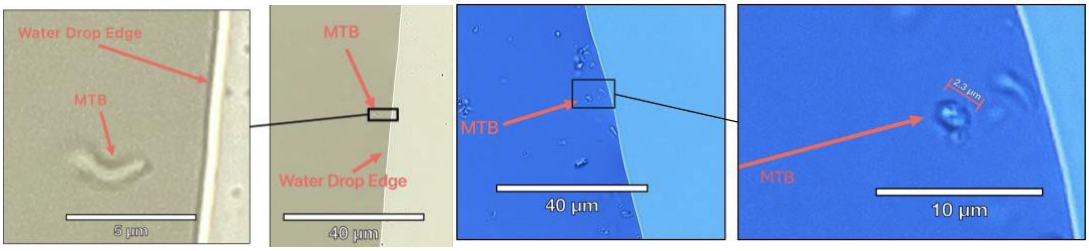


Fig. 4) Image on the left shows the AMD impacted MTB (MC3) while image on the right shows the pre-AMD MTB (MC1).

Acknowledgments

A special thank you to the Ohio Space Grant Consortium. This scholarship has allowed me to participate in and present my research, which has been an invaluable experience. Thank you to Dr. Wagner for continued support and encouragement throughout all this research. She has been a wonderful mentor who has taught me a lot. Thank you to Dr. Singer for introducing me to this Huff Run acid mine drainage site and helping with figures related to this site. Finally, thank you to Merida Keatts for training me on the SEM.

References

Goltsman, D. S. A., Comolli, L. R., Thomas, B. C., & Banfield, J. F. (2015). Community transcriptomics reveals unexpected high microbial diversity in acidophilic biofilm communities. *ISME Journal*, *9*, 1014–1023. https://doi.org/10.1038/ismej.2014.200

Time Delay in Coaxial Cables

Student Research: Auna Tack

Advisor: Dr. Saiyu Ren

Wright State University
Electrical Engineering Major

Introduction

Cable time delay is crucial in systems that require precise timing for operation. Time delay through a cable can be determined using time-domain reflectometry (TDR) theory as well as measured with network analyzer software. According to Witte, time domain reflectometry "uses the reflections of a pulse sent down a transmission line to characterize the impedance of the line [1]." Coaxial cables are included in the definition of transmission lines and will be the subject of this test [1].

Theory

Time delay is calculated using the equation below,

$$\tau = \frac{L_{mech} * \sqrt{\varepsilon}}{c}$$

where τ is the time delay, L_{mech} is the mechanical length of the cable, ε is the dielectric constant of the cable insulation, and c is the speed of light [2]. The numerator of this equation corresponds to the electrical length of the cable, due to the permittivity of practical dielectrics being greater than one, the electrical length is always longer than the mechanical length [2]. Since each cable is insulated with fluorinated ethylene propylene (FEP), each cable's dielectric constant is 2.05 [3]. The calculations for each cable are shown in the results section.

Testing Philosophy

This test was conducted on three cables, each of different length and manufacturer. Each cable under test was coaxial with a SMA termination. Cable 1 was manufactured by Mini Circuits and had a length of 12 inches, Cable 2 was manufactured by Times Microwave Systems and had a length of 24 inches, and Cable 3 was manufactured by Koaxis and had a length of 1.5 meters.

This test utilized a Rohde and Schwarz ZNA. This ZNA was equipped with additional TDR software. The ZNA number of points and span presets were determined with the phase ambiguity in mind, if the step is too large the phase cannot be distinguished if ϕ < 360 degrees [2].

This issue was mitigated by increasing the number of points [2]. To reduce external interfering signals, the ZNA was calibrated every day that testing occurred [2]. The use of two port calibrations ensured the most accurate measurements were able to be obtained [2]. The experiment also utilized a Hann low pass filter (LFP).

Results

The calculations for the time delay of each cable under test can be seen below.

$$\tau_{Mini\ Circuits} = \frac{.33 * \sqrt{2.05}}{3 * 10^8} = 1.575\text{x}10^{-9}$$

$$\tau_{Times\ Microwave\ Systems} = \frac{.67 * \sqrt{2.05}}{3 * 10^8} = 3.198\text{x}10^{-9}$$

$$\tau_{Koaxis} = \frac{1.5 * \sqrt{2.05}}{3 * 10^8} = 7.159\text{x}10^{-9}$$

The measured results of this experiment exhibited consistency with that of the theoretical delay and are compared in Table 1. The percentage error for the Mini Circuits cable was calculated to be 1.97%. The Times Microwave Systems Cable had a percentage error of 7.43%. Lastly, the Koaxis cable has the greatest error of 9.82%.

Part Number	Manufacturer	Description	Delay (ns)	Theoretical Delay (ns)
086-12SM+	Mini Circuits	12 inch Coaxial Cable	1.544	1.575
M17/152 00001	Times Microwave Systems	24 inch Coaxial Cable	2.960	3.198
AP10-KF120-AP10-1.50m-DM-MK	Koaxis	1.5 m Coaxial Cable	6.456	7.159

Table 1: Results; Source: Author

Conclusion

Time domain reflectometry characterizes the impedance of a transmission line [1]. This research report was conducted to use the theory of TDR to find the time delay of various coaxial cables. This report followed an experiment that was conducted using a ZNA which had TDR software and capabilities. Finally, this report used calculations to prove the validity of the experimental measurements.

References

[1] R. Witte, Electronic Test Instruments 2nd Edition, New Jersey, Prentice Hall, 2002.

[2] Olaf Ostwald, "Group and Phase Delay Measurements with Vector Network Analyzer ZVR," Rohde & Schwarz, https://www.rohde-schwarz.com/us/applications/group-and-phase-delay-measurements-with-vector-network-analyzer-zvr-application-note_56280-15546.html, 1997.

[3] Cheng, Tangjian, et al. "Low Dielectric Polyimide/Fluorinated Ethylene Propylene (PI/FEP) Nanocomposite Film for High-Frequency Flexible Circuit Board Application." *Macromolecular Materials & Engineering*, vol. 306, no. 7, pp. 1–9. *EBSCOhost*, https://doi.org/10.1002/mame.202100086, 2021.

Matching 2D Images and 3D Point Clouds using Feature Metric Registration

Student Researcher: Michael Tan

Advisor: Professor Jundong Liu

Ohio University
Russ College of Engineering/Computer Science

Abstract
Point clouds are 3D representations of some object or environment, typically captured by using laser camera systems or depth capturing cameras to produce such data. These point clouds are made of dots that have a coordinate relative to other dots and can cumulate together to form a complete 3D model. With point clouds, complex analysis can be conducted even in spite of a lack of a physical body, which helps to better comprehension of a large area and perform mathematical algorithms on them. This has been done to great effect in fields such as medicine to examine complex models of microorganisms, architectural design to detect flaws or improve upon critical features of buildings, and forestry and urban planning to conceptualize the health and area of their respective places.

With point clouds, many researchers have looked into how to combine two or more slightly different point clouds of the same scene in a process called registration. The combination of these point clouds can help form a more complete image of the entire environment/object, which greatly benefits techniques and tools such as computer vision, Magnetic Resonance Imaging (MRI) scans, and Computer Assisted Design (CAD) development.

Project Objectives
In this research project, matching 2D images with 3D point clouds is the ultimate objective to create a more detailed environment by meshing the dynamic colors and visual quality provided by 2D images with point clouds that can produce mechanically complex images that can only be represented in a 3D space.

One of the registration techniques used to combine point clouds is called correspondence, which essentially aligns each point from one point cloud to another point in a different point cloud. Currently, Iterative Closest Point is the most popular correspondence registration algorithm being used to combine these clouds and have shown to produce substantial results. However, ICP is prone to outliers and data-dense centers in its point clouds as a result of these algorithms attempting to match these points, even if no direct equivalent can be found between different clouds. This can result in massive transformational or rotational error that is too large to ignore in the model.

As such, our research has led us to find alternative algorithms that can reduce the outlier issue and focus on fast and accurate results. The most prominent and successful algorithms that has been tested during this project is Feature Metric Registration, a machine learning algorithm from researchers in the University of Sydney and University of Technology Sydney. This algorithm takes two point clouds that differ by rigid transformations (rotations and translations) and matches them together without correspondence and eliminate the issues of outliers that correspondence algorithms typically suffer from. Through FMR and another algorithm into transforming 2D images to 3D point clouds, a more accurate model of an environment can be achieved by combining two seemingly different ways of capturing data into one point cloud system.

Methods

1) Test typical 3D – 3D registration methods such as Iterative closest point and RANSAC to test their performance and accuracy.

2) Test FMR and compare it to ICP and other registration algorithms

3) Find ways to translate 2D images to 3D point clouds

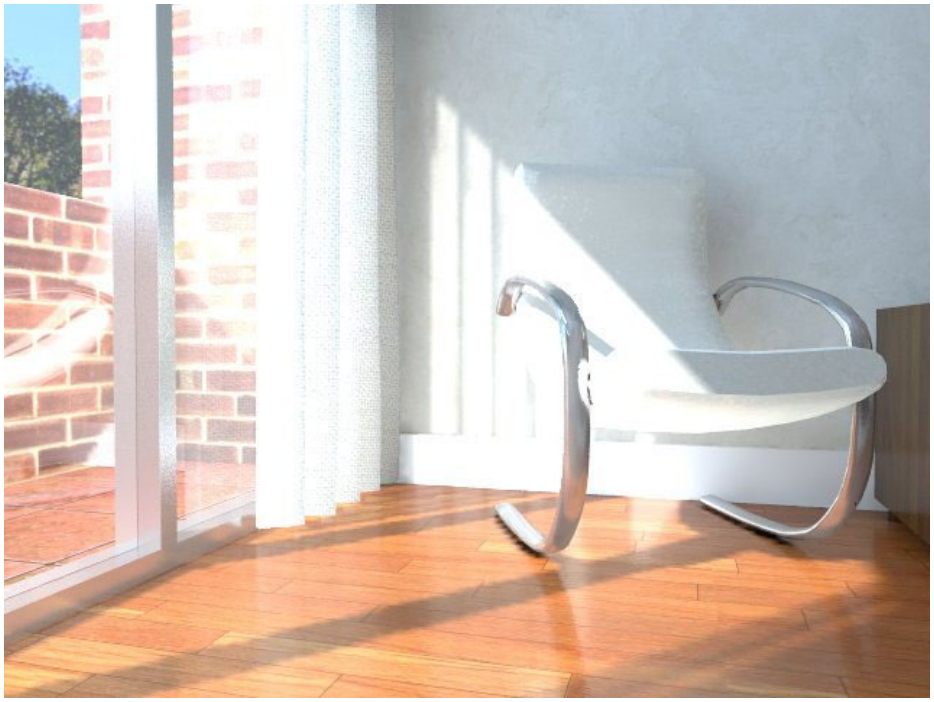
4) Perform FMR on a regular 3D point cloud obtained by traditional 3D capturing methods and a 3D point cloud of the same scene but extracted from a 2D image

Results and Discussion

Currently, 3D-3D point cloud registration has been successful as described in the paper. With FMR registration, combining 3D point clouds together have resulted in extremely low rotational and translational error, with rotational errors averaging less than a hundredth of a percentage and translational errors only around 10% and have been seen to be even less than that, all while finishing operations usually around .5 seconds for small or medium sized point clouds.

However, 2D to 3D registration is still being developed as we are still in the beginning stages of finding more information about it. FMR was developed only to register 3D point clouds with other 3D point clouds, so more information must be gathered about extracting features from a 2D image into a 3D format and performing FMR from there.

Figures/Charts



```
Time:
236194 microseconds

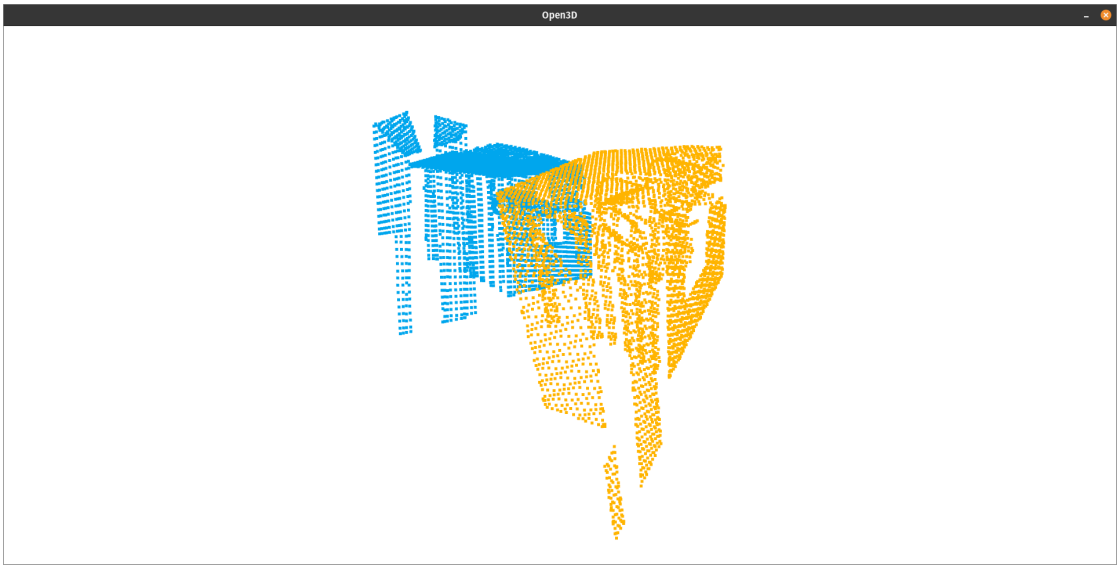
Transformation Ground truth:
tensor([[ 0.9165, -0.3875,  0.0998, -0.0031],
        [ 0.3992,  0.8684, -0.2940, -0.0615],
        [ 0.0272,  0.3093,  0.9506,  1.7707],
        [ 0.0000,  0.0000,  0.0000,  1.0000]], dtype=torch.float64)

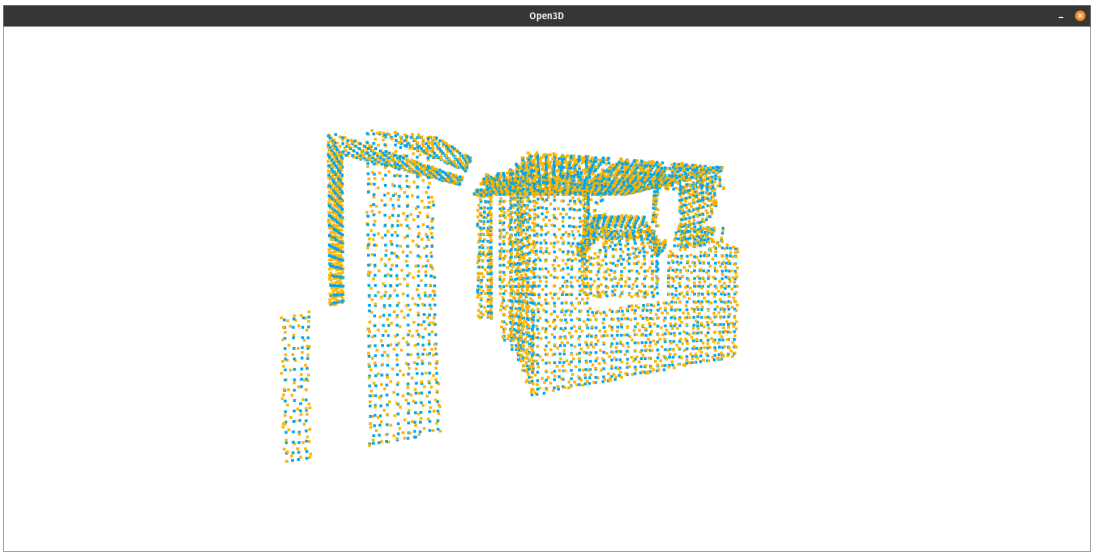
Transformation Estimated:
tensor([[ 0.9166,  0.3991,  0.0253, -0.0934],
        [-0.3866,  0.8681,  0.3115, -0.0520],
        [ 0.1024, -0.2952,  0.9499,  1.9022],
        [ 0.0000,  0.0000,  0.0000,  1.0000]])

Rotational Error:
0.0009119986753541864

Translational Error:
0.15977661921422806

RMSE:
0.3189118203939655
```





Acknowledgments

Special thanks goes to Xiaoshui Huang from The University of Sydney, Guofeng Mei from The University of Technology Sydney, and Jian Zhang from the University of Technology Sydney for introducing the concept of FMR and providing their source code that formed the basis of my current research study. Thanks also goes to Dr. Jundong Liu and Dr. Chris Bartone from Ohio University for helping me along this project and helping me to understand the parameters and finding research in this complex topic.

References

[1] X. Huang, G. Mei, and J. Zhang, "Feature-metric Registration: A Fast Semi-supervised Approach for Robust Point Cloud Registration without Correspondences." Accessed: Mar. 28, 2025. [Online]. Available: https://openaccess.thecvf.com/content_CVPR_2020/papers/Huang_Feature-Metric_Registration_A_Fast_Semi-Supervised_Approach_for_Robust_Point_Cloud_CVPR_2020_paper.pdf

Investigating the Effects of Cortical Microstructure Through Virtual Bone Scans

Student Researcher: Zachary Toth

Advisor: Dr. Joshua Gargac

Ohio Northern University
Mechanical Engineering

Abstract
The microstructural properties and cortical porosity of cortical bone are large contributors to the overall bone strength. Evaluating this contribution, however, can be difficult due to the complexity of controlling changes to pore structure in human or animal samples. This research was in the development of a computer program that is able to generate three-dimensional models of micron-scale cortical bone. A wide array of variable input parameters allows for the generation of samples with similarity to micro-CT scans of cortical bone or with specific geometric features, depending on the values used. A finite element model is also presented to demonstrate the similarities between generated and natural samples. This program aims to help provide a better understanding of how cortical bone microstructure contributes to overall bone strength, which could have major applications in future biomechanical design.

Project Objectives
Bone fractures are a significant public health issue, with some 178 million individuals being affected by them globally, as of 2019 [1]. An estimated $25 billion is spent in the United States alone on non-traumatic fractures [2,3]. One of the most common types of these fractures, stress fractures, most commonly affect elderly and physically active people, with a rate of occurrence at approximately 5.7 fractures per 1000 people per year [4,5,6]. Because stress fractures take the form of small fractures in cortical bone that propagate after repeated mechanical stress, it can be seen that their formation is influenced by factors such as the small-scale geometry and porosity of cortical bone.

Though somewhat less well-understood with respect to bone fragility than trabecular bone, cortical bone makes up approximately 80% of the human skeleton and serves as a major load-bearing component [7]. According to Augat and Schorlemmer [8], the strength of cortical bone is not only influenced by macro-scale structural properties such as bone cortex thickness and cross-sectional area but is also largely contributed to by microstructural properties such as crystallinity, incidence of microcracks, and cortical porosity. These microstructural geometries can affect continuum-level strength by altering the stress distribution in the extracellular matrix, inducing stress concentrations, and providing sites for microdamage nucleation and propagation [9–11].

There are multiple ways to measure the strength of cortical bone, but the most common is via direct measurement through mechanical testing. Especially when used alongside mechanical testing, finite element models derived from bone scans such as ultrasounds or micro-Computed Tomography (μCT) scans are well-suited to analyzing the relationship between microscale stress and macroscale strength [12–14]. Determining the exact relationship between microstructure and overall bone strength, however, is a difficult task because of the difficulty of controlling changes to pore structure in human or animal samples. In order to make research into the effects of microstructure on strength more precise, the ability to easily generate bone samples with given desired microstructural properties would be a very useful tool. This project seeks to present and evaluate a custom computer application to generate 3-dimensional models of micron-scale cortical bone based on a range of input parameters relating to cortical microstructure. These parameters can be varied to generate images similar to binarized CT scans of cortical bone, thereby allowing for more in-depth analysis and isolation of the effects of specific changes

to microstructure on overall bone strength. Overall, the objective of this project is to describe the function and abilities of the custom-built application and evaluate the application's ability to generate cores with similarity to CT scans of human cortical bone.

Methods

A custom-built program was developed using Python (Python Software Foundation, Wilmington, DE). To generate a core, the program initializes a three-dimensional binary cubic array—with each voxel representing a 10μm cube—with all cells set equal to one, representing solid bone and zero porosity overall. Then, a series of pores resembling the network of canals that makes up the Haversian systems characteristic of cortical bone is generated throughout the core. Each of these pores is generated one at a time via a repeated five-step process, as shown in Fig. 1. (1) The radius and eccentricity of the pore is chosen, establishing the cross-section of the pore. (2) Azimuthal and polar angles are chosen, orienting the pore in 3D space. (3) The x- y- and z- coordinates of the pore center are chosen, locating the pore in 3D space. (4) The pore is generated with an assigned length and the properties outlined prior, as well as with other less generalizable properties. (5) The number of sites at each end of the pore at which later pores can generate are determined. (6+) Following this process, further pores are generated until the target porosity is reached, finalizing the core. New pores are either generated in isolation or centered at the end of a previous pore, as described above. Once the target porosity has been reached, an additional routine is run to smooth the sample and merge nearby pores.

For each pore, the radius, eccentricity, orientation, location, length, pore shape, and other parameters are selected from gaussian distributions with user-assigned parameters. The values used for each of these parameters is either derived from review of the current literature [10,12,15–18] or analysis of μCT scans of human cortical bone samples. Further details about the program's parametrization, development, and implementation are described in a previous paper [19].

μCT scans of human cortical bone were acquired for comparison. The samples used were obtained from the proximal and mid-diaphysis of the femur of an 85-year-old male tissue donor with no medical history of skeletal pathology or trauma. Samples were machined into cylindrical "dog-bone" specimens with a gauge length of 10 mm and a gauge diameter of 3 mm. For each sample, μCT scans were acquired (mCT-80, Scanco Medical AG, Brüttisellen, Switzerland) at 10 μm resolution, 70 kVp voltage and 114 μA current with 1000 projections at a 600 ms integration time with slices oriented perpendicular to the longitudinal axis of the specimen [10]. The μCT scans were then imported into ImageJ (U.S. National Institutes of Health, Bethesda, MD) [20] using the "KHKs ImageJ I/O Utilities" plugin [21] and processed for comparison against generated samples. In order to process these scans, the images were smoothed, made binary, and cropped into 2 mm cubic TIFF files.

Specimen-specific finite element models were created from two generated bone cores with porosity of 5.4% and 24.8%, as well as a core taken from a μCT scan of human cortical bone with a porosity of 7.8% (Fig. 2). The STL files were imported into a general-purpose finite element program (Ansys, Canonsburg, PA). A static structural simulation was defined using an isotropic elastic material with an elastic modulus of 17.5 GPa and a Poisson's ratio of 0.3 [22]. Fixed boundary conditions were applied to all nodes along the bottom surface of each model. A distributed force of 40 N was applied to the top surface of each model.

Results and Discussion

Verification of the program's ability to generate samples with an intended porosity was performed by generating 169 bone cores with target porosities ranging from 0.667 to 20.77 percent; this target porosity and the actual porosity were recorded for each core (Fig. 3). The correlation between these values was close, with an average percent difference of 15.9% and no statistical difference observed between the

two ($p<0.001$, paired T-test). The difference between the target and actual porosity is caused by the pore smoothing routine. When disabled, the deviation between these two values disappears.

The proportional distributions of average cross-sectional pore diameter were used as a proxy for the statistical similarity between generated cores and those taken from μCT scans. When using parameter values taken from the literature, this value deviated an average of 1.67 ± 4.90% from donor samples. When parameter values were optimized for similarity, this deviation was reduced to 1.36 ± 2.39% (Fig. 4). For comparison, when two samples of donor cores were randomly selected, their deviation was 0.37 ± 0.52% from each other.

When finite element simulations were performed, the average and maximum von-Mises stresses were calculated for each core (Fig. 5). For the generated core with 5.4% porosity, the stress values were 25.3 MPa and 386 MPa, respectively. For the generated core with 24.8% porosity, the stress values were 35.2 MPa and 884 MPa, respectively. The average and maximum von-Mises stress values were measured to be 37.9 MPa and 208 MPa, respectively, for the 7.8% porosity core derived from μCT scan of donor bone. As can be expected, the high porosity generated core—representing osteoporotic bone—had a much higher maximum stress value than the other cores. For the generated core with a normal porosity value, the stress distribution profile was quite similar to that of the donor-sourced core, excepting the increased number of low-stress elements.

While promising, the evaluation and application of the model described here does have some limitations. While it is built with a large number of parameters to allow for flexibility in what can be generated, not all features of cortical bone are represented as parameters, which limit what microstructural changes can be evaluated. In addition, the point of comparison used was limited, with all μCT scan data coming from only 9 different CT scans, all from the femur of a single tissue donor. Lastly, the similarity between generated and actual samples was compared in a limited manner, with values like the distribution of average cross-sectional diameter and element-wise stress distributions used as proxies for similarity.

Given its ability to generate bone cores with highly controllable geometry, this program could be a useful tool for investigating the mechanical effects of different porosities, especially ones less common in standard samples. For example, one study tested 20 bone core samples but found that some porosity values were underrepresented due to the relatively small sample size and the natural variation of biological samples [23]. In addition, the program could also the isolation of the effects of specific variations in pore geometry, such as pore shape. For example, it is currently difficult to find samples consisting of mostly tapered pores [16], and therefore researchers are not able to quantify the effects of this microstructural change. As well as for general medicine, more in-depth investigation into the effects of cortical porosity on overall bone strength would also be a boon for the development of human space travel considering the detrimental effects of microgravity on bone porosity [24].

Figures/Charts

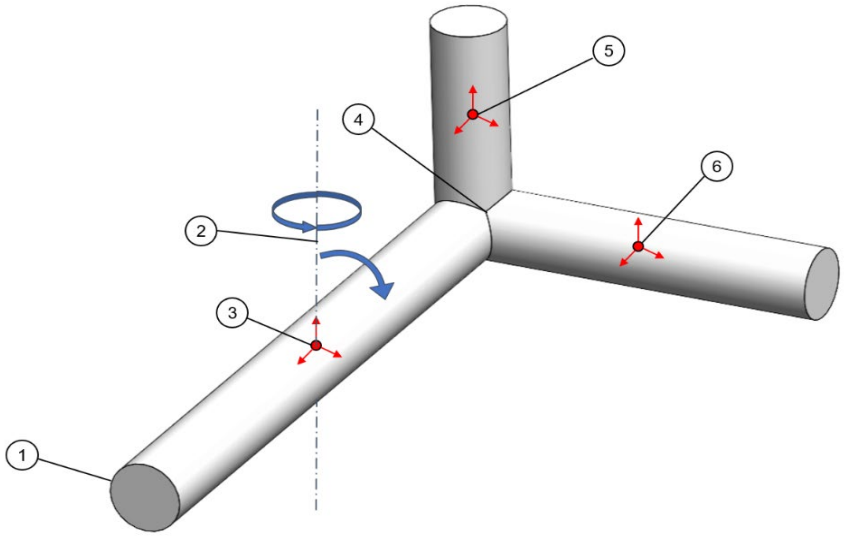


Figure 1: Illustration of the five-step algorithm used by the program to generate pores.

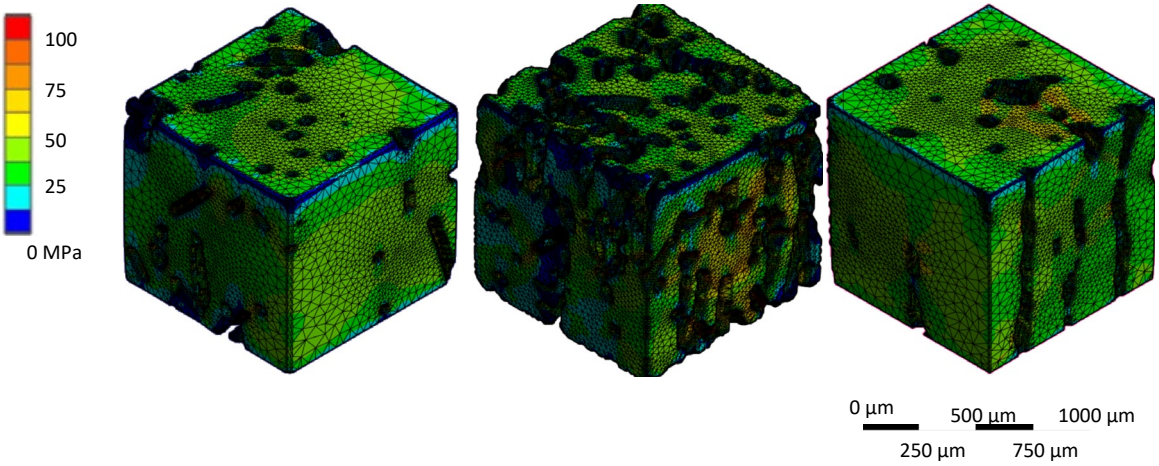


Figure 2: Finite element models of generated core with 5.4% porosity (right), donor core with 7.8% porosity (center), and generated core with 24.8% porosity (right).

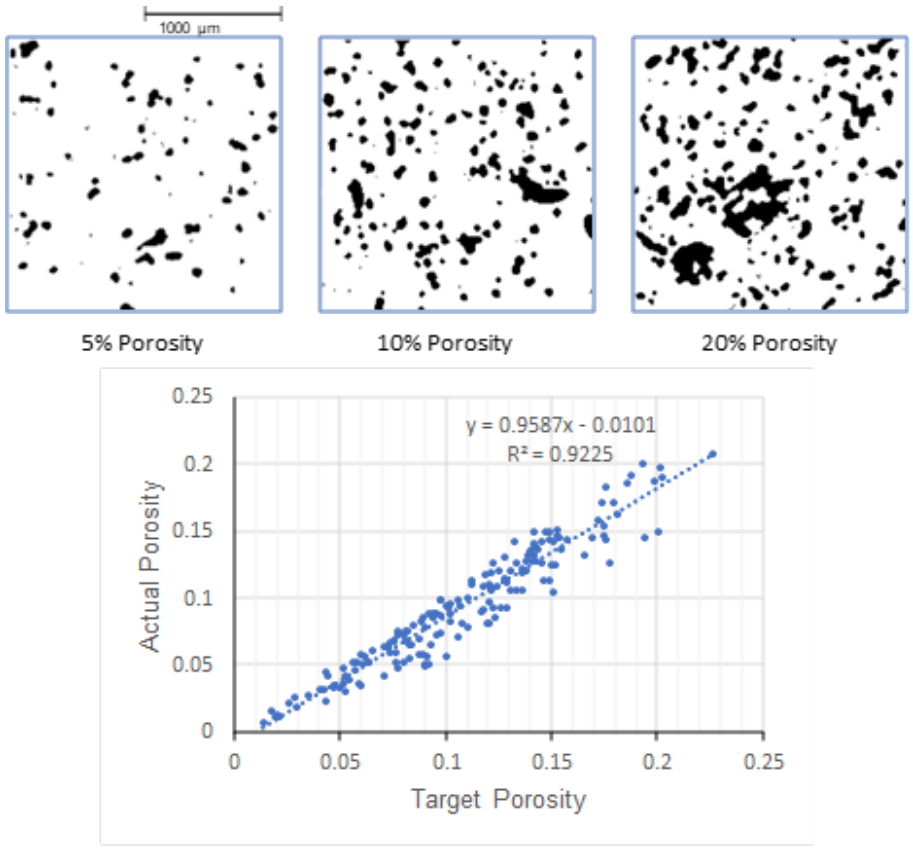


Figure 3: Demonstration of the program's ability to generate cores with desired porosity values.

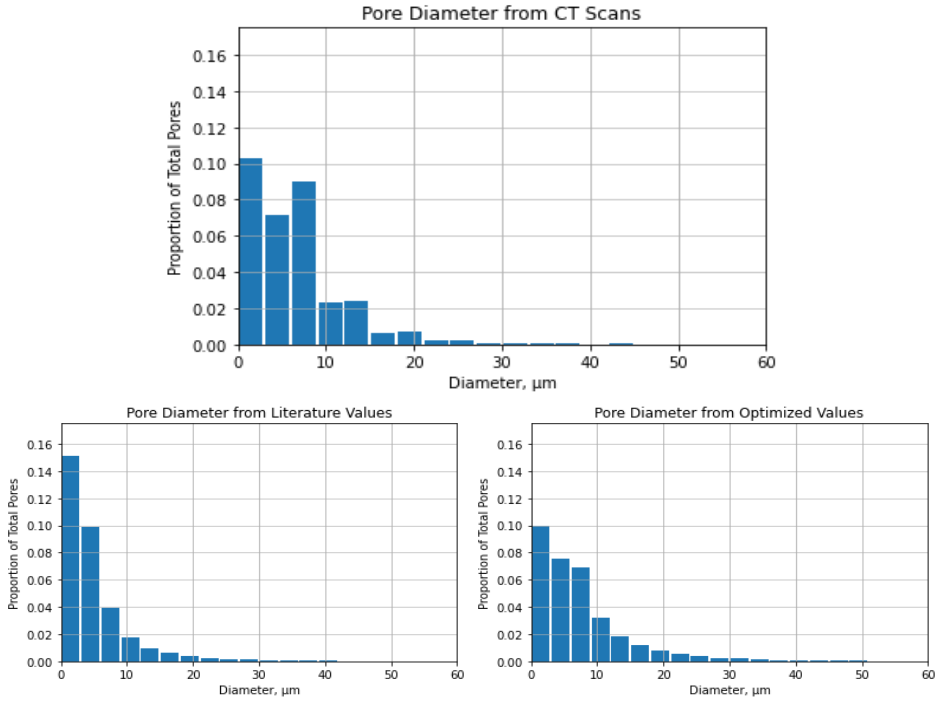


Figure 4: Comparison of proportional distributions of average cross-sectional pore diameter between donor cores and ones generated with literature-based or optimized parameter values.

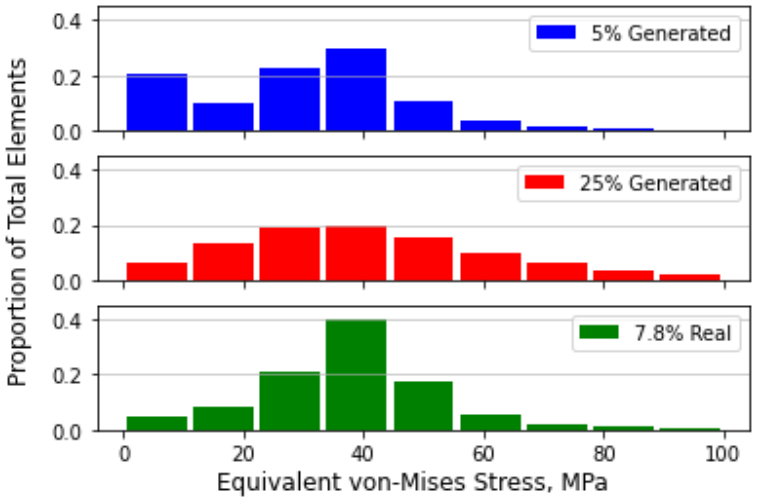


Figure 5: Distribution of von-Mises stress by element for each of the three cores analyzed.

Acknowledgments

The authors would like to thank Glen Niebur and Ryan Roeder at the University of Notre Dame for providing the human cortical bone µCT scans.

References

[1] Wu, A., et al., "Global, regional, and national burden of bone fractures in 204 countries and territories, 1990–2019: a systematic analysis from the Global Burden of Disease Study 2019," *The Lancet Healthy Longevity*, 2(9):580–592, Sept. 2021, doi: 10.1016/s2666-7568(21)00172-0

[2] Burge, R., et al., "Incidence and Economic Burden of Osteoporosis-Related Fractures in the United States, 2005–2025," *Journal of Bone and Mineral Research*, 22(3):465–475, Mar. 2007, doi: 10.1359/jbmr.061113

[3] Orsini, L. S., et al., "Health care utilization and expenditures in the United States: a study of osteoporosis-related fractures," *Osteoporosis International*, 16(4):359–371, Sept. 2004. doi: 10.1007/s00198-004-1694-2

[4] Waterman, B. R., et al., "Epidemiology of Lower Extremity Stress Fractures in the United States Military," Military Medicine, 181(10):1308–1313, Oct. 2016. doi: 10.7205/milmed-d-15-00571

[5] Rizzone, K. H., et al., "The Epidemiology of Stress Fractures in Collegiate Student-Athletes, 2004–2005 Through 2013–2014 Academic Years," *Journal of Athletic Training*, 52(10):966–975, Oct. 2017. doi: 10.4085/1062-6050-52.8.01

[6] Knowles, S. B., et al., "Issues in Estimating Risks and Rates in Sports Injury Research," *Journal of athletic training*, 41(2):207–215, June 2006. https://www.ncbi.nlm.nih.gov/pmc/articles/PMC1472638/

[7] Ott, S. M., "Cortical or Trabecular Bone: What's the Difference?," *American Journal of Nephrology*, 47(6):373–375, May 2018. doi: 10.1159/000489672

[8] Augat, P., Schorlemmer, S., "The role of cortical bone and its microstructure in bone strength," *Age and Ageing*, 35(suppl_2):ii27–ii31, Sept. 2006. doi: 10.1093/ageing/afl081

[9] Turnbull, T. L., Gargac, J. A., Niebur, G. L., Roeder, R. K., "Detection of fatigue microdamage in whole rat femora using contrast-enhanced micro-computed tomography," *J. Biomech.*, 44(13):2395–2400, Sept. 2011. doi: 10.1016/j.jbiomech.2011.06.032

[10] Turnbull, T. L., Baumann, A. P., Roeder, R. K., " Fatigue microcracks that initiate fracture are located near elevated intracortical porosity but not elevated mineralization," *J. Biomech.*, 47(12):3135–3142, Sept. 2014. doi: 10.1016/j.jbiomech.2014.06.022

[11] Gargac, J. A, Turnbull, T. L., Roeder, R. K., Niebur, G. L., “A probabilistic damage model based on direct 3-D correlation of strain to damage formation following fatigue loading of rat femora,” *J. Mech. Behavior of Miomedical Materials*, 30:234–243, Feb. 2014. doi: 10.1016/j.jmbbm.2013.11.009

[12] Grimal, Q., et al., “Assessment of cortical bone elasticity and strength: Mechanical testing and ultrasound provide complementary data,” *Medical Engineering & Physics*, 31(9):1140–1147, July 2009. doi: 10.1016/j.medengphy.2009.07.011

[13] Duchemin, L., et al., “Prediction of mechanical properties of cortical bone by quantitative computed tomography,” *Medical Engineering & Physics*, 30(3):321–328, Apr. 2008. doi: 10.1016/j.medengphy.2007.04.008

[14] Keyak, J. H., et al., “Prediction of fracture location in the proximal femur using finite element models,” *Medical Engineering & Physics*, 23(9):657–664, Sept. 2001. doi: 10.1016/s1350-4533(01)00094-7

[15] Heřt, J., Fiala, P., Petrtýl, M., “Osteon orientation of the diaphysis of the long bones in man,” *Bone*, 15(3):269–277, May 1994. doi: 10.1016/8756-3282(94)90288-7

[16] Pazzaglia, U. E., Zarattini, G., Giacomini, D., Rodella, L., Menti, A. M., Feltrin, G., “Morphometric Analysis of the Canal System of Cortical Bone: An Experimental Study in the Rabbit Femur Carried Out with Standard Histology and Micro-CT,” *Anatomia, Histologia, Embryologia*, 39(1):17–26, Jan. 2010. doi: 10.1111/j.1439-0264.2009.00973.x

[17] Pazzaglia, U. E., Congiu, T., Raspanti, M., Ranchetti, F., Quacci, D., “Anatomy of the Intracortical Canal System: Scanning Electron Microscopy Study in Rabbit Femur,” *Clinical Orthopaedics and Related Research*, 467(9):2446–2456, Sept. 2009. doi: 10.1007/s11999-009-0806-x

[18] Congiu. T., & Pazzaglia, U. E., “The Sealed Osteons of Cortical Diaphyseal Bone. Early Observations Revisited With Scanning Electron Microscopy,” *The Anatomical Record*, 294(2):193–198, Dec. 2010. doi: 10.1002/ar.21309

[19] Toth, Z. B., Gargac, J. A., “Generating Virtual Bone Scans for the Purpose of Investigating the Effects of Cortical Microstructure,” *ASME J. Biomech. Eng.*, 147(3): 034502, Mar. 2025, doi: 10.1115/1.4067576

[20] Schneider, C. A., Rasband, W. S., & Eliceiri, K. W. (2012). “NIH Image to ImageJ: 25 years of image analysis,” *Nature Methods*, 9(7):671–675, June 2012. doi:10.1038/nmeth.2089

[21] Kunzelmann, K. -H. KHKs ImageJ I/O Utilities. (2009). ProjetUrbain. Accessed: 7 June 2024. [Online]. Available: http://www.kunzelmann.de/4_software-imagej-import-export-utilities.html

[22] Bakalova, L. P. et al., “Intracortical Bone Mechanics Are Related to Pore Morphology and Remodeling in Human Bone,” Journal of Bone and Mineral Research, 33(12):2177–2185, Dec. 2018. doi: 10.1002/jbmr.3561

[23] Schaffler, M. B., & Burr, D. B., “Stiffness of compact bone: Effects of porosity and density,” *J. Biomech.*, 21(1):13–16, 1988. doi: 10.1016/0021-9290(88)90186-8

[24] Sibonga, J. D., et al., “Risk of Bone Fracture due to Spaceflight-induced Changes to Bone,” NASA JSC, Houston, TX, USA, Rep. HRP-F07-ERFT.R2, 2024.

Comparative Evaluation of 2x4 Construction Wood and Polymer Matrix Composites

Student Researcher: Sri Tyler

Advisor: Dr. Alssandro Rengan

Central State University
Industrial Technology

Abstract
This project explores the viability of replacing traditional 2x4 construction wood with high strength-to-weight Polymer Matrix Composites (PMCs). The study evaluates Carbon/Kevlar hybrid fabric in combination with various core materials-Styrofoam, Divinycell Divinymat, and balsa wood-using Vacuum Assisted Resin Infusion Molding (VARIM). Through ASTM D5045 (Fracture Toughness) and ASTM D790 (Flexural Strength) testing, the performance of PMCs is compared to wood to assess feasibility for industrial structural use.

Project Objective
The primary objective of this project is to determine whether a polymer matrix composite structure can effectively replace traditional 2x4 wood in structural applications. This involves the fabrication of composite beams using Carbon/Kevlar hybrid sleeving combined with various core materials such as Styrofoam, Divinycell Divinymat, and balsa wood. Another key aim is to conduct standardized mechanical testing using ASTM D5045-14 for evaluating fracture toughness and ASTM D790-03 for assessing flexural properties. By comparing the results for flexural strength, flexural modulus, and fracture toughness with those of standard construction lumber, the project seeks to understand the practical feasibility of replacing wood with PMCs. Additionally, considerations such as weight, sustainability, manufacturability, and durability of PMC beams in relation to wood are evaluated.

Methods
The PMC specimens were fabricated using Carbon/Kevlar hybrid sleeving as the reinforcing fiber material, filled with a variety of core options including Styrofoam, Divinycell Divinymat, and balsa wood. The resin matrix consisted of a two-to-one ratio of Resin Research 2000CE epoxy resin and a fast hardener. To manufacture the specimens, Vacuum-Assisted Resin Infusion Molding (VARIM) was employed. In this process, the fiber-sleeved core was placed within a vacuum bagging setup, which included sealant tape, flow mesh, infusion tubing, and a resin trap. Once the system was fully vacuum-sealed, the resin mixture was introduced and allowed to infuse through the fibers and core. The setup was then left to cure at room temperature for 24 hours.

After curing, the samples were cut to specific dimensions using a diamond saw and CNC milling machine to meet the requirements set forth by the ASTM testing standards. Flexural testing samples measured 5 inches by 0.5 inches by 0.5 inches, while fracture toughness samples were prepared with machined notches and pre-cracks. The two primary testing procedures used were ASTM D5045-14 for determining the plane-strain fracture toughness of plastic materials and ASTM D790-03 for assessing flexural strength and modulus. Each test sample was measured and weighed prior to testing. Mechanical testing was conducted using a load frame machine.

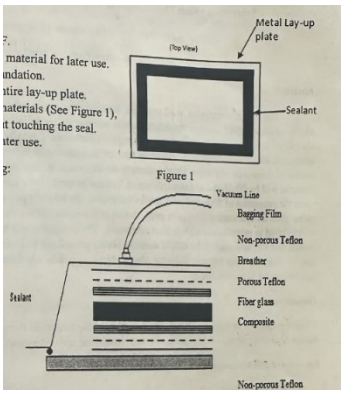
Results and Discussion

3-POINT FLEXURAL TESTING RESULTS			
SPECIMEN	FORMULA	FLEXURAL STRENGTH	FLEXURAL MODULUS
2X4 Construction Wood	$\sigma = \frac{Mh}{2I}$	310 MPa	.07 MPa
CARBON KEVLAR SLEEVE AND BALSA WOOD +DIVINITY CORE (PMC)	$E = \frac{FL^3}{48dI}$	16 MPa	7.72 MPa

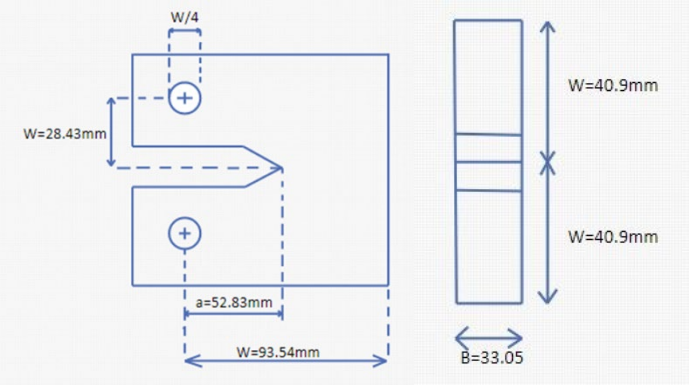
PLANE-STRAIN FRACTURE TOUGHNESS RESULTS			
SPECIMEN	FORMULA	DENSITY	FRACTURE TOUGHNESS
2x4 Construction Wood	$K_Q = \left(\frac{P_Q}{B\sqrt{W}}\right) f(x)$	$1.11 \ \frac{g}{cm^3}$	$K1c = 0.7MPa\sqrt{m}$
Carbon Kevlar sleeve and Balsa Wood + Divinity core (PMC)	$K_Q = \left(\frac{P_Q}{B\sqrt{W}}\right) f(x)$	$0.87 \ \frac{g}{cm^3}$	$K1c = 2.9MPa\sqrt{m}$

In terms of flexural performance, the wood sample demonstrated a flexural strength of approximately 310 MPa, which is nearly 19.37 times greater than that of the PMC specimen. However, the stiffness of the PMC, as indicated by its flexural modulus of around 7.72 MPa, was approximately 110 times higher than that of the wood. This suggests that the PMC beams are far more resistant to bending deformation than traditional 2x4 wood. For fracture toughness, the PMC samples significantly outperformed the wood. This highlights the PMC's superior ability to resist crack propagation, a property attributed to the reinforcing characteristics of the hybrid Carbon/Kevlar fibers and the energy dissipation capability of the resin matrix. Although the wood demonstrated high flexural strength, it exhibited low fracture toughness, meaning it was more prone to sudden brittle failure. There are limitations and areas for improvement. While the wood provides greater strength, it fails with minimal warning and lacks resistance to crack growth. The PMC, on the other hand, though weaker in absolute strength, is lighter, stiffer, and more durable under fracture-inducing conditions. Improvements could include employing multi-layered fiber layups, enhancing the bonding between the core and sleeve, and scaling up the prototypes for more realistic structural applications.

Figures and Charts



(Image of the resin transfer infusion molding)



(Specimen Engineering drawing of PMC)



(PMC)



(PMC Core)



(Constuction Wood)

Testing Standards

- Fracture Toughness: ASTM D5045-14 for Plane-Strain Fracture Toughness of Plastic Materials.
- Flexural Testing: ASTM D790-03 for determining flexural strength and modulus.

Test samples were measured and weighed prior to testing. A load frame machine was used for mechanical testing, and data was collected using it.

Acknowledgments
Special thanks to Dr.Alessandro Rengan, the Central State University Mechanical Engineering Department, for support and my appreciation also extends to OSGC for offering an extraordinary opportunity to showcase research at the OSGS symposium as well as offering scholarships.

References

1. ASTM D5045-14. "Standard Test Method for Plane-Strain Fracture Toughness and Strain Energy Release Rate of Plastic Materials."
2. ASTM D790-03. "Standard Test Methods for Flexural Properties of Unreinforced and Reinforced Plastics and Electrical Insulating Materials."
3. Resin Research Epoxy Systems. Technical Data Sheets.

Defining the Relationship between Bacterial Motility and Virulence in *V. campbellii* & *V. parahaemolyticus*.

Student Researcher: Jayanti Upadhyay

Advisor: Dr. Blake Petersen

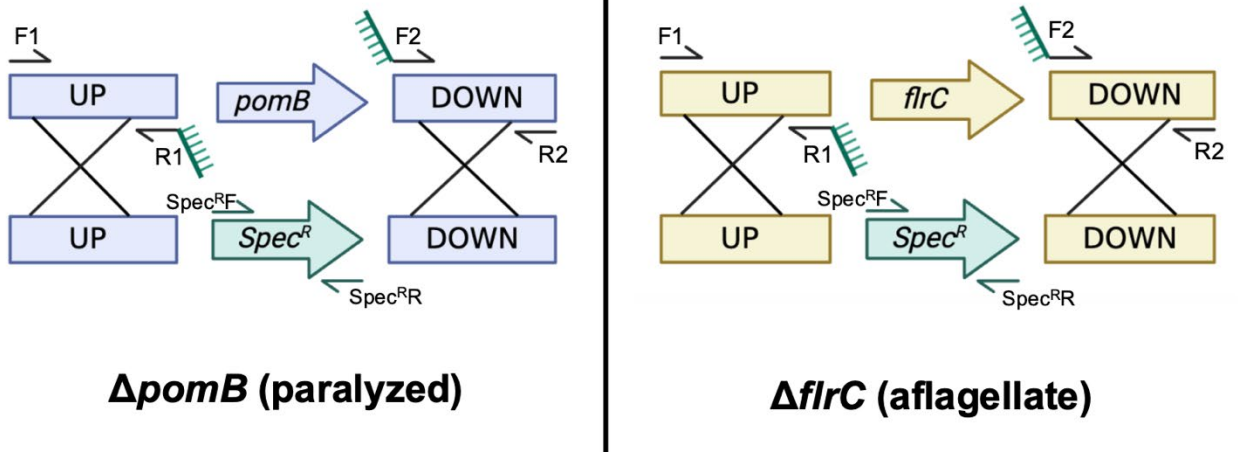
Baldwin Wallace University
Biology and Chemistry

Project Summary and Results

Vibrio campbellii is a gram-negative marine bacterium that impacts the aquaculture industry as a pathogen of various aquatic organisms. In other pathogenic *Vibrio* species, such as V. *parahaemolyticus*, bacterial flagellar motility acts as a virulence factor that aids in host colonization and escape; it serves as a promising target for developing potential antibiotics and treatments.[1] In my previous work, I infected gnotobiotic *Artemia franciscan* larvae (brine shrimp) with *V. campbellii* flagellar mutants under varying environmental conditions to clarify the relationship between flagellar motility and virulence. I found that an aflagellate mutant (Δ*flrC*) showed reduced virulence, while a mutant with a paralyzed flagellum (Δ*pomB*) exhibited significantly increased virulence. There was also an increase in biofilm formation, a multicellular matrix that aids in attachment and protection during infection, while also contributing to the rise in antibiotic resistance.[2] The increase in virulence and biofilm formation in the paralyzed flagellar mutant were abolished under turbulent conditions but not static conditions. These results suggest a mechanosensory pathway that controls *V. campbellii*'s transition between motile and sessile states during infection and changing environmental conditions.

I initially split my work into two main goals to investigate further the relationship between the motile-sessile switch in determining *Vibrio* virulence. First, the role of biofilm formation in *V. campbellii* virulence was examined to further study the potential flagellar mechanosensing pathway. I started working towards deleting VpsR, a response regulator responsible for controlling the expression of the vibrio polysaccharide (*vps*) genes that compose the exopolysaccharide matrix of biofilms in other *Vibrio* species.[3] Unfortunately, due to complexities in the construction of the gene and other roadblocks, I turned my full attention to my second goal: to determine whether the mechanosensing behavior of *V. campbellii*'s flagellum is conserved across different species. To answer this question, I am in the process of constructing aflagellate (Δ*flrC*) and paralyzed flagellar (Δ*pomB*) mutants in *V. parahaemolyticus*, which is a closely related *Vibrio* species to V. campbellii and is a human pathogen. This semester, I successfully isolated different parts of each gene from the entire V. parahaemolyticus genome through computational genetics. My next step is to take the isolated gene parts and successfully construct the two deletion mutants in the lab using various wet lab genetics techniques. These *V. parahaemolyticus* mutants will be compared alongside their homologous *V. campbellii* mutants in brine shrimp infection assays to determine whether there is a similar pattern in mechanosensing behavior between *Vibrio* species, further solidifying previous *V. campbellii* data I collected. Exploring the similarities between both *Vibrios*, one that is an aquatic pathogen and one that is a human pathogen, and replicating the relationship between motility and virulence in both can provide insight into future research impacting environmental and health conditions in society and help discover novel therapeutics targeting virulence factors in *Vibrio* species and similar bacterial pathogens, further assisting with alternate pathways to combat the antibiotic resistance crisis in the world.

Design of Deletion Mutants in *V. parahaemolyticus*



Acknowledgements

I am grateful to the NASA Ohio Space Consortium for funding my research this semester. Next, I would like to thank my research advisor, Dr. Blake Petersen, for guiding and supporting my research goals. I would also like to acknowledge the Peterjohn family, who funded my previous research that led to my current research plans and results, and the Biology, Geology, and Neuroscience Department of Baldwin Wallace University for their continued support.

References

[1] Nakamura, S., & Minamino, T. (2019). Flagella-Driven Motility of Bacteria. Biomolecules, 9(7), 279. https://doi.org/10.3390/biom9070279

[2] Valentini, M., & Filloux, A. (2016). Biofilms and Cyclic di-GMP (c-di-GMP) Signaling: Lessons from Pseudomonas aeruginosa and Other Bacteria. The Journal of biological chemistry, 291(24), 12547–12555. https://doi.org/10.1074/jbc.R115.711507

[3] Yildiz, F. H., Dolganov, N. A., & Schoolnik, G. K. (2001). VpsR, a Member of the Response Regulators of the Two-Component Regulatory Systems, Is Required for Expression of vps Biosynthesis Genes and EPS(ETr)-Associated Phenotypes in Vibrio cholerae O1 El Tor. *Journal of bacteriology*, *183*(5), 1716–1726. https://doi.org/10.1128/JB.183.5.1716-1726.2001

Hybrid Engines for Aircraft Propulsion

Student Researcher: Cael Vanderhorst

Advisor: Dr. David Sawyers, Jr.

Ohio Northern University
Mechanical Engineering

Abstract
This research seeks to evaluate the feasibility of using hybrid engines for aircraft propulsion through analyzing the performance of a basic hybrid propulsion system across varying flight parameters. The results of this analysis provide information on the general utility of hybrid systems for aircraft propulsion. As hybrid systems are becoming increasingly popular in automobiles and are being developed for aircraft, analyses such as the one presented in this study will prove important engineering design tools in the future.

This project began with a literature review to determine the energy requirements of an aircraft during different portions of flight, namely takeoff, climb, and cruise. From this review, mathematical models were created to determine the thrust and power requirements for each of these flight portions, based on variable input parameters such as aircraft weight and airspeed. These mathematical models were used to create a computer model using Microsoft Excel, allowing input parameters to be quickly varied when repeating calculations. Using the requirements during each flight portion, a series-arrangement hybrid propulsion system was developed and sized to provide the required power for the duration of flight for an example case. Using the computer model, flight parameters can be varied (and propulsion system size requirements recalculated) to determine the feasibility of such a hybrid system across different flight conditions.

Project Objectives
The overarching objective of this work was to analyze the performance of a hybrid propulsion system for aircraft. In order to do this, it was necessary to determine the power requirements of an aircraft during different stages of flight. For repeatability and increased usefulness, a model allowing the variation of input parameters (as opposed to a single solution) was desired.

Methods
Work began by breaking an aircraft's flight into different phases, for which the power requirements could be calculated. Flight was taken to have four phases: takeoff, where the aircraft accelerates up to the liftoff velocity; climb, where the aircraft climbs from the ground to its cruising altitude; cruise, where the aircraft flies towards its destination at its cruising altitude; and landing, where the aircraft descends back to ground level and slows to a stop. The power requirements at each phase were then determined using kinetics.

Assumptions:
The following assumptions were made for the kinetic analysis:

1. The aircraft was treated as a point mass.
2. The propeller provides constant thrust to the aircraft.
3. Flight during the climb phase is unaccelerated (i.e., a steady analysis was performed for climb).

4. Flight during the cruise phase is level (parallel to the ground) and unaccelerated (steady analysis for cruise).

Takeoff:

Figure 1 shows the free body diagram of the aircraft during takeoff.

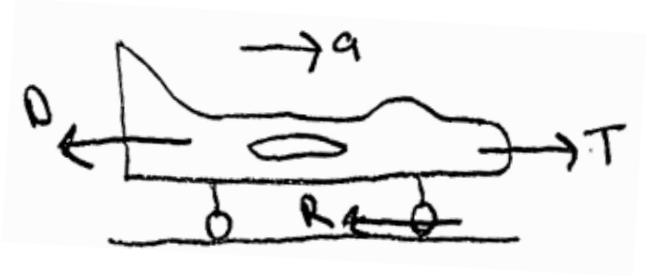


Figure 1: Takeoff free body diagram.

From standard kinematics (i.e., $\Delta s = \frac{1}{2}at^2 + v_0 t$, etc.), one can derive equation 1 [1]:

$$s = \frac{V^2 m}{2F} \tag{1}$$

where s is the distance an object has traveled (assuming an initial position of zero), V is the object's velocity at position s, m is the object's mass, and F is the constant, net force acting on the object. By definition, at the end of takeoff (when the liftoff distance is reached), the aircraft will be at the liftoff velocity. The liftoff velocity is given by equation 2 [1]:

$$V_{LO} = 1.2V_{stall} = 1.2\sqrt{\frac{2W}{\rho_\infty S C_{L,max}}} \tag{2}$$

where V_{LO} is the liftoff velocity, V_{stall} is the aircraft's stall velocity, W is the aircraft's weight, ρ_∞ is the density of the oncoming air, S is the aircraft's wing area, and $C_{L,max}$ is the aircraft's maximum lift coefficient. Applying equation 1 to an aircraft, substituting equation 2 for the velocity, and simplifying yields equation 3 [1]:

$$s_{LO} = \frac{1.44W^2}{g\rho_\infty S C_{L,max} T} \tag{3}$$

where s_{LO} is the liftoff distance, g is the gravitational acceleration constant, and T is the aircraft's thrust. It should be noted that equation 3 neglects drag and rolling resistance, which is not unreasonable [1]. Solving equation 3 for thrust yields equation 4:

$$T_{req} = \frac{1.44W^2}{g\rho_\infty S C_{L,max} s_{LO}} \tag{4}$$

where T_{req} indicates that it is the thrust required to reach V_{LO} in s_{LO}. In other words, T_{req} is the thrust required for takeoff. Using the thrust (net force), and knowing the mass of the aircraft, the acceleration was solved for using Newton's Second Law. This allowed the velocity profile of the aircraft to be found. The power required during takeoff can be found from the thrust and velocity using equation 5:

$$P_{req} = T_{req} V \tag{5}$$

where P_{req} is the power required during takeoff and V is the aircraft's velocity.

Climb:

Figure 2 shows the free body diagram of the aircraft during climb.

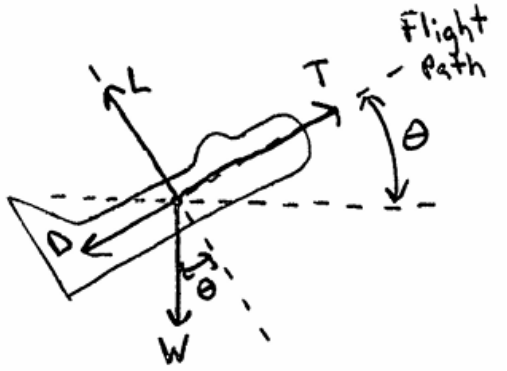


Figure 2: Climb free body diagram.

Because climbing flight is assumed to be steady for this analysis, summing forces parallel and perpendicular to the flight path yields equations 6 and 7, respectively.

$$T = D + Wsin\theta = \frac{1}{2}\rho_\infty V_\infty^2 S C_D + Wsin\theta \tag{6}$$

$$L = \frac{1}{2}\rho_\infty V_\infty^2 S C_L = Wcos\theta \tag{7}$$

where D, L, C_D, and C_L are the drag and lift forces and coefficients, respectively, θ is the climb angle, and V_∞ is the airspeed. From equations 6 and 7, the power required for climb can be found using the following steps (based on [1]):

1. Choose V_∞ (varied as an input parameter).
2. Calculate $C_L = \frac{Wcos\theta}{\frac{1}{2}\rho_\infty V_\infty^2 S}$.
3. From the aircraft's drag polar: $C_D = C_{D,0} + \frac{C_L^2}{\pi e AR}$, where $C_{D,0}$ is the drag coefficient at zero lift, e is the aircraft's Oswald efficiency factor, and AR is an aspect ratio equal to $\frac{(wingspan)^2}{wing\ area}$.
4. Calculate $D = \frac{1}{2}\rho_\infty V_\infty^2 S C_D$.
5. Calculate $T_{req} = D + Wsin\theta$.
6. Calculate $P_{req} = T_{req} V_\infty$.

Cruise:

Figure 3 shows the free body diagram of the aircraft during cruise.

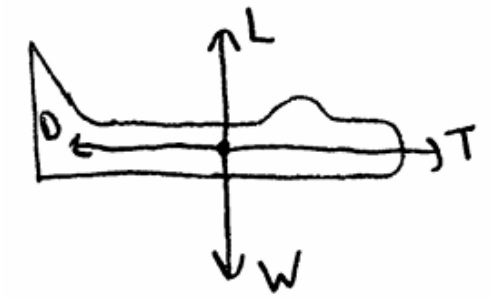


Figure 3: Cruise free body diagram.

Similar to climb, summing forces yields equations 8 and 9:

$$T = D = \frac{1}{2}\rho_\infty V_\infty^2 S C_D \tag{8}$$

$$L = \frac{1}{2}\rho_\infty V_\infty^2 S C_L = W \tag{9}$$

From equations 8 and 9, the power required for cruise can be found using the following steps (based on [1]):

1. Choose V_∞ (varied as an input parameter).
2. Calculate $C_L = \frac{W}{\frac{1}{2}\rho_\infty V_\infty^2 S}$.
3. From the aircraft's drag polar: $C_D = C_{D,0} + \frac{C_L^2}{\pi e AR}$.
4. Calculate $T_{req} = D = \frac{1}{2}\rho_\infty V_\infty^2 S C_D$.
5. Calculate $P_{req} = T_{req} V_\infty$.

Landing:

During descent, it is assumed that the aircraft is gliding downwards, meaning power is only needed for maneuvering. The power required for maneuvering is much less than the power required for delivering thrust to the aircraft during the other phases of flight. Moreover, because of the (theoretical) possibility of a regenerative system (similar to a regenerative braking system in an electric vehicle), some power could be delivered back to the aircraft. Because of this, any (small) net power requirement during descent is neglected. Similarly, during the landing ground roll, the aircraft is assumed not to use reverse-thrust to slow itself down. Therefore, any power requirements during the landing phase of flight are neglected.

From the above analyses, a flight model was created using Microsoft Excel. As input parameters, the model takes flow parameters (airspeed, air density), aircraft parameters (weight, wingspan, wing area, etc.), liftoff distance, and climb angle. The program uses the above analyses to calculate the power requirements for each phase of flight given the specified input parameters.

Propulsion System:

A simple, series-arrangement propulsion system was used for this project. Figure 4 shows a diagram of the propulsion system.

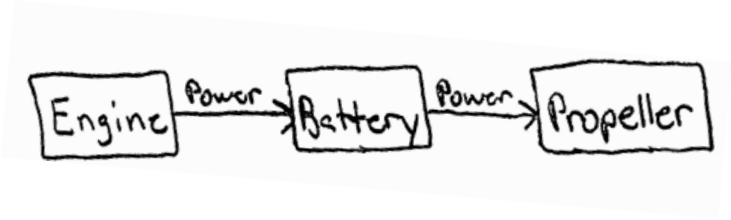


Figure 4: Propulsion system.

The engine supplies power to the battery, which in turn supplies power to the aircraft. This system is designed for the engine to run at a constant output, which means higher efficiency compared to one that must change its output to meet acceleration requirements. When the aircraft's power requirements are higher than the engine's output (during takeoff and climb), the battery depletes. Then, when the aircraft's power requirements are lower than the engine's output (cruise), the battery is recharged.

One simple way to size the engine is to have it provide the average power across the entire flight. This situation is shown in Figure 5. Sizing the engine to provide the average power ensures that the battery will be fully recharged during cruise. The minimum size of the battery is calculated as the difference between the energy required by the aircraft during takeoff and climb and the energy provided by the engine during those phases (i.e., the shaded area in Figure 5). Note that the numerical values in Figure 5 come from a test case, discussed in Results and Discussion.

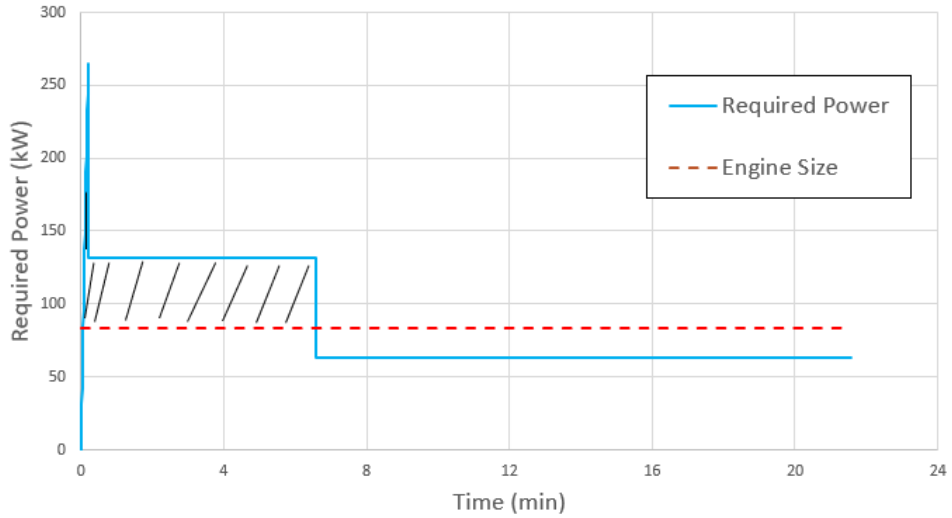


Figure 5: Power profile for test case in which the battery is fully recharged during cruise.

Because of obvious safety issues with fully depleting the battery during takeoff and climb, a 20% factor of safety was added to the battery size calculation, which is shown in equation 10:

$$Battery\ Size = 1.2A_{shaded} \tag{10}$$

Results and Discussion

In order to demonstrate the functionality of the Excel model discussed above, engine and battery sizes were determined for an example case in three scenarios:

1. Fully recharging the battery during cruise (i.e., landing with a fully recharged battery)
2. Not recharging the battery at all (landing with a fully depleted battery)
3. Recharging the battery ~20% (landing with a battery at ~20% charge)

The test case was modeled after a short flight in a small, Cessna-esque plane. The exact input parameters used are included in Appendix 1. Figure 5 in Methods shows the power profile for the fully recharged case, in which the engine is sized at the average power requirement across the entire flight. Figures 6 and 7 show the power profiles for the non-recharged (engine sized at cruise power requirement) and ~20% recharged (engine sized at one-quarter of the way between the cruise power requirement and the average power) cases, respectively. For each of the cases, the battery was sized using equation 10.

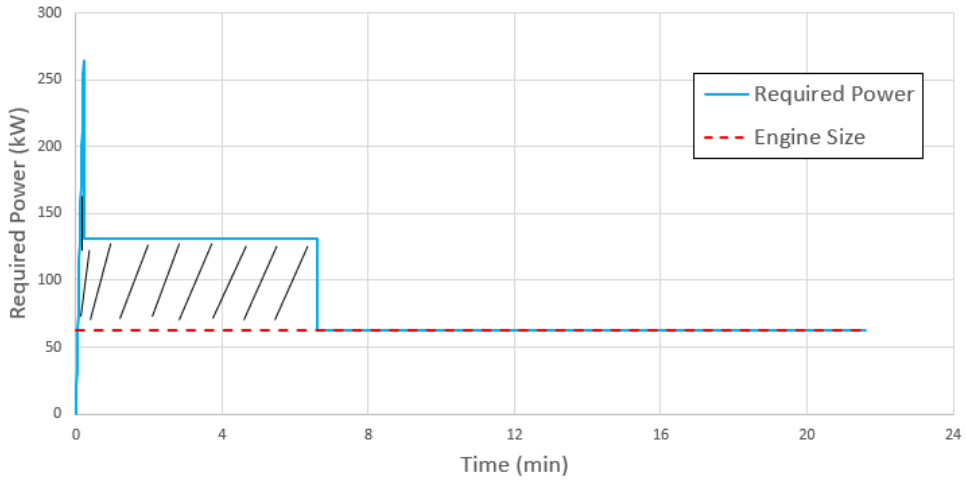


Figure 6: Power profile for test case in which the battery is not recharged during cruise.

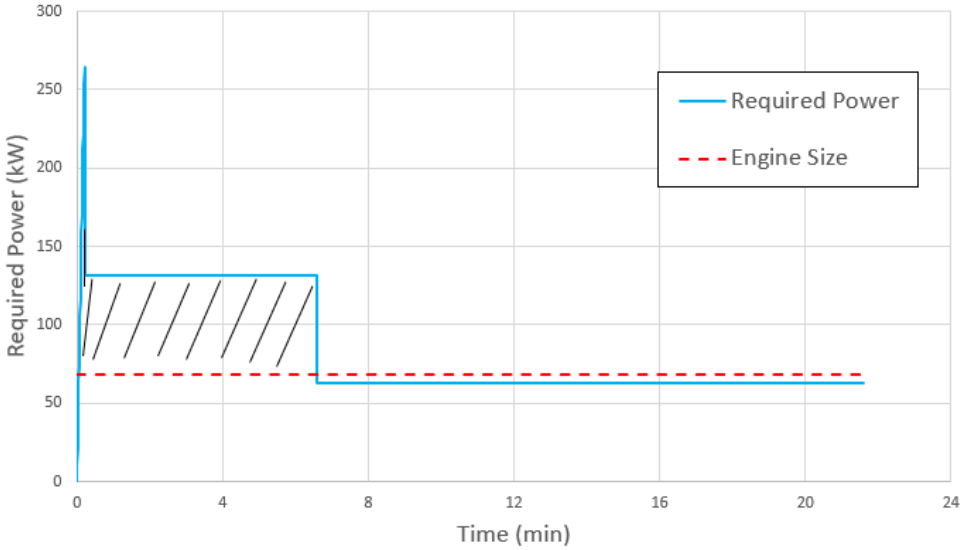


Figure 7: Power profile for test case in which the battery is recharged ~20% during cruise.

Table 1 summarizes the results of the test case calculations. The required battery size if there was no engine (meaning the battery must supply the energy equal to the full area under the required power curve) is also included for reference.

Table 1: Test Case Results

Case	Engine Size (kW)	Battery Size (MJ)
Fully Recharged	83.86	22.8
Not Recharged	62.97	32.6
20% Recharged	68.19	30.1
No Engine	-	130.4

From the results in Table 1, if the aircraft can rely on electrical power to recharge the battery between flights, a smaller engine can be used. A bigger battery is necessary to accommodate this, though. The required engine sizes above are comparable to, and generally smaller than, the engines of small, general aviation aircraft [2], after which this test case was modeled. This is promising, as it indicates aircraft could

be produced with smaller engines if using a hybrid propulsion system such as the one described here. The battery requirements are also feasible, as the sizes are well within the sizes of the batteries used in Tesla automobiles [3]. The peak power requirement during takeoff shown in Figures 5-7 is a potential area of concern, but is not outside the realm of future capabilities, as the Tesla Model 3 has been shown to provide peak power outputs of around 200 kW [4]. It should be noted, though, that the test case in this paper was performed for a small aircraft, and that larger aircraft would have increasing power requirements. This indicates that current battery technology may not be adequate for hybrid propulsion systems for large aircraft. Further analyses, such as comparing battery weights versus engine and fuel weights for different levels of recharge, can be performed by varying the input parameters in the model created in this project.

Acknowledgments

I would like to give special thanks to my advisor, Dr. David Sawyers, for providing guidance and expertise throughout my work on this project. The completion of this work would not have been possible without his advice and helping hand. I would also like to give credit to Dr. John D. Anderson, Jr., author of "Introduction to Flight," a textbook which guided much of the aircraft flight analysis. Lastly, I would like to thank Dr. Craig Murray for lending me his copy of "Introduction to Flight."

References

[1] J.D. Anderson Jr, *Introduction to Flight*, 8th ed. New York: McGraw-Hill Education, 2016.

[2] "How Much Horsepower Does an Airplane Have?," *My Aircraft Cost*, Jan. 21, 2025. https://myaircraftcost.com/how-much-horsepower-does-an-airplane-have-in-flight/

[3] E. Gibson, "Tesla Car Battery Capacity: Size, Range, And Performance Explained [Updated On- 2025]," *PoweringAutos*, 2025. https://poweringautos.com/how-much-capacity-is-tesla-car-battery/

[4] Mountain Pass Performance, "Dyno Testing The Tesla Model 3 At Various Battery SOC," *YouTube*, Aug. 16, 2018. https://www.youtube.com/watch?v=G8NaZDIL6sI

Appendix 1: Test Case Input Parameters

Table 2 gives the input parameters used for the test case described in this paper.

Table 2: Test Case Input Parameters

Airspeed	60 m/s	Wingspan [1]	35.8 ft
Air Density (takeoff, climb/cruise)	1.006, 1.225 kg/m^3	Climb Angle	5°
Aircraft Weight [1, pg. 455-456]	2950 lb	Cruise Altitude	2000 m
Wing Area [1]	174 ft^2	Liftoff Distance	300 m
Parasite Drag Coefficient at Zero Lift [1]	0.025	Max Lift Coefficient during takeoff ground roll	0.8
Oswald Efficiency Factor [1]	0.8		

LoRa Network Feasibility

Student Researcher: Justin Verhosek

Advisor: Dr. Brian Krupp

Baldwin Wallace University
Computer Science

Abstract

As the use and application of the Internet of Things (IoT) expands, the search for reliable and efficient communications between devices to provide real-time data to end users continues. Given its open-source and low-cost nature, LoRa, a popular wide-area network, is a favorable choice for providing network coverage to IoT devices. This research paper provides further analysis of the performance of one LoRa board with a spring antenna that was demonstrated to be the best of several boards and antenna combinations in previous research. An analysis is provided using a variety of boards, including a LoRa RFM9X board, a LoRa RP2040 board, and a Raspberry Pi 3 with a LoRa HAT. A variety of antennas are also utilized, including a pigtail antenna, a directly soldered spring antenna, and a simple copper wire antenna, including a dipole antenna. It is hypothesized that the RP2040 with a pigtail antenna will be the best in a network environment. This hypothesis is supported by previous research conducted with these LoRa sensors and will be put to the test in the following paper. This research aims to empower IoT enthusiasts, practitioners, and engineers to make informed decisions about the hardware they utilize, thereby enhancing the overall performance and reliability of LoRa-enabled devices in diverse environments.

Project Objectives

LoRa has been increasingly used as a means of providing connectivity to Internet of Things (IoT) devices all over the world. LoRa, or long-range low-power, belongs to a classification of networks called Low-Power Wide-Area Networks, also known as LPWANS. Unlike other LPWANS, LoRa is gaining popularity due to its open-source, low-cost nature. Since LoRa is open source, the user has the ability to configure and customize the network settings that influence the network performance, data transmission rate, and signal spread. These settings must be considered in distance and interference testing as they could sway the data, measured in RSSI or Received Signal Strength Indication. Reflected in the methodology and expanded upon from previous research, LoRa was pushed to its limit, walking across distances far beyond the reach of Wi-Fi, testing indoors and outdoors, testing with different interference methods, and testing at differing elevations. This paper relays the results of the performance tests, providing a clear answer as to which LoRa setup is more optimal. In this case, the aim was to utilize LoRa to receive real-time data from air quality sensors stationed around the city of Cleveland, Ohio. Given that the sensors exist in an urban environment, it's important that the methodology reflected how LoRa would be deployed in a city, which is why the tests were conducted across campus, where there were buildings, trees, parking lots, walls, and other obstacles that may impact direct line of sight.

Methods

To answer the questions of the expected range of commercial off-the-shelf boards, low-cost antennae, and what affects an expected range of deployed sensors, a series of tests were designed that examined changes in RSSI and packet loss. The tests included an evaluation of four different antennas: spring, pigtail, monopole copper wire, and dipole copper wire. In addition to various antenna options, several different boards as transmitters were tested, which included an Adafruit Feather RP2040 and an Adafruit Feather

M0. The tests shared a common receiver, a Raspberry Pi 3 Model B with an Adafruit Radio Bonnet. The simple spring antenna was soldered directly onto the Feather M0 board. The pigtail antenna used a SMA to IPEX connector connected to the RP2040 board. For the monopole and dipole antennas, a 3.07" piece of copper wire was soldered onto the RP2040 board, and two 3.07" pieces of copper wire were soldered onto the RP2040 board. The Raspberry Pi and Feather RP2040 used CircuitPython, while the Feather M0 used C. Both boards were powered through laptops using a USB to usb-c/micro usb connector. The Raspberry Pi 3 receiver used a single monopole antenna, and the receiver code was written in Python. The transmitter boards continuously send a packet with an integer starting at 0 to indicate the packet that was sent. The receiver consistently listens for a packet and, upon receiving a packet, will send an acknowledgement to the transmitter, where the packet number in the payload will increase by one. The transmitter will wait up to 20 seconds for an acknowledgement from the receiver before attempting to retransmit the packet. Between successful acknowledgements, the transmitter will wait only one second before transmitting the next packet. Modifications were made to the code to print out the RSSI value from the transmitter to the console, where it would then be visible from the laptop the board was connected. To measure the changes in RSSI for each test, 50 packets were transmitted and received, and each RSSI was recorded for each distance. Then the average was taken from the 50 RSSI values and recorded. The initial hypothesis was that the more expensive pigtail antenna would perform better than both the spring antenna and simple copper wire antennas. Three tests with the different antenna types were conducted, with two focused on longer ranges to determine which antenna performs the best over long ranges. The other tested shorter distances and polarities to determine which antenna works most effectively at closer range and with which polarity. The last test was the only one to include all four antennae.

Results and Discussion

After completing the three tests with each board and set of antennas, it was found that the hypothesis was incorrect, and the RFM9X board with the spring antenna outperformed the RP2040 board and pigtail antenna in every test. The results of the first test (Figure 1) rejected the proposed hypothesis, as the RFM9X and spring antenna pair kept a better RSSI value for almost all distances, except for one data point at 310 meters away from the receiver. Interestingly, although the RFM9X and spring antenna outperformed for the majority of the test, the signal dropped completely at a distance of 520 meters. On the other hand, RP2040 and the pigtail pair held the signal for a total distance of 550 meters. The second test (Figure 2) further facilitates the negation of the proposed hypothesis as here, the RFM9X remains steadily above the RP2040 and even lasts a significantly larger distance. This increase in distance contradicts the previous test (Figure 1), where the RP2040 and pigtail antenna pair exceeded the distance of the RFM9X and spring antenna pair. However, in this test, the latter lasted a total of 720m, 200m more than the previous test and 70m more than the total distance the RP2040 pigtail pair had in the same test, which dropped at 530m in this test (20m short of how it performed in the previous test). The third test (Figure 3) also furthers disproves the hypothesis, as even amongst the newly added monopole and dipole antennae, the spring antennae outperform them all decisively.

The above results strongly suggest that the proposed hypothesis is invalid and that the RFM9X spring pair is a better option for LoRa than the RP2040 pigtail pair. It was discovered during the experiments that the pigtail antenna that was used with the RP2040 board was utilizing a connector that was not meant for outdoor use. This specific connector's sole purpose was to attach to the board and the antenna in an enclosed space, as it was not meant to undergo the physical stress that it went through during these tests. If this connector was utilized correctly within such an enclosed space, it is likely that the RP2040 board and pigtail antenna could have outperformed against the RM9X and spring antenna; however, this specific test was attempting to find the ideal board and antenna pair when used alone, and thus the results are

valid for this specific question. Moving forward it will be useful to test how each board and antenna pair do within an appropriate enclosure. Additional tests can also be utilized to see how each board and antenna pair performs with different objects of interference. Whether these interferences are different types of materials or signals, it would be useful to see if different pairs perform better against different means of interference. Along with accounting for different means of interference, it would be useful to see how different settings and configurations of these boards and antennas would affect their performance. This paper addressed vertical and horizontal orientations of the antennae, but more changes can be made to how they are set up and placed in an environment that can help find the best procedure for a given deployment. Lastly, these two combinations of boards and antennae are not the only options for utilizing LoRa, and more research can be conducted to better understand other boards and antennae that may present better alternatives.

Figures/Charts

Figure 1

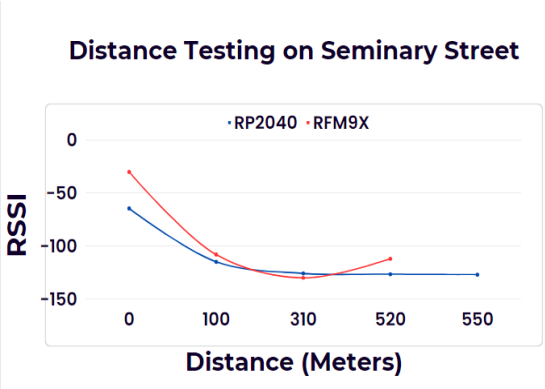


Figure 2

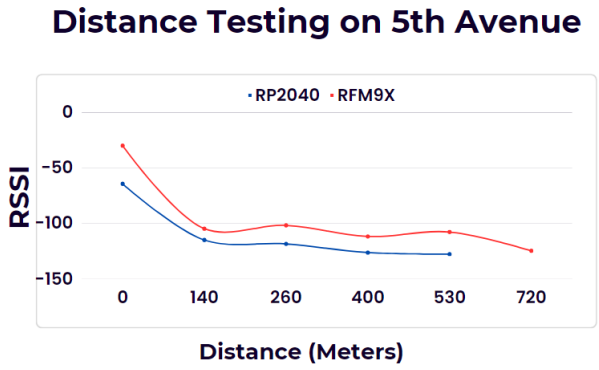
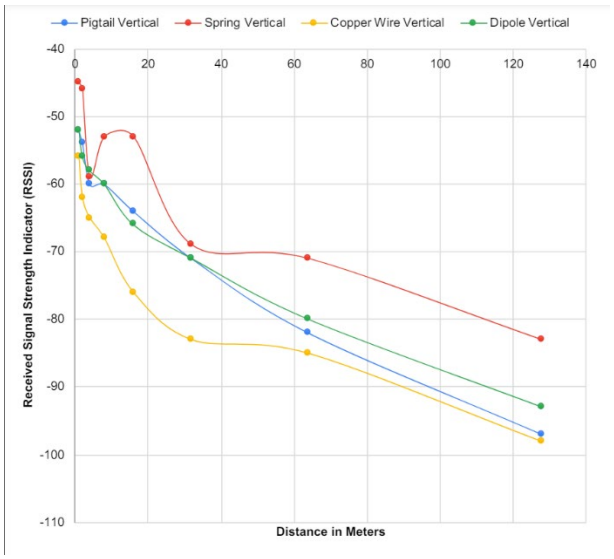
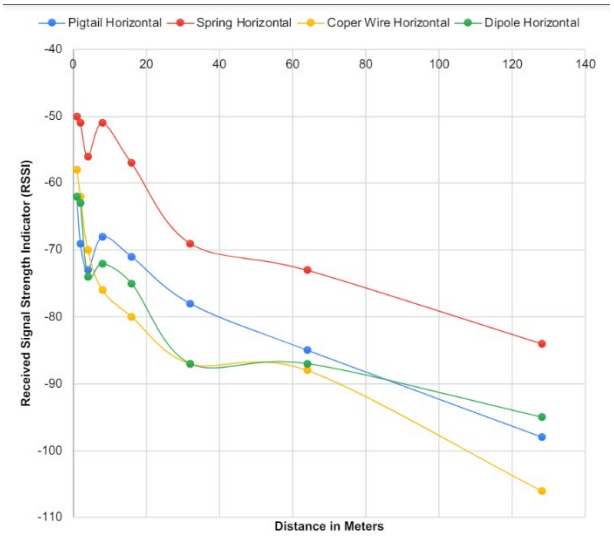


Figure 3





Acknowledgments

This research would not be possible without the funding from the Ohio Space Grant Consortium (OSGC), the help and support from my advisor, Dr. Brian Krupp, and the assistance of Alexandria Macko-Dobrovic, Joshua Buxton, and Dr. David Revta.

Development of a Multiphysics Simulation Model for Laser Welding Applications

Student Researcher: Cory Webber

Advisors: Jeong-Hoi Koo, Carter Hamilton

Miami University
Department of Mechanical and Manufacturing Engineering

Abstract
For manufacturing components for aerospace applications like lithium-ion batteries, joints need to be created with dissimilar metals to obtain lightweight and mechanically-sound structures. However, the chemical and mechanical incompatibilities of dissimilar metals can degrade weld quality through traditional fusion welding methods. Modeling and simulation of laser welding applications using COMSOL applied to 6061 aluminum alloy in lithium-ion batteries is needed to assess the correlations between properties and microstructures of the welds. By first creating a working model simulating the laser energy on the material, future adjustments to the battery casing geometry, laser parameters, and joint orientation can be made depending on the requirements. To optimize the laser parameters for 6061 aluminum alloy, the model must show the transition from the solidus, to liquidus, and back to solidus temperature at the joint surface to show fusion between the two surfaces being welded together. The purpose of this model is to improve the repeatability and quality of manufacturing lithium-ion batteries with the use of laser welding technology.
Keywords: Laser welding, Lithium-ion battery, Laser Power, Spot size, Scanning speed

Introduction
The aerospace industry is needing to manufacture at a much higher rate than in previous years. To achieve this, manufacturers need to optimize their manufacturing processes, and in turn, reduce build time and overall costs. One way this can be done is by implementing laser welding technology. Other fusion welding methods can show a compromise in the material properties due to dissimilar metal welds. Brittle intermetallic compounds form in the fusion zone during welding and compromise the mechanical performance. In the joining of aluminum alloys to magnesium alloys, for example, the formation of the brittle eutectic $Mg_{17}Al_{12}$/α-Mg phase can significantly reduce weld quality [1]. The laser welding method, which can be seen in Figure 1 below, is optimal because it offers precise control over the processing parameters and heat input.

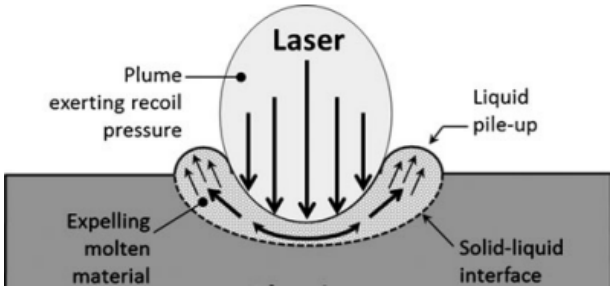


Figure 1:Schematic of laser–material interaction and associated surface [2].

An example of how laser welding can be implemented into future aerospace applications is the aid in the creation of lithium-ion batteries. Proper laser welding parameters are important because if the welding strength is weak, the internal resistance of the battery string will increase causing the power supply to be

affected [3]. Additionally, if the welding temperature is too high, the power supply can be damaged causing an electrolyte leakage, which can result in battery combustion [3]. Background information into the key welding parameters, such as laser output, welding speed, and beam diameter, on weld quality is needed to validate the computational model. First with laser output and welding speed, these parameters go hand in hand. For complete laser penetration, the relationship between laser power and welding speed is important as a lower speed and power will not work for productivity, and a quicker speed with higher power can result in solidification cracking [4]. The microstructure and mechanical properties of the weld can be affected from tendencies for porosity and solidification cracking particularly at high welding speed [4]. This can be combated by cleaning the base metal before welding and post weld aging treatment [4]. Second with beam diameter, this parameter is important in weld penetration. If the weld does not fuse along the entire cross section, it will be prone to cracking and eventual failure. When the spot size is larger, the molten material has a tendency to form a bowl shaped morphology and not fully penetrate the material [5]. When the spot size is smaller, it has a morphology similar to a hole [5]. This means that the molten material stays in a centralized location and is a more focused penetration [5]. In order for the larger spot sizes to not expand while the material is in molten form, the laser power will have to increase which can lead to further issues with mechanical properties and microstructure defects. When the spot size is smaller it provides a wider processing window with better control on penetration depth and laser power [6]. To test these findings, COMSOL, which is a Multiphysics software, will be implemented to create a working model of the laser welding system with the ability to adjust the lithium-ion battery casing geometry, laser parameters, and joint orientation.

This project has two main goals. The first goal is to determine the weld parameters and configurations to maximize the weld quality and develop an initial laser welding setup based on this information. This will help evaluate the impact of various welding parameters, such as laser output, welding speed, and focal position, on weld quality through literature review or experiments. Additionally, this will help analyze the microstructure, mechanical properties, and defects of the weld to derive the optimal welding configuration. The second goal is the preliminary development of numerical simulation of laser welding using COMSOL. By doing this, the development of an initial laser welding simulation model, which is capable of Multiphysics simulations including thermofluid flow during welding, will occur. Finally, the COMSOL model will be used to numerically evaluate the effects of each parameter and determine the conditions necessary to ensure weld quality.

COMSOL Model Setup

A. Material Properties

With the implementation of COMSOL Multiphysics, thermodynamic studies can be run to determine the effects of heat transfer on any selected material. To start the model, the user-defined material properties must be implemented into COMSOL. Properties that must be added are density, dynamic viscosity, specific heat capacity, Poisson's ratio, thermal conductivity, Young's modulus, and coefficient of thermal expansion. As shown in Table 1 and Table 2, the temperature-dependent properties of 6061 aluminum alloy can be seen.

Table 1: Temperature-dependent properties of 6061 aluminum alloy [7].

Temperature (°C)	Density ($kg \cdot m^{-3}$)	Heat Conductivity ($W \cdot m^{-1} \cdot °C^{-1}$)	Specific Heat Capacity ($J \cdot kg^{-1} \cdot °C^{-1}$)	Expansion Coefficient ($10^{-6} \cdot °C^{-1}$)	Elastic Modulus (GPa)	Yield Stress (MPa)
20.0	2700	162	945	23.45	68.54	274.4
93.3	2685	177	978	24.61	66.19	264.6
204.4	2657	192	1028	26.60	59.16	218.6
260.0	2657	201	1052	27.56	53.99	159.7
371.0	2630	217	1104	29.57	40.34	36.84
482.2	2602	226	1136	31.71	20.2	10.49

Table 2: Properties of 6061 aluminum alloy at solidus and liquidus temperatures [8].

Physical properties	Value
Thermal conductivity, k_l ($W\ m^{-1}K^{-1}$)	195
Convective heat transfer coefficient, h_c ($W\ m^{-1}K^{-1}$)	60
Solidus temperature, T_s (K)	873
Liquidus temperature, T_l (K)	915
Boiling temperature, T_b (K)	2790
Viscosity, μ ($kg\ m^{-1}s^{-1}$)	0.0013
Specific heat of the solid phase, C_s ($J\ kg^{-1}K^{-1}$)	930
Specific heat of the liquid phase, C_l ($J\ kg^{-1}K^{-1}$)	1131.8
Surface tension, γ_0 ($N\ m^{-1}$)	0.62
Temperature coefficient of surface tension, K_{sur} ($N\ m^{-1}K^{-1}$)	-2.25×10^{-4}
Solid density, ρ_s ($kg\ m^{-3}$)	2700
Liquid density, ρ_l ($kg\ m^{-3}$)	2650
Latent heat of the vapor, H_v ($J\ kg^{-1}$)	1.07×10^7
Latent heat of fusion, H_{sl} ($J\ kg^{-1}$)	5.03×10^5
Ambient temperature, T_0 (K)	300

By using the built-in piecewise function in COMSOL, the properties seen in Table 1 can be found for any temperature. With the user-defined material created, it can be assigned to any geometry created within the model.

Joint Geometry

Now that 6061 aluminum alloys have been created in the model, the geometry for the joint must be created. One of the important dimensions for the weld is the thickness of the aluminum sheets. A thinner sheet will need precise parameters in order to preserve the microstructure and joining of the materials. By using the established dimensions of 100 x 30 x 0.7 mm, the geometry can be inputted into the model. As seen below in Figure 2, the geometry of the model can be seen. This can be subject to change depending on the casing requirements. To represent the spot size of the laser beam, a cylindrical geometry is added to the surface of the aluminum sheet. The location for the laser beam can be altered, for different welding paths. In order to make the cylindrical representation of the spot size a mark on the surface instead of an extruded cylinder, the difference partition was used while keeping the interior boundaries to have a circular mark as seen in Figure 2 Below.

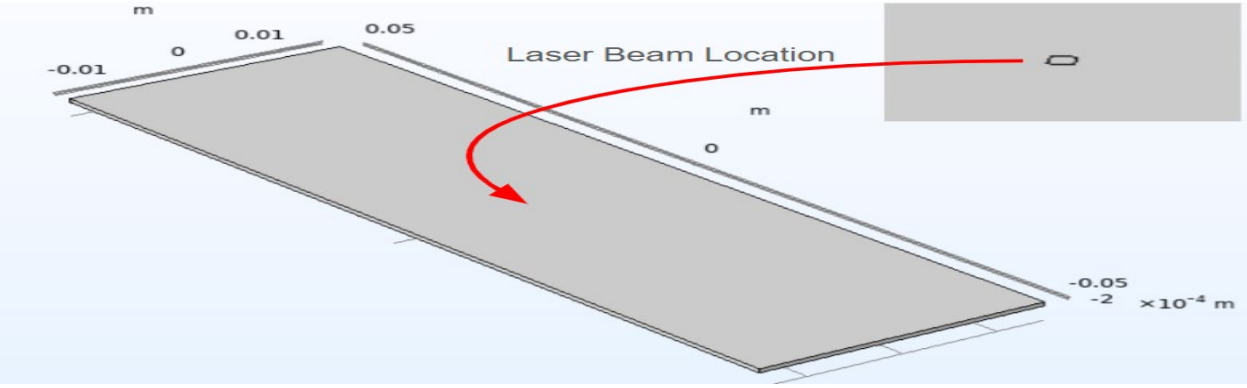


Figure 2: Geometry of the aluminum sheet with the laser beam spot.

In order to have the laser beam travel down the top face, a translational motion must be set to the entire geometry. The speed of the laser beam will be set at the scanning speed of the laser beam, which can be user-defined. By adding this, the laser beam will travel down along the surface instead of being located at a singular point.

Laser Parameters

With the base model created, the laser parameters can be implemented as global variables. This is important as these parameters must first be initialized to be used in the equations governing the creation of the laser beam. These laser parameters are dependent on the manufacturing process and can be changed as needed. Within COMSOL, the creation of the laser beam is done by the heat flux media within the heat transfer in solids physics. In order for the simulation to run smoothly and converge to a solution, a step input was added to cause the laser to start one second into the simulation. The heat flux media requires a power value to be inputted into it. This is done by creating a Gaussian distribution with an average laser density. Below in Equation 1, the expressions for the Gaussian distribution, which will be used in creating the laser beam can be seen.

Equation 1: Laser power density and rectangle function expression [2].

Average laser power density in Gaussian distribution

$$P_g = A\left[\frac{E_p}{P_w\left(\frac{\pi}{4}D^2\right)}\right]\exp\left[-\left(\frac{(x-x_r)^2}{2\phi^2}\right)\right] \text{ (in W/m}^2\text{)}$$

This equation incorporates absorptivity (A), laser power density, and Gaussian distribution. The power density includes the laser power, pulse width (Pw), which for a constant beam is equal to 1, and the area of the spot size. The Gaussian distribution includes the x coordinate with the x reference, and the standard deviation of the Gaussian laser beam, which describes the width or spread of the beam's intensity profile. With all the parameters, functions, and heat flux added, the laser beam will function until a designated stop time. After these components have been added, a study is implemented into the model that will simulate the heat flux across the surface as previously modelled.

Phase Change

An important component of the model is the ability to determine if there was a phase change due to the laser parameters. This is done by adding a phase change Multiphysics within the heat transfer in solids Multiphysics. Important features that must be added to the phase change Multiphysics are the temperature data of the material from the heat flux, and the boundaries for when the phase change will

happen, which are the solidus and liquidus temperatures. In order to have a smooth computation that converges to a solution, a second study is designated only for calculating the phase change. This study uses the temperature data from the first study to determine the phase change throughout the entire geometry. Finally, a cross-sectional view can be created to see the depth of phase change and showcase the fusion along the joint. This is done by adding a parametric surface under the results section and setting the boundaries to the desired cross-section. Below in Figure 3, an example of how COMSOL shows the phase change throughout the cross section can be seen for both when the phase change Multiphysics is and is not used.

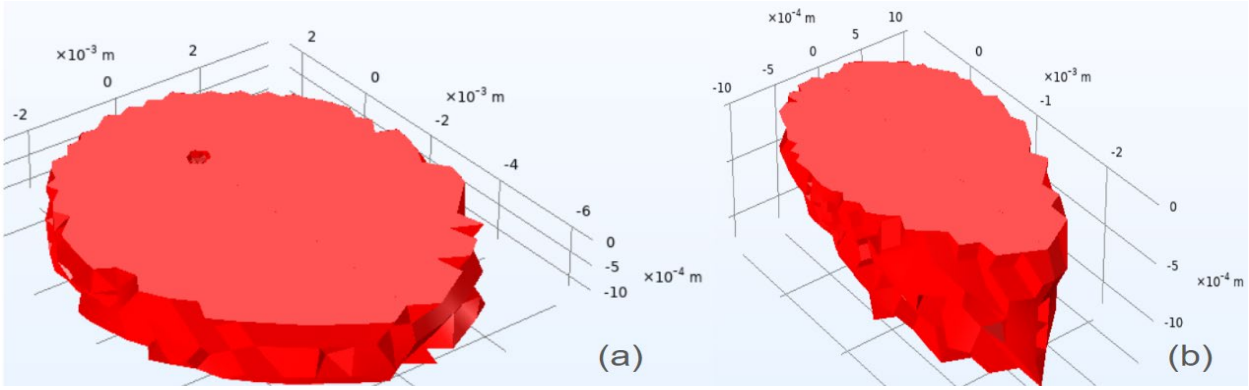


Figure 3: Phase change across the thickness (a) without phase change Multiphysics, (b) with phase change Multiphysics.

This example showcases the benefit of using the phase change Multiphysics. When the phase change Multiphysics is not used, the width of liquidation is 4 mm, and while it is used the width of liquidation is 2 mm. This shows that without the phase change Multiphysics, the simulations overestimates the phase change throughout the cross section, and this is due to it only looking at temperature data at that instant and not the phase change process. Another observation that can be made is when the phase change Multiphysics is used, the depth of liquidation forms a tear-shaped geometry, which matches molten pools seen in physical testing.

Environmental Conditions

To have an accurate model simulating the results of laser welding 6061 aluminum alloy, environmental conditions like natural air convection cooling and radiation must be applied. Similar to how the laser heat flux was added, a heat flux for convection and radiation will need to be added under the heat transfer in solids Multiphysics. Starting with natural convection, this will be caused by ambient air around the sheet metal. With a heat transfer coefficient and ambient temperature seen in Table 3, these can be inputted to the heat flux function and applied to the entire geometry of the model, as air is surrounding the sheet metal. Radiation heat flux is applied to the model in a very similar way as the natural convection was added. The same steps will be taken but with the surface emissivity, which can be seen in Table 3, in place for the convection heat transfer coefficient. The radiation heat flux will be applied to the entire geometry, as radiation is emitted all around the surface.

Simulation Analysis

The objective of the COMSOL simulation described above is to simulate the effects of a laser beam on the surface of a designated material. With a completed model, a numeric simulation can be completed to see the relationship between the material and laser parameters. Important information that can be gathered from the simulation are the joint temperature, phase change, and heat distribution. After running the

simulation, an animation can be generated showing the location and temperature intensity from the laser. Below in Figure 4, the simulated laser beam along the surface can be seen.

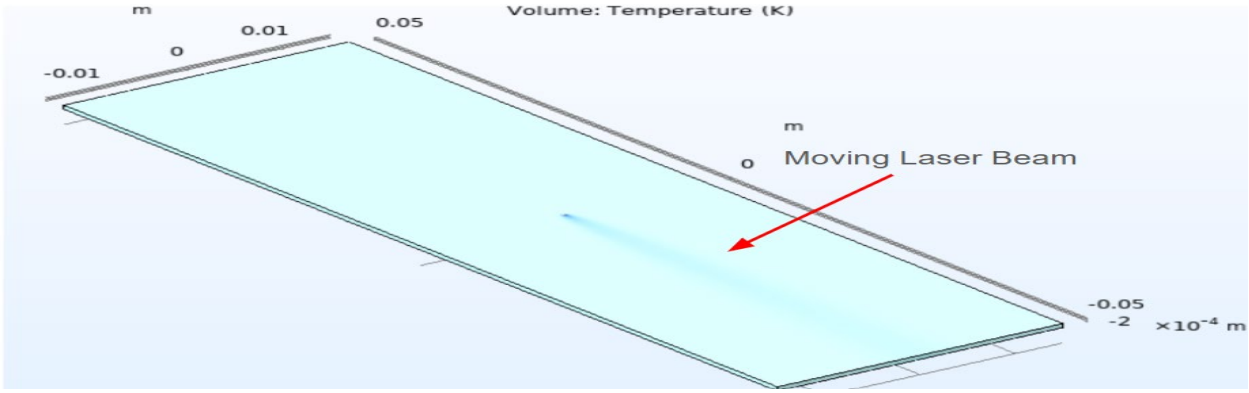


Figure 4: Simulation of the laser beam across a surface.

Model Validation

In order to establish that the model created for this project is valid, an established model was used. Comparing the laser welding model to one using a laser power of 4 KW, spot size of 0.3 mm, and scanning speed of 1.2 m/min, the simulation can be replicated and compared to determine how close the output temperatures are in relation to each model [8]. Below in Figure 5, the maximum temperature over a 160 ms time period can be seen for the established model and the model generated for this project.

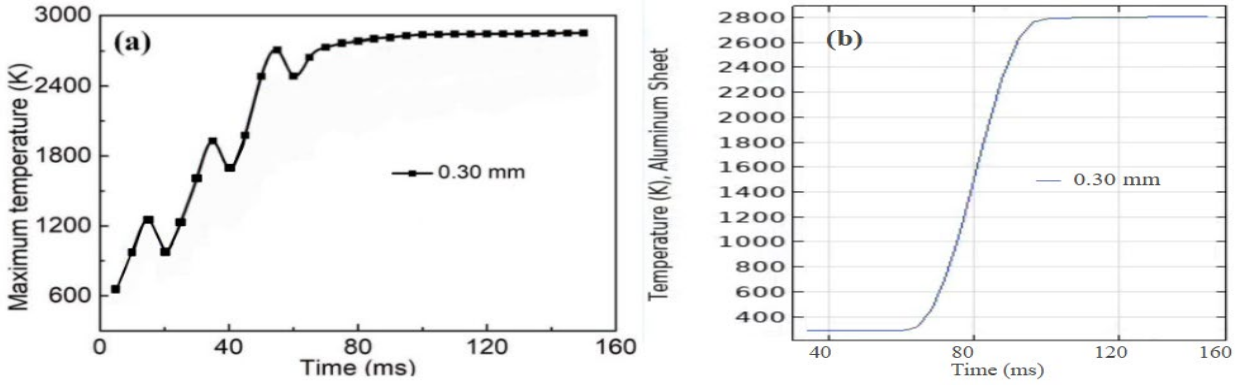


Figure 5: Maximum temperature plot with a laser power of 4 KW, spot size of 0.3 mm, and scanning speed of 1.2 m/min (a) Established Model [8], (b) Project Model.

It can be seen that at steady-state, the maximum temperature reached is roughly 2800 K meaning that the two models reach similar results. This concludes that the model established for this project will calculate accurate results for the specified parameters established for optimized manufacturing.

Summary and Future Work

With a representation of the laser welding method created in COMSOL, the model can be utilized to optimize the manufacturing process for lithium-ion batteries. The model was generated by adding heat fluxes representing the laser, natural convection, and radiation to the geometry. The laser heat flux is translated down the top surface at a set scanning speed. Future consideration can be taken in order to make the model even more adaptable to various laser paths such as oscillating. The model can be adjusted in accordance with the casing geometry and laser parameters to adapt to the changing needs in

manufacturing. The current model has proven to meet the temperature requirements needed for a phase change along the surface. In the future, the simulation will be modified to weld in a two-dimensional motion instead of the current one-dimensional. This will help when the casing geometry is altered in accordance with manufacturing. Additional future considerations that can be taken is to compare the results from the simulation with physical testing data. Currently the model has been compared to other simulated results for validation, but differences can occur between results for simulated and physical data. Finally, additional material types will be added to the model to compare laser welding parameters among the various alloys, which include Al3003-H14, and Al5052-H14, which are commonly used in manufacturing lithium-ion batteries.

References

1. Wang, D., Zhu, Q., Wei, Z., Lin, B., Jing, Y., Shi, Y., Misra, R. D. K., Li, J., Hot deformation behaviors of AZ91 magnesium alloy: constitutive equation, ANN-based prediction, processing map and microstructure evolution, J. Alloys Compd., 908, 2022, p 1 – 17.
2. Vora, H. D., Santhanakrishnan, S., Harimkar, S. P., Boetcher, S. K., & Dahotre, N. B. (2013). One-dimensional multipulse laser machining of structural alumina: Evolution of surface topography. The International Journal of Advanced Manufacturing Technology, 68(1–4), 69–83. https://doi.org/10.1007/s00170-012-4709-8.
3. Feng, J.; Zhang, P.; Yan, H.; Shi, H.; Lu, Q.; Liu, Z.; Wu, D.; Sun, T.; Li, R.; Wang, Q. Application of Laser Welding in Electric Vehicle Battery Manufacturing: A Review. Coatings 2023, 13, 1313. https:// doi.org/10.3390/coatings13081313.
4. El-Batahgy, A., Kutsuna, M., Laser Beam Welding of AA5052, AA5083, and AA6061 Aluminum Alloys, Advances in Materials Science and Engineering, 2009, 974182, 9 pages, 2009. https://doi.org/10.1155/2009/974182.
5. Yuan, B.-S., Zhang, Y., Zhang, W., Dong, Y., & Jin, G.-Y. (2018). The Effect of Spot Size Combination Mode on Ablation Morphology of Aluminum Alloy by Millisecond-Nanosecond Combined-Pulse Laser. Materials, 11(8), 1419. https://doi.org /10.3390/ma11081419.
6. Vincenzo Dimatteo, Alessandro Ascari, Erica Liverani, Alessandro Fortunato, Experimental investigation on the effect of spot diameter on continuous-wave laser welding of copper and aluminum thin sheets for battery manufacturing, Optics & Laser Technology, Volume 145, 2022, 107495, ISSN 0030-3992, https://doi.org/10.1016 /j.optlastec.2021.107495.
7. Rong, Y., Huang, Y., & Wang, L. (2021). Evolution Mechanism of Transient Strain and Residual Stress Distribution in Al 6061 Laser Welding. Crystals, 11(2), 205. https://doi.org/10.3390/cryst11020205.
8. Yang Lu, Yuchun Deng, Lin Shi, Laihege Jiang, Ming Gao. Numerical simulation of thermal flow dynamics in oscillating laser welding of aluminum alloy, Optics & Laser Technology, Volume 159, 2023, 109003, ISSN 0030-3992, https://doi.org/10.1016/j.optlastec.2022.109003.

CubeSat Missions for GNSS Research

Student Researcher: Isaac Whipkey

Advisor: Dr. Sabrina Ugazio

Ohio University
School of EECS/Electrical Engineering

Abstract
The Ohio University Avionics Engineering Center (AEC) is collaborating with the Libre Space Foundation (LSF) on the PHASMA mission. PHASMA, a spectrum monitoring and space-based situational awareness mission [1], from the Libre Space Foundation, includes two 2U CubeSats (CAD models are shown in Figures 1-3), currently under development by LSF in Athens, Greece, and is scheduled for launch in 2025 (Q4). The satellite will enter a 600 km sun-synchronous orbit (SSO), with lifetime expectancy 12-15 years after deployment. While PHASMA's primary mission centers on spectrum monitoring and transmitter localization supported by machine learning techniques, Ohio University's contribution will focus on a secondary objective, that serves as a follow-on to the Ohio University Bobcat-1 mission. The focus is on Global Navigation Satellite System (GNSS) research, including inter-constellation bias estimation and spectrum monitoring.

Project
Ohio University's mission within PHASMA builds on experimental work from the Bobcat-1 mission. The objectives include, like in Bobcat-1 [2] :

- Estimating GNSS inter-system time offsets
- Monitoring GNSS spectrum
- Outreach

Additionally, PHASMA GNSS-experiment will implement extra features enabling further analysis:

- Long-term data collections
- IQ samples data collection

Methods
The GNSS-mission carried out by Ohio University within the PHASMA project involves different phases, including:

- sub-system design and development, to support the GNSS data collections, including measurements from the receivers as well as IQ samples of the incoming RF signals
- calibration and testing of the GNSS receiver in different environmental conditions (in particular, temperature)
- design, development and testing of a ground station at Ohio University
- data collection (in space)
- algorithm development, building on the work done for the Bobcat-1 mission
- data analysis

During my work in the past months, the focus was on system development, as well on the definition of the calibration procedure.

The GNSS experiment runs on the "GNSS processor," a Linux-based ARM Cortex-A9 processor on the SatNOGS-COMMS v0.4 board. The IQ samples are sent via the SPRINKLER system, which is transferred at 100 Mbits/s with a direct Ethernet link. Figure 4 and Figure 5 show, respectively, the block diagram of the

system supporting the GNSS experiment and the selected multi-GNSS/multi-frequency receiver used in the mission, a NovAtel OEM7770.

Results and Discussion

To enable GNSS data collection, I developed a UART driver and implemented a circular buffer to handle incoming data. I also designed and tested code to parse NovAtel messages from the data stream and verify their integrity using cyclic redundancy checks (CRC). Additionally, I contributed to the design of the temperature calibration procedure to properly calibrate the GNSS receiver.

The next steps in the project are to build the ground station and implement an Ethernet driver to support higher data rates necessary for the collection of IQ samples.

Figures

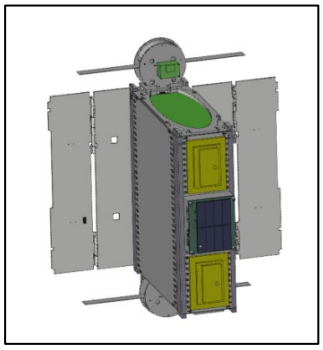


Figure 1: A model of the PHASMA CubeSat.

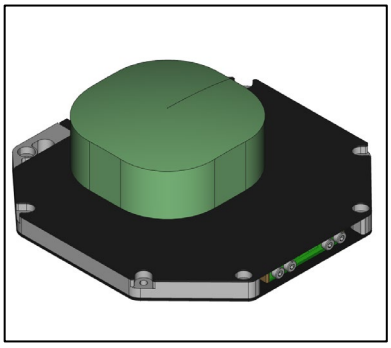


Figure 2: PHASMA GNSS antenna deployer mechanism stowed.

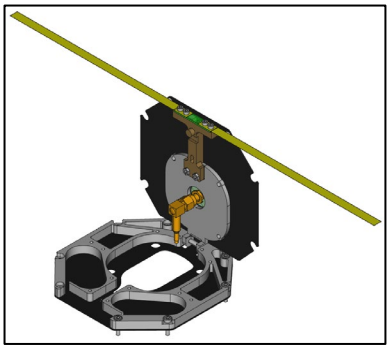


Figure 3: PHASMA GNSS antenna deployer mechanism deployed.

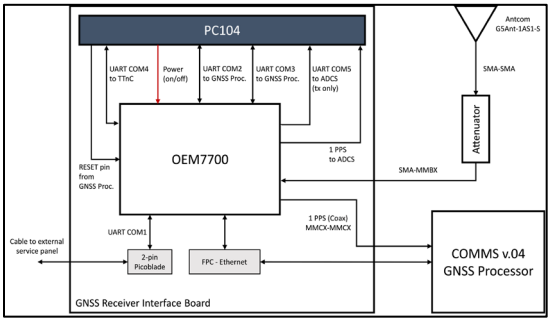


Figure 4: GNSS experiment board layout.

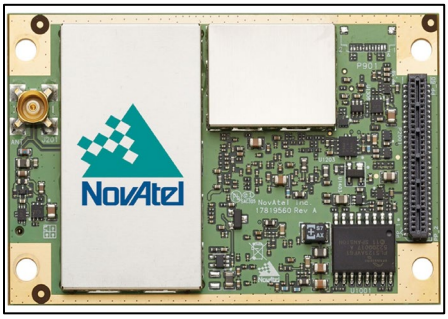


Figure 5: NovAtel OEM7770 GNSS receiver board.

Acknowledgments

The author would like to thank OSGC, Dr. Mike DiBenedetto (AEC) and Dr. Sabrina Ugazio for their support, and Brian C. Peters and Ryan McKnight for their technical guidance.

References

[1] https://libre.space/projects/phasma/

[2] Croissant, Kevin, Jenkins, Gregory, McKnight, Ryan, Peters, Brian C., Ugazio, Sabrina, van Graas, Frank, "Design and mission planning of Bobcat-1, the Ohio University CubeSat," *Proceedings of the 33rd International Technical Meeting of the Satellite Division of The Institute of Navigation (ION GNSS+ 2020)*, September 2020, pp. 1383-1393.

Implications for Martian Ocean Chemistry on Potential Hydrothermal Mineral Deposits

Student Researcher: Leo Wible

Advisor: Dr. Joseph Ortiz and Dr. Jeffrey Balcerski

Kent State University
Department of Earth Sciences

Abstract

If Mars ever had long-lasting oceans, what would its ocean chemistry have been like, and how would it affect hydrothermal deposits? While prior analysis of spectral data of the Martian surface have suggested the presence of hydrothermal deposits [1], this study investigates the potential oceanic chemistry of hypothesized large, long duration bodies of water on Mars's surface. Using data from Martian spacecraft and comparisons to Earth's early oceans, simulations of Martian ocean chemistry were used to simulate hydrothermal vent conditions found in early Martian oceans. A range of possible precipitating products from a notional Martian hydrothermal, "black smoker"-style vent, was modeled using a commercial aqueous geochemistry code, the Geochemist's Workbench 2023. These simulations were used to explore the mineralogy of potential deposits under possible Martian conditions, with a focus on carbonates, sulfides, and silicates that could form in early Martian oceans.

Project Objectives

There are two phases to this research project. The first phase was to model and predict what sorts of carbonates, sulfides, and silicates could have formed at a Martian hydrothermal vent system in the Eridania Basin. This was achieved using information gathered from previous studies and the aqueous geochemistry code the Geochemist's Workbench. This phase of the project has already been completed, and the findings of this phase will be discussed in the methods section. The second phase of this study is to use CRISM, HiRISE, and CTX data of the Eridania Basin that was taken by the Mars Reconnaissance Orbiter to find predicted minerals from the first phase of the study. As of the writing of this report, all necessary data has been gathered and is currently being processed. It is planned to use a modified VPCA code to identify predicted minerals in the CRISM data before comparing the results with previous studies.

Methods

For this study, published information on ancient conditions of hypothetical Martian oceanic conditions was used to investigate what kinds of carbonates, sulfides, and silicates had the potential to form. Using data gathered from various sources [4] [5] [1] [6] [7] [8] [9] [10], a range of dissolved species found in Earth's early oceans was constructed. By putting this information into SPECE8 and TACT in the community version of the Geochemist's Workbench 2023, multiple lists of potential equilibrium mineral products were generated. SPECE8 is a program that calculates the equilibrium distribution of dissolved elements in an aqueous fluids [11], while TACT can be used to plot data on temperature against pH or activity of a certain aqueous element or compound [11]. Nine different elements, including reduced (+2) iron, calcium, potassium, sodium, chlorine, magnesium, manganese, aluminum, and copper were used in conjunction with dissolved elemental sulfur (S^{-2}), carbonate, and aqueous silica (SiO_2) for testing. Starting concentrations for each element were selected from a variety of studies [4] [5] [6] [7] [8], and the maximum and minimum concentrations of each element were used. The selected values were run through SPECE8 to convert them to activity percent, which TACT needs to work. These elements were run in TACT under 50 bars of pressure [1], a temperature range of 100 to 300 degrees Celsius, and a pH range of 6.6 to 3.4 [3] [4].

Results and Discussion

From the lists of minerals generated, it was found that some results matched the findings of earlier studies. For instance, the Geochemist's Workbench predicted the presence of phyllosilicates like saponite and talc. These predictions align with analyzed CRISM data, which show these minerals exist in the Eridania Basin [1]. Moreover, predicted carbonates like siderite, rhodochrosite, and dolomite correspond with absorption spectra seen from possible, hydrothermally sourced magnesium, iron, calcium, and manganese-based carbonates exposed in an impact crater [1]. However, not all minerals generated in the Geochemist's Workbench have been detected in potential Martian hydrothermal deposits. While certain minerals, like quartz, are already rare on Mars [12], nesosilicates like andalusite, kyanite, sillimanite, and grossular, despite appearing consistently in results, were not reported in earlier studies. In addition, sulfides have proven difficult to detect using traditional infrared remote sensing [1], making it hard to compare previous findings with the results of this study. The next step in this study is to observe physical structures, such as mineral veins, generated by potential hydrothermal activity on Mars's surface. By using a visual light-based remote sensing technique and spectral patterns from the USGS's spectral library, evidence of predicted minerals might be found. It is hoped that future findings will help to expand the understanding of mineral formation, hydrothermal activity, and ocean chemistry of worlds beyond Earth.

Acknowledgments

The author would like to acknowledge the Ohio Space Grant Consortium for providing funding for this study.

References

[1] Michalski, J. R., Dobrea, E. Z., Niles, P. B., & Cuadros, J. (2017). Ancient hydrothermal seafloor deposits in Eridania Basin on Mars. *Nature Communications*, *8*(1). https://doi.org/10.1038/ncomms15978

[2] Lin, H., Lin, Y., Wei, Y. *et al.* Mineralogical evidence of water activity in the northern lowlands of Mars based on inflight-calibrated spectra from the Zhurong rover. *Sci. China Earth Sci.* 66, 2463–2472 (2023). https://doi.org/10.1007/s11430-023-1194-4

[3] Rollinson, H. R. (2007). *Early earth systems: A geochemical approach*. Blackwell Publishing.

[4] Ueda, H., Shibuya, T., Sawaki, Y., Shozugawa, K., Makabe, A., & Takai, K. (2021). Chemical nature of hydrothermal fluids generated by serpentinization and carbonation of komatiite: Implications for H2-rich hydrothermal system and Ocean Chemistry in the early Earth. *Geochemistry, Geophysics, Geosystems*, *22*(12).

[5] Govind, A. V., Behera, K., Dash, J. K., Balakrishnan, S., Bhutani, R., Managave, S., & Srinivasan, R. (2021b). *Trace Element and Isotope Geochemistry of Neoarchean Carbonate Rocks from the Dharwar Craton, Southern India: Implications for Depositional Environments and Mantle Influence on Ocean Chemistry*. https://doi.org/https://doi.org/10.1016/j.precamres.2021.106137

[6] Manisonneuve, J. (1981). THE COMPOSITION OF THE PRECAMBRIAN OCEAN WATERS. *Sedimentary Geology - Elsevmr Scientific Publishing Company*.

[7] Costello, L. J., Filiberto, J., Crandall, J. R., Potter-McIntyre, S. L., Schwenzer, S. P., Miller, M. A., Hummer, D. R., Olsson-Francis, K., & Perl, S. (2020). Habitability of hydrothermal systems at Jezero and gusev craters as constrained by hydrothermal alteration of a terrestrial mafic dike. *Geochemistry*, *80*(2), 125613.

[8] Burns, R. G. (1993). é *Gmckimica et Cosmochimica Ado*, *57*, 4555–4574.

[9] Morris, R. V., Rampe, E. B., Vaniman, D. T., Christoffersen, R., Yen, A. S., Morrison, S. M., Ming, D. W., Achilles, C. N., Fraeman, A. A., Le, L., Tu, V. M., Ott, J. P., Treiman, A. H., Hogancamp, J. V., Graff, T. G., Adams, M., Hamilton, J. C., Mertzman, S. A., Bristow, T. F., … Thorpe, M. (2020). Hydrothermal precipitation of Sanidine (Adularia) having full al,si structural disorder and specular hematite at Maunakea Volcano (hawai'i) and at Gale Crater (Mars). *Journal of Geophysical Research: Planets*, *125*(9).

[10] Fairén, A. G., Fernández-Remolar, D., Dohm, J. M., Baker, V. R., & Amils, R. (2004). Inhibition of carbonate synthesis in acidic oceans on early Mars. *Nature*, *431*(7007), 423–426. https://doi.org/10.1038/nature02911

[11] Bethke, C. M., Farrell, B., & Sharifi, M. (2024, March 26). GWB Essentials Guide . Champaign, Illinois ; Aqueous Solutions, LLC.

[12] Crumpler, L. S. (2021). *Missions to Mars: A new era of rover and Spacecraft Discovery on the Red Planet*. Harper Design, an imprint of HarperCollinsPublishers.

Integration of Thermoelectric Generators within Aerospace Powerplants

Student Researcher: Brady Wilson

Advisor: Dr. Randall Mathison

Ohio State University
Aerospace Engineering

Abstract
The optimization of aircraft engines represents a variety of challenges and is an ongoing effort for all major aerospace companies. Integration of thermoelectric generators (TEG's) can assist in increasing the thermal efficiency of an aircraft engine by offering a passive system that converts heat energy to electricity. By installing TEG's onboard exhaust systems of piston driven engines for general aviation (GA) aircraft, this will serve as a proving ground for the effectiveness of these energy conversion devices. In this contribution, a study was conducted in three phases that evaluates the modeling and testing procedures for TEG modules including the use of the Ansys Thermal Electric Toolbox, MATLAB analytic solver, and intensive experimentation. Phase one consisted of basic modeling and hot-plate testing of TEG modules made from Bismuth-Telluride. Phase two will take the lessons learned from phase one and integrate the modules onto a propane-air combustion burner that will help simulate flight conditions onboard an aircraft exhaust system. Finally, phase three will involve a static and flight test of the integrated TEG's onboard an ultralight aircraft and will serve as a proving ground for the power gained from the system compared to the weight penalty. The work shown here will primarily focus on the first phase of the entire study, while also exploring preliminary work for phase two.

Project Objectives:
Increasing the thermal efficiency of aircraft engines has been an ongoing challenge since the advent of aviation engines in the early 1900's. Thermal efficiency for a piston driven aircraft is defined as how well the engine converts the heat energy available in the fuel to the power input toward driving the engine cylinders. Of the total heat produced from the fuel, 40 to 45 percent of this is lost through the exhaust system (Federal Aviation Administration). Various methods have been considered to recuperate this wasted heat, most of which consist of complex hardware components that result in excessive weight and volume penalties which negate any potential gains (Buchter, Et al. 2018). Thermoelectric generators offer a relatively simple and completely passive system that can be installed on the exhaust system where the majority of the heat energy is being lost to.
A thermoelectric generator (TEG) is a passive device that converts heat energy into electricity through the Seebeck effect. The Seebeck effect is a phenomenon where a maintained temperature difference between two junctions connected in series will induce a current.

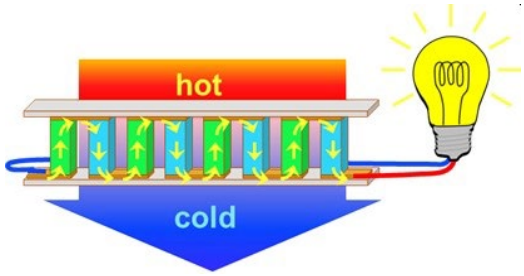


Figure 1: Current created by a maintained temperature differential across the TEG surfaces.

By integrating an energy storage unit to this circuit or simply wiring the TEG directly to an energy consuming device, power can be harnessed from the heat induced current. Research into these passive devices onboard automobile exhaust systems has resulted in promising power gains that may eventually offset the weight penalty through further experimentation (Orr, Et al. 2016). Unlike the automobile application, a TEG system installed onboard an aircraft must strongly consider any weight and volume penalties obtained. This contribution is broken into three distinct phases that are used to validate the TEG system design. The first phase consists of basic modeling and testing of these devices to gain general familiarity on their operation. Phase two will focus on creating a TEG system that can be installed onboard a cylindrical pipe that is mounted to a propane-air combustion burner. The combustion burner will assist in simulating the exhaust pipe environment seen onboard a piston drive aircraft engine. Finally, phase three will be static testing and eventual flight testing of the TEG rig onboard an ultralight aircraft. For the Ohio Space Grant Consortium, phase one and phase two will be primarily explored.

Methods

There are three methods that were used in validate the TEG system design: computational solver, analytic solver, and experimentation. Both the computational and analytic solvers will be utilized to verify what variables need to be adjusted to optimize the power output from the module and their results will be cross checked with experimental data. In combining these various methods, a TEG system that can eventually be used onboard an aircraft exhaust system can be validated.

Regarding the computational model, the Ansys Thermal-Electric Toolbox was used to simulate the power output of a TEG module under specified conditions. Unlike the steady state or transient analysis tools from Ansys, the Thermal-Electric software integrates electrical variables into the thermal system and is meant to analyze thermoelectric systems. For phase one modeling, the commercially available SP1848-27145 module was evaluated.

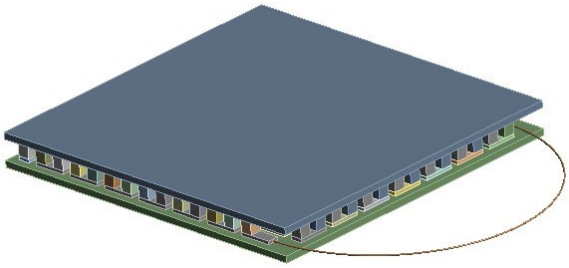


Figure 2: SP1848-27145 TEG module created through Ansys Spaceclaim. Note the load wire protruding from the module which is used to gather crucial data such as power output.

The module shown in figure 2 was created based on data provided by the SP1848-27145 manufacturer. This TEG consists of Bismuth-Telluride (BiTe), which is a widely used material combination for lower temperature capable, commercially available devices. Once the module geometry was created, a hot and cold temperature load was applied to the top and bottom surface of the module respectively. Along with the temperature load, a wire resistivity was defined which would later be used to calculate the power output.

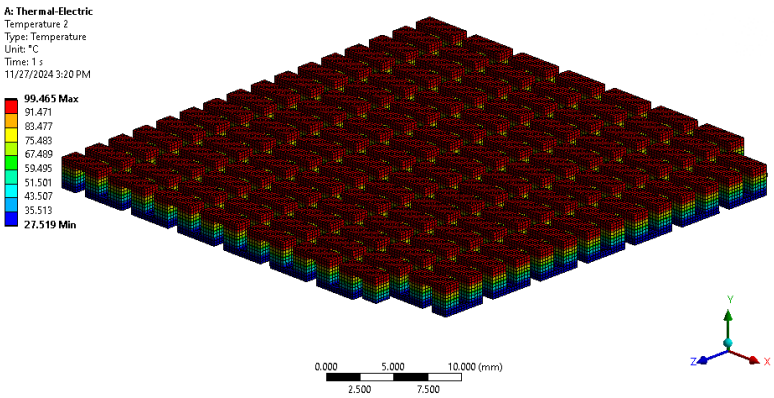


Figure 3: Example simulation showing the steady state temperature distribution of the internal junctions in the SP1848-27145 module. Note the hot side remaining on the upper junction, while the lower portion remains relatively cool.

It should be stated that the wire resistivity was defined as 4.8 ohms as this closely matched the internal resistance of the TEG module. To obtain optimal power output, the load resistance should equal the internal resistance of the device being used. The internal resistance of the SP1848-27145 is a published value and was verified through extensive testing with varying load resistors. There are a variety of outputs that can be evaluated through this software including voltage, power, current, efficiency, etc... However, the output that will be primarily explored in this contribution will be the power output as this will be the defining parameter that justifies the overall TEG system.
An analytic model through MATLAB was also used to assist in verifying the design. This model factored in published values for the SP1848-27145 TEG which include open circuit voltage as a function of temperature difference.

Table 1: Published values for the SP1848-27145 TEG. Note that the voltages are open circuit and are not the load voltage readings.

Temp Difference (C)	Open Circuit Voltage (V)
20	0.97
40	1.8
60	2.4
80	3.6
100	4.8

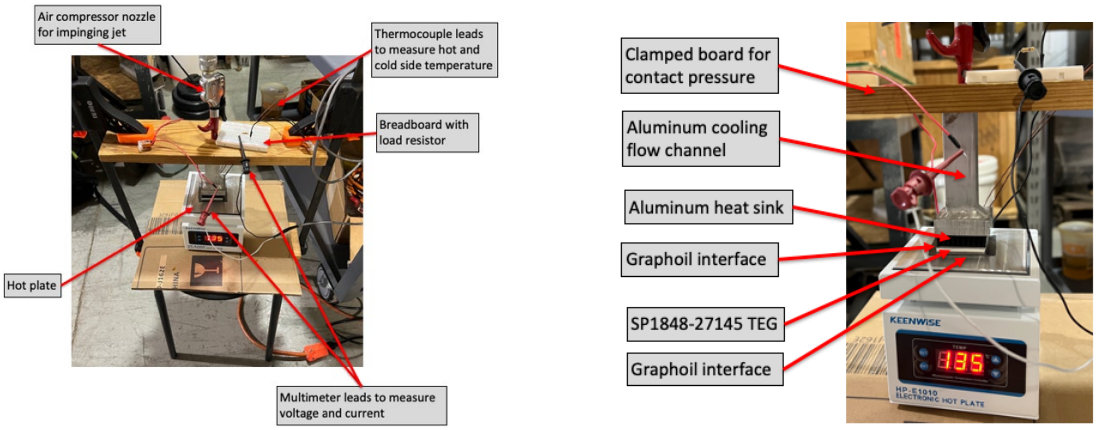
With the values shown in table 1 and a defined load and internal resistance, multiple parameters such as load voltage, Seebeck coefficient, power, current, figure of merit, and efficiency, were calculated based on known equations for thermoelectric devices (Lau, Et al. 1997). While all the outputted variables will be used for validating the overall TEG system, this study will focus on the power output.

$$Power: P = \frac{(V_{OC} * N)^2 * R_L}{(R_I * N + R_L)^2}$$

Where:
$N = Number\ of\ TEG\ modules$

$$R_L = Load\ Resistance$$
$$R_I = Internal\ Resistance$$
$$V_{OC} = Open\ Cicuit\ Voltage$$

Experimentation for phase one consisted of hot plate testing of the SP1848-27145 module along with the Hi-2 module. These evaluations were conducted to gain familiarity of the TEG devices and to establish what variables must be controlled to optimize power output. 27 separate hot plate tests were conducted on the modules, each of which provided valuable insight on what makes an efficient TEG system.



(a) *(b)*

Figure 4: Entire testing setup (a) with the TEG placed on top of hot plate (b).

It was found through testing and research that maintaining a temperature differential across the module and having ample contact pressure were crucial variables to control when wanting to optimize the power output (Cosher, Et al. 2013). The graphoil above and below the TEG provides uniform planar heat distribution to the module surface. As stated before, this test was also run with the Hi-Z 2 module as it was able to withstand a higher temperature from the hot plate compared to the SP1848-27145 TEG. The Hi-Z 2 module was not originally tested as this hardware was more expensive compared to the SP1848-27145.

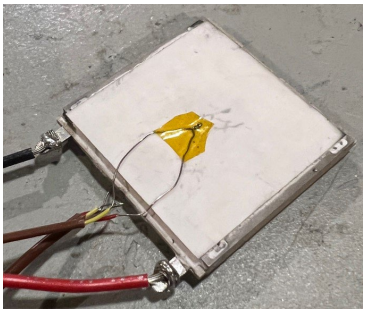


Figure 5: Hi-Z 2 TEG module with type K thermocouple wires taped to the surface to obtain temperature readings.

Phase 1 Results:

The power output data obtained through modeling and experimentation of the SP1848-27145 were compared and there was slight convergence between the results.

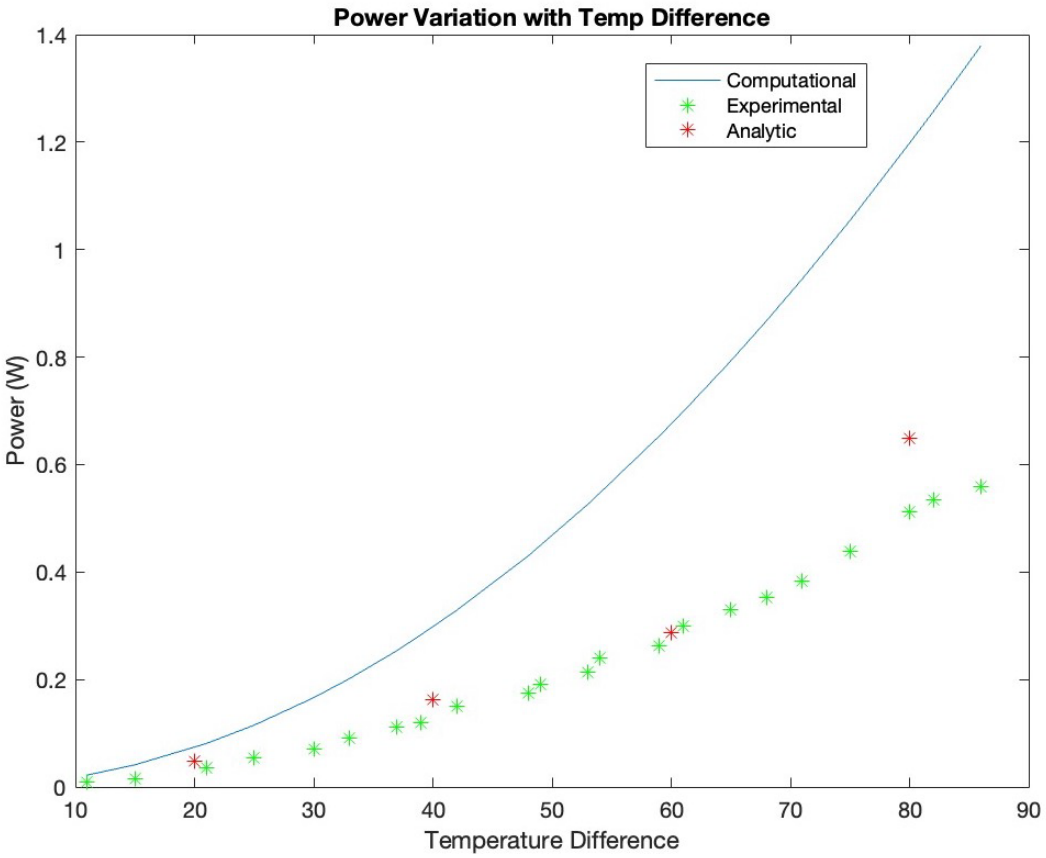
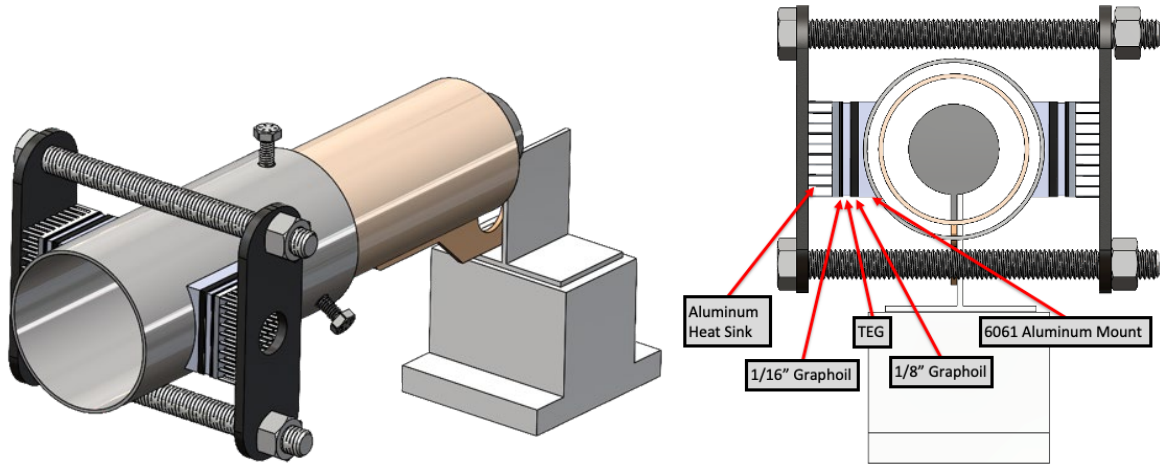


Figure 6: SP1848-27145 data comparison for modeling and experimental methods.

The data obtained analytically through MATLAB converged to the experimental results, with a slight error being seen at the higher temperature difference range. When evaluating the computational data, there is a higher output power over the entire range as this is the idealized model that does not consider any losses in the overall system. These results suggest general accuracy among each data acquisition method and will be taken into consideration when moving on to phase 2.

Phase 2 and Future Work

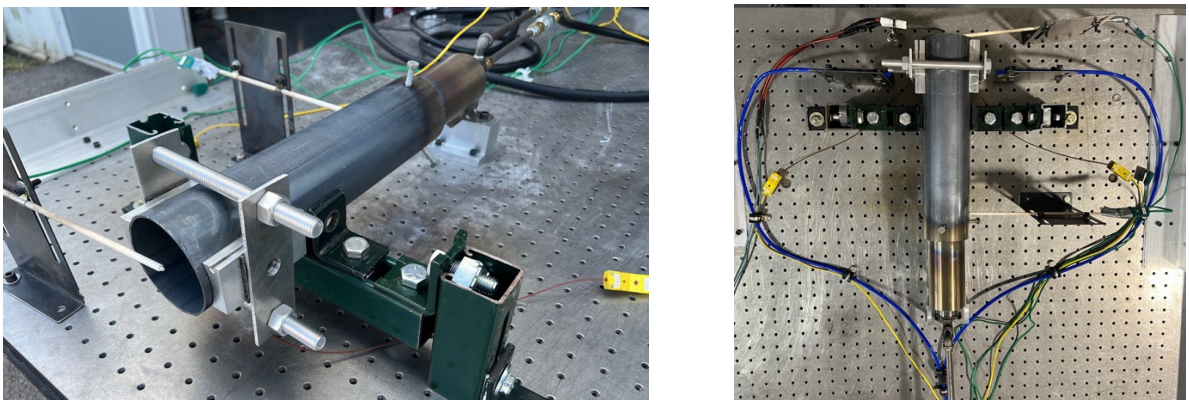
With the data and observations taken from phase 1, a TEG rig was created and mounted to a propane-air combustion burner to simulate the flight environment onboard an aircraft exhaust system. This setup utilized the clamped method for contact pressure, along with the compressed air cooling system to maintain a temperature difference across the module.



(a) *(b)*

Figure 7: CAD model of combustion burner rig isometric view (a) and front view (b).

As the clamped TEG rig will be attached to the surface of a heated steel pipe, temperature readings were taken to ensure the aluminum hardware would not melt. Ansys modeling and experimental testing showed the steel pipe surfacing being well below the 585 Celsius melting point of 6061 aluminum.



(a) *(b)*

Figure 8: Propane-Air combustion burner experimental setup. Note the blue hoses in (b) for compressed air cooling directed toward the TEG cold side surfaces.

Further 1-D heat transfer models are actively being conducted through both Ansys Transient Thermal software and MATLAB to estimate the temperatures that the TEG modules will experience. Variables such as the convective heat transfer coefficient both inside the pipe and the external ambient conditions will certainly play an important role in maintaining temperature differentials across the TEG surfaces. Another variable that will be evaluated is the thickness of aluminum interface used to mount the flat TEG module to the curved steel pipe surface. Once these variables are better understood and controlled in the combustion burner environment, a validated TEG system can then be integrated onboard an ultralight aircraft engine exhaust system.

Acknowledgements

Financial support from the Ohio Space Grant Consortium is gratefully acknowledged for funding the thermoelectric generator project. Special thanks are given to associate professor Dr. Randall Mathison who is actively serving as a research advisor to this work, along with Technology Development and

Commercialization Manager, Dr. Chris Whiting. Dr. Whiting is employed at NASA and specializes in thermoelectric systems. Support from the Ohio State University, Aerospace Research Center is also gratefully acknowledged for allowing use of their lab space and equipment.

References

U.S. Department of Transportation, Federal Aviation Administration, Aviation Maintenance Technician Handbook. Washington, DC. 2024.

Büchter, Kai-Daniel, et al. "Estimation of mission fuel savings potential using thermoelectric recuperation in aero-engines." *Transportation Research Procedia*, vol. 29, 2018, pp. 23–33.

Orr, B., et al. "An exhaust heat recovery system utilising thermoelectric generators and heat pipes." *Applied Thermal Engineering*, vol. 126, Nov. 2017, pp. 1185–1190.

Lau, P.G., and R.J. Buist. "Calculation of thermoelectric power generation performance using finite element analysis." *XVI ICT '97. Proceedings ICT'97. 16th International Conference on Thermoelectrics (Cat. No.97TH8291)*, 1997, pp. 563–566.

Cosher, Christopher, et al. *Power Take-Off for JetCat P-80SE Engine*, 2013.

Towards a More Thorough Understanding of Banded Iron Formations

Student Researcher: Johanna Wood

Advisor: Dr. John Whitmore

Cedarville University
School of Science and Math/Geology

Abstract
Banded iron formations (BIFs) are anomalous sedimentary and metamorphic rocks composed primarily of iron oxide minerals such as hematite, magnetite, and grunerite layered with silicate cherts. Often found among the oldest rocks on earth, similar iron oxides have also been recently discovered on Mars. Given that numerous recent studies are favoring microbial over chemical precipitation as a more viable formation mechanism for BIFs, these rocks contain significant implications for life origins. To determine whether chemical, microbial, or other processes are most likely to have formed the terrestrial BIFs, this project will seek to build an Excel spreadsheet of typical BIF characteristics as displayed around the world.

A dramatic shift in depositional style occurs across the Archean-Proterozoic time period, so it is important to compare criteria between these two general BIF types. However, to avoid overgeneralization of data, individual basins both stratigraphically near and far from each other were also compared. Criteria considered included chemistry, mineral texture, deposit thickness, microfossil concentration, conventionally interpreted depositional setting, and association with other mineralogically unique strata. Since the continents would have been arranged differently during the Archean and Proterozoic than they are today, possible BIF correlations across basins were accounted for to avoid double-counting formations. Upon accumulation of data, it is hypothesized that the observed qualitative trends may offer a more robust interpretation of biological and chemical signatures in the rocks. As researchers continue to study Martian iron oxides, these trends may prove useful for determining their similarities or differences from terrestrial BIFs. Future goals for this research project include developing a public BIF database and performing further chemical reactions in appropriate formation conditions to encourage more detailed comparative studies.

Project Objectives
The goal of this project is to create a set of criteria characterizing Superior-type BIFs. With this criteria list, the possible relationships between the BIFs and Martian oxides may become more apparent.

Methods
A list of 180 BIFs were compiled from geographical locations around the world. Databases such as GeoRef, Porter Geo, and Science Direct were referenced to perform a literature review to gather data regarding each BIF's thickness, iron weight percent, depositional environment, organic content, and prevalent facies. Quantitative datasets included thickness and iron weight percent, whereas depositional environment, the presence or absence of organic content, and facies types were qualitative. Only the 77 BIFs with data for all 5 criteria were included in the analysis. Their datasets were organized and analyzed in Excel, with boxplots, confidence intervals, and stacked bar plots proving the most useful for revealing relationships among data.

Results and Discussion

Out of over 180 BIFs sampled, only 77 yielded data for each category. Due to data collection taking much longer than anticipated, only thickness and organic content data were further analyzed for these BIFs. Superior type-BIFs had an average thickness of 238.9 m, Algoma-type BIFs of about 178.2 m, and Rapitan-type BIFs of about 211.6 m. These values are largely consistent with reported literature trends, with Superior-type BIFs found to be consistently thicker than Algoma-type BIFs. However, field observations describe many Rapitan BIFs as interbedded with other formations, which means that their thickness may be overexaggerated in the literature. It would be useful to verify that the data collected applied to individual beds rather than the thickness of the total occurrence of the BIF within the formation. Respective standard deviations were 271.7, 264.8, and 396.0, which indicates that thickness varies widely within each type. Each type had an outlier of over 1,000 m, which certainly contributed to the large standard deviations.

Various levels of organic content were observed in each BIF-type. The Superior-type BIFs had the most significant organic presence with 28 out of 33 containing indicators. Upon further analysis of organic indicator type, Superior-type BIFs displayed the strongest association with 15 having reported microfossils, 7 containing microbial mats, and 6 containing only organic residues. These indicators were ranked such that microfossils were more strongly indicative of organics than microbial mats and organic residues such as bitotic graphite. 14 out of 34 Algoma-type BIFs had reported organics, and 5 out of 9 Rapitan BIFs displayed organic indicators. As to be expected with the volcanic-associated Algoma-type BIFs, most of the organics were only residues, which makes a strong organic presence doubtful. Furthermore, graphite can be precipitated apart from biological means, so though the Algoma BIFs displayed ^{13}C-depleted graphite signals typical of organic origin, more rigorous review is necessary to verify whether a distinct biotic signal is present.

Studies have been published by Fallacaro and Calvin (2003), Bridges et al. (2011), and Singh et al. (2016) comparing Martian iron oxide beds to terrestrial, Superior-type banded iron formations such as the Brazilian Carájas and Indian Singhbhum deposits. However, they focused on basin geomorphology and only limited rock composition features to make this conclusion. Given the high average thickness, as well as strong organic signal, associated with Superior-type fossils, it is expected that the Martian iron oxides will display similar characteristics if they are truly analogous rocks.

Figures/Charts

Figure 1: Thickness Plot by BIF Type.

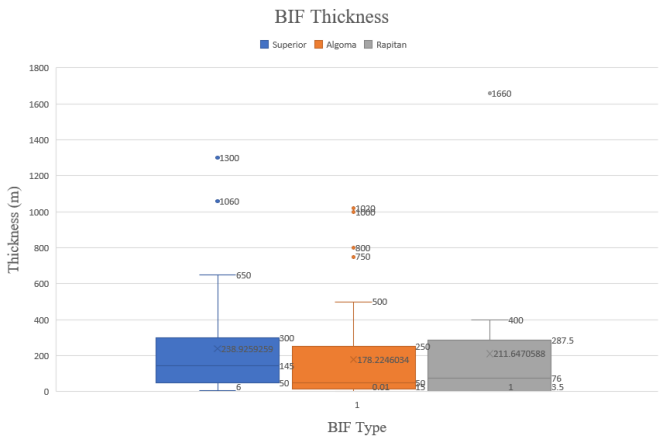


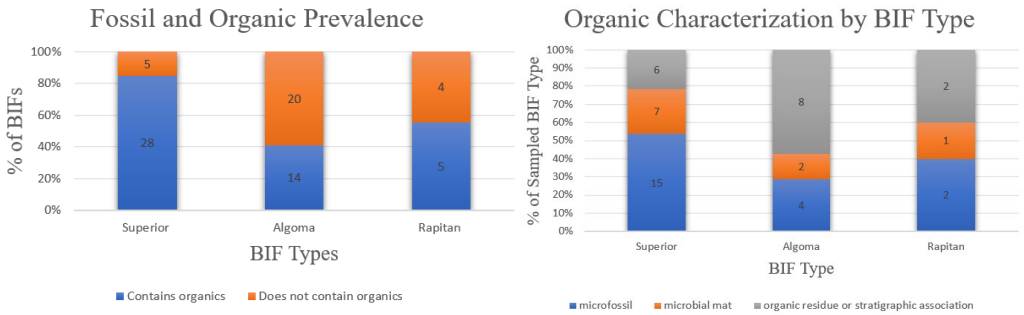
Figure 2: Example Criteria Data Entry for the Gunflint Formation

Name	Depositional Environment	Thickness	Iron Content	Facies	Type
Gunflint	storm-dominated continental shelf (marine subtidal?)	122 m	45.81%	carbonate	Superior

Figure 3: Example Organic Criteria Data Entry for the Gunflint Formation

Name	microfossils	Microbial mats	Organic association (^{13}C-depleted graphite residues, etc.)
Gunflint	yes	yes	not reported

Figures 4 and 5. Organic Signal Prevalence in Different BIF Types.



Acknowledgments

I would like to thank my advisors, Dr. John Whitmore and Dr. Robert Chasnov, for their unwavering encouragement, support, and guidance throughout the course of this project. Furthermore, I would like to thank the Ohio Space Grant Consortium and NASA for the opportunity to perform and present this research at the 2025 Scholar's Symposium in Cleveland, Ohio.

References

Bridges, N.T., Hook, S.J., Thomson, Bradley J., Crowley, James K., Filho, Carlos Roberto de Souza, Macambira, J.B., and Gilberto de Lima Pereira Silva. "Brazilian Analog for Ancient Marine Environments on Mars." *AGU: Advancing Earth and Space Sciences,* 2011. https://doi.org/10.1029/2008EO360001

Fallacaro, Alicia, and Wendy M. Calvin, "Spectral and Chemical Characteristics of Lake Superior Banded Iron Formation: Analog for Martian Hematite Outcrops." In *Sixth International Conference on Mars*, Pasadena CA, July 2023.

Singh, Mahima, Singhal, J., Prasad, K. Arun, Rajesh, V.J., Ray, D. and Priyadarshi Sahoo. "Spectral Characteristics of Banded Iron Formations in Singhbhum Craton, Eastern India: Implications for Hematite Deposits on Mars." *Geoscience Frontiers* 7(6). 2016. https://doi.org/10.1016/j.gsf.2015.11.003

Enhancing Student Experience through Human-Centered Design

Student Researcher: Isabella Wynter Mitchell

Advisor: Dr. Deng Cao

Central State University
Computer Science and Mathematics/Computer Science

Abstract
Access to campus resources is critical for student engagement, academic achievement, and overall well-being. However, many students report difficulty finding information due to fragmented digital platforms. This project used a human-centered design (HCD) approach to evaluate current information access patterns among Central State University students and create a centralized mobile app that addresses key pain points. The results reveal a strong student preference for visually organized, mobile-first formats that combine event schedules, dining information, and university resources in one place. Access to campus resources is critical for student engagement, academic achievement, and overall well-being. However, many students report difficulty finding information due to fragmented digital platforms. This project used a human-centered design (HCD) approach to evaluate current information access patterns among Central State University students and create a centralized mobile app that addresses key pain points. The results reveal a strong student preference for visually organized, mobile-first formats that combine event schedules, dining information, and university resources in one place.

Project Objectives
The project aimed to: (1) identify how students currently access campus resources, (2) assess challenges they face when locating information, (3) understand format and platform preferences, and (4) create a design prototype informed by student needs. Grounded in HCD, the study emphasized student voice and participatory feedback in building a solution that supports information accessibility and student success.

Methods
A survey was distributed to Central State University students via SurveyMonkey. It assessed how frequently students search for campus updates, which platforms they use, their difficulties in accessing information, and their preferred presentation formats. Based on these insights, a mobile-first prototype was designed using Figma. The layout was inspired by social media platforms and included interactive visual components such as daily event cards and scrollable weekly previews.

Results and Discussion
Survey results revealed that 55% of students search for campus resources at least weekly. Students struggled most with locating dining schedules and event details, citing the scattered nature of existing platforms as a key frustration. Email and social media were the most-used sources, but students preferred visual, app-based interfaces that consolidate information. This confirms existing research that supports the use of centralized, student-informed technology for improving access to academic support tools. The final design features easy navigation, push notifications, and modular updates to align with students' tech habits.

Acknowledgments
This research was supported by the Ohio Space Grant Consortium. We thank Dr. Deng Cao for his guidance and the Central State University students who participated in the study.

References

1. Bennett, S., & Maton, K. (2010). Beyond the 'digital natives' debate: Towards a more nuanced understanding of students' technology experiences. Journal of Computer Assisted Learning, 26(5), 321-331.
2. Gibbons, S. (2016). User interface design basics. Nielsen Norman Group. Retrieved from www.nngroup.com
3. Dahlstrom, E., Brooks, D. C., Grajek, S., & Reeves, J. (2015). ECAR Study of Undergraduate Students and Information Technology. EDUCAUSE Center for Analysis and Research.
4. Garrett, J. J. (2010). The Elements of User Experience: User-Centered Design for the Web and Beyond. New Riders.
5. Norman, D. A. (2013). The Design of Everyday Things (Revised and Expanded Edition). Basic Books.
6. SurveyMonkey. (2024). Online Survey Tool. www.surveymonkey.com
7. Figma. (2024). Collaborative Interface Design Tool. www.figma.com

Effect of Different Airfoil Shapes on Lift and Drag

Student Researcher: Jennifer Zayac

Advisor: Dr. Abigail Clark

Ohio Northern University
Mechanical Engineering

Abstract:
The impact of various airfoils on the effectiveness and efficiency of an aircraft wing can be significant. Airfoils play an important role in determining the aerodynamic characteristics of an airplane. By altering the shape and design of the airfoil, the lift and drag forces acting on the wing can be altered, which ultimately influences the overall performance of the aircraft. Every aircraft has a different airfoil with distinct properties that affect the performance of the wing for different conditions in flight. Some airfoils are designed for easier maneuvering while others are designed simply for high speed flying. The airfoil selection process depends on several factors, including the weight, size and purpose of the aircraft. The experiment designed will test three
separate airfoils in CFD, to analyze which one provides the most effective performance based on the lift versus drag conditions. The properties of the aircraft used will be based on the Ohio Northern University SAE Aero competition team's aircraft, using the weight, size and slow speeds.

Background:
An airfoil is a curved structure that produces lift and drag while moving through the air. It is the cross section of the wing or tail. For this research, the wing will be the focus. Airfoils are
specific to each airplane and their function. The SAE Aero Competition team at Ohio Northern University design, builds and flies a new airplane every year based on the competition rules. The research project focuses on which airfoil will allow the best outcome and lift to drag ratio. This will determine the most effective airfoil selected for the team. The analysis is done at a zero
degree angle of attack due to that being the angle that the team is using for competition.

Project Objectives:
1. Obtain three potential airfoils to analyze from statistics using airfoil tools
2. Extract the coordinate files from each airfoil
3. Generate a CAD geometry of each airfoil to import into Fidelity Pointwise
4. Mesh each airfoil in Pointwise and perform CFD analysis using COBALT on the airfoil
5. Analyze the results of the lift to drag ratio for each airfoil
6. Implement into SAE Aero Competition airplane

Methods:
Approach: In order to narrow the selection down to only three airfoils, multiple airfoil
statistics were analyzed using airfoil tools [1]. Each airfoil was analyzed at 4 different angles of attack but ultimately, the zero degree alpha is analyzed. As shown in Figure 1 below, airfoils GOE244, GOE225 and GOE448 are selected for the research.

Airfoil Name	Reynolds Number	0 Deg Alpha			3 Deg Alpha			5 Deg Alpha			7.5 Deg Alpha		
		Cof Lift	Cof Drag	L/D	Cof Lift	Cof Drag	L/D	Cof Lift	Cof Drag	L/D	Cof Lift	Cof Drag	L/D
GOE222	200000	0.89	0.02	48.92	1.20	0.018	68.510	1.38	0.019	72.943	1.60	0.022	73.566
GOE223	200000	0.71	0.02	43.63	1.05	0.018	59.308	1.25	0.019	66.047	1.48	0.021	70.476
GOE244	200000	1.22	0.017	71.76	1.46	0.022	66.364	1.65	0.026	63.462	1.87	0.031	60.323
GOE225	200000	0.9384	0.01473	63.71	1.2653	0.0154	82.162	1.465	0.01698	86.278	1.6925	0.02067	81.882
GOE226	200000	0.9301	0.01497	62.13	1.2488	0.0157	79.541	1.4416	0.017	84.800	1.6883	0.02139	78.929
GOE234	200000	0.9422	0.02551	36.93	1.3081	0.02194	59.622	1.5262	0.02142	71.251	1.7433	0.02389	72.972
GOE241	200000	1.0507	0.01811	58.02	1.3672	0.02114	64.674	1.5638	0.0232	67.405	1.7483	0.02643	66.148
GOE242	200000	0.964	0.01959	49.21	1.3096	0.02079	62.992	1.5327	0.02176	70.437	1.7639	0.02251	78.361
GOE448	200000	1.02	0.01286	79.32	1.3056	0.00946	138.013	1.4805	0.00956	154.864	1.6531	0.01209	136.733
S1221 w/o Flap	200000	0.6732	0.01496	45.00	1.0225	0.01681	60.827	1.2266	0.01832	66.954	1.502	0.02285	65.733
CH10	200000	1.175	0.02055	57.18	1.4705	0.0219	67.146	1.6551	0.02427	68.195	1.841	0.02778	66.271

Figure 1: Airfoil Statistics from Airfoil Tools

Geometry: The coordinate files were extracted from airfoil tools and imported into Solidworks to create a 2D sketch. GOE244, GOE225 and GOE448 are shown in figures 2,3 and 4 respectively.

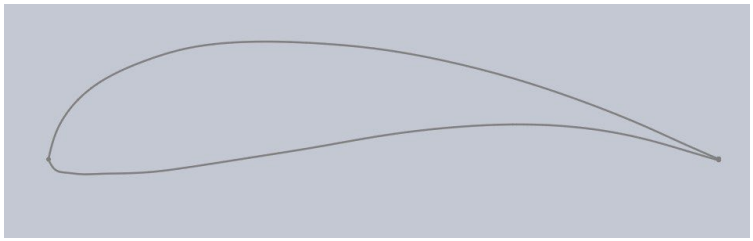


Figure 2: GOE244

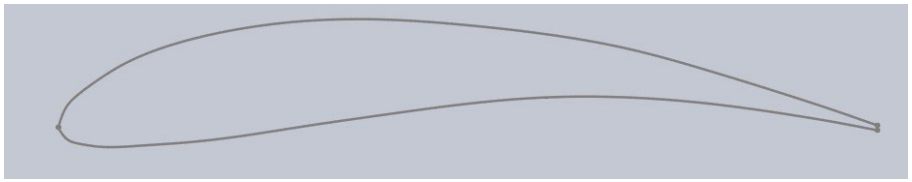


Figure 3: GOE225

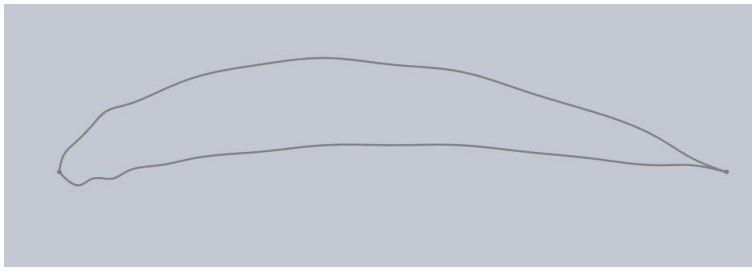


Figure 4: GOE448

CFD Meshing: Each airfoil was meshed in Fidelity Pointwise the exact same way with the same boundary conditions. Figure 5 displays the whole mesh of GOE244 and how each of the airfoils were meshed.

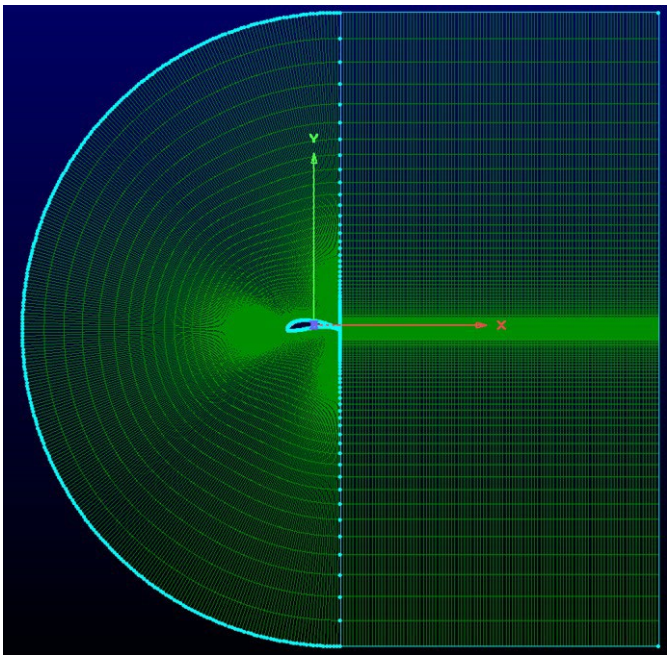


Figure 5: GOE244 mesh in Fidelity Pointwise

A closer look of the boundary layer surrounding the airfoil is depicted in figure 6. The meshed layers are closer together as they get closer to the airfoil to allow for more accurate results of airflow around the edge.

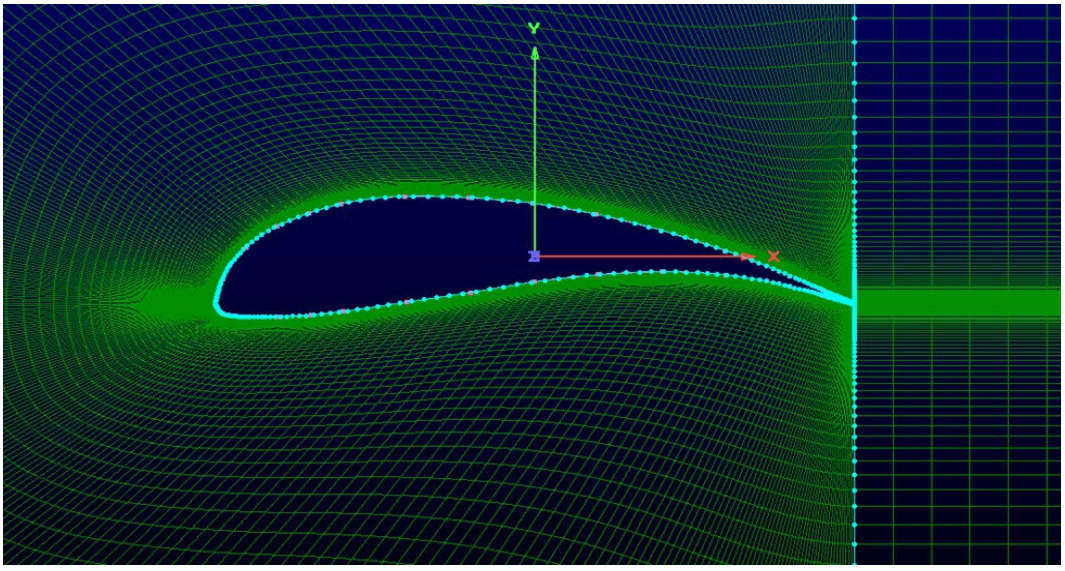


Figure 6: Up Close look at the Boundary Layer

The other two airfoils were meshed in the exact same way and can be observed in figures 7 and 8 with the up close looks in figures 9 and 10.

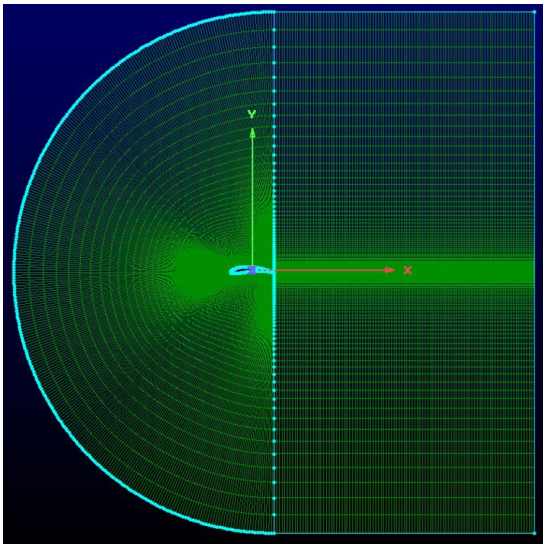


Figure 7: GOE225 mesh

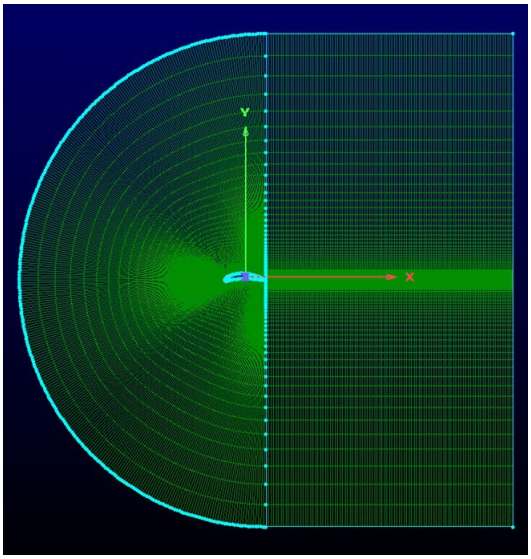


Figure 8: GOE448 mesh

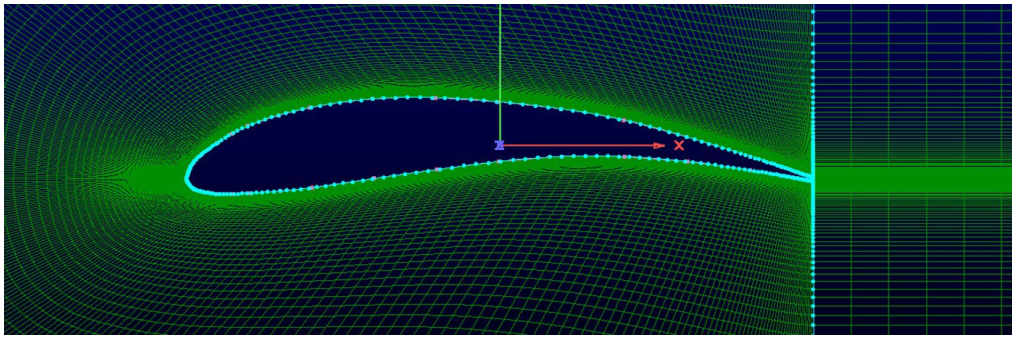


Figure 9: GOE225 Up Close Look

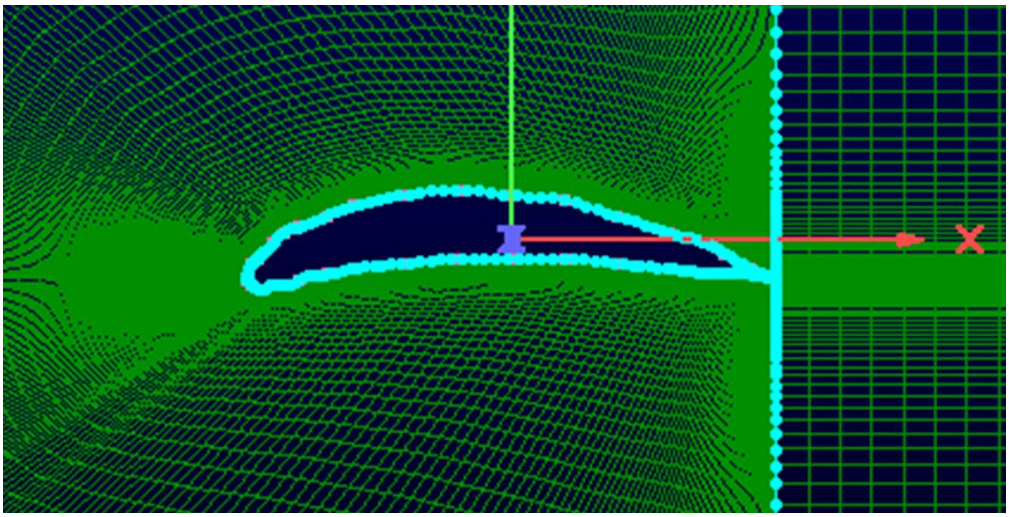


Figure 10: GOE448 Up Close Look

Boundary Conditions: After the airfoils were meshed in Fidelity Pointwise, the CFD analysis was run using COBALT software. Boundary conditions were needed to be applied to
each of the edges. Figure 11 shows where each boundary condition is. The red circles were given a Farfield - Modified Riemann boundary condition, the yellow circles were given a Wall - Slip condition and the orange circle, the airfoil, was given a Wall - Adiabatic No Slip boundary condition.

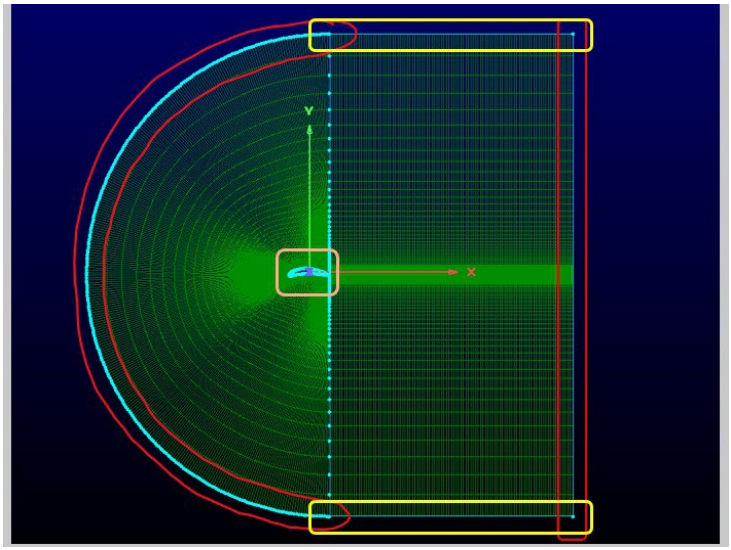


Figure 11: Boundary Conditions

Once the airfoil was meshed and the boundary conditions were applied, the CFD was run in COBALT to get the results for all of the airfoils.

Results and Discussion:
COBALT simulation was run for each airfoil, GOE244, GOE225 and GOE448. The results are displayed in Table 1 below. Each airfoil shows the coefficient of lift, drag and then finally the lift to drag ratio.

Table 1: Results at Zero Degree Angle of Attack

	GOE225	GOE244-il	GOE448
C_L	0.083711	1.6246	1.23
C_D	0.0048267	0.015878	0.01568
L/D	17.3	102.3	78.44

According to the results of CFD, GOE244 has the greatest L/D ratio. Looking back at figure 1, airfoil tools showed that GOE448 was the most effective, however, the CFD analysis expresses GOE244 as the best choice. There could be multiple reasons as to why this has happened but just to ensure the airplane has great success, GOE244 was the airfoil selected for the SAE Aero team.

Acknowledgments:
OSGC for this scholarship
Ohio Northern University Dr. David Sawyers Advisor: Dr. Abigail Clark

References:
[1] airfoiltools.com

Fabrication and Testing of 3D Printed Polymers for Torsional Dynamic Properties for Aeroelastic Prototypes

Student Researcher: Lisa Zhang

Advisor: Dr. Kumar V. Singh & Dr. Fazeel Khan

Miami University
Department of Mechanical and Manufacturing Engineering

Abstract
The evaluation of aeroelastic and aero-servo-elastic behavior in aircraft structures requires complex, multidisciplinary analysis supported by ground vibration and wind tunnel testing. Traditional approaches to testing are costly and resource intensive. Recent advances in rapid prototyping and additive manufacturing offer promising alternatives for fabricating complex aerospace components, including 3D-printed wings [1]. However, the reliability and performance of these printed structures, particularly under dynamic loading conditions, remain open research challenges.

This project investigates the dynamic response of 3D-printed polymers, with a focus on torsional loading relevant to aeroelastic applications. While additive manufacturing has gained widespread adoption across various industries, including aerospace and biomedical engineering, concerns regarding the mechanical performance and consistency of printed components persist. Most prior research emphasizes tensile and bending tests; this study expands the scope to torsional behavior [2]. By examining the influence of printing parameters on torsional stiffness and vibration characteristics, this research aims to inform the design of aeroelastic structures with improved damping and optimized natural frequencies, enhancing structural performance and extending service life.

Project Objectives
The objective of this research is to investigate how different 3D printing parameters influence the mechanical and dynamic properties of printed polymer structures, with a particular focus on determining the shear modulus (G) and damping characteristics. This study involves gathering experimental data on shear modulus and damping capacity as a function of printing parameters based on ASTM standards. It includes fabricating 3D printed samples for dynamic characterization and vibration performance, designing a fixture for vibration modal testing, and conducting vibration modal analysis to estimate natural frequencies and damping behavior. Additionally, numerical simulations will be performed to validate key experimental results. The goal is to deepen understanding of how printing parameters affect structural performance and to support the development of more accurate aeroelastic prototypes using 3D printed materials.

Methods
This research was carried out in three key stages: Preparation, Quasi-Static Testing, and Dynamic Testing.

1. Preparation Phase

The project began with a literature review focused on the mechanical and aeroelastic behavior of 3D printed materials. Emphasis was placed on prior studies involving additive manufacturing and its applications in structural dynamics. Based on the findings, relevant testing protocols were identified and implemented in accordance with ASTM standards, particularly ASTM D638-22 [3] for tensile testing of plastics and ASTM E143-20 for torsional properties [4]. Using insights from the literature and standards, we designed test specimens via CAD modeling, ensuring dimensional consistency with ASTM guidelines. The designs were printed using a Dremel 3D printer, with samples fabricated in both horizontal and

vertical orientations to evaluate the influence of build direction on mechanical performance. Four materials were selected for testing: PLA, ABS, PETG, and ONYX (a nylon-carbon fiber composite), enabling comparisons across a range of mechanical properties and compositions.

2. Quasi-Static Testing Phase

The quasi-static mechanical characterization was performed using an MTS hydraulic testing machine. Each specimen was subjected to controlled torsional loading with a rotational displacement of 2 degrees, enabling the measurement of torsional stiffness and baseline mechanical response. Torque vs. torsional angle data was collected, and the shear modulus (G) was calculated using the torsion formula for circular **cross-sections.**

where T is the applied torque, L is the length of the specimen, J is the polar moment of inertia, and ϑ is the angle of twist. This phase was critical in establishing reference mechanical properties for each material, including stiffness, yield strength, and elastic behavior.

3. Dynamic Testing Phase

The dynamic testing focused on evaluating how the materials respond under frequency-dependent loading conditions. To perform this, a custom torsional vibration fixture was designed and fabricated to securely hold the 3D printed specimens during testing. Dynamic characterization was conducted using vibration modal analysis, allowing for the extraction of natural frequencies and damping characteristics. From the frequency response data, the frequency-dependent shear modulus G(ω) was determined. This data was compared against the quasi-static results to assess how dynamic loads influence mechanical performance and to validate consistency between the two testing methods.

Results and Discussion

The quasi-static testing phase measured the shear modulus (G) of four different 3D printed polymers: ONYX, PETG, ABS, and PLA, each fabricated in both horizontal and vertical build orientations. The results showed a consistent trend across all materials: the horizontally printed samples exhibited a higher shear modulus than the vertically printed samples (Figure 1). This finding aligns with expectations based on the layered nature of the 3D printing process. Horizontally printed samples benefit from the alignment of printed filaments along the direction of applied stress, leading to greater stiffness. In contrast, vertically printed samples are more susceptible to interlayer weaknesses, resulting in lower measured G values.

Additionally, even within the quasi-static tests, there was noticeable variation in G values, with percentage differences ranging from 2% to 11% between specimens. This variability can be attributed not only to differences in printing parameters (such as layer adhesion, infill density, and build orientation) but also to the intrinsic material properties of polymers themselves. Importantly, these results emphasize a core challenge of the research: for polymer-based materials, the shear modulus is not truly constant. Polymers are viscoelastic materials, meaning their mechanical properties naturally vary with loading rate and frequency. Thus, even though quasi-static testing aims to capture a baseline "constant" G, the material's response inherently shifts when subjected to dynamic excitation.

This observation has significant implications for the dynamic testing phase. It highlights that identifying a single value of G is inherently limited when dealing with polymers. Instead, a full characterization of G(ω), the shear modulus as a function of frequency, is necessary to accurately capture the material behavior under real-world loading conditions.

Figures/Charts

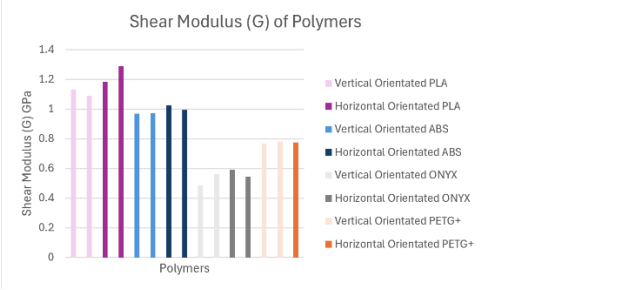


Figure 1. Vertical and Horizontal Comparison of Different Polymer of Shear Modulus (G)

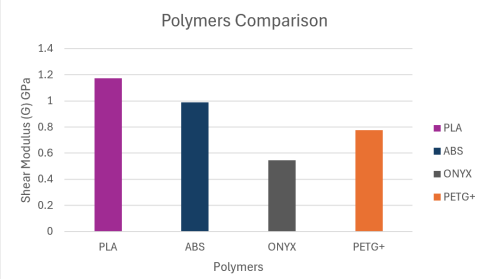


Figure 2. Polymer Comparison of Shear Modulus (G)

Future Work

We are currently conducting dynamic testing to evaluate both the frequency-dependent shear modulus G(ω) and the complex shear modulus G* of the 3D printed polymer specimens. This phase will provide deeper insight into the materials' viscoelastic behavior under dynamic loading conditions, complementing the baseline data obtained from quasi-static tests.

Acknowledgments

The author would like to thank her advisors, Dr. Kumar V. Singh and Dr. Fazeel Khan, for their invaluable guidance and mentorship throughout this research. She also appreciates the resources and support provided by the Department of Mechanical and Manufacturing Engineering at Miami University during her undergraduate studies. Finally, the author extends her gratitude to the Ohio Space Grant Consortium for their support and partnership, whose funding made this research possible.

References

[1] Black, C.*, Singh, K. V., Goodman, S., Altman, A., and Kolonay, R., "Design, Fabrication and Testing of 3D Printed Wings for Rapid Evaluation of Aeroelastic Performance", Proceedings of the AIAA/ASCE/AHS/ASC Structures, Structural Dynamics, and Materials Conference at AIAA-SciTech Forum 2018, 8-12 January 2018, Kissimmee, FL, USA.

[2] Carter, J.*, Singh, K. V., and Khan, F., "Vibration Characteristics of 3D Printed Viscoelastic Graded Polymeric Plates", Proceedings of the ASME International Design Engineering Technical Conferences & Computers and Information in Engineering Conference (IDETC-CIE 2021), Paper Number: 68460, Virtual Conference: August 17 – 19, 2021.

[3] *Standard Test Method for Tensile Properties of Plastics*. Compass. (n.d.-a). https://compass.astm.org/document/?contentCode=ASTM%7CD0638-22%7Cen-US

[4] *Standard Test Method for Shear Modulus at Room Temperature*. Compass. (n.d.-a). https://compass.astm.org/document/?contentCode=ASTM%7CE0143-20%7Cen-US

Community College

Locating PSR B0904+77 Using Regional Spectral Data from Astronomical Surveys

Student Researcher: Olivia Bogna

Advisor: Dr. Monroe Kennedy

Lorain County Community College
Universal Sciences

Abstract
PSR B0904+77 is a pulsar with a spin period almost equivalent to π/2 seconds. It was detected in 1970 but has disappeared in astronomical surveys. Using spectral data from astronomical surveys in the region from the Low Frequency Array (LOFAR) and the Very Large Array (VLA), we can test the hypothesis that this pulsar's location still corresponds to a steep spectrum source. We also propose various follow-up techniques.

Overview and Project Objectives
In 1968, two Harvard physicist discovered two new pulsars [2]. One of them, PSR B0904+77, was detected at about 111 - 112 MHz and located at approximately 09 hr 4 min RAJ, 77:40 DEC. Given the "peculiar" characteristics the pulsar exhibited, such as emitting a seemingly secondary pulse about 20% the amplitude of the primary pulse, and being unable to have a dual-frequency analysis conducted on it, the scientists were unable to deduce a dispersion measure. This pulsar has not appeared in follow-up observations using typical detection method.

Our objective is to rediscover PSR B0904+77 using radio, IR and spectroscopic data from LOFAR and VLA surveys. By collecting spectral data from radio sources located in the pulsar's region of uncertainty, we can find candidates that exhibit similar properties to PSR B0904+77 and other pulsars. Promising candidates can be chosen for deep observation using radio telescopes to confirm their correlation or identity as PSR B0904+77.

Methodology
Using Aladin, we re-analyzed NVSS (1.4 GHz), WENSS (325 MHz), TGSADR (147.4 MHz), and VLSSr (74 MHz) data for 22 candidates within 5° of PSR B0904+77 (RAJ 09:04:00, DEC +77:40:00), alongside 147 new candidates. Only sources not identified in Simbad and with NVSS, WENSS, or VLSSr counterparts were considered.

Flux densities (in mJy) were measured using Vizier's high-res mode over 20-40 pixel (1-2°) circular regions, determined by each candidate's size and brightness. Unlike earlier average-based methods, we used summed pixel data. The same NVSS-defined region was applied to all three surveys.

Noise was estimated via color dispersion graphs, identifying inflection points between background and signal. Using the equation listed below, the flux density uncertainty was then calculated:

$$\sigma_{noise} * \sqrt{Number\ of\ Pixels} = \sigma_{flux}$$

With flux and uncertainty values, AstroPy was used to generate log-log plots. With frequency on the x-axis, flux density on the y-axis and flux uncertainty used to produce error bars, an estimated slope provided a spectral index and magnitude for each candidate. Fit uncertainty was calculated using the equations listed below.

$$\Delta = \sum w \sum w x^2 - (\sum w x)^2$$

$$\sigma_B = \sqrt{\frac{\sum w}{\Delta}}$$

Considering pulsars typically have a spectral index (an indicator of how their radio emission intensity changes with frequency) ranging from -1.5 to -3, candidates with indices within this range would be strongly considered for observation.

Results and Discussion

In addition to the 22 re-analyzed candidates, 14 of 147 new candidates were examined. Many showed a spectral peak between 75 MHz and 147.4 MHz, prompting the creation of two spectral index plots per candidate, one including VLSSr (75 MHz) data and one excluding it. Exclusion plots generally resulted in steeper spectral indices.

Among the VLSSr-inclusive plots, Candidate 1.3VS had the steepest index at -1.58. For VLSSr-exclusion plots, Candidate 2.1VS-R had the steepest at -1.85. Spectral indices below -1.5 are considered favorable, with -1.75 to -3 being ideal. If pulsations are confirmed through follow-up observations, Candidate 2.1VS-R would be a strong target, unless candidates with even steeper indices are identified, alongside others within the preferred range.

Acknowledgements

I would like to thank my advisors Dr. Monroe Kennedy and Dr. Timothy Dolch their assistance with this research, along with the rest of the NANOGrav and STARS-UP faculty that support this program.

References

[1] Sibert, Nathan et al, (2024). *Investigating a Potential Pulsar Wind Nebula and Candidates for PSR B0904+77*

[2] Strasbourg astronomical Data Center. Aladin Sky Atlas. Version 12.060. Mar. 2024. url: http://aladin.cds.unistra.fr/aladin.gml.

[3] J. H. Taylor and G. R. Huguenin. “Two New Pulsating Radio Sources”. In: Nature 221 (Mar. 1969). doi: 10.1038/221816a0. url: https://doi.org/10.1038/221816a0.

[4] Duncan R. Lorimer. “Binary and Millisecond Pulsars”. In: Living Reviews in Relativity 11 (Nov. 2008), p. 11. issn: 1433-8351. url: http://www.livingreviews

Exploring the Use of Mycelium as Biodegradable Space Satellite Building Materia

Student Researcher: Tyler Fullilove

Advisor: Dr. Jeremy Huber

Cincinnati State Technical and Community College
Pre-Engineering

Abstract

As the aerospace industry continues to expand, concerns about space debris have become increasingly pressing. Satellites are a large contributor to this issue, often referred to as space pollution. Most satellites are constructed from durable materials such as metals and plastics, which can persist in the space environment for decades, if not longer. These materials not only clutter the orbital pathways around Earth but also pose significant risks to both operational spacecraft and future missions. The environmental impact of these materials extends beyond space, as the accumulation of space debris can also begin negatively affecting the environment and by degree, human life. This project seeks to address the issue of space debris by exploring the potential of mycelium, a natural, biodegradable fungus, in the development of satellite structures. Mycelium has shown remarkable promise as a sustainable alternative to conventional materials due to its ability to decompose naturally, leaving no harmful residues in space. By utilizing mycelium-based composites, we can design satellites that not only serve their intended purpose but also break down over time, minimizing their environmental footprint both in orbit and upon re-entry. The project will involve investigating the mechanical properties of mycelium, such as its strength and durability, to ensure it can withstand the requirements of space travel, including radiation exposure and extreme temperatures. Additionally, it will explore various applications of mycelium in satellite design, from structural components to insulation materials. Through this project, I aim to demonstrate that sustainable practices can be effectively integrated into aerospace engineering, paving the way for a new generation of environmentally friendly satellites that contribute to a cleaner and safer space environment.

Methods

To assess the feasibility of mycelium in aerospace, fungal composites will be grown in a laboratory setting using agricultural waste as substrate. Environmental conditions—temperature, humidity, and nutrients—will be carefully controlled to optimize strength properties (Islam et al., 2017). Post-cultivation, samples will undergo ASTM-standard mechanical testing to measure compressive strength, tensile durability, and impact resilience (Jones et al., 2017). Simulated radiation exposure, including gamma and ultraviolet light, will test survivability under cosmic radiation (Elsacker et al., 2019). Thermal conductivity tests will assess insulation performance. Microgravity effects will be explored using drop tower and parabolic flight simulations, as per ISRU applicability (Appels et al., 2019).

1. **Material Preparation:** Mycelium samples will be grown using agricultural byproducts as a substrate. Growth parameters such as humidity, temperature, and nutrient availability will be controlled to optimize material properties (Islam et al., 2017).
2. **Mechanical Testing:** Strength, flexibility, and impact resistance will be tested using standard ASTM protocols to determine structural integrity (Jones et al., 2017). Compression and tensile tests will assess whether mycelium composites can withstand space launch forces.
3. **Radiation Exposure:** Samples will be subjected to gamma radiation and UV exposure to evaluate their resistance to cosmic radiation, which is a key challenge for spacecraft materials (Elsacker et al., 2019).
4. **Microgravity Simulation:** Drop tower and parabolic flight tests will simulate microgravity effects on mycelium growth and material properties (Appels et al., 2019). Results will inform potential in-situ manufacturing applications on the Moon and Mars.
5. **Comparative Analysis:** Mycelium-based materials will be compared to traditional aerospace materials in terms of strength-to-weight ratio, thermal insulation, and sustainability metrics. It is anticipated that mycelium-based composites will demonstrate competitive mechanical properties while significantly reducing production energy and waste. These materials are expected to provide thermal insulation benefits and some degree of radiation shielding, making them suitable for spacecraft interiors and planetary habitats (Zhang et al., 2020).

6. **Potential Applications**: Applications include lightweight structural panels, impact-resistant enclosures, and self-healing spacecraft components. The use of mycelium could also enable in-situ resource utilization (ISRU), where astronauts cultivate structural materials directly on Mars or the Moon, reducing launch costs and dependency on Earth-based supplies (Islam et al., 2018).

Results and Discussion

Findings from existing literature strongly support mycelium's role in short-term space applications. It has been demonstrated how fabrication processes can tune the mechanical properties of mycelium (Haneef et al. 2017), introduced NASA's vision of growing habitats from fungal composites on the Moon or Mars using ISRU (Rothschild 2021), and confirmed that mycelium materials possess the strength and thermal resistance required for aerospace-grade applications ((Zhang et al. 2020) and (Islam et al. 2018)). While they may not yet rival metals for long-term missions, their biodegradability makes them ideal for satellites designed to de-orbit, burn up, or degrade naturally over time. This highlights their compelling promise for short-term, low-risk deployments. Future research will expand testing to long-duration spaceflight environments and explore genetic modifications to enhance mycelium structural performance. The results from this study will contribute to sustainable space architecture and reinforce the viability of biocomposites in next-generation spacecraft design.

Acknowledgments

This research is supported by NASA and the Ohio Space Grant Consortium. Special thanks to Cincinnati State Technical and Community College, Dr. Huber, and Ms. Abbey Yee for their guidance.

References

Rothschild, L. J. (2021). Growth as an Alternative Approach to the Construction of Extra-Terrestrial Habitats. *NASA Technical Reports Server (NTRS)*.
https://ntrs.nasa.gov/citations/20210021668

Yang, G., Brewer, M., El-Gharabawy, H., Griffith, G., & Jones, P. (2017). Growing and Testing Mycelium Bricks as Building Insulation Materials. *IOP Conference Series: Earth and Environmental Science, 121*, 022032.
https://doi.org/10.1088/1755-1315/121/2/022032

Islam, M. R., Tudryn, G., Bucinell, R., Schadler, L., & Picu, R. C. (2017). Morphology and Mechanics of Fungal Mycelium. *Scientific Reports, 7*, 13070.
https://doi.org/10.1038/s41598-017-13295-2

Haneef, M., Ceseracciu, L., Canale, C., Bayer, I. S., Heredia-Guerrero, J. A., & Athanassiou, A. (2017). Advanced Materials From Fungal Mycelium: Fabrication and Tuning of Physical Properties. *Scientific Reports, 7*, 41292.
https://doi.org/10.1038/srep41292

Jones, M., Huynh, T., Dekiwadia, C., Daver, F., & John, S. (2017). Mycelium Composites: A Review of Engineering Characteristics and Growth Kinetics. *Journal of Bionanoscience, 11*(4), 241-257.
https://doi.org/10.1166/jbns.2017.1440

Elsacker, E., Vandelook, S., Brancart, J., Peeters, E., & De Laet, L. (2019). Mechanical, Physical and Chemical Characterization of Mycelium-Based Composites with Different Types of Lignocellulosic Substrates. *PLOS ONE, 14*(7), e0213954.
https://doi.org/10.1371/journal.pone.0213954

Zhang, J., Hu, Y., & Ruan, X. (2020). Thermal and Mechanical Properties of Mycelium-Based Composites for Architectural Applications. *Journal of Materials in Civil Engineering, 32*(6), 04020107.
https://doi.org/10.1061/(ASCE)MT.1943-5533.0003208

Islam, M. R., Tudryn, G., Bucinell, R., Schadler, L., & Picu, R. C. (2018). Mechanical Behavior of Mycelium-Based Particulate Composites. *Journal of Materials Research, 33*(21), 3313-3321. https://doi.org/10.1557/jmr.2018.312

Girometta, C., Picco, A. M., Baiguera, R. M., Dondi, D., Babbini, S., Cartabia, M., & Pellegrini, M. (2019). Physico-Mechanical and Thermodynamic Properties of Mycelium-Based Biocomposites: A Review. *Sustainability, 11*(1), 281.
https://doi.org/10.3390/su11010281

Appels, F. V. W., Camere, S., Montalti, M., Karana, E., Jansen, K. M. B., Dijksterhuis, J., Krijgsheld, P., & Wösten, H. A. B. (2019). Fabrication Factors Influencing Mechanical, Moisture- and Water-Related Properties of Mycelium-Based Composites. *Materials & Design, 161*, 64-71. https://doi.org/10.1016/j.matdes.2018.11.027

Tavares, F. (2020, January 10). Could Future Homes on the Moon and Mars Be Made of Fungi? NASA.
https://www.nasa.gov/feature/ames/myco-architecture/

Comparative Blockchain Solutions for Enhanced Cybersecurity in Space Communications

Student Researcher: Noah Manley

Cincinnati State Technical and Community College
Cybersecurity

Abstract

Space missions depend heavily on secure communications but face critical cybersecurity threats and extreme operational constraints such as latency and limited bandwidth. This study compares blockchain technologies—Hedera Hashgraph, Hyperledger Fabric, and Ethereum—to evaluate their suitability for securing interstellar communications. Hedera's NASA-backed implementation demonstrates superior transaction throughput, minimal latency, optimal bandwidth efficiency, and robust fault tolerance compared to Ethereum and Hyperledger Fabric, highlighting its viability for space communication applications.

Introduction and Project Objectives

Interstellar communication networks underpin space exploration but suffer from severe latency, bandwidth restrictions, and persistent cybersecurity vulnerabilities. Traditional centralized communication methods lack resilience against targeted cyberattacks and single-point failures. Blockchain technology emerges as a robust solution offering decentralized, tamper-resistant data logging and resilient consensus mechanisms. This study comparatively evaluates Hedera Hashgraph, Hyperledger Fabric, and Ethereum, emphasizing Hedera's unique advantages due to NASA-backed use in space missions.

Methodology

Blockchain prototypes were simulated under four realistic space scenarios—Earth-based, Near-Earth Orbit (NEO), Deep Space (Mars), and Interstellar—using Mininet and dummynet to emulate latency and bandwidth limitations. Key metrics evaluated included Transaction Throughput (TPS), Latency, Bandwidth Efficiency, and Fault Tolerance. Hedera Hashgraph's consensus service (HCS), Hyperledger Fabric's modular consensus mechanisms (Raft, PBFT), and Ethereum's traditional blockchain were qualitatively and quantitatively assessed. Performance was monitored using Hyperledger Caliper and Wireshark, employing data compression and blockchain pruning for bandwidth optimization.

Results

Hedera Hashgraph consistently outperformed Hyperledger Fabric and Ethereum across metrics. Under optimal Earth-based conditions, Hedera achieved 949 TPS compared to Fabric's approximate 3500 TPS (optimized, permissioned conditions) and Ethereum's limited ~15 TPS. In latency-sensitive scenarios, Hedera demonstrated superior performance (Interstellar latency at 1.06 seconds) against Ethereum's impractical delays and Fabric's 1–2 seconds under controlled conditions. Bandwidth efficiency in Hedera ranged from 75–90%, surpassing traditional Ethereum's <70%. Fault tolerance was highest with Hedera (98.53% interstellar), substantially outperforming Fabric (~95%) and Ethereum (<75%).

Conclusion

Blockchain, specifically Hedera Hashgraph, offers significant cybersecurity enhancements for interstellar communication, evidenced by its high throughput, minimal latency, superior bandwidth efficiency, and robust fault tolerance. Its NASA-backed applications validate its practical suitability for space missions. Hyperledger Fabric presents viable solutions for controlled environments, whereas Ethereum requires significant scalability enhancements. Future integration strategies should consider Hedera as a primary backbone, complemented by Fabric's private channel capabilities and Ethereum's expansive smart contract ecosystem.

References

1. De La Beaujardière, J., & Mital, R. (2019). Blockchain application within a multi-sensor satellite architecture. IGARSS 2019 – IEEE Int. Geoscience and Remote Sensing Symposium, pp. 5293–5296.

2. Wang, Y., Su, Z., Ni, J., Zhang, N., & Shen, X. (2021). Blockchain-empowered space-air-ground integrated networks: Opportunities, challenges, and solutions. IEEE Comm. Surveys & Tutorials, 24(1), 160–209.

3. Li, C., Sun, X., & Zhang, Z. (2021). Effective methods and performance analysis of a satellite network security mechanism based on blockchain technology. IEEE Access, 9, 113558–113565.

4. Torky, M., et al. (2022). A Blockchain Protocol for Authenticating Space Communications between Satellite Constellations. Aerospace, 9(9), 495.

5. Hedera. (2023). How it Works – Hashgraph Consensus. Retrieved from https://hedera.com.

6. Cointelegraph. (2023). Hedera Hashgraph (HBAR) explained: A beginner's guide.

7. SpaceChain. (2021). SpaceX Launches Flight to ISS with Ethereum Node. CryptoBriefing.

8. Yesha, Y., et al. (2023). Revolutionizing Satellite Security: NASA's Groundbreaking Project to Integrate AI, Blockchain & Nanosatellites. Forbes/University of Miami.

9. Gorenflo, C., et al. (2019). FastFabric: Scaling Hyperledger Fabric to 20,000 Transactions per Second. IEEE Int. Conf. on Blockchain, pp. 1-9.

Quantifying Antioxidants in Non-Alcoholic Beers: Part 1, the Brewery, the Antioxidant, and the Analytical Method

Student Researcher: Jocelyn Mateo

Advisor: Dr. Regan Silvestri

Lorain County Community College
Department of Chemistry

Abstract

High-performance liquid chromatography (HP-LC) has been used to quantify the antioxidant xanthohumol in nonalcoholic beers provided by industry partner Surreal Brewing, San Francisco. Xanthohumol is a natural product originating from hops, an ingredient used to impart desired bitter flavors to beer. The flavonoid xanthohumol has recently attracted substantial attention regarding potential health benefits as an antioxidant. Under standard beer brewing techniques however, the concentration of xanthohumol unfortunately diminishes as xanthohumol is converted to byproducts during the brewing process. In an effort to increase the concentration of xanthohumol in beer, Surreal Brewing has produced several non-alcoholic beers via a modified brewing technique. An existing analytical method using HP-LC was applied to quantify the concentrations of xanthohumol in these various experimental beers produced by Surreal Brewing.

Project Objectives

In partnership with Surreal Brewing Company, the objective of this research project was to produce data concerning the concentration of xanthohumol that remained in their brews after applying their new brewing process.

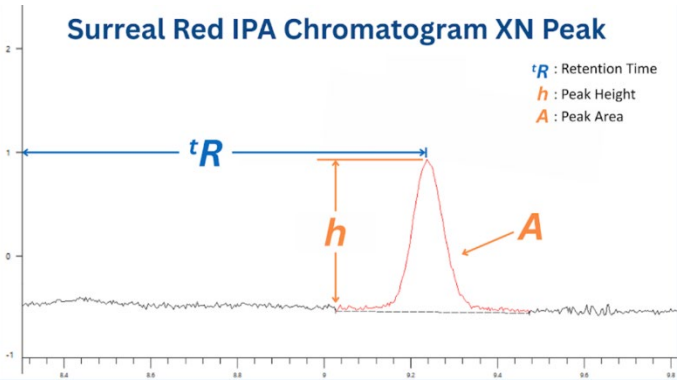
Methods

To achieve this project's objective, high-performance liquid chromatography (HP-LC) was employed to separate each beer sample's contents into chromatograms where quantity of xanthohumol was interpreted through peaks.

Results and Discussion

The resulting data showed that concentrations of xanthohumol did remain in provided beer samples from 20 µg/L to 504 µg/L where content varied in each sample. Some samples had equivalent or higher amounts of xanthohumol as commercial xanthohumol supplements.

Figures/Charts



Acknowledgments
I would like to acknowledge my advisor, Dr. Regan Silvestri, for all his support and the Ohio Space Grant Consortium for this opportunity.

References

1. Fegredo, J. A.; Meynell, R.; Lai, A. K. H.; Wong, M. C. Y.; Martin, C. R.; Wiseman, H.; Preedy, V. R. The antioxidant capacity of beer: relationships between assays of antioxidant capacity, color and other alcoholic and non-alcoholic beverages. In *Elsevier eBooks*; 2009; pp 475–481. https://doi.org/10.1016/B978-0-12-373891-2.00046-8.

2. Friedlander, B. *Nonalcoholic beer at higher risk for foodborne pathogens | Cornell Chronicle*. Cornell Chronicle. https://news.cornell.edu/stories/2023/12/nonalcoholic-beer-higher-risk-foodborne-pathogens.

3. Griffis, C. Non-Alcoholic Beer: Relapse or Rehab? thesis, University of Virginia, 2024.

4. Lobo, V.; Patil, A.; Phatak, A.; Chandra, N. Free radicals, antioxidants and functional foods: Impact on human health. *Pharmacognosy Reviews/Bioinformatics Trends/Pharmacognosy Review* **2010**, *4* (8), 118. https://doi.org/10.4103/0973-7847.70902.

5. Loureiro, P. V.; Jiménez, I. H.; Sendón, R.; De Quirós, A. R.-B.; Barbosa-Pereira, L. Determination of xanthohumol in hops, food supplements and beers by HPLC. *Foods* **2019**, *8* (10), 435. https://doi.org/10.3390/foods8100435.

6. Mellor, D. D.; Hanna-Khalil, B.; Carson, R. A review of the potential health benefits of Low Alcohol and Alcohol-Free Beer: Effects of ingredients and craft brewing processes on potentially bioactive metabolites. *Beverages* **2020**, *6* (2), 25. https://doi.org/10.3390/beverages6020025.

7. Pfizer. *Flower Power: How an ingredient in beer could fight an epidemic | Pfizer*. https://www.pfizer.com/news/articles/flower_power_how_an_ingredient_in_beer_could_fight_an_epidemic.

8. Proestos, C.; Komaitis, M. Antioxidant capacity of hops. In *Elsevier eBooks*; 2009; pp 467–474. https://doi.org/10.1016/B978-0-12-373891-2.00045-6 .

9. Shimadzu Corporation. *What is HPLC?* https://www.shimadzu.com/an/service-support/technical-support/analysis-basics/basic/what_is_hplc.html.

10. Willmoth, H. Beer might be healthier than you think. *Newsweek*. October 15, 2024. https://www.newsweek.com/beer-might-healthier-you-think-1969366.

Use of Cosmic Rays for Electric Power Generation

Student Researcher: Amari Q. Mathis

Advisor: Dr. Jeremy Huber

Cincinnati State Technical and Community College
Pre-Engineering

Abstract
This research strives to explore the potential of harvesting energy from cosmic rays, which are composed primarily of high-energy particles originating from outside the Earth's atmosphere. These rays consist of approximately 89% protons, ~10% alpha particles, and a small fraction (<1%) of heavier nuclei. Given the high amount of kinetic energy these particles carry, this project seeks to understand whether their energy can be practically captured and converted into usable electric power.

Project Objectives
The main objective of this research is to develop a conceptual and theoretical understanding of how feasible it is to generate electric power using high-energy particles, such as those found in cosmic radiation. This includes reviewing existing particle detection and energy conversion technologies, including betavoltaics and scintillator-photodiode systems used for radiation-to-energy conversion. A secondary objective is to propose a simplified and idealized schematic that demonstrates a potential method for capturing this energy in a practical system.

Methods
To support this investigation, I will examine data from a number of academic articles. These sources include both theoretical models and real-world experimental studies on devices.

Results and Discussion
This research draws from a selection of experimental studies that demonstrate how high-energy particles can be converted into electric power.

In a 2019 project at UC Berkeley's Undergraduate Lab (ULAB), a sodium iodide scintillator (NaI:Tl) was used to convert gamma radiation into visible light, which was then directed onto a photovoltaic cell. The resulting electric current was extremely small, with output power reported in the nanowatt to microwatt range—even under a controlled gamma-ray source. Voltage output varied depending on the source's distance and radiation intensity. While the concept proved functional, it was limited by the radiation flux and material sensitivity.

A more advanced system by Hirota et al. (2005) used an X-ray tube, a fluorescent screen, and an amorphous silicon solar cell. Under X-ray conditions of 40 kV and 10 mA, the system produced an open-circuit voltage of 4.7 V and a short-circuit current of 1.8 mA, yielding a maximum output of 2.7 mW. This marked an improvement over the UC Berkeley setup, likely due to stronger radiation and better conversion efficiency, though it still required a controlled lab environment and high-energy input.

Zhou et al. (2021) reviewed betavoltaic systems, which generate electricity from beta particles emitted by isotopes such as $^{90}Sr/^{90}Y$. While beta radiation is not a key component of cosmic rays, these systems demonstrate effective energy conversion principles. One example achieved 16% efficiency and 1 mW/cm² power density using a silicon junction optimized to match the beta particle penetration depth. Though

not directly applicable to cosmic radiation, this work illustrates how tuning material properties can significantly improve charge collection and output.

Interpretation and Discussion

The reviewed studies demonstrate that it is indeed possible to generate electric power from high-energy particles. While betavoltaic systems offer higher efficiencies, they require radioactive sources and radiation shielding. Scintillator-based systems are safer and more durable but typically produce power in the nanowatt to microwatt range—insufficient for most electronics, though still valuable for ultra-low-power applications. A major challenge lies in the efficiency of materials used to convert particle energy into light or electricity. Improvements in this area will likely depend on advances in materials science and semiconductor design. Until then, energy output will remain limited.

To address this, one proposed improvement is replacing standard photodiodes with avalanche photodiodes (APDs). APDs amplify weak signals through an internal avalanche effect, increasing the output current from low-intensity light. However, they require high reverse bias voltages (typically 60–100 V), adding complexity to the system. Despite these limitations, the fact that usable electric power can be harvested at all from cosmic radiation is promising. With further development, such systems could support low-power applications in remote or space environments.

Acknowledgments

I would like to thank Jeremy Huber for his support, also Cincinnati State and OSGC for the opportunity.

References

- **Mo, Sherry, et al.** "*Interplanetary Radiation Harnessing Voltaic System*." ULAB Research Poster, University of California, Berkeley, 2019. https://ulab.berkeley.edu/static/doc/posters/s195.pdf
- **Hirota, Y., et al.** "Proposal for Electric Power Generation by Using X-rays and Gamma Rays" *Japanese Journal of Applied Physics*, vol. 44, no. 7B, 2011, pp. 103-107.
- **Zhou, X., et al.** "Review—Betavoltaic Cells: The Past, Present, and Future." *ECS Journal of Solid State Science and Technology*, vol. 10, no. 2, 2021, 027005.

Galaxies: Their Formation, Evolution, and Demise

Student Researcher: Noah A. Roberts

Advisor(s): Dr. Jeremy Huber

Cincinnati State Technical and Community College
Department of Physics

Abstract
When people think of outer space, they conjure up images of strange planets, huge stars, and aliens. Many may also think of galaxies. These unfathomably large structures containing millions, even billions, of the aforementioned objects. Everyone is familiar with our own galaxy, the Milky Way, but many people do not think of how these massive collections of planets and stars came to form in the first place. What causes galaxies to form? How are they held together? What does the life cycle of a galaxy look like? The most common model for galactic formation is the Lambda-Cold Dark Matter (ΛCDM) model. This model describes how galaxies (or proto galaxies) cluster and merge in order to evolve into full-fledged galaxies. After becoming a full galaxy, there are several events that occur which eventually culminate in what could be considered the galactic equivalent of 'death.' In this project, these phenomena will be explored; through this exploration, we can gain a better understanding of our universe, its history, and its future.

Project Objective
The main goal of this research project is to construct a general understanding and timeline of events regarding galactic evolution. It will cover the birth of galaxies, their structure, phenomena and events that shape them, and how they come to an end.

Methodology Used
Using existing research gathered from various academic sources, I will construct an outline of the life of a typical galaxy.

Results Obtained
Using our current understanding of the formation of the universe itself, astronomers have devised a model of galactic formation based on Lambda-Cold Dark Matter (ΛCDM). Here, lambda (Λ) represents the cosmological constant, which is associated with dark energy, which is the main theorized form of energy driving cosmological expansion. Galaxies are vast in size with relatively low mass. As such, if we only account for visible matter, they should not be able to maintain their shapes. The CDM model solves this problem by hypothesizing that something unseen (in this case, dark matter) must be holding galaxies together by contributing to the gravitational force required to maintain their shape. In the CDM model, it is generally thought that the visible portion of galaxies is enveloped in a "halo" of dark matter. (Kauffmann & van den Bosch, 2002). In the time shortly following the Big Bang, the rate of cosmic expansion was too high to permit the formation of galaxies. This is due to the expansion pulling objects apart and gravity being unable to overcome it. This caused the density of the region of our future galaxy to decrease, although this decrease is slower than the decrease in the surrounding area. Because of this, the universe consisted of a simple cloud of light elements and fundamental particles (collectively, baryons) and dark matter. At a particular point, the region becomes overly dense compared to the surrounding area and gravity begins to overcome the cosmic expansion (Kauffmann & van den Bosch, 2002).
Our region of gas now becomes what can be considered a protogalaxy. This is a region of gas and dark matter that has become large enough to hold itself together against cosmic expansion, but star formation has yet to begin. According to our current understanding of galactic formation, protogalaxies in the early universe exerted tidal forces on one another, causing them to spin and gain angular momentum. This caused the gases that filled it to flatten and eventually begin to cool and contract. (Kauffmann & van den Bosch, 2002) This contraction allowed the gases to accumulate tightly together. From here, the galaxy begins to take shape and birth its first stars. Now the galaxy will take one of two main shapes: spiral or elliptical. Spiral galaxies are theorized to be the default form that a new galaxy takes. This is the shape of our very own Milky Way and one of our closest neighbors, Andromeda.

Spiral galaxies have a couple distinctive characteristics. These include the large spiral arms and the central bulge from which they extend. They can consist of young stars as well as old stars. Star formation itself is usually still quite active. While spiral galaxies make up a large portion of observable galaxies, the other shape, elliptical, is quite common as well. These galaxies tend to be much older than spirals and do not have as defined of a shape as spirals have. There is some debate about how elliptical galaxies are formed. One common theory is that all galaxies begin as spiral galaxies and through mergers of two or more galaxies, elliptical galaxies are born. (Kauffmann & van den Bosch, 2002) These galaxies are mostly round or oval-shaped and are comprised of almost exclusively old stars. In ellipticals, star formation is nearly halted due to the little amount of interstellar matter.



***Figure 2**: Spiral galaxy NGC 6956*



***Figure 1**: Elliptical galaxy NGC 4150*

Finally, we arrive at the end of the life cycle of the galaxy: galactic death. There are several ways in which this occurs. One such way is through a galactic merger. During this event, two or more galaxies are drawn together by their gravity; they then collide and combine to form a larger galaxy, this phenomenon puts an end to the two constituent galaxies but births a new larger one. Another notable side effect of mergers is that there is often a large burst of star formation due to the interaction of the gases and gravity of each galaxy. (Stuart, 2024)

Another possible cause of galactic death is galaxy quenching. A galaxy is considered to be "quenched" when there is little to no new star formation. These galaxies are commonly referred to as "red and dead" as they mostly consist of old, red stars. There are two theories for why quenching occurs. The first is called "halo quenching" which describes the fact that gases in the halo of a galaxy are shock-heated; thus, they are not able to fall deeper into the galaxy, preventing condensation of the gas into new stars. The second is active galactic nuclei (AGN) quenching. (Chen et al., 2020) This theory states that as the central blackhole of a galaxy grows, it either ejects gas from the galaxy or disturbs the halo gas in a way that stops it from falling into the galaxy. (Chen et al. 2020)

Significance of results

We have now examined the life cycle of a typical galaxy. From the Big Bang to the ultimate death of the galaxy, numerous events and phenomena shape and define these colossal structures. We saw how they form, what influences their shape, and two of the possible ways in which they die. There is much more to be learned of the subject, and, in doing such, we will learn more about our own place in the universe.

This literature review has only scratched the surface of galactic evolution. There is much more to learn and understand. Through further study, we can unlock the deepest secrets of the universe, such as how our universe came to be, what will happen to our own universe, and learn how to detect and quantify the mysterious dark matter and dark energy. Finding the answer to only one of these would be groundbreaking, but through extensive continued study, we can find the answers to all three and so many more.

Acknowledgements and references

Kauffmann, G., & van den Bosch, F. (2002). The life cycle of Galaxies. *Scientific American*, *286*(6), 46–58. https://doi.org/10.1038/scientificamerican0602-46

NASA, ESA, Crockett, R. M., Kaviraj, S., Silk, J., Mutchler, M., O'Connell, R., & WFC3 Scientific Oversight Committee. (2010). Hubble Captures New Life in an Ancient Galaxy. Retrieved March 25, 2025, from https://hubblesite.org/contents/news-releases/2010/news-2010-38.html.

NASA, ESA, Jones, D., & Kober, G. (2022). *NGC 6956*. Retrieved from https://esahubble.org/images/opo1038b/.

Chen, Z., Faber, S. M., Koo, D. C., Somerville, R. S., Primack, J. R., Dekel, A., Rodríguez-Puebla, A., Guo, Y., Barro, G., Kocevski, D. D., Wel, A. van, Woo, J., Bell, E. F., Fang, J. J., Ferguson, H. C., Giavalisco, M., Huertas-Company, M., Jiang, F., Kassin, S., … Yesuf, H. M. (2020). Quenching as a contest between galaxy halos and their Central Black holes. *The Astrophysical Journal*, *897*(1), 102. https://doi.org/10.3847/1538-4357/ab9633

Stuart, C. (2024, October 2). *Galaxy collisions are chaotic but crucial. without them, humanity might not exist*. BBC Sky at Night Magazine. https://www.skyatnightmagazine.com/space-science/galaxy-collisions

Cam Design for Safer and More Effective Exercise

Student Researcher: Stephen Zbornik

Advisor: Dr. Reagan Silvestri

Lorain County Community College
Physics

Abstract
This project focuses on the design and optimization of a bicep curl machine cam that provides consistent resistance throughout the range of motion. By analyzing the biomechanics of elbow flexion and applying physics principles, a non-circular cam profile was developed to ensure uniform muscle engagement. The goal was to create a cam that compensates for the changing moment arm of the biceps brachii during the curl motion, resulting in a more effective and safer resistance training experience.

Project Objectives

- To analyze the physics and biomechanics of the elbow during a bicep curl.
- To design a cam profile that provides a consistent torque throughout the movement.
- To improve muscle activation uniformity by compensating for variations in leverage.
- To evaluate the proposed cam design using physics-based modeling and calculations.

Methods

- Studied the elbow joint mechanics and torque generation during a bicep curl.
- Calculated torque requirements at different joint angles using moment arm analysis.
- Designed cam shapes in correlation with the torque-angle profile of the biceps.
- Used theoretical models and simulations to determine the required resistance at each point.
- Developed a force diagram to guide cam shape adjustment to achieve consistent torque.

Results and Discussion
The analysis revealed that torque production during a bicep curl varies significantly depending on the elbow angle due to changes in the moment arm. A circular cam fails to accommodate this change, leading to inconsistent resistance. The redesigned non-circular cam shape, based on biomechanical analysis, allows the machine to deliver near-uniform torque across the motion path. This design better matches human strength curves, potentially reducing injury risk and improving workout effectiveness. The project highlighted the importance of aligning resistance profiles with joint biomechanics in strength training equipment.

Acknowledgments
I would like to thank my advisors Dr. Monroe Kennedy and David Van Arsndale in the Physics Department for their support and feedback throughout the project.

Education Scholars

Energy of the Sun

Student Researcher: Morgan Briley

Advisor: Dr. Brandi Seither

Baldwin Wallace University
Early Childhood Education

Abstract:
This lesson introduces kindergarten students to the essential role of the sun in sustaining life on Earth. The teacher will begin by presenting an anchor chart and prompting students to share what they already know about the sun, facilitating a discussion to capture their prior knowledge. The teacher will then provide fundamental information, emphasizing that the sun is a star and the primary source of energy, heat, and light, which enables all living things to thrive. Using high-quality images from NASA, students will explore the sun's features, such as its color, texture, and sun flares, fostering curiosity and critical observation skills. Student contributions will be added to the anchor chart alongside simplified explanations of scientific concepts. Additionally, the teacher will incorporate a NASA video to further explain how the sun generates energy, reinforcing new learning through accessible and age-appropriate language.

Following the discussion and charting activity, students will engage in a hands-on art project to solidify their understanding. Using materials like paper plates, tissue paper, and markers, students will create their own representations of the sun. Each student will attach strings with stars to their sun, writing three key facts about the sun's energy on the stars with teacher guidance. This creative activity not only reinforces factual information but also encourages fine motor skills and self-expression. By the end of the lesson, students will have a foundational understanding of the sun's energy and its significance to life on Earth, bridging scientific concepts with visual and tactile learning.

Project Objectives:
In this lesson, students will learn that the sun is a star and the main source of energy, heat, and light that supports life on Earth. They will observe and describe basic features of the sun, such as its color, texture, and sun flares, using high-quality images. Through guided discussion and a shared anchor chart, students will build on their prior knowledge and begin to explain how the sun provides energy in simple terms. To reinforce their learning, students will create an artistic representation of the sun and identify three key facts about its energy. This hands-on activity will also support fine motor development and give students a chance to express scientific ideas creatively. Throughout the lesson, students will participate in collaborative conversation, develop critical observation skills, and build a foundational understanding of the sun's importance to life on Earth.

Methods:
The lesson uses a variety of methods to engage kindergarten students in learning about the sun. It begins with an anchor chart to activate and document students' prior knowledge, encouraging discussion and participation. The teacher then provides direct instruction, sharing age-appropriate facts about the sun as a star and the primary source of energy, heat, and light. Students explore high-quality NASA images to observe features like the sun's color, texture, and flares, fostering visual literacy and curiosity. A short NASA video further reinforces learning by explaining how the sun generates energy in an accessible way. Throughout the lesson, the teacher guides discussion and updates the anchor chart with new information

and simplified scientific explanations. To deepen understanding, students complete a hands-on art project where they create their own sun using craft materials and attach paper stars with three facts about the sun's energy. With teacher support, students practice writing these facts, connecting science content to literacy development and fine motor skills through creative

References:

The sun gallery: Agreicius. (2023, June 14). *The Sun - NASA Science*. NASA Science. https://science.nasa.gov/gallery/the-sun/

YouTube Video: NASA Space Place. (2017, April 13). *Where does the sun's energy come from?* [Video]. YouTube. https://www.youtube.com/watch?v=GAGFC8-wn1

Matter Properties Matter!

Student Researcher: Kiki Burkert

Advisor: Dr. Brandi Seither

Baldwin Wallace University
Dual Primary & Intervention Specialist, B.S.Ed.

Abstract
Via a slideshow, the teacher will show an image of a solid and ask the students to describe its properties. The teacher will write them on the board. This will happen again, but with a picture of a liquid then a picture of a gas. Examples given on the board are water, a moon rock, and smoke. Students provide the teacher with their observations of the objects' properties. The teacher will write them on the board to keep a running record of observations. Then the teacher will facilitate a group discussion/formative assessment. She will show multiple examples of the three states of matter, one at a time, on the board. Students will raise their hand in the shape of the ASL letter S, L, or G to tell if the object is a solid, liquid, or gas, respectively. Examples given include volcano smoke, lava lakes, glaciers, and more. This serves as the formative assessment for the lesson. Lastly, the teacher will pass three sticky notes to each student. On each note, students will write their name and either solid, liquid, or gas along with a property of each state (each state of matter gets its own sticky note). Students will stick their answers to the board in the corresponding column: gas answers under gas and so forth. This exit ticket serves as the summative assessment and allows the teacher to assess the knowledge of her students after the lesson.

Project Objectives
After the lesson, students will be able to: identify the three main states of matter, describe their properties, and give examples of each in everyday life as well as in space.

Methods
This lesson plan combines visual engagement, guided discussion, hands on exploration, and formative and summative assessments. The lesson begins with a teacher-led slideshow. For each state of matter, the teacher displays an image and students observe its properties. Each observed property is written on the board. This encourages student responses and activates prior knowledge. Following the slideshow, the teacher gives live demonstrations using real-world examples of rocks, water, and smoke. During the presentation students are shown examples from space, like lava lakes, glaciers, and volcano smoke. Students participate in an ASL answering discussion to identify the states of matter. To conclude with the summative assessment, students fill out a three-part sticky note summative assessment.

Results and Discussion
Although this lesson was unable to be taught in the field, there are still expected outcomes associated with the plan. The first outcome is that students apply their prior knowledge of the three main states of matter to the lesson and discussions. Students should interact with the slideshow and be able to identify visual and tangible properties of examples of matter. The second outcome is that students are able to demonstrate their understanding in a quick and inclusive way through the use of ASL. This visual and kinesthetic strategy would likely increase engagement and reinforce learning. The third and final outcome or expectation is that students engage in the exit ticket activity. This provides a hands-on component to their learning and gives a visual representation of their knowledge. Based on the lesson, it is expected that all or most students are able to correctly classify objects into the three states of matter and name at least one accurate physical property for each state. Students participating is the biggest expectation,

followed closely by correct answers on their assessments. If this lesson was taught, the results would include the percentage of correct answers across the class and examples of missed questions.

Acknowledgments

I applied for this scholarship with the utmost support from my Papa. He was always so proud of everything I did in school and life. This scholarship was for him as much as it was for me. Though he is no longer here to celebrate this moment with me, his unwavering belief in me continues to guide and inspire my journey. This achievement is dedicated to his memory, with love and gratitude.

References

NASA video. (2013, May 14). NASA Now: States of matter: Finding and using water on the Moon [Video]. YouTube. https://youtu.be/EkbUffRtjXk

NASA Glenn Research Center. (n.d.). States of matter. NASA. https://www.grc.nasa.gov/www/k-12/BGP/state.html

Preparation and Selection of Food for Travel in Space

Student Researcher: Elizabeth Denman

Advisor: Dr. Bridget Mulvey

Kent State University
Early Childhood Education Major

Abstract
Through this three-day lesson, students explore the importance of food preservation for space travel, focusing specifically on NASA's role and the science behind preparing food for astronauts. The lesson incorporates NASA's history and contributions through discussions, videos, and hands-on activities, while students investigate astronaut nutrition challenges and preservation techniques like dehydration and freeze-drying. They simulate space food preparation by weighing and dehydrating items, calculating moisture loss, and reflecting on the need for lightweight, long-lasting food in space. Using peer discussions, graphic organizers, and guided worksheets, students engage in inquiry-based learning, culminating in a taste-testing panel where they evaluate preserved foods and vote on which they'd take on a space mission. Through these activities, students make real-world connections and gain a deeper understanding of the science behind space food and how preservation methods contribute to astronauts' survival on long missions.

Project Objectives
By the end of this three-day lesson:

- ∉ Students will be able to generate a KWL chart displaying at least one thing they think they know, one thing they wonder, and one thing they learned about NASA, space food and/or its preparation process, and/or astronauts after participating in class discussion and watching space food video.
- ∉ After receiving a guided lab sheet with formulas for students to use, students will be able to calculate the percentage of moisture lost from three food items that have been weighed and then dehydrated.
- ∉ In 1-2 sentences, students will be able to describe why dehydrated and/or freeze dried food products are lighter in weight than their hydrated counterparts after participating in class discussions, watching educational video(s), and participating in a two day food dehydration experiment.

Methods
Several effective teaching strategies were utilized within this lesson to promote student engagement and understanding. The 5 E Instructional Model (Engage, Explore, Explain, Elaborate, Evaluate) was incorporated to guide students through the learning process, ensuring active participation and engagement over the multi-day lesson. The "I Do, We Do, You Do" gradual release strategy was also implemented to provide clear modeling, guided practice, and independent application of student knowledge. Additionally, differentiation of lesson materials and instruction methods was utilized to address the diverse needs of all learners, ensuring that each student could access the content at their own level of understanding.

Results and Discussion
After conducting this three-day lesson, I found that my students not only met the established learning objectives but they were also highly engaged and had lots of fun throughout the experience. They created thoughtful KWL charts, explored technology-based resources, and shared new understandings about space food and NASA. During the dehydration experiment, students accurately calculated moisture loss, demonstrating strong scientific reasoning, peer collaboration, and math skills. Their explanations of food weight differences showed a clear understanding of how water content affects mass, connecting their learning to real-world space challenges. Overall, the lesson was both educational and fun, sparking curiosity and collaboration through hands-on, meaningful activities with my students.

The following images were taken during the three-day lesson. These images display student engagement, exploration, and the hands-on learning that took place throughout the lesson.

Figures/Charts



Figure 1: Students calculating moisture lost from food items.



Figure 2: Student's food for space food taste testing experience.



Figure 3: Students observing their dehydrated foods.

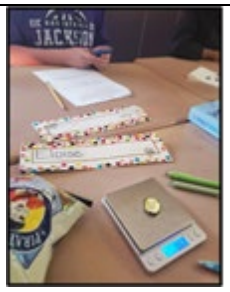


Figure 4: Students weighing food items during the experiment.

The following images were taken during the three-day lesson. These images display student engagement, exploration, and the hands-on learning that took place throughout the lesson.

Acknowledgments

I would like to thank Kent State University, NASA, the Ohio Space Grant Consortium (OSGC), my advisor Dr. Bridget Mulvey, Professor Jenny Lampe, cooperating teachers Emily Feielin and Lora Finn, and my supervisor Christina Schiltz for their continued support and guidance throughout this project.

References

Denman, E. (2024, November 1). *NASA OSGC Space Food Lesson Plan*. Google.com. https://docs.google.com/document/d/e/2PACX-1vTiDVp2w9gut-ieJCmaP3JhVDmzuZ34NnyXERF8DSyGKKoPkANCJdl92zY0iM-KAp1PjFw6Q_DMjee0/pub

This website features a lesson plan I created and implemented in a fifth-grade classroom.

NASA. (n.d.). *Educational product educators grades K-8 with activities in science and mathematics space food and nutrition*.

NASA. (2017). *The traditional NASA blue circular logo*.

NASA. (2017, October 11). *Living and Working in Space: Advanced Food Tech*. https://www.youtube.com/watch?v=zQEPKKmQGG0

Ohio Department of Education. (2020). Ohio's Learning Standards | Ohio Department of Education. Ohio.gov.

Reutov, R. (2025). *Space Lunch Game*. Nasa.gov.

Uri, J. (2020, August 14). *Space Station 20th: Food on ISS - NASA*. NASA. https://www.nasa.gov/history/space-station-20th-food-on-iss/

This article was used as a primary source of information during the development of the lesson. Additionally, images from the article were incorporated as instructional materials throughout the three-day lesson.

Weather and Our World

Student Researcher: Cora L. Gill

Advisor: Laura Dell

The University of Cincinnati
Secondary Education Integrated Sciences: Chemistry

Abstract
This lesson would be for a 7th-grade Earth Science course. It would highlight the importance of clouds for our Earth's environment. The lesson would take place over one whole week of school and begin with a few days of lectures where students will learn about the different types of clouds that exist and what they each contribute to our world. Students will also be taught the importance of clouds in global temperatures and maintaining the environment they enjoy every day. Concepts like the albedo effect, the water cycle, and global warming will all be touched on to give students a well-rounded look into the importance of clouds. After this, the students will begin the lab portion of the lesson. They will be introduced to the GLOBE program that NASA has, and will first get to explore the site and what information it offers regarding data and scientific discoveries. For the last two days of the week (weather dependent), students will be taken outside to observe and record the cloud cover for the day and the size and type of visible clouds. They will then compile all the class data and submit it to the NASA GLOBE program so that they can contribute the data that NASA uses to observe and study our world.

Project Objectives

- Students will use research to inform their learning about weather (clouds)
- Complete laboratory experiments to determine cloud cover data and submit that data to the NASA GLOBE program.

The Lesson Plan
This lesson would be during an environmental science unit and focus on weather and cloud formation. Students would be asked to draw on previous knowledge and things taught in lectures, as well as conduct their own research on clouds and cloud cover.

The Project
After this, the students will begin the lab portion of the lesson. They will be introduced to the GLOBE program that NASA has, and will first get to explore the site and what information it offers regarding data and scientific discoveries. For the last two days of the week(weather dependent), students will be taken outside to observe and record the cloud cover for the day and the size and type of visible clouds. They will then compile all the class data and submit it to the NASA GLOBE program so that they can contribute the data that NASA uses to observe and study our world.

Conclusion
The goal of this lesson is to help students participate in research opportunities in the science community. Using the NASA GLOBE program gives students the opportunity to use their research and data for real and practical purposes. This also helps students understand why their research is important to the world.

Gibbs Students' "Eyes On" Climate Change

Student Researcher: Taylor Grasse

Advisor: Bridget Mulvey
Kent State University
Early Childhood Education

Abstract
With this study, third grade students from Gibbs Elementary explored the impact of climate change by using multiple NASA climate resources to engage them in hands-on learning. The overall goal was to enhance students' understanding of climate science through interactive tools and data visualizations available on NASA's website. Students were introduced to key concepts such as the greenhouse effect, global temperature changes, and the role of human activities in climate change. Activities included exploring the satellite's NASA utilizes to study climate change and the images they produce, reviewing and breaking down real-time climate data, utilizing climate models to observe and analyze the effects of rising temperatures, melting ice caps, and shifting weather patterns, and engaging in group discussions to connect scientific information with their everyday lives. Through these guided activities and group discussions, students were able to connect the scientific data to tangible, real-world examples, gaining insight into how global warming is altering ecosystems and communities. Results indicated that students demonstrated a deeper understanding of climate change, with improved ability to identify its causes, effects, and potential solutions. For most of the students, this project marked their first exposure to the topic of climate change, by providing them with the access to interactive tools and data visualizations from NASA's website, they were able to construct foundational knowledge about environmental science and recognize the importance of taking action. The study highlights the effectiveness of using accessible, digital resources to teach complex scientific concepts to young learners, fostering environmental awareness and critical thinking skills.

Project Objectives
By the end of this lesson, students will be able to:

- Explore multiple NASA resources appropriately to enhance their understanding of climate sciences.
- Discuss in detail key concepts of what climate change is.
- Discuss in detail what changes we see happen to the Earth due to climate change.
- List two impacts they learned about during the lesson and one way they believe they can help fight climate change.

Methods
This lesson complied with third grade standards from the Ohio Department of Education State Learning Standards in Science (3.ESS.3, 3.ESS.2), English Language Arts(RI.3.4, RI.3.7), and Writing (W.3.2, W.3.7). It also utilized combining a gradual release model of instruction (i.e. "I-do, we-do, you-do") and the 5E Learning Cycle Unit (Bybee, 2018). The gradual release of instruction provided scaffolding for this group of students by allowing for the lesson to begin with an introduction to new content through explicit instruction from the teacher, then transition into guided practice where students were working alongside the teacher to build their understanding, and ended with letting the students showcase what they learned through both independent and collaborative summative assessments and discussion. The 5E Learning Cycle complimented this lesson plan because through NASA resources the students got to actively engage,

explore, explain, and extend their learning of climate science through hands-on work and research based discussions then show evidence of growth by completing a summative assessment project.

Key Questions to Guide Thinking:

- "What changes do you notice in the before and after images from NASA's Earth Observatory?"
- "How does NASA use satellites to study climate change, and why is this important?"
- "What are some simple actions we can take to reduce our impact on climate change?"

Results and Discussion

What Was Effective?

- The students having individual hands-on access to the NASA resources allowed them to discover and explore at their own pace in an effective and engaging way.
- Following a gradual release method of instruction allowed for significant comprehension of a science topic that was previously never explored.

How do I know?

- Thought-provoking and insightful questions were asked, recorded on a class collaborative *Notice & Wonder chart*
- Students were able to generate accurate and meaningful solutions during a student-led class discussion
- Proper use of NASA resources was observed during production of *Climate Change Brochure* summative assessment in which sufficient sentences were written by at least 89% of the class.

Acknowledgments

I would like to thank the Kent State University EHHS staff who nominated me for this opportunity, Dr. Bridget Mulvey for advising me on this work, and Ohio Space Grant Consortium for the opportunity and experience.

References

Bybee, R. (2018). The BSCS 5E Instructional Model: Personal Reflections and Contemporary Implications. BSCS Science Learning.
https://pimser.org/wp-content/uploads/2022/01/BSCS_5E_Instructional_Model_Bybee-article.pdf/

7-8th Grade Math Lesson on Planets and Ratios

Student Researcher: Alyssa Hart

Advisor: Professor Sarah Gilchrist

Cedarville University
Adolescent/Young Adult Mathematics Education

Abstract
The project will be centered around comparing the size of the different planets using ratios. Students will begin by doing some research using NASA's resources to learn more about the size of the planets compared to each other and their distances away from each other. During the students' Webquest, they will fill out a guided sheet and will record all of the diameters of the planets in the solar system. Then, the students will divide into groups and will be given a base model of planet earth that will be some type of sports ball. The students will measure the circumference of the model earth. Then, using the circumference of the model earth and the diameters of the actual size of earth and a planet of the students choice, the students will use ratios to calculate the circumference of the model size of the planet that they chose. The groups would then switch model earths and do more calculations. This lesson allows students to grow in their knowledge of the solar system and do a hands-on activity that involves math!

Project Objectives
This lesson is targeted for 7-8th grade math students learning ratios and proportions. The lesson will start with the students individually doing a 10 to 15 minute WebQuest exploration on the sizes of the planets and seeing how the planet sizes compare to each other. The students will be given the "WebQuest Handout" where they will write down the diameter of each planet, using the information from WebQuest. The students will be given links to articles and diagrams on the NASA website and can research planets using other NASA articles as well.

Students will be divided into groups, and each group will receive a different ball (e.g., tennis ball, soccer ball, baseball, ping pong ball) to represent Earth. Each group will measure the circumference of their ball. Each group will pick another planet in the solar system. Using the actual circumference of Earth, the circumference of their ball (model Earth), and the actual circumference of the chosen planet, students will calculate the circumference of a model planet that is proportional to their model Earth on the data sheet. Groups will then switch balls and repeat the process.

Lastly, each group will be assigned a planet, find an object that matches the size of their model planet, and bring that object to the next class. All groups will then put all the objects together to create a proportional model of the solar system.

The goal of this lesson is to deepen students' understanding of the vastness of our universe and the diverse sizes of the planets within it. The objectives are the following:

1. Students will gather and record data on the diameters of planets using reliable sources.
2. Students can use proportional reasoning and measurement conversions to find the circumference planets based on their model earth.
3. Students will use creative thinking to find everyday objects that accurately represent the proportional sizes of planets.

Methods

This lesson uses the constructivist learning theory. Students are actively engaged with hands-on activities and students work in groups, which promotes social interaction and collaboration. Additionally, the WebQuest encourages students to explore and discover information on their own, fostering curiosity and critical thinking.

Results and Discussion

Unfortunately, I have not had the opportunity to teach this lesson in a classroom setting yet. However, I would be excited to see how the students enjoy learning about the solar system and the size of the planets. I would also be interested to see how creative the students got finding an object to represent their model planet.

Figures/Charts



Name:_____

Instructions: Use the links below to learn more about the sizes and proportions of the planets in our solar system! Use the information in these NASA websites to fill in the information about each planet below. If you have time, explore other articles and resources on NASA's website as well!

Webquest Links:

Size and Distance of Planets

↳ https://science.nasa.gov/solar-system/planet-sizes-and-locations-in-our-solar-system/

Comparison of Planets Graphic

↳ https://science.nasa.gov/resource/comparison-of-planet-sizes-solar-systems/

JUPITER
Diameter:_____
___ times farther from the Sun than Earth

EARTH
Diameter:_____
_____ miles from the Sun

SATURN
Diameter:_____
___ times farther from the Sun than Earth

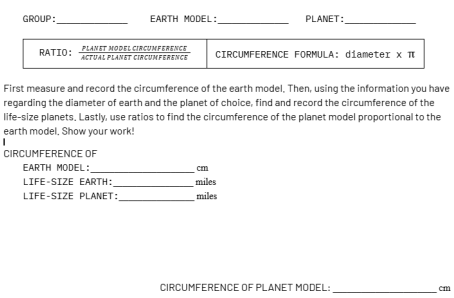
VENUS
Diameter:_____
_____ miles closer to the Sun than Earth.

URANUS
Diameter:_____
___ times farther from the Sun than Earth

MARS
Diameter:_____
_____ miles farther to the Sun than Earth

NEPTUNE
Diameter:_____
___ times farther from the Sun than Earth

MERCURY
Diameter:_____
_____ miles closer to the Sun than Earth



GROUP:_____ EARTH MODEL:_____ PLANET:_____

RATIO: $\frac{\text{PLANET MODEL CIRCUMFERENCE}}{\text{ACTUAL PLANET CIRCUMFERENCE}}$	CIRCUMFERENCE FORMULA: diameter x π

First measure and record the circumference of the earth model. Then, using the information you have regarding the diameter of earth and the planet of choice, find and record the circumference of the life-size planets. Lastly, use ratios to find the circumference of the planet model proportional to the earth model. Show your work!

CIRCUMFERENCE OF
EARTH MODEL:_____ cm
LIFE-SIZE EARTH:_____ miles
LIFE-SIZE PLANET:_____ miles

CIRCUMFERENCE OF PLANET MODEL: _____ cm

Acknowledgments

I would like to thank the Ohio Space Grant Consortium, NASA, my advisor Miss Gilchrist, and Dr. Chasnov for all their help and support.

References

NASA. (2024, November 8). *Comparison of planet sizes: Solar Systems - NASA science*. NASA. https://science.nasa.gov/resource/comparison-of-planet-sizes-solar-systems/

NASA. (2025a, March 12). *Planet sizes and locations in our Solar System - NASA Science*. https://science.nasa.gov/solar-system/planet-sizes-and-locations-in-our-solar-system/

Demolish Disasters with Knowledge

Student Researcher: Jenna Levans

Student Advisor: Dr. Nicole Whittaker

Marietta College
Early Childhood Education

Abstract

This project looks at how the results of a natural disaster can be lessened or eliminated by the work of people. The ideal that this project looks at is possibilism: the idea that we as humans can help to adapt to the Earth to better meet our needs. Through my lesson, the students go through the motions of critical thinking in order to solve a problem related to natural disasters, which in our area is mostly flooding.

Project Objectives

The objective of this project was to teach students how to be leaders in their community and how to think critically to solve a problem. Through this lesson, the students will also be working collaboratively to reach a common goal. The content that students will be interacting with and learning is related to precipitation, graphing, and scientific tools. This lesson is aimed at 3rd-grade students, so they will use a precipitation tower to graph the rainfall and look deeply at weather data from the internet to identify and track patterns in the weather.

Methods

The teaching method I used was constructivism. The students built the knowledge as they went throughout the lesson. The first step was understanding precipitation and graphing. So the students learned all about precipitation towers and how to use them. They set them outside of their classroom to measure the precipitation throughout the month. They will keep a daily log to see when throughout the month there was the most precipitation.

Then the students will track weather data for the last year. They will look at the amount of rainfall each month and week and see where the highest amounts of rain are. They will find this data through online resources and will make a graphic of some kind to show their data. They will also look at the amount of flooding that has occurred in each month, if any. The students will also briefly learn about the flooding that occurs in their local area to build background knowledge.

Then, while in groups, the students will come up with a creative idea to try to combat the damage done by a flood. They will work together and present to the class in any way they would like. Using their data, they will decide when these solutions would be most useful and look at efforts to lower the impact of natural disasters.

Results & Discussions

The result was some very creative solutions from some very deep thinkers. The students got in-depth and came up with phenomenal ideas that experts in their field would pitch to their supervisors. Many students came up with the idea of a flood wall or ways to keep the water out, like higher foundations or boarding up doors. The most creative solution was to put a large sponge in front of the river to “catch”

the water. While not all of these ideas are reasonable, the students were able to get creative and showcase their critical thinking skills and teamwork. They will be able to use these skills in their future careers and their future schoolwork for years to come.

The students did a great job presenting their information. They were very creative; one group even created a rap about a flood wall. The students were given a rubric on what they needed to include in their presentation, but their method of presenting the information was completely up to them. Some did a simple presentation, and some went far out of the box. They had to outline and explain their thinking and their process to the class, which is an effective practice, so students can understand the thinking process of others.

Acknowledgements

I would like to thank my advisor, Dr. Nicole Whitaker, for all the support and assistance in curating this idea. I would also like to thank her for introducing me to this program! I would also like to thank the OSGC for this amazing opportunity to research and come up with such an inspiring lesson for my students. Lastly, I would like to thank my students for all of their hard work and for helping me bring this idea to life.

Solving Environmental Issues in Second Grade

Student Researcher: Rachel Penno

Advisor: Dr. Todd France

Ohio Northern University
Early Childhood Education

Abstract
For this project I worked to design a mini unit plan that focused on teaching second grade students about environmental issues. I made sure to find a second grade standard that fit that topic and went to design the unit from there. I started with a backwards design template outlining what goals I wanted my students to accomplish and learn from completing this unit. I also made sure to outline different types of assessments both formative and summative that showed students growth and learning throughout the lessons. From here I was able to design my unit by separating it into three different days of learning, which I created lesson plans for. I broke the days down into the first being an introduction to living things and environmental changes, followed by a lesson that focused on recycling, finally a lesson which allows students to use what they have learned from the following lessons to design a project that focuses on recycling and solving environmental issues. For the project in the final lesson I came up with the prompt that students are to design an object, or model of an object, that is built using recycled materials that focuses on solving an environmental issue.

Project Objectives
Ohio Second Grade Standard- 2.LS.1 Living things cause changes on Earth

Methods
Within my lessons I used various teaching methods and strategies for lesson 1- Observations- the students will observe environmental changes they see outside during a nature walk. Read aloud- the teacher will read the story One Plastic Bag aloud to the class so they are able to understand the story and pick up on any new words they do not yet know. Inquiry- the teacher will ask the students what are some of the environmental changes they see and what are some living things. Group discussion- after reading the story and watching the video there will be a class discussion where students will talk about environmental changes they see and their impact on living things. For lesson 2- Play pedagogy- this can be demonstrated through the Trash or Not Trash game the students will play, along with the recycle sorting activity the students will do on their own. Student directed exploration- students will work in groups to start brainstorming ideas for their recycling project. For lesson 3- Problem Based Learning- used to describe what the students are doing during the building process. Presentation- type of verbal communication strategy that students will engage in after the completion of their project.

Results and Discussion
Currently I am placed with a second grade Intervention Specialist due to this placement I have been working with small groups of students who need interventions and was not able to directly teach these lessons to them. However because of this placement I am familiar with the tendencies and the interest of second graders. The students that I work with love any experience with hands-on activity. These vary from sensory learning, by writing in sand, to discussing the leprechaun traps they built with their general education teacher. From this knowledge I was able to take some of the interest of second graders and place aspects they like into my lesson. An example of this is listening to the teacher read,

which is done through the story in the first part of this unit. Another aspect Incorporated was student directed exploration. Students this age are starting to question more and more what they are learning and why they are learning it. They also love to explore more on their own. Students this age love using technology which is why in the second lesson they are able to use their chromebooks to help them come up with ideas for their recycling project. I have also learned from the students that they love building things as they demonstrated by talking about an activity they did with their general education teacher.

From this I took into mind that second grade students like hands-on activities which include building which lead me to add the aspect where students were able to design and build their own project in groups. Even though I was not able to directly teach this lesson to the second graders I have been working with, I was able to take what I have learned from working with them to guide my designing process for these lessons. This also helped me take into account what their ability and skill levels are for students of this age, and I was able to keep that in mind when planning activities in these lessons.

Acknowledgments

I would like to thank my advisor Dr. Todd France for helping me with this project as well as a professor from the education department Dr. Paulina Roders. I would also like to thank my cooperating teacher and the second grade students I have worked with this semester who have helped inspire my unit plan.

References

A guide for using discussion- based pedagogy. (n.d.). https://taylorinstitute.ucalgary.ca/sites/default/files/discussion based learning TI guide_final.pdf

Lev Vygotsky and Social Learning Theories. (n.d.). https://jan.ucc.nau.edu/lsn/educator/edtech/learningtheorieswebsite/vygotsky.htm

Paul, M. (2021). One plastic bag: Isatou Ceesay and the recycling women of the Gambia. CELA.

How self-directed inquiry benefits the whole child. (n.d.-b). https://files.eric.ed.gov/fulltext/EJ1213379.pdf

Lara, Gabriela. (2018, November 19). *Theory 4: Kohn's student directed learning theory*. Ms. Gabriela Lara's Classroom Management Blog. https://mslaraclassroommanagement.wordpress.com/2018/11/19/theory-4-kohns-student-directed- learning-theory/

John Dewey's theory. Structural Learning. (n.d.). https://www.structural-learning.com/post/john-deweys-theory

Uluçınar, U. (n.d.). The effect of problem-based learning in science education on academic achievement: A Meta-analytical study. Science Education

The Water Cycle

Student Researcher: Alice Somers

Advisor: Laura Dell

University of Cincinnati
Elementary Education

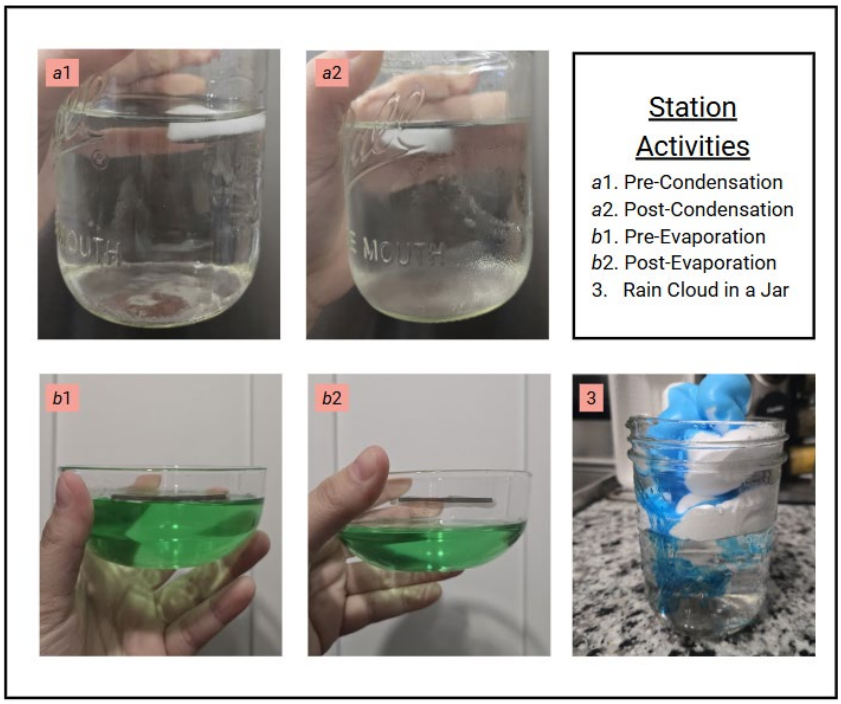
Abstract
Using NASA' Space Place. A student friendly educational website, this lesson follows Ohio's Earth Science standard 2.ESS.2. This standard focuses on students understanding that "water is present in the atmosphere". The activity created focuses particularly on the troposphere and how there is water in the atmosphere. Students will work in groups up to three to complete an exploratory worksheet while watching *How Much Water Is On Earth?,* one of the videos from Space Place. Together as a class, we will discuss previous knowledge about the water cycle and read Gail Gibbon's book *It's Raining!*. Once they have been properly introduced, students will go through a rotation of stations that will focus on various aspects of the water cycle to better understand the Earth Science standard. The different stations would include hands-on and student led opportunities including the following: A Rain Cloud in a Jar; Condensation and Evaporation observations; and a choice learning opportunity consisting of books, videos, and demonstrations. Upon completing the different activity stations, we will come back together as a group to allow students to discuss with one another the ideas and concepts they synthesized from the activity.

Project Objectives
This activity emphasizes the presence of water in the atmosphere, and the different ways it can present depending on temperature and density of the collection of water. Upon completing this activity, students will understand:

1. Water is present in the atmosphere;
2. When given time and heat, water will change from a liquid to a vapor;
3. When introduced to a cold environment, water will change from a vapor to a liquid;
4. When water evaporates and rises in the atmosphere to clouds, it is introduced to colder temperatures and changes from vapor into liquid. As more water collects in the cloud, the heavier it becomes, eventually resulting in precipitation.

Results and Discussion
Due to my current field placement in a different grade level, I was unable to implement this activity to a class. However, I believe that the implementation of the Universal Design of Learning (UDL) as a part of the activity will promote deeper understanding based on the scaffolding. I recognize that the introduction of this activity requires access to technology, so if I were to implement this activity, I would like to consider alternate ways of sharing the Space Place video. I also believe that some activities, depending on the classroom, might require additional guidance to ensure students are

Figures/Charts



Acknowledgments

I would like to extend my gratitude to the University of Cincinnati; NASA; the Ohio Space Grant Consortium; the Ohio Aerospace Institute; and my advisor Dr. Laura Dell, Associate Dean for Academic Affairs, College of Education, Criminal Justice, and Human Services, for all their continued support and encouragement.

References

Gibbons, G. (2014). *It's Raining!*. Holiday House.

NASA. (2022, August 29). *How much water is on Earth?*. NASA. https://spaceplace.nasa.gov/water/en/

Ohio's learning standards and model curriculum for Science. Ohio Department of Education. (n.d.). https://education.ohio.gov/Topics/Learning-in-Ohio/Science/Ohios-Learning-Standards-and-MC

Create Your Own Solar System

Student Researcher: Joslyn Taylor

Advisor: Dr. Todd France

Ohio Northern University
Early Childhood Education

Abstract
For my project, I decided to do a lesson plan over students creating their own solar systems. I focused on 5th grade science for this project. Although I was not able to actually teach this lesson, it was a great lesson to plan and I hope I am able to teach this sometime in my career. Through this lesson, students would have an understanding of the solar system by applying knowledge of plants, celestial bodies, and their characteristics to create an original solar system. This encourages critical thinking, creativity, and scientific reasoning for future space-related studies.

Project Objectives
The objectives of this project would be that students will be able to identify parts of the solar system with 90% accuracy and students will be able to create their own solar system using previous knowledge with 90% accuracy. The standards I used for the creation of this lesson were: 5.ESS.1 The solar system includes the sun and all celestial bodies that orbit the sun. Each planet in the solar system has unique characteristics and W.5.7 Conduct short research projects that use several sources to build knowledge through investigation of different aspects of a topic.

Methods
For the methods, I focused on think-pair-share, guided research, hands-on exploration, and student-directed projects. Think-pair-share would be used as a formative assessment. I would go around and listen to students' responses to one another's questions and listen to what they would have to say about their projects. Based on how they would answer each other, I could adjust what expectations I would need to share with the class. For my second formative assessment, I would have looked at research notes. I would look at their completeness and accuracy of their research findings. Based on that, I would determine if additional resources would be needed for them to continue their research. For my summative assessment, it would be the final solar system project. Evidence I would look for to see if learning has occurred would be creativity, accuracy, and application of knowledge. If I was not seeing those things, I would reteach the concepts and/or give my students extra time if they were to need more time on finishing the project.

Results and Discussion
Since I was not able to teach this lesson, I do not have any results. Ideally, students would have created their own solar systems based on the knowledge they have with the actual one. They would have their own planets, celestial bodies, and other characteristics that were not all in the actual solar system. The goal would be for students to bring out their creative side and show what they would want their solar system to look like.

Acknowledgments
I would like to thank Dr. Todd France for sharing this scholarship with me and being my advisor for the project. I would also like to thank my professors at Ohio Northern University for providing me with the knowledge to create potential lessons for future students!